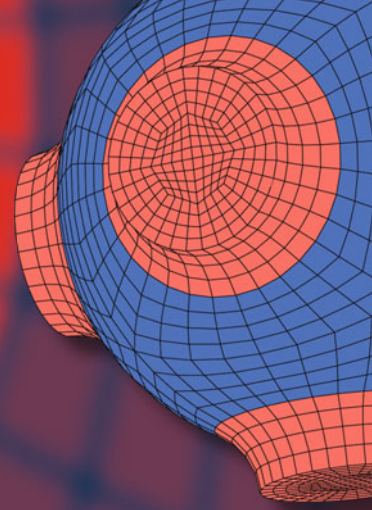Holm Altenbach
Jörg Hohe
Christian Mittelstedt *Editors*

Progress in Structural Mechanics

Springer

Advanced Structured Materials

Volume 199

Series Editors

Andreas Öchsner, Faculty of Mechanical Engineering, Esslingen University of Applied Sciences, Esslingen, Germany

Lucas F. M. da Silva, Department of Mechanical Engineering, Faculty of Engineering, University of Porto, Porto, Portugal

Holm Altenbach , Faculty of Mechanical Engineering, Otto von Guericke University Magdeburg, Magdeburg, Sachsen-Anhalt, Germany

Common engineering materials are reaching their limits in many applications, and new developments are required to meet the increasing demands on engineering materials. The performance of materials can be improved by combining different materials to achieve better properties than with a single constituent, or by shaping the material or constituents into a specific structure. The interaction between material and structure can occur at different length scales, such as the micro, meso, or macro scale, and offers potential applications in very different fields.

This book series addresses the fundamental relationships between materials and their structure on overall properties (e.g., mechanical, thermal, chemical, electrical, or magnetic properties, etc.). Experimental data and procedures are presented, as well as methods for modeling structures and materials using numerical and analytical approaches. In addition, the series shows how these materials engineering and design processes are implemented and how new technologies can be used to optimize materials and processes.

Advanced Structured Materials is indexed in Google Scholar and Scopus.

Holm Altenbach · Jörg Hohe · Christian Mittelstedt
Editors

Progress in Structural Mechanics

Springer

Editors
Holm Altenbach 🆔
Institute of Mechanics
Otto-von-Guericke University Magdeburg
Magdeburg, Sachsen-Anhalt, Germany

Jörg Hohe 🆔
Composite Materials
Fraunhofer Institute for Mechanics
of Materials
Freiburg im Breisgau, Baden-Württemberg,
Germany

Christian Mittelstedt
Fachbereich Maschinenbau
Technical University of Darmstadt
Darmstadt, Hessen, Germany

This book is dedicated to our friend and colleague Wilfried Becker on the occasion of his retirement.

Preface

At the end of September 2022 our colleague and friend Prof. Dr.-Ing.habil. Wilfried Becker, who significantly influenced the field of research with his work on the structural mechanics of composite structures, retired. Up to his retirement, he was a full professor for Mechanics and the head of the Institute of Structural Mechanics at the University of Technology Darmstadt (Germany). As a professor, he has trained several generations of undergraduate and graduate students. At the same time, as author or co-author of numerous scientific articles and books, he has significantly shaped the field and also gained international recognition.

Wilfried Becker was born on March 27, 1957. His professional and scientific career started in 1976 with entering the TH Darmstadt as a student in Mathematics and Physics. In 1982 he graduated with 1st state exam. In 1984, he continued his studies (now in Mechanics) at TH Darmstadt and obtained in 1986

Wilfried Becker

the diploma degree. From 1986 until 1989, he was a research assistant at the Institute of Mechanics at TH Darmstadt. Under supervision of Prof. Dietmar Gross he prepared his PhD thesis in the field of fracture mechanics "Dugdale-Riss-Lösungen und deren Verwendung zur mikromechanischen Modellierung von anisotropem Damage" (Dugdale crack solutions and their use for micromechanical modeling of anisotropic damage) [1].

From 1990 until 1996 he was a systems engineer at Daimler-Benz Aerospace. His research focus was on development, design and optimization of lightweight structures. In 1993, he defended his habilitation at TH Darmstadt. The title of his thesis was "Beiträge zur analytischen Behandlung ebener Laminate" (Contributions to the analytical treatment of plane laminates) [2].

In 1996, Wilfried Becker was appointed as full professor for Mechanics at University of Siegen as the successor of Prof. Hans Eschenauer. In 2003, he became a

full professor for Mechanics and head of the Institute of Structural Mechanics at TU Darmstadt. His scientific areas of work are

- Solid and Structural Mechanics
- Composite Mechanics
- Fracture Mechanics
- Structural Optimization

He has prepared (partly together with several co-authors) more than 300 publications for international peer-reviewed journals and conferences and he published three books [3–5]. In addition, he served as an editorial board member of:

- Archive of Applied Mechanics
- Composite Structures
- Composites Science and Technology
- International Journal of Advances in Mechanics and Applications of Industrial Materials
- Luftfahrttechnisches Handbuch – Faserverbund-Leichtbau

We wish Wilfried Becker many more years in good health and hope that his scientific contributions will continue to be recognized by other scientists in the future.

Magdeburg, *Holm Altenbach*
Freiburg im Breisgau, *Jörg Hohe*
Darmstadt *Christian Mittelstedt*

July 2023

References

[1] Becker, W.: Dugdale-Riss-Lösungen und deren Verwendung zur mikromechanischen Modellierung von anisotropem Damage. Düsseldorf: VDI Verlag, 1989 (Fortschritt-Berichte VDI. Reihe 18, Nr. 54)

[2] Becker, W.: Beiträge zur analytischen Behandlung ebener Laminate. Düsseldorf: VDI Verlag, 1993 (Fortschritt-Berichte VDI. Reihe 18, Nr. 121)

[3] Becker, W.; Gross, D.: Mechanik elastischer Körper und Strukturen. Berlin, Heidelberg: Springer, 2002

[4] Altenbach, H.; Becker, W.: Modern Trends in Composite Laminates Mechanics. Vienna: Springer, 2003 (International Centre for Mechanical Sciences, Courses and Lectures, Nr. 448)

[5] Mittelstedt, C.; Becker, W.: Strukturmechanik ebener Laminate. Darmstadt: Studienbereich Mechanik, Technische Universität Darmstadt, 2016

Contents

List of Contributors

Holm Altenbach
Lehrstuhl für Technische Mechanik, Institut für Mechanik (IFME), Fakultät für Maschinenbau, Otto-von-Guericke-Universität Magdeburg, Universitätsplatz 2, D-39106 Magdeburg, Germany,
e-mail: holm.altenbach@ovgu.de

Michał Basista
Institute of Fundamental Technological Research, Polish Academy of Sciences, Pawińskiego 5B, 02-106 Warsaw, Poland,
e-mail: mbasista@ippt.pan.pl

Carla Beckmann
Fraunhofer-Institut für Werkstoffmechanik IWM, Wöhlerstr. 11, 79108 Freiburg, Germany,
e-mail: carla.beckmann@iwm.fraunhofer.de

Kamil Bochenek
Institute of Fundamental Technological Research, Polish Academy of Sciences, Pawińskiego 5B, 02-106 Warsaw, Poland,
e-mail: kboch@ippt.pan.pl

Dmytro Breslavsky
Department of Computer Modelling of Processes and Systems, National Technical University "Kharkiv Polytechnic Institute", 2, Kyrpychova str., UKR-61002, Kharkiv, Ukraine,
e-mail: dmytro.breslavsky@khpi.edu.ua

Ralf Cuntze
MAN-Technologie, Augsburg, Germany,
e-mail: ralf_cuntze@t-online.de

Hossein Darban
Institute of Fundamental Technological Research, Polish Academy of Sciences,
Pawińskiego 5B, 02-106 Warsaw, Poland,
e-mail: hdarban@ippt.pan.pl

Jan Fränkle
ITM-predictive GmbH, Roonstr. 23a, 76137 Karlsruhe, Germany,
e-mail: jan.fraenkle@itm-p.ch

Dietmar Gross
Institute for Mechanics, Technical University of Darmstadt, Darmstadt, Germany,
e-mail: gross@mechanik.tu-darmstadt.de

Johannes Grygier
ITM-predictive GmbH, Roonstr. 23a, 76137 Karlsruhe, Germany,
e-mail: johannes.grygier@itm-p.com

Jörg Hohe
Fraunhofer-Institut für Werkstoffmechanik IWM, Wöhlerstr. 11, 79108 Freiburg,
Germany,
e-mail: joerg.hohe@iwm.fraunhofer.de

Angelika Humbert
Alfred-Wegener-Institut Helmholtz Zentrum für Polar- und Meeresforschung,
Bremerhaven, Germany & Department of Geoscience, University of Bremen,
Bremen, Germany,
e-mail: angelika.humbert@awi.de

Philipp Jatzlau
RayScan Technologies GmbH, Klingleweg 8, 88709 Meersburg, Germany,
e-mail: p.jatzlau@rayscan.eu

Andreas Kappel
Darmstadt University of Technology, Department of Mechanical Engineering,
Institute for Lightweight Engineering and Structural Mechanics, Germany,
e-mail: andreas.kappel@klub.tu-darmstadt.de

Vladimir A. Kolupaev
Fraunhofer Institute for Structural Durability and System Reliability (LBF),
Schloßgartenstr. 6, D-64289 Darmstadt, Germany,
e-mail: Vladimir.Kolupaev@lbf.fraunhofer.de

Stanislav Konkin
Department of Computer Modelling of Processes and Systems, National Technical
University "Kharkiv Polytechnic Institute", 2, Kyrpychova str., UKR-61002, Kharkiv,
Ukraine,
e-mail: stanislav.konkin@infiz.khpi.edu.ua

Kevin Koschalla
University of Applied Sciences Osnabrück, Institute of Materials Design and
Structural Integrity, Albrechtstraße 30, 49076 Osnabrück, Germany,
e-mail: k.koschella@hs-osnabrueck.de

Ulrich Krupp
RWTH Aachen University, IEHK Steel Institute, Intzestraße 1, 52072 Aachen,
Germany,
e-mail: krupp@iehk.rwth-aachen.de

Dominique Leguillon
Institut Jean Le Rond d'Alembert, Sorbonne Université and CNRS UMR 7190, 4
place Jussieu, 75005 Paris, France,
e-mail: dominique.leguillon@upmc.fr

Volodymyr Lysenko
Department of Data Measuring Technologies and Systems, National Technical
University "Kharkiv Polytechnic Institute", 2, Kyrpychova str., UKR-61002, Kharkiv,
Ukraine,
e-mail: volodymyr.lysenko@khpi.edu.ua

Christian Mittelstedt
Darmstadt University of Technology, Department of Mechanical Engineering,
Institute for Lightweight Engineering and Structural Mechanics, Germany,
e-mail: christian.mittelstedt@klub.tu-darmstadt.de

Ralf Müller
Institute for Mechanics, Technical University of Darmstadt, Darmstadt, Germany,
e-mail: ralf.mueller@mechanik.tu-darmstadt.de

Konstantin Naumenko
Lehrstuhl für Technische Mechanik, Institut für Mechanik (IFME), Fakultät für
Maschinenbau, Otto-von-Guericke-Universität Magdeburg, Universitätsplatz 2,
D-39106 Magdeburg, Germany,
e-mail: konstantin.naumenko@ovgu.de

Philipp L. Rosendahl
Institute of Structural Mechanics and Design, Technical University of Darmstadt,
Franziska-Braun-Str. 3, 64287 Darmstadt, Germany,
e-mail: rosendahl@ismd.tu-darmstadt.de

Christoph Sauerwein
RayScan Technologies GmbH, Klingleweg 8, 88709 Meersburg, Germany,
e-mail: c.sauerwein@rayscan.eu

Jakob C. Schilling
Technical University Darmstadt, Institute for Lightweight Engineering and Structural
Mechanics, Otto-Berndt-Straße 2, 64287 Darmstadt, Germany,
e-mail: jakob.schilling@klub.tu-darmstadt.de

Michael Schober
Fraunhofer-Institut für Werkstoffmechanik IWM, Wöhlerstr. 11, 79108 Freiburg,
Germany,
e-mail: michael.schober@gmx.net

Philip Schreiber
Technical University Darmstadt, Institute for Lightweight Engineering and Structural
Mechanics, Otto-Berndt-Straße 2, 64287 Darmstadt, Germany,
e-mail: philip.schreiber@klub.tu-darmstadt.de

Isabell Schulz
Institute of Structural Mechanics and Design, Technical University of Darmstadt,
Franziska-Braun-Str. 3, 64287 Darmstadt, Germany,
e-mail: schulz@ismd.tu-darmstadt.de

Axel Schumacher
University of Wuppertal, Germany,
e-mail: schumacher@uni-wuppertal.de

Rabea Sondershaus
Institute for Mechanics, Technical University of Darmstadt, Darmstadt, Germany,
e-mail: rabea.sondershaus@tu-darmstadt.de

Clarissa Vogelbacher
ITM-predictive GmbH, Roonstr. 23a, 76137 Karlsruhe, Germany,
e-mail: clarissa.vogelbacher@itm-p.com

Witold Węglewski
Institute of Fundamental Technological Research, Polish Academy of Sciences,
Pawińskiego 5B, 02-106 Warsaw, Poland,
e-mail: wweglew@ippt.pan.pl

Chapter 1
Numerical and Experimental Analysis of Elastic Three-layer Plate Under Static and Low Velocity Impact Loading

Holm Altenbach, Dmytro Breslavsky, Stanislav Konkin, Volodymyr Lysenko, and Konstantin Naumenko

Abstract Computational and experimental approaches to determine the values of physical and mechanical properties of three-layer sandwich plates, consisting of two outer layers of fiberglass and a core of expanded polystyrene, bonded with epoxy glue, is proposed. To measure displacements and strains, an experimental stand which uses mechanical dial gauges and strain gauges, was developed. Experimental data are presented for static and low-velocity impact loading on the plate when a spherical impactor falls on it. The finite element analysis of the plate is carried out and the results are compared with experimental data.

1.1 Introduction

Multilayer composite panels are widely used in various industrial applications, including aerospace industry. One of the fairly common types of such structural elements are three-layer plates and shells. Due to their low weight as well as increased stiffness and strength compared to the material of the core part, which occupies the main volume of the plate, they are widely used in practice [1].

Holm Altenbach · Konstantin Naumenko
Lehrstuhl für Technische Mechanik, Institut für Mechanik (IFME), Fakultät für Maschinenbau, Otto-von-Guericke-Universität Magdeburg, Universitätsplatz 2, D-39106 Magdeburg, Germany, e-mail: holm.altenbach@ovgu.de, konstantin.naumenko@ovgu.de

Dmytro Breslavsky · Stanislav Konkin
Department of Computer Modelling of Processes and Systems, National Technical University "Kharkiv Polytechnic Institute", UKR-61002, Kharkiv, Ukraine, e-mail: dmytro.breslavsky@khpi.edu.ua, stanislav.konkin@infiz.khpi.edu.ua

Volodymyr Lysenko
Department of Data Measuring Technologies and Systems, National Technical University "Kharkiv Polytechnic Institute", UKR-61002, Kharkiv, Ukraine, e-mail: volodymyr.lysenko@khpi.edu.ua

Currently, the design of structures in various fields of technology is carried out automatically, using specialized software, CAD/CAE systems. CAE modules, in most cases based on the Finite Element Method (FEM), are used for computational analysis at the design stage in order to select the best parameters in terms of ensuring the required stiffness and strength. One of the most important issues that are solved in this case is the determination of the physical and mechanical properties of composite elements for their further use in calculations.

This task is often associated with a large number of difficulties. They appeared with the complexity of the experimental determination of the properties of composite elements as a whole. Already at the manufacturing stage, from the point of view of Solid Mechanics, a multilayer panel is a composite structure, the properties of which differ significantly from the properties of the constituent materials. The methods of experimental determination of physical and mechanical properties known for homogeneous materials often do not work [1, 2].

Let us consider the main results obtained recently in the study of the stress-strain state of multilayer plates under static and dynamic loading, including impact. The main theoretical approaches and justification the methods of computational analysis are described in [3]–[4]. However, the practical implementation of the developed methods often contains a large number of special techniques and algorithms, which often combine real experimental studies. Their description in relation to multilayer panels with low velocity impacts is presented in [5]–[6].

A review of classical methods and equipment for the experimental investigations of impact deformation processes at low velocity testing, created before 2000, is presented in [5], and recently developed, in [7]. The authors of reviews note that robust and reliable non-destructive testing of composites is essential to ensure the safety concerns and maintenance costs. The most well-known non-destructive testing methods for detecting and evaluating the development of defects/damages in composites are considered, for each of which the principles, standard methods, equipment and tools used to study composites, are discussed.

A review of already created computational methods for predicting deformation under low-velocity impact contain in [8]. Next, we consider new developments in this area. The low-speed impact of a rigid impactor on three-layer sandwich panels, which causes local deflection of the front sheet and irreversible deformation of the core, was studied in [9]. The protective effect of thin plastic layers inserted between the front sheet and the core in order to compensate the deflections is considered. The problem for different core materials - foam plastic, polyurethane foam and others was solved by the FEM. It is noted that the intermediate layer of polyurethane provides better impact resistance.

The impact behavior of a deformable thin sandwich plate under low-velocity impact was studied in [10]. The fabrication method and two types of experimental setups using drop impacts with a micro-processor based data acquisition system are described. The dominant type of failure is experimentally determined, which is local sheet crushing. The experimental and FEM simulation results of the critical impact energy, the deformed shape as well as of the maximum values of deflection, contact force, intrusion and the specific absorbed energy were compared.

Dynamic responses of sandwich panels with aluminum foam cores under impact loading were studied in [11] using experiments and FE modeling. Impact tests were done using a drop weight impactor at various low velocities. In addition, experiments were carried out with different facing sheet materials. It is shown that the impact response of a sandwich panel is mainly determined by the front sheet. Calculations using FEM show that the critical impact energy, required to destroy the front sheet, increases with an increase in the density of the first core layer.

Fiber metal laminates (FML) were used in [12] as a coating on a polypropylene honeycomb core to form a sandwich structure. Impact tests at low velocity were carried out. The authors found that the maximum impact load increases to a threshold value at which it reaches a plateau. The optical images obtained after the impact were analyzed. A varying in the damaged area with an increase in the impact energy was noted.

The behavior of sandwich panels with different core structures after damage in a low-velocity impact was studied in [13]. The damage spread was determined using ultrasonic control. To assess the strength of damaged panel sandwich structures, they were tested in bending to failure.

The low-velocity impact behavior of composite sandwich panels with various types of core structures was studied in [14]. Panels made of carbon/fiber epoxy composite face sheets and polyurethane rigid core were considered. The material properties of the components were determined through tensile and compression tests. A hard impactor was dropped onto the plates. Calculations using the FEM confirmed the experimental results. The advantages of different cores are analyzed based on the analysis of impact strength.

Sandwich panels with various combinations of woven monolithic front sheets made of carbon and kevlar were considered in [15]. Low-velocity impact tests were carried out using various energy levels. The damage caused by the fracture of a multilayer structure is estimated. It is noted that the results of the calculations are consistent with the experimental data.

The study presented in [16] describes the results of numerical simulation of the response of sandwich panels with an expanded polystyrene core to low velocity impacts. The effect of foam core density on impact energy absorption by the panel was analyzed. The ABAQUS/Explicit FEA package was used in the calculations. The ability to absorb impact energy depending on the different density of the core is estimated.

Sandwich panels with a core reinforced with polyester pins were studied in [17]. The results were compared with obtained for non-reinforced plates with foam filler. The response to impact with low velocity and compression characteristics after impact were analyzed. The impact damage area was calculated using MATLAB image processing technology. Tests showed that pin reinforcement improved load-bearing capacity as well as significantly reduced the area of impact damage.

An attempt to discuss the mechanism of sandwich panels failure with fiberglass/epoxy face sheets reinforced with metal fibers during low-velocity impact and compression after impact (CAI) is made in [18]. The time dependence of the contact force, the absorbed energy and the deflection during the impact were obtained

experimentally. CAI tests are conducted using Digital Image Correlation (DIC) technology.

Investigations which are presented in [19] were devoted to the study of vibrations of three-layer composite plates in a wide frequency range. Experimentally, using Dynamic Mechanical Analysis, the equivalent complex modulus of the three-layer and polymer core characteristics were determined. Stripes under forced periodic straines were investigated. A scanning laser vibrometer was used for measurements. The measurement results are compared with the data obtained by calculation using the model of Guyader [20] and model of Ross, Kerwin and Ungar [21].

A three-layer composite plate element for FE dynamic simulation of a multilayer plate with a core made of a frequency-dependent viscoelastic material was presented in [22]. Its vibrational characteristics have also been studied experimentally. There is a satisfactory agreement between the results.

Laminated glass and photovoltaic panels are also being investigated using similar numerical and experimental methods [23, 24]. FEM was used in [25] to simulate the destruction of laminated glass loaded with an explosion. The method of separation of nodes is used, which allows solving the problem without loss of mass or momentum. The simulation data were compared with experimental results obtained in a shock tube. The results of an experimental determination of the response of multilayer plates consisting of layers of glass and polymers contains in [6].

Thus, at present, it can be considered an established approach, in which both experimental data and FEM simulation of a deformed state are used to study the behavior of thin-walled multilayer structural elements. This paper is devoted to the description of the developed experimental equipment for studying the dynamics of three-layer plates under low-velocity impact as well as the results of verification of the FEM calculations.

1.2 Description of Measurement System

The system of tensometric measurements "TENZO-21" (hereinafter referred to as the "System") is designed to conduct experimental investigations of two-dimensional structural elements in order to determine their deformed state using strain gauges [26]. In order to measure strains, strain gauges and corresponding measurement channels are combined into triplets (sockets) X,Y,XY.

The system specifications are given as follows

- number of measuring channels for connecting strain gauges is 5 x 3 = 15
- nominal resistance of strain gauges is 350 Ohm
- displaying the conditional numerical values of the selected group of sockets and the number of the socket on the LCD (liquid crystal display) (2 periods of 16 characters each)

The strain sensors (strain gauges) BF350-3AA with nominal resistance 350 Ohm were selected. As an ADC, modules based on the HX711 chip were used. Due to the

need for a sufficiently large number of ports for connecting modules, ensuring high performance and functionality, the Arduino Mega 2560 Rev3 controller was chosen. The system software includes the following components: a working program written in C language, a CH341 driver V3.1 and a program for receiving, displaying and registering measurement data.

Measurement technique. Since there are three non-zero components of the strain tensor during plate bending, sockets with three strain gauges are used, which must be glued to the surface of the plate under study. An drawing for the strain gauges placement is shown in Fig. 1.1. After carrying out the appropriate preparation of the test sample surface, the strain gauges are glued with cyanoacrylic glue. Connection of strain gauges is made by soldering POS-61 solder with rosin flux. Twisted pairs of MGTF-0.25 wire are used for connections. After soldering, a digital ohmmeter checks the serviceability of the strain gauge (obtained resistance was in the range of 350–352 Ohm). The connecting wires are fixed, and the socket is covered with a protective cover. Pairs of wires from strain gauges are connected to the corresponding socket terminals. The measured data are written in a text file.
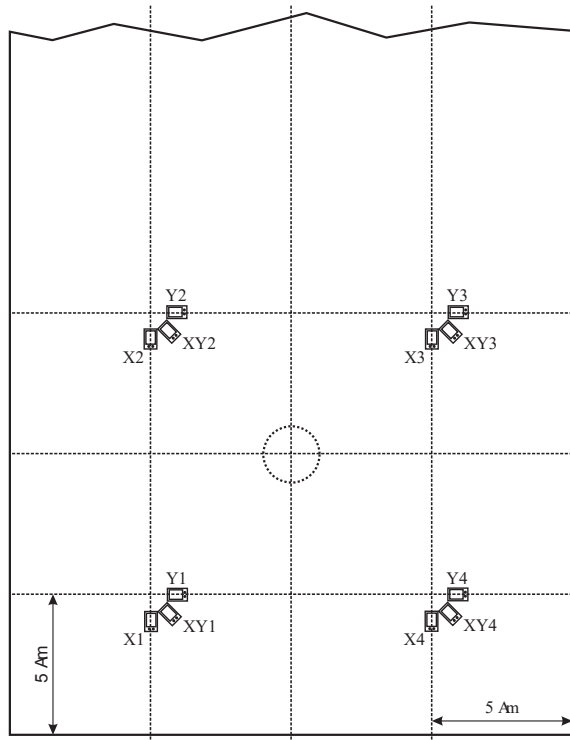
Fig. 1.1 Layout of strain gauges.

1.3 Method and Results of Measurements Using Dial Gauges

The deformed state of three-layer plates planned for use as a skin for a future heavy unmanned aerial vehicle (UAV) of a hybrid type, built on the basis of using only internal combustion engines [27], was investigated. A sketch of such vehicle is shown in Fig. 1.2. It is planned to use plates made in the laboratory of the Department of Computer Modeling of Processes and Systems NTU KhPI. The plates have three layers - two outer, made of fiberglass with 1 mm thick, and an inner one, 48 mm thick. It is made from expanded polystyrene. The layers are bonded with epoxy adhesive. For experimental tests, three plates were made, see Fig. 1.3. Their dimensions are 0.55x0.20x0.055m. The investigations of the mechanical behavior of these plates consisted of two cycles of experiments: tests under static load and under impact. The plates were rigidly fixed behind one small side. For this, clamp-type devices were used. A general view of the experimental setup with a fixed plate is shown in Fig. 1.4.

In the first experimental cycle, a static load was implemented using standard weights with an interval of 0.15 kg. They were added to a hanger connected to a hook fixed in the middle of the edge of the plate (Fig. 1.4). Plate deflections were measured using mechanical extensometers equipped with dial gauges (resolution of 0.01 mm). Measurements were made for two points located in the middle of the plate at a distance of 0.15 m and 0.25 m from the loaded edge in succession for all three plates. For each plate, three cycles of loading and unloading were carried out. The measurement data were averaged. The difference between the results both for different cycles and for different plates did not exceed 17%. The obtained averaged

Fig. 1.2 Design sketch of a heavy unmanned aerial vehicle (UAV) of a hybrid type.
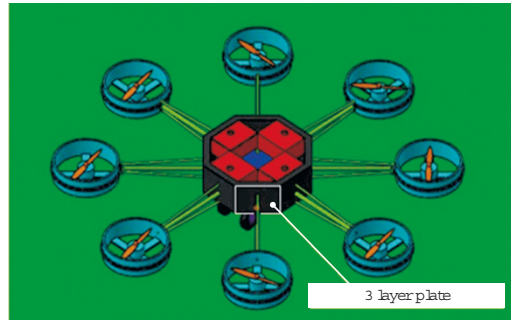
Fig. 1.3 Three-layer plates.
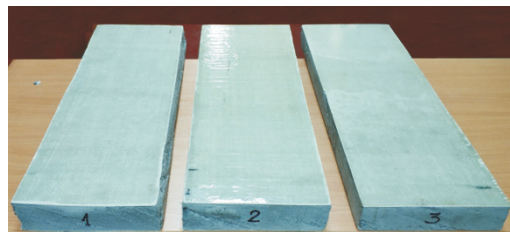
Fig. 1.4 General view of the
experimental unit with a fixed
plate under static load.
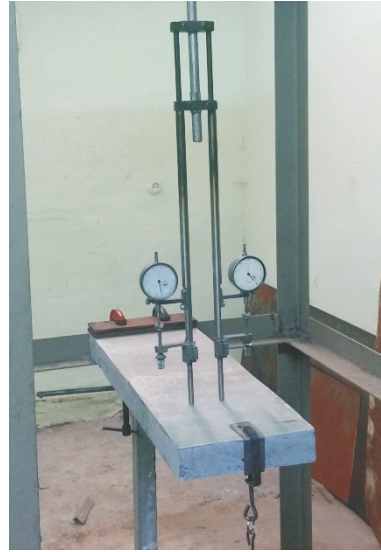
results are presented in Fig. 1.5 (point 0.15 m away from the edge of the plate) and
Fig. 1.6 (point 0.25 m away from the edge of the plate, Fig. 1.4).

1.4 Method and Results of Measurements Using Strain Gauges

With the help of the tensometric stand developed during this study (see Sect. 1.3),
an investigation of the deformed state of the three-layer plates under consideration
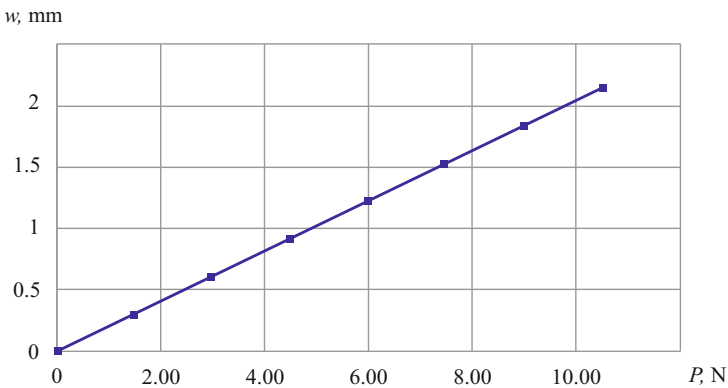
Fig. 1.5: Plate normal deflection versus load value for the point at 0.15 m distance from the edge of
the plate.

w, mm
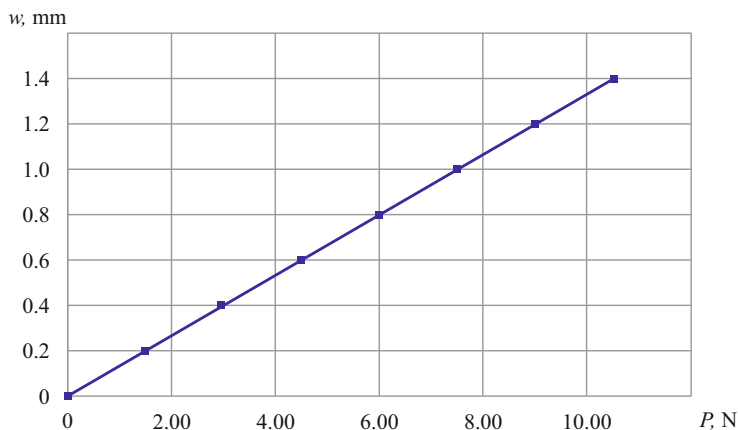
Fig. 1.6: Plate normal deflection versus load value for the point at 0.25 m distance from the edge of the plate.

was carried out. As noted, strain gauge data (the value of electrical signals on each strain gauge) is written to a text file. Further, using known methods [2] for calibrating, detecting the sensitivity of the measuring complex and determining the conversion factors for measuring the values of the strain components by strain gauges, a series of experiments on static load was carried out. In this case, similar load programs that were used when measuring static deflections were used. Three cycles of stepwise loading/unloading of the studied plate were carried out. At each load, the value of the strain gauge signal was recorded for each sensor at a given weight *m*. The general view of the experimental stand is shown in Fig. 1.7 (loaded plate with installed sensor sockets) and Fig. 1.8 (operator's workplace). For each socket, a measurement was made and the dependences of the signal value from the statically applied force during loading and unloading were obtained. With each addition of a load, measurements were made only when the motion of the device was completely stopped. As an example, Fig. 1.9 shows the data for socket #4, located on the upper surface (Fig. 1.1) as well as Fig. 1.10 demonstrates the data for #5 (plate bottom, located in the center from the bottom side of the plate). The data are presented by use of System measurement units (me). The data are averaged over 5 experiments. It can be seen from the graphs that the strain components follow a linearly elastic law. The numbers in figures show the corresponding directions of location of strain gauges :*1-x* (0°), *2-y* (90°), *12*-45°. Further, in order to prepare for the experimental-computational determination of the deformed state of the plates under dynamic (including impact) loads, an experimental study of the dynamics of the plates under consideration was carried out when a steel spherical impactor with a mass of 230 g, falls on them from a height of 0.08 m. The impact point was at the plate's midline at 0.11 m from its free edge. The impactor was released at a fixed time and moved vertically until it met the plate. The methodology for such experimental studies is described in [28].

Fig. 1.7 Loaded plate with
installed sensor sockets.

Fig. 1.8 Operator's work-
place.
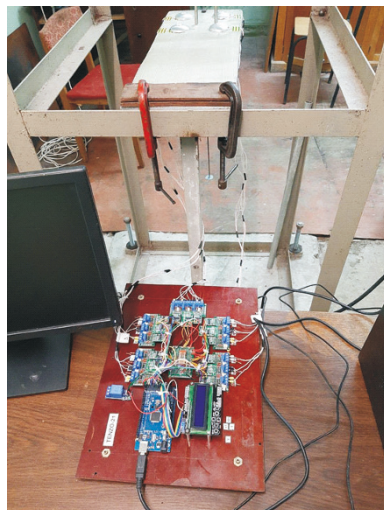
As an example, some results of measurements of linear strains are shown in Fig.
1.11 (socket #5) and Fig. 1.12 (socket #4). Similar results were obtained for sockets
1, 2, 3. The data are averaged over five measurements. The curve numbers mark the
corresponding directions of location of strain gauges $1 - x$ (0°), $2 - y$ (90°). Due to
the fact that the main task is to determine the maximum strain values upon impact,
we present data only for the area of their growth. Consequently, according to the

me
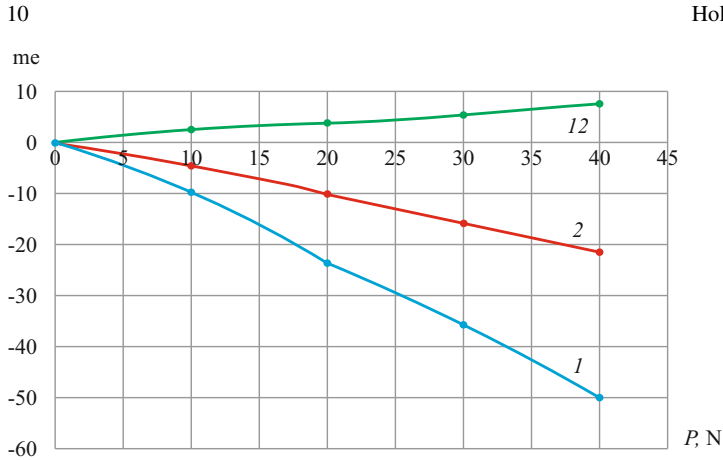
Fig. 1.9: Signal values versus statically applied force. Socket #4.

me
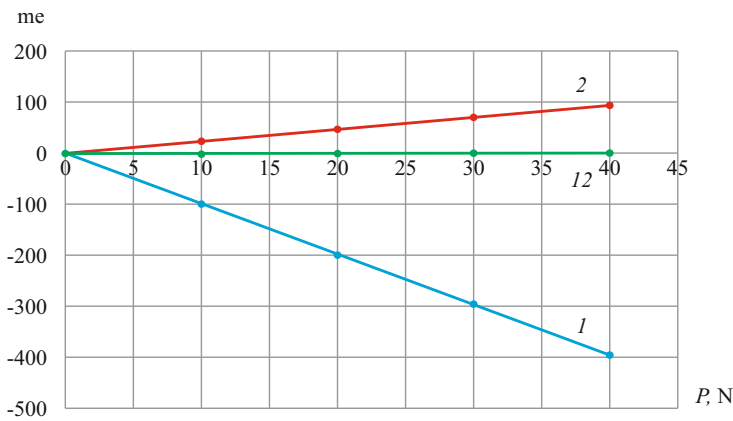
Fig. 1.10: Signal values versus statically applied force. Socket #5.

results of measurements on the developed experimental equipment, it was possible to obtain the values of the voltage on strain gauges under impact loading.

1.5 Sensor Calibration Method and Numerical Analysis

Due to the fact that a composite three-layer plate is a rather complex object, which, firstly, acquires its physical and mechanical properties after the completion of the manufacturing process, and secondly, due to the thickness of the plate (50 mm), it is not possible to manufacture an experimental one-dimensional specimen (its thickness will be of the same order with a standard length of 100 mm for specimens tested in tension or bending), the following calculation and experimental method for

me
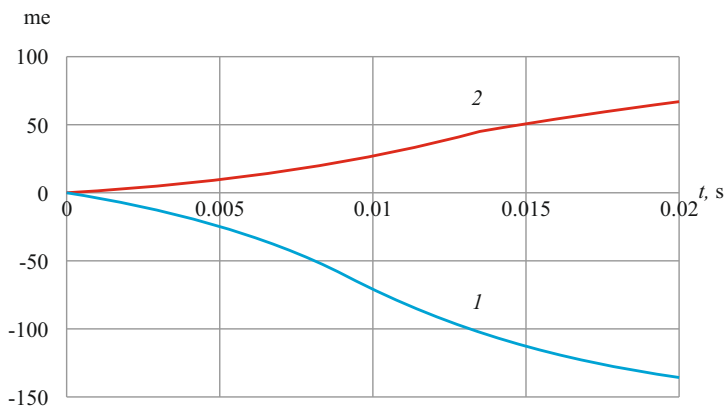
Fig. 1.11: Impact loading. Signal values versus time. Socket #5.

me
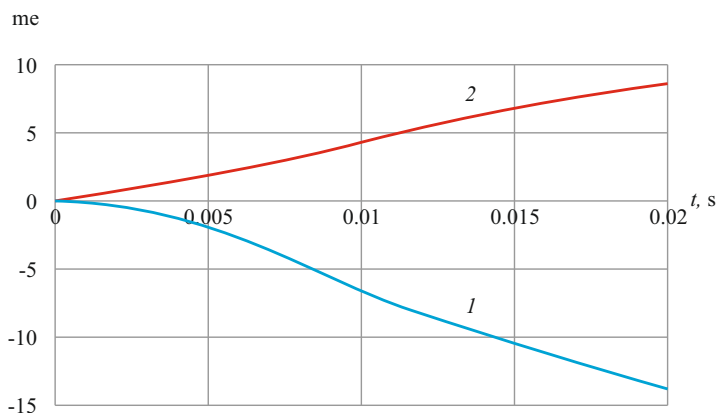
Fig. 1.12: Impact loading. Signal values versus time. Socket #4.

calibrating strain gauge sensors was adopted in the work. It is based on the use of a comprehensively tested engineering software package ANSYS [29] for the numerical assessment of the stress-strain state of the considered three-layer plates.

Briefly, the methodology is as follows. At first stage the set of numerical experiments for the determining the material elastic moduli was done. As is known, the material of such plates is described with a sufficient degree of accuracy by the model of an orthotropic material [1]. So, the number of typical numerical experiments (tension, compression and torsion) for the FE models of the material specimens were done and the elastic moduli E_x, E_y and the shear moduli G_{xy}, $G_{xz}=G_{yz}$ and Poisson's ratios $\nu_{xy}=\nu_{yz}=\nu_{xz}$ were determined.

At the second stage, the experimental results were obtained on tests with the static loaded plates (see Sect. 1.3) were compared with FEM numerical data for such problem. After comparisons the values of material elastic moduli were insignificantly varied in order to obtain the best results fitting.

Let us consider the results of the final simulation of the plate deformation process under static load. Note that this structural element from the point of view of the Solid Mechanics can be considered a thin plate (its thickness is much less than the dimensions in the plane). In this regard, it is appropriate to use finite elements for modeling, the main relations for which are obtained from the theory of plates [30]. On the other hand, when analyzing the impact interaction processes, when the impactor contacts precisely with the outer layer made of fiberglass, and the stress state in the vicinity of the contact is three-dimensional, the three-dimensional formulation of the problem is necessary.

So, in connection with the above arguments, we consider the solution of the problem with two formulations: using the theory of plates and the general three-dimensional one. In the first case, we use the FE SHELL 181, in the second - SOLID 185.

Figure 1.13 contains the calculation scheme of the plate when using FE SHELL 181. This scheme was chosen after a cycle of calculations designed to establish the convergence of solutions. The dots indicate the nodes, the values of the normal deflections in which were used to plot the dependence of the normal deflection on the coordinate. For example, for the value of the force applied inside the edge of the plate with a value of 10.5N, such a graph is shown in Fig. 1.14 The solid line indicates the calculated data, the dots are the results of deflection measurements at points 0.15 m and 0.25 m away from the edge of the plate, respectively. As can be seen from Fig. 1.14, the calculated results are quite close to the experimental ones, the difference in deflection values does not exceed 2.3%.

Than the calculation was made using the FE SOLID 185. The mesh selected after convergence studies is shown in Fig. 1.15. In this case, the dependence of the deflection of the upper points of the plate on the coordinates along the midline is almost similar to presented on Fig. 1.14.

After refining the values of the components of the matrix included in the formulation of the generalized Hooke's law, the following values were obtained: $E_x = E_y = 68$ MPa, $E_z = 3.4$ MPa, $G_{xy} = 29$ MPa, $G_{xz} = G_{yz} = 1.44$ MPa, $\nu_{xy} = \nu_{yz} = \nu_{xz} = 0.15$. It should be noted a significant increase in the elasticity moduli E_x, E_y of the composite material compared to the value of this modulus for expanded polystyrene at a tension (23.6 MPa). This, of course, reflects the influence of two thin layers of fiberglass.

Next, a similar cycle of experiments on the static load of the plates as well FE data were used for the case of the strain measurements by strain gauges. According to
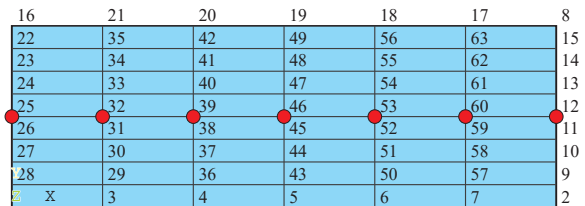
Fig. 1.13 Finite Element mesh of the plate with SHELL181 elements.

w, mm
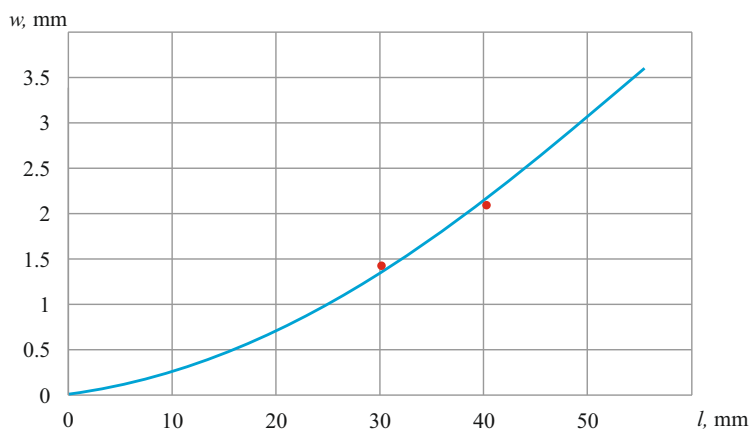
Fig. 1.14: Dependence of the normal deflection of the plate on the coordinate for the applied force of 10.5N using the plate theory.

Fig. 1.15 Solid Finite Element mesh of the plate using SOLID185 elements.
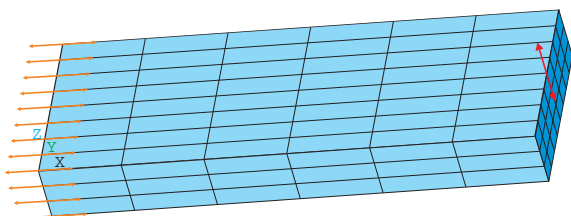
the obtained sets of numerically and experimentally determined components of the strain tensor at the points of location of the of strain gauges sockets, the coefficients k_1, k_2, k_{12} are calculated as proposed in [2]

$$k_1 = \frac{\varepsilon_x}{u_1}, \qquad k_2 = \frac{\varepsilon_y}{u_2}, \qquad k_{12} = \frac{\varepsilon_x \cdot l^2 + \varepsilon_y \cdot m^2 + \gamma_{xy} \cdot l \cdot m}{u_{12}}, \qquad (1.1)$$

where ε_x, ε_y, γ_{xy} - calculated values of strain tensor components, u_1, u_2, u_{12} are measured values of voltage and

$$l, m = \frac{\sqrt{2}}{2}.$$

After determining the coefficients of correspondence between the values of the voltage and the numerically obtained strain components, it becomes possible to verify the results of numerical simulation of non-stationary dynamic processes. For this, the results of an experimental study of the process of impact loading of plates by a spherical impactor are used. When a satisfactory convergence of experimental and numerical data is obtained, it becomes possible to consider computer simulation data as reliable and subsequently apply them in the analysis of various design options. In this paper, the technique under consideration is used to verify the data of the

computational analysis of the impact load of three-layer plates planned for the skin of a new UAV.

Next, consider the results of calculating the deformed state of the plate. To determine the coefficients for recalculating the data for determining the data from strain gauges, we use FEA with new grids, the location of the nodes in which corresponds to the location of the centers of the strain gauge sockets. The view of the mesh for the problem using a plate element with a similar cross section for the three-dimensional problem is shown in Fig. 1.16. Dots show the location of the specified nodes. The numbers in the figure reflect the corresponding dimensions of the sides of the elements.

Tables 1.1 and 1.2 present the results of calculating the values of the strain tensor components at the nodes of the model, corresponding to the location of the centers of the strain gauges sockets. Table 1.1 contains the results obtained using the FE SHELL181, as well as Table 1.2 - for use of FE SOLID185.

From the analysis of the data given in the tables, it can be concluded that the results when using different approaches are quite similar. The difference in signs between the measurement data (Figs. 1.9 and 1.10) and calculations is due to the applied directions of the axes in the coordinate systems used. When using the plate element, it is considered that all calculations are made for the middle surface, so the strain's sign for the socket #5 s the same as the signs at the points of sockets #1-4. Next, we will use the calculation data in the general three-dimensional formulation to determine the coefficients for converting the values of signal measurements to the values of strains.
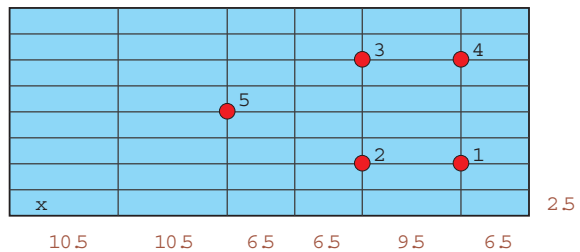
Fig. 1.16 FE mesh of the plate. Determining the strain tensor components.

Table 1.1: Data for the components of the strain tensor using SHELL 181 elements.

Socket	$\epsilon_x.10^{-3}$	$\epsilon_y.10^{-3}$	$\gamma_{xy}.10^{-3}$
1	-0.137	0.0389	0.0121
2	-0.284	0.0495	0.0446
3	-0.137	0.0389	-0.0121
4	-0.284	0.0495	-0.0446
5	-0.560	0.0887	0

Table 1.2: Data for the components of the strain tensor using SOLID 185 elements.

Socket	$\epsilon_x.10^{-3}$	$\epsilon_y.10^{-3}$	$\gamma_{xy}.10^{-3}$
1	-0.122	0.071	0.0702
2	-0.249	0.05	0.0062
3	-0.122	0.071	-0.0702
4	-0.249	0.05	-0.0062
5	0.492	-0.109	0

Using dependencies (1.1), the average values of these coefficients were obtained. For strain gauges of sockets *#1-4* located on the upper surface of the plate, the value of $k_1 = k_2 = k_{12} = 2 \cdot 10^{-5}$ was determined. For strain gauges of the socket #5 located on the lower surface of the plate, the value was: $k_1 = k_2 = k_{12} = 5 \cdot 10^{-6}$. In this case, when processing the data, the determined values of the coefficients deviated in the range of 4-7% for each direction.

Further, due to the obtained possibility of strain determining in the impact mode, a comparison of the experimental data with the data of numerical simulation was performed for the considered plate. The description of the experiment is presented in Sect. 1.4.

The impact loading process was modeled according to the experimental conditions. A spherical impactor fell from a height of 0.08 m onto a plate (Fig. 1.17). The values of stresses, strains and displacements in the nodes of the FE model were calculated. The obtained components of the strain tensor at the points corresponding to the location of the strain gauges were compared with the values obtained experimentally and calculated by use determined coefficients. As an example, the results of comparing the values of linear strains for a point on the plate's bottom corresponding to the location of the socket #5 (Fig. 1.18) are presented. Numerical data are represented by solid lines, experimental data by points. Here curve *1* corresponds to the component ε_x, curve *2* to ε_y. As can be seen from the graphs, there is a satisfactory correspondence between the calculated and experimental data: for the components ε_x the difference
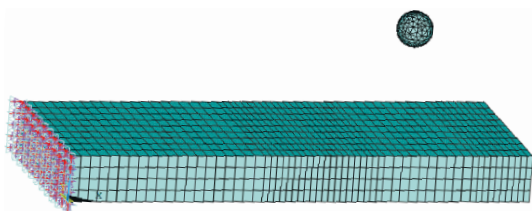
Fig. 1.17 Model for impact loading analysis.
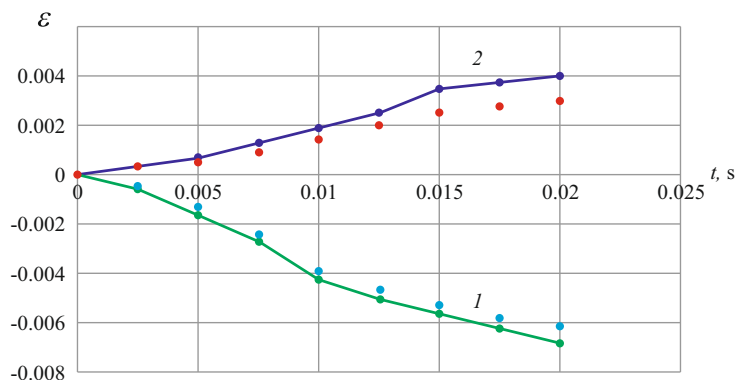
Fig. 1.18: Comparison of numerical (solid lines) and experimental (points) values of strains at the point of the plate, which corresponds to the location of the socket #5.
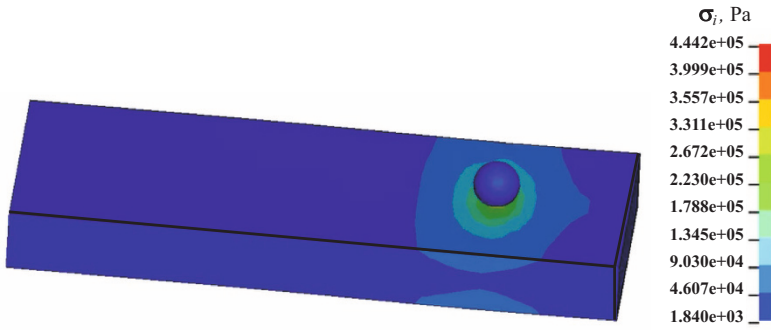
Fig. 1.19: Distribution of the maximum von Mises equivalent stresses on the surface of the plate at the time of impact.

does not exceed 12%, for the components ε_y it equal to 20%. In general, the divergence for all strain gauge sockets points do not exceed 20%. Thus, based on the results of the comparisons, we obtain a conclusion about the possibility of the numerical estimation of the stress-strain state of the plates made from the three-layer material under consideration.

As an example, let us give the distributions of the von Mises equivalent stresses (Fig. 1.19) on the surface of the plate at the time of impact contact with it. Note the essential localization of stresses at the point of impact. The maximum values of von Mises stresses do not exceed 0.44 MPa.

1.6 Conclusions

The deformed state of three-layer composite plates, made for the the body part of the UAV under design, loaded by static and impact loading, was experimentally determined. Plate structure consist of two outer fiberglass layers and a core of expanded polystyrene bonded with epoxy glue are considered. An experimental stand using clock-type mechanical sensors and strain gauges was developed to measure displacements and strains. The numerical-experimental approach for the choice of the values of the orthotropy parameters of the material is discussed. The results of verification studies conducted to analyze the reliability of the results of impact loading are described. The obtained results show a satisfactory convergence of experimental and calculated finite element data, which allows us to conclude that it is possible to use the developed approach and the experimental stand when designing the new parts of aircraft bodies.

References

[1] Altenbach H, Altenbach J, Kissing W (2018) Mechanics of Composite Structural Elements, 2nd edn. Springer
[2] Sharpe WN (2008) Handbook of Experimental Solid Mechanics. Springer Science and Business Media, New York
[3] Allen HG (1969) Analysis and Design of Structural Sandwich Panels. The Commonwealth and International Library: Structures and Solid Body Mechanics Division, Elsevier
[4] Abrate S (1998) Impact on Composite Structures. Cambridge University Press, Cambridge
[5] Espinosa HD, Nemat-Nasser S (2000) Low-velocity impact testing. ASM Handbook **8**:539–559
[6] Hána T, Janda T, Schmidt J, Zemanová A, Šejnoha M, Eliášová M, Vokáč M (2019) Experimental and numerical study of viscoelastic properties of polymeric interlayers used for laminated glass: Determination of material parameters. Materials **12**(14):2241
[7] Wang B, Zhong S, Lee TL, Fancey KS, Mi J (2020) Non-destructive testing and evaluation of composite materials/structures: A state-of-the-art review. Advances in Mechanical Engineering **12**(4):1687814020913,761
[8] Elder DJ, Thomson RS, Nguyen MQ, Scott ML (2004) Review of delamination predictive methods for low speed impact of composite laminates. Composite Structures **66**(1-4):677–683
[9] Dvorak GJ, Suvorov AP (2006) Protection of sandwich plates from low-velocity impact. Journal of Composite Materials **40**(15):1317–1331
[10] Ahn D, Nam G, Kim S, Han G, Seoung D, Yang D (2011) Low–velocity impact behaviors of a deformable thin metallic sandwich plate. In: Proceedings of the 18th International Conference on Composite Material, pp 21–26
[11] Sun G, Wang E, Wang H, Xiao Z, Li Q (2018) Low-velocity impact behaviour of sandwich panels with homogeneous and stepwise graded foam cores. Materials & Design **160**:1117–1136
[12] Tan C, Akil HM (2012) Impact response of fiber metal laminate sandwich composite structure with polypropylene honeycomb core. Composites Part B: Engineering **43**(3):1433–1438
[13] Göttner W, Reimerdes HG (2005) Low velocity impact investigations of sandwich panels with different cores. In: Sandwich Structures, vol 7: Advancing with Sandwich Structures and Materials, Springer, pp 661–670
[14] Usta F, Türkmen HS, Scarpa F (2021) Low-velocity impact resistance of composite sandwich panels with various types of auxetic and non-auxetic core structures. Thin-Walled Structures **163**:107,738
[15] Samlal S, Santhanakrishnan R (2022) Low-velocity impact behavior of foam core sandwich panels with inter-ply and intra-ply carbon/kevlar/epoxy hybrid face sheets. Polymers **14**(5):1060
[16] Çalışkan U (2017) FEM analyses of low velocity impact behaviour of sandwich panels with eps foam core. Journal of Thermal Engineering **3**(6):1544–1552

[17] Jayaram R, Nagarajan V, Kumar KV (2022) Low velocity impact and compression after impact behaviour of polyester pin-reinforced foam filled honeycomb sandwich panels. Journal of Sandwich Structures & Materials **24**(1):157–173

[18] Wu Y, Wan Y (2019) The low-velocity impact and compression after impact (cai) behavior of foam core sandwich panels with shape memory alloy hybrid face-sheets. Science and Engineering of Composite Materials **26**(1):517–530

[19] Ege K, Roozen N, Leclere Q, Rinaldi RG (2018) Assessment of the apparent bending stiffness and damping of multilayer plates; modelling and experiment. Journal of Sound and Vibration **426**:129–149

[20] Guyader JL, Cacciolati C (2007) Viscoelastic properties of single layer plate material equivalent to multi-layer composites plate. In: INTER-NOISE and NOISE-CON Congress and Conference Proceedings, Institute of Noise Control Engineering, vol 3, pp 4190–4199

[21] Ross D (1959) Damping of plate flexural vibrations by means of viscoelastic laminae. Structural Damping pp 49–97

[22] Huang Z, Wang X, Wu N, Chu F, Luo J (2020) The finite element modeling and experimental study of sandwich plates with frequency-dependent viscoelastic material model. Materials **13**(10):2296

[23] Aßmus M, Naumenko K, Altenbach H (2016) A multiscale projection approach for the coupled global–local structural analysis of photovoltaic modules. Composite Structures **158**:340–358

[24] Naumenko K, Eremeyev VA (2017) A layer-wise theory of shallow shells with thin soft core for laminated glass and photovoltaic applications. Composite Structures **178**:434–446

[25] Osnes K, Holmen JK, Hopperstad OS, Børvik T (2019) Fracture and fragmentation of blast-loaded laminated glass: An experimental and numerical study. International Journal of Impact Engineering **132**:103,334

[26] Tumanski S (2006) Principles of Electrical Measurement. CRC press

[27] Andrjejew Y, Breslavsky D, Larin A, Mietielov V (2021) Computer modelling of UAV flight. In: 2021 IEEE 2nd KhPI Week on Advanced Technology (KhPIWeek), IEEE, pp 455–459

[28] Breslavsky D, Morachkovsky O, Naumov I, Ganilova O (2018) Deformation and fracture of square plates under repetitive impact loading. International Journal of Non-Linear Mechanics **98**:180–188

[29] Lee HH (2018) Finite Element Simulations with ANSYS Workbench 18. SDC publications

[30] Timoshenko S, Woinowsky-Krieger S (1959) Theory of Plates and Shells, 2nd edn. McGraw-Hill New York

Chapter 2
Reviewing Yield Criteria in Plasticity Theory

Holm Altenbach and Vladimir A. Kolupaev

Abstract Mathematical plasticity theory assumes in many cases that deformation occurs without a change in volume. A yield surface, which limits elasticity under arbitrary combinations of stresses, is thus the function of the deviatoric components of the stress tensor. The yield criteria define this limit surface in the principal stress space. The commonly accepted criteria are Tresca, von Mises and Schmidt-Ishlinsky. Nowadays, they are not sufficient for modelling of real material behaviour in critical components and are generalized in the different ways.

Numerous criteria proposed over the last 150 years are hardly used because their utility is not obvious. In addition, the cost of material testing, parameter adjustment and complexity of criterion implementation often outweighs the benefits of accurate material description. Furthermore, there is no clear procedure for selecting the best criterion for a particular application.

This paper summarises frequently discussed yield criteria and assigns them to five derivation paths. Based on the introduced nomenclature, a verification standard for these criteria is outlined and the number of yield criteria is reduced to a few manageable cases. The criteria are classified into criteria of trigonal and hexagonal symmetry in the π-plane with C^0- and C^1-continuity for solving various problems.

Four missing criteria are identified, but their mathematical formulation is still subject to discussion. Four other yield criteria, which best meet plausibility requirements, are recommended instead. These criteria are suitable for all pressure-insensitive isotropic materials. The development and selection of particular criteria for certain groups of materials are therefore no longer necessary.

Holm Altenbach

Lehrstuhl für Technische Mechanik, Institut für Mechanik (IFME), Fakultät für Maschinenbau, Otto-von-Guericke-Universität Magdeburg, Universitätsplatz 2, D-39106 Magdeburg, Germany, e-mail: holm.altenbach@ovgu.de

Vladimir A. Kolupaev

Fraunhofer Institute for Structural Durability and System Reliability (LBF), Schloßgartenstr. 6, D-64289 Darmstadt, Germany, e-mail: Vladimir.Kolupaev@lbf.fraunhofer.de

19

There are many paths leading to the peak
of Mount Fuji, but the goal is the same.
MORIHEI UESHIBA [1]

2.1 Introduction

The design of components manufactured from ductile materials is based on the methods of plasticity theory. One of the cornerstones of this theory is the concept of the yield surface, which sets the elasticity limit under arbitrary combinations of stresses [2, 3]. Phenomenological criteria describe the yield surface in a simplified way. In mathematical plasticity theory for isotropic materials the yield criterion is only a function of the deviatoric components of the stress tensor since pressure-insensitivity can be assumed [3].

The choice of yield surface is crucial for reliable material description, optimization routines and design results. This choice depends on the available measured data of the material, the engineer's knowledge of the state of the art and some subjective preferences. The aim of this work is to reduce bias in the modelling.

For academic purposes and in simplified design, TRESCA and VON MISES criteria and sometimes also SCHMIDT-ISHLINSKY criterion are applied, which do not differentiate between tension and compression loads. These basic criteria are only functions of the equivalent stress σ_{eq}. The equivalent stress σ_{eq} is equated to the yield stress under uniaxial load, e.g. tensile load (T)

$$\sigma_{eq} = \sigma_0^T. \tag{2.1}$$

The subscript 0 in σ_0^T refers to the stress angle as a function of the deviatoric stresses – the geometric property of the tensile load. It is futile to discuss on the basis of a single test which of these criteria is the best for a particular application, see [4–10] and cf. [11–18].

To distinguish the basic criteria, an additional test is necessary, e.g. shear test (S). As a rule, these criteria show deviations from the shear yield data σ_{30}^S. In this case, a criterion as a function of σ_{eq} and one setting parameter is required. For real materials, a difference is also measured in tensile (T) and compressive (C) properties

$$\sigma_0^T \neq \sigma_{60}^C. \tag{2.2}$$

In this case, a criterion as a function of σ_{eq} and two parameters should be applied for reliable material description.

Numerous yield criteria have been proposed over the last 150 years. The best known are the criteria of DRUCKER [19], FREUDENTHAL-GOU [20], SAYIR-SOBOTKA [21, 22], SPITZIG-RICHMOND [23–25], DODD–NARUSE [26] and YU [9, 27] with one parameter in addition to the equivalent stress. Yield criteria with two parameters are PODGÓRSKI [28–31], ALTENBACH-ZOLOCHEVSKY [32] and

the cosine ansatz [33–37], among other. Some authors have introduced several criteria which complicates their identification by the researchers' name.

Behind the legion of names, the background of the criteria gets lost. The lack of systematisation has led to the same criteria being proposed by various authors, e.g.:

- FREUDENTHAL-GOU criterion is developed later in [38–42],
- SAYIR-SOBOTKA criterion is introduced also in [43–51],
- SPITZIG-RICHMOND criterion – in [32, 52–55],
- PODGÓRSKI criterion – in [56–58],
- the cosine ansatz – in [59, 60].

In some of the references above, the impact of the pressure-sensitivity in the formulations of the strength criteria is neglected to obtain the yield criteria for comparison.

A large number of reviews are known on the subject of yield and strength criteria, see [4, 9, 10, 13, 27, 32, 33, 61–75], among others. These reviews are mainly a list of criteria: superficial analyses of properties or preferences are indicated. The lists are either structured by publication year, alphabetically by researchers' name or a number of parameters [32, 76–78]. First, YU introduced a classification of yield criteria into single, octahedral and twin-shear stress criteria [9, 27]. Later, the systematisation of the criteria according to the power of the stress n in polynomially formulated criteria has been proposed, but only $n \leq 12$, $n \in \mathbb{N}$ are recommended [36].

It is considered that "our present knowledge of initial yield criteria for isotropic ductile materials is quite good, and fortunately these yield criteria are of a reasonably simple nature" [67], yet all of the above systematisations are not universal and do not answer the question which criterion is best for a given application. Moreover, they do not highlight the shortcomings of the criteria.

The second aim of this work is to discover paths in the derivation of a "very general criterion" [67] for isotropic materials – unus pro omnibus casibus, see the statements in [13, 74, 79, 80]. It is postulated that possible geometric shapes of the criterion should maintain extreme convexity limits [81, 82]. Further, this criterion should be obvious and numerically trivial, and the function of a few parameters that can be determined from simple tests. Then, no particular criteria for thermoplastics, metals or alloys are necessary. The "special theories" can be later obtained by suitable parameter restrictions [36].

The peculiarity of our work is the introduced nomenclature with a subsequent reduction of all reviewed yield criteria to fundamental cases, which contain the known criteria or approximate them closely. The criteria are classified into criteria of trigonal and hexagonal symmetry in the π-plane (deviatoric plane) that do or do not distinguish between tensile and compressive loads. Further, these criteria with C^0- and C^1- continuity can be used for solving various problems.

With the help of the introduced systematization, four missing yield criteria are identified, but their appropriate formulations are unknown. Pragmatically, they are replaced by four yield criteria, which meet the plausibility assumptions in the best known way. These criteria are suitable for all pressure-insensitive isotropic materials. Other criteria are not general enough and therefore redundant.

The present work is organized as follows

- invariants of the stress tensor (Sect. 2.2),
- methods, requirements and restrictions in the formulation of the criteria (Sect. 2.3),
- nomenclature and designation of yield criteria and geometric values for their comparison (Sect. 2.4),
- five typical paths of deriving the yield criteria (Sect. 2.5).

The most important points of our work are refreshed in conclusion (Sect. 2.6).

2.2 Invariants of Stress Tensor

Criteria for isotropic material behaviour must be invariant with respect to an arbitrary rotation of the coordinate system [10, 83, 84]. Therefore, they are established using the invariants of the symmetric second-rank stress tensor $\boldsymbol{\sigma}$. As a result of the eigenvalue problem, the principal values (principal stresses) are obtained and denoted by σ_I, σ_II and σ_III [32, 61, 85]. For uniqueness, the following order is assumed [86–91]

$$\sigma_\mathrm{I} \geq \sigma_\mathrm{II} \geq \sigma_\mathrm{III}. \tag{2.3}$$

The invariants of the stress tensor play an important role in the formulation of the equivalent stress expressions.

2.2.1 Axiatoric-Deviatoric Invariants

The axiatoric-deviatoric invariants [10, 32, 61]: the trace (axiator) I_1 of the stress tensor

$$I_1 = \sigma_\mathrm{I} + \sigma_\mathrm{II} + \sigma_\mathrm{III} \tag{2.4}$$

and the invariants I_2' and I_3' of the stress deviator

$$
\begin{aligned}
I_2' &= \frac{1}{6}\left[(\sigma_\mathrm{I} - \sigma_\mathrm{II})^2 + (\sigma_\mathrm{II} - \sigma_\mathrm{III})^2 + (\sigma_\mathrm{III} - \sigma_\mathrm{I})^2\right] = \\
&= \frac{1}{2}\left[\left(\sigma_\mathrm{I} - \frac{1}{3}I_1\right)^2 + \left(\sigma_\mathrm{II} - \frac{1}{3}I_1\right)^2 + \left(\sigma_\mathrm{III} - \frac{1}{3}I_1\right)^2\right]
\end{aligned} \tag{2.5}
$$

and [85, 92]

$$
\begin{aligned}
I_3' &= \left(\sigma_\mathrm{I} - \frac{1}{3}I_1\right)\left(\sigma_\mathrm{II} - \frac{1}{3}I_1\right)\left(\sigma_\mathrm{III} - \frac{1}{3}I_1\right) = \\
&= \frac{1}{3}\left[\left(\sigma_\mathrm{I} - \frac{1}{3}I_1\right)^3 + \left(\sigma_\mathrm{II} - \frac{1}{3}I_1\right)^3 + \left(\sigma_\mathrm{III} - \frac{1}{3}I_1\right)^3\right]
\end{aligned} \tag{2.6}
$$

are often used in the modelling. The first invariant I_1 is employed to model pressure-sensitivity. The second and third invariants can be interpreted as "the average quadratic" and "cubic deviation of a given state of stress from the mean hydrostatic stress" [85, 93–95].

The stress tensor $\boldsymbol{\sigma}$ can be decomposed into hydrostatic and deviatoric components [10, 32]

$$
\begin{bmatrix} \sigma_{\mathrm{I}} & 0 & 0 \\ 0 & \sigma_{\mathrm{II}} & 0 \\ 0 & 0 & \sigma_{\mathrm{III}} \end{bmatrix} = \begin{bmatrix} \frac{1}{3}I_1 & 0 & 0 \\ 0 & \frac{1}{3}I_1 & 0 \\ 0 & 0 & \frac{1}{3}I_1 \end{bmatrix} + \begin{bmatrix} \sigma_{\mathrm{I}} - \frac{1}{3}I_1 & 0 & 0 \\ 0 & \sigma_{\mathrm{II}} - \frac{1}{3}I_1 & 0 \\ 0 & 0 & \sigma_{\mathrm{III}} - \frac{1}{3}I_1 \end{bmatrix} \tag{2.7}
$$

to highlight their impact in the criterion. With the stresses of the deviator

$$
s_{\mathrm{I}} = \sigma_{\mathrm{I}} - \frac{1}{3}I_1, \qquad s_{\mathrm{II}} = \sigma_{\mathrm{II}} - \frac{1}{3}I_1 \quad \text{and} \quad s_{\mathrm{III}} = \sigma_{\mathrm{III}} - \frac{1}{3}I_1 \tag{2.8}
$$

the invariants I'_2 and I'_3 can be expressed as [96–101]

$$
\begin{aligned}
I'_2 &= \frac{1}{6}\left[(s_{\mathrm{I}} - s_{\mathrm{II}})^2 + (s_{\mathrm{II}} - s_{\mathrm{III}})^2 + (s_{\mathrm{III}} - s_{\mathrm{I}})^2\right] = \\
&\frac{1}{2}\left(s_{\mathrm{I}}^2 + s_{\mathrm{II}}^2 + s_{\mathrm{III}}^2\right) = -\left(s_{\mathrm{I}}\,s_{\mathrm{II}} + s_{\mathrm{II}}\,s_{\mathrm{III}} + s_{\mathrm{III}}\,s_{\mathrm{I}}\right)
\end{aligned} \tag{2.9}
$$

and [98, 100–102]

$$
I'_3 = \frac{1}{3}\left(s_{\mathrm{I}}^3 + s_{\mathrm{II}}^3 + s_{\mathrm{III}}^3\right) = s_{\mathrm{I}}\,s_{\mathrm{II}}\,s_{\mathrm{III}}. \tag{2.10}
$$

The expression of the second invariant of the deviator I'_2 in the principal shear stresses [9, 88, 96, 103–105]

$$
\tau_{12} = \frac{1}{2}\left(\sigma_{\mathrm{I}} - \sigma_{\mathrm{II}}\right), \qquad \tau_{23} = \frac{1}{2}\left(\sigma_{\mathrm{II}} - \sigma_{\mathrm{III}}\right), \qquad \tau_{31} = \frac{1}{2}\left(\sigma_{\mathrm{III}} - \sigma_{\mathrm{I}}\right) \tag{2.11}
$$

as, cf. [104, 106–108],

$$
I'_2 = \frac{2}{3}\left(\tau_{12}^2 + \tau_{23}^2 + \tau_{31}^2\right) \tag{2.12}
$$

is useful for various interpretations. Note, the sign of the shear stresses does not affect the result of I'_2. The principal shear stresses are the extreme values of the shear stresses, i.e. these take on their maximum or minimum value. If the principal shear stresses occur, the normal stresses assume their mean value. The stress state τ_{12}, τ_{23}, $\tau_{31} \neq 0$ with $\sigma_{11} = \sigma_{22} = \sigma_{33} = 0$ is impossible, cf. [42].

The transformation (2.11) has the following linear-algebraic properties: the equations allow to obtain the principal shear stresses from the principal normal stresses in a unique way. The same is not true for the inverse transformation. It is necessary

to consider the expressions (2.11) as a system of linear equations with respect to the principal stresses, assuming that the shear stresses are known. Because of the condition [6, 88, 100, 109–111]

$$\tau_{12} + \tau_{23} + \tau_{31} = 0 \tag{2.13}$$

this system is not of full rank, so it has an infinite number of solutions, which means that the transformation is not unique [112]. We obtain with [112]

$$s_{\mathrm{I}} = \frac{2}{3}\,(\tau_{12} - \tau_{31}), \quad s_{\mathrm{II}} = \frac{2}{3}\,(\tau_{23} - \tau_{12}) \quad \text{and} \quad s_{\mathrm{III}} = \frac{2}{3}\,(\tau_{31} - \tau_{23}) \tag{2.14}$$

the third invariant of the deviator I_3', cf. [106, 107, 113]

$$I_3' = -\frac{2^3}{3^3}\,(\tau_{12} - \tau_{23})\,(\tau_{23} - \tau_{31})\,(\tau_{31} - \tau_{12}). \tag{2.15}$$

2.2.2 Normalized Functions of Invariants

Normalized functions of the invariants (2.4) to (2.6) are obtained from a transformation of the coordinate system $(\sigma_{\mathrm{I}}, \sigma_{\mathrm{II}}, \sigma_{\mathrm{III}})$ to (ξ_1, ξ_2, ξ_3), (Fig. 2.1)

- the scaled axiator I_1 (2.4) of the stress tensor [36, 114]

$$\xi_1 = I_1/\sqrt{3} \tag{2.16}$$

  describes the coordinate of load $(\sigma_{\mathrm{I}}, \sigma_{\mathrm{II}}, \sigma_{\mathrm{III}})$ on the hydrostatic axis (space diagonal of the normal stress space),
- the root of the scaled second invariant of the stress deviator (2.5)

$$\rho_{\mathrm{HW}} = \sqrt{2\,I_2'} \tag{2.17}$$

  as radius in the plane orthogonal to the hydrostatic axis at the cross section $\xi_1 = \text{const.}$

Instead of the invariant (2.17), the invariant

$$\rho = \sqrt{3\,I_2'} \tag{2.18}$$

is often used [36, 115]. This scaling is preferred due to the equivalence

$$I_1^2 = 3\,I_2' \tag{2.19}$$

valid for the uniaxial tensile limit load (T)

$$\sigma_{\mathrm{I}} = \sigma_0^{\mathrm{T}}, \qquad \sigma_{\mathrm{II}} = \sigma_{\mathrm{III}} = 0 \tag{2.20}$$

and uniaxial compressive limit load (C)

$$\sigma_{\mathrm{I}} = \sigma_{\mathrm{II}} = 0, \qquad \sigma_{\mathrm{III}} = -\sigma_{60}^{\mathrm{C}}. \tag{2.21}$$

The subscript 0 in σ_0^{T} and 60 in σ_{60}^{C} refer to the corresponding stress angles as a geometric property of the load, which will be introduced in Subsect. 2.2.3.

The invariants (2.16) and (2.17) are sometimes preferred because of the interpretation of the loads in the principal stress space (HAIGH-WESTERGAARD coordinates [36, 114]). The invariant (2.18) is used for comparison the measured data with the uniaxial tensile test.

The third invariant of the deviator I_3' (2.6) has no physical or geometric meaning. Note, this invariant is an odd function of the stresses. The apparently logical normalisation by power as a consequence of (2.16) and (2.17)

$$\vartheta_3 = \mathrm{sign}[I_3'] \left(\frac{3^3}{2} \, |I_3'| \right)^{1/3}$$

in the formulation of the criterion is not recommended because it leads to non-convex surfaces [36, 116], cf. [23, 24, 50, 65, 85, 117, 118]. Other invariants are given for instance in [10, 32, 61, 119].

2.2.3 Dimensionless Invariants

Dimensionless invariants are crucial for analysing stress states and comparing measured data from different materials in the same diagrams:

- the elevation ψ in BURZYŃSKI-plane $\left(I_1, \sqrt{3 I_2'} \right)$ [120, 121], see also [10, 61, 122–126]

$$\tan \psi = \frac{\sqrt{3 I_2'}}{I_1}, \qquad \psi \in [\, 0, \pi \,] \tag{2.22}$$

  or the stress triaxiality factor [119, 127–130]

$$\eta = \frac{1}{\tan \psi} \tag{2.23}$$

  and

- the stress angle θ in the π-plane (deviatoric plane or plane with $I_1 = \mathrm{const.}$) [131–133], see also [10, 101, 134–137]

$$\cos 3\theta = \frac{3\sqrt{3}}{2} \frac{I_3'}{(I_2')^{3/2}}, \qquad \theta \in \left[0, \frac{\pi}{3} \right]. \tag{2.24}$$

They result from the utilisation of the spherical (ξ_1, ψ, θ) and cylindrical $(\xi_1, \rho_{\mathrm{HW}}, \theta)$ coordinate systems. The subscripts in the loads σ_0^{T}, σ_{30}^{S} and σ_{60}^{C} with the designation

T – uniaxial tension, S – shear and C – uniaxial compression correspond to the respective stress angle θ in degrees [81, 82].

Further stress angle invariants [51, 101, 138], see also [10] are obtained with a double-angle function [139]

$$\cos 6\theta = 2\cos^2 3\theta - 1 = 2\,\frac{3^3}{2^2}\,\frac{(I_3')^2}{(I_2')^3} - 1 \tag{2.25}$$

and

$$\cos 12\theta = 2\cos^2 6\theta - 1 = 2\left(2\cos^2 3\theta - 1\right)^2 - 1 = 2\left(2\,\frac{3^3}{2^2}\,\frac{(I_3')^2}{(I_2')^3} - 1\right)^2 - 1 \tag{2.26}$$

and can be used to consistently represent the criterion as a function of only $\cos 3\theta$ or $\cos 6\theta$.

The third invariant of deviator I_3' (2.5) can be expressed as a function of ρ (2.18) and $\cos 3\theta$ [51, 101]

$$I_3' = \frac{2}{3\sqrt{3}}\,\sqrt{(I_2')^3}\,\cos 3\theta = \frac{2}{3^3}\,\rho^3\cos 3\theta, \tag{2.27}$$

what is usable for some generalizations [81].

The principal stresses σ_{I}, σ_{II} and σ_{III} in the criterion can be replaced using the invariants I_1, ρ and θ [140], see also [141, 142]

$$\begin{aligned}
\sigma_{\text{I}} &= \frac{1}{\sqrt{3}}\left(\xi + \rho_{\text{HW}}\cos\left[\theta\right]\right), \\
\sigma_{\text{II}} &= \frac{1}{\sqrt{3}}\left(\xi + \rho_{\text{HW}}\cos\left[\theta - \frac{2}{3}\pi\right]\right), \\
\sigma_{\text{III}} &= \frac{1}{\sqrt{3}}\left(\xi + \rho_{\text{HW}}\cos\left[\theta + \frac{2}{3}\pi\right]\right).
\end{aligned} \tag{2.28}$$

The particular stress states at the stress angle [136]

$$\begin{aligned}
\theta &= 0 &&\text{if } \sigma_{\text{I}} > \sigma_{\text{II}} = \sigma_{\text{III}}, \\
\theta &= \frac{\pi}{6} &&\text{if } I_3' = 0, \\
\theta &= \frac{\pi}{3} &&\text{if } \sigma_{\text{I}} = \sigma_{\text{II}} > \sigma_{\text{III}}
\end{aligned} \tag{2.29}$$

are used for the experimental set-up and analysis of the limit surfaces.

2.3 Formulation of and Assumptions in Yield Criteria

For safe design, possible stress states in the component must be within the limit surface defined by the yield or strength criterion. A criterion is an engineering tool: there are no physical principles underlying such a formulation. Only plausibility assumptions provide reliable criteria for meaningful applications.

2.3.1 Formulation of Yield Criteria

The criteria for isotropic materials are formulated using invariants of the stress tensor (Sect. 2.2):

- the principal stresses (principal invariants) σ_I, σ_{II} and σ_{III} [10, 32, 143, 144]

$$\Phi\left(\sigma_I, \sigma_{II}, \sigma_{III}, \sigma_{eq}\right) = 0, \tag{2.30}$$

- the trace I_1 of the stress tensor and the invariants I_2', I_3' of the stress deviator (2.4) – (2.6) [4, 72, 136, 145–148]

$$\Phi\left(I_1, I_2', I_3', \sigma_{eq}\right) = 0, \tag{2.31}$$

- the cylindrical invariants ξ_1, ρ and θ (2.16) – (2.24) [128, 133, 136, 149–151]

$$\Phi\left(\xi_1, \rho, \theta, \sigma_{eq}\right) = 0 \tag{2.32}$$

  and
- the spherical invariants ξ, ψ and θ (2.16), (2.24) and (2.22) [36, 61, 128, 152]

$$\Phi\left(\xi_1, \psi, \theta, \sigma_{eq}\right) = 0. \tag{2.33}$$

In the formulations (2.32) and (2.33), the invariant ξ_1 (2.16) is the scaled invariant I_1 that describes the coordinate of the load on the hydrostatic axis, the radius ρ in the π-plane (2.17) is the scaled root of the second invariant I_2' and θ (2.24) is the corresponding stress angle in the π-plane. The radius ρ can be replaced by the stress triaxiality factor ψ (2.22) or (2.23), which gives a description of the surface in terms of the spherical invariants.

All these formulations (2.30)–(2.33) are, from a mathematical point of view, equivalent. Formulation (2.30) has a historical origin and is primarily mentioned in textbooks of strength of materials and plasticity theory in the discussion of the classical criteria:

- RANKINE criterion or the maximum normal stress criterion,
- TRESCA criterion based on the maximum shear stress,
- VON MISES criterion of the maximum distortion energy and

- SCHMIDT-ISHLINSKY criterion of the absolute value of the maximum deviatoric stress.

Formulations according to (2.31) were intensively elaborated until the beginning of the XXI century. Although such criteria are still being developed, they are not user-friendly [81].

The formulations (2.32) and (2.33) allow for the manipulation of the geometric properties of the surface Φ. The formulation (2.32) is very effective in terms of applicability and satisfying plausibility assumptions [81]. The formulation (2.33) has found hardly any practical application and is included here for the sake of completeness: it will be omitted from our discussion. One or the other of the formulations (2.30)–(2.33) may be preferred depending on the academic goals, the modelling concept, the consideration of plausibility assumptions or the desired application.

If pressure-insensitivity is assumed, the first invariant I_1 has no effect on yielding or failure [10, 84]. For this property, the formulations (2.31) and (2.32) can be reduced to the criteria

$$\Phi(I_2', I_3', \sigma_{\mathrm{eq}}) = 0 \qquad \text{or} \qquad \Phi(\rho, \theta, \sigma_{\mathrm{eq}}) = 0. \qquad (2.34)$$

Polynomial formulations of $\Phi(I_2', I_3', \sigma_{\mathrm{eq}})$ in terms of series of the deviatoric invariants I_2' and I_3' are well elaborated [36] but cannot be recommended for application because of additional outer contours around the physically meaningful surface in the π-plane. As a rule, the equivalent stress σ_{eq} is implicit in such equations, which increases the numerical effort.

For the sake of completeness, the formulation of the yield criteria (2.34) in the principal shear stresses (2.11)

$$\Phi(\tau_{12}, \tau_{23}, \tau_{31}, \sigma_{\mathrm{eq}}) = 0 \qquad (2.35)$$

is mentioned here. The criteria of TRESCA, VON MISES and SCHMIDT-ISHLINSKY are formulated in this way, see [96, 109, 111, 153]. Although all yield criteria can be expressed in terms of principal shear stresses, this method has lost its relevance for modelling and is now only used for academic purposes.

2.3.2 Plausibility Assumptions

There are no physical principles underlying the formulation of the yield and strength criteria Φ, which has led to their remarkable number [154, 155]. In order to select the best possible and most suitable criteria for the application, several requirements were stated in the past. These requirements can be interpreted as plausibility assumptions: they are not mandatory, but the quality of the criteria can be assessed taking into account the plausibility assumptions.

The known plausibility assumptions (PA) are summarized in [81]. We limit ourselves to the essentials

PA1: explicit solvability of the criterion w.r.t. the equivalent stress $\sigma_{eq} > 0$,

PA2: single surface in principal stress space without any additional outer contours and plane intersections: the equivalent stress σ_{eq} has only one root,

PA3: no case discrimination in the formulation,

PA4: possible reformulation of the yield criterion (2.30) or (2.35) in the invariants of deviator I'_2 and I'_3 or ρ and θ for any parameter setting,

PA5: restriction of the hydrostatic tensile stress,

PA6: numerical robustness in the application,

PA7: surface convexity restriction,

PA8: maximum generality and

PA9: requirements on the parameters:

  PA9.1: no parameters as power,

  PA9.2: minimum number of parameters,

  PA9.3: clear parameter restriction,

  PA9.4: non-dimensional parameters,

  PA9.5: geometric meaning of the parameters and

  PA9.6: unique assignment of the limit surface to parameters of the criterion.

The criteria that meet all PAs are not found. However, these PAs reduce the known criteria to a manageable number [81].

To satisfy the assumption PA1 and PA2, the equivalent stress σ_{eq} of the yield criterion can be specified explicitly:

$$\sigma_{eq} = \Phi(\tau_{12}, \tau_{23}, \tau_{31}), \tag{2.36}$$

$$\sigma_{eq} = \Phi(\sigma_I, \sigma_{II}, \sigma_{III}) \qquad \text{or} \qquad \sigma_{eq} = \Phi(s_I, s_{II}, s_{III}), \tag{2.37}$$

$$\sigma_{eq} = \Phi(I'_2, I'_3) \tag{2.38}$$

and

$$\sigma_{eq} = \Phi(\rho, \theta). \tag{2.39}$$

Such formulations are advantageous for iterative computations, e.g. in FEM codes.

With PA2, numerous polynomial formulations as a series development of I'_2 and I'_3 are excluded. PA3 prohibits the use of the max, min and modulus functions, which cause singularities. The PA4 and PA9.1 are related: the formulations with the parameter as power are not numerically stable (PA6) and this parameter in (2.36) and (2.37) does not allow a reformulation with the invariants in the general case.

PA5 can be derived from the bonding breaking mechanisms [68, 118, 128, 156–161]. In this case, the criteria are the functions of the first invariant (2.4). It is not discussed here as we have limited our review to consideration of the criteria for pressure-insensitive materials.

PA7 states that the convexity constraints should be given to the criterion and PA8 requires the extreme yield surfaces to be included. PA9.2 limit the number of tests necessary to fit the parameter of the criterion. PA9.3 prohibits the function of parameters as a constraint. PAs9.4 and 9.5 allow interpretation of the parameters for

"mastery" of the criterion and comparison of different fitting results. PA9.6 ensures unambiguity in fitting.

Consistent application of the PAs reduces the possible equations to the formulation (2.39). We may further postulate a multiplicative split of the yield criteria into a function of the radius $\Psi(\rho)$ and a function of the stress angle $\Omega(\theta)$ [10]

$$\sigma_{\text{eq}} = \Psi(\rho)\,\Omega(\theta). \qquad (2.40)$$

To highlight deviations of the surface' shape in the π-plane from the circle of VON MISES criterion (Fig. 2.1) [109, 162]

$$\sigma_{\text{eq}} = \sqrt{3I_2'} \qquad \text{with} \qquad \Omega(\theta) = 1, \qquad (2.41)$$

the function of $\Psi(\rho)$ is often replaced by $\sqrt{3I_2'}$ [128, 155, 163, 164], which yields

$$\sigma_{\text{eq}} = \sqrt{3I_2'}\,\Omega(\theta). \qquad (2.42)$$
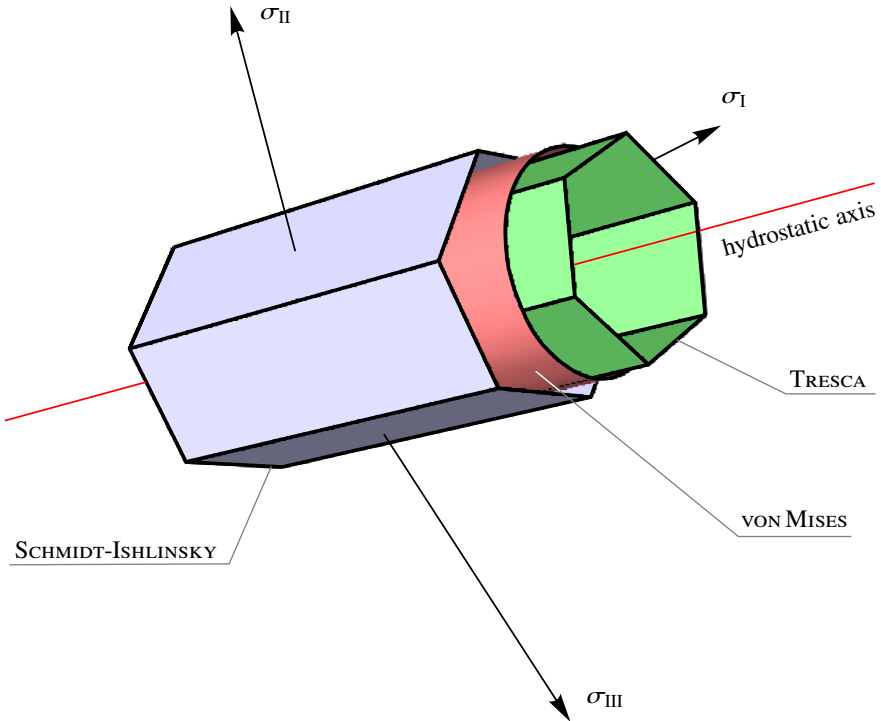
Fig. 2.1: Criteria of TRESCA, VON MISES and SCHMIDT-ISHLINSKY in the principal stress space (σ_{I}, σ_{II}, σ_{III}) [36, 61].

Normalizing criteria with respect to the appropriate uniaxial tensile limit load, e.g., the tensile yield or strength σ_0^{T} (2.1) leads to the final formulation

$$\sigma_{\mathrm{eq}} = \sqrt{3I_2'}\,\frac{\Omega(\theta)}{\Omega(0)}, \tag{2.43}$$

which includes several known yield criteria and is useful for application. Possible pressure-sensitive extensions of the yield criterion, e.g. with the linear I_1-substitution [36, 81]

$$\sigma_{\mathrm{eq}} \to \frac{\sigma_{\mathrm{eq}} - \gamma_1\,I_1}{1 - \gamma_1} \qquad \text{with} \qquad \gamma_1 \in [0, 1[, \tag{2.44}$$

which limits the hydrostatic tensile stress (PA5), are not a part of our discussion.

2.4 Designation and Comparison of Yield Criteria

A clear designation of the yield criteria is proposed, which provides a consistent overview and simplifies their selection for application [81]. The useful criteria are systematized in tables and diagrams. A method of comparing yield criteria is presented allowing the identification of missing criteria.

2.4.1 Nomenclature of Yield Criteria

The mathematical expressions for the yield criteria Φ can be very different, which makes their comparison in terms of best fit not directly possible, cf. [27, 142, 163, 165–168] among others. A unique nomenclature and consequent designation of the criteria is performed based on their geometric shapes in the π-plane [81].

The possible shapes of the yield criteria in the π-plane are constrained by the convexity requirement. The global upper and lower convexity restrictions are referred to as extreme yield figures [57, 82, 128, 129, 169, 170]. Extreme yield figures can take the shape of isogonal and isotoxal polygons of trigonal or hexagonal symmetry. Regular polygons are limit cases of the extreme yield figures.

Isogonal polygons are equiangular. An isotoxal polygon is equilateral, i.e. all sides are of the same length [171–173]. In general, isogonal and isotoxal hexagons are of trigonal symmetry (Fig. 2.2a). The regular hexagons of TRESCA and SCHMIDT-ISHLINSKY criteria have an additional symmetry axis and are of hexagonal symmetry (Figs. 2.2b and 2.3). Hexagonal symmetry is also present in isogonal and isotoxal dodecagons (twelve-sided polygons).

In this paper, the basic (regular) yield figures are labelled according to their shapes in the π-plane, cf. [82]:

- the designation $\bigcirc$ reflects VON MISES criterion with its circular cross section in the π-plane,
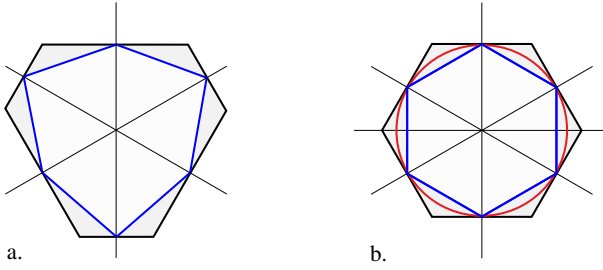
Fig. 2.2: Yield criteria in the π-plane normalized with respect to the tensile stress σ_0^{T}: a. Isogonal (black) and isotoxal (blue) hexagons of trigonal symmetry, b. Regular hexagons of SCHMIDT-ISHLINSKY (black) and TRESCA (blue) criteria of hexagonal symmetry and the circle of VON MISES criterion (red) of rotational symmetry [82].
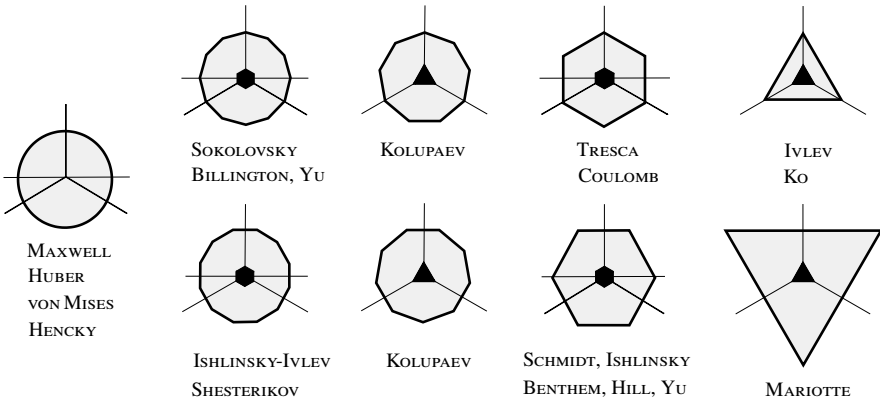
Fig. 2.3: Basic yield figures described by a circle and regular polygons of trigonal or hexagonal symmetry in the π-plane [81]. The symbols of symmetry follow according to [174].

- regular triangles in the π-plane are denoted with 3,
- regular hexagons with 6,
- regular enneagons with 9,
- regular dodecagons with 12,
- regular icositetragons with 24, etc.

Further regular polygons with the number of corners divisible by three are also accepted as yield criteria for isotropic materials, but they are particular.

Circumflex ˆ and macron ¯ refer to an upward pointing tip or upward facing flat base of the criterion shape in the π-plane, respectively: $\hat{3}$, $\bar{3}$, $\hat{6}$, etc. (Fig. 2.3 and Table 2.1).

The purpose of the designation is to provide a visual representation of the basic yield figures included in the discussed criteria (Table 2.2).

Limit surfaces for isotropic materials can be characterized by the regular polygons and the circle in the π-plane they contain. The criteria involving less than three of the

Table 2.1: Basic criteria in the π-plane (Fig. 2.3) with the values r_{15}, r_{30} and r_{60} (2.46) [81, 82].

Designation	r_{15}	r_{30}	r_{60}	References
$\hat{3}$ (△)	$\sqrt{2}/2$	$1/\sqrt{3}$	$1/2$	[175], see also [21, 91, 176–180]
$\bar{3}$ (▽)	$\sqrt{2}\left(\sqrt{3}-1\right)$	$2/\sqrt{3}$	2	[181], see also [32, 175, 182–185], [10, 21, 71, 170, 186, 187]
$\hat{6}$ (hexagon)	$\sqrt{3/2}\left(\sqrt{3}-1\right)$	$\sqrt{3}/2$	1	[99, 146, 188–191], see also [3, 10, 75, 106, 109, 111, 131, 192] and [78, 177, 193–197], [100, 126, 198–202]
$\bar{6}$ (hexagon)	$\sqrt{2}\left(\sqrt{3}-1\right)$	$2/\sqrt{3}$	1	[3, 9, 96, 145, 203–207], see also [7, 83, 106, 208–210], [42, 72, 136, 211–216]
$\hat{9}$	$\dfrac{\cos\dfrac{\pi}{9}}{\cos\dfrac{\pi}{36}}$	$\dfrac{\cos\dfrac{\pi}{9}}{\cos\dfrac{\pi}{18}}$	$\cos\dfrac{\pi}{9}$	[36, 81, 82]
$\bar{9}$	$\sqrt{2}\left(\sqrt{3}-1\right)$	$\sec\dfrac{\pi}{18}$	$\sec\dfrac{\pi}{9}$	[36, 81, 82]
$\hat{12}$	$\dfrac{1}{2}\sqrt{2+\sqrt{3}}$	1	1	[205]*, see also [217–222], [68, 212, 223–228]
$\bar{12}$	$\sqrt{2}\left(\sqrt{3}-1\right)$	1	1	[229, 230], see also [231, 232]
$\hat{24}$	1	1	1	[36, 81, 82]
$\bar{24}$	1	1	1	[81, 82]
(circle)	1	1	1	[109, 162, 233–237], see also [64, 88, 98, 103, 114, 145, 198, 238, 239], [72, 74, 75, 99, 111, 202, 240, 241] and [10, 85, 87, 194, 196, 242–244]

* – The criterion is named SOKOLOVSKY criterion (Fig. 2.3) following PISARENKO-LEBEDEV [68] "... it was attempted to introduce some intermediate criteria by replacing the hexagonal prism of COULOMB with a dodecagonal prism [100] (inscribed in VON MISES cylinder) ... " [36].

Table 2.2: Designation of the most important yield criteria and number of parameter in addition to the equivalent stress σ_{eq} [36, 81, 82].

Name	Abbrevi-ation	Designation	Eq.	Para-meters	References
Capurso (Ivlev)	Cap	$\hat{3} - \hat{6} - \bar{3}$	(2.141)	1	[21, 175, 177, 245]
Sayir-Sobotka cubic criterion	CC	$\hat{3} - \bigcirc - \bar{3}$	(2.133)	1	[21, 43, 49, 246], [22, 170, 247], see also [44–46], [29, 47, 48, 50]
Haythornthwaite	Hay	$\hat{3} - \bar{6} - \bar{3}$	(2.143)	1	[21, 210, 248, 249]
Yu yield criterion	YYC	$\hat{6} - \hat{12} - \bar{6}$	(2.146)	1	[9, 27, 250, 251]
Szwed bicubic criterion*	BCC	$\hat{6} - \bigcirc - \bar{6}$	(2.138)	1	[51, 101, 252, 253]
Multiplicative ansatz criterion	MAC	$\hat{6} - \bar{12} - \bar{6}$	(2.149)	1	[36, 254–256]
Podgórski**	Pdg	$\hat{3} - \hat{6} \mid \bigcirc - \bar{3}$	(2.153)	2	[28–31]
Rosendahl	Rsn	$\hat{6} - \hat{12} \mid \bigcirc - \bar{6}$	(2.159)	2	[81, 82, 257]
C^0-criterion of trig. sym.	C^0-CTS	$\hat{3} - \hat{6} \mid \hat{12} \mid \bar{6} - \bar{3}$	(2.164)	2	[36, 82, 155]
Capurso-Haythornthwaite	C^1-CTS	$\hat{3} - \hat{6} \mid \bigcirc \mid \bar{6} - \bar{3}$	(2.144)	2	[33, 35, 36]
C^0-criterion of hex. sym.	C^0-CHS	$\hat{6} - \hat{12} \mid \hat{24} \mid \bar{12} - \bar{6}$	(2.170)	2	[82, 257]
YYC + MAC	C^1-CHS	$\hat{6} - \hat{12} \mid \bigcirc \mid \bar{12} - \bar{6}$	(2.151)	2	[36, 112]

Comments: * - supplementary sources [48, 49, 258–265] and our references [35, 36, 115, 254]; ** - supplementary sources [51, 56–58, 101, 142, 252, 266] and our investigations [36, 82, 155, 257]. The symbol | refers the vertical line in the diagrams Figs. 2.7 and 2.8.

regular geometries are considered as particular cases of the general formulation and excluded from our discussion, see PA8. The limitation to three regular geometries is motivated in Table 2.2 and Subsect. 2.4.2.

Generalized yield criteria involving three to five basic geometries are significant for application. Only twelve such criteria are known (Table 2.2). The number of their parameters does not exceed one in the first case and two – in the other two cases (PA9.2) in addition to σ_{eq}. However, the assumption PA2, that the criteria should be a single surface in the principal stress space with no case discrimination in the formulation (PA3), is only fulfilled for criteria as functions of the stress angle θ (2.43).

In our view, further criteria are not effective for application. For example, Lemaitre-Chaboche yield criterion "intermediary between those of von Mises and Tresca" as a function of I_2' and I_3' invariants with one parameter in addition to σ_{eq} [196, 267], see also [32, 33, 268–271] describing the transition

$$\hat{6} - \bigcirc$$

can be replaced with SZWED criterion with also one parameter (Table 2.2)

$$\hat{6} - \bigcirc - \bar{6}$$

and is therefore obsolete. ALTENBACH-ZOLOCHEVSKY C^0-criterion (C^0-CTS) with two parameters [32, 61, 154]

$$\hat{3} - \hat{6} \,|\, \bigcirc - \bar{3}$$

can be replaced with the modified ALTENBACH-ZOLOCHEVSKY C^0-criterion with the same number of parameters [36, 81, 82, 155, 164]

$$\hat{3} - \hat{6} \,|\, \hat{12} \,|\, \bar{6} - \bar{3}.$$

The symbol | is explained in Table 2.2, comments. Here, only one C^1-criterion of VON MISES is replaced with the regular dodecagon $\hat{12}$. The definition range of the modified formulation is significantly larger.

2.4.2 Shapes of Yield Criteria in π-plane

Cross sections of pressure-insensitive criteria may be described in the π-plane as functions $\rho(\theta)$ (Fig. 2.4). Let us introduce geometric properties on any cross section $I_1 = $ const. as relations of radii at the angles

$$\theta = \frac{\pi}{24}, \frac{\pi}{12}, \frac{\pi}{8}, \frac{\pi}{6}, \frac{\pi}{4} \quad \text{and} \quad \frac{\pi}{3} \tag{2.45}$$

to the radius $\rho(0)$ as

$$r_{7.5} = \frac{\rho(\pi/24)}{\rho(0)}, \, r_{15} = \frac{\rho(\pi/12)}{\rho(0)}, \, r_{22.5} = \frac{\rho(\pi/8)}{\rho(0)},$$
$$r_{30} = \frac{\rho(\pi/6)}{\rho(0)}, \quad r_{45} = \frac{\rho(\pi/4)}{\rho(0)}, \quad r_{60} = \frac{\rho(\pi/3)}{\rho(0)}. \tag{2.46}$$

Fig. 2.4 Isogonal (black) and isotoxal (blue) hexagons in the π-plane normalized by the uniaxial limit tensile load σ_0^T (Fig. 2.2a): Enlarged detail with VON MISES criterion (red) and the stress states T, CC on the 0-meridian, S, Tt and Cc on the $\pi/6$-meridian and C, TT on the $\pi/3$-meridian for comparison (Table 2.3) [82].
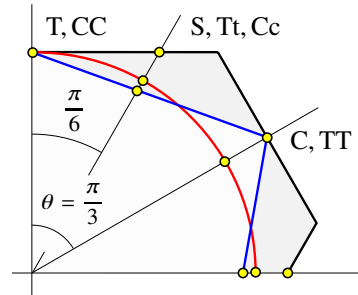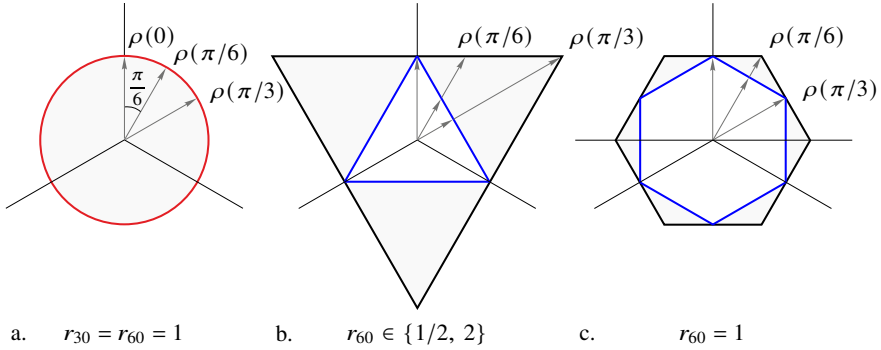
Fig. 2.5: Basic surfaces with the same radius $\rho(0)$ in the π-plane: a. Rotationally symmetric VON MISES criterion (2.41), b. Regular triangles $\hat{3}$ and $\bar{3}$, and **c.** Regular hexagons $\hat{6}$ and $\bar{6}$. The values r_{30} and r_{60} (2.46) are given for comparison [82].

The subscripts of r

$$7.5, \quad 15, \quad 22.5, \quad 30, \quad 45, \quad \text{or} \quad 60$$

correspond to the stress angle θ (2.45) of the respective radius in degrees. These values (2.46) can be used to compare different yield criteria in appropriate diagrams. The chosen angles θ are fractions $\pi/24$ of the angle $\pi/3$ between the symmetry axes in the π-plane (Figs. 2.5 and 2.6). Certain fractions are left as superfluous.
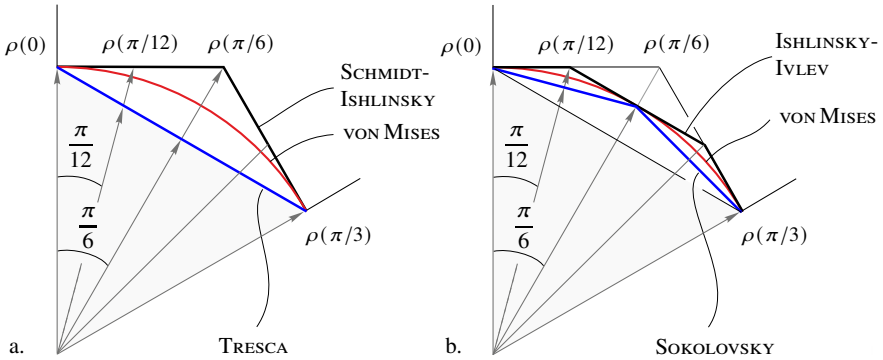
Fig. 2.6: Basic surfaces of hexagonal symmetry in the π-plane: a. Regular hexagons $\hat{6}$ and $\bar{6}$ and b. Regular dodecagons $\hat{12}$ and $\bar{12}$ with VON MISES criterion (2.41). Because of hexagonal symmetry a cut-out of the angle $\theta \in [0, \pi/3]$ is representative [36, 82].

All radii of VON MISES criterion (2.41) are equal (Fig. 2.5a)

$$r_{7.5} = r_{15} = r_{22.5} = r_{30} = r_{45} = r_{60} = 1. \tag{2.47}$$

For the direct comparison of the yield criteria of trigonal symmetry (Fig. 2.5b), the values r_{30} and r_{60} are significant. The values r_{15} and r_{45} can be used in refined analysis [81, 82].

For the criteria of hexagonal symmetry (Fig. 2.6), the radii at the angles $\theta = 0$ and $\pi/3$ are equal $\rho(0) = \rho(\pi/3)$, which gives

$$r_{60} = 1, \tag{2.48}$$

and since $\rho(\pi/12) = \rho(\pi/4)$, we obtain

$$r_{15} = r_{45}. \tag{2.49}$$

In this case, the values $r_{7.5}$ and $r_{22.5}$ are sometimes needed for the refined comparison of the shapes and, because of hexagonal symmetry, the values at the angles $5\pi/24$ and $7\pi/24$ are excluded from consideration.

Figures 2.7 and 2.8 show convexity restrictions for yield criteria of trigonal symmetry in the $r_{60} - r_{30}$ diagram and for yield criteria of hexagonal symmetry in the $r_{15} - r_{30}$ diagram, respectively. These diagrams allow a comparison of all yield criteria for isotropic materials. The shapes

$$\bigcirc, \quad \hat{1}2, \quad \bar{1}2, \quad \hat{2}4 \quad \text{and} \quad \bar{2}4$$

coincide in the $r_{60} - r_{30}$ diagram (Fig. 2.7), while the shapes

$$\bigcirc, \quad \hat{2}4, \quad \text{and} \quad \bar{2}4$$

coincide in the $r_{15} - r_{30}$ diagram (Fig. 2.8). The $r_{15} - r_{7.5}$ diagram for the criteria of hexagonal symmetry with $r_{60} = r_{30} = 1$ is conceivable for theoretical investigations.
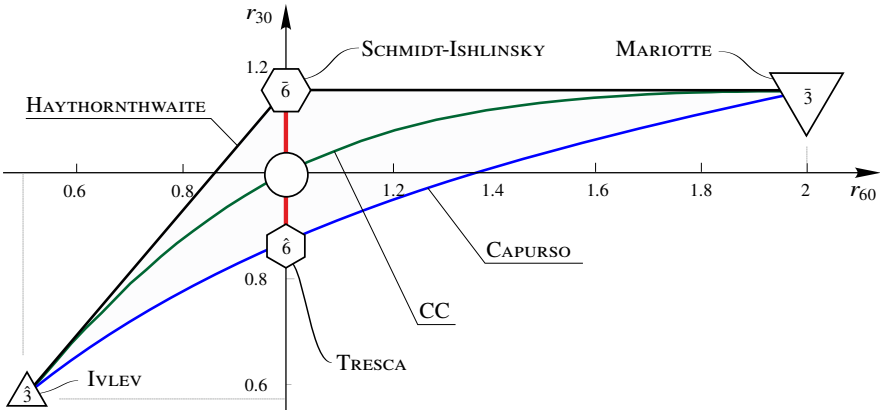
Fig. 2.7: Diagram $r_{60} - r_{30}$ for convex criteria of trigonal symmetry compared to VON MISES criterion with $r_{30} = r_{60} = 1$ [36]. The global upper and lower convexity restrictions are given with $\hat{3} - \bar{6} - \bar{3}$ and $\hat{3} - \hat{6} - \bar{3}$ criteria. Denotation follows according Table 2.2.
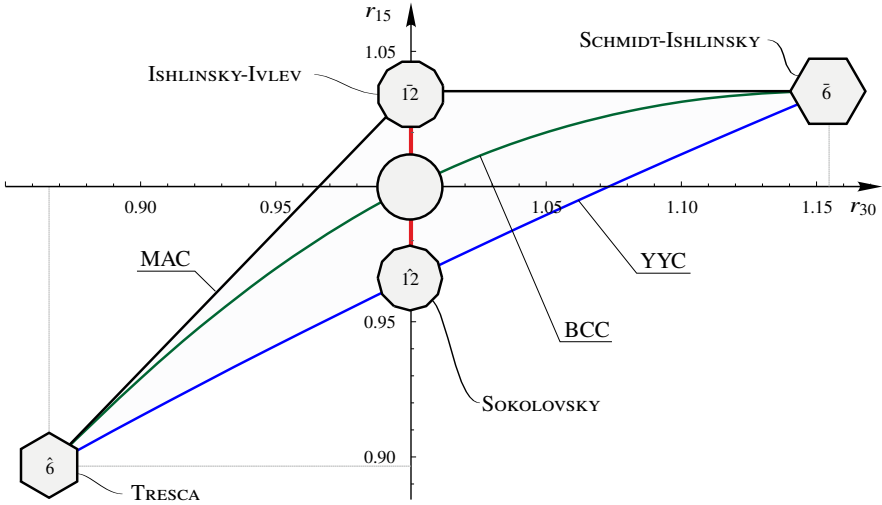
Fig. 2.8: Diagram $r_{30} - r_{15}$ for convex criteria of hexagonal symmetry ($r_{60} = 1$) compared to VON MISES criterion with $r_{15} = r_{30} = 1$ [82]. The global upper and lower convexity restrictions are given with $\hat{6} - \bar{12} - \bar{6}$ and $\hat{6} - \hat{12} - \bar{6}$ criteria. Denotation of the criteria follows according Table 2.2.

2.4.3 Geometric Properties and Basic Experiments

For comparison of the limit surfaces with the setting $\sigma_{\mathrm{eq}} = \sigma_0^{\mathrm{T}}$ (2.1), test results, approximations and extrapolations, measured data is normalized by the appropriate tensile limit load σ_0^{T}

$$\left(\frac{\sigma_{\mathrm{I}}}{\sigma_0^{\mathrm{T}}}, \frac{\sigma_{\mathrm{II}}}{\sigma_0^{\mathrm{T}}}, \frac{\sigma_{\mathrm{III}}}{\sigma_0^{\mathrm{T}}} \right), \tag{2.50}$$

so that mechanical properties become dimensionless. The surfaces Φ for different isotropic materials can be now compared in the same diagrams.

Let us introduce the following limit load values normalized with respect to the corresponding uniaxial tensile limit load σ_0^{T} (Table 2.3):

$$r_{60}^{\mathrm{C}} = \frac{\sigma_{60}^{\mathrm{C}}}{\sigma_0^{\mathrm{T}}} \qquad \text{and} \qquad r_{60}^{\mathrm{TT}} = \frac{\sigma_{60}^{\mathrm{TT}}}{\sigma_0^{\mathrm{T}}}, \tag{2.51}$$

where σ_{60}^{C} is the uniaxial compressive limit and $\sigma_{60}^{\mathrm{TT}}$ is the limit under equibiaxial tensile load,

$$r_{30}^{\mathrm{S}} = \sqrt{3} \, \frac{\sigma_{30}^{\mathrm{S}}}{\sigma_0^{\mathrm{T}}}, \qquad r_{30}^{\mathrm{Cc}} = \frac{\sqrt{3}}{2} \frac{\sigma_{30}^{\mathrm{Cc}}}{\sigma_0^{\mathrm{T}}}, \qquad \text{and} \qquad r_{30}^{\mathrm{Tt}} = \frac{\sqrt{3}}{2} \frac{\sigma_{30}^{\mathrm{Tt}}}{\sigma_0^{\mathrm{T}}}, \tag{2.52}$$

Table 2.3: Basic stress states with the corresponding stress angle θ and the dimensionless invariants η (2.23), $\cos 3\theta$ (2.24), $\cos 6\theta$ (2.25), $\cos 9\theta$, and $\cos 12\theta$ (2.26) [36, 81, 115, 272].

Designation	CCC	CC	Cc	C	S	T	Tt	TT	TTT
$\dfrac{\sigma_I}{\sigma_0^T}$	$-r^{CCC}$	$-r_0^{CC}$	$-\dfrac{2}{\sqrt{3}}r_{30}^{Cc}$	$-r_{60}^{C}$	$\dfrac{1}{\sqrt{3}}r_{30}^{S}$	1	$\dfrac{2}{\sqrt{3}}r_{30}^{Tt}$	r_{60}^{TT}	r^{TTT}
$\dfrac{\sigma_{II}}{\sigma_0^T}$	$-r^{CCC}$	$-r_0^{CC}$	$-\dfrac{1}{\sqrt{3}}r_{30}^{Cc}$	0	$-\dfrac{1}{\sqrt{3}}r_{30}^{S}$	0	$\dfrac{1}{\sqrt{3}}r_{30}^{Tt}$	r_{60}^{TT}	r^{TTT}
$\dfrac{\sigma_{III}}{\sigma_0^T}$	$-r^{CCC}$	0	0	0	0	0	0	0	r^{TTT}
θ	-	0	$\dfrac{\pi}{6}$	$\dfrac{\pi}{3}$	$\dfrac{\pi}{6}$	0	$\dfrac{\pi}{6}$	$\dfrac{\pi}{3}$	-
η	$-\infty$	-2	$-\sqrt{3}$	-1	0	1	$\sqrt{3}$	2	∞
$\cos 3\theta$	-	1	0	-1	0	1	0	-1	-
$\cos 6\theta$	-	1	-1	1	-1	1	-1	1	-
$\cos 9\theta$	-	1	0	-1	0	1	0	-1	-
$\cos 12\theta$	-	1	1	1	1	1	1	1	-

Designation: C - uniaxial compression, Cc - biaxial compression in the stress relation 1:2, CC - equibiaxial compression, CCC - hydrostatic compression, S or TC - shear, T - uniaxial tension, Tt - biaxial tension in the stress relation 1:2, TT - equibiaxial tension, TTT - hydrostatic tension.

where σ_{30}^S is the shear limit, σ_{30}^{Tt} and σ_{30}^{Cc} are the limit load of thin-walled tube with closed ends under inner (Tt) and outer pressure (Cc), respectively, and

$$r_0^{CC} = \frac{\sigma_0^{CC}}{\sigma_0^T}, \tag{2.53}$$

where σ_0^{CC} is the limit load under equibiaxial compression (Table 2.3). The subscripts of r refer to the stress angles of the load in degrees $\theta = 0, 30,$ and $60°$ (2.24), see Table 2.3. These values are characteristic properties of the material.

For VON MISES criterion (2.41), it follows

$$r_{60}^C = r_{60}^{TT} = r_{30}^S = r_{30}^{Cc} = r_{30}^{Tt} = r_0^{CC} = 1, \tag{2.54}$$

and is exactly the same as the values (2.47). It means that all meridians of the cylindrical surface coincide in BURZYŃSKI-plane $\left(I_1, \sqrt{3 I_2'}\right)$ and this straight line is parallel to the I_1-axis [81].

While a hydrostatic tensile test

$$\sigma_I = \sigma_{II} = \sigma_{III} > 0$$

and a hydrostatic compression test

$$\sigma_{\mathrm{I}} = \sigma_{\mathrm{II}} = \sigma_{\mathrm{III}} < 0$$

until failure can only be realised in special cases [36, 67, 264, 273–277], the corresponding properties are important for comparison of extrapolations. We may introduce

$$r^{\mathrm{TTT}} = \frac{\sigma^{\mathrm{TTT}}}{\sigma_0^{\mathrm{T}}} \qquad \text{and} \qquad r^{\mathrm{CCC}} = -\frac{\sigma^{\mathrm{CCC}}}{\sigma_0^{\mathrm{T}}}. \tag{2.55}$$

where σ^{TTT} and σ^{CCC} are the limit load under hydrostatic tension and compression, respectively. Except for porous and granular materials, hydrostatic compressive failure does not typically occur for relevant load and

$$r^{\mathrm{CCC}} \to \infty$$

is assumed. The upper limitation of the hydrostatic tensile stress follows from the bonding breaking mechanisms (PA5). This property is commonly ignored in plasticity theory and it is assumed that

$$r^{\mathrm{TTT}} \to \infty.$$

Now, the values r_0, r_{30}, and r_{60} (2.46) describe the shape of the surface Φ in the π-plane and the values

$$r_{60}^{\mathrm{C}}, \quad r_{60}^{\mathrm{TT}}, \quad r_{30}^{\mathrm{S}}, \quad r_{30}^{\mathrm{Cc}}, \quad r_{30}^{\mathrm{Tt}}, \quad r_0^{\mathrm{CC}}, \quad r^{\mathrm{CCC}}, \quad \text{and} \quad r^{\mathrm{TTT}}$$

characterise the material properties. If

$$r^{\mathrm{CCC}}, r^{\mathrm{TTT}} \to \infty,$$

pressure-sensitive criteria degenerate to pressure-insensitive criteria: the meridians of the surface Φ are parallel to the hydrostatic axis. Equal stress angles θ share the same radius ρ (2.17) and collapse onto one point in the π-plane (Fig. 2.4):

$$r_{60} = r_{60}^{\mathrm{C}} = r_{60}^{\mathrm{TT}}, \qquad r_{30} = r_{30}^{\mathrm{S}} = r_{30}^{\mathrm{Cc}} = r_{30}^{\mathrm{Tt}} \qquad \text{and} \qquad r_0^{\mathrm{CC}} = 1. \tag{2.56}$$

Pressure-insensitive criteria of hexagonal symmetry do not distinguish between tensile and compressive properties

$$r_{60} = r_{60}^{\mathrm{C}} = r_{60}^{\mathrm{TT}} = r_0^{\mathrm{CC}} = 1. \tag{2.57}$$

The meridians $\theta = 0$ and $\pi/3$ coincide in BURZYŃSKI-plane ($I_1, \sqrt{3I_2'}$) and together with other meridians are parallel to the I_1-axis. For fitting and comparison of the approximations, the shear load with the stress angle $\theta = \pi/6$ is significant. The superimposed loads of the plane stress state tension-shear (TS) and compression-shear (CS) at the stress angles $\theta = \pi/24, \pi/12, \pi/8$ and $5\pi/24, \pi/4, 7\pi/24$ respectively can be included in the test set-up for data comparison and improved material modelling.

2.4.4 Values for Comparison

The details on the stress calculation for comparison of the geometric properties of the yield criteria Φ obtained from the basic experiments are given below [81, 82]. The normalized stresses (2.50) of the plane stress state

$$\sigma_{\text{III}} = 0$$

and the normalized equivalent stress (2.1)

$$\frac{\sigma_{\text{eq}}}{\sigma_0^{\text{T}}} = 1$$

are evaluated with the setting of VON MISES criterion (2.41)

$$3I_2' = 1 \tag{2.58}$$

for selected stress angles (2.45). Here, the stress order (2.3) is not considered.

   The value r_0 with the stress angle $\theta = 0$ is obtained by setting in (2.24)

$$\cos[3 \cdot 0] = 1$$

with the stresses

$$\sigma_{\text{II}} = 0, \qquad \sigma_{\text{I}} = 1 \tag{2.59}$$

or

$$\sigma_{\text{I}} = \sigma_{\text{II}} = -1. \tag{2.60}$$

The value $r_{7.5}$ is obtained by setting [278]

$$\cos\left[3\,\frac{\pi}{24}\right] = \frac{1}{2}\sqrt{2 + \sqrt{2}}$$

with the stresses

$$\sigma_{\text{I}} = \pm\sqrt{\frac{1}{3}\left(2 + \sqrt{2}\right)}, \qquad \sigma_{\text{II}} = \pm\sqrt{\frac{1}{3}\left(2 \mp \sqrt{2 \pm \sqrt{3}}\right)} \tag{2.61}$$

or

$$\sigma_{\text{I}} = -\sqrt{\frac{1}{3}\left(2 - \sqrt{2 + \sqrt{3}}\right)}, \qquad \sigma_{\text{II}} = \sqrt{\frac{1}{3}\left(2 + \sqrt{2 - \sqrt{3}}\right)}. \tag{2.62}$$

The value r_{15} is obtained by setting

$$\cos\left[3\,\frac{\pi}{12}\right] = \frac{\sqrt{2}}{2}$$

with the stresses

$$\sigma_{\mathrm{I}} = \sqrt{\frac{2}{3}}, \qquad \sigma_{\mathrm{II}} = -\frac{1}{\sqrt{2}} + \frac{1}{\sqrt{6}}, \tag{2.63}$$

$$\sigma_{\mathrm{I}} = -\sqrt{\frac{2}{3}}, \qquad \sigma_{\mathrm{II}} = -\sqrt{\frac{2}{3} + \frac{1}{\sqrt{3}}} \tag{2.64}$$

or

$$\sigma_{\mathrm{I}} = \sqrt{\frac{2}{3} + \frac{1}{\sqrt{3}}}, \qquad \sigma_{\mathrm{II}} = \sqrt{\frac{2}{3} - \frac{1}{\sqrt{3}}}. \tag{2.65}$$

The value $r_{22.5}$ is obtained by setting [278]

$$\cos\left[3\frac{\pi}{8}\right] = \frac{1}{2}\sqrt{2 - \sqrt{2}}$$

with the stresses

$$\sigma_{\mathrm{I}} = \pm\sqrt{\frac{1}{3}\left(2 - \sqrt{2}\right)}, \qquad \sigma_{\mathrm{II}} = \sqrt{\frac{1}{3}\left(2 \pm \sqrt{2 \pm \sqrt{3}}\right)} \tag{2.66}$$

or

$$\sigma_{\mathrm{I}} = -\sqrt{\frac{1}{3}\left(2 + \sqrt{2 + \sqrt{3}}\right)}, \qquad \sigma_{\mathrm{II}} = -\sqrt{\frac{1}{3}\left(2 - \sqrt{2 - \sqrt{3}}\right)}. \tag{2.67}$$

The value r_{30} is obtained by setting

$$\cos\left[3\frac{\pi}{6}\right] = 0$$

with the stresses

$$\sigma_{\mathrm{I}} = -\sigma_{\mathrm{II}} = \frac{1}{\sqrt{3}}, \tag{2.68}$$

or

$$\sigma_{\mathrm{I}} = 2\,\sigma_{\mathrm{II}} = \pm\frac{2}{\sqrt{3}}. \tag{2.69}$$

The value r_{45} is obtained by setting

$$\cos\left[3\frac{\pi}{4}\right] = -\frac{\sqrt{2}}{2}$$

with the stresses

$$\sigma_{\mathrm{I}} = \sqrt{\frac{2}{3}}, \qquad \sigma_{\mathrm{II}} = \frac{1}{\sqrt{2}} + \frac{1}{\sqrt{6}} \tag{2.70}$$

or

$$\sigma_{\mathrm{I}} = \pm\sqrt{\frac{2}{3}}, \qquad \sigma_{\mathrm{II}} = \sqrt{\frac{2}{3} \pm \frac{1}{\sqrt{3}}}. \tag{2.71}$$

The value r_{60} is obtained by setting

$$\cos\left[3\,\frac{\pi}{3}\right] = -1$$

with the stresses

$$\sigma_{\mathrm{II}} = 0, \qquad \sigma_{\mathrm{I}} = -1 \tag{2.72}$$

or

$$\sigma_{\mathrm{I}} = \sigma_{\mathrm{II}} = 1. \tag{2.73}$$

Further setting can be formulated for the multiaxial stress states, e.g. for different elevations ψ (2.22) or the cross sections $I_1 = \text{const.}$ [81].

2.5 Five Derivation Paths

In Sect. 2.3 the schemas in the formulation of the yield criteria are outlined. Although the yield criteria Φ are a function either of

- three principal shear stresses $(\tau_{12}, \tau_{23}, \tau_{31})$ with the linear dependence (2.13),
- three principal normal stresses $(\sigma_{\mathrm{I}}, \sigma_{\mathrm{II}}, \sigma_{\mathrm{III}})$ with the pressure-insensitivity condition $I_1 = 0$ or, what the same, three deviatoric stresses $(s_{\mathrm{I}}, s_{\mathrm{II}}, s_{\mathrm{III}})$ or
- two invariants of the stress deviator (I_2', I_3') or (ρ, θ),

their formulation possibilities are almost endless. The PAs (Subsect. 2.3.2) limit this diversity (Table 2.2). Five typical derivation paths

I.   criteria as function of the principal shear stresses (2.36),
II.   criteria as a power function of the deviatoric stresses (2.37),
III. ○-criteria without extreme yield figures (2.38) or (2.39),
IV.   polynomial criteria as a series of I_2' and I_3' (2.34) and
V.   criteria as solution of equations with trigonometric identity (2.39)

are compared in terms of which of them is closest to the PAs. Pros and contras are explained.

The usual techniques for generalising the known criteria:

- linear (convex) combination of two or three criteria - a mixture rule [36, 279] and
- superposition (overlay) of two criteria realised as a product of equations [36, 280].

can also be used. However, the number of parameters increases and they have no direct geometric meaning, cf. PA9.2 and PA9.5.

2.5.1 Criteria in Shear Stress Space

The formulation of the yield criteria in the principal shear space $(\tau_{12}, \tau_{23}, \tau_{31})$ is intended more as a thought-provoking tool. The classical yield criteria $\hat{6}$, ○ and $\bar{6}$ are most easily interpreted in this space. According to LÜPFERT, the shear

stress considerations can be carried out uniformly and further yield criteria can be introduced [281]. R A D A E V wrote, that "the most general forms of the yield criterion of an isotropic solid are: the form in principal shear stresses" [110], see also [264]. However, the shear stress space is practically untouched scientific subject: a few authors contributed to it [9, 96, 100, 106, 107, 109, 111, 282], see also [113, 283–287].

When discussing this space, the sum of the shear stresses is referred to as

$$\zeta = \tau_{12} + \tau_{23} + \tau_{31}. \tag{2.74}$$

Only the ζ_0-plane with

$$\zeta = 0 \tag{2.75}$$

has a physical meaning [288], which describes a linear dependence (2.13). The stress states can be mapped in the ζ_0-plane [88, 100, 109, 111, 289].

2.5.1.1 Open Surfaces in Shear Stress Space

The yield criteria can be represented as cylinder and prisms along the space diagonal $\tau_{12} = \tau_{23} = \tau_{23}$ in the principal shear stress space:

• criterion $\bigcirc$

$$\frac{2^m}{2 + 2^m} \left[(\tau_{12} - \tau_{23})^m + (\tau_{23} - \tau_{31})^m + (\tau_{31} - \tau_{12})^m \right] = \sigma_{\text{eq}}^m \tag{2.76}$$

with the power $m = 2$ and 4,
• criterion $\hat{3}$

$$2 \max \left[\tau_{12} - \tau_{23}, \ \tau_{23} - \tau_{31}, \ \tau_{31} - \tau_{12} \right] = \sigma_{\text{eq}}, \tag{2.77}$$

• criterion $\bar{3}$

$$\max \left[-\tau_{12} + \tau_{23}, \ -\tau_{23} + \tau_{31}, \ -\tau_{31} + \tau_{12} \right] = \sigma_{\text{eq}}. \tag{2.78}$$

If yielding depends only on the modulus of the shear stresses, the yield surface is of hexagonal symmetry [39]. The prisms of hexagonal symmetry are:

• criterion $\hat{6}$ [96]

$$\frac{2}{3} \max \left[|2\,\tau_{12} - \tau_{23} - \tau_{31}|, \ |-\tau_{12} + 2\,\tau_{23} - \tau_{31}|, \ |-\tau_{12} - \tau_{23} + 2\,\tau_{31}| \right] = \sigma_{\text{eq}}, \tag{2.79}$$

• criterion $\bar{6}$ [96]

$$\max \left[|\tau_{12} - \tau_{23}|, \ |\tau_{23} - \tau_{31}|, \ |\tau_{31} - \tau_{12}| \right] = \sigma_{\text{eq}}, \tag{2.80}$$

• criterion $\hat{12}$ follows as a linear combination of (2.79) and (2.80)

$$(1-\alpha)\,\frac{2}{3}\,\max\left[|2\,\tau_{12}-\tau_{23}-\tau_{31}|,\,|-\tau_{12}+2\,\tau_{23}-\tau_{31}|,\,|-\tau_{12}-\tau_{23}+2\,\tau_{31}|\right]+$$

$$\alpha\,\max\left[\left(|\tau_{12}-\tau_{23}|,\,|\tau_{23}-\tau_{31}|,\,|\tau_{31}-\tau_{12}|\right)\right]=\sigma_{\text{eq}}\quad\text{with}\quad\alpha=2\left(2-\sqrt{3}\right)$$

$$(2.81)$$

and

- criterion $\bar{1}2$ follows as a intersection of (2.79) and (2.80)

$$\max\left[\frac{2}{3\,\alpha}\,|2\,\tau_{12}-\tau_{23}-\tau_{31}|,\,\frac{2}{3\,\alpha}\,|-\tau_{12}+2\,\tau_{23}-\tau_{31}|,\,\frac{2}{3\,\alpha}\,|-\tau_{12}-\tau_{23}+2\,\tau_{31}|,\right.$$

$$\left.|\tau_{12}-\tau_{23}|,\,|\tau_{23}-\tau_{31}|,\,|\tau_{31}-\tau_{12}|\right]=\sigma_{\text{eq}}\quad\text{with a scaling}\quad\alpha=2/\sqrt{3}.$$

$$(2.82)$$

The prisms (2.77)–(2.82) are regular.

2.5.1.2 Closed Surfaces in Shear Stress Space

The representation of the sphere and the convex polyhedra with three orthogonal planes of symmetry in the principal normal stress space $(\sigma_{\text{I}}, \sigma_{\text{II}}, \sigma_{\text{III}})$ for stress analysis is known:

- the sphere [12, 241, 273, 289–299],
- the cube [90, 299], see also [18, 283],
- the octahedron[1] [99, 289, 299, 300], see also [5, 9, 18, 98, 213, 239, 279, 281, 283, 301–303],
- the rhombic dodecahedron[2] [9, 16, 27, 80, 206, 207, 289, 299, 304, 305], see also [279, 281, 283, 306],
- the cuboctahedron[3] [306],
- the tetrakis hexahedron[4]
- the disdyakis dodecahedron[5]
- the great rhombicuboctahedron[6] and the small rhombicuboctahedron[7] [18, 306],
- the hexaicosahedron[8] [283].

---

[1] https://mathworld.wolfram.com/RegularOctahedron.html

[2] https://mathworld.wolfram.com/RhombicDodecahedron.html

[3] https://mathworld.wolfram.com/Cuboctahedron.html

[4] https://mathworld.wolfram.com/TetrakisHexahedron.html

[5] https://mathworld.wolfram.com/DisdyakisDodecahedron.html

[6] https://mathworld.wolfram.com/GreatRhombicuboctahedron.html

[7] https://mathworld.wolfram.com/SmallRhombicuboctahedron.html

[8] polyhedron with 8 triangles, 6 square and 12 octagons leading to $8+6+12=26$ faces, $8\times3+6\times4+12\times4=96$ edges and $8\times3+4\times6=48$ vertices.

The yield criteria can also be represented as closed bodies in the principal shear stress space: spheres and polyhedra. This representation is often preferred for academic purposes, despite the linear dependence of three principal shear stresses (2.13), (2.75):

• criterion ◯

$$2^{m-1} \left[(\tau_{12})^m + (\tau_{23})^m + (\tau_{31})^m \right] = \sigma_{eq}^m, \qquad m = 2, 4 \qquad (2.83)$$

with the circle in the ζ_0-plane (Fig. 2.9, left and right below), see [5, 6, 17, 100, 106, 109, 111, 288, 307–309] for $m = 2$ and Table 2.4 for $m = 4$:
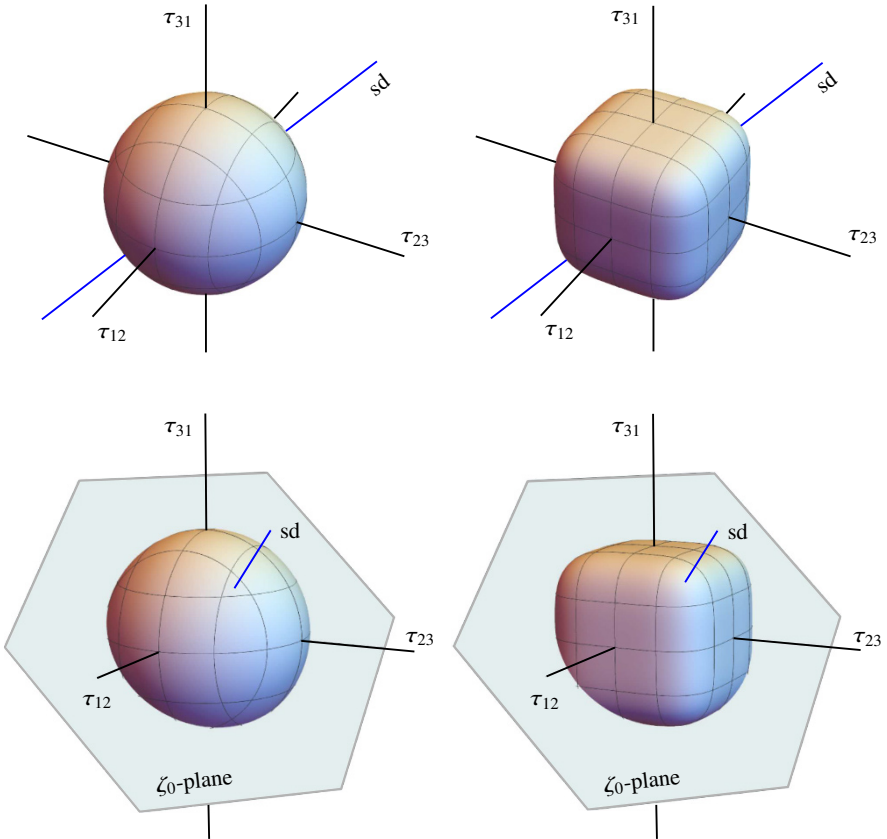
Fig. 2.9: Spheres of von Mises criterion ◯ (2.83) with the power $m = 2$ (left) and $m = 4$ (right) in the principal shear stress space (τ_{12}, τ_{23}, τ_{31}). sd – space diagonal, ζ_0 – plane (2.75) through the origin orthogonal to the space diagonal is shown for better clarity.

• criterion $\hat{3}$ as a triangular dipyramid (Fig. 2.10, left)

Table 2.4: HERSHEY criterion $\hat{6} - \bigcirc$ (2.95): setting of the power $n \geq 1$ with the corresponding values r_{30} (2.97) and r_{15} (2.98).

n	r_{30}	r_{15}	Cross section	Remarks	References
1	0.8660	0.8966	$\hat{6}$	TRESCA	[38, 258, 261, 310–312], [49, 68, 280, 313–315]
1.0824	0.8888	0.9161	–	inflection point V_n	–
1.5416	0.9671	0.9779	–	cf. r_{30} in $n = 6$	–
1.6	0.9731	0.9821	–	–	[261]
1.7	0.9819	0.9882	–	–	[261]
2	1	1	$\bigcirc$	VON MISES	[38, 97, 108, 258, 310, 311], [259–262, 316] [49, 263, 312, 313, 317], [10, 68, 264, 315, 318]
2.7230	1.0136	1.0076	–	max(r_{15})	–
2.7670	1.0137	1.0076	–	max(r_{30})	[261, 318, 319]
3	1.0129	1.0070	–	–	[316, 319]
4	1	1	$\bigcirc$	cf. $n = 2$	[38, 258, 261, 310, 311, 316], [10, 49, 312, 315, 318]
4.4719	0.9919	0.9958	–	inflection point r_{30}	–
4.5496	0.9905	0.9951	–	inflection point r_{15}	–
5	0.9828	0.9911	–	–	[260, 319]
6	0.9671	0.9826	–	–	[258, 310, 320–323], [97, 108, 260, 311, 316, 319], [263, 312, 317, 324], [10, 313, 325]
8	0.9435	0.9681	–	–	[97, 258, 311, 320, 322, 326], [108, 312, 313, 319, 324, 325]
10	0.9280	0.9568	–	–	[263, 280, 319, 321]
11	0.9223	0.9521	–	–	[316]
12	0.9175	0.9480	–	–	[108, 280, 319]
14	0.9100	0.9412	–	–	[327]
16	0.9044	0.9359	–	–	[263]
20	0.8966	0.9281	–	–	[320, 321]
26	0.8894	0.9208	–	–	[328]
30	0.8863	0.9175	–	–	see Table 2.5
32	0.8850	0.9162	–	–	[263]
40	0.8812	0.9122	–	–	[327]
41	0.8808	0.9119	–	–	see Table 2.5
100	0.8720	0.9028	–	–	–
∞	0.8660	0.8966	$\hat{6}$	TRESCA	[38, 97, 108, 258, 310, 311, 323], [259–261, 263, 280, 312] [10, 49, 264, 313–315]

$$2 \max \left[\tau_{12} - \tau_{23} + a\,\zeta, \; \tau_{23} - \tau_{31} + a\,\zeta, \; \tau_{31} - \tau_{12} + a\,\zeta, \right.$$

$$\left. \tau_{12} - \tau_{23} - a\,\zeta, \; \tau_{23} - \tau_{31} - a\,\zeta, \; \tau_{31} - \tau_{12} - a\,\zeta \right] = \sigma_{\mathrm{eq}}, \qquad a \in \mathbb{R}, \tag{2.84}$$
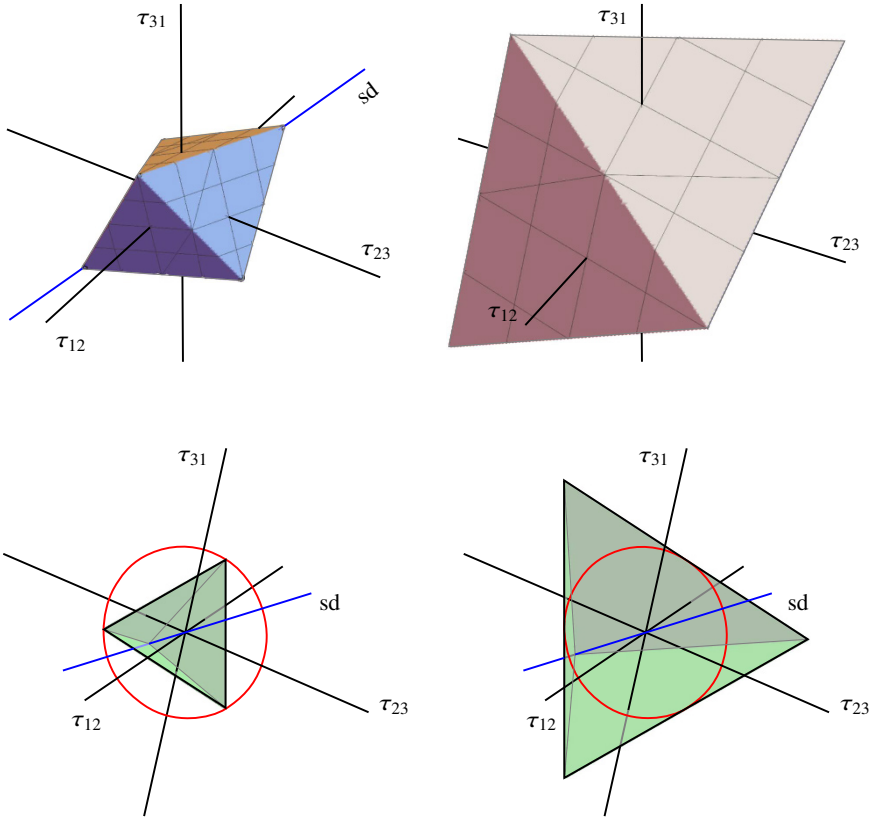
Fig. 2.10: IVLEV criterion $\hat{3}$ (2.84) as triangular dipyramid (left) and MARIOTTE criterion $\bar{3}$ (2.85) as triangular dipyramid (right) with $a = 1/3$ in the principal shear stress space (τ_{12}, τ_{23}, τ_{31}). The cross-sections with the ζ_0 – plane (2.75) through the origin orthogonal to the space diagonal is shown. The colour of both polyhedra below is changed for better clarity.

- criterion $\bar{3}$ as a triangular dipyramid (Fig. 2.10, right)

$$\max \left[-\tau_{12} + \tau_{23} + a\,\zeta, \; -\tau_{23} + \tau_{31} + a\,\zeta, \; -\tau_{31} + \tau_{12} + a\,\zeta, \right.$$

$$\left. -\tau_{12} + \tau_{23} - a\,\zeta, \; -\tau_{23} + \tau_{31} - a\,\zeta, \; -\tau_{31} + \tau_{12} - a\,\zeta \right] = \sigma_{\mathrm{eq}}, \quad a \in \mathbb{R}, \tag{2.85}$$
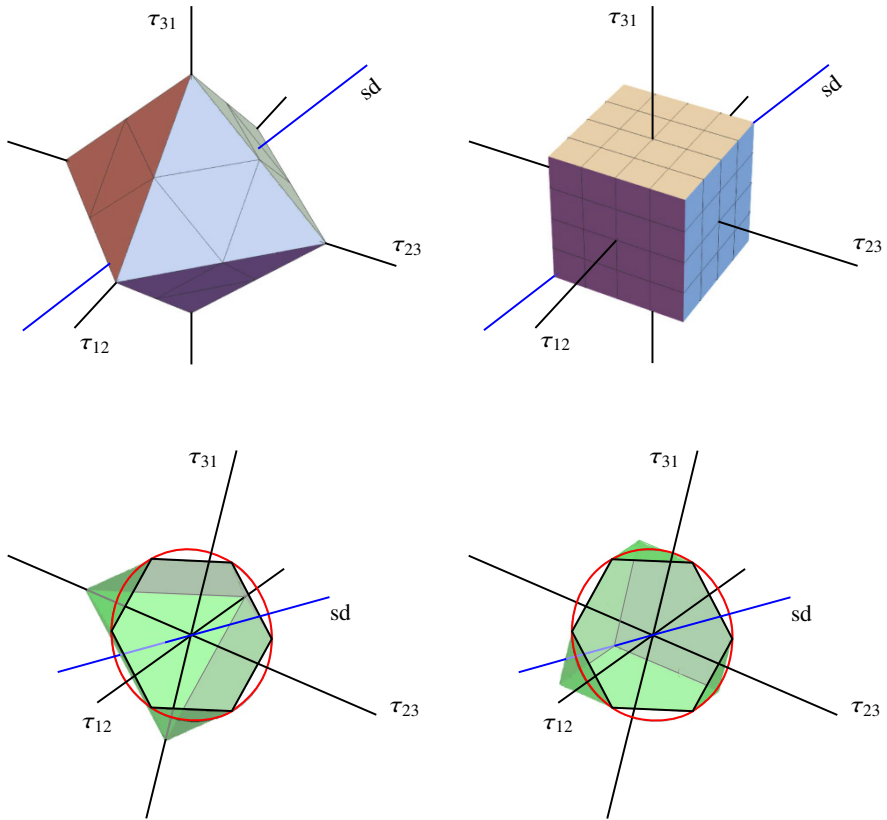
Fig. 2.11: TRESCA criterion $\hat{6}$ (2.86) as octahedron (left) and (2.88) as cube (right) in the principal shear stress space (τ_{12}, τ_{23}, τ_{31}), sd – space diagonal. The cross-sections with the ζ_0 – plane (2.75) through the origin orthogonal to the space diagonal is shown. The circle of VON MISES criterion (red) is presented for better comparison. The colour of both polyhedra below is changed for better clarity.

- criterion $\hat{6}$ with three options
  - as a octahedron (Fig. 2.11, left)

$$|\tau_{12}| + |\tau_{23}| + |\tau_{31}| = \sigma_{\text{eq}} \tag{2.86}$$

  or

$$\max \left[|\tau_{12} + \tau_{23} + \tau_{31}|, \ |\tau_{12} - \tau_{23} - \tau_{31}|, \ |\tau_{12} + \tau_{23} - \tau_{31}|, \right.$$
$$\left. |\tau_{12} - \tau_{23} + \tau_{31}| \right] = \sigma_{\text{eq}}, \tag{2.87}$$

  - as a cube (Fig. 2.11, right) [96, 100, 109, 111, 288, 307–309, 329]

$$2 \max \left[|\tau_{12}|, |\tau_{23}|, |\tau_{31}| \right] = \sigma_{eq} \tag{2.88}$$

and

– as a rhombohedron (trigonal trapezohedron) (Fig. 2.12, left), cf. (2.87)

$$\max \left[|\tau_{12} - \tau_{23} - \tau_{31}|, |\tau_{12} + \tau_{23} - \tau_{31}|, |\tau_{12} - \tau_{23} + \tau_{31}| \right] = \sigma_{eq}, \tag{2.89}$$

• criterion $\bar{6}$ as a rhombic dodecahedron (Fig. 2.12, right) [9, 27]
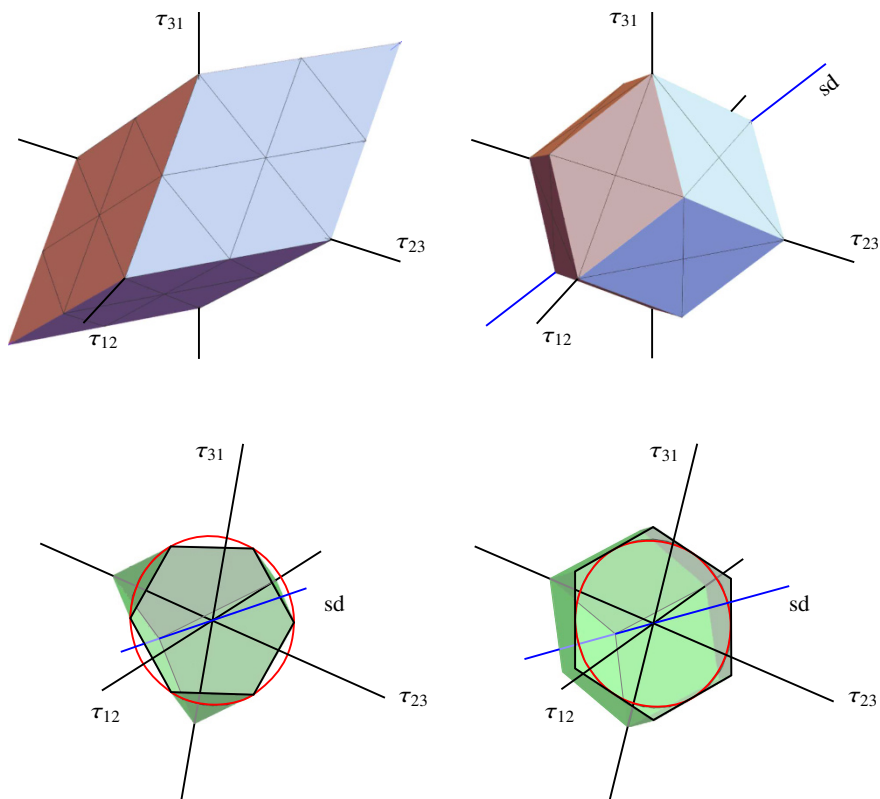
Fig. 2.12: Tresca criterion $\hat{6}$ as rhombohedron (2.89) (left) and Schmidt-Ishlinsky criterion $\bar{6}$ (2.90) as Yu rhombic dodecahedron (right) in the principal shear stress space $(\tau_{12}, \tau_{23}, \tau_{31})$, sd – space diagonal. The cross-sections with the ζ_0 – plane (2.75) through the origin orthogonal to the space diagonal is shown. The circle of von Mises criterion (red) is presented for better comparison. The colour of both polyhedra below is changed for better clarity.

$$\max \left[\, |\tau_{12} + \tau_{23}| \,, \, |\tau_{12} - \tau_{23}| \,, \, |\tau_{23} + \tau_{31}| \,, \, |\tau_{23} - \tau_{31}| \,, \right.$$
$$\left. |\tau_{31} + \tau_{12}| \,, \, |\tau_{31} - \tau_{12}| \, \right] = \sigma_{\mathrm{eq}}, \tag{2.90}$$

- criterion $\hat{1}2$ as a linear combination of

  - octahedron $\Phi_{\mathrm{octhahedron}}$ (2.86) and rhombic dodecahedron $\Phi_{\mathrm{rhombic\ dodecahedron}}$ (2.90): triakis octahedron (Fig. 2.13, left))

$$(1 - \alpha)\,\Phi_{\mathrm{octhahedron}} + \alpha\,\Phi_{\mathrm{rhombic\ dodecahedron}} = \sigma_{\mathrm{eq}}, \qquad \alpha = 4 - 2\sqrt{3}, \tag{2.91}$$
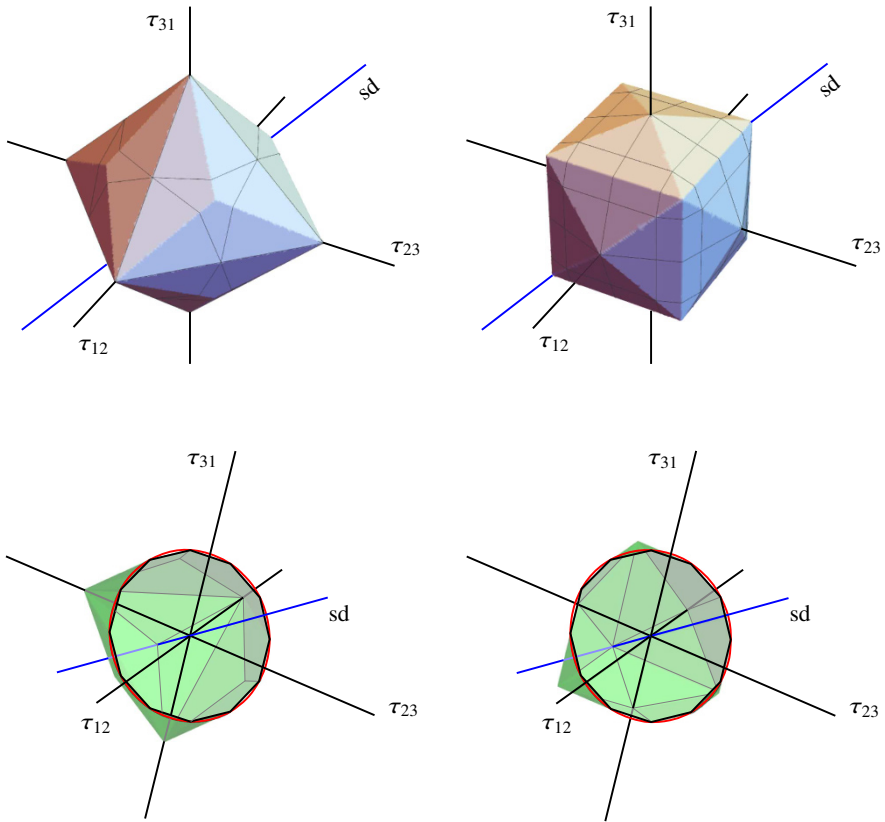
Fig. 2.13: S O K O L O V S K Y criterion $\hat{1}2$ as triakis octahedron (2.91) (left) and tetrakis hexahedron (2.92) (right) in the principal shear stress space (τ_{12}, τ_{23}, τ_{31}), sd – space diagonal. The cross-sections with the ζ_0 – plane (2.75) through the origin orthogonal to the space diagonal is shown. The circle of V O N M I S E S criterion (red) is presented for better comparison. The colour of both polyhedra below is changed for better clarity.

- cube (2.88) and rhombic dodecahedron (2.90): tetrakis hexahedron (Fig. 2.13, right)

$$(1-\alpha)\,\Phi_{\text{cube}} + \alpha\,\Phi_{\text{rhombic dodecahedron}} = \sigma_{\text{eq}}, \qquad \alpha = 4 - 2\sqrt{3}, \qquad (2.92)$$

- criterion $\bar{1}2$ with the edge truncations of octahedron or cube by a rhombic dodecahedron:

  - octahedron (2.86) or (2.87) and rhombic dodecahedron (2.90) (Fig. 2.14, left)

$$\max\left[\frac{\sqrt{3}}{2}\big(|\tau_{12}| + |\tau_{23}| + |\tau_{31}|\big),\, |\tau_{12}+\tau_{23}|,\, |\tau_{12}-\tau_{23}|,\right.$$
$$\left.|\tau_{23}+\tau_{31}|,\, |\tau_{23}-\tau_{31}|,\, |\tau_{31}+\tau_{12}|,\, |\tau_{31}-\tau_{12}|\right] = \sigma_{\text{eq}}, \qquad (2.93)$$

  - cube (2.88) and rhombic dodecahedron (2.90) (Fig. 2.14, right)

$$\max\left[\sqrt{3}\,|\tau_{12}|,\, \sqrt{3}\,|\tau_{23}|,\, \sqrt{3}\,|\tau_{31}|,\, |\tau_{12}+\tau_{23}|,\, |\tau_{12}-\tau_{23}|,\right.$$
$$\left.|\tau_{23}+\tau_{31}|,\, |\tau_{23}-\tau_{31}|,\, |\tau_{31}+\tau_{12}|,\, |\tau_{31}-\tau_{12}|\right] = \sigma_{\text{eq}}, \qquad (2.94)$$

No regular polyhedron is found for the criterion $\bar{1}2$.

The discussed formulations offer numerous possibilities for generalisation (Table 2.2):

- Hershey criterion $\hat{6} - \bigcirc$ (Subsect. 2.5.2) as a generalization of (2.83) for $m \geq 1$,
- Yu yield criterion (YYC) $\hat{6} - \hat{1}2 - \bar{6}$, see (2.91) or (2.92),
- multiplicative ansatz criterion (MAC) $\hat{6} - \bar{1}2 - \bar{6}$, see (2.93) or (2.94),
- C^0-CHS $\hat{6} - \hat{1}2|\hat{2}4|\bar{1}2 - \bar{6}$ as linear combination of YYC and MAC, etc.

Further polyhedra with three orthogonal planes of symmetry in the principal shear stress space are also known, e.g. [35], however, they do not reveal any physical evidence. Regular polyhedra are sometimes preferred in modelling because the equations are uniform, but their consideration provides only particular setting of the known criteria that can be used for comparison with the fitting results. Rhombicuboctahedron and hexaicosahedron have no sense in $(\tau_{12}, \tau_{23}, \tau_{31})$ space, since the intersections of octahedron and cube always lead to Tresca criterion $\hat{6}$ (Fig. 2.15).

Certain analogies of various foam structures or material defects to polyhedra with subsequent derivation of the relationships can be found in the literature, e.g. [13, 330, 331], among others. Sometimes space-filling polyhedra are preferred [9, 112]. However, the physical explanation for the polyhedra as yield restriction is unknown.

The figures in the principal shear stress space are deceptive and need a good 3D imagination (Figs. 2.9–2.15). Different 3D objects can lead on the same criterion. The cross section $\zeta = 0$ (2.75) in $(\tau_{12}, \tau_{23}, \tau_{31})$ space does not provide any new insights
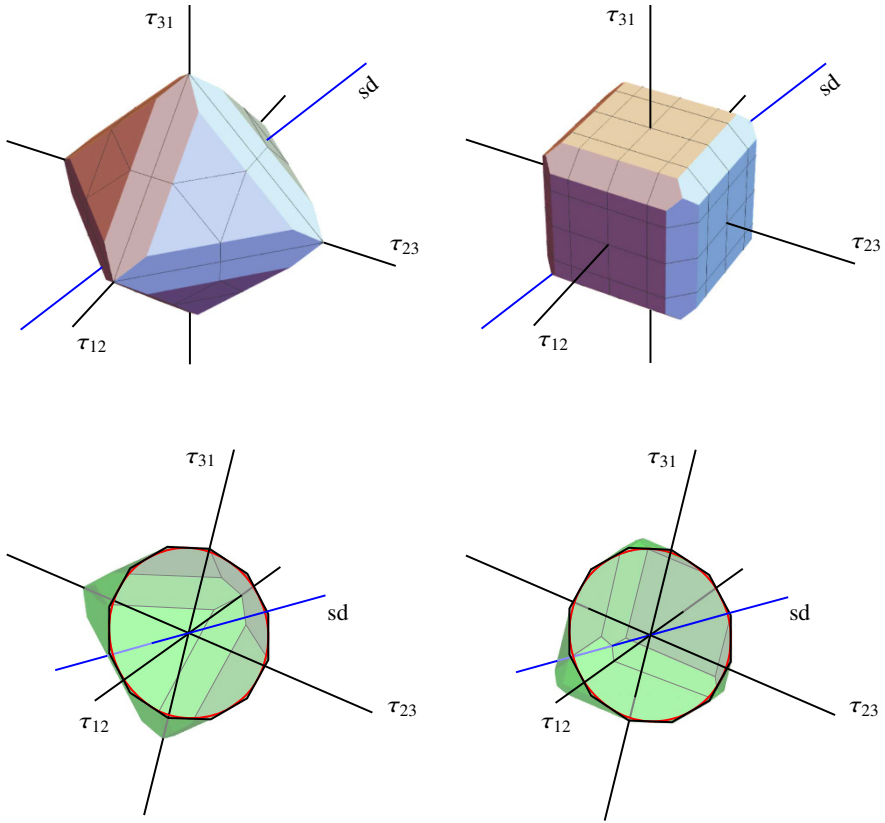
Fig. 2.14: Ishlinsky-Ivlev criterion $\bar{1}2$ with the edge truncations of octahedron (2.93) (left) and c«ube (2.94) (right) by a rhombic dodecahedron in the principal shear stress space $(\tau_{12}, \tau_{23}, \tau_{31})$, sd – space diagonal. The cross-sections with the ζ_0 – plane (2.75) through the origin orthogonal to the space diagonal is shown. The circle of von Mises criterion (red) is presented for better comparison. The colour of both polyhedra below is changed for better clarity.

compared to the π-plane. This derivation path "seems very pretty … but it's rather hard to understand" [332]. For this reason, such representations have not caught on.

2.5.2 Criteria as Power Functions

The criteria discussed below have prevailed in application because they meet PA1 and PA2. The major disadvantages are that they contradict PA3, PA4 and PA9.1. The formulation of these criteria in the deviatoric stresses s_I, s_II and s_III can be confusing and ambiguous. Most of the relationships are challenging in a numerical sense.

2.5.2.1 Hershey criterion $\hat{6} - \bigcirc$

Hershey criterion of hexagonal symmetry [260]

$$|\sigma_\mathrm{I} - \sigma_\mathrm{II}|^n + |\sigma_\mathrm{II} - \sigma_\mathrm{III}|^n + |\sigma_\mathrm{III} - \sigma_\mathrm{I}|^n = 2\,\sigma_\mathrm{eq}^n, \qquad n \geq 1 \tag{2.95}$$

is equivalent to the criterion formulated in the deviatoric stresses (2.8)

$$|s_\mathrm{I} - s_\mathrm{II}|^n + |s_\mathrm{II} - s_\mathrm{III}|^n + |s_\mathrm{III} - s_\mathrm{I}|^n = 2\,\sigma_\mathrm{eq}^n, \qquad n \geq 1. \tag{2.96}$$

The values of the criterion (2.95) are $r_{60} = 1$,

$$r_{30} = \sqrt{3}\left(1 + 2^{n-1}\right)^{-1/n} \tag{2.97}$$

and

$$r_{15} = 2^{1/n}\left[\left(\frac{2}{3} - \frac{1}{\sqrt{3}}\right)^{n/2} + \left(2 - \sqrt{3}\right)^{n/2}\frac{1 + \left(\sqrt{3} - 1\right)^n}{\left(2\sqrt{3} - 3\right)^n}\right]^{-1/n}. \tag{2.98}$$

The particular setting of the power n is summarized in Table 2.4 and shown in Fig. 2.16.

The setting $n = 4$ in (2.95) leads to [38]

$$2 \times \left(3\,I_2'\right)^2 = 2\,\sigma_\mathrm{eq}^4,$$

see (2.83) with $n = 4$ and Fig. 2.9 on the right and cf. von Mises criterion (2.41) with $n = 2$. The setting $n = 6$ results in the invariant formulation [38]

$$66\left(I_2'\right)^3 + 3^4\left(I_3'\right)^2 = 2\,\sigma_\mathrm{eq}^6,$$
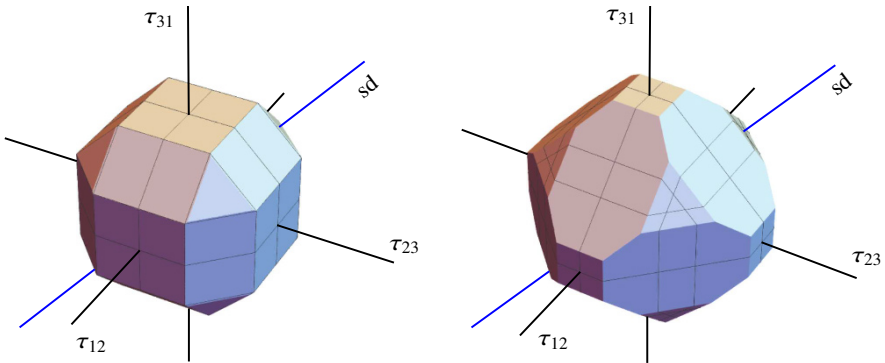
Fig. 2.15: Rhombicuboctahedron and hexaicosahedron in the principal shear stress space $(\tau_{12}, \tau_{23}, \tau_{31})$, sd – space diagonal.

what corresponds to DRUCKER criterion [2, 19, 333, 334]

$$\frac{\left(3I_2'\right)^3 + c_6\left(I_3'\right)^2}{1 + c_6\left(\dfrac{2}{3^3}\right)^2} = \sigma_{eq}^6 \qquad \text{and} \qquad c_6 \in \left[-\frac{3^5}{2^2}, \frac{3^6}{2^3}\right], \qquad (2.99)$$

with the setting $c_6 = -3^6/22$ (Table 2.4).

The surfaces with the powers $n = 1, 1.5416, 2, 4, 6$ and ∞ are shown in the π-plane (Fig. 2.17). The powers $n = 1.5416$ and 6 with the same value

$$r_{30} = \frac{3^{1/3}}{11^{1/6}} \approx 0.9671$$

are chosen for the better comparison (Table 2.4). Even though the powers $n = 1$ and $n \to \infty$ as well as $n = 2$ and 4 provide respective the same surfaces in the principal normal stress space, the resulting surfaces in the principal shear stress space differ.

HERSHEY criterion (2.95) is formulated in the principal shear stress space, cf. (2.83)

$$2^{n-1}\left[|\tau_{13}|^n + |\tau_{23}|^n + |\tau_{31}|^n\right] = \sigma_{eq}^n, \qquad n \geq 1 \qquad (2.100)$$

The volume of the closed surfaces (2.100) in the principal shear stress space [335]
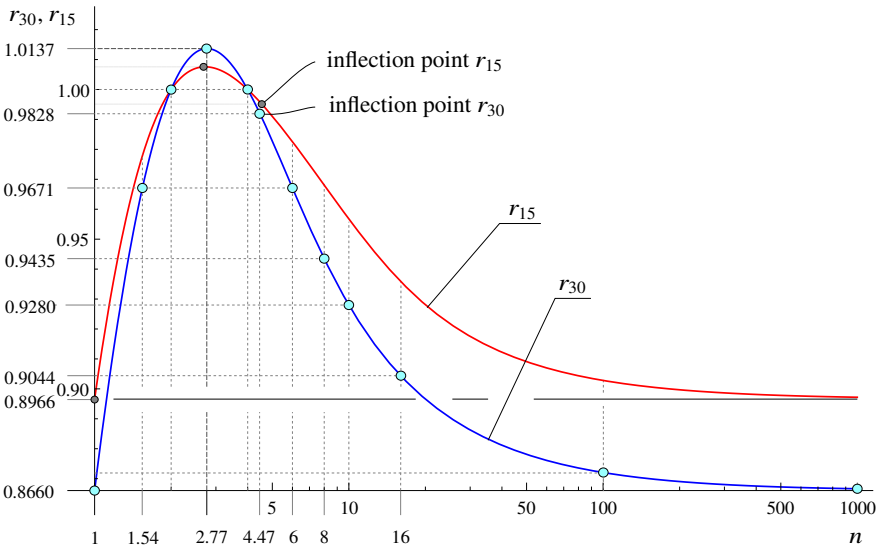
Fig. 2.16: HERSHEY criterion $\hat{6} - \bigcirc$ (2.95): log-linear plot of the values r_{30} (2.97) and r_{15} (2.98) as function of the power $n \geq 1$. Some particular points are depicted for clarity (Table 2.4).

$$V_n = 2^3 \frac{\left[\Gamma\left(1+\dfrac{1}{n}\right)\right]^3}{\Gamma\left(1+\dfrac{3}{n}\right)} \tag{2.101}$$

with Γ for the gamma function [139] increases with increasing power n (Fig. 2.18)

$$\frac{V_n}{V_2} \in \left[\frac{1}{\pi}, 2^3 \times \frac{3}{4\pi}\right]. \tag{2.102}$$

The inflection point results numerically in $n \approx 1.0824$.

HERSHEY criterion (2.95) includes two basic shapes $\hat{6}$ and $\bigcirc$ and is designated as $\hat{6} - \bigcirc$, cf. LEMAITRE-CHABOCHE criterion (Subsect. 2.4.1). For numerical robustness in the application (PA6), it is advisable to restrict the power n as $n \in [1, 12]$. This criterion with modulus (PA3) and the parameter n as a power (PA9.1) can not be recommended due to high numerical effort with limited fitting possibilities. According to PAUL [264], HERSHEY criterion (2.95) is rather "of academical interest" and has nowadays "any great practical advantage". It should be replaced by the more effective SZWED criterion $\hat{6} - \bigcirc - \bar{6}$, which also has one parameter (Table 2.2).

The values r_{30} (2.97) and r_{15} (2.98) of HERSHEY criterion are easy to calculate. For any $n \in \mathbb{N}$, HERSHEY criterion (2.95) can be formulated as a function of the invariants $\Phi\left(I_2', I_3'\right)$ [38], but such formulation in the general case $n \geq 1$ is
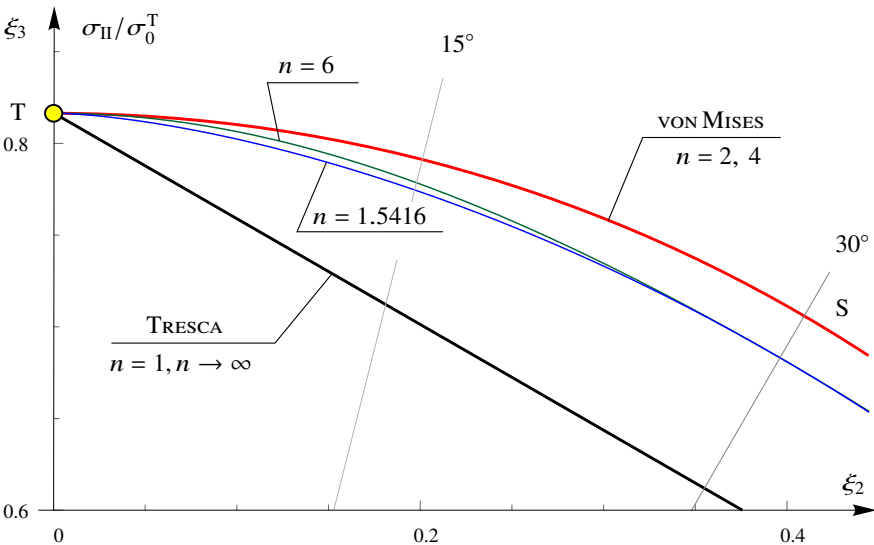
Fig. 2.17: HERSHEY criterion $\hat{6} - \bigcirc$ (2.100) in the π-plane. The diagram is cropped to highlight differences of the surfaces with the setting $n = 1.5416$ and 6 at the stress angle $\theta = \pi/12$ (Table 2.4).

unknown (PA4). The criterion $\hat{6} - \bigcirc$ is considered here because it is applied in Subsubsect. 2.5.2.2.

2.5.2.2 KARAFILLIS-BOYCE criterion $\hat{6} - \hat{1}\hat{2}| \bigcirc |\bar{1}\bar{2} - \bar{6}$

KARAFILLIS-BOYCE criterion of hexagonal symmetry [263], see also [9, 27, 49, 97, 108, 256, 280, 310] among other,

$$\frac{1-\alpha}{2} \left(|s_{\mathrm{I}} - s_{\mathrm{II}}|^m + |s_{\mathrm{II}} - s_{\mathrm{III}}|^m + |s_{\mathrm{III}} - s_{\mathrm{I}}|^m \right) +$$
$$\frac{\alpha}{2} \frac{3^m}{2^{m-1}+1} \left(|s_{\mathrm{I}}|^m + |s_{\mathrm{II}}|^m + |s_{\mathrm{III}}|^m \right) = \sigma_{\mathrm{eq}}^m, \quad m \geq 1, \quad \alpha \in [0, 1] \tag{2.103}$$

yields the values

$$r_{60} = 1 \qquad \text{and} \qquad r_{30} = \sqrt{3} \left[(1-\alpha)\left(1+2^{m-1}\right) + \alpha \frac{3^m}{1+2^{m-1}} \right]^{-1/m}. \tag{2.104}$$

The value $r_{60} = 1$ results for any $m \geq 1$ because of the modulus function [280], cf. [97, 263]. The equations for the values r_{15} and $r_{7.5}$ are omitted due to complexity.

It follows with (2.104) for the setting $r_{30} = 1$
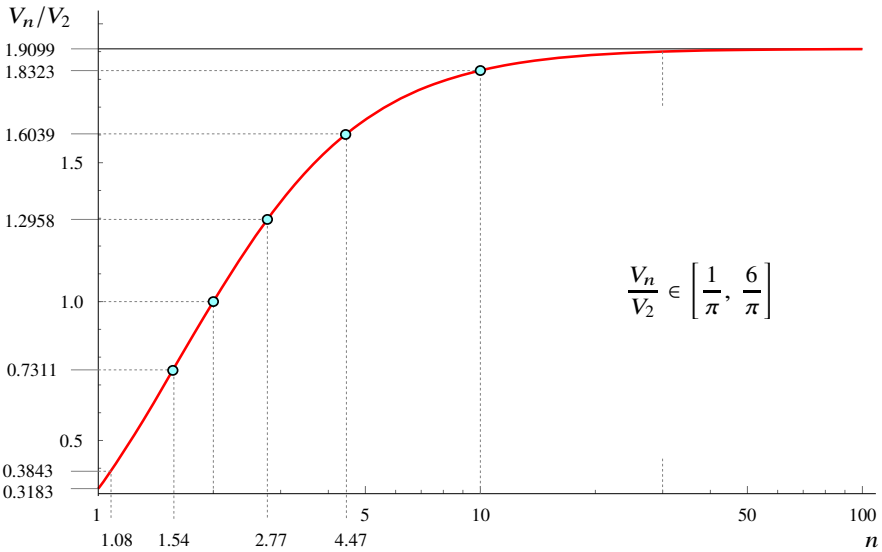
Fig. 2.18: HERSHEY criterion $\hat{6} - \bigcirc$ (2.95): log-linear plot of the volume relation V_n/V_2 (2.102) in the principal shear stress space as function of n. Some particular points are shown for clarity (Table 2.4).

$$\alpha = \left(1 + \frac{3^{m/2}}{1+2^{m-1}}\right)^{-1}$$

and VON MISES $\bigcirc$, SOKOLOVSKY $\hat{12}$ and ISHLINSKY-IVLEV $\bar{12}$ criteria can be obtained (Table 2.5).

Although some problems are treated with the criterion (2.103), it cannot be recommended for practice: the computation is unstable with the higher powers of m because of loss of order (PA6). The parameters α and m have no geometric or mechanical meaning (PA9.5). A straightforward physical interpretation of the criterion (2.103) is unknown. This criterion with $m \geq 2$ can not be recommended for use: no clear relationship between the geometry and the parameters (PA9.6), but the application can be thought of in the range $m \in [1, 2]$.

The particular points $P_6, P_{12}, P_{16}, P_{26}, P_{30}, T_{30}$ and T_{41} (Table 2.5) in the $r_{30} - r_{15}$ diagram (Fig. 2.19) lie outside the range with $\alpha \in [0, 1]$ and $m \in [1, 2]$ and the convexity range of ROSENDAHL C^1-criterion (Table 2.2). If required, they can be described with the C^0-criterion $\hat{6} - \hat{12} \,|\, \bigcirc \,|\, \bar{12} - \bar{6}$ of hexagonal symmetry (Table 2.2).

The extreme value r_{15} with $r_{30} = 1$ is reached at $m = 41$. For $m > 41$ the level lines $m = $ const. move in the direction $\hat{6} - \bar{12}$ and, with increasing power, on to the criterion $\hat{6}$. The transition $\bigcirc - \bar{12}$ can not be described with (2.103). The criterion $\hat{6} - \bar{12} - \bar{6}$ with $\alpha \in [0, 1]$ and $m \to \infty$ is obtained numerically with $\alpha \in [1 - 10^{-500}, 1 - 10^{-1}]$ and $m = 1000$, which lies in the realm of mathematical curiosity, i.e. no possibility of practical use. The criterion $\bar{12}$ follows then with $\alpha = 10^{-62}$ (Table 2.5).

YU [9, 27] compared KARAFILLIS-BOYCE criterion (2.103) with TAN criterion $\hat{6} - \bigcirc - \bar{6}$ [265]

$$\sigma_{\text{eq}} = \begin{cases} \max\left[(4\eta^2 - 9)\,\tau_i^2 + (\tau_k - \tau_j)^2\right], & \frac{3}{2} \leq \eta \leq \sqrt{3},\ \bar{6} - \bigcirc; \\ \max\left[\eta^2\,\tau_i^2 + (4 - \eta^2)\,(\tau_k - \tau_j)^2\right], & \sqrt{3} \leq \eta \leq 2,\ \bigcirc - \hat{6} \end{cases} \tag{2.105}$$

with the denotation

$$\tau_i = \frac{1}{2}\,(\sigma_j - \sigma_k), \qquad i \neq j \neq k, \qquad i, j, k = 1, 2, 3.$$

The values r_{30} and r_{15} follows for the criterion (2.105) with

$$r_{30} = \frac{\sqrt{3}}{\eta}, \qquad \eta \in \left[\frac{3}{2}, 2\right]$$

and

$$r_{15} = \begin{cases} \left(-1 + \sqrt{3} + \dfrac{2 - \sqrt{3}}{r_{30}^2}\right)^{-1/2}, & \dfrac{2}{\sqrt{3}} \geq r_{30} \geq 1,\ \bar{6} - \bigcirc; \\[4mm] \left(2 - \sqrt{3} + \dfrac{-1 + \sqrt{3}}{r_{30}^2}\right)^{-1/2}, & 1 \geq r_{30} \geq \dfrac{\sqrt{3}}{2},\ \bigcirc - \hat{6}. \end{cases} \tag{2.106}$$

Table 2.5: KARAFILLIS-BOYCE criterion $\hat{6} - \widehat{12}\,|\,\bigcirc\,|\,\overline{12} - \overline{6}$ (2.103): setting of the parameter.

Designation	Criterion	α	m	r_{30}	r_{15}	Comments
			Particular setting			
-	HERSHEY	0	≥ 1	-	-	Eqs. (2.95, (2.96)
-	-	0.4904	3	1	1.0006	-
P_6	-	0.17	6	0.9765	0.9877	[108, 263]
P_{12}	-	0.3	12	0.9410	0.9652	[108, 263, 311]
-		0.7376		1	1.0004	-
P_{16}	-	0.5	16	0.9421	0.9662	[328]
-		0.8332		1	1.0023	-
P_{26}	-	0.63	26	0.9240	0.9538	[328]
-		0.9546		1	1.0098	-
-		[0, 1]		-	-	recommended [263]
P_{30}	-	0.8350	30	0.9410	0.9702	[108, 263, 311]
T_{30}		0.9480		0.9776	0.9992	[263, 311]
-		0.9740		1	1.0125	-
-	-	0.9803	32	1	1.0137	-
P_{41}	-	0.9945	41	1	1.0181	cf. ISHLINSKY-IVLEV
			Basic criteria			
$\overline{12}$	ISHLINSKY-IVLEV	$1 - 10^{-62}$	∞	1	$\sqrt{2}\left(\sqrt{3}-1\right)$	unstable*
$\hat{6}$	TRESCA	0	$\dfrac{1}{\infty}$	$\sqrt{3}/2$	$\sqrt{3/2}\left(\sqrt{3}-1\right)$	Table 2.4
$\overline{6}$	SCHMIDT-ISHLINSKY	1	$\dfrac{1}{\infty}$	$2/\sqrt{3}$	$\sqrt{2}\left(\sqrt{3}-1\right)$	[280]
$\widehat{12}$	SOKOLOVSKY	$4 - 2\sqrt{3}$	1	1	$\dfrac{1}{2}\sqrt{2+\sqrt{3}}$	-
		[0, 1]	2			[259, 263, 280]
		[0, 1]	4			[280]
$\bigcirc$	VON MISES	11/20	6	1	1	-
		43/70	8			-
		19/28	10			-

* – obtained with $m = 1000$.

The lines $r_{15}\,(r_{30})$ lie below the lines $\alpha = 0$ and $\alpha = 1$ in the $r_{30} - r_{15}$ diagram (Fig. 2.19, the level lines (2.106) are not shown). TAN criterion $\hat{6} - \bigcirc - \bar{6}$ (2.105) can not be recommended due to the case discrimination and the max function (PA3).

YU $\hat{6} - \hat{12} - \bar{6}$ criterion can be obtained from (2.103) with

$$(1 - \alpha) \max \left[|s_{\mathrm{I}} - s_{\mathrm{II}}|, |s_{\mathrm{II}} - s_{\mathrm{III}}|, |s_{\mathrm{III}} - s_{\mathrm{I}}| \right] +$$

$$\alpha \frac{3}{2} \max \left[|s_{\mathrm{I}}|, |s_{\mathrm{II}}|, |s_{\mathrm{III}}| \right] = \sigma_{\mathrm{eq}}, \qquad \alpha \in [0, 1] \tag{2.107}$$

and yields the values

$$r_{30} = \frac{2\sqrt{3}}{4 - \alpha}, \qquad r_{15} = \frac{6\sqrt{2}}{2\left(3 + \sqrt{3}\right) - \alpha\left(3 - \sqrt{3}\right)}.$$

SOKOLOVSKY criterion $\hat{12}$ follows with $r_{30} = 1$ or $\alpha = 4 - 2\sqrt{3}$, see (2.91) and (2.92).

The formulation (2.107) is not recommended for practice because of the max and modulus functions. It makes sense to replace (2.107) by ROSENDAHL C^1-criterion $\hat{6} - \hat{12} | \bigcirc - \bar{6}$ as function of two parameters in addition to σ_{eq} (Table 2.2).

KARAFILLIS-BOYCE $\hat{6} - \hat{12} | \bigcirc | \bar{12} - \bar{6}$ criterion (2.103) can be reformulated in the principal shear stresses
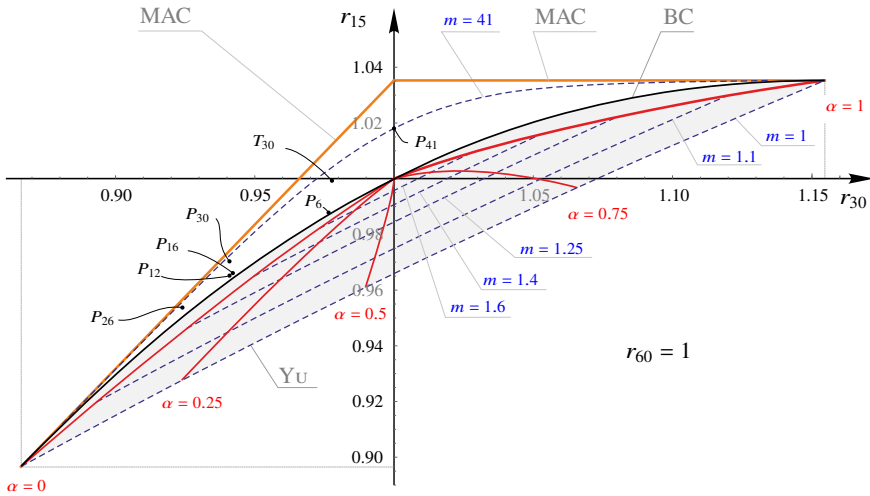
Fig. 2.19: KARAFILLIS-BOYCE criterion $\hat{6} - \hat{12} | \bigcirc | \bar{12} - \bar{6}$ (2.103) in the $r_{30} - r_{15}$ diagram (Fig. 2.8). The lines $\alpha = $ const., $m \in [1, 2]$ (solid red) and $m = $ const., $\alpha \in [0, 1]$ (dashed blue) are shown. The shaded area corresponds to ROSENDAHL C^1-criterion $\hat{6} - \hat{12} | \bigcirc - \bar{6}$ (Subsubsect. 2.5.5.2).

$$\sigma_{\text{eq}}^m = \frac{1-\alpha}{2} F_1 + \frac{\alpha}{2} \frac{3^m}{2^{m-1}+1} F_2 \tag{2.108}$$

with the terms (2.100)

$$F_1 = 2^m \left[|\tau_{12}|^m + |\tau_{23}|^m + |\tau_{31}|^m \right] \tag{2.109}$$

and (2.76) based on (2.14)

$$F_2 = \left(\frac{2}{3}\right)^m \left[|\tau_{12} - \tau_{23}|^m + |\tau_{23} - \tau_{31}|^m + |\tau_{31} - \tau_{12}|^m \right] \tag{2.110}$$

or, subject to the condition $\tau_{12} + \tau_{23} + \tau_{31} = 0$ (2.13), as

$$\begin{aligned} F_2 = \frac{1}{2} \left(\frac{2}{3}\right)^m &\left[|2\,\tau_{12} + \tau_{23}|^m + |2\,\tau_{12} + \tau_{31}|^m + |2\,\tau_{31} + \tau_{12}|^m + \right. \\ &\left. |2\,\tau_{31} + \tau_{23}|^m + |2\,\tau_{23} + \tau_{12}|^m + |2\,\tau_{23} + \tau_{31}|^m \right]. \end{aligned} \tag{2.111}$$

With F_2 in (2.110) and (2.111), different polyhedra result in the principal shear stress space, but the cross-section with the ζ_0-plane (2.75) remains the same at the given setting. However, Schmidt-Ishlinsky $\bar{6}$ and Ishlinsky-Ivlev $\bar{12}$ criteria can not be obtained as a polyhedra.

2.5.2.3 Cazacu et al. Criterion $\hat{3} - \bigcirc | \bar{6} - \bar{3}$

Cazacu et al. criterion [39, 108, 311, 322, 336–338]

$$3^m \frac{(|s_1| - \kappa\,s_1)^m + (|s_2| - \kappa\,s_2)^m + (|s_3| - \kappa\,s_3)^m}{2\,(1+\kappa)^m + 2^m\,(1-\kappa)^m} = \sigma_{\text{eq}}^m \tag{2.112}$$

is a function of two parameters

$$m \geq 1 \qquad \text{and} \qquad \kappa \in [-1, 1]. \tag{2.113}$$

The values r_{60} and r_{30} follows with [108]

$$r_{60} = \left(\frac{2^m\,(1-\kappa)^m + 2\,(1+\kappa)^m}{2\,(1-\kappa)^m + 2^m\,(1+\kappa)^m} \right)^{1/m}, \tag{2.114}$$

$$r_{30} = \frac{1}{\sqrt{3}} \left(\frac{2^m\,(1-\kappa)^m + 2\,(1+\kappa)^m}{(1-\kappa)^m + (1+\kappa)^m} \right)^{1/m}. \tag{2.115}$$

The parameter setting for the basic criteria is given in Table 2.6. The substitution

Table 2.6: Cazacu et al. criterion $\hat{3} - \bigcirc | \bar{6} - \bar{3}$ (2.112): parameter setting for the basic criteria.

Designation	Criterion	κ	m	r_{60}	r_{30}	Comments and References
		0	2			[39, 108, 311, 336–338]
$\bigcirc$	von Mises	0	4	1	1	-
		∞	2			cf. (2.113)
		0	∞			-
$\bar{6}$	Schmidt-Ishlinsky	$[-1, 1]$	1	1	$2/\sqrt{3}$	[39]
		$\pm\infty$	∞			cf. (2.113)
$\hat{3}$	Ivlev	1	∞	1/2	$1/\sqrt{3}$	[39]
$\bar{3}$	Mariotte	-1	∞	2	$2/\sqrt{3}$	[39]

$$\eta = \frac{1-\kappa}{1+\kappa}, \qquad \kappa \neq -1 \tag{2.116}$$

in Eqs. (2.114) and (2.115)

$$r_{60} = \left(\frac{2^m \eta^m + 2}{2\eta^m + 2^m} \right)^{1/m}, \qquad r_{30} = \frac{1}{\sqrt{3}} \left(\frac{2^m \eta^m + 2}{\eta^m + 1} \right)^{1/m}. \tag{2.117}$$

resolved with respect of η^m results in

$$\eta^m = \frac{-2 + 2^m r_{60}^m}{2^m - 2 r_{60}^m} \qquad \text{and} \qquad \eta^m = \frac{-2 + 3^{a/2} r_{30}^m}{2^m - 3^{a/2} r_{30}^m}, \tag{2.118}$$

and finally combined, in

$$\frac{-2 + 2^m r_{60}^m}{2^m - 2 r_{60}^m} = \frac{-2 + 3^{a/2} r_{30}^m}{2^m - 3^{a/2} r_{30}^m}. \tag{2.119}$$

The numerical solution of (2.119) depends on the starting point, see e.g. the parameter sets for the particular points A_2 and A_4, B_2 and B_4, F_2 and F_6, G_2 and G_6, J_2 and J_3 with the same values r_{60} and r_{30}, respectively (Table 2.7).

With the predefined powers m_1 and m_2 in the system of Eqs. (2.114) and (2.115)

$$\begin{cases} \left[\dfrac{2^{m_1} (1-\kappa_1)^{m_1} + 2 (1+\kappa_1)^{m_1}}{2 (1-\kappa_1)^{m_1} + 2^{m_1} (1+\kappa_1)^{m_1}} \right]^{m_2/m_1} = \dfrac{2^{m_2} (1-\kappa_2)^{m_2} + 2 (1+\kappa_2)^{m_2}}{2 (1-\kappa_2)^{m_2} + 2^{m_2} (1+\kappa_2)^{m_2}}, \\[4mm] \left[\dfrac{2^{m_1} (1-\kappa_1)^{m_1} + 2 (1+\kappa_1)^{m_1}}{(1-\kappa_1)^{m_1} + (1+\kappa_1)^{m_1}} \right]^{m_2/m_1} = \dfrac{2^{m_2} (1-\kappa_2)^{m_2} + 2 (1+\kappa_2)^{m_2}}{(1-\kappa_2)^{m_2} + (1+\kappa_2)^{m_2}} \end{cases} \tag{2.120}$$

Table 2.7: CAZACU et al. criterion $\hat{3} - \bigcirc\,|\,\bar{6} - \bar{3}$ (2.112): setting of the parameters κ and m.

Designation	Criterion	κ	m	r_{60}	r_{30}	Comments and References
-	-	0.2	2	0.8790	0.9337	[39, 311]
-	-	-0.2	2	1.1376	1.0622	[39, 311]
A_2	-	0.3098	2	0.8264	0.9009	[39, 338]
B_2	-	-0.3098	2	1.2101	1.0902	[39, 338]
-	-	0.4	2	0.7913	0.8776	[39, 311]
-	-	-0.4	2	1.2637	1.1090	-
C_2	-	0.4340	2	0.7800	0.8698	[108]
D_2	-	-0.4340	2	1.2821	1.1151	[108]
E_2	-	0.4514	2	0.7745	0.8776 *	[108]
-	-	-0.4514	2	1.2910	1.1180	-
F_2	-	0.5176	2	0.7564	0.8531	-
G_2	-	-0.5176	2	1.3221	1.1279	-
H_2	-	0.9	2	0.7086	0.8176	[39, 336]
I_2	-	-0.9	2	1.4113	1.1539	[39, 336]
-	-	1	2	0.7071	0.8165	[39]
-	-	-1	2	1.4142	1.1547 **	-
J_2	-	-0.0770	2.5982	1.0799	1.0237	cf. point J_3
-	-	0	2.7670	1	0.9865	$\dfrac{dr_{30}}{dm} = 0$
-	-	0	3	1	0.9873	$\dfrac{dr_{30}}{dm} = 0,\, m \in \mathbb{N}$
-	-	0.0645	3	0.9260	0.9479	-
J_3	-	-0.0645	3	1.0799	1.0237	[39, 311, 338]
-	-	0.1995	3	0.7987	0.8776 *	-
-	-	-0.1995	3	1.2521	1.0844	-
-	-	0	4.6087	1	1.0106	$\dfrac{dr_{30}}{dm} = 0$
B_4	-	-0.1141	4.6618	1.2101	1.0902	cf. point B_2
A_4	-	0.1142	4.6643	0.8264	0.9009	cf. point A_2
F_6	-	0.1531	6	0.7564	0.8531	-
G_6	-	-0.1531	6	1.3221	1.1279	-
-	-	1/7	∞	0.75	0.8776 *	-

* – This value corresponds to the value $r_{30} = \sqrt{3}/2$ of TRESCA criterion (Table 2.1).
** – This value corresponds to the value $r_{30} = 2/\sqrt{3}$ of SCHMIDT-ISHLINSKY criterion.

the parameters κ_1 and κ_2 for the coinciding points in the $r_{60} - r_{30}$-diagram can be obtained (Fig. 2.20). The solution of (2.120) also depends on the starting point, see e.g. the points F_2 and F_6, G_2 and G_6 with $m_1, m_2 \in \mathbb{N}$ (Table 2.7). Differences for the sets of the points discussed above (Table 2.7) in the value r_{15}

$$r_{15} = \left(\frac{\left(2 - \sqrt{3}\right)^{-m/2} \left[2^m (1-\kappa)^m + 2(1+\kappa)^m\right]}{\left(2 + \sqrt{3}\right)^m (1-\kappa)^m + \left[1 + \left(1 + \sqrt{3}\right)^m\right] (1+\kappa)^m} \right)^{1/m} \tag{2.121}$$

lie in the third decimal place and are thus negligible.

The criterion (2.112) can be reformulated in the principal shear stresses with (2.14)

$$3^m \left(\frac{2}{3}\right)^m \frac{1}{2(1+\kappa)^m + 2^m (1-\kappa)^m} \left[\left(|\tau_{12} - \tau_{23}| + \kappa (\tau_{12} - \tau_{23})\right)^m + \right.$$
$$\left. \left(|\tau_{23} - \tau_{31}| + \kappa (\tau_{23} - \tau_{31})\right)^m + \left(|\tau_{31} - \tau_{12}| + \kappa (\tau_{31} - \tau_{12})\right)^m \right] = \sigma_{\text{eq}}^m. \tag{2.122}$$

This formulation (2.122) describes open surfaces along the space diagonal $\tau_{12} = \tau_{23} = \tau_{23}$ in the principal shear stress space (Subsubsect. 2.5.1.1).

The disadvantages of CAZACU et al. criterion (2.112) are

- the criterion (2.112) includes the modulus function (PA3),
- it cannot be expressed as a function of the invariants in general case (PA4),
- the parameter $m \geq 1$ is a power (PA9.1),
- SAYIR C^1-criterion $\hat{3} - \bigcirc - \bar{3}$ (Table 2.2) can not be described with (2.112) as function of one parameter,
- the level lines $\kappa = $ const. intersect in the $r_{60} - r_{30}$ diagram (Fig. 2.20): same points can be obtained with different parameter setting (PA9.6) and
- the parameter κ is oversensitive in the area around 0 and the parameter m has low sensitivity in the range $m > 20$.

Equations (2.119) and (2.120) of the criterion (2.112) are numerically challenging and, due to the ambiguity of the calculation, rather impractical, although some results are obtained for particular applications. Recommended setting is $m = 2$ and 3 (Table 2.7) [338].

HAYTHORNTHWAITE criterion $\hat{3} - \bar{6} - \bar{3}$ (Table 2.2) results with $m \to \infty$ in (2.112)

$$3 \frac{\max\left[|s_1| - \kappa s_1, |s_2| - \kappa s_2, |s_3| - \kappa s_3\right]}{\max\left[2(1-\kappa), 1+\kappa\right]} = \sigma_{\text{eq}}, \qquad \kappa \in [-1, 1]. \tag{2.123}$$

The values of the criterion (2.123) are

$$r_{60} = \frac{\max\left[2(1-\kappa), 1+\kappa\right]}{\max\left[2(1+\kappa), 1-\kappa\right]}, \qquad r_{30} = \frac{\max\left[2(1-\kappa), 1+\kappa\right]}{\max\left[1+\kappa, 1-\kappa\right]}. \tag{2.124}$$
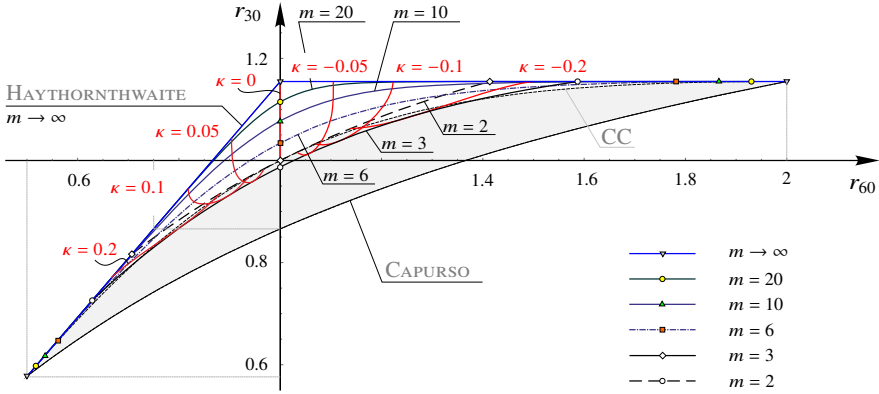
Fig. 2.20: CAZACU et al. criterion $\hat{3} - \bigcirc | \bar{6} - \bar{3}$ (2.112) in the $r_{60} - r_{30}$ diagram. The lines $\kappa = \text{const.}$, $\kappa \in [-1, 1]$ (solid red) and $m = \text{const.}$, $m \geq 1$ (black and blue) are shown.

Equation of the criterion $\hat{3} - \bar{6} - \bar{3}$ (2.123) cannot be recommended for use because of the case discrimination with the max and modulus functions (PA3).

2.5.3 $\bigcirc$-Criteria

The C^1-criteria according to the schemata (2.38)–(2.39) and containing only one basic shape $\bigcirc$ can be grouped together with (Table 2.8)

$$\left(\sqrt{3 I_2'}\right)^m \frac{1 + c_n \left[\dfrac{3\sqrt{3}}{2} \dfrac{I_3'}{\left(I_2'\right)^{3/2}} \right]^n}{1 + c_n} = \sigma_{\text{eq}}^m, \qquad m \in \mathbb{R}, \qquad n \in \mathbb{N}. \tag{2.125}$$

The parameter c_n is weighted with $\left(3\sqrt{3}/2\right)^n$ according to the invariant $\cos 3\theta$ (2.24) for the following generalization. The values are

$$r_{60}^m = \frac{1 + c_n}{1 + (-1)^n c_n} \tag{2.126}$$

$$r_{30}^m = 1 + c_n \tag{2.127}$$

and

$$r_{15}^m = \frac{2^n \left(1 + c_n\right)}{2^n + \left(2 - \sqrt{3}\right)^{n/2} \left(1 + \sqrt{3}\right)^n c_n}. \tag{2.128}$$

Table 2.8: Power setting for the $\bigcirc$-criterion (2.125) with the parameter limits and corresponding values. The extreme values r_{60} and the extreme values r_{30} and r_{15} with $r_{60} = 1$ are highlighted in bold.

Name	m	n	c_n	r_{60}	r_{30}	r_{15}	References
GENIEV-KISSJUK	-2	1	-2/11	1.2019	1.1055	1.0320	[339, 340],
			2/11	0.8321	0.9199	0.9772	see also [35, 341–343]
–	-2	2	-1/10	1	1.0541	1.0274	[35]
			1/9		0.9487	0.9747	
related to LEYTES	-1	1	-1/10	1.2222	1.1111	1.0325	[343–346],
			1/10	0.8181	0.9091	0.9734	see also [340–342, 347]
	-1	2	-1/19	1	1.0556	1.0278	
			1/18	1	0.9474	0.9737	
–	1	1	-1/8	0.7778	0.8750	0.9598	[348–350]
			1/8	1.2857	1.1250	1.0336	
CAZACU–REVIL-BAUDARD	1	2	-1/18	1	0.9444	0.9714	[351]
			1/17		1.0588	1.0286	
–	1	4	-0.0490	1	0.9510	0.9628	[36, 112]
			1/35		1.0286	1.0213	
–	2	1	-2/7	0.7454	0.8452	0.9461	[116, 352, 353]
			2/7	1.3416	1.1339	1.0342	
PRAGER	2	2	-1/9	1	0.9428	0.9703	[354, 355], see also
			1/8		1.0607	1.0290	[3, 116, 197, 352]
–	2	4	-0.0963	1	0.9507	0.9623	[36, 112]
			1/17		1.0290	1.0215	
FREUDENTHAL–GOU	3	1	-1/2	0.6934	0.7937	0.9179	[20], see also [4, 310, 356, 357],
			1/2	1.4423	1.1477	1.0348	[38–40, 40–42, 63, 311, 358, 359]
–	3	2	-1/6	1	0.9410	0.9687	[36, 112]
			1/5		1.0627	1.0294	
–	3	4	-0.1417	1	0.9504	0.9619	[36, 112]
			1/11		1.0294	1.0218	
–	6	1	-0.8563	**0,6528**	0.7237	0.8451	[35, 36]
			0.8563	**1.5319**	1.1086	1.0245	
DRUCKER	6	2	-1/3	1	0.9347	0.9635	[2, 19, 333, 334], see also
			1/2		1.0699	1.0309	[4, 108, 116, 131, 310, 357, 360, 361],
							[10, 98, 138, 264, 352, 359, 362]
–	6	4	-0.2671	1	0.9495	0.9605	[36, 112]
			1/5		1.0309	1.0225	
CAZACU	8	2	-4/9	1	0.9292	0.9588	[97, 108, 363, 364]
			4/5		1.0762	1.0319	
RANIECKI-MRÓZ	9	3	-0.4506	0.8977	0.9357	0.9538	[359]
			0.4506	1.1139	1.0422	1.0252	
-	12	1	-0.9211	0.7664	0.8092	0.8835	[35, 36]
			0.9211	1.3048	1.0559	1.0127	
-	12	2	-2/3	1	**0.9125**	**0.9439**	[36, 112]
			2		**1.0959**	**1.0344**	
DODD-NARUSE	12	4	-0.4716	1	0.9482	0.9582	[26], see also
			1/2		1.0344	1.0243	[36, 112, 359]
STOCKTON-DRUCKER	72	2	-0.9679	1	0.9533	0.9622	[334]
			30.1205		1.0489	1.0092	

A criterion of hexagonal symmetry results with even power $n = 2$ or 4 leading to $r_{60} = 1$, see (2.126). Powers $m > 12$, $n > 4$ are possible but not of interest, see PA6 and cf. [359].

A generalization of (2.125) follows with the cosine ansatz [33–37], see also [59, 60, 116, 343, 345, 365] and cf. [101, 359, 366]:

- the criterion of trigonal symmetry

$$\sqrt{3\,I_2'}\left[\frac{1+c_3\cos 3\theta+c_6\cos^2 3\theta}{1+c_3+c_6}\right]^{1/m} = \sigma_{\text{eq}}, \qquad m \in \mathbb{R} \qquad (2.129)$$

with the values

$$r_{60}^m = \frac{1+c_3+c_6}{1-c_3+c_6} \qquad \text{and} \qquad r_{30}^m = 1+c_3+c_6 \qquad (2.130)$$

includes the third invariant of the deviator I_3' (2.6) in the even and odd powers. The parameters of (2.129) result as

$$c_3 = \frac{1}{2}\left(r_{60}^m-1\right)\left(\frac{r_{30}}{r_{60}}\right)^m \qquad \text{and} \qquad c_6 = \frac{1}{2}\left[r_{30}^m+\left(\frac{r_{30}}{r_{60}}\right)^m - 2\right].$$

- the criterion of hexagonal symmetry as function of I_3' in the even powers

$$\sqrt{3\,I_2'}\left[\frac{1+c_6\cos^2 3\theta+c_{12}\cos^4 3\theta}{1+c_6+c_{12}}\right]^{1/m} = \sigma_{\text{eq}}, \qquad m \in \mathbb{R} \qquad (2.131)$$

with the values

$$r_{60} = 1, \qquad r_{30}^m = 1+c_6+c_{12} \qquad \text{and} \qquad r_{15}^m = 2^2\,\frac{1+c_6+c_{12}}{2^2+2\,c_6+c_{12}}. \qquad (2.132)$$

The parameters of (2.131) result as

$$c_6 = \left(\frac{2^2}{r_{15}^m}-1\right)r_{30}^m-3 \qquad \text{and} \qquad c_{12} = 2+2\left(r_{15}^m-2\right)\left(\frac{r_{30}}{r_{15}}\right)^m.$$

The criterion (2.131) can be reformulated as function of $\cos 6\theta$ (2.25).

Although both cosine series in (2.129) and (2.131) can be developed, the number of parameters is pragmatically limited to two (PA9.2). Note that the power m is not a fitting parameter (PA9.1): it is recommended as $m = 6$ in (2.129) and $m = 12$ in (2.131) to cover the maximum convexity range of the surface (PA8) and set prior to applying the criterion (Table 2.8, values highlighted in bold).

The parameter constraint in (2.129) is symmetric to the c_3-axis and convex (Fig. 2.21). The analytical equation for the lower boundary in Fig. 2.21 is unknown but can be approximated at will, e.g. with the hyperbola

$$c_6 = \frac{1}{3} \left(1 + \frac{c_3^2}{a_2^2}\right)^{1/2} - \frac{2}{3} \qquad \text{with} \qquad a_2 = \frac{1}{3}\sqrt{\frac{11}{15}}$$

and two straight lines

$$c_6 = \frac{215}{1000} \frac{\pm\sqrt{\frac{11}{15}} - c_3}{\pm\sqrt{\frac{11}{15}} \mp \frac{57}{50}}.$$

The (r_{60}, r_{30})-diagram with the constraints (Fig. 2.21) is shown in Fig. 2.22 [35, 36].

The parameter restrictions of the criterion (2.131) with $m = 12$ is convex in the $c_6 - c_{12}$ diagram (Fig. 2.23), cf. the parameter restrictions of this criterion with $m = 6$ [36, 112]. The analytical equation for the boundary $c_{12} < 0$ (green solid line) is unknown. The restrictions (Fig. 2.23) are shown in the (r_{30}, r_{15})-diagram (Fig. 2.24): the line $T_3 - T_4 - P_2 - P_3 - T_1$ is not convex.

Both criteria (2.129) and (2.131) are explicitly formulated (PA1) and have no surrounding surfaces outside the physically sensible area (PA2). However, they do not include extreme yield figures (PA8). The parameter restrictions are not straightforward
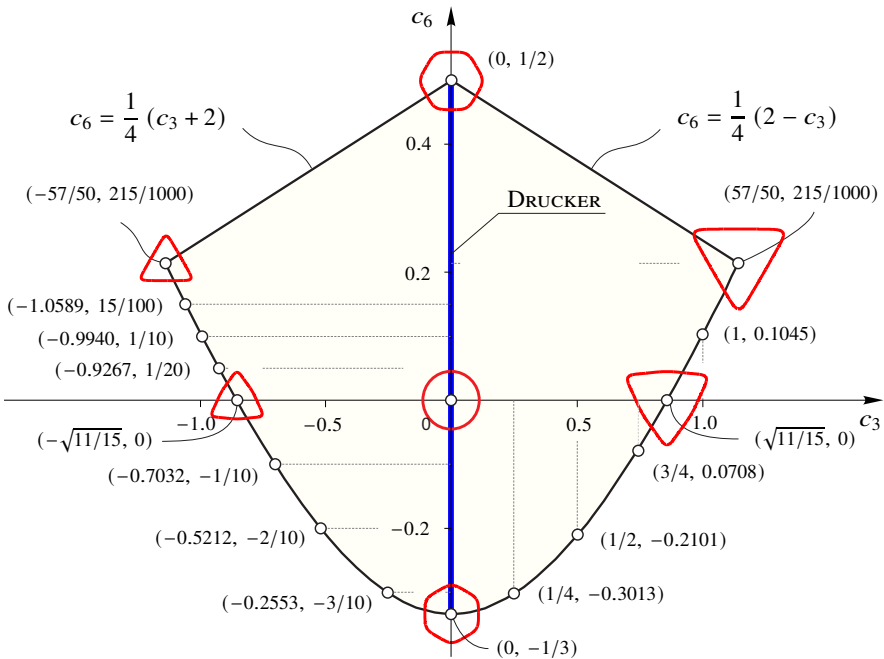
Fig. 2.21: Convexity region of the cosine ansatz (2.129) with the power $m = 6$ [36, 254, 367]. Particular cross sections in the π-plane are shown for clarity. DRUCKER criterion (2.99) is shown for comparison.
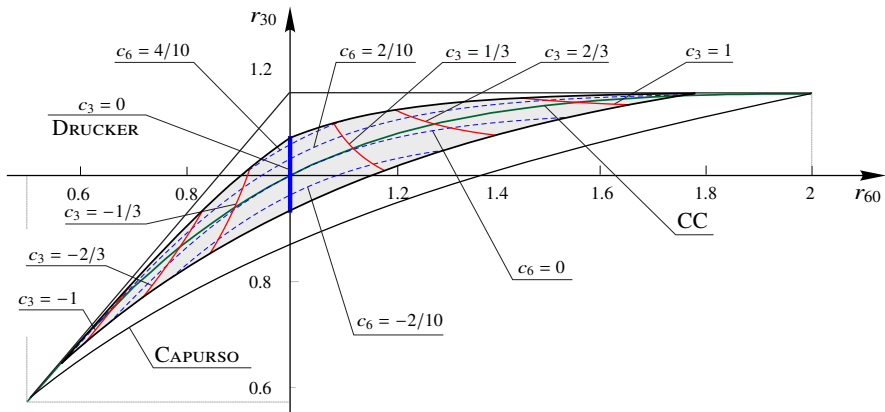
Fig. 2.22: Convexity conditions (Fig. 2.21) of the cosine ansatz (2.129) with the power $m = 6$ in the diagram $r_{60} - r_{30}$ [36]. DRUCKER criterion (2.99) and the cubic C^1-criterion (CC) $\hat{3} - \bigcirc - \bar{3}$ (2.133) are shown for comparison.
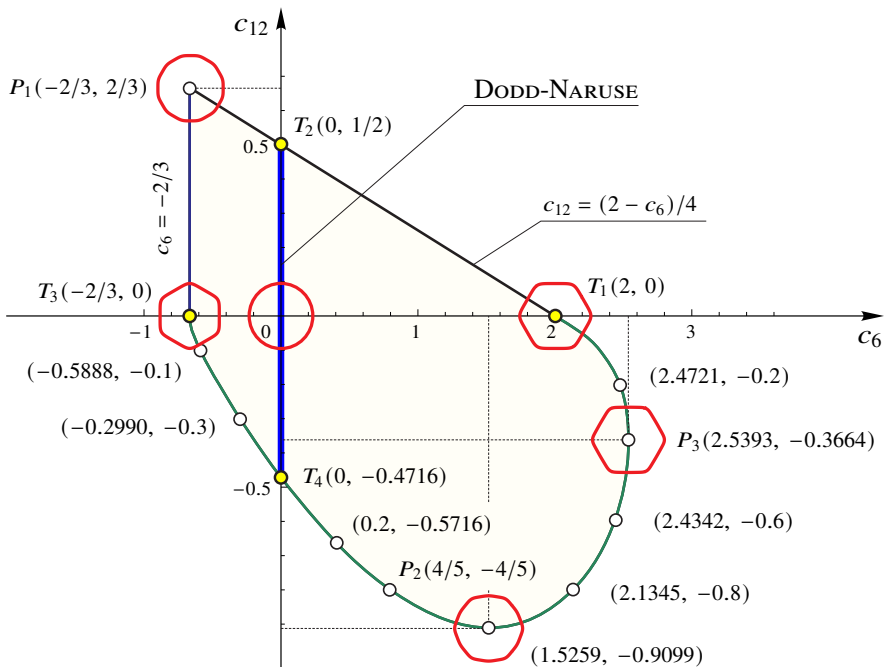
Fig. 2.23: Convexity region of the cosine ansatz (2.131) with the power $m = 12$. Some particular cross sections in the π-plane are shown for clarity. DODD-NARUSO criterion (Table 2.8) is shown for comparison.
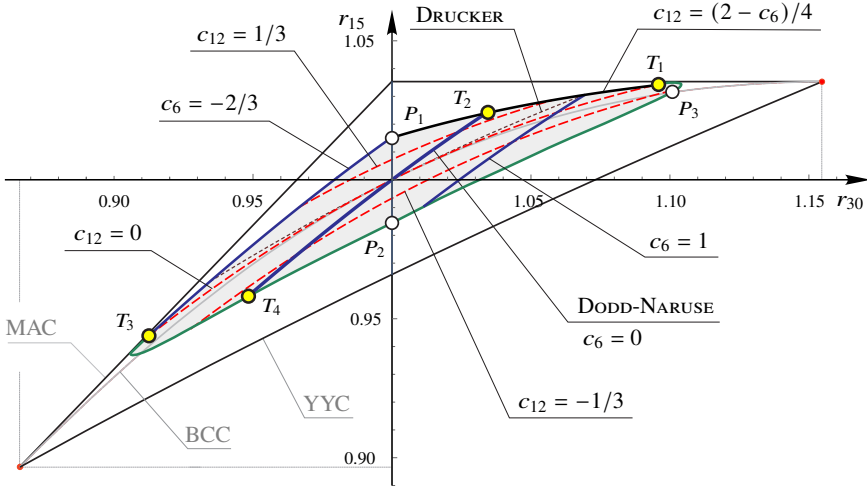
Fig. 2.24: Cosine ansatz (2.131) with the power $m = 12$ in the $r_{30} - r_{15}$ diagram (Fig. 2.8). The lines $c_{12} = $ const. (dashed red) and $c_6 = $ const. (solid blue) are shown. DRUCKER criterion (2.99) (thin dashed brown) is plotted for comparison. BCC – SZWED bicubic criterion, MAC – multiplicative ansatz criterion (Table 2.2). Some particular points from the $c_6 - c_{12}$-diagram (Fig. 2.23) are given.

(PA9.3) and the parameters have no geometric meaning (PA9.5). Due to these reasons, the ⃝-criteria (2.129) and (2.131) are numerically challenging (PA6) and cannot be recommended for solving common problems, although some particulate applications are reported. Nowadays, the ⃝-criteria have lost their significance.

2.5.4 Polynomial Criteria

The polynomially formulated criteria are characterised by the same power of the stress $n \geq 2$, $n \in \mathbb{N}$ in each term. To achieve this, the terms with the invariant I_2', I_3' or their products are weighted with σ_{eq} in the corresponding power. An absolute term (the term without invariants) is weighted with σ_{eq} by the maximal power, see e.g. VON MISES criterion (2.41) with $n = 2$, DRUCKER criterion (2.99) with $n = 6$ or DODD-NARUSE criterion with $n = 12$ (Table 2.8).

Excluded from VON MISES criterion, only the CC $\hat{3} - \bigcirc - \bar{3}$ and BCC $\hat{6} - \bigcirc - \bar{6}$ (Table 2.2) allow an analytical solution with respect of σ_{eq} (PA1). All polynomially formulated criteria violate PA2 and are difficult to fit parameters and implement.

The linear combination of the polynomially formulated extreme criteria (Table 2.2)

- of trigonal symmetry $\hat{3} - \hat{6} - \bar{3}$ and $\hat{3} - \bar{6} - \bar{3}$ and
- of hexagonal symmetry $\hat{6} - \hat{12} - \bar{6}$ and $\hat{6} - \bar{12} - \bar{6}$

leads to the criteria $\hat{3} - \hat{6}|\bigcirc|\bar{6} - \bar{3}$ and $\hat{6} - \hat{12}|\bigcirc|\bar{12} - \bar{6}$. Although both criteria meet PA7, PA8, PA9.1, PA9.2 and PA9.3, they violate PA1. It means that they are not

suitable for iterative procedures and can only be recommended for use to a limited extent. Because of PA6, the power can be limited as $n \in [2, 12]$. The upper limit results from the $\hat{1}2$ and $\bar{1}\bar{2}$ criteria (Table 2.1) formulated as the intersection of twelve planes.

2.5.4.1 Cubic C^1-Criterion $\hat{3} - \bigcirc - \bar{3}$

SAYIR-SOBOTKA criterion of trigonal symmetry (Table 2.2)

$$\frac{\sigma_{\text{eq}} \left(3I_2'\right) + c_3\, I_3'}{1 + \dfrac{2}{3^3}\, c_3} = \sigma_{\text{eq}}^3 \qquad \text{with} \qquad c_3 \in \left[-3^2,\, \frac{3^2}{2}\right] \qquad (2.133)$$

represents a convex combination of the polynomially formulated IVLEV $\hat{3}$ and MARIOTTE $\bar{3}$ criteria as an intersection of the three planes in the principal stress space. It has the structure of a reduced cubic equation [139] with respect to the equivalent stress $\sigma_{\text{eq}} = \sigma_0^{\text{T}}$ (2.1). The values r_{60} and r_{30} are calculated as follows

$$r_{60} = \frac{3^3 + 2\,c_3 - \sqrt{3\,(3^2 - 2\,c_3)\,(3^3 + 2\,c_3)}}{2^2\, c_3} \qquad \text{and} \qquad (r_{30})^2 = 1 + \frac{2}{3^3}\, c_3 \quad (2.134)$$

which, when reformulated, gives

$$r_{30} = \frac{r_{60}}{\sqrt{1 - r_{60} + (r_{60})^2}} \qquad \text{with} \qquad r_{60} \in \left[\frac{1}{2},\, 2\right]. \qquad (2.135)$$

The CC separates the $r_{60} - r_{30}$ diagram into two areas (Fig. 2.7). The basic shapes follows with

- $c_3 = -3^2$ – IVLEV criterion $\hat{3}$ with $r_{60} = 1/2$,
- $c_3 = 0$ – VON MISES criterion $\bigcirc$ with $r_{60} = 1$ and
- $c_3 = 3^2/2$ – MARIOTTE criterion $\bar{3}$ with $r_{60} = 2$.

The parameter c_3 in (2.133) can be substituted in (2.133) as follows

$$c_3 = \frac{3^3\,(r_{60} - 1)}{2 + 2\,r_{60}\,(r_{60} - 1)} \qquad \text{with} \qquad r_{60} \in \left[\frac{1}{2},\, 2\right] \qquad (2.136)$$

or

$$c_3 = \frac{3^3}{2}\left[(r_{30})^2 - 1\right] \qquad \text{with} \qquad r_{30} \in \left[\frac{1}{\sqrt{3}},\, \frac{2}{\sqrt{3}}\right] \qquad (2.137)$$

in order to obtain the geometric meaning, see Fig. 2.5 and PA9.5.

2.5.4.2 Bicubic C^1-Criterion $\hat{6} - \bigcirc - \bar{6}$

Szwed criterion of hexagonal symmetry (Table 2.2) is obtained with a convex combination of polynomially formulated Tresca $\hat{6}$ and Schmidt-Ishlinsky $\bar{6}$ criteria each of them as an intersection of the six planes in the principal stress space [36]

$$
\begin{aligned}
(1-\xi) & \left[\left(I_2' - \sigma_{\text{eq}}^2\right)^2 \left(2^2\, I_2' - \sigma_{\text{eq}}^2\right) - 3^3\, I_3'^2\right] \\
+ \xi & \left[\frac{3^3}{2^3}\, I_3' + \frac{3^2}{2^2}\, I_2'\, \sigma_{\text{eq}} - \sigma_{\text{eq}}^3\right] \left[\frac{3^3}{2^3}\, I_3' - \frac{3^2}{2^2}\, I_2'\, \sigma_{\text{eq}} + \sigma_{\text{eq}}^3\right] = 0
\end{aligned}
\tag{2.138}
$$

using the parameter $\xi \in [0, 1]$. It contains the equivalent stress σ_{eq} to the power of 2, 4 and 6 and therefore allows an explicit solution with respect of σ_{eq} (PA1).

The values r_{30} and r_{15} are given with the bicubic equations

$$
2^4 \cdot 3^3 + 2^3 \cdot 3^3 \left(r_{30}^2\right) (\xi - 2^2) + 2^6 \left(r_{30}^2\right)^3 (\xi - 1) - 3^3 \left(r_{30}^2\right)^2 (7\xi - 2^4) = 0 \tag{2.139}
$$

and

$$
2^5 \cdot 3^3 + 2 \cdot 3^3 \left(r_{15}^2\right)^2 (2^4 - 7\xi) + 2^4 \cdot 3^3 \left(r_{15}^2\right) (\xi - 2^2) + \left(r_{15}^2\right)^3 (37\xi - 2^6) = 0 \tag{2.140}
$$

as the lowest positive solutions, which are restricted as follows (Table 2.1)

$$
r_{30} \in \left[\frac{\sqrt{3}}{2}, \frac{2}{\sqrt{3}}\right] \qquad \text{and} \qquad r_{15} \in \left[\sqrt{\frac{3}{2}}\left(\sqrt{3}-1\right), \sqrt{2}\left(\sqrt{3}-1\right)\right].
$$

The analytical solutions of (2.139) and (2.140) are laborious and hence omitted.

The BCC divides the $r_{30} - r_{15}$ diagram into two areas (Fig. 2.8). The criteria of Tresca $\hat{6}$ and Schmidt-Ishlinsky $\bar{6}$ are obtained with $\xi = 0$ and $\xi = 1$. The value $r_{30}^S = 1$ of the criterion $\bigcirc$ results in

$$
\xi = 2^6/(7 \cdot 13) \approx 0.7033.
$$

2.5.4.3 C^1-criterion $\hat{3} - \hat{6} | \bigcirc | \bar{6} - \bar{3}$

Capurso criterion $\hat{3} - \hat{6} - \bar{3}$ (Table 2.2)

$$
\begin{aligned}
\Phi_{\text{CAP}} = {} & \alpha_{41}\, \sigma_{\text{eq}}^4\, I_2' + \alpha_{31}\, \sigma_{\text{eq}}^3\, I_3' + \alpha_{21}\, \sigma_{\text{eq}}^2\, (I_2')^2 \\
& + \alpha_{11}\, \sigma_{\text{eq}}\, I_2'\, I_3' + \beta_{21}\, (I_2')^3 + \beta_{31}\, (I_3')^2 - \sigma_{\text{eq}}^6 = 0
\end{aligned}
\tag{2.141}
$$

with the coefficients

$$\alpha_{41} = 6\,\frac{(r_{60}-1)^2 + r_{60}}{r_{60}^2}, \qquad\qquad \alpha_{31} = 3^3\,\frac{r_{60}-1}{r_{60}^2},$$

$$\alpha_{21} = -3^2\,\frac{\left((r_{60}-1)^2 + r_{60}\right)^2}{r_{60}^4}, \qquad \alpha_{11} = -3^4\,\frac{(r_{60}-1)\left((r_{60}-1)^2 + r_{60}\right)}{r_{60}^4}, \quad (2.142)$$

$$\beta_{21} = \frac{(1-2\,r_{60})^2\,(r_{60}-2)^2\,(1+r_{60})^2}{r_{60}^6}, \qquad \beta_{31} = -3^3\,\frac{\left((r_{60}-1)^2 + r_{60}\right)^3}{r_{60}^6}$$

and HAYTHORNTHWAITE criterion $\hat{3}-\bar{6}-\bar{3}$ (Table 2.2)

$$\Phi_{\mathrm{HAY}} = \frac{3^6}{2^6}\,\frac{1}{r_{60}^3}\,(I_3')^2 - \frac{3^5}{2^5}\,\frac{r_{60}-1}{r_{60}^3}\,I_2'\,I_3'\,\sigma_{\mathrm{eq}} - \frac{3^4}{2^4}\,\frac{1}{r_{60}^2}\,(I_2')^2\,\sigma_{\mathrm{eq}}^2$$
$$- \frac{3^3}{2^3}\,\frac{1-r_{60}^3}{r_{60}^3}\,I_3'\,\sigma_{\mathrm{eq}}^3 + \frac{3^2}{2^2}\,\frac{1+r_{60}^2}{r_{60}^2}\,I_2'\,\sigma_{\mathrm{eq}}^4 - \sigma_{\mathrm{eq}}^6 \tag{2.143}$$

are functions of the value $r_{60} \in [1/2, 2]$. With the convex combination (2.143) and (2.141)

$$\Phi_6 = (1-\xi)\,\Phi_{\mathrm{CAP}} + \xi\,\Phi_{\mathrm{HAY}}, \qquad \xi \in [0, 1] \tag{2.144}$$

one obtains the C^1-criterion $\hat{3}-\hat{6}|\bigcirc|\bar{6}-\bar{3}$ with the power of stress $n = 6$ in each term. The resulting criterion describes all points in the $r_{60} - r_{30}$ diagram (Fig. 2.7) with the convex shapes in the π-plane by using two parameters (r_{60}, ξ). The analytical solution for the value $r_{30}(r_{60}, \xi)$ is cumbersome and therefore omitted.

The criterion (2.144) contains (Table 2.1 and 2.2)

- SZWED criterion $\hat{6}-\bigcirc-\bar{6}$ of hexagonal symmetry in the π-plane (Subsubsect. 2.5.4.2) with the value $r_{60} = 1$ and the parameter

$$\xi = 1 - \frac{2}{r_{30}^2} + \frac{270 - 115\,r_{30}^2}{216 - 189\,r_{30}^2 + 64\,r_{30}^4}, \qquad r_{30} \in \left[\frac{\sqrt{3}}{2}, \frac{\sqrt{2}}{3}\right] \tag{2.145}$$

including

  - TRESCA criterion $\hat{6}$ with $\xi = 0$,
  - SCHMIDT-ISHLINSKY criterion $\bar{6}$ with $\xi = 1$ and
  - VON MISES criterion $\bigcirc$ with $\xi = 2^6/(7 \cdot 13) \approx 0.7033$,

- IVLEV criterion $\hat{3}$ with $r_{60} = 1/2$,
- MARIOTTE criterion $\bar{6}$ with $r_{60} = 2$ and
- an approximation of SAYIR-SOBOTKA criterion $\hat{3}-\bigcirc-\bar{3}$ (Subsubsect. 2.5.4.1) following with $r_{60} \in [1/2, 2]$ and $\xi = 2^6/(7 \cdot 13)$.

2.5.4.4 C^1-Criterion $\hat{6}-\hat{12}|\bigcirc|\bar{12}-\bar{6}$

The YYC $\hat{6}-\hat{12}-\bar{6}$ (Table 2.2)

$$\Phi_{\text{YYC}} = (\alpha_{41}\,\sigma_{\text{eq}}^4\,I_2' + \alpha_{21}\,\sigma_{\text{eq}}^2\,I_2'^2 + \beta_{21}\,I_2'^3 + \beta_{31}\,I_3'^2 - \sigma_{\text{eq}}^6)^2$$
$$- (\alpha_{31}\,\sigma_{\text{eq}}^3\,I_3' + \alpha_{11}\,\sigma_{\text{eq}}\,I_2'\,I_3')^2 \tag{2.146}$$

is the function of the value

$$r_{30} \in \left[\frac{\sqrt{3}}{2}, \frac{2}{\sqrt{3}}\right] \tag{2.147}$$

with the coefficients

$$\alpha_{41} = \frac{2\times3^2}{r_{30}^2}\left(1 - \sqrt{3}\,r_{30} + r_{30}^2\right), \qquad \alpha_{31} = -\frac{2\times3^3}{r_{30}^2}\left(r_{30} - \frac{\sqrt{3}}{2}\right)\left(r_{30} - \sqrt{3}\right),$$
$$\alpha_{21} = -\frac{3^4}{r_{30}^4}\left(1 - \sqrt{3}\,r_{30} + r_{30}^2\right)^2,$$
$$\alpha_{11} = \frac{2\times3^5}{r_{30}^4}\left(r_{30} - \frac{\sqrt{3}}{2}\right)\left(r_{30} - \sqrt{3}\right)\left(1 - \sqrt{3}\,r_{30} + r_{30}^2\right),$$
$$\beta_{21} = \frac{3^5}{r_{30}^6}\left(r_{30} - \frac{1}{\sqrt{3}}\right)^2\left(r_{30} - \frac{2}{\sqrt{3}}\right)^2, \quad \beta_{31} = -\frac{3^6}{r_{30}^6}\left(1 - \sqrt{3}\,r_{30} + r_{30}^2\right)^3. \tag{2.148}$$

The parameter $\eta \in [1, 4/3]$ in the MAC $\hat{6} - \bar{1}\bar{2} - \bar{6}$ (Table 2.2)

$$\Phi_{\text{MAC}} = \left[\left(I_2' - (\eta\,\sigma_{\text{eq}})^2\right)^2 \left(2^2\,I_2' - (\eta\,\sigma_{\text{eq}})^2\right) - 3^3\,I_3'^2\right]$$
$$\times \left[\frac{3^3}{2^3}\,I_3' + \frac{3^2}{2^2}\,I_2'\,\sigma_{\text{eq}} - \sigma_{\text{eq}}^3\right]\left[\frac{3^3}{2^3}\,I_3' - \frac{3^2}{2^2}\,I_2'\,\sigma_{\text{eq}} + \sigma_{\text{eq}}^3\right] \tag{2.149}$$

is replaced by r_{30} (2.147) with

$$\eta = \frac{2}{\sqrt{3}}\,r_{30}. \tag{2.150}$$

With the linear (convex) combination of two latter criteria (2.146) and (2.149)

$$\Phi_{12} = (1 - \xi)\,\Phi_{\text{YYC}} + \xi\,\Phi_{\text{MAC}}, \qquad \xi \in [0, 1] \tag{2.151}$$

the C^1-criterion $\hat{6} - \hat{1}\hat{2}|\bigcirc|\bar{1}\bar{2} - \bar{6}$ with the power of stress $n = 12$ in each term is obtained. It covers all convex shapes in the $r_{30} - r_{15}$ diagram (Fig. 2.8) with two parameters (r_{30}, ξ). The analytical solution for the value $r_{15}(r_{30}, \xi)$ is cumbersome and therefore omitted.

The values $r_{30} = r_{15} = 1$ result in the parameter $\xi \approx 0.3901$, which corresponds to von Mises criterion $\bigcirc$ (Fig. 2.8). With $\xi = 0.3901$ and r_{30} (2.147) one gets the approximation of the BCC (2.138). With $r_{30} = 1$ and $\xi \in [0, 1]$ a criterion $\hat{1}\hat{2} - \bigcirc - \bar{1}\bar{2}$ is obtained, which links Sokolovsky $\hat{1}\hat{2}$ and Ishlinsky-Ivlev $\bar{1}\bar{2}$ regular dodecagons leading to (Table 2.1)

$$r_{15} \in [0.9659, 1.0353].$$

These relatively small deviations from $r_{15} = 1$ describe the maximum gap between the MAC and YYC (Fig. 2.8). It falls within the range of the measured data scatter and is of relevance for theoretical studies.

2.5.5 Criteria with Trigonometric Identity

The criteria discussed below meet PAs 1-9 in the best known way, rendering them the most effective in practice.. Their equations and the parameter restrictions are clear. The number of basic geometries included in these criteria is sufficient for many applications.

Implementing the trigonometric criteria is critical to ensure reliable material description and minimise bias in the modelling (Sect. 2.1). Their use significantly reduces ambiguity in the material description and optimisation procedure.

These criteria are grouped into the criteria with C^0- and C^1-continuity: for certain problems it is convenient to use the "piecewise linear" criteria [67]. The C^1-criteria can be approximated with increasing accuracy by the polygons of trigonal or hexagonal symmetry using the values r_{60}, r_{30} and r_{15} to calculate the parameters.

2.5.5.1 C^1-Criterion $\hat{\mathbf{3}} - \hat{\mathbf{6}} \,|\, \bigcirc - \bar{\mathbf{3}}$

Normalized with respect to the uniaxial tensile yield stress $\sigma_{eq} = \sigma_0^T$ (2.1), PODGÓRSKI criterion (Table 2.2) reads

$$\sigma_{eq} = \sqrt{3 I_2'} \, \frac{\Omega_3(\theta, \beta_3, \eta_3)}{\Omega_3(0, \beta_3, \eta_3)} \tag{2.152}$$

with the shape function of trigonal symmetry

$$\Omega_3(\theta, \beta_3, \eta_3) = \cos\left[\frac{1}{3}\left(\pi\beta_3 - \arccos[\eta_3 \cos 3\theta]\right)\right] \tag{2.153}$$

and the parameter restrictions

$$\beta_3 \in [0, 1], \quad \eta_3 \in [-1, 1]. \tag{2.154}$$

The criterion (2.152)–(2.154) is obtained by solving the cubic equation (2.133) in σ_{eq} with the trigonometric identity [139]. The values r_{60} and r_{30} are

$$r_{60} = \frac{\cos\left[\frac{1}{3}\left(\pi\beta_3 - \arccos \eta_3\right)\right]}{\cos\left[\frac{1}{3}\left(\pi\beta_3 - \arccos[-\eta_3]\right)\right]}, \quad r_{30} = \frac{\cos\left[\frac{1}{3}\left(\pi\beta_3 - \arccos \eta_3\right)\right]}{\sin\left[\frac{1}{3}\pi\left(\beta_3 + 1\right)\right]}. \tag{2.155}$$

To avoid numerical issues, the real value function can be introduced in (2.153)

$$\Omega_3(\theta, \beta_3, \eta_3) = \Re\left[\cos\left[\frac{1}{3}\left(\pi\beta_3 - \arccos[\eta_3 \cos 3\theta]\right)\right]\right]. \tag{2.156}$$

Replacing the parameter η_3 with

$$\eta_3 = \sin\left[\kappa_3 \frac{\pi}{2}\right], \qquad \kappa_3 \in [-1, 1] \tag{2.157}$$

results in improved parameter sensitivity and numerical stability (PA6).

The criterion (2.152)–(2.154) contains the criteria (Fig. 2.25, Table 2.1 and 2.2)

- SAYIR-SOBOTKA cubic criterion $\hat{3} - \bigcirc - \bar{3}$ with $\beta_3 = \{0, 1\}$, cf. [102, 136, 368–370],
- CAPURSO criterion $\hat{3} - \hat{6} - \bar{3}$ with $\eta_3 = \{-1, 1\}$ and
- TRESCA-VON MISES transition $\hat{6} - \bigcirc$ with $\beta_3 = 1/2$, $\eta_3 \in [0, 1]$.

PODGÓRSKI criterion (2.152)–(2.154) has received great recognition from the professional community (Table 2.2, Comments). The number of the basic geometries (Table 2.1) included in the criterion is sufficient for many applications. The parameter restriction (2.154) is practical.

The disadvantage is that the parameters β_3 and η_3 can only be numerically determined by known values r_{60} and r_{30}. Furthermore, HAYTHORNTHWAITE criterion $\hat{3} - \hat{6} - \bar{3}$, which contains SCHMIDT-ISHLINSKY criterion $\bar{6}$, cannot be described with PODGÓRSKI criterion limiting its application in the general case.
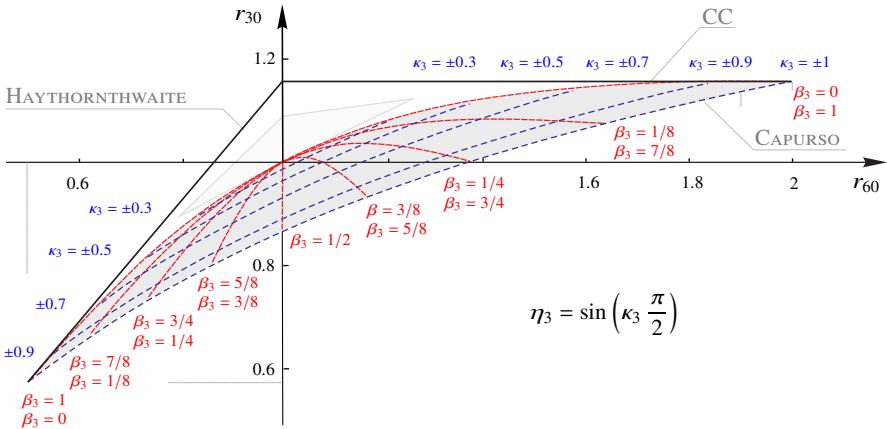
Fig. 2.25: PODGÓRSKI yield criterion (2.152) in the $r_{60} - r_{30}$ diagram (Fig. 2.7). The lines $\beta_3 = \text{const.}$, $\kappa_3 \in [-1, 1]$ (solid red) and $\kappa_3 = \text{const.}$, $\beta_3 \in [0, 1]$ (dashed blue) are shown [82], cf. [29, 30], adapted from [36, 155]. CC - SAYIR-SOBOTKA cubic criterion (Table 2.2).

2.5.5.2 C^1-Criterion $\hat{6} - \hat{12} \mid \bigcirc - \bar{6}$

Normalized with respect to the uniaxial tensile yield stress $\sigma_{eq} = \sigma_0^T$ (2.1), ROSEN-DAHL criterion (Table 2.2) reads

$$\sigma_{eq} = \sqrt{3\,I_2'} \, \frac{\Omega_6(\theta,\beta_6,\eta_6)}{\Omega_6(0,\beta_6,\eta_6)} \tag{2.158}$$

with the shape function of hexagonal symmetry

$$\Omega_6(\theta,\beta_6,\eta_6) = \cos\left[\frac{1}{6}\left(\pi\beta_6 - \arccos[\,\eta_6\cos6\theta\,]\right)\right]. \tag{2.159}$$

The parameter restrictions are

$$\beta_6 \in [0,1], \quad \eta_6 \in [-1,1]. \tag{2.160}$$

The criterion (2.158)-(2.160) is obtained by solving the bicubic equation (2.138) with respect to σ_{eq} using the trigonometric identity, cf. PODGÓRSKI criterion (2.152)–(2.154). The values r_{30} and r_{15} are

$$r_{30} = \frac{\cos\left[\frac{1}{6}\left(\pi\beta_6 - \arccos\eta_6\right)\right]}{\cos\left[\frac{1}{6}\left(\pi\beta_6 - \arccos[-\eta_6]\right)\right]}, \qquad r_{15} = \frac{\cos\left[\frac{1}{6}\left(\pi\beta_6 - \arccos\eta_6\right)\right]}{\sin\left[\frac{1}{12}\pi\left(2\beta_6+5\right)\right]}. \tag{2.161}$$

In analogy to (2.156), the real value function can be introduced in (2.159)

$$\Omega_6(\theta,\beta_6,\eta_6) = \Re\left[\cos\left[\frac{1}{6}\left(\pi\beta_6 - \arccos[\,\eta_6\cos6\theta\,]\right)\right]\right]. \tag{2.162}$$

Replacing the parameter η_6 with

$$\eta_6 = \sin\left[\kappa_6\,\frac{\pi}{2}\right], \qquad \kappa_6 \in [-1,1] \tag{2.163}$$

results in improved parameter sensitivity and numerical stability, cf. (2.157).

The criterion (2.158)–(2.160) contains the criteria (Fig. 2.26, Table 2.1 and 2.2)

- SZWED bicubic criterion $\hat{6} - \bigcirc - \bar{6}$ with $\beta_6 = \{0,1\}$,
- YU yield criterion $\hat{6} - \hat{12} - \bar{6}$ with $\eta_6 = \{1,-1\}$ and
- SOKOLOVSKY-VON MISES transition $\hat{12} - \bigcirc$ with $\beta_3 = 1/2$, $\eta_6 \in [0,1]$.

The criterion (2.158)–(2.159) is suitable for solving several problems of plasticity theory. The number of basic geometries included in the criterion is sufficient for many applications. The parameter restriction (2.160) is convenient for the practice, cf. (2.154).

The disadvantage is that the parameters β_6 and η_6 in (2.158)–(2.160) can only be numerically determined by the known values r_{30} and r_{15}. Furthemore, the MAC $\hat{6} - \bar{12} - \bar{6}$ containing ISHLINSKY-IVLEV criterion $\bar{12}$ cannot be described by ROSEN-DAHL criterion, which limits the application of the criterion in the general case.
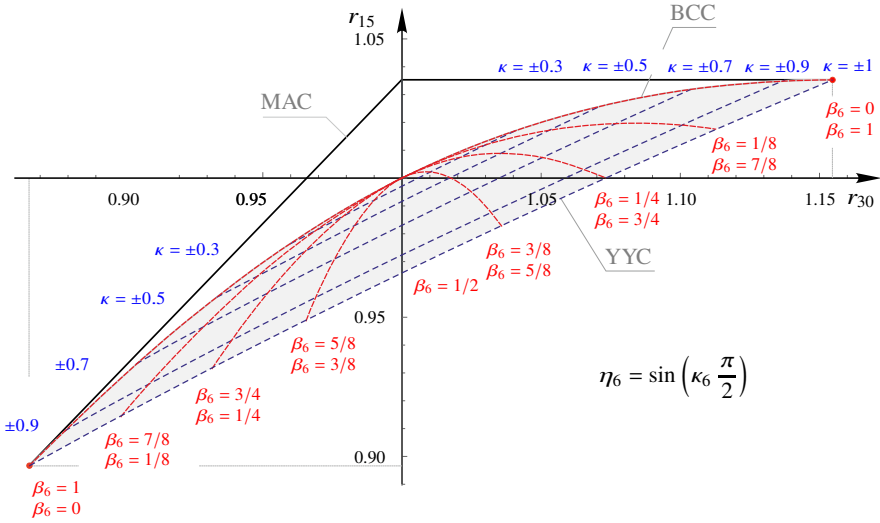
Fig. 2.26: ROSENDAHL criterion (2.159) in the $r_{30} - r_{15}$ diagram (Fig. 2.8). The lines $\beta_6 = $ const., $\kappa_6 \in [-1, 1]$ (solid red) and $\kappa_6 = $ const., $\beta_6 \in [0, 1]$ (dashed blue) are shown [81], cf. Fig. 2.25. BCC – SzweD bicubic criterion, MAC – multiplicative ansatz criterion (Table 2.2).

2.5.5.3 C^0-Criterion $\hat{3} - \hat{6} \,|\, \hat{12} \,|\, \bar{6} - \bar{3}$

A linear combination of the criteria $\hat{3} - \hat{6} - \bar{3}$ and $\bar{6}$, cf. [36, 82, 155]

$$\Phi_3 = \sqrt{3I_2'} \left[(1-\alpha) \frac{\cos\left[\frac{1}{3}(\pi\beta_3 - \arccos[\cos 3\theta])\right]}{\cos\left[\frac{1}{3}\pi\beta_3\right]} + \alpha \cos\left[\frac{1}{6}\arccos[\cos 6\theta]\right] \right] - \sigma_{\text{eq}}$$

(2.164)

with the parameter restriction

$$\alpha \in [0, 1] \qquad \text{and} \qquad \beta_3 \in [0, 1] \qquad (2.165)$$

provides the C^0-criterion $\hat{3} - \hat{6} \,|\, \hat{12} \,|\, \bar{6} - \bar{3}$ of trigonal symmetry. The values are

$$r_{60} = \frac{2}{1 + \alpha + \sqrt{3}(1-\alpha)\tan\dfrac{\pi\beta_3}{3}} \quad \text{and} \quad r_{30} = \frac{2}{\sqrt{3} + (1-\alpha)\tan\left[\dfrac{\pi\beta_3}{3}\right]}. \quad (2.166)$$

We obtain the parameters α and β_3 with the known values r_{60} and r_{30} as

$$\alpha = 2 - \frac{2\sqrt{3}}{r_{30}} + \frac{2}{r_{60}} \qquad \text{and} \qquad \beta_3 = \frac{3}{\pi}\arctan\left[\frac{r_{60}(\sqrt{3}r_{30} - 2)}{(2 + r_{60})r_{30} - 2\sqrt{3}r_{60}}\right]. \quad (2.167)$$

SOKOLOVSKY criterion $\hat{12}$ with $r_{60} = r_{30} = 1$ (Fig. 2.6 b and Table 2.1) follows with

$$\alpha = 4 - 2\sqrt{3} \approx 0.5359 \qquad \text{and} \qquad \beta_3 = 0.5. \tag{2.168}$$

The criterion (2.164) describes all points in the $r_{60} - r_{30}$ diagram (Figs. 2.7 and 2.27). It contains the criteria (Table 2.2)

- CAPURSO criterion $\hat{3} - \hat{6} - \bar{3}$ with $\alpha = 0$ and $\beta_3 \in [0, 1]$,
- YU yield criterion $\hat{6} - \hat{12} - \bar{6}$ with $\alpha \in [0, 1]$, $\beta_3 = 1/2$ and
- approximation of HAYTHORNTHWAITE criterion $\hat{3} - \bar{6} - \bar{3}$ with $\alpha \in [0, 1]$ and

$$\beta_3 = \begin{cases} 1, & \text{for} \quad \hat{3} - \bar{6}, \\ 0, & \text{for} \quad \bar{6} - \bar{3} \end{cases} \tag{2.169}$$

leading to the enneagons in the π-plane [81, 82, 155].

The equations and the parameter constraints (2.164)–(2.167) are simple, so this criterion is advocated for use in practice. The function $\cos 6\theta$ in (2.164) can be replaced with (2.25) for a consistent expression of the criterion as a function of $\cos 3\theta$.

The disadvantage is, that the geometry of HAYTHORNTHWAITE criterion cannot be exactly reproduced with the criterion (2.164), although both criteria coincide in the $r_{60} - r_{30}$ diagram [36, 82, 155]. It is also detrimental that the criterion (2.164) does not include VON MISES criterion $\bigcirc$.

2.5.5.4 C^0-Criterion $\hat{6} - \hat{12}\,|\,\hat{24}\,|\,\hat{12} - \bar{6}$

A linear combination of the criteria $\hat{6} - \hat{12} - \bar{6}$ and $\bar{12}$, cf. the C^0-criterion $\hat{3} - \hat{6}\,|\,\hat{12}\,|\,\bar{6} - \bar{3}$ (Subsubsect. 2.5.5.3)
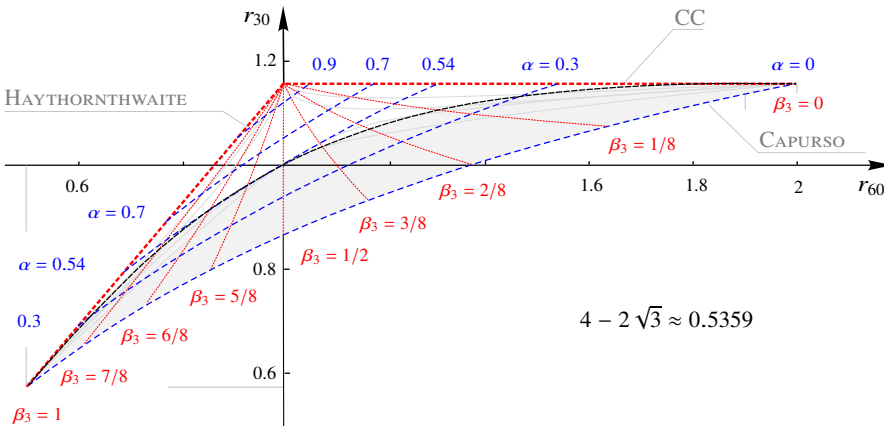
Fig. 2.27: C^0-criterion $\hat{3} - \hat{6}\,|\,\hat{12}\,|\,\bar{6} - \bar{3}$ (2.164) in the $r_{60} - r_{30}$ diagram. The lines $\beta_3 = \text{const.}$, $\alpha \in [0, 1]$ (solid red) and $\alpha = \text{const.}$, $\beta_3 \in [0, 1]$ (dashed blue) are shown. CC – cubic criterion (Table 2.2).

$$\Phi_6 = \sqrt{3I_2'}\left[(1-\alpha)\,\frac{\cos\left[\frac{1}{6}(\pi\beta_6-\arccos[\cos 6\theta])\right]}{\cos\left[\frac{1}{6}\pi\beta_6\right]} + \alpha\cos\left[\frac{1}{12}\arccos[\cos 12\theta]\right]\right] - \sigma_{\text{eq}}$$
(2.170)

with the parameter restriction

$$\alpha \in [0,\,1] \qquad \text{and} \qquad \beta_6 \in [0,\,1] \tag{2.171}$$

provides the C^0-criterion $\hat{6} - \hat{1}\hat{2}\,|\,\hat{2}\hat{4}\,|\,\bar{1}\bar{2} - \bar{6}$ of hexagonal symmetry. The values are

$$r_{60} = 1, \qquad r_{30} = 2\left[\sqrt{3} - \alpha\left(\sqrt{3}-2\right) + (1-\alpha)\tan\left[\frac{\pi\beta_6}{6}\right]\right]^{-1} \tag{2.172}$$

and

$$r_{15} = 2\sqrt{2}\left[1 + \sqrt{3} + (1-\alpha)\left(\sqrt{3}-1\right)\tan\left[\frac{\pi\beta_6}{6}\right]\right]^{-1}. \tag{2.173}$$

We obtain the parameters α and β_6 with the known values r_{30} and r_{15} as

$$\alpha = 1 - \frac{2\left(2+\sqrt{3}\right)^{3/2}}{r_{15}} + \frac{\left(2+\sqrt{3}\right)\left(2+\sqrt{3}\,r_{30}\right)}{r_{30}}, \tag{2.174}$$

$$\beta_6 = \frac{6}{\pi}\arctan\left[\frac{\sqrt{2}\left(3\sqrt{3}-5\right) + \left(\sqrt{3}-2\right)r_{15}}{\sqrt{2}\left(\sqrt{3}-1\right)r_{30} + r_{15}\left(2\sqrt{3}-4+3r_{30}-2\sqrt{3}\,r_{30}\right)}\,r_{30}\right]. \tag{2.175}$$

The criterion $\hat{2}\hat{4}$ with the values $r_{15} = r_{30} = 1$ (Table 2.1) follows with

$$\alpha = 2\left(2+\sqrt{3}\right)\left(2 - \sqrt{2+\sqrt{3}}\right) \approx 0.5087 \qquad \text{and} \qquad \beta_6 = 0.5. \tag{2.176}$$

The criterion (2.170) describes all points in the $r_{30} - r_{15}$ diagram (Fig. 2.8 and 2.28). It contains the criteria (Table 2.2):

- Y u yield criterion $\hat{6} - \hat{1}\hat{2} - \bar{6}$ with $\alpha = 0$, $\beta_6 \in [0,\,1]$,
- C^0-criterion $\hat{1}\hat{2} - \hat{2}\hat{4} - \bar{1}\bar{2}$ with $\alpha \in [0,\,1]$, $\beta_6 = 1/2$ and
- approximation of the MAC $\hat{6} - \hat{1}\bar{2} - \bar{6}$ with $\alpha \in [0,\,1]$ and

$$\beta_6 = \begin{cases} 1, & \text{for} \quad \hat{6} - \bar{1}\bar{2}, \\ 0, & \text{for} \quad \hat{1}\hat{2} - \bar{6}. \end{cases} \tag{2.177}$$

The Eqs. (2.170)–(2.175) are simple, so this criterion is recommended for practical use. The functions $\cos 6\theta$ and $\cos 12\theta$ can be replaced with (2.25) and (2.26) for uniform presentation of the criterion as function of $\cos 3\theta$ or $\cos 6\theta$.

The disadvantage is, that the geometry of the MAC (Table 2.2) cannot be exactly described with the criterion (2.170), although both criteria coincide in the $r_{30} - r_{15}$ diagram. It is detrimental, that the criterion (2.170) does not include the $\bigcirc$-criterion.
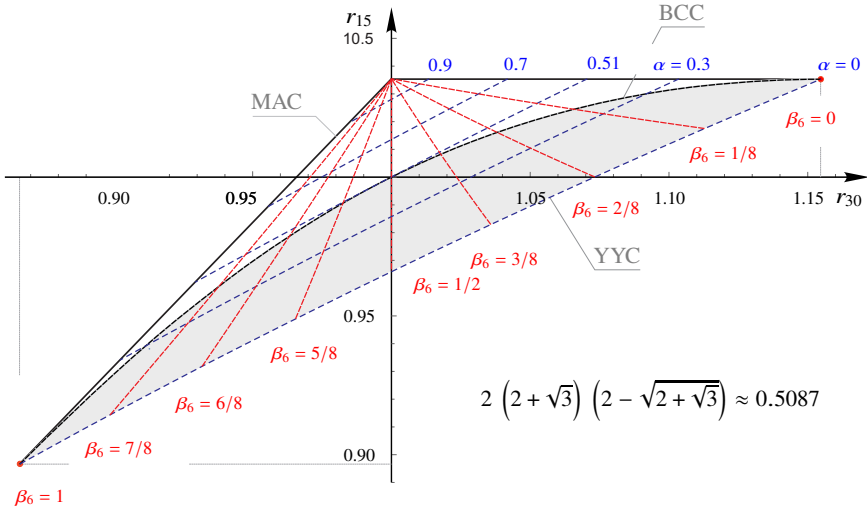
Fig. 2.28: C^0-Criterion $\hat{6} - \hat{1}\hat{2}\,|\,\hat{2}\hat{4}\,|\,\bar{1}\bar{2} - \bar{6}$ (2.170) in the $r_{30} - r_{15}$ diagram (Fig. 2.8). The lines $\beta_6 = \text{const.}$, $\alpha \in [0, 1]$ (solid red) and $\alpha = \text{const.}$, $\beta_6 \in [0, 1]$ (dashed blue) are shown. The criterion $\hat{2}\hat{4}$ follows with $\alpha \approx 0.5087$ and $\beta_6 = 1/2$ (2.176). BCC – bicubic criterion (Table 2.2).

2.6 Conclusion

The present work reviews the yield criteria of mathematical plasticity theory. These criteria are pressure-insensitive: the influence of the first invariant of the stress tensor I_1 (2.4) is neglected. This assumption, which is tacitly omitted in numerous publications and is also not considered in this paper, can be applied to very ductile materials in the range $I_1 \leq 0$ [87, 145, 236–238], see also [64, 85, 148, 194, 239, 241, 242, 302, 371] or, in certain circumstances, in the range $I_1 \leq \sigma_0^{\mathrm{T}}$ [36, 81, 82, 272]. Pressure-sensitivity can be achieved by the I_1-substitution (2.44) in the yield criteria (PA5).

Firstly, the geometric properties of the yield surfaces calculated at the stress angles $\theta = \pi/3, \pi/4, \pi/6, \pi/12$ and 0

$$r_{60}, r_{45}, r_{30}, r_{15} \quad \text{and} \quad r_0$$

are examined and assigned to the mechanical properties at the basic states of the plane stress

$$r_{60}^{\mathrm{C}}, r_{60}^{\mathrm{TT}}, r_{45}^{\mathrm{CS}}, r_{30}^{\mathrm{Cc}}, r_{30}^{\mathrm{S}}, r_{30}^{\mathrm{Tt}}, r_{15}^{\mathrm{TS}} \quad \text{and} \quad r_0^{\mathrm{CC}}$$

(Table 2.3). The use of these dimensionless values simplifies the fitting procedure and comparison of material properties.

Secondly, a nomenclature for isotropic yield criteria is refined (Table 2.1). The regular polygons of trigonal and hexagonal symmetry in the π-plane are represented schematically depending on the number of their edges and orientation, e.g. $\hat{3}$, $\bar{3}$,

$\hat{6}$ and $\bar{6}$. The rotationally symmetric VON MISES criterion is denoted as a circle (Subsect. 2.4.1). The yield criteria involving three or more basic geometries are of relevance, which limits the number of appropriate yield criteria to twelve (Table 2.2), but the methods of their derivation are different.

In the next step, numerous yield criteria are assigned to five derivation paths (Sect. 2.5). The dimensionless parameters r_{60}, r_{30} and r_{15} (2.46) help to compare the criteria of trigonal symmetry in the (r_{60}, r_{30})-diagram (Fig. 2.7) and the criteria of hexagonal symmetry – in the (r_{30}, r_{15})-diagram (Fig. 2.8). Considering these diagrams, it is obvious that the criteria should be the functions of two parameters additional to the equivalent stress $\sigma_{\mathrm{eq}} = \sigma_0^{\mathrm{T}}$ (Table 2.2).

In summary about the derivation paths:

I.   The easiest way to interpret the classical yield criteria (Fig. 2.1) is using the principal shear space (Subsect. 2.5.1). The representation of the polyhedra in this space is elegant but not very useful for generalization. Spatial imagination is required to recognise the resulting shape in the cross section $\zeta = 0$ (2.13). Since the meaning of polyhedra in $(\tau_{12}, \tau_{23}, \tau_{31})$-space is unclear, this derivation path has no further reach and is left to academic purposes.

II.   The criteria of KARAFILLIS-BOYCE (Subsubsect. 2.5.2.2) and CAZACU et al. (Subsubsect. 2.5.2.3) as power functions of stresses lie in the realm of mathematical trickery. They can be safely used with the powers $m \in [1, 2]$ in the first case and $m \in \{2, 3\}$ in the second. The meaning of the parameters is missing. The reformulation of the criteria in the invariants (I_2, I_3') or (I_2, θ) is only possible for the powers $n \in \mathbb{N}$. Together, these drawbacks negate the utility of both criteria.

III. The $\bigcirc$-criteria (Subsect. 2.5.3) have a rather historical significance. Numerous practical problems have been treated with these criteria. The development of such criteria is known as the cosine ansätze (2.129) and (2.131) but is no longer necessary.

IV. The polynomial formulated SAYIR-SOBOTKA C^1-criterion $\hat{3} - \bigcirc - \bar{3}$ (2.133) and SZWED C^1-criterion $\hat{6} - \bigcirc - \bar{6}$ (2.138) can be solved analytically with respect of σ_{eq} using CARDANO formula (Subsubsect. 2.5.4.1 and 2.5.4.2). However, PA2 is violated here.

The C^1-criteria $\hat{3} - \hat{6}| \bigcirc |\bar{6} - \bar{3}$ (2.144) and $\hat{6} - \hat{12}| \bigcirc |\bar{12} - \bar{6}$ (2.151) include the extreme yield figures. The implementation of these two criteria involves unnecessary mathematical effort (PA1 and PA2), however, they can be applied while searching for a convex shape of Φ by fitting.

V.   The equations of SAYIR-SOBOTKA and SZWED criteria can be resolved on the basis of the trigonometric identity (Subsubsect. 2.5.5.1 and 2.5.5.2). These solutions lead to

    – PODGÓRSKI C^1-criterion $\hat{3} - \hat{6}| \bigcirc -\bar{3}$ (2.152) and
    – ROSENDAHL C^1-criterion $\hat{6} - \hat{12}| \bigcirc -\bar{6}$ (2.158)

as function of the stress angle θ (2.24). Both criteria are crucial for modelling because they fulfil several PAs (Sect. 2.3.2), especially PA1 and PA2.

The linear combination of CAPURSO C^0-criterion $\hat{3} - \hat{6} - \bar{3}$ with SCHMIDT-ISHLINSKY criterion $\bar{6}$ leads to C^0-criterion $\hat{3} - \hat{6}|\hat{12}|\bar{6} - \bar{3}$ (2.164). By analogy,

the linear combination of the YYC C^0-criterion $\hat{6} - \hat{1}\hat{2} - \bar{6}$ with I s h l i n s k y-I v l e v criterion $\bar{1}\bar{2}$ leads to C^0-criterion $\hat{6} - \hat{1}\hat{2}\,|\hat{2}\hat{4}|\,\bar{1}\bar{2} - \bar{6}$ (2.170). However, the upper convexity restriction $\hat{3} - \bar{6} - \bar{3}$ of the criterion (2.164) and $\hat{6} - \bar{1}\bar{2} - \bar{6}$ of the criterion (2.170) do not fit the criteria of H a y t h o r n t h w a i t e and MAC respectively. This shows the limitations of the introduced nomenclature (Subsect. 2.4.1).

The proposed nomenclature (Table 2.1 and 2.2) highlights the fact that numerous criteria have been suggested more than once and provides hints for finding new derivation paths. PA8 expects the criteria to include the extreme yield figures. This means that they should encompass the upper and lower convexity limits:

- $\hat{3} - \hat{6} - \bar{3}$ and $\hat{3} - \bar{6} - \bar{3}$ for criteria of trigonal symmetry (Fig. 2.7) and
- $\hat{6} - \hat{1}\hat{2} - \bar{6}$ and $\hat{6} - \bar{1}\bar{2} - \bar{6}$ for criteria of hexagonal symmetry (Fig. 2.8).

Therefore, the missing criteria are:

- C^0- and C^1-criteria $\hat{3} - \hat{6}|\bigcirc|\bar{6} - \bar{3}$ and
- C^0- and C^1-criteria $\hat{6} - \hat{1}\hat{2}|\bigcirc|\bar{1}\bar{2} - \bar{6}$

which include H a y t h o r n t h w a i t e criterion in the first case and the MAC in the second one. It is expected that they should meet the PAs. Since these explicitly formulated criteria are not known, they are replaced by four criteria (Subsect. 2.5.5).

The above results in six yield criteria with one parameter in addition to $\sigma_{\text{eq}} = \sigma_0^{\text{T}}$ (Table 2.2) becoming obsolete as being particular. The criteria with two parameters are state of art. Further generalisations of the yield criteria are possible, but the number of parameters increases making them unusable. The question of whether there is a yield criterion that generalises all known criteria is therefore not relevant.

The recommended yield criteria (Subsect. 2.5.5) allow a consistent numerical verification in component design and the search for component weak points with various parameter setting. The approximation of the measured data with these criteria for ductile isotropic materials is then unambiguous and the comparison of the properties between different materials is clear.

Although the development of computing technology is making enormous progress, the elegant criteria are still preferred. Using the criteria, that PAs meet, significantly reduces implementation errors: they are easier to master. In any case, the search for the most suitable yield criteria and new derivation paths continues [372].

References

[1] Ueshiba M (2007) The Art of Peace, Stevens, J. (ed.). Shambhala, Boston & London

[2] Drucker DC (2001) Background on isotropic criteria. In: Lemaitre J (ed) Handbook of Materials Behavior Models: Deformations of Materials, vol 1, Academic Press, San Diego, pp 129–136

[3] Hill R (1950) LXVI. On the inhomogeneous deformation of a plastic lamina in a compression test. The London, Edinburgh, and Dublin Philosophical Magazine and J of Science, Series 7 **41**(319):733–744

[4] Backhaus G (1983) Deformationsgesetze. Akademie-Verlag, Berlin

[5] Belyaev NM (1959) Strength of Materials (in Russ.: Soprotivlenije Materialov). Gosudarstvennoe Izdatel'stvo Fisiko-Matematicheskoj Literatury, Moscow

[6] Gvozdev AA (1949) Computation of Bearing Capacity of Structures by the Method of Limiting Equilibrium (in Russ.: Raschet nesusshhej sposobnosti konstrukzij po metody predel'nogo ravnovesija). Strojizdat, Moscow

[7] Ivlev DD (1958) On the development of a theory of ideal plasticity. J of Applied Mathematics and Mechanics **22**(6):1221–1230

[8] Kachanov LM (1969) Foundations of the Theory of Plasticity (in Russ.: Osnovy teorii plastichnosti). Nauka, Moscow

[9] Yu MH (2004) Unified Strength Theory and its Applications. Springer, Berlin

[10] Zyczkowski M (1981) Combined Loadings in the Theory of Plasticity. PWN-Polish Scientific Publ., Warszawa

[11] Beer F, Johnston E, DeWolf J, Mazurek DE, Sanghi S (2020) Mechanics of Materials. McGraw-Hill, Upper Saddle River

[12] Calladine CR (2010) Plasticity for Engineers: Theory and Applications. Woodhead Publishing, Oxford

[13] Christensen RM (2013) The Theory of Materials Failure. University Press, Oxford

[14] Gorshkov AG, Starovojtov AI, Tarlakovskij DB (2002) Theory of Elasticity and Plasticity (in Russ.: Teorija uprugosti i plastichnosti). Fismatlit, Moscow

[15] Housner GW, J VT (1966) The Analysis of Stress and Deformation. McMillan, New York

[16] Kettunen PO, Kuokkala VT (2003) Plastic Deformation and Strain Hardening. Trans Tech Publications, Uetikon-Zuerich

[17] Serensen SV (1937) Metal Strength and Calculation of Machine Components (in Russ. Prochnost' metalla i raschet detalej mashin). ONTI NKTP, Moscow, Leningrad

[18] Szczepiński W, Szlagowski J (1990) Plastic Design of Complex Shape Structures. PWN-Polish Scientific Publishers and Ellis Horwood Limited, Warszawa, Chichester

[19] Drucker DC (1949) Relation of experiments to mathematical theories of plasticity. J of Applied Mechanics **16**:349–357

[20] Freudenthal AM, Gou RF (1969) Second order effects in the theory of plasticity. Acta Mechanica **8**(1):34–52

[21] Sayir M (1970) Zur Fließbedingung der Plastizitätstheorie. Ingenieur-Archiv **39**(6):414–432

[22] Sobotka Z (1967) The cubic yield condition for incompressible bodies. Acta Techica CSAV, Ceskoslovenskáá Akademie Ved, Praha **12**(6):830–832

[23] Spitzig W, Sober R, Richmond O (1975) Pressure dependence of yielding and associated volume expansion in tempered martensite. Acta Metallurgica **23**(7):885–893

[24] Spitzig WA, Richmond O (1979) Effect of hydrostatic pressure on the deformation behavior of polyethylene and polycarbonate in tension and in compression. Polymer Engineering & Science **19**(16):1129–1139

[25] Spitzig WA, Sober RJ, Richmond O (1976) The effect of hydrostatic pressure on the deformation behavior of maraging and HY-80 steels and its implications for plasticity theory. Metallurgical Transactions A **7**(11):1703–1710

[26] Dodd B, Naruse K (1989) Limitation on isotropic yield criteria. Int J of Mechanical Sciences **31**(7):511–519

[27] Yu MH (2002) Advances in strength theories for materials under complex stress state in the 20th century. Applied Mechanics Reviews **55**(5):169–218

[28] Podgórski J (1983) Ogólny warunek stanu granicznego dla materiałów izotropowych. Prace IPPT PAN, IFTR Reports, Instytut Podstawowych Probłemów Techniki Polskiej Akademii Nauk **17**:4–21

[29] Podgórski J (1984) Limit state condition and the dissipation function for isotropic materials. Archives of Mechanics **36**(3):323–342

[30] Podórski J (1985) General failure criterion for isotropic media. J of Engineering Mechanics **111**(2):188–201

[31] Podórski J (1986) Critical states in bodies with internal friction, (in Polish: Stany krytyczne w ciałach z tarciem wewnętrznym). Praca doctorska, Prace IPPT, IFTR Reports, Instytut Podstawowych Problemów Techniki Polskiej Akademii Nauk, 25, Warszawa

[32] Altenbach H, Altenbach J, Zolochevsky A (1995) Advanced Deformation Models and Failure Criteria in Material Mechanics (in German: Erweiterte Deformationsmodelle und Versagenskriterien der Werkstoffmechanik). Deutscher Verlag für Grundstoffindustrie, Stuttgart

[33] Altenbach H, Bolchoun A, Kolupaev VA (2014) Phenomenological yield and failure criteria. In: Altenbach H, Öchsner A (eds) Plasticity of Pressure-Sensitive Materials, Springer, Berlin Heidelberg, Engineering Materials, pp 49–152

[34] Altenbach H, Kolupaev VA (2009) Fundamental forms of strength hypotheses. In: Indeitcev DA, Krivtsov AM (eds) Proc. of XXXVI Summer School Advanced Problems in Mechanics, Institute for Problems in Mechanical Engineering RAS, St. Petersburg, pp 32–45

[35] Bolchoun A, Kolupaev VA, Altenbach H (2011) Convex and non-convex flow surfaces (in Germ.: Konvexe und nichtkonvexe Fließflächen). Forschung im Ingenieurwesen **75**(2):73–92

[36] Kolupaev VA (2018) Equivalent Stress Concept for Limit State Analysis. Springer, Cham

[37] Kolupaev VA, Bolchoun A (2008) Combined yield and fracture criteria (in Germ.: Kombinierte Fließ- und Grenzbedingungen). Forschung im Ingenieurwesen **72**:209–232

[38] Cazacu O, Barlat F (2004) A criterion for description of anisotropy and yield differential effects in pressure-insensitive metals. Int J of Plasticity **20**(11):2027–2045

[39] Cazacu O, Plunkett B, Barlat F (2006) Orthotropic yield criterion for hexagonal closed packed metals. Int J of Plasticity **22**(7):1171–1194

[40] Hu W, Wang ZR (2005) Multiple-factor dependence of the yielding behavior to isotropic ductile materials. Computational Materials Science **32**(1):31–46

[41] Wang Z, Hu W (1989) A general yield criterion, in Chinese. Chinese J of Theoretical and Applied Mechanics (Acta Mechanica Sinica) - Li xue xue bao: shuang yue kan **21**(S1, SUP):213–219

[42] Wang ZR, Hu W, Yuan SJ, Wang X (2018) Engineering Plasticity: Theory and Applications in Metal Forming. Wiley, Higher Education Press, Singapore

[43] Betten J (1976) Plastische Anisotropie und Bauschinger-Effekt; allgemeine Formulierung und Vergleich mit experimentell ermittelten Fließortkurven. Acta Mechanica **25**(1-2):79–94

[44] Haythornthwaite RM (1985) A family of smooth yield surfaces. Mechanics Research Communications **12**(2):87–91

[45] Haythornthwaite RM (1992) Isotropic yield criteria developed from simple shear. Mechanics Research Communications **19**(1):59–64

[46] Krenk S (1996) Family of invariant stress surfaces. J of Engineering Mechanics **122**(3):201–208

[47] Krenk S (2000) Characteristic state plasticity for granular materials. Part I: Basic theory. Int J of Solids and Structures **37**(43):6343–6360

[48] Lagzdiņš A, Zilaucs A (1996) Constructing convex limit surfaces in material mechanics. Mechanics of Composite Materials **32**(3):233–241

[49] Lagzdin' A (1997) Smooth convex limit surfaces in the space of symmetric second-rank tensors. Mechanics of Composite Materials **33**(2):119–127

[50] Richmond O, Spitzig WA (1980) Pressure dependence and dilatancy of plastic flow. In: Rimrott FPJ, Tabarrok B (eds) Theoretical and Applied Mechanics, North-Holland Publishing Co., Amsterdam, IUTAM, Proceedings of the XVth Int. Congress of Theoretical and Applied Mechanics, University of Toronto, Canada, August 17-23, 1980, pp 377–386

[51] Szwed A (2013) Construction of the deviatoric shape function for the cross-sections of the limit surfaces, (in Polish: Konstrukcja funkcji kształtu przekrojów dewiatorowych powierzchni granicznych). In: Jemioło S, Szwed A (eds) Seria Monografie Zakładu Wytrzymałości Materiałów, Teorii Sprężystości i Plastyczności ZWMTSiP, Deformacje i Wytrzymałość Materiałów i Elementów Konstrukcji, Wydział Inżynierii Lądowej Politechniki Warszawskiej, Warszawa, 3, pp 51–66

[52] Altenbach H (2001) A nonclassical model for creep-damage processes. Materials Physics and Mechanics **3**:25–35

[53] Altenbach H, Schieße P, Zolochevsky AA (1991) Zum Kriechen isotroper Werkstoffe mit komplizierten Eigenschaften. Rheologica Acta **30**(4):388–399

[54] Brünig M, Berger S, Obrecht H (2000) Numerical simulation of the localization behavior of hydrostatic-stress-sensitive metals. Int J of Mechanical Sciences **42**(11):2147–2166

[55] Maitra M, Majumdar K, Das A (1973) Unified plastic yield criterion for ductile solids. AIAA J **11**(10):1428–1429

[56] Bigoni D, Piccolroaz A (2003) A new yield function for geomaterials. In: Viggiani C (ed) Constitutive Modeling and Analysis of Boundary Value Problems in Geotechnical Engineering, Hevelius Edizioni, Benevento, Italy, pp 266–281

[57] Bigoni D, Piccolroaz A (2004) Yield criteria for quasibrittle and frictional materials. Int J of Solids and Structures **41**(11):2855–2878

[58] Piccolroaz A, Bigoni D (2009) Yield criteria for quasibrittle and frictional materials: a generalization to surfaces with corners. Int J of Solids and Structures **46**(20):3587–3596

[59] Carney K, Du Bois P, Sengoz K, Wang L, Kan CD (2020) Development of a generalized yield surface for isotropic, pressure-insensitive metal plasticity with differing tension, compression, and shear yield strengths. Report dot/faa/tc-19/42, Federal Aviation Administration, William J. Hughes Technical Center, Aviation Research Division, Atlantic City International Airport, New Jersey

[60] Sengoz K (2017) Development of a generalized isotropic yield surface for pressure insensitive metal plasticity considering yield strength differential effect in tension, compression and shear stress states. Diss., The School of Engineering and Applied Science, The George Washington University, Washington

[61] Altenbach H, Kolupaev VA (2014) Classical and non-classical failure criteria. In: Altenbach H, Sadowski T (eds) Failure and Damage Analysis of Advanced Materials, Springer, Wien, Heidelberg, Int. Centre for Mechanical Sciences CISM, Courses and Lectures Vol. 560, pp 1–66

[62] Banabic D, Bunge HJ, Pöhlandt K, Tekkaya AE (2000) Formability of Metallic Materials: Plastic Anisotropy, Formability Testing, Forming Limits. Springer, Berlin

[63] Bertram A (2012) Elasticity and Plasticity of Large Deformations. Springer, Berlin

[64] Fromm H (1931) Grenzen des elastischen Verhaltens beanspruchter Stoffe. In: Auerbach F, Hort W (eds) Statik und Dynamik elastischer Körper nebst Anwendungsgebieten. II. Teil. Zum Gebrauch für Ingenieure, Physiker und Mathematiker, vol 4, Barth-Verlag, Leipzig, pp 359–435

[65] Gol'denblat II, Kopnov VA (1968) Yield and Strength Criteria for Structural Materials (in Russ.: Kriterii prochnosti i plastichnosti konstrukzionnych materialov). Mashinostroenie, Moscow

[66] Huber MT (1948) Strength criteria in technical stereomechanics (in Polish: Kryteria wytrzymałościowe w stereomechanice technicznej). Instytut Wydawniczy SIMP, Warszawa pp 1–18

[67] Paul B (1968) Generalized pyramidal fracture and yield criteria. Int J of Solids and Structures **4**(2):175–196

[68] Pisarenko GS, Lebedev AA (1976) Deformation and Strength of Materials under Complex Stress State (in Russ.: Deformirovanie i prochnost' materialov pri slozhnom naprjazhennom sostojanii). Naukowa Dumka, Kiev

[69] Pisarenko GS, Lebedev AA (1968) On the shape of a limit surface for a mechanical strength criterion (in Russ.: O forme predel'noj poverchnosti mekhanicheskogo kriterija prochnosti). Prikladnaja Mekhanika **4**(3):45–50

[70] Potapova LB, Yarzev VP (2005) Mechanics of Materials under Complex Stress State. How Predict the Limit Stresses? (in Russ.: Mekhanika materialov pri slozhnom naprjazhennom sostojanii. Kak prognozirujut predel'nye naprjazhenija?). Mashinostroenie-1, Moscow

[71] Sähn S, Göldner H, Nickel J, Fischer K (1993) Bruch- und Beurteilungskriterien in der Festigkeitslehre. Fachbuchverlag, Leipzig, Köln

[72] Skrzypek JJ (1993) Plasticity and Creep: Theory, Examples and Problems. CRC Press, Boca Raton

[73] Shen ZJ (1995) Summary on the failure criteria and yield functions (in chinese). Chinese J of Geotechnical Engineering **17**(1):1–8

[74] Timoshenko SP (1953) History of Strength of Materials: With a Brief Account of the History of Theory of Elasticity and Theory of Structure. McGraw-Hill, New York

[75] Yagn YI (1933) Strength of Materials: Theory and Problems (in Russ.: Soprotivlenie materialov: teorija i zadachnik). Kubuch, Leningrad

[76] Brandt AM, Dzieniszewski W, Jendo S, Marks W, Owczarek S, Wasiutyński Z (1986) Criteria and Methods of Structural Optimization. Martinus Nijhoff Publishers, PWN - Polish Scientific Publishers, Dordrecht, Warszawa

[77] Chen WF (1984) Constitutive modelling in soil mechanics. In: Desai CS, Gallagher RH (eds) Mechanics of Engineering Materials, Numerical Methods in Eingieering, Wiley, Chichester, pp 91–120

[78] Mang HA, Hofstetter G (2013) Festigkeitslehre, 4. aktualisierte Auflage. Springer, Berlin

[79] Voigt W (1901) Zur Festigkeitslehre. Annalen der Physik **309**(4):567–591

[80] Yu MH (2023) Soil Mechanics: New Concept and Theory. Zhejiang University Press, Springer Nature Singapure

[81] Altenbach H, Kolupaev VA (2022) General forms of limit surface: Application for isotropic materials. In: Altenbach H, Beitelschmidt M, Kästner M, Naumenko K, Wallmersperger T (eds) Material Modeling and Structural Mechanics, Springer, Cham, Advanced Structured Materials, pp 1–76

[82] Rosendahl PL, Kolupaev VA, Altenbach H (2019) Extreme yield figures for universal strength criteria. In: Altenbach H, Öchsner A (eds) State of the Art and Future Trends in Material Modeling, Advanced Structured Materials, Springer Nature, Cham, 100, pp 259–324

[83] Malinin NN (1975) Applied Theory of Plasticity and Creep (in Russ.: Prikladnaja teorija plastichnosti i polzuchesti). Mashinostroenije, Moscow

[84] Mālmeisters A, Tamužs V, Teters G (1977) Mechanik der Polymerwerkstoffe. Akademie-Verlag, Berlin

[85] Filonenko-Boroditsch MM (1961) Mechanical Theories of Strength (in Russ.: Mechanicheskie teorii prochnosti). Izdatel'stvo Moskovskogo Universiteta MGU, Moscow

[86] Burzyński W (1929) Theoretical foundations of the hypotheses of material effort (in Polish: Teoretyczne podstawy hipotez wytężenia). Czasopismo Techniczne **47**:1–41

[87] Burzyński W (2009) Selected passages from Włodzimierz Burzyński's doctoral dissertation "Study on Material Effort Hypotheses" printed in Polish by the Academy of Technical Sciences, Lwów, 1928, 1-192. Engng Trans Polish Academy of Sciences **57**:3–4, 127–157

[88] Geiringer H (1937) Fondements mathématiques de la théorie des corps plastiques isotropes. Mémorial des Sciences Mathématiques, Gauthier-Villars, Paris **86**:1–91

[89] Mesnager A (1927) Limites de rupture et de déformation permanente. Congrès International pour L'essai des Matériaux, La Have M Nijhoff **I**:15–38

[90] Nadai A (1933) Theories of strength. Applied Machanics, Transactions of the American Society of Mechanical Engineers pp 111–129, APM-55-15

[91] Rendulic L (1938) Eine Betrachtung zur Frage der plastischen Grenzzustände. Der Bauingenieur **19**(11/12):159–164

[92] Filonenko-Boroditsch MM (1954) On the strength criteria for materials with different strength under tension and compression (in Russ.: Ob uslovijach prochnosti materialov, obladajushhikh razlichniym soprotivleniem rastjazheniju i szhatiju). Inzhenernyj Sbornik **19**:13–36

[93] Filonenko-Borodich MM (1960) Theory of Elasticity. P. Noordhoff W. N., Groningen

[94] Novozhilov VV (1952) On the physical meaning of invariants of stress used in the theory of plasticity (in Russ.: O fizicheskom smysle invariantov naprjazhenija, ispol'zuemykh v teorii plastichnosti). Prikladnaja Matematika i Mekhanika **XVI**(5):617–619

[95] Ponomarev SD (1953) On the interpretation of the so-called "strength theory of energy of form change" (in Russ.: K voprosu o traktovke tak nazyvaemoj "teorii prochnosti energii formoizmenenija"). Vestnik inzhenerov i tekhnikov, NTO VSNITO, Moskovskoe politechnicheskoe obshhestvo (1):25–26

[96] Benthem JP (1951) On the stress-strain relations of plastic deformation. Tech. Rep. S.398, Ordernumber 295.110, Nationaal Luchtvaartlaboratorium, Amsterdam

[97] Cazacu O (2020) New expressions and calibration strategies for Karafillis and Boyce (1993) yield criterion. Int J of Solids and Structures **185**:410–422

[98] Jones RM (2009) Deformation Theory of Plasticity. Bull Ridge Publishing, Blacksburg, Virginia

[99] Prager W, Hodge P (1954) Theorie ideal plastischer Körper. Springer, Wien

[100] Sokolovsky VV (1950) Theory of Plasticity (in Russ.: Teorija plastichnosti). Gos. Izdatelstvo techn.-teoret. lit., Moscow, Leningrad

[101] Szwed A (2000) Strength hypotheses and constitutive relations of materials including degradation effects, (in Polish: Hipotezy wytężeniowe i relacje konstytutywne materiałów z uwzględnieniem efektów degradacji). Praca doctorska, Wydział Inżynierii Lądowej Politechniki Warszawskiej, Warszawa

[102] Xiaoping Y, Ottosen NS, Thelandersson S, Nielsen MP (1989) Review of constructive models for concrete, Final report. Tech. rep., European Communities Commission EUR 12394 EN, Office for Official Publications of the European Communities, Luxembourg, Series: Nuclear Science and Technology

[103] Geiringer H (1953) Some recent results in the theory of an ideal plastic body. Advances in Applied Mechanics **3**:197–294

[104] Troost A, Betten J (1973) Zur Schreibweise von Flußbedingungen bei Isotropie und Anisotropie. Zeitschrift für Naturforschung A **28**(2):319–320

[105] Yu MH, Ma GW, Li JC (2009) Structural Plasticity. Limit, Shakedown and Dynamic Plastic Analyses of Structures. Springer, Berlin

[106] Annin BD (1999) Theory of ideal plasticity with a singular yield surface. J of Applied Mechanics and Technical Physics **40**(2):347–353

[107] Annin BD, Zhigalkin VM (1999) Material Behaviour under Complex Loading Conditions (in Russ.: Povedenie materialov v uslovijach slozhnogo nagruzhenija. Izdatel'stvo SO RAN, Novosibirsk

[108] Cazacu O, Revil-Baudard B (2020) Plasticity of Metallic Materials: Modeling and Applications to Forming. Elsevier

[109] von Mises R (1913) Mechanik des festen Körpers im plastischen deformablen Zustand. Nachrichten der Königlichen Gesellschaft der Wissenschaften Göttingen, Mathematisch-physikalische Klasse pp 582–592

[110] Radaev YN (2007) On the Ishlinsky commutative equations in the mathematical theory of plasticity (in Russ.: O sootnoshenijach perestanovochnosti Ishlinskogo v matematicheskoj teorii plastichnosti. Vestnik SamGu, Estestvennonauchnaja serija **56**(6):102–114

[111] Sokolovsky VV (1946) Theory of Plasticity (in Russ. and English: Teorija plastichnosti). Izdatelstvo Akademii Nauk SSSR, Moscow

[112] Kolupaev VA, Yu MH, Altenbach H (2013) Yield criteria of hexagonal symmetry in the π-plane. Acta Mechanica **224**(7):1527–1540

[113] Troost A, Betten J (1975) Mögliche Deutungen quadratischer Fließbedingungen bei Isotropie und Anisotropie. Zeitschrift für Naturforschung A: Physik, physikalische Chemie, Kosmophysik **30**(8):996–1000

[114] De Boer R (2000) Theory of Porous Media: Highlights in Historical Development and Current State. Springer, Berlin

[115] Kolupaev VA (2006) 3D-Creep Behaviour of Parts Made of Non-Reinforced Thermoplastics (in Germ.: Dreidimensionales Kriechverhalten von Bauteilen aus unverstärkten Thermoplasten). Diss., Martin-Luther-Universität Halle-Wittenberg, Halle-Saale

[116] Gupta NK, Meyers A (1990) Fitting of experimental yield surfaces. ZAMM J of Applied Mathematics and Mechanics / Zeitschrift für Angewandte Mathematik und Mechanik **70**(3):181–187

[117] Irmay S (1968) Failure criteria of plastic solids in the space of stress invariants. Israel J of Technology **6**(3):165–173

[118] Goldenblat II, Kopnov VA (1971) General theory of strength criteria of isotropic and anisotropic materials (in Russ.: Obshaja teorija kriteriev prochosti isotropnykh i anizotropnykh materialov). Problemy Prochnosti **5**:65–69

[119] Yagn YI, Vinogradov IN (1954) Influence of the shape of the stress deviator upon the strength of metals at plastic deformations (in Russ.: Vlijanie vida deviatora naprjazhenij na soprotivlenie metallov plasticheskomy deformierovaniju). Doklady Akademii Nauk SSSR (Moskva) **96**(3):515–517

[120] Klębowski Z (1934) Obecny stan wytrzymałościowego obliczenia materiałów o własnościach uogólnionych; uogólnione obliczenie osiowo symetrycznego cienkościennego naczynia pod ciśnieniem. Przegląd Techniczny (11):7–31

[121] Klębowski Z (1950) Energetyczne hipotezy wytężenia, a możność opracowania ogólnej teorii wytężenia. Księga jubileuszowa dla uczczenia zasług naukowych prof dr inz M T Hubera z okazji 50 - lecia pracy naukowej pp 165–179

[122] Hencky H (1943) Ermüdung, Bruch, Plastizität. Stahlbau **16**(23/24):95–97

[123] Marciniak Z (1971) Graphical representation of states of stress and strain. Archives of Mechanics **3**:261–274

[124] Mendera Z (1966) Wytężenie spoiny czołowej w interpretacji powierzchni granicznych. Przegląd Spawalnictwa SIMP **XVIII(1)**:6–13

[125] Pełczyński T (1957) The effect of the stress state on the transition of the material to a state of plasticity (in Polish: Wpływ stanu napięcia na przejście materiału w stan plastyczny). Przeglad Mechaniczny **7**:204–208

[126] Pełczyński T (1962) Issues of material strength. Historical background (in Polish: Zagadnienia wytężenia materiałów. Rys historyczny). Obróbka Plastyczna **3**:9–49

[127] Davis EA, Connelly FM (1959) Stress distribution and plastic deformation in rotating cylinders of strain-hardening material. Transactions of the ASME, J of Applied Mechanics **26**:25–30

[128] Lebedev AA (2010) Development of the theories of strength in the mechanics of materials. Strength of Materials **42**(5):578–592

[129] Lebedev AA, Koval'chuk BI, Lamashevsky VP, Giginjak FF (1979) Computation of Complex Stress State: Determining of Equivalent Stresses. Akademija Nauk Ukrainskoj SSR, Institut Problem Prochnosti, Kiew

[130] Stommel M, Stojek M, Korte W (2018) FEM zur Berechnung von Kunststoff- und Elastomerbauteilen. Hanser, München

[131] Freudenthal AM, Geiringer H (1958) The mathematical theories of the inelastic continuum. In: Flügge S (ed) Handbuch der Physik, Elastizität und Plastizität, vol 6, Springer, Berlin, pp 229–433

[132] Fromm H (1933) Stoffgesetze des isotropen Kontinuums, inbesondere bei zähplastischem Verhalten. Ingenieur-Archiv **4**(5):432–466

[133] Novozhilov VV (1951) On the principles of the statical analysis of the experimental results for isotropic materials (in Russ.: O prinzipakh obrabotki rezultatov staticheskikh ispytanij izotropnykh materialov). Prikladnaja Matematika i Mekhanika **XV**(6):709–722

[134] Chen WF, Zhang H (1991) Structural Plasticity - Theory, Problems, and CAE Software. Springer, New York

[135] Nayak GC, Zienkiewicz OC (1972) Elasto-plastic stress analysis. a generalization for various contitutive relations including strain softening. Int J for Numerical Methods in Engineering **5**(1):113–135

[136] Ottosen NS, Ristinmaa M (2005) The Mechanics of Constitutive Modeling. Elsevier, Amsterdam

[137] Zienkiewicz OC, Pande GN (1977) Some useful forms of isotropic yield surfaces for soil and rock mechanics. In: Gudehus G (ed) Finite Elements in Geomechanics, Wiley, London, New York, pp 179–198

[138] Jemioło S, Szwed A (1999) Application of convex isotropic functions in failure theory for isotropic materials: Yield criteria for metals, (in Polish: O zastosowaniu funkcji wypukłych w teorii wytężenia materiałów izotropowych: Propozycja warunków plastyczności metali). Prace Naukowe Politechniki Warszawskiej, Budownictwo **133**:5–52

[139] Bronstein IN, Semendjajew KA (2007) Handbook of Mathematics. Springer, Berlin

[140] Chen WF, Mizuno E, et al (1990) Nonlinear Analysis in Soil Mechanics: Theory and Implementation. Developments in Geotechnical Engineering 53, Elsevier, Amsterdam

[141] Geiringer H, Prager W (1934) Mechanik isotroper Körper im plastischen Zustand. Ergebnisse der Exakten Naturwissenschaften, Schriftleitung der Naturwissenschaften **13**:310–363

[142] Lagioia R, Panteghini A (2016) On the existence of a unique class of yield and failure criteria comprising Tresca, von Mises, Drucker-Prager, Mohr-Coulomb, Galileo-Rankine, Matsuoka-Nakai and Lade-Duncan. Proceedings of the Royal Society of London, Series A **472**(2185):20150,713

[143] Haigh BP (1920) The strain-energy function and the elastic limit. Engineering **109**:158–160

[144] Westergaard HM (1920) On the resitance of ductile materials to combined stress in two or three directions perpendicular to one another. J of the Franklin Institute **189**:627–640

[145] Burzyński W (1928) Study on Material Effort Hypotheses, (in Polish: Studjum nad Hipotezami Wytężenia). Akademia Nauk Technicznych, Lwów

[146] Reuss A (1933) Vereinfachte Beschreibung der plastischen Formänderungsgeschwindigkeiten bei Voraussetzung der Schubspannungsfließbedingung. ZAMM **13**(5):356–360

[147] Sawczuk A (1982) Introduction to Mechanics of Plastic Structures (in Polish: Wprowadzenie do mechaniki konstrukcji plastycznych). Panstwowe Wydawnictwo Naukowe PWN, Warszawa

[148] Yagn YI (1931) New methods of strength prediction (in Russ.: Novye metody pascheta na prochnost'). Vestnik inzhenerov i tekhnikov **6**:237–244

[149] Murzewski J (1957) Une theorie statistique du corps fragile quasihomogene. In: IXe Congrès Int. de Mécanique Appliquée, ICAM-1956, Université de Bruxelles, vol 5, pp 313–320

[150] Murzewski J (1960) A probabilistic theory of plastic and brittle behaviour of quasi-homogeneous materials. Archiwum Mechaniki Stosowanej **3**(12):203–227

[151] Novozhilov VV (1951) On the connection between stresses and strains in a nonlinear-elastic continuum (in Russ.: O svjazi mezhdu naprjazhenijami i deformazijami v nelinejno-uprugoj srede). Prikladnaja Matematika i Mekhanika **XV**(2):183–194

[152] Lagzdin' AZ, Tamuzh VP (1971) Construction of a phenomenological theory of the fracture of an anisotropic medium (in Russ.: K postroeniju fenomeno-logicheskoj teorii razrushenija anizotropnoj sredy). Mekhanika Polimerov **7**(4):563–571

[153] Yu MH, Mao GW, Qiang HF, Zhang YQ (2006) Generalized Plasticity. Springer, Berlin

[154] Altenbach H (2001) A generalized limit criterion with application to strength, yielding, and damage of isotropic materials. In: Lemaitre J (ed) Handbook of Materials Behaviour Models. Academic Press, San Diego, pp 175–186

[155] Kolupaev VA (2017) Generalized strength criteria as functions of the stress angle. J of Eng Mechanics **143**(9):04.017.095

[156] Awaji H, Sato S (1978) A statistical theory for the fracture of brittle solids under multi-axial stresses. Int J of Fracture **14**(1):R13–R16

[157] Gurson AL (1977) Continuum theory of ductile rupture by void nucleation and growth: Part I - Yield criteria and flow rules for porous ductile media. J of Engineering Materials and Technology, Transactions of ASME **99**:2–15

[158] Lindsey GH, Schapery RA, Williams ML, Zak AR (1963) The triaxial tension failure of viscoelastic materials. Tech. Rep. DTIC Document ARL 63-152, California Institute of Technology Passadena, California

[159] Oh KPL, Vardar O, Finnie I (1973) Failure of brittle solids under biaxial stresses. Int J of Fracture **9**(3):372–375

[160] Reiner M (1960) Deformation, Strain and Flow: An Elementary Introduction to Rheology. Lewis & Co., London

[161] Williams ML, Schapery RA (1965) Spherical flaw instability in hydrostatic tension. Int J of Fracture Mechanics **1**(1):64–72

[162] von Mises R (1928) Mechanik der plastischen Formänderung von Kristallen. J of Applied Mathematics and Mechanics, ZAMM **8**:161–185

[163] Giraldo-Londoño O, Paulino GH (2020) A unified approach for topology optimization with local stress constraints considering various failure criteria: von Mises, Drucker-Prager, Tresca, Mohr-Coulomb, Bresler-Pister and Willam-Warnke. Proceedings of the Royal Society A **476**(2238):20190,861

[164] Kolupaev VA, Yu MH, Altenbach H, Bolchoun A (2018) Comparison of strength criteria based on the measurements on concrete. J of Eng Mechanics (ASCE) **144**(6)

[165] Kolupaev VA, Bolchoun A, Altenbach H (2009) Unified representation and evaluation of the strength hypotheses. In: Elboujdaini M, Tyson B, Patnaik P (eds) 12th Int. Conference on Fracture ICF 12, 10 p., National Research Council Canada, Ottawa

[166] Matsuoka H, Nakai T (1985) Relationship among Tresca, Mises, Mohr-Coulomb and Matsuoka-Nakai failure criteria. Soils and Foundations **25**(4):123–128

[167] Zhang J, Zhang ZX, Huang CP (2011) Representation based classification of strength theories of concrete. In: Advanced Materials Research, vol 168, pp 74–77

[168] Xu P, Sun Z, Shao S, Fang L (2021) Comparative analysis of common strength criteria of soil materials. Materials **14**(15):4302

[169] Marti P (1980) Zur plastischen Berechnung von Stahlbeton, Institut für Baustatik und Konstruktion, vol 104. Birkhäuser, Basel, Diss. ETH Zürich

[170] Sayir M, Ziegler H (1969) Der Verträglichkeitssatz der Plastizitätstheorie und seine Anwendung auf räumlich unstetige Felder. Zeitschrift für angewandte Mathematik und Physik ZAMP **20**(1):78–93

[171] Conway JH, Burgiel H, Goodman-Strauss C (2008) The Symmetries of Things. Peters, Ltd., Wellesley

[172] Koca M, Koca NO (2011) Quasi regular polygons and their duals with Coxeter symmetries D_n represented by complex numbers. In: J. of Physics: Conference Series, Group 28: Physical and Mathematical Aspects of Symmetry, IOP Publishing, vol 284, pp 1–10

[173] Tóth LF (1964) Regular Figures. Pergamon Press, Oxford

[174] Nye JF (1985) Physical Properties of Cristals: Their Representation by Tensors and Matrices. Oxford University Press, Oxford

[175] Ivlev DD (1959) The theory of fracture of solids (in Russ.: K teorii razrushenija tverdykh tel). J of Applied Mathematics and Mechanics **23**(3):884–895

[176] Bishop AW (1966) The strength of soils as engineering materials. Geotechnique **16**(2):91–130

[177] Capurso M (1967) Yield conditions for incompressible isotropic and orthotropic materials with different yield stress in tension and compression. Meccanica **2**(2):118–125

[178] Cicala P (1961) Presentazione geometrica delle relazioni fondamentali d'elastoplasticità. Giornale del Genio Civile **99**:125–137

[179] Ko WL (1963) Application of the finite elastic theory to the behavior of rubber-like materials. PhD thesis, California Institute of Technology, Pasadena

[180] Ziegler H (1969) Zum plastischen Potential der Bodenmechanik. Zeitschrift für angewandte Mathematik und Physik ZAMP **20**:659–675

[181] Mariotte E (1718) Traité du Mouvement des Eaux et des Autres Corps Fluides. J. Jambert, Paris

[182] Benvenuto E (1991) An Introduction to the History of Structural Mechanics. Springer, New York

[183] Birger IA, Shopp BF, Iosilevich GB (1993) Strength Computations for Machine Components. Handbook (in Russ.: Raschet na prochnost' detalej mashin. Spravochnik). Mashinostroenie, Moscow

[184] Finnie I, Heller WR (1959) Creep of Engineering Materials. McGraw-Hill, New York

[185] Ponomarev SD, Biderman VL, Likharev KK, Makushin VM, Malinin NN, Feodosjev VI (1957) Strength Analysis in Mechanical Engineering (in Russ.: Rascety na procnost' v masinostroenii), vol 1. Gosudarstvennoe nauchno-technicheskoe izdatel'stvo mashinostroitel'noj literaturi, Moskow

[186] Sauter J, Winterger N (1990) Neue und alte statische Festigkeitshypothesen. VDI, Reihe 1: Konstruktionstechnik / Maschinenelemente Nr. 191, Düsseldorf

[187] Shanley FR (1957) Strength of Materials. McGraw-Hill, New York

[188] Coulomb CA (1776) Essai sur une application des regles des maximis et minimis a quelques problemes de statique relatifs, a la architecture. Mem Acad Roy Div Sav **7**:343–387

[189] Lévy M (1871) Extrait du mémoire sur les équations générales des mouvements intérieurs des corps solides ductiles au delà des limites où l'élasticité pourrait les ramener à leur premier état; présenté le 20 juin 1870. J de mathématiques pures et appliquées **16**:369–372

[190] de Saint Venant B (1870) Mémoire sur l'etablissement des equations différentielles des mouvements inérieurs opérés dans les corps ductiles au délà des limites où l'élasticité pourtait les ramener à leur premier état. Comptes Rendus de l'Academie des Sciences Paris **70**:473–480

[191] Tresca H (1868) Mémoire sur l'ecoulement des corps solides. Mémoires Pres par Div Savants **18**:733–799

[192] Marin J (1942) Mechanical Properties of Materials and Design. McGraw-Hill, New York

[193] Artemov MA, Baranovskii ES, Yakubenko AP (2015) Alternative forms of the piecewiwe-linear conditions of plasticity and their generalizations (in Russ.: Al'ternativnye formy zapisi kusochno-linejnych uslovij plastichnosti i ich obobshhenija). Vestnik Voronezhskogo gosudarstvennogo universiteta Serija: Fisika Mathematika (1):71–82

[194] Filin AP (1975) Applied Mechanics of Solid Deformable Bodies (in Russ.: Prikladnaja mekhanika tverdogo deformiruemogo tela), vol 1. Nauka, Moscow

[195] Dankert J, Dankert H (2013) Technische Mechanik: Statik, Festigkeitslehre, Kinematik/Kinetik. Springer, Vieweg, Wiesbaden

[196] Lemaitre J, Chaboche JL (1990) Mechanics of Solid Materials. Cambridge University Press, Cambridge

[197] Malvern LE (1969) Introduction to the Mechanics of a Continuous Medium. Prentice-Hall, New Jersey

[198] Marin J (1957) Theories of strength for combined stresses and nonisotropic materials. J of the Aeronautical Sciences **24**(4):265–268, 274

[199] Markowitz J (1968) Singular surfaces in perfectly plastic solids for general yield criteria. PhD thesis, Department of Engineering Mechanics, The Pennsylvania State University

[200] Massonnet C, Olszak W, Phillips A (2014) Plasticity in Structural Engineering, Fundamentals and Applications, vol 241. Springer, Wien

[201] Radaev YN (2007) Spatial Problem of the Mathematical Theory of Plasticity (in Russ.: Prostranstvennaja zadacha matematicheskoj teorii plastichnosti). Samarskij universitet, Samara

[202] Theocaris PS (1995) Failure criteria for isotropic bodies revisited. Eng Fracture Mechanics **51**(2):239–264

[203] Ishlinsky AY (1940) Hypothesis of strength of shape change (in Russ.: Gipoteza prochnosti formoizmenenija). Uchebnye Zapiski Moskovskogo Universiteta, Mekhanika **46**:104–114

[204] Schmidt R (1932) Über den Zusammenhang von Spannungen und Formänderungen im Verfestigungsgebiet. Ingenieur-Archiv **3**(3):215–235

[205] Yu MH (1961) General behaviour of isotropic yield function (in Chinese). Scientific and Technological Research Paper of Xi'an Jiaotong University pp 1–11

[206] Yu MH (1983) Twin shear stress yield criterion. Int J Mech Sci **25**(1):71–74

[207] Yu MH (1983) Twin shear stress yield criterion. Reply to Prof. Hill's comments. Int J of Mechanical Sciences **25**(11):845–846

[208] de Araújo FC (1962) Elasticidade e Plasticidade. Imprensa Portuguesa, Porto

[209] Haythornthwaite RM (1961) The range of the yield condition in stable, ideally plastic solids. Technical report, ORA Project 04403, University of Michigan, College of Engineering, Department of Engineering Mechanics, Detroit

[210] Haythornthwaite RM (1961) Range of yield condition in ideal plasticity. Proc ASCE J Eng Mech Division EM6 **87**:117–133

[211] Mendelson A (1968) Plasticity: Theory and Application. Macmillan, New York

[212] Prokudin A (2021) Schmidt-Ishlinskii yield criterion and a rotating cylinder with a rigid inclusion. J of Applied and Computational Mechanics **7**(2):858–869

[213] Rabotnov YN (1979) Mechanics of Deformable Solids (in Russ.: Mekhanika deformiruemogo tverdogo tela). Nauka, Moscow

[214] Troost A, Betten J (1975) Zur allgemeinen Formulierung der Fließbedingung unter Berücksichtigung der Anisotropie und des Bauschinger-Effekts. Zeitschrift für Naturforschung A: Physik, physikalische Chemie, Kosmophysik **30**(4):492–496

[215] Yan Z, Bu X (1996) An effective characteristic method for plastic plane stress problems. J of Engineering Mechanics **122**(6):502–506

[216] Zhang YQ, Hao H, Yu MH (2003) A unified characteristic theory for plastic plane stress and strain problems. J of Applied Mechanics, ASME **70**(5):649–654

[217] Berdzenishvili GG, Penkov HA, Semka EV, Fathudinov DB (2019) Mathematical modelling for the rotating disc state (in Russ.: Matematicheskoe modelierovanie sostojanija vrashhayshhegos'ja diska). In: Borisov D (ed) Informatics: Problems, Methodology, Technology. Materials XIX Int. scientific-methodical conference, 14-15 February 2019, Voronezh, pp 210–216

[218] Billington EW (1986) Introduction to the Mechanics and Physics of Solids. Adam Hilger Ltd., Bristol

[219] Desai CS, Siriwardane HJ (1984) Constitutive Laws for Engineering Materials, with Emphasis on Geologic Materials. Prentice Hall, Englewood Cliffs, New Jersey

[220] Haythornthwaite RM (1983) Piecewise linear yield criteria in invariant form. J of Eng Mechanics **109**(4):1016–1022

[221] Hui-er X (1994) A linearized and unified yield criterion of metals and its application. Applied Mathematics and Mechanics **15**:485–489

[222] Kiriakov P, Yakhno A (2006) Symmetries of the plane plasticity system with a general yield criterion. In: Agarwal RP, Perera K (eds) Differential & Difference Equations and Applications, Hindawi Publishing, New York, pp 555–564

[223] Li G, Zeng X, Li J, Huang L (1988) Elastoplastic analysis of an open-ended cylinder from the twelve polygonal yield condition. Int J of Pressure Vessels and Piping **33**(2):143–152

[224] Modarres-Motlagh A (1997) Lower bound to collapse load for structures. PhD thesis, School of Mechanical and Manufacturing Engineering, Faculty of Engineering, University of New South Wales UNSW

[225] Owen DRJ, Hinton E (1986) Finite Elements in Plasticity, Theory and Practice. Pineridge Press Limited, Swansea

[226] Semka EV, Artemov MA, Babkina YN, Baranovskii ES, Shashkin AI (2020) Mathematical modeling of rotating disk states. J of Physics: Conference Series **1479**(1):1–16

[227] Prager W (1956) A new method of analyzing stresses and strains in work-hardening plastic solids. J of Applied Mechanics **23**:493–496

[228] Zeng X, Li JX, Li JW, Li G, Yang Z, Li JY (1993) The application of the twelve-angled polygonal yield criterion to pressure vessel problems. Int J of Pressure Vessels and Piping **55**(3):385–393

[229] Ivlev DD (1960) On extremum properties of plasticity conditions (in Russ.: Ob ekstremal'nykh svojstvakh uslovii plastichnosti). J of Applied Mathematics and Mechanics **24**(5):1439–1446

[230] Shesterikov SA (1960) On the theory of ideal plastic solid (in Russ.: K postroeniju teorii ideal'no plastichnogo tela). Prikladnaja Matematika i Mekhanika, Otdelenie Tekhnicheskikh Nauk Akademii Nauk Sojusa SSR **24**(3):412–415

[231] Ishlinsky AY, Ivlev DD (2003) Mathematical Theory of Plasticity (in Russ.: Matematicheskaja teorija plastichnosti). Fizmatlit, Moscow

[232] Yu MH (1999) Engineering Strength Theory (in Chinese). Higher Education Press, Beijing

[233] Beltrami E (1885) Sulle condizioni di resistenza dei corpi elastici. Il Nuovo Cimento **18**(1):145–155

[234] Hencky H (1924) Zur Theorie plastischer Deformationen und der hierdurch im Material hervorgerufenen Nachspannungen. J of Applied Mathematics and Mechanics ZAMM **4**(4):323–334

[235] Hencky H (1925) Über langsame stationäre Strömungen in plastischen Massen mit Rücksicht auf die Vorgänge beim Walzen, Pressen und Ziehen von Metallen. ZAMM **5**(2):115–124

[236] Huber MT (1904) Specific strain work as a measure of material effort (in Polish: Właściwa praca odkształcenia jako miara wytężenia materyału). Czasopismo

Techniczne, Lwów, Organ Towarzystwa Politechnicznego we Lwowie **22**:34–40, 49–50, 61–62, 80–81

[237] Huber MT (2004) Specific work of strain as a measure of material effort. Archives of Mechanics **56**(3):173–190

[238] Föppl A, Föppl L (1920) Drang und Zwang: Eine höhere Festigkeitslehre für Ingenieure. R. Oldenbourg, München

[239] Pisarenko GS, Lebedev AA (1969) Deformation and Fracture of Materials under Combined Stress (in Russ.: Soprotivlenie materialov deformirovaniju i razrusheniju pri slozhnom naprjazhennom sostojanii). Naukowa Dumka, Kiev

[240] Sachs G (1928) Zur Ableitung einer Fließbedingung. Zeitschrift VDI **72**(22):734–736

[241] Timoshenko S (1947) Strength of Materials: Advanced Theory and Problems, Part II, vol II. D. Van Nostrand Co., Toronto

[242] Filonenko-Boroditsch MM, Isjumow SM, Olissow BA, Malginow LI (1954) Festigkeitslehre, vol II. VEB Verlag Technik, Berlin

[243] Malinin NN (2000) Who is Who in Strength of Materials (in Russ.: Kto est' kto v soprotivlenii materialov). Izdatel'stvo MGTU im. Baumana N. E., Moscow

[244] Rychlewski J (2011) Elastic energy decomposition and limit criteria. Eng Transactions, Polish Academy of Sciences **59**(1):31–63

[245] Sarkissian MS (1972) On the theory of perfect plasticity of solids with different tensile and compressive strengths. Izvestija Akademii Nauk Armjanskoj SSR, Mechanika, Erevan **25**(4):53–67

[246] Lankford J, Ko WL, Lindholm US (1973) A study of the dynamic strength and fracture properties of rock. Report AD-766 048, DTIC Document, Southwest Research Institute, San Antonio

[247] Willam KJ, Warnke EP (1975) Constitutive model for the triaxial behaviour of concrete (Stoffmodell für das mehrachsiale Verhalten von Beton). In: Proc. Int. Association for Bridge and Structural Engineering IABSE AIPC IVBH, Concrete Structures Subjected to Triaxial Stress, 17th-19th May 1974, ISMES, Bergamo, vol 19, pp 1–30

[248] Candland CT (1975) Implications of macroscopic failure criteria which are independent of hydrostatic stress. Int J of Fracture **11**(3):540–543

[249] Haythornthwaite RM (1962) Range of yield condition in ideal plasticity. Transactions of the American Society of Civil Engineers ASCE **127**(1):1252–1269

[250] Yu MH (2017) Unified strength theory (UST). In: Feng XT (ed) Rock Mechanics and Engineering, Volume 1: Principles, CRC Press, Balkema, Leiden, pp 425–452

[251] Yu MH, Yu SQ (2019) Introduction to Unified Strength Theory. CRC Press, London

[252] Szwed A (2010) General strengh criterion for incompressible materials. In: Szcześniak WE, Zbiciak A (eds) Theoretical Foundations of Civil Engineering : Polish-Ukraïnian-Lithuanian Transactions, Oficyna Wydawnicza Politechniki Warszawskiej, Warsaw, 18, pp 313–318

[253] Unger DJ (2022) Generalized Tresca yield condition as a family of elliptic curves with application to mode I crack problems. Zeitschrift für angewandte Mathematik und Physik ZAMP **73**(5):184

[254] Kolupaev VA, Altenbach H (2010) Considerations on the Unified Strength Theory due to Mao-Hong Yu (in Germ.: Einige Überlegungen zur Unified Strength Theory von Mao-Hong Yu). Forschung im Ingenieurwesen **74**(3):135–166

[255] Kolupaev VA, Bolchoun A, Altenbach H (2013) Yield criteria for incompressible materials in the shear stress space. In: Öchnser A, Altenbach H (eds) Experimental and Numerical Investigation of Advanced Materials and Structures, Springer, pp 107–119

[256] Lequeu PH, Gilormini P, Montheillet F, Bacroix B, Jonas JJ (1987) Yield surfaces for textured polycrystals. Acta Metallurgica **35**(2):439–451, 1159–1174

[257] Rosendahl PL (2020) From bulk to structural failure: Fracture of hyperelastic materials. Diss., Fachgebiet Strukturmechanik, Technische Universität Darmstadt

[258] Barlat F, Lege DJ, Brem JC (1991) A six-component yield function for anisotropic materials. Int J of Plasticity **7**(7):693–712

[259] Habraken AM (2004) Modelling the plastic anisotropy of metals. Archives of Computational Methods in Engineering **11**(1):3–96

[260] Hershey AV (1954) The plasticity of an isotropic aggregate of anisotropic face-centered cubic crystals. J of Applied Mechanics **21**(3):241–249

[261] Hosford WF (1972) A generalized isotropic yield criterion. Transactions of the ASME, J of Applied Mechanics **39**(June):607–609

[262] Hosford WF (1979) On yield loci of anisotropic cubic metals. In: 7th North American Metalworking Research, SME, Proc. NAMRC, Dearborn, 7, pp 191–196

[263] Karafillis AP, Boyce MC (1993) A general anisotropic yield criterion using bounds and a transformation weighting tensor. J of the Mechanics and Physics of Solids **41**(12):1859–1886

[264] Paul B (1968) Macroscopic plastic flow and brittle fracture. In: Liebowitz H (ed) Fracture: An Advanced Treatise, vol II, Academic Press, New York, pp 313–496

[265] Tan JJ (1990) Unified form of yield criteria for metallic materials (in Chinese). Chinese Science Bulletin **35**(7):555–557

[266] Lagioia R, Panteghini A, Puzrin AM (2014) The I_3 generalization of the Galileo-Rankine tension criterion. Proceedings of the Royal Society A: Mathematical, Physical and Engineering Sciences **470**(2172):20140,568

[267] Lemaitre J, Chaboche JL (1985) Mécanique des Matériaux Solides. Dunod, Paris

[268] Jirásek M, Bažant ZP (2002) Inelastic Analysis of Structures. Wiley, London and New York

[269] Koval'chuk BI (1981) Criterion for the limiting state of some hull steels under combined strain at room and elevated temperatures. Strength of Materials **13**(5):548–554

[270] Kroon M, Faleskog J (2013) Numerical implementation of a J_2- and J_3-dependent plasticity model based on a spectral decomposition of the stress deviator. Computational Mechanics **52**(5):1059–1070

[271] Takeda T, Kikuchi S, Nasu Y (1986) Experimental evaluation of yield condition containing third invariant of deviatoric stresses. In: Proceedings of the Thirtieth Japan Congress on Materials Research, Society of Materials Science, Japan, Kyoto, pp 13–18

[272] Bulla M, Kolupaev VA (2021) Stress analysis in design with plastics: Accessible method with huge impact. Kautschuk, Gummi Kunststoffe KGK, Hüthig GmbH **74**(5):32–39

[273] Balandin PP (1937) On the strength hypotheses (in Russ.: K voprosu o gipotezakh prochnosti). Vestnik inzhenerov i tekhnikov **1**:19–24

[274] Drass M (2020) Constitutive Modelling and Failure Prediction for Silicone Adhesives in Façade Design, Diss., FB 13 Bauingenieurwesen, Technical University of Darmstadt, Mechanik, Werkstoffe und Konstruktion im Bauwesen, vol 55. Springer, Vieweg, Wiesbaden

[275] Feodosiev VI (1975) Ten lecture and talk sessions on strength of materials (in Russ.: Desjat' lekzij-besed po soprotivleniju materialov). Nauka, Moscow

[276] Kolupaev VA, Becker W, Massow H, Dierkes D (2014) Design of test specimens from hard foams for the investigation of biaxial tensile strength (in Germ.: Auslegung von Probekörpern aus Hartschaum zur Ermittlung der biaxialen Zugfestigkeit). Forschung im Ingenieurwesen **78**(3-4):69–86

[277] Torre C (1950) Grenzbedingung für spröden Bruch und plastisches Verhalten bildsamer Metalle. Österreichisches Ingenieur-Archiv **IV**(2):174–189

[278] Weisstein EW (2021) Trigonometry Angles – Pi/8. https://mathworld.wolfram.com/ TrigonometryAnglesPi8.html

[279] Lüpfert HP (1994) Beurteilung der statischen Festigkeit und Dauerfestigkeit metallischer Werkstoffe bei mehrachsiger Beanspruchung. Deutscher Verlag für Grundstoffindustrie, Leipzig

[280] Hou Y, Min J, Guo N, Shen Y, Lin J (2021) Evolving asymmetric yield surfaces of quenching and partitioning steels: Characterization and modeling. J of Materials Processing Technology **290**:116,979

[281] Lüpfert HP (1991) Schubspannungs-Interpretationen der Festigkeitshypothese von Huber / v. Mises / Hencky und ihr Zusammenhang. Technische Mechanik **12**(4):213–217

[282] Sokolovskij VV (1955) Theorie der Plastizität. VEB Verlag Technik, Berlin

[283] Besuchov NI (1961) Fundamentals of Theory of Elasticity, Plasticity and Creep (in Russ: Osnovy teorii urugosti, plastichnosti i polzuchesti. Vysshaja Shkola, Moscow

[284] Blinowski A, Rychlewski J (1998) Pure shears in the mechanics of materials. Mathematics and Mechanics of Solids **3**(4):471–503

[285] Kolosov GV (1933) On the surfaces showing the distribution of the shear stresses in a point of a continuous deformable body (in Russ.: O poverchnostjach demonstrirujushhich raspredelenije srezyvajushhich usilij v tochke sploshnogo deformiruemogo tela). Prikladnya Matematika i Mekhanika **1**(1):125–126

[286] Troost A (1961) Bemerkungen zu einer Anstrengungsbedingung. Naturwissenschaften **48**(21):664

[287] Ziółkowski AG (2022) Parametrization of Cauchy stress tensor treated as autonomous object using isotropy angle and skewness angle. Engineering Transactions **70**(3):239–286

[288] Johnson W, Mellor PB (1973) Engineering Plasticity. van Nostrand Reinhold, London

[289] Nadai A (1937) Plastic behavior of metals in the strain-hardening range. Part i. J of Applied Physics **8**(3):205–213

[290] Becker AJ (1916) The strength and stiffness of steel under biaxial loading. University of Illinois, Engineering Experiment Station, Urbana **XIII, 32**(Bulletin No. 85):1–68

[291] Becker AJ (1916) The action of mild steel under combined stress. The Quarterly J of the University of North Dakota **6**(3):208–219

[292] Botkin AI (1940) Theories of elastic failure of gramelar and of brittle materials (in Russ.: O prochnosti sypuchikh i khrupkikh materialov). Transactions of the Scientific Research Institute of Hydrotechnics, Izvestija NIIG, Leningrad **26**:205–236

[293] Lade PV (1977) Elasto-plastic stress-strain theory for cohesionless soil with curved yield surfaces. Int J of Solids and Structures **13**(11):1019–1035

[294] Love AEH (1952) A Treatise on the Mathematical Theory of Elasticity. University Press, Cambridge

[295] Marin J (1936) Failure theories of materials subjected to combined stresses. American Society of Civil Engineers Trans **101**(1):1162–1194, paper No. 1947

[296] Theocaris PS, Philippidis TP (1991) On the validity of the tensor polynomial failure theory with stress interaction terms omitted. Composites Science and Technology **40**(2):181–191

[297] Tsybul'ko AE, Romanenko EA (2020) Pespective strength criterion in engineering applications for calculation of technical and civil objects (in Russ.: Perspektivnyj kriterij prochnosti v inzhenernych prilozhenijach dlja rascheta technicheskich i stroitel'nych objektov). Technicheskie nauki, Elektronnyj innovazionnyj vestnik (5):6–9

[298] Wehage H (1905) Die zulässige Anstrengung eines Materials bei Belastung nach mehreren Richtungen. Zeitschrift VDI **49**(26):1077–1080

[299] Nadai A (1950) Theory of Flow and Fracture of Solids, vol 1. McGraw-Hill, New York

[300] Roš M, Eichinger A (1927) Versuche zur Klärung der Frage der Bruchgefahr. In: Eidg. Materialprüfungsanstalt an der E.T.H., Sonderdruck aus den Verhandlungen des 2. Int. Kongresses für technische Mechanik, Zürich, 1926, Orell Füssli, Zürich, Leipzig, pp 1–14

[301] Feldmann M (2022) Anstrengungs-und Bruchtheorie. In: Petersen S (ed) Stahlbau: Grundlagen der Berechnung und baulichen Ausbildung von Stahlbauten, Springer, Vieweg, Wiesbaden, pp 1837–1909

[302] Seely FB, Smith JO (1952) Advanced Mechanics of Materials. Wiley, New York

[303] Timoshenko S (1956) Strength of Materials, Part II: Advanced Theory and Problems. D. Van Nostrand Company, New York

[304] Yu MH, He L, Song L (1985) Twin Shear Stress Theory and its generalization. Scientia Sinica, Series A-Mathematical, Physical, Astronomical and Technical Sciences **28**(11):1174–1183

[305] Yu MH (1988) Researches on the Twin Shear Stress Strength Theory (in Chinese). Xi'an Jiaotong University Press, Xi'an

[306] Milner PR (1992) A linear algebra approach to stress and strain at a point and theories of yield. Strain **28**(1):3–8

[307] Fuchs HO (1985) On the definition of planes of maximum shear strain. In: Miller KJ, Brown MW (eds) Multiaxial Fatigue, vol 853, ASTM Special Technical Publication, Philadelphia, pp 5–8, symposium sponsored by ASTM Committees E-9 on Fatigue and E-24 on Fracture Testing, San Francisco, CA, 15–17 Dec. 1982

[308] Keil S (2017) Dehnungsmessstreifen. Springer, Vieweg, Wiesbaden

[309] Seelhofer-Schilling B (2008) Umschnürte Stahlbetonstützen: Geschichtliche Entwicklung. Institut für Baustatik und Konstruktion, Eidgenössische Technische Hochschule Zürich, Zürich

[310] Barlat F, Cazacu O, Zyczkowski M, Banabic D, Yoon JW (2004) Yield surface plasticity and anisotropy. In: Raabe D, Roters F, Barlat F, Chen LQ (eds) Continuum Scale Simulation of Engineering Materials: Fundamentals – Microstructures – Process Applications, Wiley, pp 145–183

[311] Cazacu O, Revil-Baudard B, Chandola N (2019) Plasticity-damage Couplings: From Single Crystal to Polycrystalline Materials. Springer, Cham

[312] Hosford WF (2010) Mechanical Behavior of Materials. Cambridge University Press, Cambridge

[313] Lou Y, Huh H, Yoon JW (2013) Consideration of strength differential effect in sheet metals with symmetric yield functions. Int J of Mechanical Sciences **66**:214–223

[314] Lou Y, Zhang S, Yoon JW (2019) A reduced Yld2004 function for modeling of anisotropic plastic deformation of metals under triaxial loading. Int J of Mechanical Sciences **161**:105,027

[315] Paul B (1972) Discussion: "A generalized isotropic yield criterion" (Hosford, W. F, 1972, ASME J. Appl. Mech., 39, pp. 607-609). J of Applied Mechanics **39**(4):1172

[316] Davis EA (1961) The Bailey flow rule and associated yield surface. J of Applied Mechanics **28**(2):310

[317] Logan RW, Hosford WF (1980) Upper-bound anisotropic yield locus calculations assuming <111>-pencil glide. Int J of Mechanical Sciences **22**(7):419–430

[318] Sauter J, Kuhn P (1991) Formulierung einer neuen Theorie zur Bestimmung des Fließ- und Sprödbruchversagens bei statischer Belastung unter Angabe der Übergangsbedingung. Zeitschrift für angewandte Mathematik und Mechanik **71**(4):T383–T387

[319] Emmens WC, van den Boogaard AH (2014) A yield criterion based on mean shear stress. In: Key Engineering Materials, Trans Tech Publications Ltd, Switzerland, vol 611–612, pp 3–10

[320] Alexandrov S, Barlat F (1999) Modeling axisymmetric flow through a converging channel with an arbitrary yield condition. Acta Mechanica **133**(1):57–68

[321] Alexandrov S, Rynkovskaya M (2022) Review of the upper bound method for application to metal forming processes. Metals MDPI **12**(11):1962

[322] Barlat F, Yoon JW, Cazacu O (2007) On linear transformations of stress tensors for the description of plastic anisotropy. Int J of Plasticity **23**(5):876–896

[323] Barlat F, Kuwabara T (2016) Anisotropic yield conditions in mathematical theory of plasticity. Plasticity and Processing, J of the Japan Society for Plasticity Processing JSTP **57**(662):230–243

[324] Lou Y, Huh H (2009) Yield loci evaluation of some famous yield criteria with experimental data. KSME-KSAE, KSAE09-J0003, wwwdbpiacokr (5):1–5

[325] Lou Y, Yoon JW (2018) Anisotropic yield function based on stress invariants for BCC and FCC metals and its extension to ductile fracture criterion. Int J of Plasticity **101**:125–155

[326] Barlat F, Richmond O (1987) Prediction of tricomponent plane stress yield surfaces and associated flow and failure behavior of strongly textured fcc polycrystalline sheets. Materials Science and Engineering **95**:15–29

[327] Owen DRJ, Perić D (1994) Recent developments in the application of finite element methods to nonlinear problems. Finite Elements in Analysis and Design **18**(1–3):1–15

[328] Cao J, Yao H, Karafillis A, Boyce MC (2000) Prediction of localized thinning in sheet metal using a general anisotropic yield criterion. Int J of Plasticity **16**(9):1105–1129

[329] Ivlev DD, Maksimova LA, Nepershin RI, Radaev YN, Senashov SI, Shemjakin EI (2008) Limit State of Deformable Solids and Rocks (in Russ.: Predel'noe sostojanie deformiruemych tel i gornych porod). Fismatlit, Moscow

[330] Daxner T, Bitsche RD, Böhm HJ (2006) Space-filling polyhedra as mechanical models for solidified dry foams. Materials Transactions: Special Issue on Porous and Foamed Metals – Fabrication, Characterization, Properties and Application **47**(9):2213–2218

[331] Shahbeyk S (2012) Yield/failure criteria, constitutive models, and crashworthiness applications of metal foams. In: Dukhan N (ed) Metal Foams: Fundamentals and Applications, DEStech Publications Inc, Lancaster, pp 131–214

[332] Carroll L (2010) Through the looking glass and what Alice found there. Penguin

[333] Edelman F, Drucker DC (1951) Some extensions of elementary plasticity theory. J of the Franklin Institute **251**(6):581–605

[334] Stockton FD, Drucker DC (1950) Fitting mathematical theories of plasticity to experimental results. J of Colloid Science **5**(3):239—250

[335] Wang X (2005) Volumes of generalized unit balls. Mathematics Magazine **78**(5):390–395

[336] N'souglo KE, Rodríguez-Martínez JA, Cazacu O (2020) The effect of tension-compression asymmetry on the formation of dynamic necking instabilities under plane strain stretching. Int J of Plasticity **128**:102,656

[337] Plunkett B, Lebensohn RA, Cazacu O, Barlat F (2006) Anisotropic yield function of hexagonal materials taking into account texture development and anisotropic hardening. Acta Materialia **54**(16):4159–4169

[338] Plunkett B, Cazacu O, Barlat F (2008) Orthotropic yield criteria for description of the anisotropy in tension and compression of sheet metals. Int J of Plasticity **24**(5):847–866

[339] Geniev GA, Kissjuk VN (1965) On the generalization of the strength theory for concrete (in Russ.: K voprocu obobshhenija teorii prochnosti betona). Beton i Zhelezobeton pp 16–19

[340] Geniev GA, Kissjuk VN, Tjupin GA (1974) Plasticity Theory for Concrete and Reinforced Concrete (in Russ.: Teorija plastichnosti betona i zhelezhobetona). Strojizdat, Moscow

[341] Korsun VI, Karpenko SN, Makarenko SY, Nedorezov A (2021) Modern strength criteria for concrete under triaxial stress states, (in Russ.: Sovremennye kriterii prochnosti dlja betonov pri ob'emnych naprlazhennych sostojanijach). Strojtel'stvo I rekostrukzija **97**(5):16–30

[342] Korsun VI, Nedorezov AV, Makarenko SY (2014) Comparative analysis of strength criteria for concrete (in Russ: Sopostavitel'nyj analys kriteriev prochnosti dlja betonov). Modern industrial and civil construction **10**(1):65–78

[343] Leytes ES (1971) On the condition of concrete strength, (in Russ.: Ob uslovii prochnosti betona). Central'nyj institut nauchnoj informacii po Stroitel'stvu i Architekture, Gosstroj SSSR, Referativnyj sbornik Mezhotraslevye voprosy stroitelstva (otechestvennyj opyt) ZINIS, Cross-industry problems of construction (domestic experience) / CINIS (9):31–35

[344] Leytes ES (1978) Variant of the theory of plastic yielding in concrete, (in Russ.: Variant teorii plasticheskogo techenija betona). Stroitel'naja mechanika i raschet sooruzhenij, Izdatel'svo literatury po stroitel'stvu (3):34–37

[345] Leytes ES (1980) To clarify one of the conditions of concrete strength (in Russ.: K utochneniju odnogo iz uslovij prochnosti betona). In: Gvozdev AA, Krylov S (eds) Concrete and Reinforced Concrete Structure Components Behaviour under Effect of Different Durations: Povedenie betonov i elementov zhelezobetonnych konstrukzij pri vozdejsvii razlichnoj dlitel'nosti, USSR Gosstroi Research Institute of Concrete and Reinforced Concrete, Moscow, pp 37–40

[346] Leytes ES (1983) Evaluation of the long-term strength of concrete at complex stress state, (in Russ.: Ocenka dlitel'noj prochnosti betona pri slozhnom

naprjazhennom sostojanii). Stroitel'naja mechanika i raschet sooruzhenij, Izdatel'svo literatury po stroitel'stvu **25**(4):21–24

[347] Alikov YA (2002) Hypotheses of Strength and Plasticity of Solids, Their Development Applied to Concrete (in Russ. Gipotezy prochnosti i plastichnosti tverdych tel, ich razvitie primenitel'no k betony). Wolgogradskaja gosudarstvennaja architekturno-stroitelnaja akademija, Wolgograd

[348] Helwany S (2007) Applied soil mechanics with ABAQUS applications. Wiley, Hoboken, New Jersey

[349] Hibbitt, Karlsson, Sorensen (1997) ABAQUS Theory Manual: Critical state models. Pawtucket, Rhode Island, version 5.7

[350] Rizzi E, Papa E, Corigliano A (2000) Mechanical behavior of a syntactic foam: experiments and modeling. Int J of Solids and Structures **37**(40):5773–5794

[351] Cazacu O, Revil-Baudard B (2017) New analytic criterion for porous solids with pressure-insensitive matrix. Int J of Plasticity **89**:66–84

[352] Gupta NK, Meyers A, Wichtmann A (1995) A function for representing experimental yield surfaces. European Jl of Mechanics A Solids **14**(1):45–53

[353] Matchenko HM, Tolokonnikov LA (1968) On the relation between stress and strain in isotropic continua with different moduli of elasticity at tension and compression. (in Russ. o svjasi mezhdu naprjazhenijami i deformazijami v raznomodul'nych izotropnych sredach). Mechanika tverdogo tela MTT (6):108 – 110

[354] Prager W (1937) Mécanique des solides isotropes au delà du domaine élastique. Mémorial des sciences mathématiques **87**:1–66

[355] Prager W (1945) Strain hardening under combined stresses. J of Applied Physics **16**(12):837–840

[356] Auricchio F, Petrini L (2004) A three-dimensional model describing stress-temperature induced solid phase transformations: Solution algorithm and boundary value problems. Int J for Numerical Methods in Engineering **61**(6):807–836

[357] Barlat F, Lee MG (2014) Constitutive description of isotropic and anisotropic plasticity for metals. In: Altenbach H, Sadowski T (eds) Failure and Damage Analysis of Advanced Materials, Springer, Heidelberg, CISM, pp 67–118

[358] Ehlers W (1993) Constitutive equations for granular materials in geomechanical context. In: Hutter K (ed) Continuum Mechanics in Environmental Science and Geophysics, CISM Courses and Lectures No. 337, Springer, Wien, pp 313–402

[359] Raniecki B, Mróz Z (2008) Yield or martensitic phase transformation conditions and dissipation functions for isotropic, pressure-insensitive alloys exhibiting SD effect. Acta Mechanica **195**:81–102

[360] Betten J (1979) Über die Konvexität von Fließkörpern isotroper und anisotroper Stoffe. Acta Mech **32**:233–247

[361] Betten J (2001) Kontinuumsmechanik, 2nd edn. Springer, Berlin

[362] Gao X, Zhang T, Zhou J, Graham SM, Hayden M, Roe C (2011) On stress-state dependent plasticity modeling: Significance of the hydrostatic stress, the third

invariant of stress deviator and the non-associated flow rule. Int J of Plasticity **27**(2):217–231

[363] Cazacu O (2018) New yield criteria for isotropic and textured metallic materials. Int J of Solids and Structures **139**:200–210

[364] Oliveira MC, Cazacu O, Chandola N, Alves JL, Menezes LF (2021) On the effect of the ratio between the yield stresses in shear and in uniaxial tension on forming of isotropic materials. Mechanics Research Communications **114**:103,693

[365] Hu Q, Li X, Han X, Li H, Chen J (2017) A normalized stress invariant-based yield criterion: Modeling and validation. Int J of Plasticity **99**:248–273

[366] Hou Y, Min J, Lin J, Lee MG (2022) Modeling stress anisotropy, strength differential, and anisotropic hardening by coupling quadratic and stress-invariant-based yield functions under non-associated flow rule. Mechanics of Materials **174**:104,458

[367] Kolupaev VA, Bolchoun A, Altenbach H (2009) New trends in application of strength hypotheses (in Germ.: Aktuelle Trends beim Einsatz von Festigkeitshypothesen). Konstruktion, Springer-VDI-Verlag **61**(5):59–66

[368] Ottosen NS (1975) Failure and elasticity of concrete. Report Risø-M-1801, Danish Atomic Energy Commission, Research Establishment Risö, Engineering Department, Roskilde

[369] Ottosen NS (1977) A failure criterion for concrete. J of the Engineering Mechanics Division **103**(4):527–535

[370] Ottosen NS (1980) Nonlinear finite element analysis of concrete structures. Tech. rep., Forskningscenter Risoe. Risoe-R, No. 411, Roskilde: Risø National Laboratory

[371] Birger IA, Mavlytov PP (1986) Strength of Materials (in Russ.: Soprotivlenije Materialov). Nauka, Moscow

[372] Altenbach H (2010) Strength hypotheses - a never ending story. Czasopismo Techniczne Mechanika Wydawnictwo Politechniki Krakowskiej **107**(20):5–15

Chapter 3

Minimum Test Effort-Based Derivation of Constant-Fatigue-Life Curves - Displayed for the Brittle UD Composite Materials

Ralf Cuntze

Abstract Series production of safety-relevant structural parts requires a Design Verification (DV) guaranteeing Structural Integrity. This means, it is to demonstrate that *No relevant limit failure state is met considering all Dimensioning Load Cases (DLCs)*. These DLCs involve static, dynamic, and cyclic loading focusing lifetime. However, lifetime prediction is a pain point for a better use especially of laminated composites in lightweight design. A generally practical tool is not available. Hence, each novel high-performance UD-lamina (ply)-composed laminate requires a new effortful test campaign. Therefore, the idea of the author-founded Germany-wide group BeNa (in 2010) was to base fatigue life prediction embedded and lamina-wise in order to become more general in future. This idea also fits to Cuntze's "modal" Failure-Mode-Concept (FMC), which is based on material symmetry facts dedicating a 'generic' number to ideally homogeneous materials, namely 2 for the isotropic material and 5 for the transversely-isotropic UD lamina material. Fracture morphology gives evidence: Each strength property corresponds to a distinct strength failure mode or to a strength failure type Normal Fracture (NF) or Shear Fracture (SF). In the case of UD materials 2 FiberFailure (FF) and 3 InterFiberFailure (IFF) modes are faced.

In lifetime prediction strain-life and stress-life models are used. For ductile materials one single plastic strain-linked yield mechanism dominates and strain-life models are applied. However for brittle materials the elastic strain becomes dominant and stress-life models are used. Micro-damage mechanisms drive fatigue failure and several fracture mechanisms come to act. This asks for a so-called modal approach that captures all fracture failure modes.

The automatic establishment of the not piecewise straight Constant Fatigue Life (CFL) curves is the challenging task. All SN-curves' information and all the CFL curves (N = const) are captured by the Haigh Diagram $\sigma_a(\sigma_m)$, with σ_a the stress

Ralf Cuntze
MAN-Technologie, Augsburg, Germany,
e-mail: ralf_cuntze@t-online.de

amplitude and σ_m the mean stress. The author's idea for the generation of such an automatically deducible SFC-curve includes to provide:

1. At minimum one single SN-curve as Master curve of each mode (by measurement).
2. A strength failure criterion (SFC) that can quantify the micro-damage portions under cyclic loading (due to experience, in the brittle case given by a static one).
3. A model that can predict other SN-curves on the basis of a mode Master Curve (by Kawai's Model 'Modified Fatigue Strength Ratio Ψ').
4. A physical model to map the test data in the transition domain as most problematic region in the Haigh diagram, where the modes interact and the CFL curve heavily decays (a decay function was found).

A first model validation of this private investigation, using test data from Dr. C. Hahne, AUDI, looks very promising and asks for funding.

3.1 Introduction

3.1.1 Fatigue Design Verification (DV) Task with Terms

Designing involves Design Dimensioning and Design Verification (DV). Focus in design is the strength DV of non-cracked structural parts and the fracture mechanics-based DV of cracked structural parts by Damage Tolerance Tools, see [1]. The size of the damage decides whether it is to apply a SFC for Onset-of-failure in a critical material 'Hot Spot' of the un-cracked (probably still micro-damaged) structural part or a fracture mechanics-based Damage Tolerance Condition in case of a technical crack (macro-damaged). Estimation of lifetime here means to assess the growth of the micro-damage before reaching a technical (macro-damage) crack size.

Domains of fatigue scenarios and analyses are:

LCF: high stressing and straining,
HCF: intermediate stressing $10.000 < n < 2.000.000$ cycles (rotor tubes, bridges, large towers, off-shore structures, planes, etc.), and
VHCF: low stress and low strain amplitudes (see SPP1466, VeryHighCycleFatigue $> 10^7$ cycles, in centrifuges, wind energy rotor blades, etc.).

Design Verification demands for reliable reserve factors RF which demand for reliable SFCs. Such a SFC is the mathematical formulation $F = 1$ of a failure curve or of a failure surface (body). Generally required are a yield SFC and fracture SFCs. A yield SFC usually describes just one mode, i.e. for isotropic materials Mises describes shear yielding SY. Fracture SFCs for isotropic materials usually have to describe two independent fracture modes, shear fracture SF and normal fracture NF. For the here focused transversely-isotropic uni-directionally reinforced UD-lamina materials one counts five [1–5].

Principally, in order to avoid either to be too conservative or too un-conservative, a separation is required of the always needed analysis of the average structural behavior

in Design Dimensioning (*using average properties and average stress-strain curves*) in order to obtain best information, being a *50% expectation value*, from the mandatory single Design Verification analysis of the final design, where statistically minimum values for strength and minimum, mean or maximum values for other task-demanded properties are to apply as so-called Design Values. Cyclic fatigue Life consists of three phases. This means for a laminate [1, 6]:

Phase I: Increasing micro-damage acts in a lamina embedded in a laminate up to a discrete micro-damage onset. Determination of the accumulating micro-damage portions initiated at the end of the elastic domain and dominated by diffuse micro-cracking + matrix yielding inclusively cavitation under 3D-tensile stressing, and finally little cracks such as micro-delaminations. Degradation begins with the onset of the diffuse micro-cracking above in the strain hardening domain until Inter-Fiber-Failure (IFF1, IFF3) occurs.

Phase II: Stable local discrete micro-damage growth within the laminate up to the growth of the width of the dominating discrete micro-cracks (*after localization*) including micro-delaminations. Phase II is usually dedicated to fatigue and basically linked to discrete micro-damage growth. (In cyclic loading, degradation is more diffuse than in static loading).

Phase III: Final in-stable fracture of the laminate initiated by Fiber-Failure (FF) and probably by the compressive IFF2 of a lamina and possible criticality of the loaded laminate due to the macro-damage delamination. This phase is usually dedicated to fracture mechanics, to macro-damage and macro-cracking.

Methods for the prediction of durability, regarding the lifespan of the structural material and thereby of the structural part, involves long time static loading which is linked to *Static Fatigue* and further *(cyclic) Fatigue*. Fatigue failure requires a Procedure for Fatigue Life Estimation necessary to perform the cyclic DV.

3.1.2 Fatigue Micro-Damage Drivers of Ductile and Brittle behaving Materials

As still mentioned, there are <u>strain-life</u> (plastic deformation decisive) and *stress-life* models used. For ductile materials strain-life (plastic strain-based) models are applied because a single yield mechanism dominates. For brittle materials the elastic strain amplitude becomes dominant and stress-life models are applied. With brittle materials inelastic micro-damage mechanisms drive fatigue failure and several fracture mechanisms may come to act. This asks for a modal approach that captures all failure modes which are here fracture failure modes.

Above two models can be depicted in a Goodman diagram and in a Haigh diagram. The Goodman diagram provides the maximum tolerable stresses σ_{max} of the material (it is commonly used in construction specifically for concrete). Here, the Haigh diagram with its double information $(\sigma_{\mathrm{a}}, \sigma_{\mathrm{m}})$ will be applied, because just to use a single information σ_{a} or $\Delta\sigma = 2\sigma_{\mathrm{a}}$ or σ_{max} is not sufficient for the DV-analysis.

A Haigh Diagram represents all SN curve information by its *Constant Fatigue Life (CFL) curves* and this is the focus of this investigation.

Firstly, the basic differences between ductile and brittle materials are to consider [1, 3]:

- Ductile Material Behavior, isotropic materials: mild steel
  1 1micro-damage mechanism acts ≡ "slip band shear yielding" and drives micro-damage under tensile, compressive, shear and torsional cyclic stresses: This single mechanism is primarily described by 1 SFC, a <u>yield</u> failure condition (criterion) of Mises!
- Brittle Material Behavior, isotropic materials: concrete, grey cast iron, etc.
  2 *micro-damage* driving mechanisms act ≡ 2 fracture failure modes Normal Fracture failure (NF) and Shear Fracture failure (SF) under compression described by 2 fracture failure conditions, the 2 SFCs for NF and SF, where porosity is always to consider.
- Brittle Material Behavior, transversely-isotropic UD-materials:
  5 micro-damage driving fracture failure mechanisms act ≡ 5 fracture failure modes described by 5 SFCs = strength <u>fracture</u> failure conditions.

3.1.3 Short State-of-the-Art Regarding Cyclic Strength of UD-Laminates

Experience with composites of fiber-reinforced plastics FRP monitors: UD ply-composed laminates behave brittle, experience early fatigue damage, but show benign fatigue failure behavior in case of 'well-designed' laminates until finally a pretty 'Sudden Death' occurs (fiber-dominated laminates are used in high performance stress applications whereby fiber-dominated means that there are 0°-plies in all significant loading directions, which requires > 3 fiber direction angles α).

No Lifetime Prediction Method is available, that is applicable to any lamina (the physical ply or the lamella in construction) and UD ply-composed laminate. The procedures base on specific laminate lay-ups and therefore Short test results cannot be generally applied. Embedded ply-degradation must be non-linearly considered. Endurance strength procedures base – as with metals – on σ_a, σ_m.

<u>Present</u> in Mechanical Engineering as an Engineering Approach: Applying a Static Design Limit Strain of $\varepsilon < 0.3\%$ in multi-axial laminate design practically means negligible matrix-micro-cracking in the cases of > 3 fiber-directions. Design experience proved: Then, practically no IFF-caused fatigue danger of a laminate is given [4, 7, 8].

<u>Future</u> in Mechanical Engineering: Design Limit Strain shall be increased beyond $\varepsilon \approx 0.5\%$ (EU-project: MAAXIMUS to better exploit UD-materials). Then, dependent on the matrix, first filament breaks may change the early diffuse matrix micro-cracking to a discrete and more critical localized one.

Present Engineering Approach in Civil Engineering (Construction) for FRP materials and its semi-finished reinforcement products such as a pultruded rod, a strand cut-out of a fiber-grid, lamella (= tape) etc: In the case of a so-called 'not predominantly static loading' the required fatigue life must be demonstrated by measured SN-curves (*Stress-failure cycle N*), the given operational loading spectrum and a hypothesis for the accumulation of the micro-damages. Bounds are set by the required minimum micro-crack width of the Serviceability Limit State SLS and deformation restrictions for instance in case of bridge bending. If there are only carbon-fibers used for the reinforcement, where corrosion is no problem, then the SLS micro-crack size could be increased a little for future design, if not steel is used in the structural part at the same time.

Considering the high-performance UD lamina-composed laminates the classical fatigue tests are performed on each novel laminate. In this context the author invited German colleagues in 2000 to discuss the fatigue strength design situation during a special meeting, according to the VDI guideline 2014, sheet 3, [7]. Then, an idea of the author-founded Germany-wide group BetriebsfestigkeitsNachweis (BeNA) in 2010 was, to base the fatigue life prediction embedded lamina-wise in order to be more general in fatigue life design in future and to save test costs and time. Distinct laminate test specimens shall capture the interface effect of the lamina *embedded* in the laminate.

3.1.4 Constant Amplitude Loading and Variable Amplitude Loading

Cyclic loadings are most often given by an operational loading spectrum with its automatic loss of the stress-time relationship. In Fig. 3.1 variable amplitude loading of the structure in operation or service is displayed ending with *the operational fatigue life curve* after *Gaßner*. Further depicted is the harsher *constant amplitude loading*. A loading spectrum-representing block-loading instead of mapping the loading spectrum by a single constant amplitude loading stands for more realistic fatigue life estimation. Good information about the loading spectrum pays off.

The more brittle the material is the more mean stress influence acts. This is why micro-damage is not anymore caused by the strength failure mode yielding alone (1 mode, quantified by $\sigma_{eq}^{vonMises}$) but by micro-cracking which is caused by many strength fracture failure modes. Brittle materials like the transversely-isotropic UD material with its five fracture failure modes possess strong mean stress sensitivity. That requires a failure mode-linked treatment which cannot be captured by a mean stress correction as usually still performed with not fully ductile materials. See later in Subsect. 3.5.3 the example CFRP-lamina in the Haigh diagram, where the huge effect of the mean stress sensitivity of brittle materials is very impressively demonstrated if the so-called strength ratio, the ratio of compressive strength and tensile strength, is high.
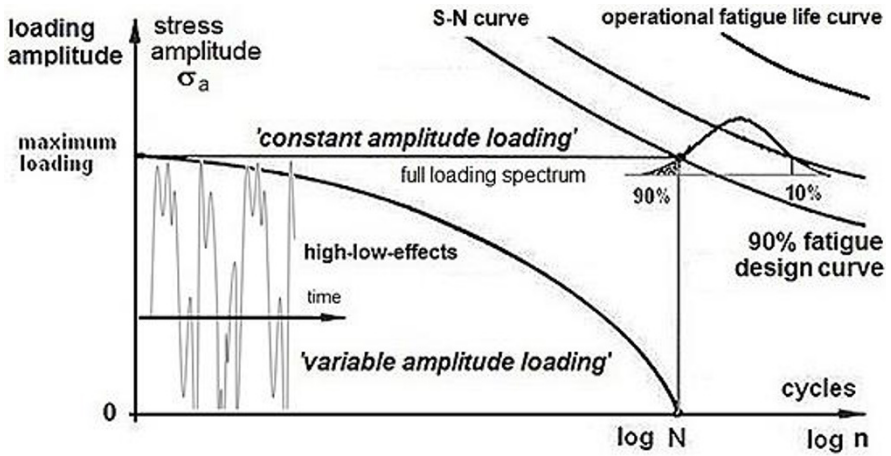
Fig. 3.1: Display of constant amplitude loading and load history-linked variable amplitude loading.

3.1.5 SN-curve, Load Spectrum and Fatigue-Driving Equivalent Stress

The SN curve is a so-called constant amplitude curve. Unfortunately in practice, the SN curve parameter, termed stress ratio R, is indicated by the capital roman letter R, too. The reason for this is that R is now the Ratio of $\sigma_{min}/\sigma_{max}$. The strengths are capitel italic letters denoted R from strength <u>R</u>esistance.

In service, a huge number of ups and downs may be given as varying stress input (Fig. 3.1). Counting methods help to reduce the number of turning points in this time-domain in order to achieve a set of simple stress reversals. The rain-flow counting method from Endo-Matsuishi, 1968, is the most often used method to obtain a spectrum. The resulting load spectrum allows the application of a Miner Rule to estimate fatigue life under complex loading or stressing, respectively.

Analogous to the ductile material case where a multi-axial stress state is captured by an equivalent stress $\sigma_{eq}^{vonMises}$ for the yield mode it may be assumed that for anisotropic materials the same is valid for each single fracture mode, if equivalent stresses can be formulated such as it is possible with the FMC-based SFCs of the author. For brittle isotropic and anisotropic <u>materials</u> a change from the uni-axial stresses σ_a, σ_{max} to a multi-axial, equivalent mode stress $\sigma_{eq\,max}^{mode}$ is welcomed and will improve the analysis.

3.1.6 Proportional and Non-Proportional Loading and Mean Stress Sensitivity

3.1.6.1 Proportional and Non-Proportional Loading (Stressing)

The so-called *proportional loading* is a concept, where all stresses are altered proportionally. Compared to the proportional stressing a non-proportional stressing (e.g. 90° out-of-phase) may lead to a significant life reduction, at least for isotropic structural materials. Due to the time-dependent, differently oriented stress states the growing flaws may have a better chance for coalescence viewing slip bands in ductile materials under strain-controlled fatigue testing or viewing micro-cracks in brittle materials.

3.1.6.2 Mean Stress Sensitivity

Not fully ductile isotropic materials show an influence of the mean stress on the fatigue strength depending on the (static) tensile strength and the material type. Mean stresses in the tensile range $\sigma_m > 0$ MPa lead to a lower permanently sustainable amplitude, whereas compressive mean stresses $\sigma_m < 0$ MPa increase the permanently sustainable amplitude or in other words: A tensile mean stress lowers the fatigue strength and a compressive mean stress increases the fatigue strength.

3.2 Modeling of SN-Curves in the Three Fatigue Domains and Choice

3.2.1 Modeling of SN-Curves

3.2.1.1 General Modeling of SN-Curves

SN-curves can be modelled linearly and non-linearly in semi-log and log-log diagrams. Possible mapping formulations describe non-linear curves such as the Weibull-model and the Wearout-model [7] and linear curves in the log-log diagram. The author investigated five models when mapping SN curve data sets, see §10.2 in [1]. The computation of the mapped curves with its curve parameters was performed by the code Mathcad.

For brittle materials it is physically optimum to use the strength $\overline{R}$ (average value, marked by a bar over) as maximum stress σ_{max} at $n = N = 1$, being the origin of a SN-curve. This, on top, reduces the number of free parameters by one. However, in aerospace standards, like the HSB [8], the strength $\overline{R}$ of not so brittle structural materials is not taken as origin in order to get more freedom for a better mapping in the domain of highest interest, namely the higher LCF domain. If at the end of the HCF domain a lack of data is faced, then, a so-called 'Haibach-correction' is often

performed by halving the HCF curve-determining decay angle beyond $n = 2 \cdot 10^6$ cycles.

3.2.1.2 Modeling Final HCF-Domain with VHCF

Some materials could have an endurance limit which represents a stress level below which the material does not fail and can be cycled infinitely. If the applied stress level is below the endurance limit the material is said to have an infinite life. This might have been acceptable in some cases for the maximum HCF-level of $2 \cdot 10^6$ cycles, however needs to be checked for VHCF because the failure mechanism might be not fully the same as for HCF. From this can be deduced that above endurance limit is an *apparent* fatigue strength.

Performing an extrapolation out of the HCF regime, for $n > 2 \cdot 10^6$ cycles, the choice of the mapping function determines the obtained lifetime value, see the investigated SN-curve mapping models in § 10.2 of [1]!

The choice of the SN-model mainly depends on the fact whether an endurance limit in the VHCF domain is to map or not. Such a limit seems to exist for cyclic tensioning of CFRP (Carbon Fiber Reinforced Polymer).

Cyclic failure always depends on the amount and distribution of flaws at the surface (formerly often termed Weibull surface effect) of the structural part and on those flaws within the critical material volume (formerly often termed Weibull volume effect), which seem to drive VHCF. This is especially to consider for the novel 3D-printed parts.

A dedication to surface-generated failure at HCF and to volume-generated failure at VHCF looks reasonable supported by novel VHCF experiments, where it became known for metals: The failure origin for VHCF changes from surface flaws and notches to internal flaws such as the different inclusion types [9]. This forced the material scientists to think about applying two different SN curves, one associated to the surface flaws and the other associated to the volume flaws. Such a change of the destructive mechanism may require the mapping of two distributions that describe the micro-damage accumulation. However, regarding the mapping of the test results, the author believes: A *physical average curve* is the result of a probabilistically-driven strength problem, and the transition zone is smooth because it is not like a sudden instability problem. Therefore, the course of the cyclic failure test data cannot show some sudden downward jump. Hence, the continuous four parameter Weibull mapping approach of the SN test data can capture the full course

$$R = \mathrm{const.} : \sigma_{\max}(R, N) = c_1 + (c_2 - c_1)/\exp(\lg N / c_3)^{c_4}.$$

Fatigue curves are given for un-notched test specimens (notch factor $K_t = 1$, *like the later examples*) and for notched ones. The loading can be a uniaxial stress state or a multi-axial stress state and a suitable permitted stress criterion is to apply.

3.2.2 Relation of the Material Stressing Effort Eff with the Micro-damage D

There are practically two possibilities to present SN curves: Using in the case of ductile materials (1) the stress amplitude $\sigma_a(R, N)$, also termed alternating stress, and in the case of brittle materials (2) the maximum or upper stress $\sigma_{max}(R, N)$, usually termed fatigue strength. The maximum stress is physically simpler to understand by the 'stress man' than the amplitude, according to smooth transfer from the static to the cyclic behavior, Fig. 3.2. Namely, a decaying SN curve is interpretable like a decaying static strength after a micro-damage process with n cycles.

Thereby, the static material stressing effort Eff (Werkstoffanstrengung, $N_f = 1$) is replaced by the accumulated cyclic micro-damage sum $D(N)$. Applied here is the classical 4-parameter Weibull curve with one parameter still fixed as strength point origin, because for brittle materials the strength value $\overline{R}^t = \sigma_{max}(n = N = 1)$ is preferably used as origin in the tension domain and as anchor point of the SN curve and in the compression domain - $\overline{R}^c = \sigma_{min}(n = N = 1)$. In detail, Fig. 3.2 visualizes the transfer from the static load-driven increase of the material stressing effort $(n = N = 1)$ $Eff = 100\%$ (corresponds to the average expectance value of 50%) at the strength point to the cycle-driven micro-damage sum $D_{mapping} = 100\%$ (= expectance value 50%) of the SN curve. The evolution of Eff is not linked to the accumulation of the micro-damage. At onset-of-micro-cracking Eff is still $> 0!$.
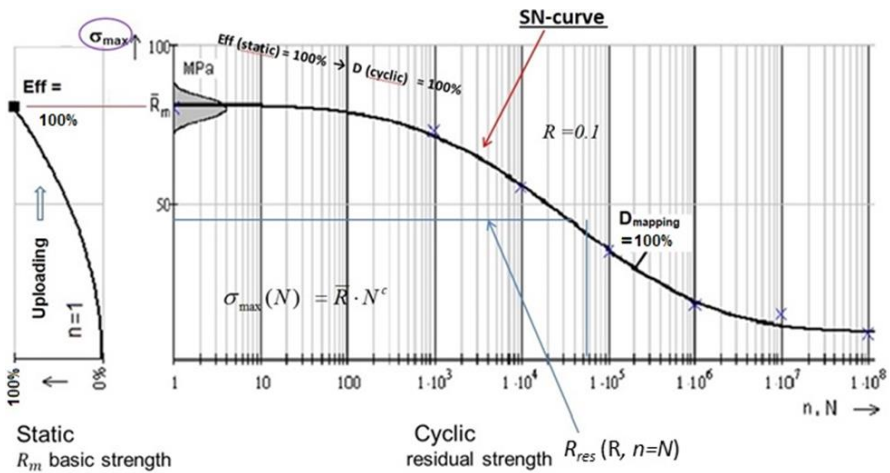
Fig. 3.2: Mapping: Eff versus $D \equiv D_{mapping}$, mapping deals with averages, 50% expectance value.

3.2.3 Statistical Properties in Design Verification (DV)

As the average SN curve cannot be applied in fatigue life DV, a statistically reduced curve is to determine as design curve, see Fig. 3.3. This curve is applied as a $D_{design} = 100\%$-SN-curve.

Conclusion: It is essential to discriminate mapping and designing.

Mapping (50%, 50%): Static failure, max $\sigma = \overline{R}, Eff_{mapping} = 1 \Rightarrow$ cyclic failure, max $\sigma = \overline{R}_{res}, D_{mapping} = 1$,

Designing (50%, 50%): Static failure, max $\sigma = R, Eff_{designing} = 1 \Rightarrow$ cyclic failure, max $\sigma = R_{res}, D_{design} = 1$.

In design verification very often as fractiles (quantiles), to meet a distinct survival failure probability P, values of 5% or 10% are taken in order to capture some of the uncertainty on the <u>resistance side</u> compared to the average of 50%. To fully capture the uncertainty on the resistance side, for instance a Design Factor of Safety FoS $j_{Life} > 5$ is imposed. On the action (loading) side the FoS j_{load} captures the uncertainty of the loading together with the 'safe' derivation of the Design Limit Load (DLL).

Capturing the uncertainty of the resistance quantities, the following is performed: Denoting P the survival probability and C the confidence level applied, when esti-
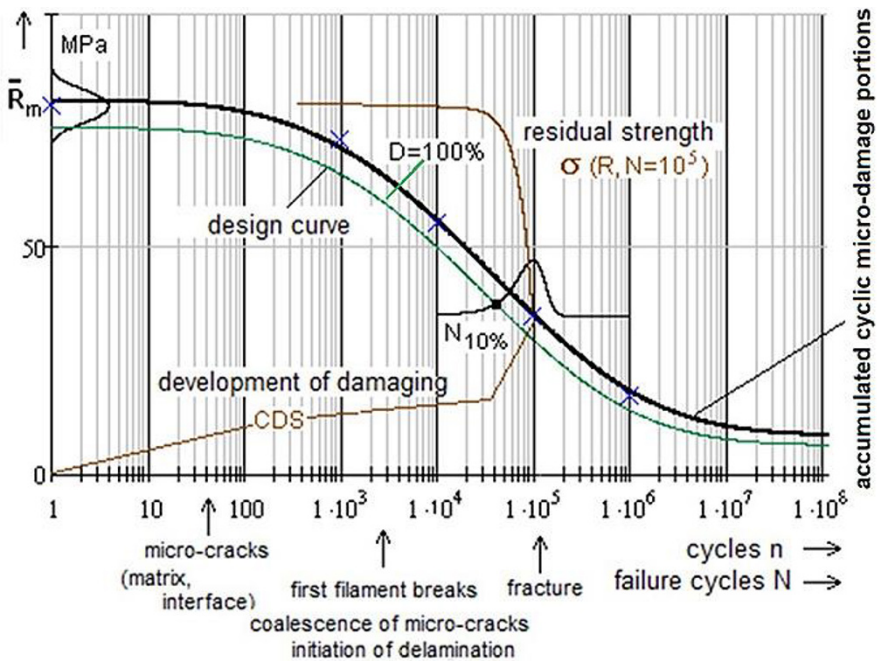
Fig. 3.3: Design Verification: Fatigue average curve and design curve. $D = D_{design}$ *for a survival probability P with a confidence level C. CDS is 'characteristic damage state' of a lamina.*

mating a basic population value from several test samples, partly enriched by some knowledge of the basic population and regarding C a one-sided tolerance level it eventually reads for the resistance side:

- Static → Statistical reduction of average strength from (P = 50%, C= 50%) to e.g. (P = 90%, C = **95**%).
- Cyclic → Statistical reduction of average SN-curve from (P =50%, C= 50%) to e.g. (P = 90%, C= **50**%). In order to obtain a safer side the maximum permitted accumulated micro-damage is further reduced in DV to a feasible value $D_{\text{feasible}} <$ $D = 100\%$, a value that is linked to the green marked design curve (P= 90%, C= **50**%) in Fig. 3.

Some Lessons Learned:

- The Palmgren-Miner rule cannot account for loading sequence effects, residual stresses, and not for stresses below the fatigue limit (life → ∞?)
- Whether a material has an endurance fatigue limit is usually open regarding the lack of VHCF tests. As an apparent fatigue strength the strength at $2 \cdot 10^6$ cycles might be only called. However, e.g. CFRP could possess a fatigue limit.
- Designing light-weight structures means a reduction of dead mass. Therefore, the ratio 'variable load/dead load' reduces, fatigue becomes more decisive and fatigue life prediction procedures become also more mandatory in construction industry, for instance!
- In the LCF regime non-linearity causing effects such as creeping, relaxation are to consider.
- Due to lack of information: Whether the material's micro-damage driver remains the same from LCF until VHCF must be verified in each given material design case.

3.3 Failure-Mode-Concept (FMC) and Static Strength Failure Criteria (SFC)

3.3.1 Features of the Author's Failure-Mode-Concept

For a better common understanding at first some terms shall be added here

- Failure condition (usually termed criterion): Condition on which a failure becomes effective, meaning $F = 1$ or $Eff = 100\%$ for one distinct limit state.
- Layer: Physical element from winding, tape-laying process, other depositing procedures. Lamina: Designation of the single UD ply as computational element of the laminate, used as laminate subset or building block for modeling. It might capture several equal plies.
- First-Ply-Failure FPF: First Inter-Fiber-Failure IFF in a lamina of the laminate (Tsai [10] did not exclude FF to be a FPF!).

Regarding the difference of Simulation and Analysis:

- *Simulation:* Process, that consists of several analysis loops and lasts until the system behavior is imitated in the Design Dimensioning process. The model parameters are adjusted hereby to the 'real world' parameter set.
- *Analysis:* Computation that uses fixed model parameters, such as the analysis of the final design.

Modeling of the variety of laminates is a challenge. In this context, essential for the interpretation of the failures faced after testing, is the knowledge about the lay-up of the envisaged laminate, because crimped and not-crimped materials behave differently. It is further extremely necessary to provide the material-modeling design engineer and his colleague in production (*for his Ply Book*) with a clear, distinguishing description of UD-lay-ups, of NonCrimpFabrics NCFs (stitched multi-UD-layer) and of Fabric layers (*crimped*). Due to unclear descriptions the author unfortunately could often not use valuable test results of fiber-reinforced materials. As editor of the VDI guideline 2014 the author makes the following proposal for a clear optical designation in order to enable a realistic material modelling:

The description of a UD-lamina-composed laminate follows the well-known lay-up denotation $[0/90/90/0] = [0/90]_s$, and an angle-ply laminate is denoted $[45/-45]_s$ with index *s* for symmetric (*targeting coupling reduction in [K]*). Analogously follows for a symmetrically stacked woven fabric $\begin{bmatrix} 0 \\ 90 \end{bmatrix}$ (*plain weave, which is symmetric in itself*) or for an angle-ply semi-finished product $[\pm 45]_s$. The survey below shall visualize by some examples how one can distinguish the various types. Square bracket [...] and wavy bracket {...} optically help here to distinguish NCF {stitched UD-stack} from those woven fabrics where one practically cannot mechanically separate the single woven layers within one fabric layer:

- Single UD-layers-*deposited* stack $[0/90]_s = [0/90/90/0]$-lay-up
- Semi-finished product, *stitched* NCF: $\{0/90\} + \{90/0\}$ symmetrically stacked deliverable 'building blocks': $\{0/45/-45/90\}$, *novel* C-ply^{TM} $\{\varphi/-\psi/-\varphi/\psi\}$ etc.
  two stacked NCFs, "*Bi-Ax*" $[\{75/-75\}/\{-15/15\}]_r$
  one NCF, r = repetition $[\{75/-75/-15/15\}]_r$
- Semi-finished product, woven Fabric: $\begin{bmatrix} 0 \\ 90 \end{bmatrix}$, $\begin{bmatrix} 0 \\ 90 \end{bmatrix}_s = \begin{bmatrix} 0 \\ 90 \end{bmatrix}_2$, $\begin{bmatrix} 45 \\ -45 \end{bmatrix}_s$
  $\Rightarrow$ Combination: $\begin{bmatrix} 45 \\ -45 \end{bmatrix}/\{75/-75/-15/15\}_3/[0/90/90/0]/\begin{bmatrix} 0 \\ 90 \end{bmatrix}_2$.

In the development of structural parts the application of 3D-validated SFCs is one essential pre-condition for achieving the required reliable DV. This includes a Yield Failure Condition (*ductile behavior*) for non-linear analysis of the material and also for design verification at the limit state 'Onset-of-Yielding'. It further includes conditions to verify that 'Onset-of-Fracture' is not met in the case of brittle and of ductile behavior.

Under the design-simplifying presumption 'Homogeneity is a permitted assessment for the material concerned´, and regarding the respective material tensors, it

follows from Material Symmetry that the number of strengths equals the number of elasticity properties! Fracture morphology gives further evidence 'Each strength property corresponds to a distinct strength failure mode and thereby to a distinct strength failure type, to Normal Fracture (NF) or to Shear Fracture (SF)'. This means, a characteristic number of quantities is fixed: 2 for isotropic material and 5 for the transversely-isotropic UD lamina (≡ lamellas in civil engineering). In the case of ideally homogeneous materials a 'generic' number seems to be faced. Hence, the applicability of material symmetry involves that in general just a minimum number of properties needs to be measured (*cost + time benefits*), which is helpful when setting up strength test programs. Of course, this is also beneficial regarding the material modeling work.

The basic features of the FMC, derived about 1995 [1, 2, 11] are:

- Each failure mode represents 1 independent failure mechanism and thereby represents 1 piece of the complete failure surface.
- A failure mechanism at the micro-scopic mode level shall be considered in the desired macro-scopic SFC applied
- Each failure mechanism or mode is governed by 1 basic strength R, only, and witnessed!
- Each failure mode can be represented by 1 SFC. Therefore, equivalent stresses can be computed for each mode. This is of advantage when deriving SN curves and generating Haigh diagrams in fatigue with minimum test effort in order to relatively effortless obtain Constant Fatigue Life curves for lifetime estimation. Modal SFCs lead to a clear mode strength-associated equivalent stress.
- Of course, a modal FMC-approach requires an interaction in all the mode transition zones or mixed failure domains, respectively, reading

$$Eff = \sqrt[m]{(Eff^{\text{mode}\,1})^m + (Eff^{\text{mode}\,2})^m + \ldots} = 1 = 100\% \text{ for Onset}-\text{of}-\text{Failure}.$$

It employs the so-called 'material stressing effort' (artificial term, generated in the WWFE in order to get an English term for the meaningful German term Werkstoffanstrengung) with a mode interaction exponent m, also termed rounding-off exponent, the size of which is high in case of low scatter and vice versa. The value of m is obtained by curve fitting of test data in the transition zone of the interacting modes. General FRP mapping experience delivered that $2.5 < m < 3$. A lower value chosen for the interaction exponent is more on the safe Reserve Factor RF side or more design verification conservative. For CFRP, $m = 2.6$ is recommended from mapping experience.

From engineering reasons m is chosen the same in all transition zones of adjacent mode domains. Using the interaction equation is leading again to a pseudo-global failure curve or surface. In other words, a 'single surface failure description' is achieved again, such as with Tsai/Wu but without the shortcomings of this global SFC.

Analogous to 'von Mises' it reads:

$$Eff^{\text{yield mode}} = \sigma_{\text{eq}}^{\text{von Mises}} / R_{0.2} \rightarrow Eff^{\text{fracture mode}} = \sigma_{\text{eq}}^{\text{fracture mode}} / R.$$

Above interaction of adjacent failure modes is modelled by the *series failure system*. That permits to formulate the total material stressing effort Eff, generated by all activated failure modes, as 'accumulation' of $Eff = \sum Eff^{\text{modes}} \equiv$ sum of the single mode failure danger proportions. $Eff = 100\% = 1$ represents the mathematical description of the complete surface of the failure body [1, 3]. In practice, i.e. in thin UD laminas, at maximum, 3 modes of the 5 modes ($2FF + 3IFF$) will physically interact. Considering 3D-loaded thick laminas embedded in laminates, there, all 3 IFF modes might interact.

3.3.2 'Global' and 'Modal' SFCs

The HMH yield failure condition can be termed a modal SFC. It captures just one failure mode. The author choose the term 'Global' as a play on words to 'modal' and to being word-self-explaining. Present SFCs can be basically separated into above two groups, the global (the German ZTL-SFC in the HSB also belongs to it) and the modal SFC ones, [1, 11].

  Figure 3.4 presents the main differences between these SFC types. Global SFCs describe the full failure surface by one single mathematical equation. This means that for instance a change of the UD tensile strength $\overline{R}_{\perp}^{t}$ affects the failure curve in the compression domain, where no physical impact can be! In this context, the computed RF may not be on the safe side in this domain. This shortcoming of the global SFCs caused the author to create modal SFCs.

  Often, global SFCs employ just strengths and no friction value. This is physically not accurate. Mohr-Coulomb acts in the case of compressed brittle materials! The undesired consequence in Design Verification again is: The computed RF may be not on the safe side.

3.3.3 FMC-Based Failure Modes, SFCs and SFC-Visualization

3.3.3.1 Types of Failure Modes

Since two decades the author believes in a macroscopically-phenomenological 'complete classification' system, where all strength failure types are included, see Fig. 3.5. In his assumed system several relationships may be recognized:

1. shear stress yielding SY, followed by shear fracture SF viewing 'dense' materials. For porous materials under compression, the SF for dense materials is replaced by crushing fracture CrF.
2. However, to complete a system beside SY also NY should exist. This could be demonstrated by the author for PMMA (plexiglass) with its chain-based texture showing NY due to crazing failure [1].

All modes are married in the Global formulation.
Any change hits all mode domains NF and SF of the fracture body surface

Drucker-Prager, Ottosen, Willam-Warnke, Tsai-Wu,
Altenbach/Bolchun/ Kulupaev, Yu , etc.

1 Global SFC : $F(\{\sigma\},\{R\})=1$ global formulation, usually

Set of Modal SFCs : $F(\{\sigma\},\{R^{mode}\})=1$ model formulation in the FMC

Mises,Puck,Cuntze   All modes are separately formulated.
Any change hits only the relevant domain of the fracture body surface

$$F(\{\sigma\},\{R^{mode};\mu^{mode}\})=1 \quad \text{more precise formulation}$$

by direct introduction of the friction value
considering Mohr-Coulomb for brittle materials under compression

$UD:\quad \{\sigma\}=(\sigma_1,\sigma_2,\sigma_3,\tau_{23},\tau_{31},\tau_{21})^T,\quad \{\overline{R}\}=(\overline{R}_{\parallel}^t,\overline{R}_{\parallel}^c,\overline{R}_{\perp}^t,\overline{R}_{\perp}^c,\overline{R}_{\perp\parallel};\mu_{\perp\parallel},\mu_{\perp\perp})^T$

$Isotrop:\{\sigma\}=(\sigma_x,\sigma_y,\sigma_z,\tau_{yz},\tau_{zx},\tau_{xy})^T =(\sigma_I,\sigma_{II},\sigma_{III})^T,\quad \{\overline{R}\}=(\overline{R}^t,\overline{R}^c;\mu)^T$

Needs an interaction of Failure Modes:
This is performed by a probabilistic approach (series failure system) in the transition zones
between neighboring modes NF and SF

Fig. 3.4: 'Global' and 'Modal' SFCs.

Fig. 3.5: Proposed scheme of macro-scopic strength failure modes of isotropic materials and transversely-isotropic UD-materials (generated 1998).

The right side of the scheme shows that a full similarity of the 'simpler' isotropic materials with transversely-isotropic UD materials exists. The strength failure modes involve a similar variety of fracture strength failure types such as SF, NF.

Of interest is not only the interaction of the fracture surface portions in a mixed failure domain or transition zone of adjacent failure modes, respectively, but failure in a multi-fold failure domain (superscript MfFD) such as at $\sigma_I = \sigma_{II}$. There the associated mode material stressing effort acts twofold. It activates failure in two orthogonal directions which is to consider by adding a multi-fold failure term in each of the present global and modal SFCs, as described and performed in [11, 12] for isotropic materials. It can be applied as well to brittle UD-materials in the quasi-isotropic transversal plane $\sigma_2 = \sigma_3$.

3.3.3.2 FMC-Based SFCs and Their Visualization

First and usual assumption for the material models is an ideally homogeneous solid. Following Beltrami and Mohr-Coulomb the solid material element may experience, generated from different energy portions, a shape change, a volume change and friction and these can be linked to invariants, which is of great advantage in material modeling, see [1, 12].

For the here envisaged UD material the applied invariants (personal note from J.P. Boehler) read:

$$I_1 = \sigma_1, I_2 = \sigma_2 + \sigma_3, I_3 = \tau_{31}^2 + \tau_{21}^2, I_4 = (\sigma_2 - \sigma_3)^2 + 4\tau_{23}^2,$$
$$I_5 = (\sigma_2 - \sigma_3) \cdot (\tau_{31}^2 - \tau_{21}^2) - 4\tau_{23}\tau_{31}\tau_{21}.$$

Table 3.1 collects the FMC-derived 5 UD-SFC formulations, $\sigma_2 = \sigma_\perp$. Treating 'Porous' UD materials, see [1, 4], IFF2 is to replace by

Table 3.1: 'Dense' UD materials: SFC formulations for FF1, FF2 and IFF1, IFF2, IFF3.

FF1: $Eff^{\|\sigma} = \breve{\sigma}_1 / \bar{R}_\|^t = \sigma_{eq}^{\|\sigma} / \bar{R}_\|^t$ with $\breve{\sigma}_1 \cong \varepsilon_1^t \cdot E_\|$ (matrix neglected)

FF2: $Eff^{\|\tau} = -\breve{\sigma}_1 / \bar{R}_\|^c = +\sigma_{eq}^{\|\tau} / \bar{R}_\|^c$ with $\breve{\sigma}_1 \cong \varepsilon_1^c \cdot E_\|$ (corresponds to a SF)

IFF1: $Eff^{\perp\sigma} = [(\sigma_2 + \sigma_3) + \sqrt{\sigma_2^2 - 2\sigma_2 \cdot \sigma_3 + \sigma_3^2 + 4\tau_{23}^2}] / 2\bar{R}_\perp^t = \sigma_{eq}^{\perp\sigma} / \bar{R}_\perp^t$

IFF2: $Eff^{\perp\tau} = [a_{\perp\perp} \cdot (\sigma_2 + \sigma_3) + b_{\perp\perp}\sqrt{\sigma_2^2 - 2\sigma_2\sigma_3 + \sigma_3^2 + 4\tau_{23}^2}] / \bar{R}_\perp^c = \sigma_{eq}^{\perp\tau} / \bar{R}_\perp^c$

IFF3: $Eff^{\perp\|} = \{[b_{\perp\|} \cdot I_{23-5} + (\sqrt{b_{\perp\|}^2 \cdot I_{23-5}^2 + 4 \cdot \bar{R}_{\perp\|}^2 \cdot (\tau_{31}^2 + \tau_{21}^2)^2}] / (2 \cdot \bar{R}_{\perp\|}^3)\}^{0.5} = \sigma_{eq}^{\perp\|} / \bar{R}_{\perp\|}$

$\left\{\sigma_{eq}^{mode}\right\} = \left(\sigma_{eq}^{\|\sigma}, \sigma_{eq}^{\|\tau}, \sigma_{eq}^{\perp\sigma}, \sigma_{eq}^{\perp\tau}, \sigma_{eq}^{\perp\|}\right)^T$, $I_{23-5} = 2\sigma_2 \cdot \tau_{21}^2 + 2\sigma_3 \cdot \tau_{31}^2 + 4\tau_{23}\tau_{31}\tau_{21}$

Inserting the compressive strength point $(0, -\bar{R}_\perp^c) \rightarrow a_{\perp\perp} \cong \mu_{\perp\perp} / (1 - \mu_{\perp\perp})$, $b_{\perp\perp} = a_{\perp\perp} + 1$

from a measured fracture angle $\rightarrow \mu_{\perp\perp} = \cos(2 \cdot \theta_{fp}^c{}^\circ \cdot \pi / 180)$, for $50° \rightarrow \mu_{\perp\perp} = 0.174$.

$b_{\perp\|} \cong 2 \cdot \mu_{\perp\|}$. Typical friction value ranges: $0 < \mu_{\perp\|} < 0.25$, $0 < \mu_{\perp\perp} < 0.2$.

$$Eff_{\text{porosity}}^{\text{SF}} = \sqrt{a_{\perp\perp\text{por}}^2 \cdot I_2^2 + b_{\perp\perp\text{por}}^2 \cdot I_4 - a_{\perp\perp\text{por}}^2 \cdot I_2]/\overline{R}\perp^{\text{c}}}$$

A measurable friction value μ tells the engineer much more than a fictitious friction parameter b. This encouraged the author to transfer the structural stresses-formulated UD-fracture curve $\sigma_2(\sigma_3)$ into a Mohr-Coulomb one obtaining $\tau_{nt}(\sigma_n)$, [1], §7. This novel, mathematically pretty effortful transformation enabled to link the parameter b of the respective SFCs via a determined shear fracture angle to the measurable physical friction value μ.

Delamination within a laminate may occur in tensile-shear cases and in compression-shear cases (*remember the so-called wedge failure IFF2 of Puck with its inclined fracture plane* [7, 13]). Investigating such a delamination a 3D stress state is to consider. This is the case if bends in the structure are stretched or compressed which generates stresses across the wall thickness. Further, if load introduction for instance at supports occurs (*high spatial shear, tiles of the heat shield of launchers like experience with X38, Hermes*). These inter-laminar stress states are delamination-critical $\{\sigma\}_{\text{lamina}} = (0, \sigma_2, \sigma_3, \tau_{23}, \tau_{31}, \tau_{21})^{\text{T}}$ and the designer may face relatively low strengths in the thickness direction (*3-direction*).

Before using UD-SFCs some pre-requisites are to check to really achieve reliable results. This is still valid for the SFC model-validation by the test specimens and for the verification of the laminate designs:

- Good fiber placement and alignment, and uniform stress distribution
- '*Fabrication signatures*' such as fabrication-induced fiber waviness and wrinkles are small and do not vary in the test specimens
- If applicable, residual stresses from the curing cycle are to be computed for the difference '*stress free temperature to room temperature 22°C*' as an effective temperature difference. Considering curing stresses or moisture stresses, the test specimens are most often assumed to be well conditioned
- The stress-strain curves are average curves in design dimensioning, which is also the type one needs for test data mapping in order to obtain the best estimation of the structural response, namely 50%.

Figure 3.6 depicts the fracture failure body of UD materials. The upper picture contains the failure body of the plane 2D stress state and the lower picture the failure surface or body of the 3D stress state. These look the same and are the same. One must just replace the UD-lamina stresses of the 2D-case by equivalent stresses.

3.3.3.3 Static Validation of the FMC-Based SFCs in the World-Wide-Failure-Exercises

The author mapped with his FMC-based SFCs a large variety of isotropic brittle structural materials such as plexiglass, porous concrete stone, cast iron, Normal Concrete, UHPC sandstone, mild steels, foam, monolithic ceramics and for the transversely-isotropic UD fiber-reinforced polymers Lamina (ply, lamella) and orthotropic ceramic
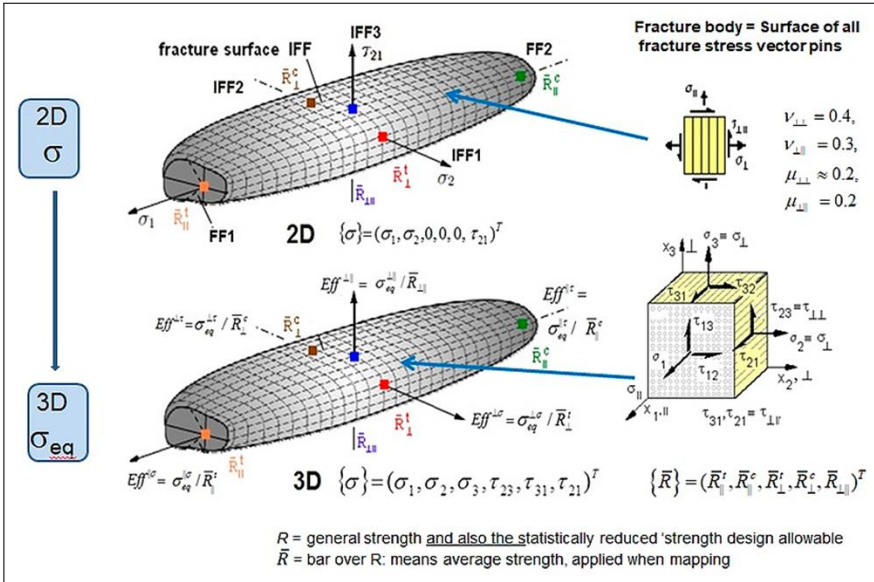
Fig. 3.6: 2D and 3D fracture failure surface (body) and essential UD entities.

Fabrics. This was possible as far as reliable multi-axial fracture test data could be obtained, see [1, 4].

Basis for the validation of the SFCs for the UD lamina material were own test data and those from the WWFEs. There are three WWFEs that have been executed since 1992: WWFE-I (2D stress states) for testing strength fracture criteria by checking the mapping quality of 2D-fracture stress states of the lamina. Then WWFE-II (*3D stress states*) for achieving 3D-lamina model validation and by laminate Test Cases for achieving some laminate wall design verification. The still ongoing WWFE-III is on SFCs generated from Continuum (micro-)Damage Mechanic models. The author contributed to WWFE-I and –II.

Addressing the WWFE it must be noted again: Model validation means *qualification* of a created model by well mapping realistic physical test results with this model. DV means fulfilment of a set of design requirement data, which does not work without model validation. In this context, regarding above two WWFEs, it is to note considering the SFC mapping task:

- Part A, a blind prediction: Mapping had to be carried out without the provision of all physically needed properties. With the provided strength values alone a SFC cannot be validated, compression requires friction information, which was not given.
- Part B, the comparison Theory-Test: Test data sets were partly not applicable or even involved false failure points. More than 50% could not be used without specific care. Further, for instance in WWFE-I (Test Case) TC1, there apples and oranges have been put together. One cannot depict in the same diagram 90°-wound

tube test specimen data together with 0°- wound tube data. The 0°-stresses have to
be transformed in the 2D-plane due to the fact that shearing under torsion loading
turns the fiber direction and the lamina CoS is not anymore identical with the
structural CoS of the tube. In order to also use the 0°-test data set the author
transformed the fracture test point data by the occurring twisting angle using a
non-linear CLT-analysis. Then he could achieve a good mapping of both the data
sets in the lamina CoS. → Due to careful checking of the provided test data the
author achieved the highest number of points in WWFE-I.

In order to solve the task WWFE-II, TC2 through TC4 the necessary average
stress-strain curve has not been provided, but could be effortful deduced from the
different test information.

In the WWFE-II, TC3, above mistake of mixing different tube test data happened
again, but here the much more complicated 3D-stress situation was to face. The
3D-transformation of the 0°-data set was very complicated but successfully carried
out and again different tube test data sets could put together in one graph. → In
the WWFE-II a real assessment of the various SFC-contributions is more or less
missing. The author was again top-ranked.

3.3.4 Application of Static UD-SFCs to Determine Cyclic Micro-Damage Portions

A very essential question in the estimation of lifetime is a means to assess the micro-
damage portions occurring under cycling. For brittle behavior, the response from
practice is: "It is possible to apply validated static SFCs if the failure mechanism
of a mode cyclically remains the same as in the static case. Then the fatigue micro-
damage-driving failure parameters are the same and the applicability of static SFCs
is allowed for quantifying micro-damage portions". Here it is to note that FMC-based
static SFCs apply the equivalent stresses of a mode SF or NF.

For clarification, the determination of the Eff^{mode}-values, representative later also
for the estimation of micro-damage portions is exemplarily described below for a
simple example (Table 3.2).

Table 3.2: Static Design Verification-procedure with determination of Eff^{mode}-values.

Asssumption: Linear analysis permitted, design FoS $j_{ult} = 1.25$

* Design loading (action): $\{\sigma\}_{design} = \{\sigma\} \cdot j_{ult}$

* 2D-stress state: $\{\sigma\}_{design} = (\sigma_1, \sigma_2, \sigma_3, \tau_{23}, \tau_{31}, \tau_{21})^T \cdot j_{ult} = (0, -75, 0, 0, 0, 52)^T\,MPa$

* Residual stresses: 0 *(effect vanishes with increasing micro − cracking)*

* Strengths (resistance) : $\{\overline{R}\} = (1378, 950, 40, 125, 97)^T\,MPa$ from mesurement

$\{R\} = (R_{\|}^t, R_{\|}^c, R_{\perp}^t, R_{\perp}^c, R_{\perp\|})^T = (1050, 725, 32, 112, 79)^T\,MPa$

* Friction values : $\mu_{\perp\|} = 0.3$, $(\mu_{\perp\perp} = 0.35)$, Mode interaction exponent: $m = 2.7$

$\{Eff^{mode}\} = (Eff^{\|\sigma},\ Eff^{\|\tau},\ Eff^{\perp\sigma},\ Eff^{\perp\tau},\ Eff^{\|\perp})^T = (0.88,\ 0,\ 0,\ 0.21,\ 0.20)^T$

$Eff^m = (Eff^{\|\sigma})^m + (Eff^{\|\tau})^m + (Eff^{\perp\sigma})^m + (Eff^{\perp\tau})^m + (Eff^{\|\perp})^m = 100\%$.

The results above deliver the following material reserve factors f_{RF}

* $Eff^{\perp\sigma} = \dfrac{\sigma_2 - |\sigma_2|}{2 \cdot \overline{R}_{\perp}^t} = 0$, $Eff^{\perp\tau} = \dfrac{-\sigma_2 + |\sigma_2|}{2 \cdot \overline{R}_{\perp}^c} = 0.60$, $Eff^{\perp\|} = \dfrac{|\tau_{21}|}{\overline{R}_{\perp\|} - \mu_{\perp\|} \cdot \sigma_2} = 0.51$

$Eff = [(Eff^{\perp\sigma})^m + (Eff^{\perp\tau})^m + (Eff^{\perp\|})^m]^{1/m} = 0.72$.

$\Rightarrow$ $f_{RF} = 1 / Eff = 1.39 \rightarrow$ RF $= f_{RF}$ (if linearity permitted) $\rightarrow$ MoS $= RF - 1 = \quad > 0.39\ 0!$

3.4 FMC-Based Constant-Fatigue-Life Estimation Model for UD-Ply–Composed Laminates

3.4.1 Idea of an Automatic Establishment of Constant Fatigue Life Curves

Basic aim in fatigue design is to reduce the test amount of SN-curves to a minimum. This was a long-lasting task for the author and was firstly solved some years ago. Its solution steps are:

- A validated static SFC is applicable to assess the micro-damage portions. This was the first hurdle to tackle. Here, the author's SFCs, based on a consistent failure mode thinking, support the fatigue analysis
- As second challenge an analytical, automatic establishment of a continuous Constant Fatigue Life (CFL) curve $\sigma_a(\sigma_m), N =$ const - basis of lifetime estimation – was then to determine (N is failure cycle number and n running cycle number). A suitable function for mapping the course of provided SN-curve test data was searched. Chosen was the 4-parameter Weibull curve model.
- A further task in order to reduce the test amount was finding a physically-based model to predict other SN curves, required for fatigue analysis, on basis of probably just one Master SN curve for each mode. This model became Kawai's 'Modified Fatigue Strength Ratio Ψ.
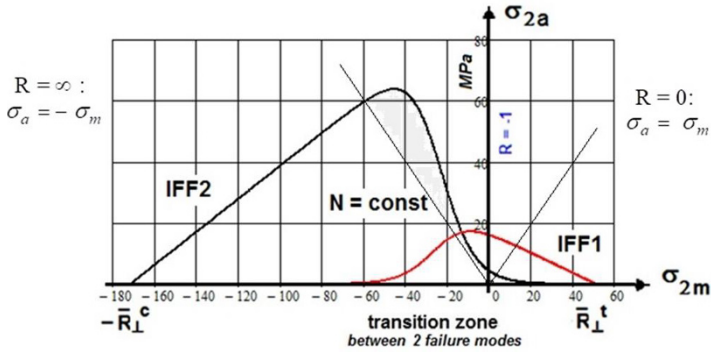
Fig. 3.7: Effect of the decay function in the transition zone $-\infty < R < 0$.

- Finally, a challenging task was the very difficult mapping of the test data decrease in the so-called transition zone where the modes interact around the stress ratio beam $R_{transition} = -R_c/R_t < R = \sigma_{min}/\sigma_{max} = -1$. The traditional investigated beam $R = -1$ is too more right in the Haigh diagram, see Fig. 3.7, and therefore does not accurately characterize the transition zone in the case of large strength ratio R_c/R_t. The transition zone is the most problematic modeling region in the Haigh diagram. A solution became possible by a mode decay function which physically terminates the influence of the SF part (*compression*) in the Haigh diagram when the NF part begins to act at $R = 0$ and vice versa for the NF part (*tension*) at $R = \infty$.

In aircraft industry, for a design-necessary interpolation in order to achieve CFL curves, much effort is spent to map them piece-by-piece by straight lines, see for instance the respecting sheets on metals in the HSB (H. Hickethier: Interpolation and Extrapolation of SN data). Regarding curved lines, the dissertation of C. Hahne [14] is recommended. Therefore, an automatic possibility to generate realistic continuous CFL-curves is highly desired in order to avoid difficult interpolations between the curves. A reliable procedure would help to save test cost and development time.

For the *multiple failure modes suffering* brittle materials an automatic establishment of the non-piecewise straight CFL curves in Haigh Diagrams is searched, generally applicable to brittle isotropic materials including for instance concrete and here for UD-materials.

Finally, as detailed points for achieving these CFL curves are to list:

- Measurement of a minimum number of Master SN curves (R =const) for each acting failure mode domain, namely compression (SF) and tension (NF)
- Finding a physically-based model to predict other SN curves, required for fatigue analysis, on basis of a measured 'Master SN curve' of each mode
- Provision of a means how the cycling-caused micro-damage portions can be quantified (see Subsect. 3.3.4 before)

- Mathematical mapping procedure of the test data in the transition domain *as most problematic region in the Haigh diagram*, where the modes interact. Search of a practicable mode domain decay function of the two modes in the Haigh diagram
- Final step is the provision of a program that automatically delivers the CFL curves on basis of the preceding fulfilled points.

3.4.2 SN Curves, Derived with Kawai's "Modified Fatigue Strength Ratio Ψ_J

Some years ago, Misamichi Kawai [15] informed the author on his physically-based model to capture SN-curves. It was dedicated to UD material. His first step was to formulate a 'Fatigue Strength Ratio' Ψ. This means a normalization of the fatigue strength $\sigma_{\max}(N)$ by a static strength $\Psi = \sigma_{\text{static}}/\overline{R} = 1 = Eff$ and such referring to Eff. The second step was the formulation of his 'Modified Fatigue Strength Ratio' Ψ, which is a reformulation in order to get the stress ratio R into the static concept $\Psi = (\sigma_a + \sigma_m)/\overline{R} = 1 \Rightarrow 1 = (\sigma_a + \sigma_m)/\overline{R} \Rightarrow \sigma_a/R - \sigma_m = \Psi$ as ratio cyclic part/static part. For visualization of Ψ see Fig. 3.8.
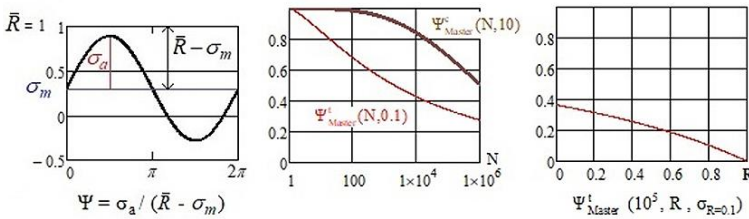
Fig. 3.8: Definition and visualization of 'Modified Fatigue Strength Ratio Ψ' (ordinate).

Each measured SN-curve is normalized by its static strength R and the 'bulk' of available SN curves then fitted to obtain the Master curve (hopefully it is more than one SN curve measured within the domains and in the transition zone). Kawai used all R-curves to obtain $\Psi = \Psi(R_{\text{fit}})$, independent of the inherent failure mode. Whether it practically makes sense to determine a Master curve by globally fitting all curves is to check, if enough test data sets will be available considering tension with $R = 0.1, 0.5$, compression with $R = 10$ and in the transition zone $R = -1$ and R_{trans}. Due to sticking to the FMC means to stick to a mode domain separation. This requires to tackle the transition zone between the modes separately. Table 3.3 presents the determination of SN-curves on basis of Ψ-model with Master SN-curve.

To justify the general applicability of the Kawai model-predicted SN curves, here the FMC mode-dedicated ones, the curves in Fig. 3.9 have been numerically derived. Figure 3.9 shows the Master SN curves and the predicted SN curves. With

Table 3.3: Determination of SN curves on basis of Kawai's Ψ-model with Master SN-curve. Full procedure of the automatic determination of a CFL curve.

---

* Relationships with stress ratio R

$$\sigma_{max} = \Delta\sigma / (1-R) \equiv 2\cdot\sigma_a / (1-R) \quad \text{with} \quad \Delta\sigma = \text{stress range}, \sigma_a \text{ is positive}$$

$$R = (\sigma_m - \sigma_a)/(\sigma_m + \sigma_a), \quad \sigma_a = \sigma_m \cdot (1-R)/(1+R)$$

$R = -1$, fully reversed alternating stress. $R = 0$, $R = 100\ (\infty)$, extreme swelling stresses.

$$\bar{R}^t = \sigma_{max}(n = N = 1), \quad \bar{R}^c = \sigma_{min}(n = N = 1)$$

$$\sigma_a = 0.5\cdot\sigma_{max}\cdot(1-R),\ \sigma_m = 0.5\cdot\sigma_{max}\cdot(1+R)\ ;\ \sigma_a = -0.5\cdot\sigma_{min}\cdot(1-R^{-1}),\ \sigma_m = \sigma_{min}(1-0.5\cdot(1-R^{-1}))$$

* Choice of problem-adequate mapping function and individual mapping of course of test data

$$\sigma_{max}(N) = c1 + (\bar{R} - c1)/\exp\left(\frac{log(N)}{c3}\right), \quad \sigma_{min}(N) = c1 + (-\bar{R} - c1)/\exp\left(\frac{log(N)}{c3}\right)^{c2}$$

* Test input and mapping of available Master curves (usually just available for R=0.1 and 10)

$$\sigma_{R=0.1} = c_1^{NF} + (\bar{R}^t - c_1^{NF})/\exp\left(\frac{log(N)}{c_3^{NF}}\right)^{c_2^{NF}}, \quad \sigma_{R=10} = c_1^{SF} + (-\bar{R}^c - c_1^{SF})/\exp\left(\frac{log(N)}{c_3^{SF}}\right)^{c_2^{SF}}$$

* Mode dedicated Application of Kawai's model $\psi = \sigma / \bar{R}$; ψ, Ψ positive

Static failure occurs at $\sigma_{max} = \bar{R}^t = \sigma_a + \sigma_m$ and $\sigma_{min} = -\bar{R}^c = -\sigma_a + \sigma_m$.

$$\sigma_{max} = \bar{R}^t = \sigma_a + \sigma_m \rightarrow \sigma_a = \bar{R}^t - \sigma_m \rightarrow 1 = \sigma_a / (\bar{R}^t - \sigma_m) \equiv \text{cyclic / 'static'}$$

Kawai 's *cyclic* danger intensity to fail $(N > 1)$ is given for tension and compression

$$\Psi_{Master}^t = \sigma_a / (\bar{R}^t - \sigma_m) \quad \text{and} \quad \Psi_{Master}^c = \sigma_a / (\bar{R}^t + \sigma_m).$$

* Relationship of available Master curves with Ψ

Inserting σ_a, σ_m brings the stress ratio R into the model

$$\Psi_{Master}^t = 0.5\cdot\sigma_{max}^{Master}\cdot(1-R)/[\bar{R}^t - 0.5\cdot\sigma_{max}^{Master}(1+R)]$$

$$\Psi_{Master}^c = \sigma_{min}^{Master}\cdot(1-R)/[2\cdot R\cdot\bar{R}^c + \sigma_{min}^{Master}\cdot(1+R)].$$

* Resolution of above equations for a novel S-N curve or of a CFL curve (inserting σ_a, σ_m)

$$\sigma_{NFdomain} = 2\cdot\bar{R}^t\cdot\Psi_{Master}^t / (\Psi_{Master}^t - R + R\cdot\Psi_{Master}^t + 1), \quad 0 < R < 1$$

$$\sigma_{SFdomain} = -2\cdot\bar{R}^c\cdot R\cdot\Psi_{Master}^c / (\Psi_{Master}^c + R + R\cdot\Psi_{Master}^c - 1)$$

$$\sigma_{R=0} = 2\cdot\bar{R}^t\cdot\Psi_{Master}^t / (\Psi_{Master}^t - 0 + 0\cdot\Psi_{Master}^t + 1) \quad \text{for } R = 0$$

$$\sigma_{R=100} = -2\cdot\bar{R}^c\cdot 100\cdot\Psi_{Master}^c / (\Psi_{Master}^c + 100 + 100\cdot\Psi_{Master}^c - 1) \quad \text{for } R = 100\ (\approx\infty).$$

---

respect to the authors mode dedication and separation the transition beam $R = -1$ is consequently not depicted in the figure.

The application results for IFF mode domains demonstrate:

- Limit Curves $R = 0, 100(\infty)$ and 1 are automatically captured
- The question, whether the intermediate Kawai-curves in the range between the limit curves and $R = 1$ are good enough, can be only responded by further test results and associated modeling research work
- The question, whether Kawai's global fit of all available SN curves is satisfactory could be not supported due to lack of test data. If successful, the Kawai's model
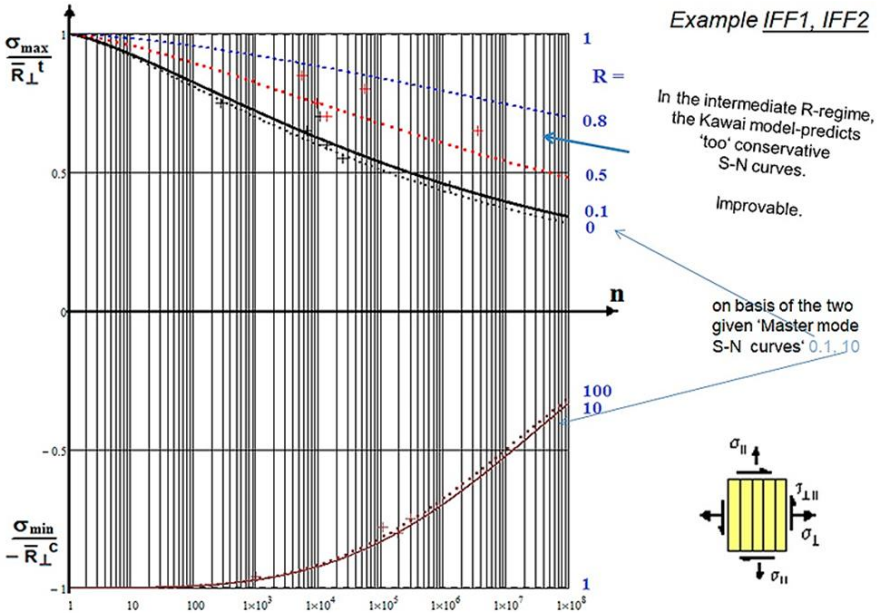
Fig. 3.9: Mode-dedicated Kawai model-derived SN curves. +R = 0.5 test data, +R = 0.1 test data.

would make it possible to also estimate SN-curves in the transition zone ($\infty >$ R > 0).

Anyway, Kawai's model quality looks very promising.

Mind, please:

Testing conventionally requires 5 different UD stress amplitude levels for a distinct SN- curve with three repetitions at each level considered as the minimum.

To become practical, an IFF work case fatigue life estimation shall be depicted. It represents the Design Verification of a critically cycled UD lamina embedded within a chosen laminate (Table 3.4).

3.4.3 Derivation of Constant Fatigue Life Curves in the Transition Domain

There is no problem to establish Haigh diagrams for FF1 with FF2 and for IFF3 due to the fact that the strength values are of similar size in each case. Application of the static mode interaction formula was almost sufficient. However for a Haigh Diagram for really brittle materials, indicated by the beam R_{trans}, practically very different to R = −1, a solution procedure has to be looked for. Chosen was a mode-linked exponentially decaying function fd, that practically ends where the other pure mode begins to reign. As the employment of the decay function is too lengthy in the work

Table 3.4: Lifetime Design Verification-procedure for a tensioned UD lamina.

IFF1: Test data, courtesy C. Hahne

* Given: $\sigma_2 = \sigma_{2a} + \sigma_{2m}$, $\bar{R}_{\perp}^t = 51$ MPa

  $n_1 = 50000$ cycles, R = 0.5, $\sigma_2 = 32$ MPa; $n_2 = 100000$ cycles, R = 0, $\sigma_2 = 30$ MPa

$$\sigma_{max}^{Master} = c1 + (\bar{R}_{\perp}^t - c1) / \exp\left(\frac{log(N)}{c3}\right)^{c2} \text{ with } c1 = 7.1, c2 = 1.34, c3 = 6.05$$

$$\Psi_{Master}^t = \frac{\sigma_{2a}}{\bar{R}_{\perp}^t - \sigma_{2m}} = 0.5 \cdot \sigma_{max}^{Master} \cdot (1-R) / (\bar{R}_{\perp}^t - 0.5 \cdot \sigma_{max}^{Master} (1+R))$$

and after resolution an equation for the determination of a desired S-N curve, inserting R

$$\sigma_{max} = 2 \cdot \bar{R}_{\perp}^t \cdot \Psi_{Master}^t / (\Psi_{Master}^t - R + R \cdot \Psi_{Master}^t + 1), \quad 0 < R < 1$$

* Estimation of fracture cyles N at $D_i = n_i / N_i = 100\%$

$$\sigma_{R=0.5} = 2 \cdot \bar{R}_{\perp}^t \cdot \Psi_{Master}^t / (\Psi_{Master}^t - 0.5 + 0.5 \cdot \Psi_{Master}^t + 1) = \sigma_2 \rightarrow N_1 = 4.6 \cdot 10^5$$

$$\sigma_{R=0} = 2 \cdot \bar{R}_{\perp}^t \cdot \Psi_{Master}^t / (\Psi_{Master}^t - 0 + 0 \cdot \Psi_{Master}^t + 1) = \sigma_2 \rightarrow N_2 = 1.7 \cdot 10^6 .$$

* Summing up the micro-damage portions $\rightarrow$ total$D_i = \Sigma \, n_i / N_i = 0.17 < 1 = 100\%$
* From experience with the SN-scatter $\rightarrow$ RF$_{Life}$ should be > 5 (termed 'Relative Miner').

  Design Verification delivers $\rightarrow$ RF$_{Life}$ = 100% / total D = 1 / 0.17 = 6 > 5 !

case above (Table 3.4) just two SN curves in the pure domains NF and SF were investigated.

Table 3.5 informs about the steps for an example IFF1-IFF2, where mode interaction has to be taken into account. In Table 3.6 the determination of the curve

Table 3.5: Mode decay function f_d for tension and compression domain in the Haigh diagram.

$$Eff = [(Eff^{NF})^m + (Eff^{SF})^m]^{m^{-1}} = 100\%$$

formulated in amplitude and mean stresses reads

$$\left(\frac{-(\sigma_{2m} - \sigma_{2a}) + |\sigma_{2m} - \sigma_{2a}|}{2 \cdot \bar{R}_{\perp}^c \cdot f_d}\right)^m + \left(\frac{\sigma_{2m} + \sigma_{2a} + |\sigma_{2m} + \sigma_{2a}|}{2 \cdot \bar{R}_{\perp}^t \cdot f_d}\right)^m = 1$$

delivering the CFL curve for N = 1 cycle, $f_d = 1$, activating both NF with SF.

To obtain a CFL curve for higher N and larger ratios such as $R_{trans} = -\bar{R}^c / \bar{R}^t$ above

interaction formula, working in the transition zone, is engineering-like to adjust because the

action of a mode ends where the other mode begins. Chosen is an exponential decay function f_d

that decays from the end of the pure SF mode at $R = \infty$ (R=10 possible) down to zero at

the beginning of the pure NF mode at R = 0 (R=0.1 possible) and vice versa

$$\rightarrow f_d = 1 / [1 + \exp(\frac{c_1 + \sigma_m}{c_2})] .$$

Table 3.6: Numerical derivation of the parameters of the decay function.
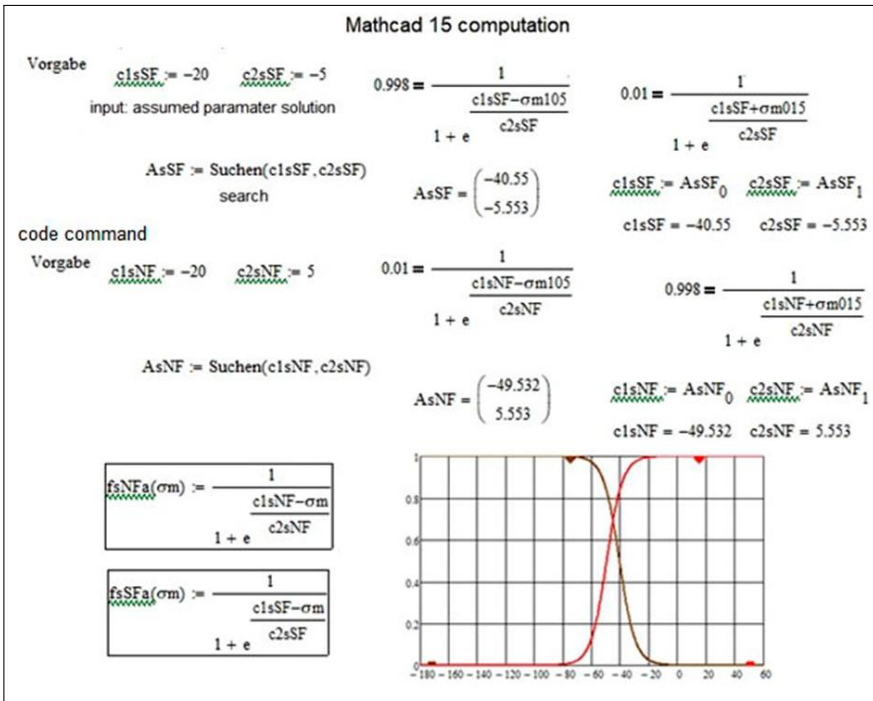
parameters of the mode decay function are derived in the SF and the NF domain and then visualized. In the included figure the resulting curves are displayed. For fully ductile materials no transition zone between 2 modes exists, because just one single mode reigns, namely 'shear yielding'. There, it is no mean stress effect to correct.

Eventually in Fig. 3.7 mode decay functions fd for the tension and the compression domain are displayed. The straight lines in the figure present the extreme SN curve beams, $R = \infty$ for the SF domain and $R = 0$ for the NF domain. In between the slightly colored transition zone is located. The quality of the approach for the transition zone is practically checked by "How good is the test data course along the stress ratio beam R_{trans}-line mapped?"

The author now proposes his procedure in Table 3.7 for deriving part-CFL curve estimates on basis of one Master SN curve provided for each mode. As example a UD-material serves which is stressed in the pure modes IFF1 and IFF2, only.

Table 3.7: Estimation of a CFL curve for IFF, $N = 10^5$ cycles.

- S-N curves in the two Mode Domains IFF1, IFF2
  * From FMC reasons - in contradiction to Kawai - a strict mode separation is to apply.
  * S-N curves are generally given for domains IFF1, IFF2 and sometimes $R = -1$, R_{trans}.
    Available Master curves are usually just the standard ones $R = 0.1$ (IFF1), $R = 10$ (IFF2)
  * Computation of the CFL curve parameters for the 2 domains (example $N = 10^5$, indexed 5)

$$\sigma_{max,5}^{Master} (10^5, R=0.1) = \sigma_{R=0.1}(10^5, R=0.1) = c_1^{NF} + (\bar{R}^t - c_1^{NF}) / \exp\left(\frac{log(10^5)}{c_i^{NF}}\right)^{c_2^{NF}} = \bar{R}^t \cdot \Psi_{Master}^{t,5}$$

$$\sigma_{min5}^{Master} (10^5, R=10) = \sigma_{R=10}(10^5, R=0.1) = c_1^{SF} + (\bar{R}^c - c_1^{SF}) / \exp\left(\frac{log(10^5)}{c_i^{SF}}\right)^{c_2^{SF}} = -\bar{R}^c \cdot \Psi_{Master}^{c,5} \cdot$$

  * The fatigue strengths $\sigma_{max}^5(R, 10^5)$, $\sigma_{min}^5(R, 10^5)$ replace static strengths

$$\sigma_{max}^5(R) = 2 \cdot \bar{R}^t \cdot \Psi_{Master}^{t,5} / (\Psi_{Master}^{t,5} - R + R \cdot \Psi_{Master}^{t,5} + 1), \quad 0 < R < 1$$

$$\sigma_{min}^5(R) = -2 \cdot \bar{R}^c \cdot \Psi_{Master}^{c,5} / (\Psi_{Master}^{c,5} + R + R \cdot \Psi_{Master}^{c,5} - 1), \quad 1 < R < 100 \ (\infty).$$

$$\text{with } R = (\sigma_m - \sigma_{2a,5}) / (\sigma_m + \sigma_{2a,5}).$$

- CFL curves $\sigma_{max}^5(R, 10^5)$ within the 2 IFF domains $\bar{R} \to \sigma^5(R)$

$$\frac{-(\sigma_{2m} - \sigma_{2a}) + |\sigma_{2m} - \sigma_{2a}|}{2 \cdot \bar{R}_\perp^c} = 1 \quad \text{and} \quad \frac{\sigma_{2m} + \sigma_{2a} + |\sigma_{2m} + \sigma_{2a}|}{2 \cdot \bar{R}_\perp^t} = 1 \text{ static}$$

$$\frac{-(\sigma_{2m} - \sigma_{2a}) + |\sigma_{2m} - \sigma_{2a}|}{2 \cdot \sigma_{min}^5(R)} = 1 \quad \text{and} \quad \frac{\sigma_{2m} + \sigma_{2a} + |\sigma_{2m} + \sigma_{2a}|}{2 \cdot \sigma_{max}^5(R)} = 1 \text{ cyclic.}$$

- Modelling in the Transition Zone between the mode domains
  * The transition zone where both the modes interact requires the interaction equation

$$Eff = [(Eff^{NF})^m + (Eff^{SF})^m]^{m^{-1}} = 100\% = 1.$$

    Formulated in CFL coordinates σ_a and σ_m the static interaction equation reads

$$\left(\frac{-(\sigma_{2m} - \sigma_{2a}) + |\sigma_{2m} - \sigma_{2a}|}{2 \cdot \bar{R}_\perp^c}\right)^m + \left(\frac{\sigma_{2m} + \sigma_{2a} + |\sigma_{2m} + \sigma_{2a}|}{2 \cdot \bar{R}_\perp^t}\right)^m = 1 \text{ static curve, n = 2N}_f.$$

  * For the $N = n = 1$ cycle with $n = 2 \cdot N_f$: Static interaction equation delivers a curve which still
    runs through the full Haigh diagram.
- CFL curves in the full Haigh diagram
  * To obtain a CFL curve for higher N and larger ratios $R_{trans} = -\bar{R}^c / \bar{R}^t$ the two opposite
    mode decays in the transition zone are to adjust by $f_d = 1 / [1 + \exp((c_1 + \sigma_m)/c_2)]$.
  * Inserting $R = (\sigma_m - \sigma_{2a,5}) / (\sigma_m + \sigma_{2a,5})$ for $\sigma_m \to \sigma_{2m}$ as running variable the CFL curve
    $\sigma_{2a}(\sigma_{2m}, N = const)$ is to determine by solving the complicate implicit equation for σ_{2a} below

$$\left(\frac{-(\sigma_{2m} - \sigma_{2a,5}) + |\sigma_{2m} - \sigma_{2a,5}|}{2 \cdot \sigma_{max}^5(R) / (1 + e^{\frac{c_{1SF} + \sigma_{2m}}{c_{2SF}}})}\right)^m + \left(\frac{(\sigma_{2m} + \sigma_{2a,5}) + |\sigma_{2m} + \sigma_{2a,5}|}{2 \cdot \sigma_{max}^5(R) \cdot / (1 + e^{\frac{c_{1NF} + \sigma_{2m}}{c_{2NF}}})}\right)^m = 1 .$$

3.5 Complete CFL-Curve Model Using the Decay Functions f_d in the Haigh-Diagram

3.5.1 Derivation of the Full Procedure

Figure 3.10 shall schematically exhibit the pure domains and the transition zone in the Haigh diagram. This shows the maximum tolerable stress (loading) amplitudes of the material $\sigma_a(\sigma_m)$. For $N = 1$ the static procedure is applicable using the strength failure envelope represented by the interaction formula, whereby in the negative domain lie the SF-determined SN-curves, in the positive domain the NF determined ones. In the transition zone 2 modes are principally activated which shows either a more SF- or a more NF-determined interaction visualized by the two pale colors. The domain limits are given by the straight SN-lines for:

$$R = \infty : \sigma_a = -\sigma_m \quad \text{and} \quad R = 0 : \sigma_a = \sigma_m.$$

The representative SN-beams in the transition zone are R_{trans} and $R = -1$.

Of highest interest are the SN-beams in the transition zone around R_{trans} and $R = -1$ which have other origin values than the basic strengths of the modes. The R_{trans} origin is not given and has to be determined before mapping. Applied was the static interaction curve, $N = 1$, because points on the boundary must fulfill the static equilibrium. The derivation of the origin points on the side lines reads for the two transition zone beams:

NF = Normal Fracture, SF = Shear Fracture, N = fracture cycle number
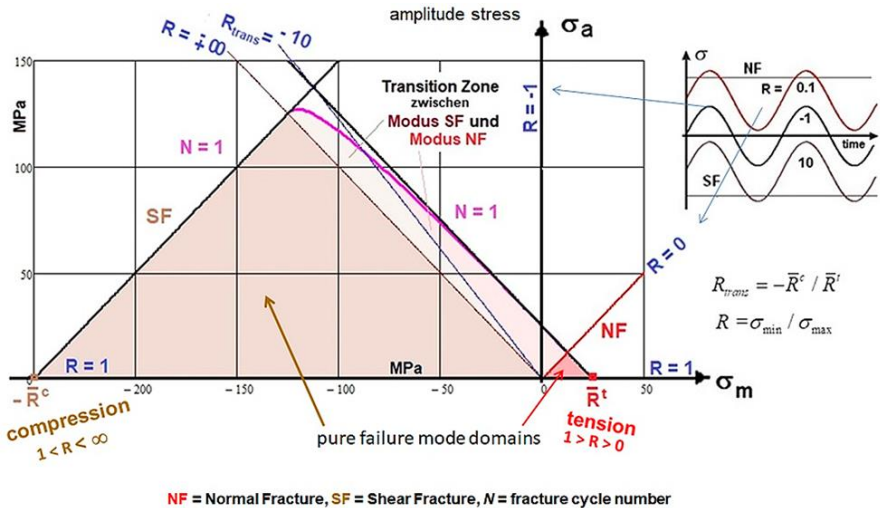
Fig. 3.10: Scheme for understanding a Haigh diagram of a brittle isotropic material. Up right: alternating stress states of 3 R curves.

$$R_{\text{trans}} = -\overline{R}_{\perp}^{c}/\overline{R}_{\perp}^{t} = -3.4 : \left(\frac{\sigma_{2\,\text{fr}}}{\overline{R}_{\perp}^{t}}+\right)^{m} + \left(\frac{\sigma_{2\,\text{fr}}R_{\text{trans}}}{\overline{R}_{\perp}^{c}}+\right)^{m} = 1 \rightarrow \sigma_{2\,\text{fr}} = -131\,\text{MPa},$$

$$R = -1 : \qquad \left(\frac{\sigma_{2\,\text{fr}}}{\overline{R}_{\perp}^{t}}+\right)^{m} + \left(\frac{\sigma_{2\,\text{fr}}R}{\overline{R}_{\perp}^{c}}+\right)^{m} = 1 \rightarrow \sigma_{2\,\text{fr}} = 50.1\,\text{MPa}$$

In Fig. 3.11 two CFL-curves are displayed, the envelope $N = 1$ and $N = 10^7$ cycles. The pure mode domains are colored and the transition zone is separated by R_{trans} into two influence parts. The course of the R-value in the Haigh diagram is represented by the bold dark blue lines.

The CFL curve $N = 1$ is the cyclic envelope. It is curved at top because 2 modes act in the case of brittle materials. This is in contrast to uniaxial static loading, depicted by the straight static envelopes $N \neq N_f$. One micro-damage cycle results from the sum of 2 micro-damage portions, one comes from uploading and one from unloading! (The associated MathCad 15 program, which involves test data evaluation, parameter determination of Weibull curves, of Master curves, of decay functions, computation operations and visualization afforded more than 30 pages). The full procedure is collected in the Table 3.8. Here, and this is reasonable for brittle materials, all the SN-curves have their origin in the strength points $\overline{R}_{\perp}^{t}$ and $\overline{R}_{\perp}^{c}$

The following points are to consider thereby:

- Assumption: If the failure mechanism of a mode cyclically remains the same as in the brittle static case, then the micro-damage-driving fatigue failure parameters
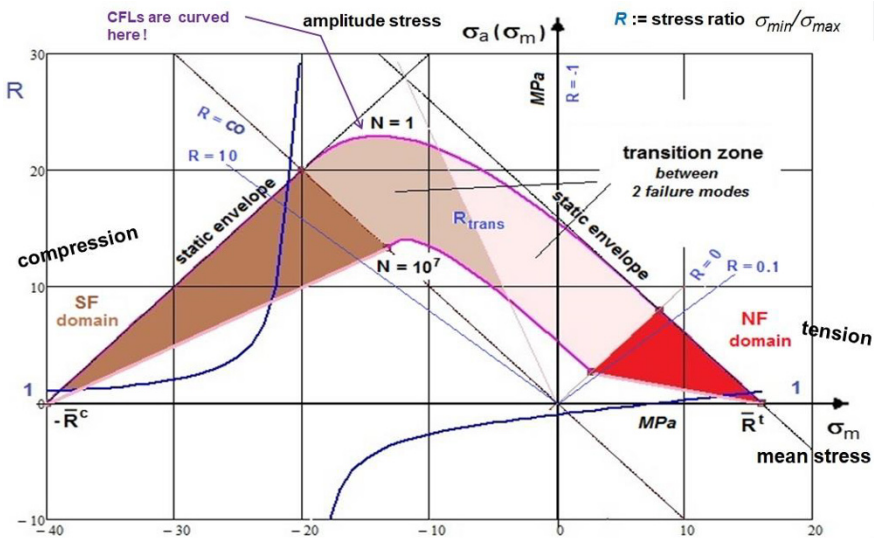
Fig. 3.11: Scheme of pure mode domains, course of R and transition zone parts.

Table 3.8: Full procedure of the automatic determination of a CFL curve. IFF, $N = 10^5$ cycles.

---

1 Choice of the distinct CFL (example $N = 10^5$)

2 Determination of the 2 Master curves

  Assumption: usual test curves R=0.1 (NF), R=10 (SF) are sufficient instead of R=0, R=1000 $\cong \infty$

$$\sigma_{max}^{Master}(N, R = 0.1) \rightarrow = \sigma_{R=0.1} = c_1^{NF} + (\bar{R}^t - c_1^{NF})/\exp\left(\frac{log(N)}{c_1^{NF}}\right)^{c_2^{NF}}$$

$$\sigma_{min}^{Master}(N, R = 10) \rightarrow = \sigma_{R=10} = c_1^{SF} + (-\bar{R}^c - c_1^{SF})/\exp\left(\frac{log(N)}{c_1^{SF}}\right)^{c_2^{SF}}.$$

3 Assumption: Straight asymptotic side lines in the 2 mode domains $\sigma_a(\sigma_m) = c_1 + c_2 \cdot \sigma_m$

  2 strength points are given and 2 mean $\sigma_a(\sigma_m, N)$ of R=0.1 and R=10 are to compute

    as a fixed point of each side line

4 Computation of the fixed points in the domains NF, SF (n MPa)

$$\sigma_{R=0.1}^{100000} = 27.3 \rightarrow \sigma_{a_{R=0.1}}^{100000} = 0.5 \cdot \sigma_{R=0.1}^{100000} \cdot (1-0.1) = 12.3, \quad \sigma_{m_{R=0.1}}^{100000} = \sigma_{R=0.1}^{100000} - \sigma_{a_{R=0.1}}^{100000} = 15.0,$$

$$\sigma_{R=10}^{100000} = -136.5 \rightarrow \sigma_{a_{R=10}}^{100000} = -0.5 \cdot \sigma_{R=10}^{100000} \cdot (1-1/10) = 61.4, \quad \sigma_{m_{R=10}}^{100000} = \sigma_{R=10}^{100000} + \sigma_{a_{R=10}}^{100000} = -75.$$

5 Function for the decay of mode influences $\sigma_a(\sigma_m)$ over the transition zone

  Parameters sets from the strength point and a fixed point $f_d = 1/[1+\exp((c_1 + \sigma_m)/c_2)]$.

    $f_d(SF): (\sigma_a, \sigma_m, N, R=10) \rightarrow 0.99$ with $(\sigma_a, \sigma_m, N, R=0.1) \rightarrow 0.01$;

    $f_d(NF): (\sigma_a, \sigma_m, N, R=10) \rightarrow 0.01$ with $(\sigma_a, \sigma_m, N, R=0.1) \rightarrow 0.99$.

6 'Static' envelope curve: Solving the interaction equation for $\sigma_a(\sigma_m, N=1)$

$$\left(\frac{-(\sigma_{2m} - \sigma_{2a}) + |\sigma_{2m} - \sigma_{2a}|}{2 \cdot \bar{R}_\perp^c}\right)^m + \left(\frac{\sigma_{2m} + \sigma_{2a} + |\sigma_{2m} + \sigma_{2a}|}{2 \cdot \bar{R}_\perp^t}\right)^m = 1 \rightarrow \sigma_{2a}(\sigma_{2m}, \bar{R}_\perp^c, \bar{R}_\perp^t).$$

7 Assymptotic side line approach for the decaying curves $\sigma_a(\sigma_m, N > 1)$

$$[\sigma_{2a}(\sigma_{2m}, N)]^m = (c_{1SF} + c_{2SF} \cdot \sigma_{2m})^m + (c_{1NF} + c_{2NF} \cdot \sigma_{2m})^m$$

  Work case $N = 10^5$ cycles, $m = 2.5$

  $c_{1SF} = 0.63 = c_{2SF}, \quad c_{1NF} = 0.34 = -c_{2NF}; \quad c_{1SFS} = -40.6, \quad c_{2SFS} = -5.56, \quad c_{1NFS} = -49.5, \quad c_{2NFS} = 5.55$

$$\sigma_{2a}(\sigma_{2m}, N=10^5, c_i) = \left[\left(\frac{c_{1SF} + c_{2SF} \cdot \sigma_{2m}}{1 + \exp(\frac{c_{1SFS} + \sigma_{2m}}{c_{2SFS}})}\right)^m + \left(\frac{c_{1NF} + c_{2NF} \cdot \sigma_{2m}}{1 + \exp(\frac{c_{1NFS} + \sigma_{2m}}{c_{2NFS}})}\right)^m\right]^{1/m}.$$

---

are the same and the applicability of static SFCs is allowed for quantifying micro-damage portions

- Presumption: An appropriate Master SN curve for each failure mode domain compression (SF) and tension (NF) is available at minimum. This means measurement of just a minimum number of SN curves is required

- The helpful model, searched by the author, became the 'Modified Fatigue Strength Ratio Ψ model' of Kawai [15], which enables to estimate SN curves. Kawai captures all SN curves in tension (NF) and in compression (SF) domain by one Ψ

and then he can also determine SN-curves in the transition zone around Rtrans. The boundary R-curves are automatically captured by the model

- According to his 'modal FMC thinking' Cuntze dedicated a Ψto each single failure mode domain SF and NF. Other necessary SN-curves, necessary for the verification of the usually faced variable amplitude operational loading, can then be derived from the mode Master SN-curve
- Cuntze separates the mode regimes to stay better physically-based in the mode domains. However, then he needs above mentioned decay function

$$f_{\text{decay}} = 1/(1 + \exp(c_1 + m/c_2)$$

in both the domains to make the determination of SN-curves and of CFL-curves in the transition zone possible

- A quality check of the two approaches is possible if enough SN-curves, distributed over the full Haigh diagram, will be available in literature for a material with a large strength ratio.

3.5.2 CFL Curves, Applying the Mode Decay Functions f_d in Various UD Haigh-Diagrams

3.5.2.1 FF SN Curves and Associate Haigh Diagram

Some examples of SN-curves, 'feeding' the associated Haigh-Diagrams, are presented Fig. 3.12. These belong to the failures FF and IFF and capture the failure types NF (tension) and SF (compression). In Fig. 3.12 FF-test data from Kawai-Suda [15]) the bulk of measured SN curves usually looks. It further shows how the mapped curves are running in the higher VHCF regime. Mind, please: There is no fidelity given when simply using extrapolated values far off the tested range.

Figure 3.13 presents failure mode-linked CFL-curves $\sigma_a(\sigma_m, N = \text{const})$. The computed SN curve points, marked by X, are fixed points (anchors) for mapping the CFL-curves to be predicted. The blue curve is for $N = 10^5$ cycles. The used SN-curves are from Fig. 3.12.

3.5.2.2 IFF3 SN Curves and Associate Haigh Diagram

Figure 3.14 presents two mapped IFF3 SN-curves. Here, at first the author likes to thank Dr.-Ing. Clemens Hahne, AUDI, for his valuable UD test effort making the generation of the following figures possible and thereby the application of the author's CFL model. The reader is invited to read the content-rich and imaginative dissertation [14] and this not only for comparing the different CFL modeling ideas of Hahne and Cuntze.
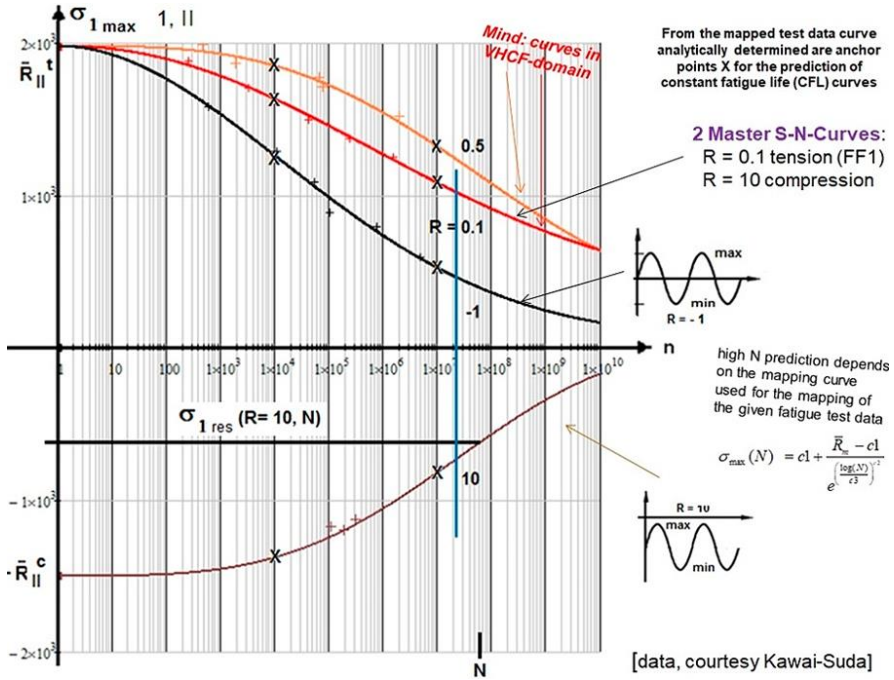
Fig. 3.12: Test example UD: Individually lin-log mapped FF1-FF2-linked SN-curves [15].

Figure 3.15 depicts the associated IFF3 CFL-curves derived. Obvious is the symmetry and that the two-fold IFF3 mode micro-damage effect flattens the curve at $\sigma_m = 0$.

3.5.2.3 IFF1, IFF2 SN-Curves and Associated Haigh Diagram

In Fig. 3.16 the mapped IFF1 (tension)- and IFF2 (compression)-linked SN-curves are presented. Figure 3.17 displays the differently colored failure mode domains IFF1-IFF2 in a UD IFF Haigh diagram. The available test data set along R_{trans} in the transition zone is represented by the crosses. The decay model quality in Fig. 3.17 proves the efficiency of the decay functions in the transition zone. For proving this the author is very thankful because this was only possible because he got access to the test results in [14]).

By the way:

The decaying course of the curve in the graph below for UD material is similar to concrete due to their large strength ratios R^c/R^t! Similar behavior permits similar description!
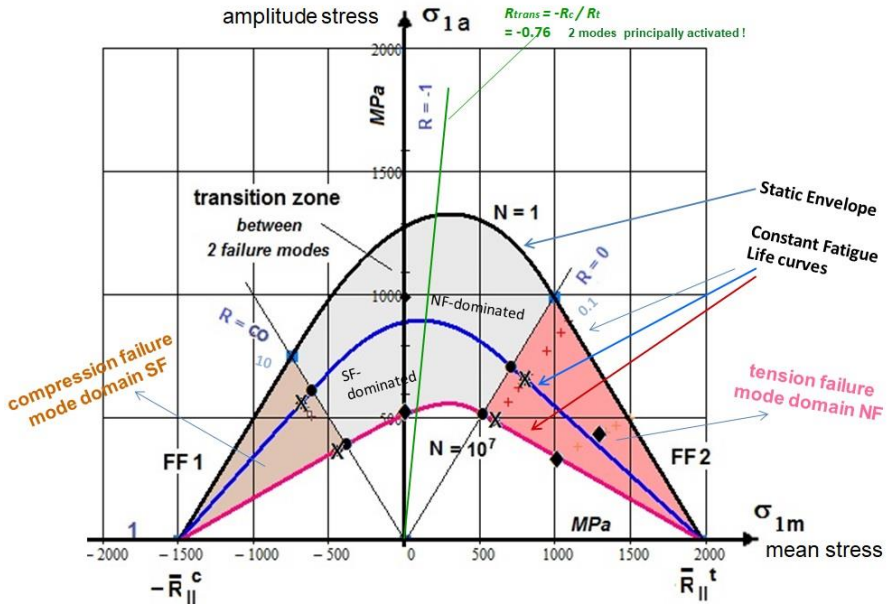
Fig. 3.13: Rigorous Interpretation of the Haigh diagram for the UD-example FF1-FF2 displaying failure mode domains and transition zone [15]: CFRP/EP, $\overline{R}^t = 1980, \overline{R}^c = 1500, \overline{R}_\perp^t = 51,$ $\overline{R}_\perp^c = 172, \overline{R}_\perp = 71$ MPa.
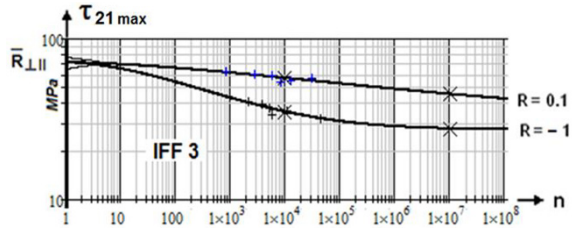
Fig. 3.14 Log-log IFF3-linked SN-curves (data, courtesy C. Hahne [14])

3.5.3 Steps of the FMC-based Fatigue Life Estimation Procedure

Some steps of the fatigue life estimation procedure are depicted in the following figures. Step 1 is searching measured SN-curves. Figure 3.18 presents such a measured SN-curve that serves as Master SN curve. This SN-curve can be mapped here (Step 2) by a straight line in a log-log diagram.

In the case of variable amplitude loading several SN-curves are needed. This will be performed exemplarily for the tension domain FF1 alone, see Fig. 3.19, by application of Kawai's model, however here by a mode-wise application, Step 3. Zero-crossing which needs interaction and micro-crack closing effects are bypassed in this simple case.
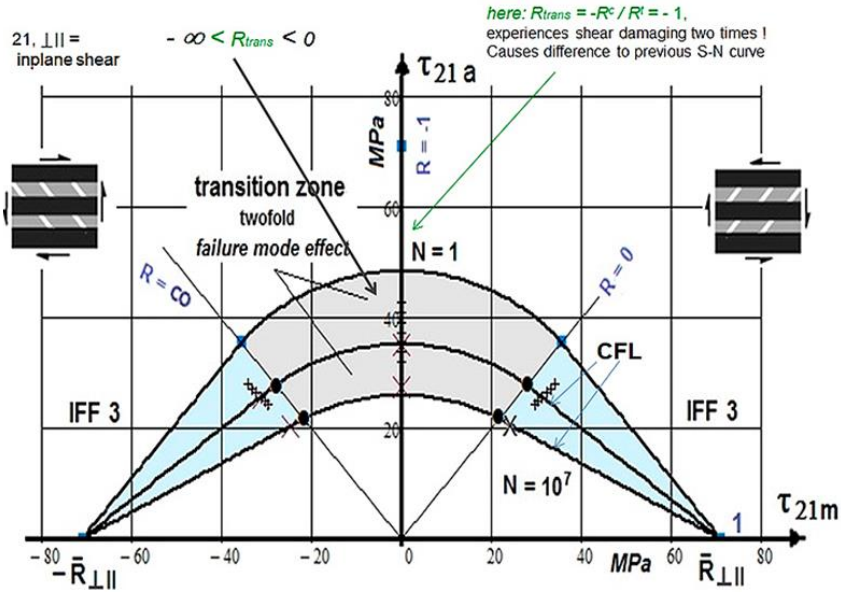
Fig. 3.15: IFF3 UD Haigh diagram, Display of a two-fold mode effect (a:= amplitude, m:= mean, N := number of fracture cycles, $\overline{R}$:= strength and R:= stress ratio $\sigma_{min}/\sigma_{max}$). Test data CF/EP, courtesy Hahne [14].
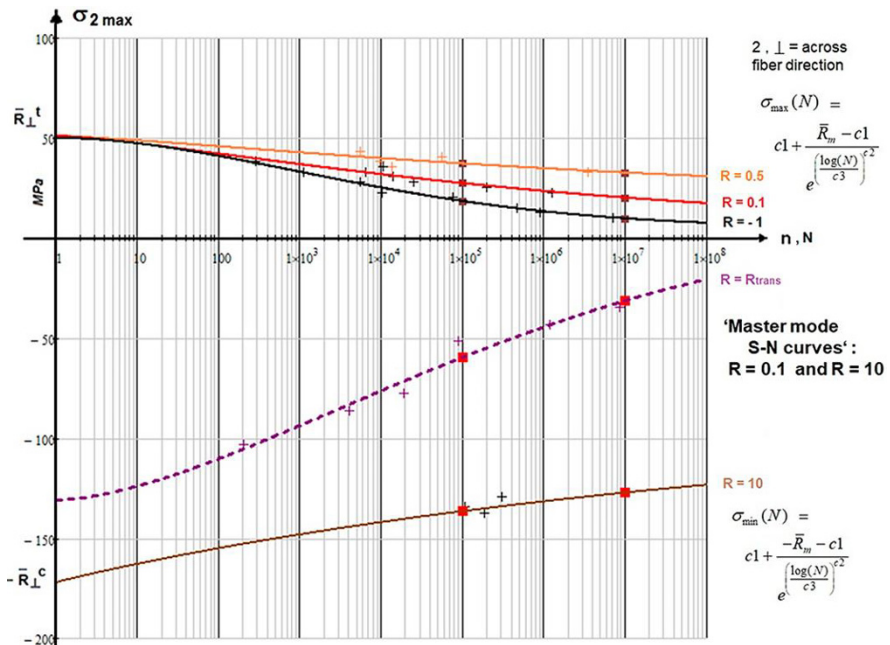
Fig. 3.16: Mapping of lin-log IFF1-IFF2-linked SN-curves [test data, courtesy C. Hahne].
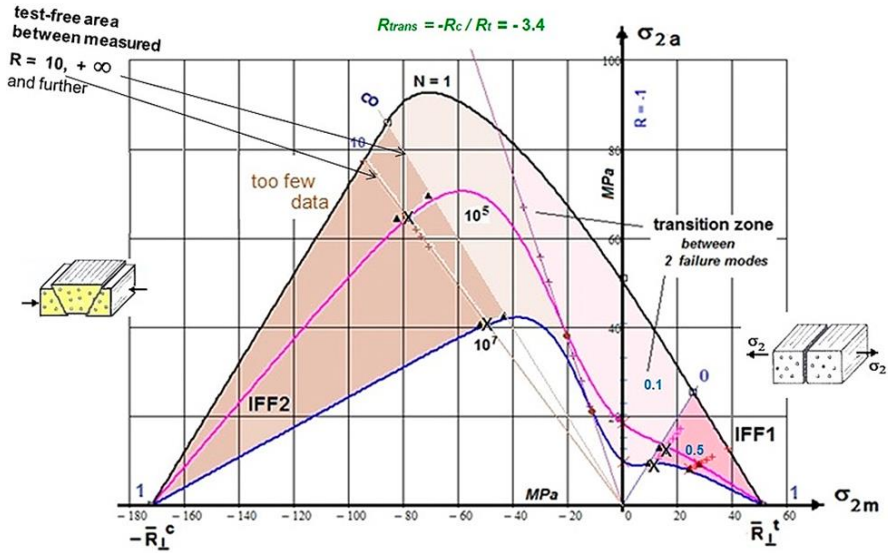
Fig. 3.17: IFF1- IFF2 UD Haigh diagram (similar for UD, lamella and concrete) displaying the failure mode domains, transition zone [test data, courtesy C. Hahne].
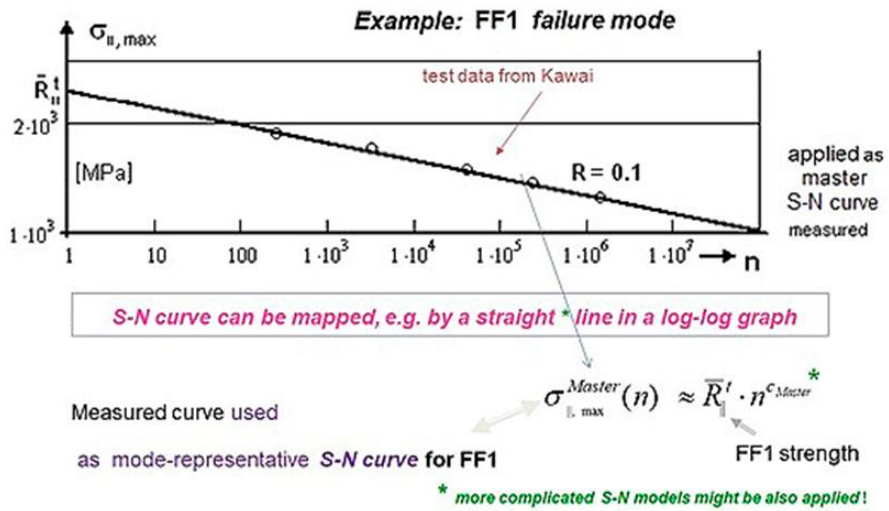
Fig. 3.18: Mapping of UD FF1 SN-data and mode-representative master SN-curve.
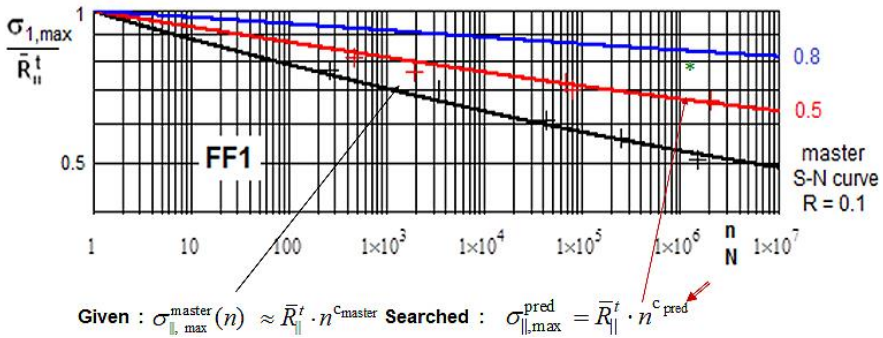
Fig. 3.19: Prediction of other needed FF1 SN curves from Master mode SN-curve and Cuntze's mode-dedicated Kawai model (Ψ curve).

The last step after the determination of the micro-damage portions is their accumulation. Statistical analyses have shown that the fatigue life estimation using the linear accumulation method of Palmgren-Miner tends to be too optimistic, see Fig. 3.20. However a satisfactory reason could not yet found. One explanation is the 'right use of the right SFC'. A more severe explanation is the loss of the loading sequence which is different for ductile and brittle materials. This is practically considered in design by the application of the Relative Miner with a $D_{\text{feasible}} < 100\%$.

Note 3.1. Dependent on the lay-up, the length of the individual fiber and on the chosen matrix fatigue resistance builds up. "Well-designed" (optimal fiber directions and minimum amount of fiber reinforcement for all load cases) high-performance UD lamina-composed laminates are less endangered, FF practically rules fatigue behavior and IFF less. Concerning the mode-representative Master SN-curves: These should
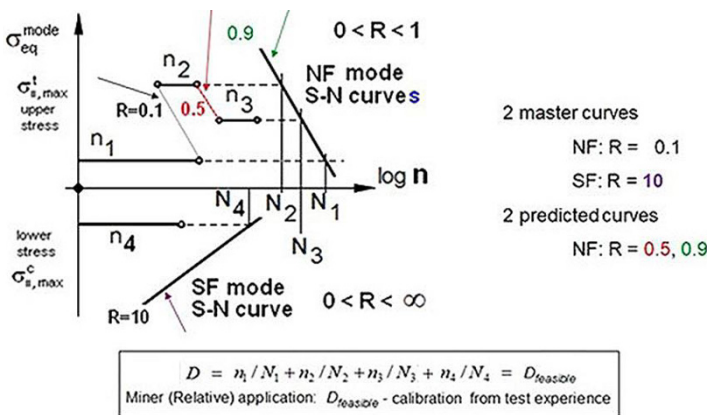
Fig. 3.20: Lifetime Prediction (estimation) Method. Schematic application by a simple example, 4 blocks, D_{feasible} from test experience derived).
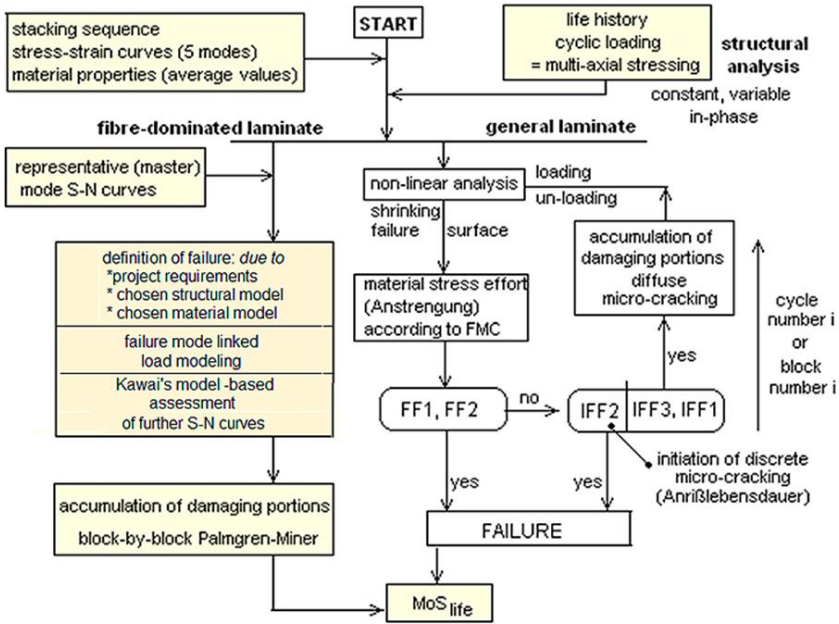
Fig. 3.21: Non-linear estimation of a laminate's fatigue life.

be derived from sub-laminate test specimen results, which capture the embedding (in-situ) effects.

Finally, Fig. 3.21 shall briefly give the fatigue life estimation procedure for the example laminate.

3.6 Conclusions on the Elaborated Novel Ideas

Novel simulation-driven product development shifts the role of physical testing to virtual testing. This requires High Fidelity concerning the material models used, such as the static strength criteria (SFC) and the lifetime estimation criteria. Based on his FMC ideas the author successfully derived static SFCs for a large variety of isotropic brittle structural materials such as plexiglass, porous concrete stone, cast iron, Normal Concrete, Ultra-High-Performance-Concrete, sandstone, mild steels, foam, monolithic ceramics and for the transversely-isotropic UD fiber-reinforced polymers Lamina (ply, lamella) and orthotropic Ceramic Fabrics. Available multi-axial fracture test data for above materials data were mapped to validate the SFCs. Practical experience showed, that for brittle materials these static SFCs are applicable to quantify the micro-damage portions under cyclic loading.

Basic idea in this paper was the generation of automatically deduced, numerically constructed Constant Fatigue Life (CFL)-curves using just one Master SN-curve for each mode, at minimum. The author was only able to realize this when he became aware of a general SN-curve modeling method, namely Kawai's method, which was physically better based than the predecessors used by the author. This method is used by the author in each mode domain separately, due to his strict failure mode thinking.

Challenging was the description of the R-beams in the transition zone between the tension and the compression mode domain, where a huge decay of the CFL-curve is faced from the compression domain down to the tension domain if the *strength ratio* is high. Therefore, a physically-based decay function has been applied to describe this. In addition, in contrast to the mode domain-linked SN-beams, the associated static origin point of a R-beam in the transition zone, which represents a mixed failure domain, was especially to determine to obtain a good transition beam description.

The application of the presented procedure was successful in several UD Haigh Diagrams and invites for more investigation. Hopefully, the author has posted to the industrial and the university reader a message which is understandable, concise and memorable to let them convincingly search for the necessary research funding.

With this document, the author attempts to redirect the thinking resulting from ductile material behavior in "Mean Stress Influence" into thinking with fracture modes for brittle materials. If the material is pretty ductile one faces one mode yielding and if pretty brittle one faces many modes of fracture.

Finally, a survey on the various Haigh diagram essentials shall be presented of isotropic and transversely-isotropic UD materials:

---

ductile **Isotropic material** brittle

$$R = R_{0.2}^t \qquad \{\sigma\} = (\sigma_I, \sigma_{II}, \sigma_{III})^T \qquad \{R\} = (R^t, R^c)^T \quad \text{with} \quad \mu$$

1 mode yielding 2 fracture modes

1 yield mode domain 2 fracture mode domains with transition zone

Increasing 'Mean stress influence' with increasing strength ratio number R^c/R^t

Interaction of *stresses* by Strength Failure Criteria (SFC)

1 SFC ('von Mises') yield failure mode 2 SFCs, fracture failure modes,

NF +SF

$$Eff^{\text{yield mode}} = \sigma_{eq}^{\text{von Mises}} \qquad \leftrightarrow \qquad Eff^{\text{fracture mode}} = \sigma_{eq}^{\text{frecture mode}}/R$$

Interaction of *failure modes* for determination of "Onset-of-failure" by an interaction equation

$$Eff = \sqrt{\frac{3J_2}{\overline{R}_{0.2}^t}} = \frac{\sigma_{eq}^{\text{von Mises}}}{\overline{R}_{0.2}^t} = 1 = 100\% \Leftrightarrow Eff = \sqrt[m]{(Eff^{\text{mode 1}})^m + (Eff^{\text{mode 2}})^m} = 1$$

1 Haigh Diagram is required.

Transversely-isotropic UD material, *brittle (no edge effect)*

$$\{\sigma\} = (\sigma_1, \sigma_2, \sigma_3, \tau_{23}, \tau_{31}, \tau_{21})^T \leftrightarrow \{R\} = (R_\parallel^t, R_\parallel^c, R_\perp^t, R_\perp^c, R_{\perp\parallel})^T \text{ with } \mu_{\perp\parallel}, \mu_{\perp\perp}$$

$$\{\sigma_{eq}^{mode}\} = (\sigma_{eq}^{\parallel\sigma}, \sigma_{eq}^{\parallel\tau}, \sigma_{eq}^{\perp\sigma}, \sigma_{eq}^{\perp\tau}, \sigma_{eq}^{\perp\parallel})^T \qquad 5 \text{ fracture modes}$$

FF1 : $Eff^{\parallel\sigma} = \breve{\sigma}_1 / \overline{R}_\parallel^t = \sigma_{eq}^{\parallel\sigma} / \overline{R}_\parallel^t$ with $\breve{\sigma}_1 \cong \varepsilon_1^t E_\parallel$ (matrix neglected)

FF2 : $Eff^{\parallel\tau} = -\breve{\sigma}_1 / \overline{R}_\parallel^c = \sigma_{eq}^{\parallel\sigma} / \overline{R}_\parallel^c$ with $\breve{\sigma}_1 \cong \varepsilon_1^c E_\parallel$

IFF1 : $Eff^{\perp\sigma} = [(\sigma_2 + \sigma_3) + \sqrt{\sigma_2^2 - \sigma_2\sigma_3 + \sigma_3^2 + 4\tau_{23}}]/2\overline{R}_\perp^t = \sigma_{eq}^{\perp\sigma} / \overline{R}_\perp^t$

IFF2 : $Eff^{\perp\tau} = [a_{\perp\perp}(\sigma_2 + \sigma_3) + b_{\perp\perp}\sqrt{\sigma_2^2 - \sigma_2\sigma_3 + \sigma_3^2 + 4\tau_{23}}]/2\overline{R}_\perp^c = \sigma_{eq}^{\perp\tau} / \overline{R}_\perp^c$

IFF3 : $Eff^{\perp\parallel} = \sqrt{2\mu_\perp I_{23-5} + \sqrt{b_{\perp\parallel} I_{23-5}^2 + 4\overline{R}_{\perp\parallel}^2 (\tau_{31}^2 + \tau_{21}^2)^2}}/(2\overline{R}_{\perp\parallel}^3) = \sigma_{eq\perp}/\overline{R}_\perp$

with $a_{\perp\perp} \cong \mu_{\perp\perp}/(1 - \mu_{\perp\perp}), b_{\perp\perp} = a_{\perp\perp} + 1, I_{23-3} = 2\sigma_2\tau_{21}^2 + 2\sigma_3\tau31^2 + 4\tau_{23}\tau_{31}\tau_{21}$

3 Haigh Diagrams required: FF1 with FF2, IFF1 with IFF2 and IFF3.

Consequently, the FMC-approach requires an interaction of all modes which reads

$$Eff = \sqrt[m]{(Eff^{mode\,1})^m + (Eff^{mode\,2})^m + \ldots} = 1 \quad \text{for} \quad Onset-of-Failure$$

Analogous to "von Mises", combining the acting stresses, above the equivalent stresses are applied. This requires future research work.

Mathematically maximum and minimum lamina failure stresses (strengths) replace the failure stresses of isotropic materials. The absolute UD-equivalent stress values replace the single UD-lamina stresses in order to capture a 3D stress state that includes the delamination-causing fatigue-relevant inter-laminar stresses. NF-linked-equivalent mode stresses are placed on the positive abscissa and SF-linked on the negative abscissa.

The transition from one layer to the next, when the fiber direction changes, is captured in the 2D- CLT analysis or a 3D-stress analysis and is thus considered via the computed micro-damage portions in the fatigue calculation.

References

[1] Cuntze R (2023) Life-Work Cuntze - a compilation. https://www.carbon-connected.de/Group/Prof.Ralf.Cuntze

[2] Cuntze R (1998) Application of 3D-strength criteria, based on the so-called "Failure Mode Concept", to multi-axial test data of sandwich foam, concrete, epoxy, CFRP-UD lamina, CMC-Fabric Lamina. In: ICCE/5, Las Vegas

[3] Cuntze R (2006) Failure Conditions for Isotropic Materials, Unidirectional Composites, Woven Fabrics - their Visualization and Linksn. https://www.ndt.net/article/cdcm2006/papers/cuntze.pdf

[4] Cuntze R (2017) Fracture Failure Bodies of Porous Concrete (foam-like), Normal Concrete, Ultra-High-Performance-Concrete and of the Lamella - generated on basis of Cuntze's Failure-Mode-Concept (FMC). In: NWC2017, NAFEMS, Stockholm

[5] Cuntze R (2007) Strength failure conditions of the various structural materials: Is there some common basis existing? SID Structural Integrity and Durability **3**(2):87–105

[6] Cuntze R (2015) Static & fatigue failure of UD-ply-laminated parts – a personal view and more. ESI Group, Composites Expert Seminar, Technical University Stuttgart, keynote presentation

[7] IASB (ed) (2022) Handbuch Strukturberechnung. Luftfahrttechnisches Handbuch, Ottobrunn

[8] VDI (2006) German guideline, sheet 3 "development of fibre-reinforced plastic components, analysis". Tech. rep., Beuth-Verlag

[9] Pyttel B, Schwerdt D, Berger C (2011) Very high cycle fatigue – is there a fatigue limit? International Journal of Fatigue **33**(1):49–58

[10] Tsai SW, Wu EM (1971) A general theory of strength for anisotropic materials. Journal of Composite Materials **5**(1):58–80

[11] Cuntze R (2019) Fachbegriffe für Kompositbauteile – Technical terms for composite parts. Springer Vieweg, Wiesbaden

[12] Cuntze R (2013) Comparison between experimental and theoretical results using cuntze's "failure mode concept" model for composites under triaxial loadings—part b of the second world-wide failure exercise. Journal of Composite Materials **47**(6-7):893–924

[13] Puck A (1996) Festigkeitsanalyse von Faser-Matrix-Laminaten - Modelle für die Praxis. Carl Hanser, München

[14] Hahne C (2015) Zur Festigkeitsbewertung von Strukturbauteilen aus Kohlenstofffaser-Kunststoff-Verbunden unter PKW-Betriebslasten. Dissertation, TU Darmstadt, Schriftenreihe Konstruktiver Leichtbau mit Faser-Kunststoff-Verbunden, Herausgeber Prof. Dr.-Ing Helmut Schürmann

[15] Kawai M (2004) A phenomenological model for off-axis fatigue behavior of unidirectional polymer matrix composites under different stress ratios. Composites Part A: Applied Science and Manufacturing **35**(7):955–963

Chapter 4

Experimental Evaluation and Phase-Field Model of Fracture Behavior of Alumina-Aluminium Graded Composite

Hossein Darban, Kamil Bochenek, Witold Węglewski, and Michał Basista

Abstract Multilayered metal-ceramic composites belong to the class of functionally graded materials with a step-wise gradient in material composition. These advanced structural materials can be tailored to meet design requirements. Aluminum-matrix composites are one of the most attractive metal-ceramic composites due to low specific weight, good thermal conductivity, enhanced specific strength, and low cost of the constituent materials. A comprehensive investigation of the fracture properties and mechanisms of layered aluminum-matrix composites is required to enhance their utilization in practical applications.

    This chapter is focused on experiments and modeling of fracture in functionally graded AlSi12-Al_2O_3 composites. Three-layer bulk disks with 10, 20, and 30% volume fractions of Al_2O_3 are manufactured through powder metallurgy. Single-edge notched samples (SEVNB) are prepared from the bulk material and tested under four-point bending. The fracture tests are simulated using the phase-field modeling of brittle fracture. In the phase-field models, individual layers are considered homogeneous linear elastic isotropic materials with effective properties estimated by the rule of mixture. The length scale parameter is calibrated by fitting the numerically determined fracture loads to the experimental data. The phase-field model is then used to investigate the impact of the stacking sequence on the load-displacement curves of the fracture specimens. It is revealed that the stacking sequence may significantly affect the load-displacement curves, including changes to the maximum load and post-peak response. The ability of the phase-field model to capture the crack arrestment, branching, and deflection in functionally graded layered materials is shown.

Hossein Darban · Kamil Bochenek · Witold Węglewski · Michał Basista
Institute of Fundamental Technological Research, Polish Academy of Sciences, Pawińskiego 5B, 02-106 Warsaw, Poland,
e-mail: hdarban@ippt.pan.pl, kboch@ippt.pan.pl, wweglew@ippt.pan.pl, mbasista@ippt.pan.pl

4.1 Introduction

Metal-ceramic composites are an innovative type of engineering materials that possess outstanding characteristics, such as high stiffness and excellent resistance to wear. These enhanced properties make them ideal for use under aggressive environments in various industries, including aerospace, automotive, and energy [1]. These composites can be produced using either liquid-state processes like spray deposition, stir casting, squeeze casting, and gas pressure-assisted infiltration, or solid-state processes like powder metallurgy, extrusion, and forging. A subgroup of metal-ceramic composites, called functionally graded materials, became popular recently due to their ability to deliver optimal performance for components under different service conditions [2].

In the past few decades, substantial research works have been conducted on functionally graded metal-ceramic composites (FGMs). Both experimental and modeling techniques have been used to better understand the mechanical behavior of such materials. This class of composite materials exhibits spatially varying properties, which can be either continuous or step-wise. The production of functionally graded metal-ceramic composites with continuous material gradation requires advanced manufacturing techniques. However, functionally graded metal-ceramic composites with a step-wise gradient can be produced using conventional manufacturing methods by employing a multilayered material architecture. For instance, different powder metallurgy techniques have been used in [3] to produce layered metal-ceramic composites. Layered metal-ceramic composites are highly attractive for various applications owing to their ability to meet specific design requirements. These composites are being used in industries such as aerospace, automotive, biomedical, and electronics. Many of these applications require materials with high resistance against fracture. Therefore, this is of the utmost importance to study fracture initiation and propagation in functionally graded metal-ceramic composites.

While numerous experimental studies have investigated the influence of microstructure on the properties of homogeneous metal-ceramic composites (e.g., [4]), experimental investigations on functionally graded metal-ceramic composites have been limited. One pioneering study focused on thermal fracture properties and was reported in [5]. In a more recent study [6], functionally graded samples with three layers were manufactured by hot pressing sintering of Al6061 and SiC with different reinforcement volume fractions. These samples were tested under tension at different temperatures to characterize their mechanical properties such as tensile strength, elongation, and fracture mechanisms [6]. Additionally, fatigue crack propagation in six-layered Al-SiC composites was studied in [7] using three-point bending specimens. In another study, the fracture behavior of five-layered metal-ceramic Ti-TiB$_2$ functionally graded samples was studied using three-point bending specimens [8]. Quasi-static and dynamic fracture tests were conducted on Ti-TiB functionally graded samples with seven layers under different temperatures in [9]. The Digital Image Correlation technique was used in [10, 11] to measure in-situ displacement and strain fields during the bending and tensile tests of layered Ti-TiB samples and to study the effect of the material gradation direction with respect to the crack axis on the fracture response of the samples.

Due to the challenges of conducting experiments on functionally graded metal-ceramic composites, analytical and numerical modeling of these materials are highly valued by the engineering community. An example is the XFEM modeling of fracture in layered Ti-TiB samples, as reported in [11]. However, the XFEM model and similar discrete methods in fracture mechanics are computationally expensive and require ad hoc criteria for crack initiation and propagation, making them less applicable to layered structures. To address these limitations, this chapter presents a phase-field model to simulate fracture in functionally graded AlSi12-Al$_2$O$_3$ composites.

The phase-field approach is a powerful computational tool for modeling crack initiation and propagation in materials. It mainly originated in seminal works [12, 13] in its current form. The formulation involves the regularization of the sharp crack by using an exponential regularization function defined by a length scale and a phase-field parameter. The phase-field parameter ranges from 1 to 0 in the fully broken and intact phases, respectively, and smoothly varies in a transition zone whose width depends on the length scale parameter. Consequently, the crack is smeared out over the domain, and the theoretical crack surface is represented by the diffuse crack topology. One of the key advantages of the phase-field modeling approach is that it does not require the geometrical description of the crack, allowing for the simulation of complex fracture mechanisms and their interactions, such as crack branching, arrestment, deflection, and coalescence, without the need for any ad hoc criteria. This makes the phase-field model a useful tool for studying fracture in a wide range of materials, including functionally graded and heterogeneous materials [14, 15].

Recent developments in phase-field modeling of fracture have focused on improving its accuracy and computational efficiency. For instance, a dynamic crack propagation model has been developed in [16] that simulates the time evolution of crack growth. Machine learning algorithms have also been used to enhance the accuracy and efficiency of the phase-field method by reducing the computational cost of simulations and optimizing model parameters [17]. Additionally, new hybrid models (e.g., [18]) combine the phase-field formulation with other modeling techniques, such as physics-informed neural networks, to further enhance the efficacy of the simulations.

Compared to conventional fracture modeling techniques, the phase-field model offers a more realistic description of crack initiation and propagation by considering the material degradation and damage accumulation that take place in the fracture process zone. The fracture process zone in metal-ceramic composites typically exhibits phenomena such as local plasticity in the metal matrix, fracture of the matrix and reinforcement, void and crack nucleation and coalescence, and interfacial debonding. The extent of material degradation in the phase-field model is determined by the length scale parameter, which plays a crucial role in accurately representing fracture behavior. The concept of the phase-field length scale has been a subject of debate in the literature. While some researchers view it as an arbitrary regularization parameter, others consider it a physically meaningful quantity that can be experimentally determined. Experimental determination of the length scale parameter in phase-field modeling can be approached in two ways. The first method involves global measures

and calibrates the length scale parameter by fitting numerically obtained fracture loads or load-displacement curves to experimental results. Another approach focuses on fitting local fields, such as the strain field, near the crack tip to experimental data. Additionally, a recent novel approach in [15] utilizes fractography analysis through scanning electron microscopy to measure the size of the process zone and use that value as the length scale parameter in the phase-field modeling.

The phase-field model enables the prediction of complex crack paths and their sensitivity to various factors, including loading conditions, material properties, and architecture. Unlike traditional fracture models that rely on pre-defined crack paths or assumptions about crack propagation, the phase-field model allows cracks to naturally evolve and propagate based on energy minimization. This predictive capability plays a vital role in optimizing material design and evaluating structural performance. By conducting simulations with different scenarios and varying parameters, scientists can assess the influence of factors such as material anisotropy, heterogeneity, and stress states on crack growth behavior. This valuable information empowers engineers and designers to make informed decisions regarding material selection, design modifications, and structural integrity assessments. In the context of this chapter, the phase-field model's predictive capability is employed to investigate the effects of stacking sequences on load-displacement curves and crack growth paths in multilayered metal-ceramic composites.

4.2 Experiment

4.2.1 Material Preparation

To fabricate the three-layered bulk disks, commercial powders of AlSi12 and Al_2O_3 were used. The mean particle size of AlSi12 was approximately 5 μm with a purity of 99.99%, while the average particle size of aluminum oxide was 10 μm with a purity of 99.99%. Powder mixtures with varying volume fractions of Al_2O_3 (10%, 20%, and 30%) were mixed using a planetary ball mill. To prevent contact of pure AlSi12 with oxygen during high-energy ball milling, the powders were closed in steel vials with ⌀10 mm balls in an environmental chamber partially filled with heptane. A rotational speed of 100 rpm, a ball-to-powder ratio of 5:1, and a mixing time of 5 h were used to obtain homogeneous powder mixtures. After milling, the powders were dried in a vacuum oven. Each layer was compacted individually using a uniaxial hand press to obtain a flat disc, which was then placed into a graphite mold before sintering. Preliminary tests showed that omitting this step resulted in an irregular interface between each layer. The hot pressing (HP) process was carried out in a vacuum atmosphere at a temperature of 600°C with a 5°C/min heating rate, a sintering pressure of 30 MPa, and a 180 min dwelling time. The final products are highly compacted discs with a relative density exceeding 99%, a diameter of approximately 33 mm, and a thickness of 4 mm.

A typical SEM image of the microstructure of the individual composite layer made of AlSi12+20%Al$_2$O$_3$ is shown in Fig. 4.1(a), while Fig. 4.1(b) shows a higher magnification image. The SEM images reveal that the Al formed almost a uniform continuous phase, likely due to the sintering temperature of 600°C being close to its melting temperature of approximately 660°C. The Si and Al$_2$O$_3$ powders are well dispersed within the Al phase, and the interfaces between different constituent phases appear smooth and regular in the images.

The SEM images in Fig. 4.2 show the microstructure of the produced functionally graded composite in the region between layers with different reinforcement volume fractions. The region close to the layers with 10% and 20% ceramic content is shown in Fig. 4.2(a), while Fig. 4.2(b) depicts the region between the layers with 20% and 30% ceramic. The difference in reinforcement volume fraction between the layers is visible in the images. The matrix phases between every two layers appear continuous, while the transition of the reinforcement volume fraction between the layers is sharp. These observations suggest that the functionally graded composite does not have any imperfect interface between the layers with different reinforcement

(a)   (b)
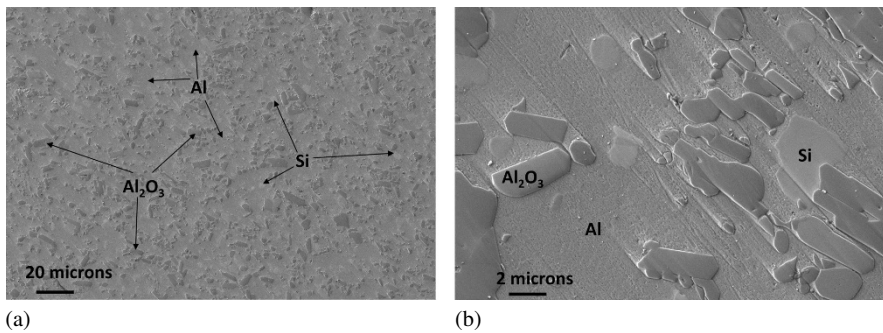
Fig. 4.1: (a) SEM image of the microstructure of the individual composite layer AlSi12-20%Al$_2$O$_3$. (b) The microstructure with a higher magnification.

(a)   (b)
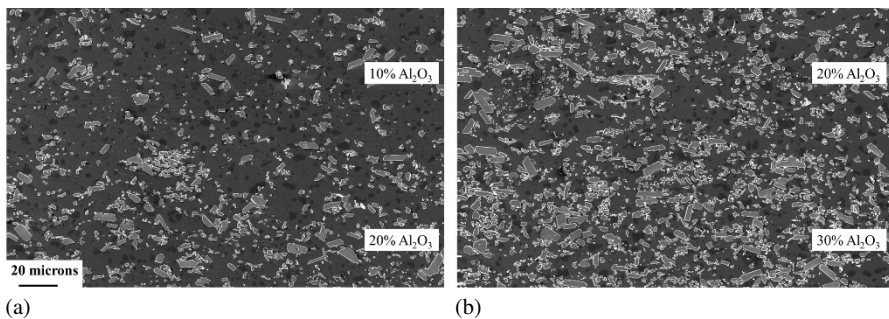
Fig. 4.2: SEM image of the microstructure at the region between the layers with (a) 20% and 10%, and (b) 30% and 20% of Al$_2$O$_3$ reinforcement volume fraction.

volume fractions, thereby avoiding any possible damage inherent in layered systems, such as delamination.

4.2.2 Fracture Tests

Initially, prismatic specimens are prepared from sintered layered disks by cutting them to, approximately, a length of 25 mm, an in-plane thickness of 4 mm, and an out-of-plane width of 3 mm. The cutting procedure is conducted in such a way that the material gradation occurs along the in-plane thickness of specimens (see Fig. 4.3). The specimens are then notched within the bottom layer made of $AlSi12+30\%Al_2O_3$

(a)

(b)

(c)
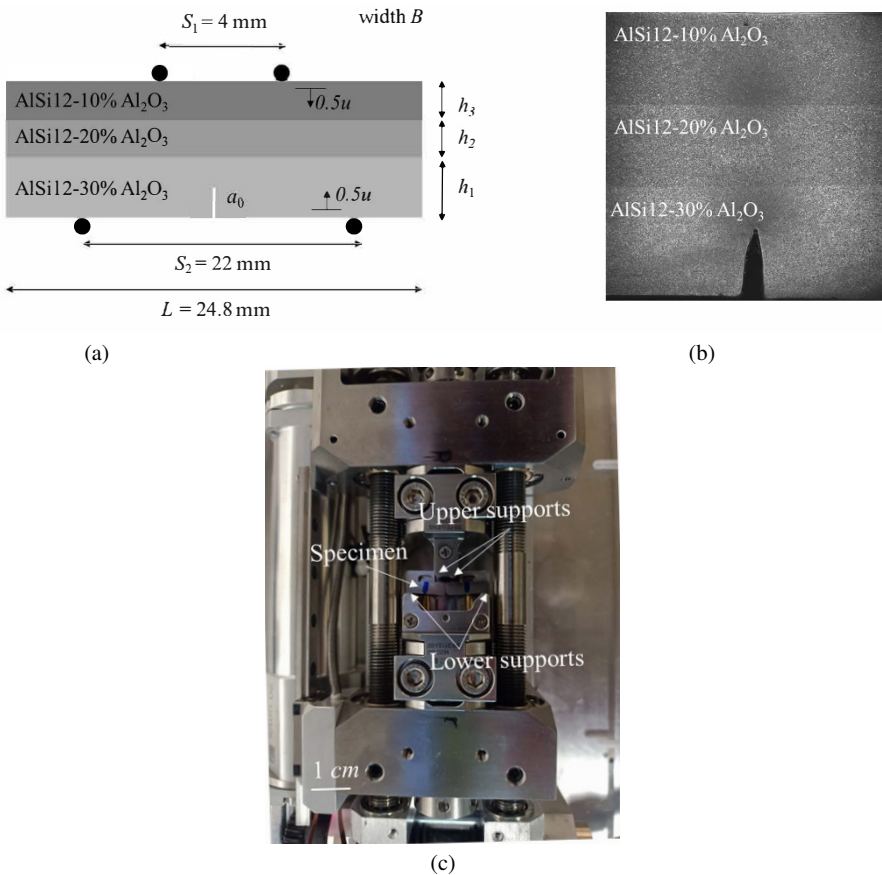
Fig. 4.3: (a) The geometry and stacking sequence of the fracture specimens (the figure is not scaled), and (b) the SEM image of the region near the notch. The three layers of the specimen with different reinforcement volume fractions are distinguishable by their colors. (c) The fracture specimen under the four-point bending testing device.

composite using wire cutting and a sharp crack is induced at the notch tip using a razor blade coated with diamond paste. To ensure smooth and even surfaces for testing, the side surfaces of each specimen are subsequently ground and polished using 1µm diamond paste. The geometry of the final fracture specimens is depicted in Fig. 4.3(a), and the dimensions are provided in Table 4.1. Three different fracture samples are produced, all of which have the same stacking sequence as depicted in Fig. 4.3. However, these samples differed in their layer thicknesses, initial crack length, and crack tip radius, as specified in Table 4.1. A close-up SEM image of the region near the notch is shown in Fig. 4.3(b). In this image, the layers with different reinforcement volume fractions are distinguishable by different brightness.

The configuration of the experimental set-up is illustrated in Fig. 4.3(c). The fracture samples are tested in-situ in four-point bending experiments using a miniaturized bending modulus operating under SEM. The support spans, S_1 and S_2, depicted in Fig. 4.3(a), are 4 mm and 22 mm, respectively. During the tests, a displacement-controlled load is applied to the samples by moving both upper and lower supports at a constant rate of 1 micron/second. The crack initiation and propagation are monitored by SEM throughout the experiments. In each test, the maximum (fracture) load, F_{Max}, associated with the initiation of crack propagation is recorded. The recorded maximum load values for all conducted tests are listed in Table 4.1.

4.3 Phase-Field Modeling

The phase-field modeling is a continuum mechanics-based approach which tackles the fracture phenomenon as an energy minimization problem. This formulation eliminates the need for ad hoc criteria for crack initiation and propagation, which are always required when discrete approaches are used. Therefore, the phase-field modeling can readily capture complex fracture events as natural outcomes of the formulation. In the following, the phase-field approach used in this work to model the macroscale fracture in functionally graded AlSi12-Al$_2$O$_3$ composites is briefly introduced and the solution technique is described. Then, after a convergence study, the model is used to simulate the fracture tests on the three-layer single-edge V-notched beams under four-point bending. Lastly, the model is used to investigate the effect of the stacking sequence on the load-displacement response and the crack growth path of the specimens.

Table 4.1: The geometry and fracture load of the fracture specimens.

Sample No.	h_1 [mm]	h_2 [mm]	h_3 [mm]	B [mm]	a_0 [mm]	Crack tip radius [mm]	F_{Max} [N]
1	1.651	0.917	1.360	2.94	1.103	0.00893	203
2	1.989	1.028	1.102	2.78	0.858	0.01451	230
3	1.798	0.985	1.182	2.84	0.880	0.01350	253

4.3.1 Formulation

The general idea of the phase-field modeling of fracture is to introduce an additional scalar parameter d that is namely the phase-field parameter, so that it takes the value of zero at the undamaged portions of the domain and 1 at the fully broken parts. The transition of the phase-field parameter between these two regions is continuous and usually assumed to have an exponential form in terms of a length scale parameter l_c. The width of the transition zone across which the phase-field parameter takes a non-negligible value depends on the length scale parameter. A higher value of the length scale parameter increases the width of the transition zone, resembling a wider fracture process zone in the vicinity of the crack. Using the phase-field modeling, a sharp crack Γ that is defined over a surface can be approximated by the diffuse crack topology defined through a volumetric integral. In this work, the AlSi12-Al$_2$O$_3$ composite with a sharp crack in a domain Ω (see Fig. 4.4(a)) is assumed to be a homogeneous isotropic linear elastic material with effective elastic properties and a diffuse crack topology, as shown in Fig. 4.4(b).

Therefore, the sharp crack is approximated by the following integral [12, 13]:

$$\Gamma \approx \Gamma_{l_c}(d) = \int_{\Omega} \left(\frac{1}{2l_c} d^2 + \frac{l_c}{2} |\nabla d|^2 \right) d\Omega \qquad (4.1)$$

Using the crack topology approximation above, the crack initiation and propagation can be defined by solving the resulting energy minimization problem through the variational approach and the finite element technique. As the material undergoes damage, its local stiffness gradually decreases. Therefore, the calculation of the strain energy in the finite element implementation must take into account not only the strains but also the phase-field parameter. Hence, the governing equations of the
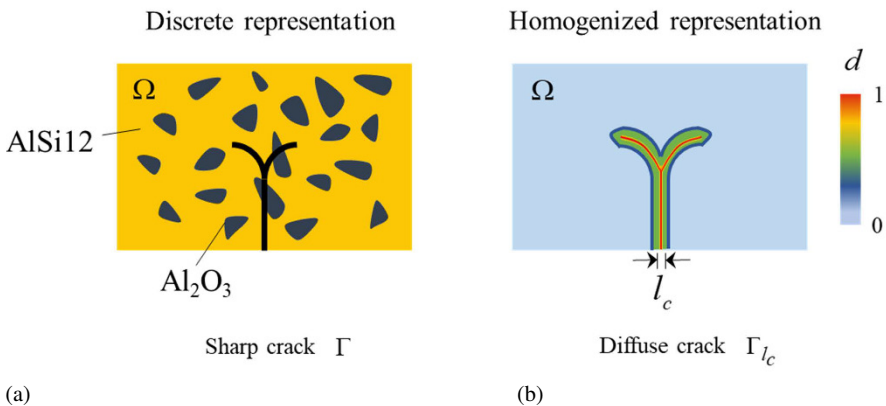
Fig. 4.4: (a) Discrete representation of the AlSi12-Al$_2$O$_3$ composite with a sharp crack within the domain and (b) its homogenized representation with a diffuse crack.

phase-field modeling of fracture are coupled. The degradation in strain energy should only affect the positive portion, which corresponds to tension, as it is assumed that no cracking occurs in compression. For brittle fracture, the degradation function is usually a quadratic function given by $(1 - d^2)$.

Two main techniques, namely, monolithic and staggered, have been developed to solve the coupled mechanical/phase-field equations. The non-convexity of the total potential energy functional can cause convergence and robustness issues in the monolithic scheme, particularly for unstable crack growth problems. Staggered schemes, based on alternating minimization, are more feasible and use a local history field to weakly couple the phase-field and elasticity problems as two quasi-independent minimization procedures. The implicit staggered finite element solution scheme developed in [16, 19] is used in this work to simulate macroscale fracture in functionally graded AlSi12-Al$_2$O$_3$ composite beams. Mathematical details of the staggered scheme can be found in [16, 19]. The solution depends on the mesh size and loading rate, and small mesh size and load increments are necessary to reach converged solutions, especially for unstable crack growth. Therefore, before comparing the numerical results with the experimental data, a sensitivity analysis is first conducted in the next section to ensure that convergence in the numerical results is reached.

4.3.2 Sensitivity Analysis

The numerical model used to simulate the fracture specimens is shown in Fig. 4.5. The simulations are conducted under plane strain conditions. Each layer is modeled as an isotropic homogeneous linear elastic material with effective properties calculated by the rule of mixture and given in Table 4.2. The fracture properties of the layers
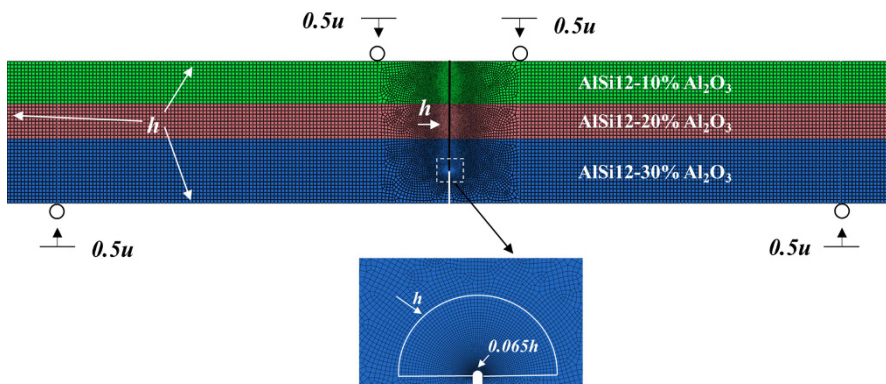
Fig. 4.5: Four-node quadrilateral elements used to mesh the three-layer V-notched specimen under four-point bending. The average mesh size is h. The mesh size close to the crack tip is refined to approximately 0.065 h. Different mesh colors indicate layers with different reinforcement volume fractions.

Table 4.2: The effective elastic moduli and fracture properties of the composite layers. Young's modulus and Poisson's ratio are determined by the rule of mixture, whereas the fracture toughness is evaluated from the SEVNB experiment. The critical energy release rate is calculated from the fracture toughness and effective elastic properties using $G_c = (1 - v^2)K_{IC}/E$.

Material	Young's modulus [GPa]	Poisson's ratio	K_{IC} [MPa$\sqrt{m}$]	G_c [N/mm]
AlSi12	75 [20–22]	0.35 [20–22]	-	-
Al$_2$O$_3$	383 [23]	0.2 [24]	-	-
AlSi12-10% Al$_2$O$_3$	105.8	0.292	12.40	1.3298
AlSi12-20% Al$_2$O$_3$	136.6	0.262	9.26	0.5848
AlSi12-30% Al$_2$O$_3$	167.4	0.243	8.75	0.4303

are determined experimentally and also given in Table 4.2.

Four-node quadrilateral elements are used to mesh the domain, as shown in Fig. 4.5. Near the crack tip the mesh is finer than in the rest of the domain to accurately capture the crack tip stress fields with high gradients. The mesh size along the expected crack growth path (straight line ahead of the initial crack axis) is always less than half of the length scale. This is the mesh size requirement to model the crack growth with reasonable accuracy using phase-field modeling [12].

Sample no. 1 (see Table 4.1) is used to conduct a convergence study on the mesh size and loading rate. The load-displacement curve of sample no. 1 determined by the phase-field model is shown in Fig. 4.6 for different mesh sizes h (see Fig. 4.5). In the numerical simulations, the length scale parameter of all layers with different reinforcement volume fractions is taken equal to 100 microns. The study in [15] showed that the volume fraction of the Al$_2$O$_3$ reinforcement has a negligible effect on the length scale parameter for the phase field modeling of global fracture in similar metal-ceramic composites.

The simulations are stopped before the advancement of the crack into the second layer (the post-peak response of the fracture samples will be studied in detail in the
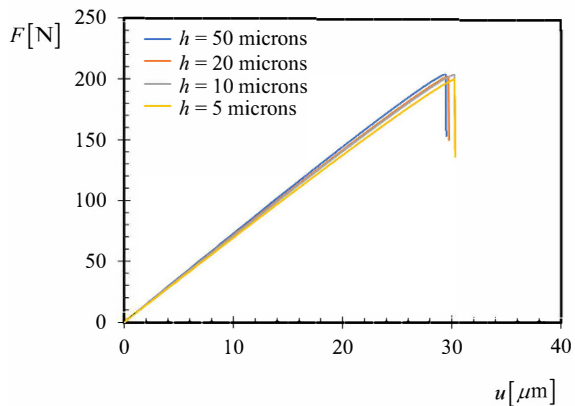
Fig. 4.6 Load-displacement curve of sample no. 1 determined by the phase-field model for $l_c = 100$ microns. Results are presented for different mesh sizes h (see Fig. 4.5)

following section, see Fig. 4.7 for instance). As can be seen in Fig. 4.6, reducing the mesh size from 50 to 5 microns reduces the global stiffness of the load-displacement curve. The displacement at the onset of crack propagation increases with decreasing mesh size from 50 to 10 microns, but does not change when the mesh size is further refined to 5 microns. To avoid a problem with excessive computational time, the simulations in the rest of the chapter are done using the mesh size $h = 10$ microns.

Since the solution technique used in this work is based on a staggered finite element formulation, the effect of the load increment on the results of the phase-field modeling of sample no. 1 is also investigated. The numerically obtained load-displacement curves of sample no. 1 are shown in Fig. 4.7(a) for different loading rates and $l_c = 100$ microns. As can be seen in the figure, the load-displacement response of the three-layer SEVNB specimen has five different regions:

1. A linear response from the initial configuration to point A where the fracture load is reached.
2. A nonlinear post-peak response from A to B where the crack advances into the first layer and the load drops suddenly. At point B, the crack penetrates the second layer without any obvious crack arrestment. However, due to the different elastic and fracture properties of the layers, the load-displacement curve is characterized by a local irregularity at point B.
3. A nonlinear response from B to C corresponding to the crack advancement within the second layer and further reduction of the load.
4. A stiffening behavior from C to D due to the crack arrest at the interface between the second and third layers due to the higher fracture energy of the third layer.
5. The crack propagation within the third layer results in a further decrease in the load from point D to E.
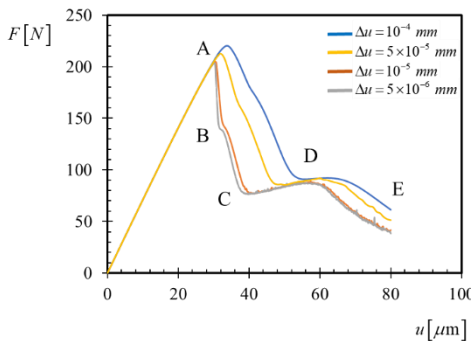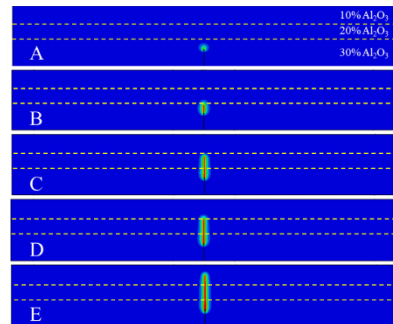
(a)   (b)

Fig. 4.7: (a) Load-displacement curve of sample no. 1 determined by the phase-field model for $l_c = 100$ microns. Results are presented for different loading rates. (b) Exemplary crack growth path corresponding to different regions of the load-displacement curve. The dashed lines indicate the interface between different layers.

When the loading rate is high, e.g., $\Delta u = 10^{-4}$ mm, the fracture load and the corresponding fracture displacement are higher and the post-peak behavior is smoother. In this case, the effect of the crack penetration into the second layer (point B in the figure) on the load-displacement response is less noticeable. The fracture load and the corresponding fracture displacement decrease as the loading rate decreases so that they become almost identical for the loading rates equal to 10^{-5} and 5×10^{-6} mm. In addition, the post-peak responses of the sample corresponding to these two loading rates are only slightly different. Therefore, considering the computational time, the phase-field simulations in the remaining parts of the chapter are conducted using a loading rate equal to 5×10^{-6} mm, except otherwise stated. Using lower loading rates is not necessary since they improve the accuracy of the results negligibly while considerably increasing the computational time.

4.3.3 Modeling Experiments

The phase-field model is used to predict the fracture loads of the three specimens. Based on the conducted convergence study in the previous section, the average mesh size (see h in Fig. 4.5) and the loading rate are, respectively, 10 microns and 5×10^{-6} mm. The geometry and the experimentally measured fracture loads of these specimens are given in Table 4.1. In the modeling, each layer is considered homogeneous and isotropic with linear elastic properties given in Table 4.2. The experimentally determined fracture energies of each layer are also given in Table 4.2. The only remaining modeling parameter is the length scale parameter which will be calibrated so that the numerical fracture loads will be in reasonable agreement with the experimental data. The fracture loads predicted by the phase-field model for the three specimens are presented in Table 4.3 on varying the length scale parameter.

To choose the best length scale parameter, the average difference between the experimental and numerical results is considered. The average difference for the length scale parameter equal to 500, 100, and 25 microns are, respectively, equal to 15, 14, and 16 N. Generally, the fracture loads are not highly dependent on the length scale value for these three cases. Here, the length scale equal to 100 microns, which

Table 4.3: The phase-field fracture loads for different length scale parameters and the experimental results.

Sample no.	F_{Max} [N] Experiment	F_{Max} [N] $l_c = 500\mu\mathrm{m}$	F_{Max} [N] $l_c = 100\mu\mathrm{m}$	F_{Max} [N] $l_c = 25\mu\mathrm{m}$
1	203	208	203	207
2	230	247	252	259
3	253	231	234	239

results in the minimum average difference was considered a reasonable choice for modeling the three-layer fracture specimens.

4.3.4 Effect of Stacking Sequence

Having successfully verified the phase-field model, this section employs it to investigate the effect of stacking sequence on the load-displacement response of cracked specimens with three layers. The geometry of sample no. 1, as specified in Table 4.1, is considered for this purpose. A total of 27 stacking sequences will be studied by varying the reinforcement volume fractions of the layers at 10%, 20%, and 30%. The length scale parameter is fixed at 100 microns, and Table 4.2 presents the fracture energies of the layers. The load-displacement curves in Fig. 4.8 refer to the cases where the crack is located in the bottom layer with $30\%Al_2O_3$.

Nine different cases were examined by varying the reinforcement volume fractions of the other two layers. All the cases exhibited an initial linear elastic response. The specimen made entirely of $AlSi12-30\%Al_2O_3$ composite exhibited the stiffest initial response due to its highest Young's modulus value (Table 4.2). It has been demonstrated in [15] through phase-field modeling that increasing the bending stiffness of the specimen results in higher fracture loads. This explains why the specimen with the stacking sequence of 30/30/30 exhibits the highest fracture load. It can be understood from the figure that the fracture load is generally controlled by the bending stiffness of the specimen. In other words, specimens with higher bending stiffness have higher fracture loads.

The stacking sequence has a significant impact on the post-peak response of the specimens. When an $AlSi12-10\%Al_2O_3$ composite layer is present, a stiffening phase is observed in the load-displacement curves in which the crack arrests at the

Fig. 4.8 Numerical load-displacement curves obtained for a three-layer specimen with the same geometry as sample no.1, but with different stacking sequences. The legend shows the percentage volume fraction of the ceramic in each layer, starting from the bottom layer, as illustrated in the inset on the left-hand side of the figure. The bottom layer of all the specimens is reinforced with 30% ceramic. The phase-field length scale parameter is $l_c = 100\mu m$ and the fracture energies of layers are listed in Table 4.2.
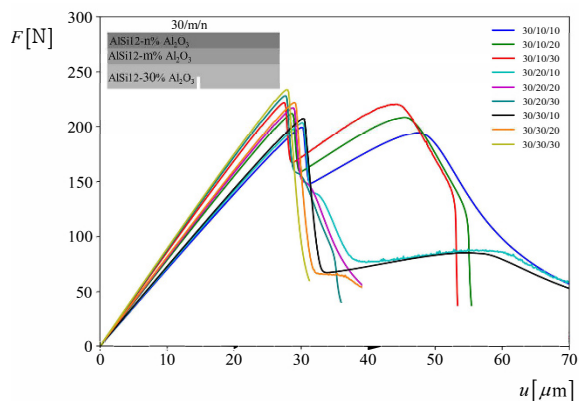
interface before penetrating the layer. This behavior is more pronounced when the AlSi12-10%Al$_2$O$_3$ layer is located between the other two layers. In this case, the load-displacement curve has two local maximum loads corresponding to (i) the onset of the propagation of the initial crack in the bottom layer, and (ii) the initiation of the crack propagation into the second layer after the crack arrestment. The values of these two local maximum loads are close to each other. In other words, the AlSi12-10%Al$_2$O$_3$ layer acts as a shield for crack propagation and prevents the specimen from sudden catastrophic fracture. This understanding might be important for potential applications of such layered structure, e.g. in braking disks in vehicles. If the first layer is in contact with the rotor cracks, the stronger interior layers can prevent catastrophic failure of the braking system, allowing for partial operation and giving the driver time to stop the vehicle, thus avoiding fatal accidents.

For the 30/10/30 and 30/10/20 stacking sequences, crack propagation accelerates upon reaching the third layer, which has lower fracture energy than the second layer. This acceleration is reflected in the load-displacement response by a sudden drop at the end of the curve. However, the crack is not arrested when it reaches the interface between the AlSi12-30%Al$_2$O$_3$ and AlSi12-20%Al$_2$O$_3$ layers.

The load-displacement curves of the specimens with the bottom layer containing the initial crack made of AlSi12-20%Al$_2$O$_3$ and AlSi12-10%Al$_2$O$_3$ are shown in Fig. 4.9(a) and (b). As also observed from Fig. 4.8, the specimens with the stiffest stacking sequences, namely 20/30/30 and 10/30/30, exhibit the highest fracture loads in Fig. 4.9.

In the specimens with the AlSi12-20%Al$_2$O$_3$ bottom layer (Fig. 4.9(a)), crack arrest occurs whenever an AlSi12-10%Al$_2$O$_3$ layer is present in the specimen. However, if the bottom layer containing the initial crack is made of AlSi12-10%AAl$_2$O$_3$ (Fig. 4.9(b)), crack arrest only occurs for the specimen with the stacking sequence of 10/30/10. For the remaining stacking sequences, the post-peak response is characterized by a sudden drop in load.

Comparing the load-displacement curves in Figs. 4.8 and 4.9 reveals that the fracture load is highly dependent on the fracture energy of the bottom layer where the crack is located. As the reinforcement volume fraction increases, the fracture energy of the AlSi12-Al$_2$O$_3$ composite decreases (see Table 4.2). Therefore, the specimens with an AlSi12-10%Al$_2$O$_3$ bottom layer exhibit the highest fracture loads. The post-peak response of the specimens depends greatly on the stacking sequence. This variety in the post-peak response of the layered composites allows for the material architecture to be tailored for various design purposes.

The functionally graded composite materials in the form of layered structures have the potential to be used in the construction of modern braking disks. The design of a layered braking disk includes optimizing the stacking sequence to enhance the capability of the disk to resist higher loads and dissipate heat generated during use due to friction. To improve fracture toughness, the stacking sequence may be adjusted, as considered above, to create a stronger composite structure against crack initiation and propagation. On the other hand, to improve heat dissipation, the stacking sequence may be also tailored to better facilitate heat transfer between layers and to the surrounding environment. Therefore, there is a possibility for designing a

(a)

(b)
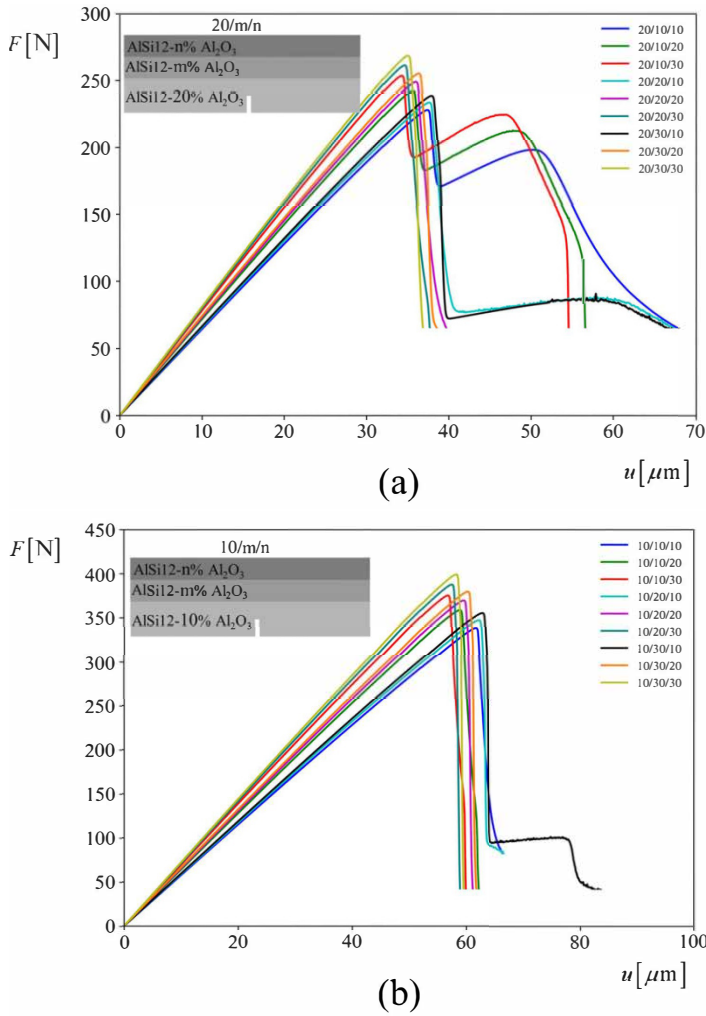
Fig. 4.9: The numerical load-displacement curves obtained for a three-layer specimen with the same geometry as sample no. 1, but with different stacking sequences. The legend shows the percentage volume fraction of the ceramic in each layer, starting from the bottom layer, as illustrated in the inset on the left-hand side of the figure. The bottom layer of all the specimens is reinforced with (a) 20% and (b) 10% ceramic. The phase-field length scale parameter used is $l_c = 100$ microns and the fracture energies of layers are listed in Table 4.2.

modern braking disk, by carefully balancing these two factors, which is both strong and effective at dissipating heat. These two features are crucial for preserving reliable braking performance over extended periods of use.

4.3.5 Crack Branching

It has been observed in the previous section that crack arrestment occurs before the crack penetration into a layer with higher fracture energy. This observation implies that when the difference between the fracture energies of two layers is significant, crack branching is likely to occur so that two new crack tips will be created and propagated along the interface between the layers. The propagation of the two new crack tips can lead to the crack deflection into the stronger layer. To evaluate the ability of the phase-field model to capture the crack branching and crack deflection in the functionally graded metal-ceramic composites, the three-layer sample with AlSi12-30%Al$_2$O$_3$ bottom layer is considered. The other two layers are considered to be made of pure AlSi12 alloy with the elastic properties given in Table 4.2. The critical energy release rate of pure AlSi12 is considered to be equal to 2.7 N/mm. Note that the assumed value of 2.7 N/mm does not accurately represent the energy release rate of AlSi12. Instead, it is selected only for illustrative purposes, to create a significant enough difference in energy release rates between the layers to induce crack branching. The length scale parameter is assumed to be 100 microns for all three layers and the loading rate is 1.25×10^{-4} mm. The load-displacement curve predicted by the phase-field model is illustrated in Fig. 4.10.

The curve can be divided into different phases, each with particular characteristics. The initial phase of the curve, from the start of the modeling to point A, represents the initial linear response of the structure before the crack propagation. Once the load reaches the first critical value at point A, the initial crack located at the AlSi12-30%Al$_2$O$_3$ bottom layer begins to propagate. From point A to B the initial crack propagates within the bottom layer until it reaches the interface between the AlSi12-30%Al$_2$O$_3$ and AlSi12 layers. At this interface, the crack is arrested due to the significant difference between the fracture energies of the two layers, causing the load to increase again. Once the crack driving force becomes sufficient for creating two crack tips, the crack branches. An exemplary snapshot of the crack branching is shown at point C. The two new cracks propagate along the interface until point D, where the left crack tip deflects into the second layer. After this point, the deflected crack propagates into the second layer, causing a sharp drop in the applied load. Point E depicts a snapshot of the deflected crack reaching the third layer. Note that because of the unstructured and asymmetric mesh pattern as depicted in Fig. 4.5, the crack deflection into the second layer only occurs at the left crack tip rather than both.
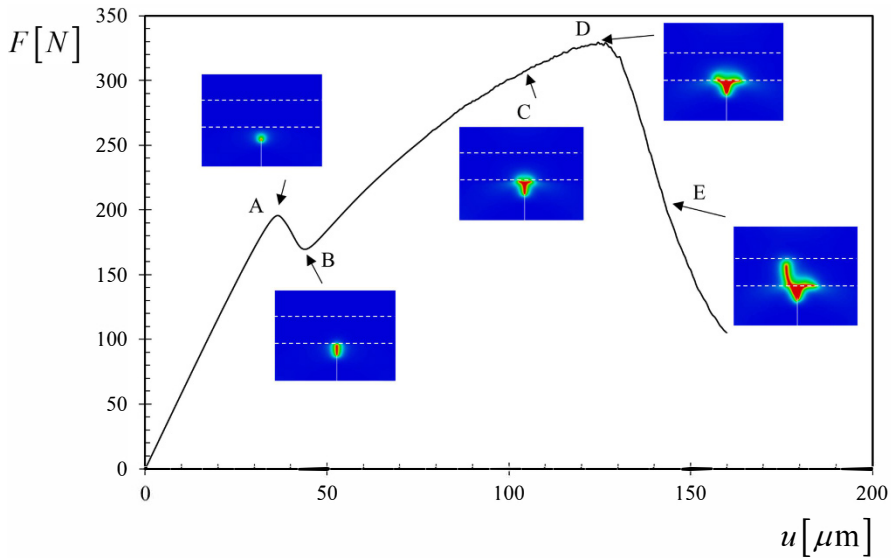
Fig. 4.10: The numerical load-displacement curve obtained for a three-layer sample with AlSi12-30%Al$_2$O$_3$ bottom layer. The other two layers are made of pure AlSi12 with the elastic properties given in Table 4.2. The critical energy release rate of pure AlSi12 is considered to be equal to 2.7 N/mm. The phase-field length scale parameter used is $l_c = 100$ microns and the fracture energy of the AlSi12-30%Al$_2$O$_3$ layer is listed in Table 4.2. The loading rate is 1.25×10^{-4} mm. The dashed lines indicate the interface between different layers.

4.4 Conclusion and Future Work

The fracture behavior of the functionally graded AlSi12-Al$_2$O$_3$ composites in the form of three-layered single-edge notched beams has been studied using the four-point bending SEVNB test and the phase-field modeling of brittle fracture. The functionally graded bulk composite with layers reinforced with 10, 20, and 30% Al$_2$O$_3$ has been manufactured through the hot press sintering technique. The fracture tests have been conducted on three different samples with the same stacking sequence and maximum loads sustained by each sample have been recorded. The phase-field modeling of brittle fracture has been applied to simulate the experiments. In the numerical modeling, the microstructure of the composites has not been explicitly simulated. Instead, each layer of the samples is modeled as a homogeneous linear elastic isotropic material with effective properties determined by the rule of mixture. In this manner, the model captures only global fracture characteristics, such as the macroscale load-displacement curve. The convergence study has been conducted to determine sufficiently small mesh size and loading rate. The length scale parameter of the phase-field models has been identified by fitting the numerically predicted maximum loads to the experimental data.

The phase-field model has been applied to study the effect of the stacking sequence on the load-displacement curves of the samples. It has been shown that the stacking sequence may greatly affect the load-displacement curve, particularly, the post-peak response. It has been found that when the crack tip reaches a layer with high fracture energy (for the considered composites, the layer made of AlSi12-10%Al$_2$O$_3$), a crack arrest occurs. In this case, the load-displacement curve is characterized by two local maximum loads:

(i)   the load corresponding to the onset of the propagation of the initial crack, and
(ii) the load corresponding to the onset of the crack propagation into the AlSi12-10%Al$_2$O$_3$ layer.

It has been discussed that this toughening mechanism might be beneficial for the design of modern mechanical elements such as braking disks. It has been shown that if the difference between the fracture energy of two adjacent layers is significant, the crack arrest might be followed by crack branching resulting in the generation of two new crack tips and their propagation along the interface between the layers.

In future work, plastic deformations will be taken into account. For this purpose, the effective elastoplastic properties of composites will be determined experimentally, as well as numerically using FE-based homogenization of the real microstructure. Furthermore, in addition to comparing fracture loads, the entire load-displacement curves obtained by the Digital Image Correlation technique will be compared with the load-displacement curves predicted by the phase-field model. This will enable the validation of the numerical predictions of complex fracture mechanisms, such as crack arrestment, branching, and deflection.

References

[1] Rosso M (2006) Ceramic and metal matrix composites: Routes and properties. Journal of Materials Processing Technology **175**(1):364–375, Achievements in Mechanical & Materials Engineering
[2] Zygmuntowicz J, Winkler H, Wachowski M, Piotrkiewicz P, Kaszuwara W (2021) Novel functionally gradient composites Al$_2$O$_3$-Cu-Mo obtained via centrifugal slip casting. Metallurgical and Materials Transactions A **52**(8):3628–3646
[3] Slawik T, Bergner A, Puschmann R, Franke P, Raethel J, Behnisch T, Scholl R, Berger LM, Moritz T, Zelm R, Gude M, Michaelis A, Beyer E, Leyens C, Großmann H, Kieback B (2014) Metal–ceramic layered materials and composites manufactured using powder techniques. Advanced Engineering Materials **16**(10):1293–1302

[4] Travitzky NA (2001) Effect of metal volume fraction on the mechanical properties of alumina/aluminum composites. Journal of Materials Science **36**(18):4459–4463

[5] Kawasaki A, Watanabe R (2002) Thermal fracture behavior of metal/ceramic functionally graded materials. Engineering Fracture Mechanics **69**(14):1713–1728

[6] Wu T, Hu Y, Wang S, Leng Y, Wang M (2020) Effect of SiC content and interlayer difference on microstructural characterization and mechanical properties of functionally graded 6061Al/SiC$_p$ composites. Applied Physics A **126**(9):673

[7] Xu F, Zhu S, Zhao J, Qi M, Wang F, Li S, Wang Z (2004) Effect of stress ratio on fatigue crack propagation in a functionally graded metal matrix composite. Composites Science and Technology **64**(12):1795–1803

[8] Ma J, He Z, Tan G (2002) Fabrication and characterization of Ti-TiB$_2$ functionally graded material system. Metallurgical and Materials Transactions A **33**(3):681–685

[9] Kidane A, Shukla A (2010) Quasi-static and dynamic fracture initiation toughness of Ti/TiB layered functionally graded material under thermo-mechanical loading. Engineering Fracture Mechanics **77**(3):479–491

[10] Koohbor B, Kidane A, Mallon S (2014) Effect of elastic properties of material composition on the fracture response of transversely graded ceramic/metal material. Materials Science and Engineering: A **619**:281–289

[11] Koohbor B, Rohanifar M, Kidane A (2019) Characterizing fracture response of cracked transversely graded materials. Composite Structures **229**, 111439

[12] Miehe C, Welschinger F, Hofacker M (2010) Thermodynamically consistent phase-field models of fracture: Variational principles and multi-field FE implementations. International Journal for Numerical Methods in Engineering **83**(10):1273–1311

[13] Miehe C, Hofacker M, Welschinger F (2010) A phase field model for rate-independent crack propagation: Robust algorithmic implementation based on operator splits. Computer Methods in Applied Mechanics and Engineering **199**(45):2765–2778

[14] Hirshikesh, Natarajan S, Annabattula RK, Martínez-Pañeda E (2019) Phase field modelling of crack propagation in functionally graded materials. Composites Part B: Engineering **169**:239–248

[15] Darban H, Bochenek K, Węglewski W, Basista M (2022) Experimental determination of the length-scale parameter for the phase-field modeling of macroscale fracture in Cr–Al$_2$O$_3$ composites fabricated by powder metallurgy. Metallurgical and Materials Transactions A **53**(6):2300–2322

[16] Molnár G, Gravouil A, Seghir R, Réthoré J (2020) An open-source Abaqus implementation of the phase-field method to study the effect of plasticity on the instantaneous fracture toughness in dynamic crack propagation. Computer Methods in Applied Mechanics and Engineering **365**, 113004

[17] Feng Y, Wang Q, Wu D, Luo Z, Chen X, Zhang T, Gao W (2021) Machine learning aided phase field method for fracture mechanics. International Journal of Engineering Science **169**, 103587

[18] Goswami S, Anitescu C, Chakraborty S, Rabczuk T (2020) Transfer learning enhanced physics informed neural network for phase-field modeling of fracture. Theoretical and Applied Fracture Mechanics **106**, 102447

[19] Molnár G, Gravouil A (2017) 2D and 3D Abaqus implementation of a robust staggered phase-field solution for modeling brittle fracture. Finite Elements in Analysis and Design **130**:27–38

[20] Huber T, Degischer HP, Lefranc G, Schmitt T (2006) Thermal expansion studies on aluminium-matrix composites with different reinforcement architecture of SiC particles. Composites Science and Technology **66**(13):2206–2217

[21] Lasagni F, Degischer HP (2010) Enhanced Young's modulus of Al-Si alloys and reinforced matrices by co-continuous structures. Journal of Composite Materials **44**(6):739–755

[22] Nikanorov SP, Volkov MP, Gurin VN, Burenkov YA, Derkachenko LI, Kardashev BK, Regel LL, Wilcox WR (2005) Structural and mechanical properties of Al–Si alloys obtained by fast cooling of a levitated melt. Materials Science and Engineering: A **390**(1):63–69

[23] Węglewski W, Krajewski M, Bochenek K, Denis P, Wysmołek A, Basista M (2019) Anomalous size effect in thermal residual stresses in pressure sintered alumina-chromium composites. Materials Science and Engineering: A **762**, 138111

[24] Węglewski W, Basista M, Chmielewski M, Pietrzak K (2012) Modeling of thermally induced damage in the processing of Cr–Al$_2$O$_3$ composites. Composites Part B: Engineering **43**(2):255–264

Chapter 5
On the Potential of Machine Learning Assisted Tomography for Rapid Assessment of FRP Materials with Defects

Jörg Hohe, Carla Beckmann, Michael Schober, Johannes Grygier, Clarissa Vogelbacher, Jan Fränkle, Philipp Jatzlau, and Christoph Sauerwein

Abstract The present contribution is concerned with the development of methods for a rapid assessment of defects in carbon fiber reinforced materials detected during a nondestructive inspection regarding their effect on the structural integrity of the components. The nondestructive inspection is performed by means of X-ray computed tomography. Subsequently, machine learning methods are employed to assess the effect of the detected defects on the strength of the material. The training data base for the machine learning scheme is determined numerically by the analysis of representative volume elements containing selected relevant defects. Their strength is characterized in terms of the Puck failure envelope. The method is demonstrated and validated against experimental data for a space grade CFRP material containing manufacturing induced defects.

5.1 Introduction

Laminates consisting of unidirectionally fiber reinforced plastics (FRP) with carbon, glass or other fibers are popular lightweight and high strength materials used in many technological fields such as aerospace, road and rail transport, in naval or even in civil

Jörg Hohe, Carla Beckmann, Michael Schober
Fraunhofer-Institut für Werkstoffmechanik IWM, Wöhlerstr. 11, 79108 Freiburg, Germany,
e-mail: joerg.hohe@iwm.fraunhofer.de, carla.beckmann@iwm.fraunhofer.de, michael.schober@gmx.net

Johannes Grygier, Clarissa Vogelbacher, Jan Fränkle
ITM-predictive GmbH, Roonstr. 23a, 76137 Karlsruhe, Germany
e-mail: johannes.grygier@itm-p.com, clarissa.vogelbacher@itm-p.com, jan.fraenkle@itm-p.ch

Philipp Jatzlau, Christoph Sauerwein
RayScan Technologies GmbH, Klinglweg 8, 88709 Meersburg, Germany
e-mail: p.jatzlau@rayscan.eu, c.sauerwein@rayscan.eu

engineering. Their main advantage – further to their superior stiffness and strength to weight ratio – is the possibility to design materials with tailored properties by a tailored design of their microstructure, especially the laminate stacking sequence. On the other hand CFRP and other laminates may feature inherent, manufacturing induced defects depending on the respective manufacturing process which cannot be avoided completely. These defects affect the mechanical performance of the material significantly. Hence, a significant body of literature is concerned with the effects of such defects.

A frequent defect type are ondulations. In an experimental and numerical study, Hörmann et al. [1] showed that a fiber waviness and the corresponding formation of matrix rich areas might have a significant impact on the fatigue response of the material. Altmann et al. [2] provided an analytical model for the effects of fiber ondulations on the effective strength using Puck's criterion [3, 4]. A finite element analysis by Lemanski et al. [5] revealed that fiber ondulations may also affect the delamination toughness of the ply interfaces significantly. In addition to ondulations and fiber waviness, the entire fiber orientation may deviate from its index value. In this context, e.g. Falcó et al. [6] showed that already small fiber misalignments result in a significant decrease in the effective stiffness and strength of the material.

The effect of delaminations in the ply interfaces as manufacturing defects has been analyzed e.g. by Bui et al. [7] using a numerical approach based on cohesive zone modelling of the interfaces. An experimental analysis into the effects of internal manufacturing or loading induced local delamination defects in cross-ply laminates has been provided more recently by Seon et al. [8], using micro computed tomography for the defect identification. Other frequent manufacturing defects during fiber and tape placement processes include the formation of gaps and undesired overlays of rovings. These defects might have negative but in some occasions also positive effects on the material performance as it has been shown by Croft et al. [9] or Lan et al. [10]. Both studies were directed to laminates manufactured in tape laying processes.

All defects mentioned so far are defects located in between different plies or at least in between different tapes or rovings. Further manufacturing defects may occur inside the individual plies or rovings. The most important (micro-) defects in this sense are fiber agglomerations, matrix rich areas between the fibers, pores or the incomplete wetting of fibers and suboptimum infiltration. The effect of inhomogeneous fiber distributions have been analyzed by Fast et al. [11] and Gommer et al. [12]. In both cases, micro computed tomography has been used for characterization of the microstructure, followed by a micromechanical simulation of the material response on the microstructural level. A similar approach has been provided by Huang and Talreja [13] using the Mori-Tanaka [14] mean field approach for numerical homogenization. Infiltration faults in laminates manufactured by resin transfer molding (RTM) have been considered by Baranger et al. [15]. Together with delaminations and fiber breakages, they were identified as the most significant manufacturing induced defects for the RTM process.

In structural application, the detection of manufacturing induced defects e.g. during non-destructive inspection of the manufactured component results in the crucial question whether or not the component will be able to withstand the service

loads even with the observed defects, i.e. whether the component has to be considered as a reject part. For this purpose, a reliable and fast method for assessment of the criticality of the respective manufacturing defect is required. The present study is concerned with an investigation into the potential of an artificial intelligence (AI) assisted defect assessment to allow an efficient and reliable evaluation of defects detected by a non-destructive inspection. In this procedure, images obtained by high resolution X-ray computed tomography are assessed for the local strength reduction caused by their presence using a machine learning algorithm. The training data base for the machine learning approach is provided by a numerical analysis of a large number of representative volume elements containing relevant defects. The approach is demonstrated on the example of a CFRP laminate containing worm pore networks due to a manufacturing mistake.

5.2 Strategy for Defect Assessment

The proposed strategy for component assessment comprises two steps. In a first step, a non-destructive inspection is performed using X-ray computed tomography. In a second step, the images of the detected defects are evaluated with respect to the reduction of the effective strengths caused by the flaw using a machine learning algorithm. The machine learning algorithm has been trained before by a numerical analysis of a large number of volume elements containing different flaw geometries where the effective parameters for Puck's failure criterion [3, 4] were determined by a homogenization approach.

5.2.1 Nondestructive Investigation

The nondestructive evaluation is performed by X-ray computed tomography (CT). In the conventional form of this nondestructive inspection technique, the specimen is placed on a rotation fixture in between an X-ray source and the corresponding detector (see Fig. 5.1). Using this device, the specimen is irradiated under different angles. From the resulting radiographic images, the internal structure is computationally reconstructed resulting in voxel-based grey scale images.

In a competitive approach, different types of X-ray computed tomography were applied in order to assess the capabilities of different scanning procedures. The objective was not only to determine whether the different approaches were applicable but also an optimum choice of the parameters in the irradiation, reconstruction and visualization of the defects in the microstructure. At the same time, the computer memory requirements had to be kept within acceptable bounds in order to enable a numerically efficient assessment by means of the machine learning approach defined in Sec. 5.2.4.

In a first step, different test specimens made from scratch material were scanned using conventional X-ray CT. In a parametric study, the minimum resolution of the reconstructed three-dimensional images of the internal defect structure was investigated that provided a sufficient quality for the automated assessment by means of the artificial intelligence tool. In this study, the reconstruction parameters interpolation accuracy, binning and the number of projections were varied systematically to obtain a reasonably accurate 3D image concerning contrast, white noise and flaw detectability.

The conventional X-ray computed tomography (Fig. 5.1, right) is convenient for specimens fitting completely into the X-ray cone. Typically, components with dimensions up to 300 mm can be investigated. However, the nondestructive inspection of larger objects typically made from fiber reinforced plastics such as structures in aircraft, wind turbine technology or even larger shell-like components in the automotive industry also is desirable. In this context, the transversal X-ray computed tomography method is advantageous. In this method, the planar or shell-like specimen is kept fixed whereas both the X-ray source and detector are moved in opposite directions on parallel planes. By this means, the specimen depth information is acquired by means of inclined radiography (see Fig. 5.1, right). In this method only those elements (i.e. defects) lying on a desired plane inside the specimen are focussed whereas the elements in other planes appear in a blurred mode.

5.2.2 Image Preprocessing

For the use in the machine learning tool, the X-ray computed tomography images are preprocessed by

- alignment to the ply orientation if the respective image is not perfectly aligned,
- black and white filtering in order to assign each voxel either to a defect (void volume) or the surrounding material,
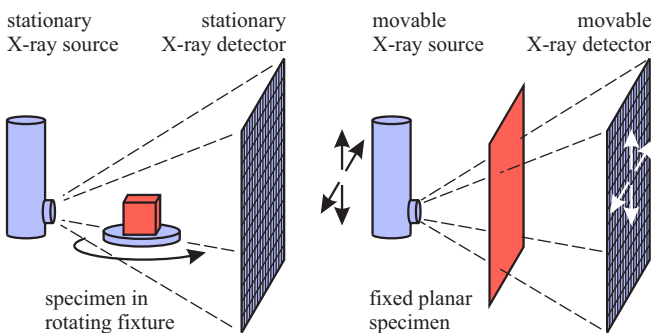
Fig. 5.1: Conventional and transversal X-ray computed tomography.

- trimming and scaling in order to ensure the same dimensions and the same scale as for the images in the training data base.

The pre-processing is necessary in order to provide a unique standardized form of the images obtained in the nondestructive inspection and the images in the training data base obtained by a finite element analysis of selected defects or defect networks using voxel-based microstructural samples. As a standard size, volume elements containing two complete adjacent plies with a total thickness of 2×0.125 mm and in-plane dimensions of 1.5 mm $\times 1.5$ mm was chosen. The standard resolution was $24 \times 150 \times 150 = 540\,000$ voxels.

An example for the alignment and filtering procedures is presented in Fig. 5.2. The original grey scale image (transversal cut through a laminate) and the corresponding grey-scale spectrum for the voxels are shown on the left hand side. Obviously, the image is slightly misaligned due to the non perfect positioning in the X-ray CT device. The grey scale histogram features two distinct maxima representing the (black) void volume voxels towards the lower end and the non-void volume voxels towards the upper end. Nevertheless, a non-negligible number of voxels featuring intermediate grey scale values were identified. The processed counterparts of the two figures for the unprocessed image are presented on the right hand side of Fig. 5.2. The CT image is now aligned to the coordinate axes. Furthermore, it has been converted to a binary black or white form.

5.2.3 Integrity Criterion

The integrity of the material is assessed by means of the well-known Puck criterion [3, 4]. In the reduced form restricted to the in-plane stresses σ_{11}, σ_{22} and σ_{12} with x_1
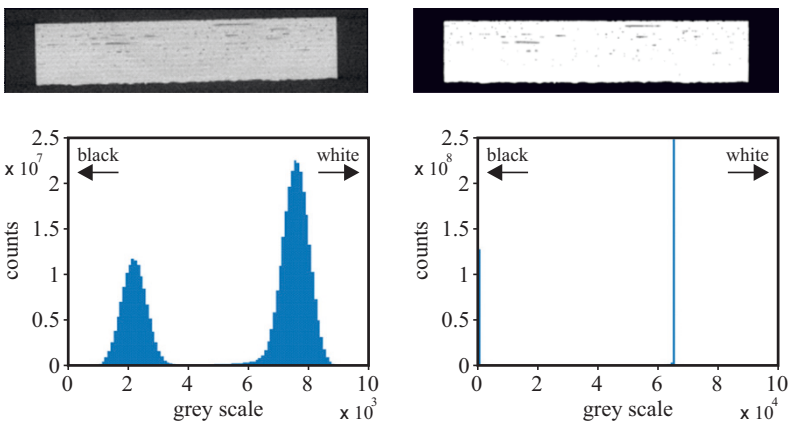
Fig. 5.2: Pre-processing of X-ray computed tomography images – left hand side: unprocessed image and grey scale histogram, right hand side: processed black and white image.

being the fiber direction, Puck's criterion is constituted by the five particular criteria

$$\left(\frac{\sigma_{11}}{R_{\parallel}^{\mathrm{t}}}\right)^2 \leq 1 \tag{5.1}$$

$$\left(\frac{\sigma_{11}}{R_{\parallel}^{\mathrm{c}}}\right)^2 \leq 1 \tag{5.2}$$

$$\left(\left(\frac{\sigma_{12}}{R_{\perp\parallel}^{\mathrm{s}}}\right)^2 + \left(1 - p_{\perp\parallel}^{(+)}\frac{R_{\perp}^{\mathrm{t}}}{R_{\perp\parallel}^{\mathrm{s}}}\right)^2 \left(\frac{\sigma_{22}}{R_{\perp}^{\mathrm{t}}}\right)^2\right)^{\frac{1}{2}} + p_{\perp\parallel}^{(+)}\frac{\sigma_{22}}{R_{\perp\parallel}^{\mathrm{s}}} \leq 1 - \left|1 - \frac{\sigma_{11}}{\sigma_{11}^{\mathrm{D}}}\right| \tag{5.3}$$

$$\left(\left(\frac{\sigma_{12}}{R_{\perp\parallel}^{\mathrm{s}}}\right)^2 + \left(p_{\perp\parallel}^{(-)}\frac{\sigma_{22}}{R_{\perp\parallel}^{\mathrm{s}}}\right)^2\right)^{\frac{1}{2}} + p_{\perp\parallel}^{(-)}\frac{\sigma_{22}}{R_{\perp\parallel}^{\mathrm{s}}} \leq 1 - \left|1 - \frac{\sigma_{11}}{\sigma_{11}^{\mathrm{D}}}\right| \tag{5.4}$$

$$\left(\left(\frac{\sigma_{12}}{2(1+p_{\perp\perp}^{(-)})R_{\perp\parallel}^{\mathrm{s}}}\right)^2 + \left(\frac{\sigma_{22}}{R_{\perp}^{\mathrm{c}}}\right)^2\right)\frac{R_{\perp}^{\mathrm{c}}}{-\sigma_{22}} \leq 1 - \left|1 - \frac{\sigma_{11}}{\sigma_{11}^{\mathrm{D}}}\right| \tag{5.5}$$

for fiber tensile and compressive failure within the fiber direction, tensile failure perpendicular to the fiber direction, interfiber shear failure and compressive/shear failure perpendicular to the fiber direction, respectively. The tensile and compressive strengths $R_{\parallel}^{\mathrm{t}}$ and $R_{\parallel}^{\mathrm{c}}$ within the fiber diresction, tensile and compressive strengths $R_{\perp}^{\mathrm{t}}$ and $R_{\perp}^{\mathrm{c}}$ perpendicular to the fiber direction, the interfiber shear strength $R_{\perp\parallel}^{\mathrm{s}}$ as well as the parameters $p_{\perp\parallel}^{(-)}$ und $p_{\perp\parallel}^{(+)}$ are material properties. For simplicity and in order to attain a smooth failure envelope, it was assumed that $p_{\perp\parallel}^{(-)} = p_{\perp\parallel}^{(+)}$. The corresponding failure envelope in in-plane stress space together with the underlying failure modes for the different partial criteria (5.1) to (5.5) is sketched in Fig. 5.3.
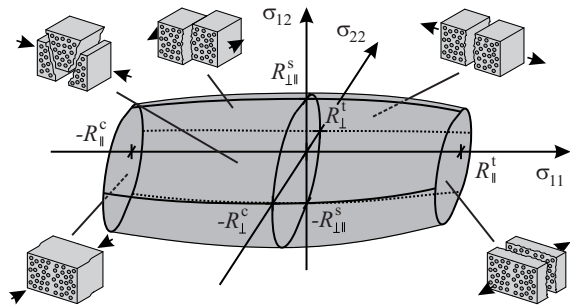
Fig. 5.3 Failure envelope for Puck's criterion [3, 4] in in-plane stress space.

5.2.4 Assessment Using a Deep Artificial Neural Network

In the presence of defects, the parameters defining Puck's failure envelope in stress space will be shrinked to different amounts. The degree of local strength reduction will be related to the geometry and topology of the underlying local defect. Due to the wide range of possible defect types, geometries and topologies, a wide range of effects on the seven parameters defining the Puck failure envelope is possible. For a numerically efficient determination of the strength reduction of defects detected during a non-destructive investigation, an artificial intelligence (AI) scheme based on deep learning is proposed. The artificial neural network approach should define the relation between the $150 \times 150 \times 24 = 540\,000$ black or white voxels and the 2×6 relevant material parameters defining the strength of the two plies in the considered volume elements in terms of Puck's criterion (5.1) to (5.5).

Considering the large number of input data, i.e. the binary information for the $540\,000$ voxels, training of an artificial neural network constitutes a highly challenging task. In order to perform this task with reasonable resources within a reasonable time, a deep learning approach is used. Deep artificial neural networks feature a larger number of specialized layers than traditional "shallow" artificial neural networks.

For the present analysis, a convolutional neural network is employed. This type of approach accounts for the requirements of automated digital image processing in an enhanced manner. The basic idea of this approach is to identify small structures and patterns on the lower levels of the artificial neural network. Subsequently, the relevant output properties are computed on the upper layers of the artificial neural network.

For this purpose, several filters are applied to small subsets of the digital images on the first layer, convolving the input voxel information onto a second layer. On the second layer, a data reduction is performed. For this purpose, only a limited amount of data is kept for small subsets, keeping only the relevant data. By means of this pooling step, the complexity of the problem is reduced. The convolution and pooling steps are repeated several times. In all of these repetitions, the complexity is reduced whereas all relevant information is preserved in abstracted form. In a final step, all points in the network are connected to enable the algorithm to recombine the information in a "dense" or "fully connected" layer.

The main challenge in the present problem is the three dimensionality of the input data and the dimensional asymmetry of the spatial extension in the transverse direction compared to the laminate in-plane directions. Therefore, the following topology for the artificial neural network is chosen:

- convolutional
- pooling
- convolutional
- pooling
- dense
- dense
- dense (output)

Since all 2×6 strength parameters may be affected by the geometry and topology of manufacturing induced defects in the laminate, the identical approach is employed for all 12 output parameters at once with one single network. This guarantees approximately the same forecast accuracy with efficient computation consumption during the training. For reasons of numerical stability, all parameters are normalized during the training of the artificial neural network.

5.3 Reference Material

As a reference material for the present study, a space grade carbon fiber reinforced material has been selected. The material consists of high strength HexTow IM7 fibers embedded into a HexPly 8552 epoxy matrix with a fiber volume fraction of $\rho_f = 58\%$. The material was supplied in form of a symmetric $[0°/90°]_{4s}$ cross ply laminate featuring a nominal ply thickness of $t_{ply} = 0.125\,\mu m$ and thus a total thickness of approximately $t_{tot} = 3\,mm$. The material may be considered as a relevant material not only for spacecraft applications but also for other high strength, high performance applications such as filament wound CFRP overwrapped pressure vessels for storage and transport in hydrogen technology and similar applications.

The material was manufactured from semi-finished prepreg using an autoclav process. Due to a production defect, the material contains worm pores of different length and diameter. A possible cause of the pore development is suspected to be an inappropriate pressure or incomplete evacuation during the manufacturing process. As an example for the defects, an X-ray computed tomography result featuring a section along a selected internal ply interface is presented in Fig. 5.4. For a clearer visibility, the original grey scale picture has been filtered to black and white where black ranges indicate pores whereas white ranges indicate undamaged material ranges. The worm pores are aligned with the fiber orientations of the respective plies. They are mostly located at the ply interfaces where a large number of pore intersections for two or more pores were observed, partially forming pore networks with possible larger void volumes at the worm pore intersections.
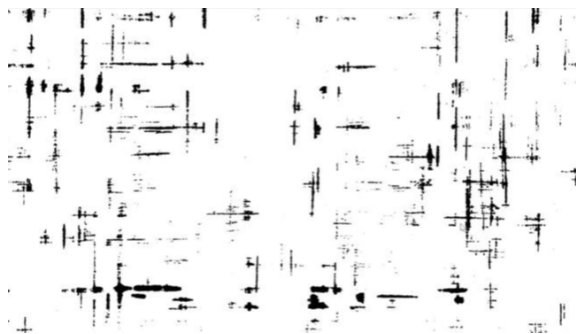
Fig. 5.4 Worm pore network at an internal ply interface of the reference material.

Fig. 5.5 Experimental results and Puck failure envelope in the biaxial failure plane and the interfiber failure planes in stress space (re-drawn from data presented by [16], assuming a prismatic shape of the failure envelope).
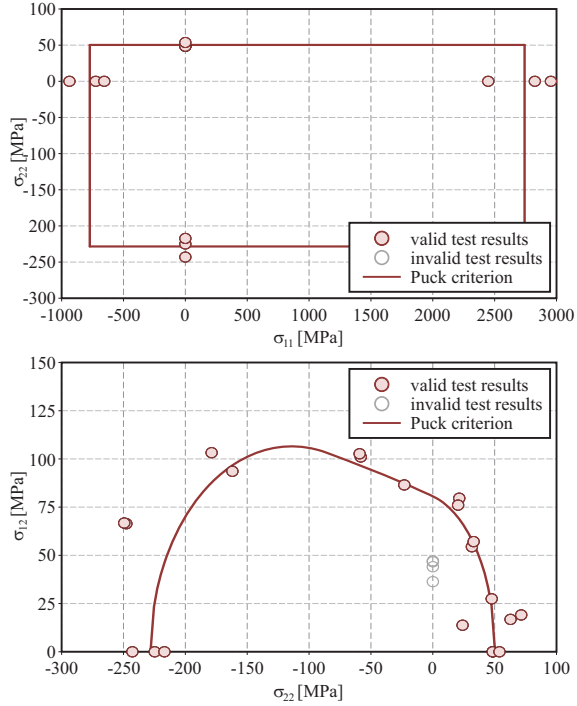
Unidirectionally fiber reinforced material from the same batch has extensively been characterized in previous contributions [16, 17]. In contrast to the material plate used as reference material in the present contribution, the plates used in the previous investigation had been found to be free from any production defects. In [16, 17], the material has been tested on single ply level within and perpendicular to the fiber direction under both, tensile and compressive loads. In addition, off-axis experiments in different test angles were performed. From the results, the parameters for the Puck criterion [3, 4] were determined using a maximum likelihood procedure [18]. The experimental results from [16] obtained at ambient temperature are compiled in Fig. 5.5 considering the biaxial failure and inter fiber failure planes in stress space, respectively. Since no reliable data was available for the determination of $\sigma_{11}^{D}(\sigma_{11})$ in Eqs. (5.3) to (5.5), the simplifying assumption $\sigma_{11}^{D} = \sigma_{11}$ was applied, i.e. it was assumed that the failure envelope is perfectly prismatic with respect to the σ_{11}-direction in stress space.

5.4 Artificial Neural Network Training Data Base

The training data base for the deep learning approach described in Sect. 5.2.4 is determined numerically. For this purpose, a sufficiently large number of defects

observed in a tomographic investigation of the reference material is analyzed with respect to the effect of the respective defects on shape and size of the Puck failure envelope (Figs. 5.3, 5.5). The analysis is performed numerically by simulating the mechanical response of stochastic volume elements (SVE) containing the respective defect or defect network by means of the finite element method.

In order to enable the analysis of a large number of stochastic volume elements, a semi-automatic procedure is implemented. The procedure is based on voxel-based volume elements each having the identical discretization and boundary conditions. The individual voxels coincide with cuboid finite elements of the same size. The respective defect is introduced by assuming a material with negligible stiffness for all elements with centroids inside the defect volume.

The stochastic volume elements consist of square cutouts of the laminate containing two complete plies, i.e. one ply with $0°$ and one ply with $90°$ fiber direction each. The in-plane are of the volume elements is $150\,\text{mm} \times 150\,\text{mm}$ with a total thickness of two plies, i.e. $2 \times 0.125\,\text{mm}$. The voxel size for both the numerical analysis and the experimental defect characterization by X-ray computed tomography is chosen to be $10\,\mu\text{m} \times 10\,\mu\text{m} \times 10\,\mu\text{m}$ resulting in finite element models consisting of $150 \times 150 \times 24$ finite elements. Standard 8-node displacement-based volume elements with tri-linear shape functions were used. The stochastic volume elements were supplied with periodic boundary conditions introducing the macroscopic strain components as direct degrees of freedom as presented in an earlier contribution (Beckmann and Hohe [19]) using a dummy node approach. By this means the corresponding effective stresses (times the SVE volume) are obtained as the energy conjugate resulting "forces" to the "displacements" of the dummy node representing the effective strains. The material for the individual plies is modelled by orthotropic linear elasticity using the material parameters for the defect free unidirectionally (UD) fiber reinforced material as determined in a previous contribution (Hohe et al. [16]). For the elements within the respective defects, the elastic moduli were scaled down to negligible however finite, non-zero values to avoid numerical instabilities. An example of a modelled worm pore network is presented in Fig. 5.6. Notice that due to the voxel-based modelling technique the defect surface is not entirely smooth. Examples for the choice of different types of defects and defect networks from tomographic data are presented in Fig. 5.7.
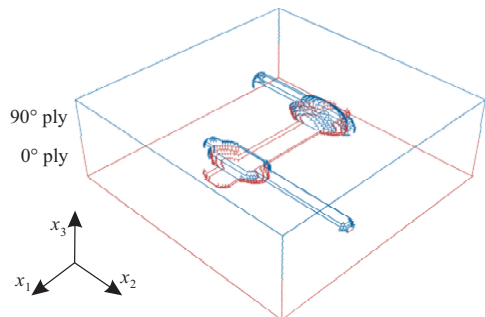
Fig. 5.6 Internal defect structure in a regular voxel-based statistical volume element for defect assessment (two adjacent plies), meshed with $150 \times 150 \times 24$ cuboidal finite elements.

Fig. 5.7 Examples for the choice of volume elements with different degrees of defect complexity.
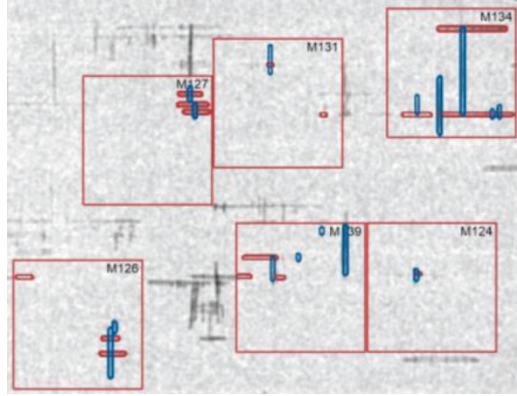
The finite element models of the stochastic volume elements are subjected to different reference strain states on the macroscopic level including uniaxial tensile and compressive stress states in both the x_1- and x_2-directions as well as in-plane shear strain states. Adopting the weakest link principle, a critical state of the volume element is assumed once Puck's criterion [3, 4] on ply level is violated for the strengths for the defect free material (Fig. 5.5). In order to avoid numerical artefacts due to unrealistic stress concentrations induced by the rough surfaces of the defects due to the voxel-based modelling failure of the respective ply is assumed once Puck's criterion is violated for 10% of the finite elements in the respective ply. The evaluation is performed separately for either of the two plies. As a result, estimates for the reduced strengths for both plies of the volume element with the respective defect or defect network are available.

An example for the shrinked Puck failure envelope is presented in Fig. 5.8. The defect network with a high degree of complexity analyzed here is the defect at the top right hand side of Fig. 5.7. For both plies, the failure envelope is found to be shrinked significantly by the presence of the defect network. Slightly more pronounced effects are observed for the (upper) 90° degree ply. For both plies, the strength reduction caused by the defect network is slightly more severe for the in-plane normal tensile and compressive stresses in both directions compared to the in-plane shear stress. The shear strength $R^s_{\perp\|}$ is found to be reduced by approximately 50% compared to a at least 60% reduction of the normal strengths $R^t_{\|}$, $R^c_{\|}$, $R^t_{\perp}$ and $R^c_{\perp}$. Thus, the failure envelope is not only shrinked by the presence of the defect network but also changes its shape.

A total of 400 different types of pores and pore networks with low and high degrees of complexity considering all types observed in the X-ray computed tomography inspection of the reference material is analyzed. In order to enhance the data base for training of the neural network further, it is considered that the observed networks may positioned not only at the positions where they were observed but at in-plane shifted positions anywhere in the volume element with the identical effect on the effective strengths. Furthermore mirror images of the observed networks with respect to either

Fig. 5.8 Shrinked Puck failure envelope for selected large worm pore network with high complexity.
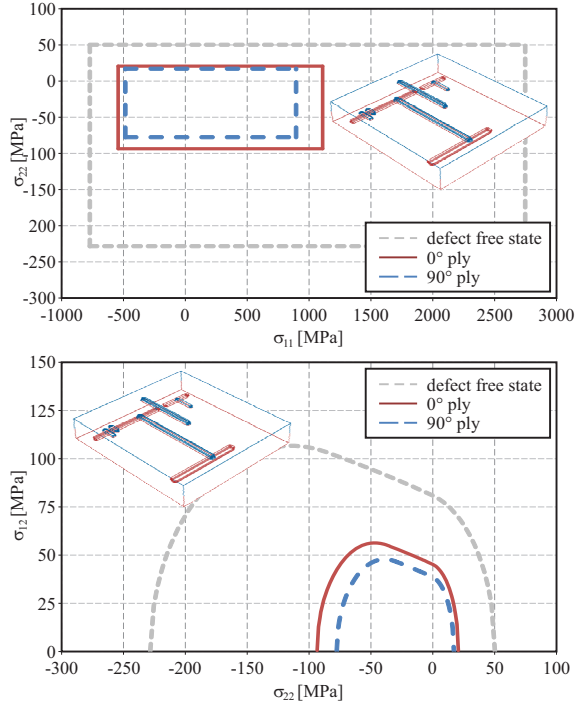
of the x_1-x_3- or x_2-x_3-planes will give the same results on the effective strength. By these considerations, the training data base can be enhanced significantly.

5.5 Example

In order to demonstrate the approach and as a basis for a critical discussion of its capabilities, it is applied to the example of notched laboratory specimens. The specimens were manufactured, scanned by X-ray computed tomography assessed by the machine learning tool and the tested mechanically to failure to provide a validation data base.

5.5.1 Experimental investigation

For the experimental investigation, five tensile test specimens are manufactured from the cross-ply laminate with worm pore networks according to Fig. 5.4. The specimens are supplied with shallow notches in order to obtain a non homogeneous stress distribution. The specimen geometry is presented in Fig. 5.9.

Fig. 5.9 Geometry of the
tensile test specimens.
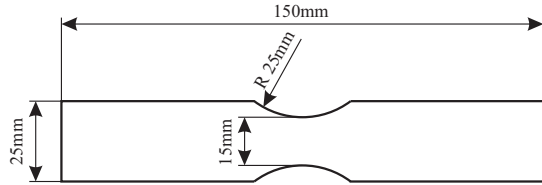
Prior to mechanical testing, the test sections of the specimens were scanned
by X-ray computed tomography. In a competitive approach, both conventional and
transversal X-ray tomography were applied (see Sect. 5.2.1). An example for the
results on the test section is presented in Fig. 5.10. Although being more efficient
especially for larger samples than the laboratory specimens considered here, the
results obtained by transversal computed tomography proved to be not evaluable by
the machine learning approach as proposed in Sect. 5.2.4 without additional depth
information. Therefore, conventional X-ray computed tomography was used in the
present experimental investigation. The test sections of all five test specimens were
scanned for defect networks using a voxel edge length of 10 μm. The CT images were
subsequently assessed by the deep learning approach for a prediction of the failure
loads (Sect. 5.5.2).

Subsequently, the specimens were tested mechanically till failure using an elec-
tromechanical testing machine (Hegewald & Peschke inspekt table 250) with a wedge
clamping system. For the tests, the specimens were supplied with cap strips to prevent
slipping in the grips. The specimens were tested till failure under quasi-static condi-
tions at a crosshead velocity of 1 mm/min. During the experiments, the applied force,
the crosshead displacement as well as the relative displacement of two points with
a distance of 50 mm across the notch were continuously recorded. From the force
measurements, a nominal (average) stress was determined for the notch root cross
section. A nominal strain across the notched section was determined by normalizing
the relative displacement across the notched section by the initial distance of 50 mm.
Notice that due to the presence of the notches the nominal strain does not constitute
a true strain measure, however, is more reliable than the crosshead displacement as a
deformation measure acquired directly on the specimen surface.
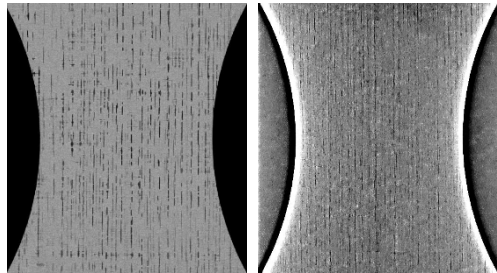
Fig. 5.10 Results of conven-
tional (left) and transversal
(right) X-ray computed tomog-
raphy of the test specimens.

Table 5.1: Tensile test results.

specimen	F^{max} [kN]	$\sigma_{\mathrm{avg}}^{\mathrm{max}}$ [MPa]	$\sigma_{0°}^{\mathrm{max}}$ [MPa]	$\sigma_{90°}^{\mathrm{max}}$ [MPa]
AVE-CFK-Zug-01	43.31	976.8	1853.5	100.1
AVE-CFK-Zug-02	42.13	953.1	1808.4	97.7
AVE-CFK-Zug-03	42.72	960.3	1822.2	98.4
AVE-CFK-Zug-04	41.96	945.6	1794.3	96.9
AVE-CFK-Zug-05	37.62	846.6	1606.4	86.8

The results in terms of the nominal stress vs. nominal strain curves and the failure modes are presented in Fig. 5.11. The failure forces and nominal failure stresses are compiled in Table 5.1. In addition to the average stress $\sigma_{\mathrm{avg}}^{\mathrm{max}}$ at failure, the failure stresses $\sigma_{0°}^{\mathrm{max}}$ and $\sigma_{90°}^{\mathrm{max}}$ were computed for the 0°- and 90°-plies, respectively.

In all five cases, linear nominal stress-strain curves with almost identical slopes were obtained. In all cases, failure occurs in a brittle mode without development of nonlinearities. The failure loads for specimens no. AVE-CFK-Zug-01 to -04 are of similar magnitude whereas specimen AVE-CFK-Zug-05 exhibits a significant pop-in at a lower failure load, followed by a limited re-increase of the load level prior to final failure.
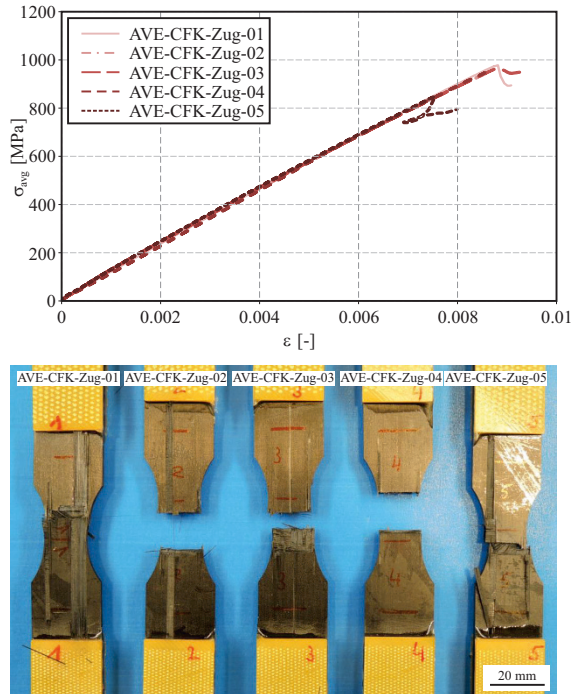
Fig. 5.11 Tensile test results – nominal average stress-strain curves and failure modes.

The fracture pattern for specimens no. AVE-CFK-Zug-02 and -04 consist in a smooth failure of all plies in the same cross section. A similar pattern is observed for specimen no. AVE-CFK-Zug-03, however, with a different fracture plane for the top plies and thus a delamination in the depth where the transition between the two different failure planes is made. The change in the position of the fracture plane is probably caused by the presence of defect induced weak spots at different in-plane locations for the front and rear plies. The delamination necessary for the transition in the fracture planes increases the fracture energy required for complete failure despite the probably lower work to failure due to the presence of significant weak spots. For specimen no. AVE-CFK-Zug-01 and especially specimen no. AVE-CFK-Zug-05 featuring the lower failure load (see Table 5.1) a more complex, rough fracture pattern is observed. In both cases, specimen failure involves failure of the different plies in different locations along with surface break-outs and shear pull-outs (see Fig. 5.11).

The obtained maximum stresses $\sigma_{90°}^{max}$ for the 90°-ply are in all cases found beyond the corresponding inter fiber tensile strength $R_\perp^t$ for the defect free material (see Figs. 5.5 and 5.8) indicating that inter fiber failure of the 90°-plies prior to complete specimen failure is likely. Since the inter fiber cracks were bridged by the neighboring 0°-plies, they did not trigger total specimen failure.

5.5.2 Integrity Assessment and Discussion

The strength of the test sections of the tested laboratory specimens AVE-CFK-Zug-01 to -05 are assessed using the deep artificial neural network constituted in Sec. 5.2.4. Since the specimees were loaded in tensile axial modes, the tensile strength $R_{||}^t$ within the fiber direction of the 0°-plies is the relevant strength property. The predictions for the local distributions of $R_{||}^t$ for an approximately 13.5 mm × 33 mm wide and long area in the test section of specimen AVE-CFK-Zug-01 to -05 are presented in Figs. 5.12 to 5.16, respectively.   In this context, the individual subfigures are related to the different depth positions through the thickness of the specimens. The specimen orientation in Figs. 5.12 to 5.16 is identical to Fig. 5.9, i.e. the loading direction is the horizontal direction with the notch root in the center of the subfigures.

Due to variation in the local defect state, strong local variations in the strength distribution are obtained. In some areas, clustering of high or low values, i.e. a distinct local correlation is observed. This correlation is caused by worm pore networks where the individual worm pores stretch across more than one of the neighboring scanned volumes. For all specimens, the lowest value for the predicted strength $R_{||}^t$ is found in the range of 500 MPa and thus far below the measured strengths in the range between 1600 MPa and 1850 MPa. Hence, an integrity assessment based directly on the weakest-link principle and thus assuming failure of the entire specimen once the first volume element fails would result in highly over-conservative results.

On the other hand, even for the rather brittle CFRP material considered here, the (early) failure of a one or few volume elements with a strength in the range of 500 mm embedded into a neighborhood of volume elements with significantly

Fig. 5.12 Local distribution of the tensile strength in fiber direction through the thickness of specimen AVE-CFK-Zug-01.
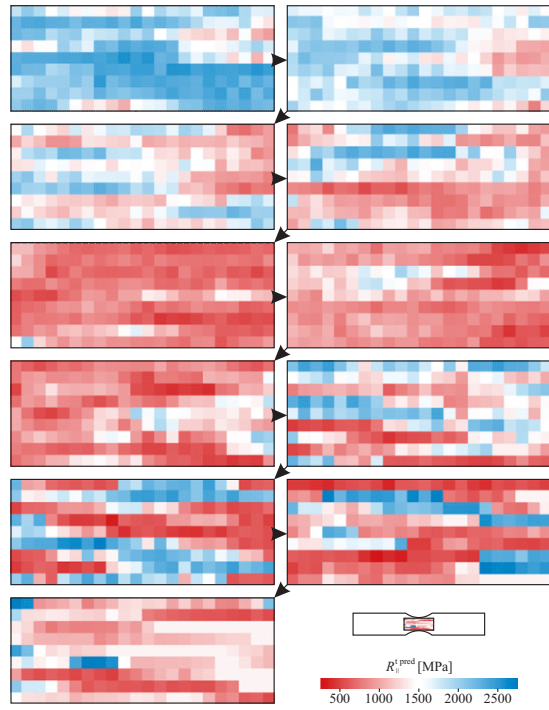
Fig. 5.13 Local distribution of the tensile strength in fiber direction through the thickness of specimen AVE-CFK-Zug-02.
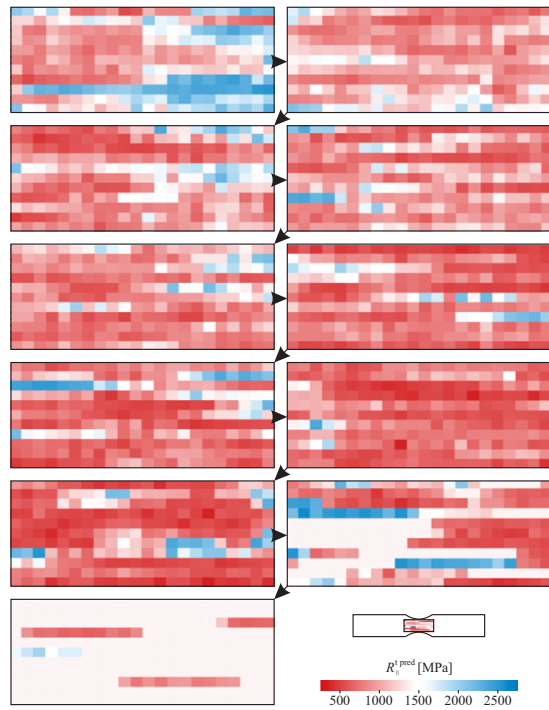
Fig. 5.14 Local distribution of the tensile strength in fiber direction through the thickness of specimen AVE-CFK-Zug-03.
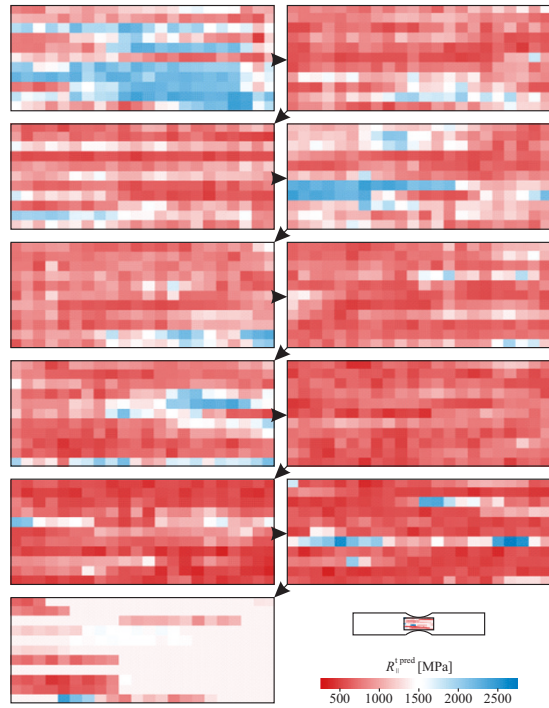
Fig. 5.15 Local distribution of the tensile strength in fiber direction through the thickness of specimen AVE-CFK-Zug-04.
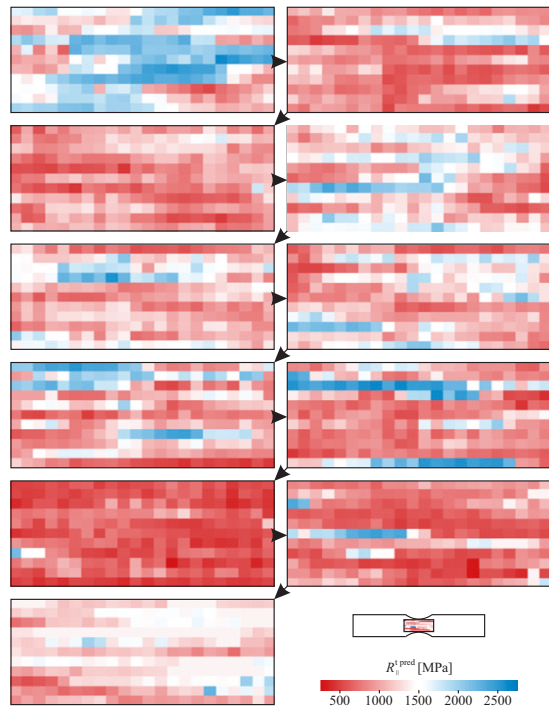
Fig. 5.16 Local distribution
of the tensile strength in fiber
direction through the thickness
of specimen AVE-CFK-Zug-
05.
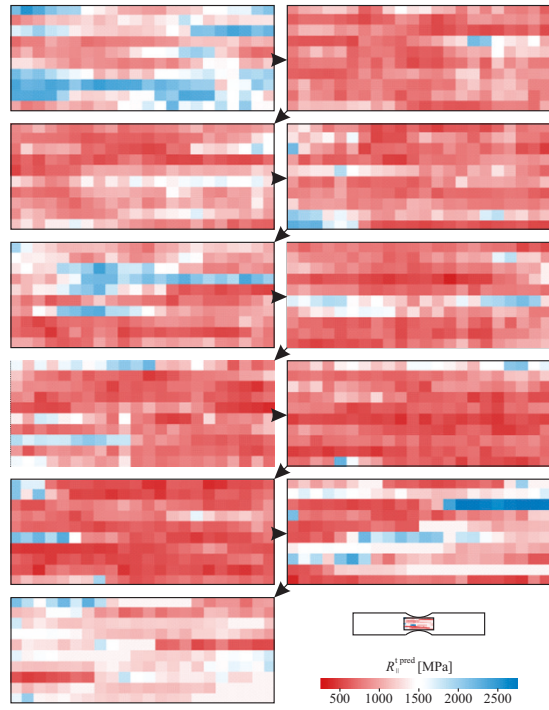
higher strength does not necessarily result in overloading of the neighborhood due
to stress re-distribution from the failed element. Furthermore, the training of an
artificial neural network is not a rigorously deterministic process but a statistical
approximation. Hence, the training result as well as all predictions based thereon are
also supplied with similar uncertainties.

For this reason, the prediction results are assessed in a stochastic manner. The
histograms for the strength evaluation of the test sections of the specimens AVE-CFK-
Zug-01 to -05 are presented in Fig. 5.17. In Table 5.2, the median values $Q_{50\%}(R_{||}^{t})$
are compiled, together with the 25%- and 75%-quantiles representing the scatter

Table 5.2: Stochastic evaluation of the assessment results for the individual test specimens.

specimen	$Q_{25\%}(R_{||}^{t})$ [MPa]	$Q_{50\%}(R_{||}^{t})$ [MPa]	$Q_{75\%}(R_{||}^{t})$ [MPa]	$R_{||}^{t,exp}$ [MPa]
AVE-CFK-Zug-01	956	1254	1704	1853.5
AVE-CFK-Zug-02	904	1321	1704	1808.4
AVE-CFK-Zug-03	773	933	1201	1822.2
AVE-CFK-Zug-04	1008	1359	1797	1794.3
AVE-CFK-Zug-05	818	994	1298	1606.4

Fig. 5.17 Histograms for the predicted reduced strength longitudinally to the fibers in the test direction.
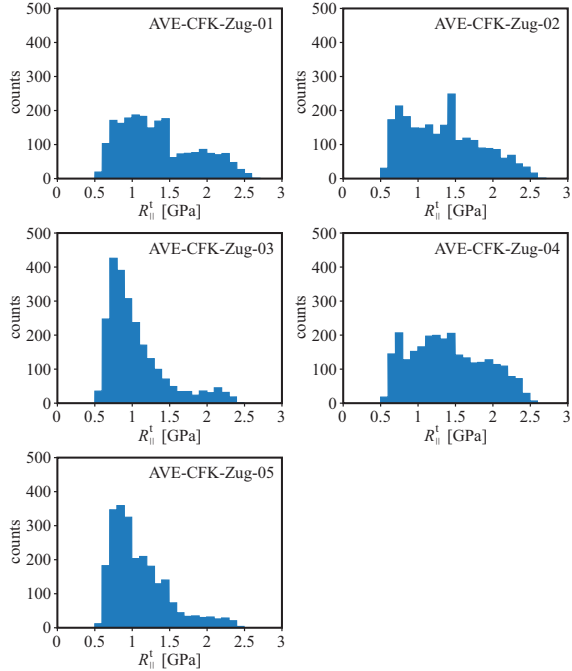
band with. For comparison, the respective experimentally determined strength $R_{\parallel}^{\mathrm{t,exp}}$ from Table 5.1 is added.

The histograms for specimens AVE-CFK-Zug-01, -02 and -04 feature a shallow characteristic with similar probabilities for a wide range of local strength values. All three distributions have median values $Q_{50\%}$ in the range of 1300 MPa. The distributions for the specimens AVE-CFK-Zug-03 and -05 feature a more distinct peak with lower median values at approximately $Q_{50\%} \approx 950$ MPa.

A comparison of the predicted median strengths $Q_{50\%}$ with the experimental strength results $R_{\parallel}^{\mathrm{t,exp}}$ yields a qualitatively similar distribution across the specimen set except for specimen AVE-CFK-Zug-03 for which a similar median strength is predicted as for specimen AVE-CFK-Zug-05, although a failure load in the same range as for specimens AVE-CFK-Zug-01, -02 and -04 has been obtained in the experimental investigation. A possible explanation for this outlier could be the delamination between the top plies and the central and lower plies visible in the fracture pattern in Fig. 5.11. The crack leading to the final separation of the specimen ran in two different intralaminar planes connected by an interlaminar delamination. For development of the delamination, additional fracture energy is required which is not included in the analytical assessment based on Puck's intralaminar failure criterion. The intralaminar criterion basically predicts a "first ply failure", however, does not account for interlaminar effects. The increase in the fracture stress caused by the additional energy consumed by the delamination is not accounted for.

In the quantitative view, the failure predictions for all five specimens in term of the predicted median strengths are still strongly conservative. Again, the reason is the limitation of Puck's criterion – as for all classical intralaminar composite failure criteria – to the prediction of first ply failure. A failure prediction for the entire structure (or, in this case, the entire specimen) could only be made if the weakest link principle would apply in the rigorous sense. This would require that the failure of a first volume element would trigger the immediate failure of its neighborhood due to stress re-distribution. Nevertheless, if the strength distribution is inhomogeneous, the neighboring volume elements might feature a significantly higher strength so that first ply failure does not necessarily trigger complete failure of the entire structure.

Another feature yielding conservatisms in the present analysis is the assumption of the weakest link principle already in the numerical generation of the training data base for the deep neural network. In the same manner as on the structural level, failure of the stochastic volume elements was assumed once a limited number of finite elements in the microstructural analysis reached their local failure load. Hence, the training data base for the neural network already contains conservative approximations.

5.6 Conclusions

The objective of the present study was an investigation into the potential of modern artificial intelligence methods for a fast, efficient and reliable assessment of defects in CFRP structures detected during non-destructive inspection. For this purpose, a machine learning approach based on a deep artificial neural network was developed and implemented. The procedure is based on a non-destructive inspection using X-ray computed tomography to provide three-dimensional information about geometry and topology of the possible internal defect structure. The observed defects are then assessed by the AI tool regarding their effect on the parameters governing Puck's failure envelope in stress space. The training data base for the AI tool is provided numerically by a multiscale analysis of a large number of stochastic volume elements containing different characteristic defects or defect networks.

The approach has been demonstrated and assessed in an experimental study on notched tensile specimens consisting of a cross-ply laminate containing worm pore networks due to a manufacturing inaccuracy. For all tested specimens, conservative results were obtained. The qualitative differences between the failure loads for the different specimens were mainly reproduced. From the quantitative point of view, the analytical predictions were found to be highly conservative. The conservatism are caused by conservatism on several levels. First, the numerical data base used for training of the artificial neural network is based on the weakest link principle, assuming the entire failure of a volume element once the microscopic failure load is exceeded on the microscale for a prescribed volume fraction of the volume element. Hence, the artificial neural network "learned" to link the defect geometry and topology to the conservative microscopic failure predictions. In a similar manner, the assessment on the structural level – again – is based on the weakest link principle. Thus, it

is assumed that failure of the first volume element necessarily triggers failure of the entire structure. Neither a stable fracture by a successive failure of the volume elements forming the structure nor fracture modes involving interlaminar failure in addition to intralaminar modes can be described by the Puck criterion employed for the integrity assessment of the composite material. The conservatism induced by the employment of the weakest link principle on the microstructural level may be overcome by using an improved simulation strategy on the microstructural level for generation of the AI training data base. An integrity assessment on the macroscopic level accounting not only on intralaminar but also for interlaminar modes as well as for successive stable fracture could improve the prediction accurracy and thereby reduce the amount of conservatism.

In general, the proposed scheme for fast and numerically efficient assessment of tomographic inspection results using a trained artificial neural network provides a promising approach. Care has to be taken in the choice of the training data base since simplifications involved will be retained in the application of the approach. The multi-step procedure for training of the neural network is a challenging procedure. In its present form, the approach is restricted to the considered defect types. Nevertheless, a generalization to other defect types can be made in a straightforward manner. Further, a continued training of the artificial neural network also using data obtained in repeated nondestructive inspection of components in service might be used for a continuous improvement of the prediction accuracy.

References

[1] Hörrmann S, Adumitroaie A, Viechtbauer C, Schagerl M (2016) The effect of fiber waviness on the fatigue life of cfrp materials. International Journal of Fatigue **90**:139–147

[2] Altmann A, Gesell P, Drechsler K (2015) Strength prediction of ply waviness in composite materials considering matrix dominated effects. Composite Structures **127**:51–59

[3] Puck A, Schürmann H (1998) Failure analysis of FRP laminates by means of physically based phenomenological models. Composites Science and Technology **58**(7):1045–1067

[4] Puck A, Schürmann H (2002) Failure analysis of FRP laminates by means of physically based phenomenological models. Composites Science and Technology **62**(12):1633–1662

[5] Lemanski SL, Wang J, Sutcliffe MPF, Potter KD, Wisnom MR (2013) Modelling failure of composite specimens with defects under compression loading. Composites Part A: Applied Science and Manufacturing **48**:26–36

[6] Falcó O, Mayugo JA, Lopes CS, Gascons N, Costa J (2014) Variable-stiffness composite panels: Defect tolerance under in-plane tensile loading. Composites Part A: Applied Science and Manufacturing **63**:21–31

[7] Bui VQ, Marechal E, Nguyen-Dang H (1999) Imperfect interlaminar interfaces in laminated composites: bending, buckling and transient reponses. Composites Science and Technology **59**(15):2269–2277

[8] Seon G, Makeev A, Nikishkov Y, Lee E (2013) Effects of defects on interlaminar tensile fatigue behavior of carbon/epoxy composites. Composites Science and Technology **89**:194–201

[9] Croft K, Lessard L, Pasini D, Hojjati M, Chen J, Yousefpour A (2011) Experimental study of the effect of automated fiber placement induced defects on performance of composite laminates. Composites Part A: Applied Science and Manufacturing **42**(5):484–491

[10] Lan M, Cartié D, Davies P, Baley C (2015) Microstructure and tensile properties of carbon–epoxy laminates produced by automated fibre placement: Influence of a caul plate on the effects of gap and overlap embedded defects. Composites Part A: Applied Science and Manufacturing **78**:124–134

[11] Fast T, Scott AE, Bale HA, Cox BN (2015) Topological and euclidean metrics reveal spatially nonuniform structure in the entanglement of stochastic fiber bundles. Journal of Materials Science **50**(6):2370–2398

[12] Gommer F, Endruweit A, Long A (2014) Analysis of filament arrangements and generation of statistically equivalent composite micro-structures. Composites Science and Technology **99**:45–51

[13] Huang H, Talreja R (2005) Effects of void geometry on elastic properties of unidirectional fiber reinforced composites. Composites Science and Technology **65**(13):1964–1981

[14] Mori T, Tanaka K (1973) Average stress in matrix and average elastic energy of materials with misfitting inclusions. Acta Metallurgica **21**(5):571–574

[15] Baranger E, Allix O, Blanchard L (2009) A computational strategy for the analysis of damage in composite pipes. Composites Science and Technology **69**(1):88–92, mechanical Response of Fibre Reinforced Composites

[16] Hohe J, Schober M, Fliegener S, Weiss KP, Appel S (2021) Effect of cryogenic environments on failure of carbon fiber reinforced composites. Composites Science and Technology **212**:108,850

[17] Hohe J, Schober M, Weiss KP, Appel S (2022) Verification of Puck's criterion for CFRP laminates under multiaxial loads at ambient and cryogenic temperatures. Composites Science and Technology **228**:109,631

[18] Findeisen C, Schober M, Appel S, Hohe J, Weiss KP (2023) Development and implementation of a parameter estimation and post-processing tool for the failure analysis of composite materials. In: Proc. 17th Europ. Conf. Spacecraft Structures Materials and Environmental Testing (Toulouse, March 28-30, 2023), electronic publication, pp 1–5

[19] Beckmann C, Hohe J (2014) Numerical prediction of disorder effects in solid foams using a probabilistic homogenization scheme. Mechanics of Materials **78**:22–43

Chapter 6
On the Semi-Analytical Modelling of the Free-Edge Stress Field in Cross-Ply Laminated Shells Under Mechanical Loads

Andreas Kappel and Christian Mittelstedt

Abstract This contribution provides a semi-analytical model for the assessment of the three-dimensional stress field in thick, cylindrically curved cross-ply laminated shells subjected to different kinds of mechanical loadings under consideration of the free-edge effect. The model superimposes a closed-form analytical solution with a layerwise approach and the governing equations as well as the boundary conditions are derived by means of the minimum total potential energy principle utilizing the general Euler-Lagrange equations. Numerical results for thick cross-ply laminated shells undergoing uniform edge loadings and sinusoidal outer pressure are presented and the accuracy is verified by comparisons with full-scale, three-dimensional finite element computations. Those reveal an excellent agreement between the highly efficient semi-analytical model and the finite element approach for the free-edge stress fields in cross-ply laminated shells.

6.1 Introduction

In the last decades, fiber-polymer composite structures have attracted more and more attention due to the social demand to protect the limited resources of the earth. Their favorable specific material properties, the low total energy consumption and their ability to arbitrarily tailor the stacking sequence of composite laminates in order to meet given design aims make fiber-polymer composite structures the ideal lightweight engineering material in order to realize a weight loss of all kinds of structures and thus lower the overall fuel consumption of vehicles or machines. However, several experimental investigations of composite laminated plates and shells undergoing dif-

Andreas Kappel · Christian Mittelstedt
Darmstadt University of Technology, Department of Mechanical Engineering, Institute for Lightweight Engineering and Structural Mechanics, Germany,
e-mail: andreas.kappel@klub.tu-darmstadt.de,
christian.mittelstedt@klub.tu-darmstadt.de

ferent loading conditions clearly indicated that those safety-critical structures exhibit complex failure modes with an interaction of micro- as well as ply cracking, which eventually lead to a degradation of the material properties of the composite structure and to the delamination of adjacent laminate layers. In this context, it was observed that the delamination was triggered by the three-dimensional stress concentrations at the traction-free edges. This phenomenon, commonly referred to as the free-edge effect, is omnipresent since it is a consequence of the dissimilar deformation properties of composite structures wherein the high modulus fibers are aligned in different directions. It is for this reason, that the free-edge effect and especially the interlaminar stress concentrations have to be taken into consideration throughout the whole development process. Thus, given the importance of this problem, a multitude of analytical, numerical and especially experimental investigations have been performed in order to investigate the complex three-dimensional free-edge stress field in fiber-reinforced composite structures.

While for the free-edge effect in composite laminated plates an impressive body of knowledge has been established over the last decades [1–3], comparatively little research can be found on the topic of the free-edge effect in composite laminated shells. Due to its localized and three-dimensional nature, numerical computations require huge computational efforts in order to deliver an adequate depiction of the underlying structural response of composite structures. Nonetheless, in order to gain an initial and efficient insight into the interlaminar stress field in the boundary-layer region, it is often useful to examine the structural behavior by means of closed-form two-dimensional approaches assuming a plane strain condition.

In this regard, Srinivas [4] was one of the first who developed an exact three-dimensional Frobenius series solution for the static and dynamic analysis of simply supported cross-ply laminated shells subjected to transverse sinusoidal loadings. Ren [5] also presented an exact solution for circular cylindrical cross-ply laminated shells in cylindrical bending and compared the numerical results to the ones obtained through Classical Shell Theory (CST). Based on the insights of Lekhnitskii [6, 7] for curved, anisotropic beams, Ko and Jackson [8] developed an analysis method for cross-ply laminated beams undergoing bending moments and end forces. Varadan and Bhaskar [9], on the other hand, adopted the elasticity solution by [4] and also investigated the structural response of finite length, cross-ply laminated shells in cylindrical bending.

Up to this day, there exists only a small number of publications in the open literature that enable an accurate depiction of the three-dimensional state variables in composite laminated shells under consideration of the free-edge effect. Several approximate analysis methods were developed by Miri and Nosier [10, 11]. Herein, they investigated the decaying behavior of the interlaminar stress gradients of cylindrically curved composite shell panels with traction-free edges in the circumferential direction which were subjected to an extension in the axial direction and hygrothermal loadings [12]. They employed linear displacement-based layerwise formulations and solved the governing equations by means of the state-space approach. The accuracy was verified by comparison with different analytical elasticity solutions. Tahani et al [13], on the other hand, utilized the three-dimensional multi-term extended Kantorovich

method in order to study the state variables of finite length, circular cylindrical composite laminated shells with arbitrary boundary conditions undergoing sinusoidal or constant outer pressure. The developed method was also able to accurately capture the localized free-edge effect which was verified through finite element computations. Based on the two-dimensional closed-form analytical solution by Ko and Jackson [8], Schnabel et al. [14] as well as Kappel and Mittelstedt [15, 16] developed linear and higher-order, layerwise displacement field models in order to investigate the interlaminar stress field of finite length, cross-ply laminated shells with traction-free axial ends. They obtained the governing equations as well as boundary conditions through the minimum total potential energy principle and solved the quadratic eigenvalue problem numerically. Comparisons of the different semi-analytical methods with highly detailed three-dimensional finite element computations clearly indicated an excellent agreement between both methods. Ahmadi [17] presented a Galerkin-based layerwise formulation to describe the out-of-plane stresses in thick composite cylindrical shell panels with general layer stacking subjected to a pure bending moment in the axial direction, which was also extended to levy-type loaded cross-ply laminated shells [18].

This contribution aims at presenting a generalized semi-analytical model which enables the reliable prediction of the interlaminar stress fields in thick, finite length circular cylindrical cross-ply laminated shells subjected to different kinds of mechanical loadings. Initially, by assuming a plane strain condition without consideration of the free-edge effect, a closed-form analytical solution for cross-ply laminated shells is introduced and then modified through a higher-order displacement-based layerwise approach. The governing equations are obtained through the application of the minimum total potential energy principle and solved by means of the state-space approach. Finally, the free constants are determined by enforcing the underlying boundary conditions at the traction-free edges. The accuracy of the semi-analytical model concerning the prediction of the free-edge stress field is verified by comparison with three-dimensional finite element computations.

6.2 Structural Situation

This paper considers cross-ply laminated shells of finite length with N perfectly bonded, homogeneous laminate layers, wherein the corresponding geometric parameters R, h, $2\theta_0$ and $2z_0$ refer to the radial position of the mid-plane, the total thickness, the opening angle and the length of the composite shells (Fig. 6.1). A cylindrical $r\theta z$-coordinate system is assigned to the generator of the shell and it is stated that the unidirectional fibers of a $0°$ laminate layer are oriented along the circumferential coordinate θ. The plies are numbered sequentially starting from the innermost one at the inner radius $R_i = R - h/2$. The considered cross-ply laminated shells have traction-free edges at their axial ends $z = 0, 2z_0$ and are subjected to either an arbitrary surface load $q(\theta)$ based on a series expansion of sine and cosine functions or
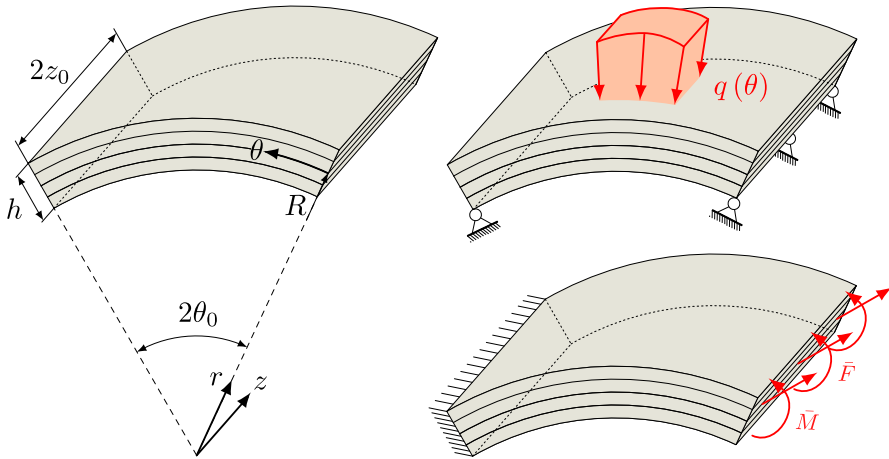
Fig. 6.1: Structural situation of the considered circular cylindrically curved cross-ply laminated shells.

uniform edge loads $\bar{M}$ and $\bar{F}$ at $\theta = 0$. It should be noted that all considered loading conditions do not vary along the length of the composite shells.

6.3 Theoretical Formulation

This section presents the semi-analytical model by, firstly, introducing the closed-form analytical solution which is then modified by a displacement-based layerwise approach in order to enable the assessment of the free-edge stress fields in cross-ply laminated shells. The complete formulation is derived within the perimeters of geometric linearity and linear elastic material behavior.

6.3.1 Closed-Form Analytical Solutions

By considering circular cylindrical composite laminated shells of infinite length undergoing solely mechanical loadings acting in the planes normal to the generator, a generalized plane state of strain with respect to the axial direction is obtained and the displacement components [6] of the lth laminate layer can be described as:

$$u^{(l)}(r,\theta) = U_{\infty}^{(l)}(r,\theta) + u_0 \cos(\theta) + v_0 \sin(\theta) \tag{6.1}$$

$$v^{(l)}(r,\theta) = V_{\infty}^{(l)}(r,\theta) + \omega_3 r - u_0 \sin(\theta) + v_0 \cos(\theta) \tag{6.2}$$

$$w^{(l)}(r,\theta) = W_{\infty}^{(l)}(r,\theta) + w_0 \tag{6.3}$$

Herein, the displacement field is characterized by $u^{(l)}(r,\theta)$, $v^{(l)}(r,\theta)$ and $w^{(l)}(r,\theta)$ which refer to the radial, circumferential and axial displacements of a material point located at a sufficient distance from the boundary-layer region at (r,θ) in the lth laminate layer of the composite laminated shell. The rigid-body translations u_0, v_0 and w_0 and the rigid-body rotation ω_3 about the z-axis are determined by the underlying displacement boundary conditions. The displacement functions $U_\infty^{(l)}(r,\theta)$, $V_\infty^{(l)}(r,\theta)$ and $W_\infty^{(l)}(r,\theta)$, on the other hand, specify the local displacements of an individual laminate ply (l) and are described in a closed-form manner by means of the stress functions $F^{(l)}$ and $\Xi^{(l)}$ that are obtained by solution of following governing equations [6]:

$$L_4'^{(l)} F^{(l)} = 0 \tag{6.4}$$

$$L_2'^{(l)} \Xi^{(l)} = 0 \tag{6.5}$$

Herein, $L_4'^{(l)}$ and $L_2'^{(l)}$ are partial differential operators

$$L_4'^{(l)} = \tilde{S}_{22}^{(l)} \frac{\partial^4}{\partial r^4} + \left(2\tilde{S}_{12}^{(l)} + \tilde{S}_{66}^{(l)}\right) \frac{1}{r^2} \frac{\partial^4}{\partial r^2 \partial \theta^2} + \tilde{S}_{11}^{(l)} \frac{1}{r^4} \frac{\partial^4}{\partial \theta^4} + 2\tilde{S}_{22}^{(l)} \frac{1}{r} \frac{\partial^3}{\partial r^3} - \left(2\tilde{S}_{12}^{(l)} + \right.$$
$$\left. \tilde{S}_{66}^{(l)}\right) \frac{1}{r^3} \frac{\partial^3}{\partial r \partial \theta^2} - \tilde{S}_{11}^{(l)} \frac{1}{r^2} \frac{\partial^2}{\partial r^2} + \left(2\tilde{S}_{11}^{(l)} + 2\tilde{S}_{12}^{(l)} + \tilde{S}_{66}^{(l)}\right) \frac{1}{r^4} \frac{\partial^2}{\partial \theta^2} + \tilde{S}_{11}^{(l)} \frac{1}{r^3} \frac{\partial}{\partial r}$$

$$L_2'^{(l)} = \tilde{S}_{44}^{(l)} \frac{\partial^2}{\partial r^2} + \tilde{S}_{55}^{(l)} \frac{1}{r^2} \frac{\partial^2}{\partial \theta^2} + \tilde{S}_{44}^{(l)} \frac{1}{r} \frac{\partial}{\partial r}$$

and $\tilde{S}_{ij}^{(l)}$ are reduced compliance constants of the corresponding composite material:

$$\tilde{S}_{ij}^{(l)} = S_{ij}^{(l)} - \frac{S_{i3}^{(l)} S_{j3}^{(l)}}{S_{33}^{(l)}} \tag{6.6}$$

Solution of the governing equations (6.4) and (6.5) leads to following formulation of the stress functions:

$$F^{(l)}(r,\theta) = {}^0 f^{(l)}(r) + {}_s^1 f^{(l)}(r) \sin(\theta) + {}_c^1 f^{(l)}(r) \cos(\theta) +$$
$$\sum_\beta {}_s^\beta f^{(l)}(r) \sin(\beta\theta) + \sum_\beta {}_c^\beta f^{(l)}(r) \cos(\beta\theta) \tag{6.7}$$

$$\Xi^{(l)}(r,\theta) = {}^0 \xi^{(l)}(r) + {}_s^1 \xi^{(l)}(r) \sin(\theta) + {}_c^1 \xi^{(l)}(r) \cos(\theta) +$$
$$\sum_\beta {}_s^\beta \xi^{(l)}(r) \sin(\beta\theta) + \sum_\beta {}_c^\beta \xi^{(l)}(r) \cos(\beta\theta) \tag{6.8}$$

with $\beta \in \left\{\frac{n\pi}{\theta_0}\right\}$ $(n = 1, 2, ...)$. It should be emphasized that for $\beta \in \{0,1\}$ and $\beta \geq 2$ as well as for a $90°$ laminate layer wherein $\tilde{S}_{11}^{(l)} = \tilde{S}_{22}^{(l)}$ and $\tilde{S}_{44}^{(l)} = \tilde{S}_{55}^{(l)}$ holds, the governing equations (6.4) and (6.5) and especially the formulations of $f^{(l)}(r)$ and

$\xi^{(l)}(r)$ change. All approaches can be found in the appendix. By making use of (6.7) and (6.8), the stress field

$$\sigma_{rr,\infty}^{(l)}(r,\theta) = \frac{1}{r}\frac{\partial F^{(l)}}{\partial r} + \frac{1}{r^2}\frac{\partial^2 F^{(l)}}{\partial \theta^2},\ \ \sigma_{\theta\theta,\infty}^{(l)}(r,\theta) = \frac{\partial^2 F^{(l)}}{\partial r^2},$$

$$\tau_{r\theta,\infty}^{(l)}(r,\theta) = -\frac{1}{r}\frac{\partial^2 F^{(l)}}{\partial r \partial \theta},\ \ \tau_{\theta z,\infty}^{(l)}(r,\theta) = -\frac{\partial \Xi^{(l)}}{\partial r},\ \ \ \tau_{rz,\infty}^{(l)}(r,\theta) = \frac{1}{r}\frac{\partial \Xi^{(l)}}{\partial \theta}, \quad (6.9)$$

$$\sigma_{zz,\infty}^{(l)}(r,\theta) = -\frac{1}{S_{33}^{(l)}}\left(S_{13}^{(l)}\sigma_{rr,\infty}^{(l)} + S_{23}^{(l)}\sigma_{\theta\theta,\infty}^{(l)}\right)$$

as well as the displacement functions

$$U_\infty^{(l)}(r,\theta) = \int_r \left(\tilde{S}_{11}^{(l)}\sigma_{rr,\infty}^{(l)} + \tilde{S}_{12}^{(l)}\sigma_{\theta\theta,\infty}^{(l)}\right) dr \tag{6.10}$$

$$V_\infty^{(l)}(r,\theta) = \int_\theta \left(r\left(\tilde{S}_{12}^{(l)}\sigma_{rr,\infty}^{(l)} + \tilde{S}_{22}^{(l)}\sigma_{\theta\theta,\infty}^{(l)}\right) - U_\infty^{(l)}(r,\theta)\right) d\theta \tag{6.11}$$

$$W_\infty^{(l)}(r,\theta) = \int_\theta \tilde{S}_{44}^{(l)}\tau_{\theta z,\infty}^{(l)} r\, d\theta \tag{6.12}$$

can be specified. Finally, the constants have to be determined by enforcing the continuity of the displacements and interlaminar stress components in the interfaces of the composite shell as well as through the admissible boundary conditions.

6.3.2 Layerwise Approach

Since the closed-form analytical solution was developed by assuming a generalized plane strain condition, it cannot capture the localized, three-dimensional stress concentrations in the boundary-layer region of the cross-ply laminated shells. Therefore, the presented method has to be upgraded by a layerwise approach. In this regard, the composite shell needs to be discretized with respect to the thickness direction by subdividing each of the N laminate layers into M mathematical layers. For each of the mathematical layers (k) an additional higher-order displacement field is introduced which is specified by means of a product approach (see Fig. 6.2):

$$u^{(k)}(r,\theta,z) = U_\infty^{(l(k))}(r,\theta) + \sum_j U^{(j)}(\theta,z)\,\Phi^{(j)}(r) + u_0(\theta) \tag{6.13}$$

$$v^{(k)}(r,\theta,z) = V_\infty^{(l(k))}(r,\theta) + \sum_j V^{(j)}(\theta,z)\,\Phi^{(j)}(r) + u_0(r,\theta) \tag{6.14}$$

$$w^{(k)}(r,\theta,z) = W_\infty^{(l(k))}(r,\theta) + \sum_j W^{(j)}(\theta,z)\,\Phi^{(j)}(r) + w_0, \tag{6.15}$$
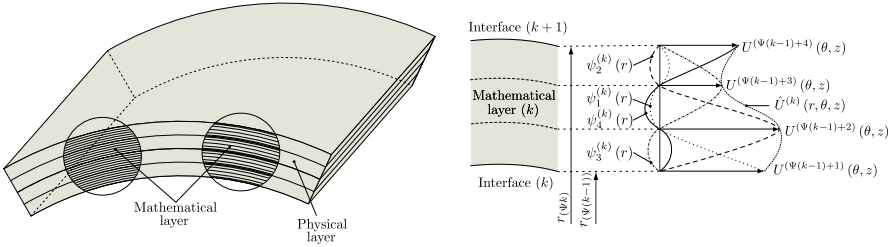
Fig. 6.2: Variable discretisation scheme of the composite laminated shells into mathematical layers and higher-order displacement field of the mathematical layer (k) by the example of $\hat{U}^{(k)}(r,\theta,z)$ with $\Psi = 3$ (adapted from Kappel et al [19]).

wherein $(l(k))$ defines the lth lamina of the according mathematical layer (k) and $j \in \{I(k)+1,...,I(k)+\Psi+1\}$. The parameter Ψ, on the other hand, denotes the order of the global Lagrangian interpolation vector $\Phi^{(j)}(r)$ which is composed of the local shape functions $\psi^{(k)}$ utilized in the course of the layerwise approach and $I(k) = \psi^{(k)}(k-1)$ describes the last grid point of the $(k-1)^{th}$ mathematical layer [15]. By taking the kinematic relations

$$\varepsilon_{rr}^{(k)} = \frac{\partial u^{(k)}}{\partial r}, \; \varepsilon_{\theta\theta}^{(k)} = \frac{1}{r}\left(\frac{\partial v^{(k)}}{\partial \theta} + u^{(k)}\right), \; \varepsilon_{zz}^{(k)} = \frac{\partial w^{(k)}}{\partial z},$$

$$\gamma_{\theta z}^{(k)} = \frac{\partial v^{(k)}}{\partial z} + \frac{1}{r}\frac{\partial w^{(k)}}{\partial \theta}, \; \gamma_{rz}^{(k)} = \frac{\partial w^{(k)}}{\partial r} + \frac{\partial u^{(k)}}{\partial z}, \tag{6.16}$$

$$\gamma_{r\theta}^{(k)} = \frac{1}{r}\left(\frac{\partial u^{(k)}}{\partial \theta} - v^{(k)}\right) + \frac{\partial v^{(k)}}{\partial r},$$

as well as Hooke's generalized law

$$\begin{pmatrix}\sigma_{rr}^{(k)}\\\sigma_{\theta\theta}^{(k)}\\\sigma_{zz}^{(k)}\\\tau_{\theta z}^{(k)}\\\tau_{rz}^{(k)}\\\tau_{r\theta}^{(k)}\end{pmatrix} = \begin{bmatrix}C_{11}^{(k)} & C_{12}^{(k)} & C_{13}^{(k)} & 0 & 0 & 0\\C_{12}^{(k)} & C_{22}^{(k)} & C_{23}^{(k)} & 0 & 0 & 0\\C_{13}^{(k)} & C_{23}^{(k)} & C_{33}^{(k)} & 0 & 0 & 0\\0 & 0 & 0 & C_{44}^{(k)} & 0 & 0\\0 & 0 & 0 & 0 & C_{55}^{(k)} & 0\\0 & 0 & 0 & 0 & 0 & C_{66}^{(k)}\end{bmatrix}\begin{pmatrix}\varepsilon_{rr}^{(k)}\\\varepsilon_{\theta\theta}^{(k)}\\\varepsilon_{zz}^{(k)}\\\gamma_{\theta z}^{(k)}\\\gamma_{rz}^{(k)}\\\gamma_{r\theta}^{(k)}\end{pmatrix}, \tag{6.17}$$

into account, the strain and stress field for each mathematical layer (k) can be computed by means of the unknown two-dimensional displacement functions $U^{(j)}(\theta,z)$, $V^{(j)}(\theta,z)$ and $W^{(j)}(\theta,z)$. Based on (6.16) and (6.17), the total potential energy can be specified as:

$$\Pi_i = \frac{1}{2} \sum_k \int_0^{2z_0} \int_0^{\theta_0} \int_{r_{(k-1)}}^{r_{(k)}} \underline{\varepsilon}^{(k)^T} \underline{\sigma}^{(k)} r \, dr \, d\theta \, dz$$

$$\Pi_e = -\frac{1}{2} \sum_k \int_0^{2z_0} \int_{r_{(k-1)}}^{r_{(k)}} \left(\bar{M} \frac{\partial v^{(k)}}{\partial r} + \bar{F}_r u^{(k)} + \bar{F}_\theta v^{(k)} \right) dr - \tag{6.18}$$

$$\frac{1}{2} \sum_k \int_0^{2z_0} \int_0^{\theta_0} q\left(\theta\right) u^{(k)}|_{r=r_o} r \, d\theta \, dz$$

Employing the minimum total potential energy principle under consideration of the general Euler-Lagrange equations, following governing equations as well as admissible boundary conditions for each grid point (i) can be derived:

$$\delta U^{(i)} : \sum_j \left(-D_{66}^{ij\,(k)} \frac{\partial^2 U^{(j)}}{\partial \theta^2} - A_{55}^{ij\,(k)} \frac{\partial^2 U^{(j)}}{\partial z^2} + \left(\bar{B}_{12}^{ji\,(k)} - \bar{B}_{66}^{ij\,(k)} + D_{22}^{ij\,(k)} + \right. \right.$$

$$D_{66}^{ij\,(k)} \Big) \frac{\partial V^{(j)}}{\partial \theta} + \left(\bar{A}_{13}^{ji\,(k)} - \bar{A}_{55}^{ij\,(k)} + B_{23}^{ij\,(k)} \right) \frac{\partial W^{(j)}}{\partial z} + \left(\tilde{A}_{11}^{ij\,(k)} + \right. \tag{6.19}$$

$$\bar{B}_{12}^{ij\,(k)} + \bar{B}_{12}^{ji\,(k)} + D_{22}^{ij\,(k)} \Big) U^{(j)} \Big) = \bar{F}_r^{(i)} - \tilde{N}_{rr,\infty}^{(i)} - \bar{N}_{\theta\theta,\infty}^{(i)} +$$

$$q \sin\left(\beta\theta\right) \Phi^{(N_I)} \Big|_{r=r_o}$$

$$\delta V^{(i)} : \sum_j \left(-D_{22}^{ij\,(k)} \frac{\partial^2 V^{(j)}}{\partial \theta^2} - \left(B_{23}^{ij\,(k)} + B_{44}^{ij\,(k)} \right) \frac{\partial^2 W^{(j)}}{\partial \theta \partial z} - A_{44}^{ij\,(k)} \frac{\partial^2 V^{(j)}}{\partial z^2} + \right.$$

$$\left(\bar{B}_{66}^{ji\,(k)} - \bar{B}_{12}^{ij\,(k)} - D_{22}^{ij\,(k)} - D_{66}^{ij\,(k)} \right) \frac{\partial U^{(j)}}{\partial \theta} + \left(\tilde{A}_{66}^{ij\,(k)} - \bar{B}_{66}^{ij\,(k)} - \right. \tag{6.20}$$

$$\bar{B}_{66}^{ji\,(k)} + D_{66}^{ij\,(k)} \Big) V^{(j)} \Big) = \bar{F}_\theta^{(i)} + \bar{M}^{(i)} - \tilde{Q}_{r\theta,\infty}^{(i)} + \bar{Q}_{r\theta,\infty}^{(i)}$$

$$\delta W^{(i)} : \sum_j \left(-D_{44}^{ij\,(k)} \frac{\partial^2 W^{(j)}}{\partial \theta^2} - \left(B_{23}^{ij\,(k)} + B_{44}^{ij\,(k)} \right) \frac{\partial^2 V^{(j)}}{\partial \theta \partial z} - A_{33}^{ij\,(k)} \frac{\partial^2 W^{(j)}}{\partial z^2} + \right.$$

$$\left(\bar{A}_{55}^{ji\,(k)} - \bar{A}_{13}^{ij\,(k)} - B_{23}^{ij\,(k)} \right) \frac{dU^{(j)}}{dz} + \tilde{A}_{55}^{ij\,(k)} W^{(j)} \Big) = \tilde{Q}_{rz,\infty}^{(i)}$$

$$\tag{6.21}$$

$$\delta U^{(i)} : \sum_j \int_0^{\theta_0} \left(A_{55}^{ij\,(k)} \frac{\partial U^{(j)}}{\partial z} + \bar{A}_{55}^{ij\,(k)} W^{(j)} + Q_{rz,\infty}^{(i)} \right) \Big|_{z=0}^{z=2z_0} r \, d\theta = 0 \tag{6.22}$$

$$\delta V^{(i)} : \sum_j \int_0^{\theta_0} \left(B_{44}^{ij\,(k)} \frac{\partial W^{(j)}}{\partial \theta} + A_{44}^{ij\,(k)} \frac{\partial V^{(j)}}{\partial z} + Q_{\theta z,\infty}^{(i)} \right) \Big|_{z=0}^{z=2z_0} r \, d\theta = 0 \tag{6.23}$$

$$\delta W^{(i)} : \sum_j \int_0^{\theta_0} \left(B_{23}^{ij\,(k)} \frac{\partial V^{(j)}}{\partial \theta} + A_{33}^{ij\,(k)} \frac{\partial W^{(j)}}{\partial z} + \left(\bar{A}_{13}^{ij\,(k)} + B_{23}^{ij\,(k)} \right) U^{(j)} + \right.$$

$$N_{zz,\infty}^{(i)} \Big) \Big|_{z=0}^{z=2z_0} r \, d\theta = 0 \tag{6.24}$$

with $j \in \{I(k)+1, ..., I(k)+\Psi+1\}$. The abbreviations are specified in the appendix. In order to solve the coupled system of partial differential equations, following approach for the a priori unknown displacement functions has to be utilized:

$$U^{(j)}(\theta,z) = {}^{0}U^{(j)}(z) + \sum_{\beta}\left({}^{\beta}_{s}U^{(j)}(z)\sin(\beta\theta) + {}^{\beta}_{c}U^{(j)}(z)\cos(\beta\theta)\right) \qquad (6.25)$$

$$V^{(j)}(\theta,z) = {}^{0}V^{(j)}(z) + \sum_{\beta}\left({}^{\beta}_{s}V^{(j)}(z)\sin(\beta\theta) + {}^{\beta}_{c}V^{(j)}(z)\cos(\beta\theta)\right) \qquad (6.26)$$

$$W^{(j)}(\theta,z) = {}^{0}W^{(j)}(z) + \sum_{\beta}\left({}^{\beta}_{s}W^{(j)}(z)\sin(\beta\theta) + {}^{\beta}_{c}W^{(j)}(z)\cos(\beta\theta)\right) \qquad (6.27)$$

with $\beta \in \left\{1, \frac{n\pi}{\theta_0}\right\}$ ($n = 1, 2, ...$). This leads to following ordinary differential equation systems

$$\left({}^{0}\underline{\underline{\tilde{K}}}_1\,{}^{0}\underline{\tilde{U}}_{,zz} + {}^{0}\underline{\underline{\tilde{K}}}_2\,{}^{0}\underline{\tilde{U}}_{,z} + {}^{0}\underline{\underline{\tilde{K}}}_3\,{}^{0}\underline{\tilde{U}} - {}^{0}\underline{\tilde{R}}\right) +$$

$$\sum_{\beta}\left({}^{\beta}_{s}\underline{\underline{\tilde{K}}}_1\,{}^{\beta}_{s}\underline{\tilde{U}}_{,zz} + {}^{\beta}_{s}\underline{\underline{\tilde{K}}}_2\,{}^{\beta}_{s}\underline{\tilde{U}}_{,z} + {}^{\beta}_{s}\underline{\underline{\tilde{K}}}_3\,{}^{\beta}_{s}\underline{\tilde{U}} - {}^{\beta}_{s}\underline{\tilde{R}}\right)\sin(\beta\theta) + \qquad (6.28)$$

$$\sum_{\beta}\left({}^{\beta}_{c}\underline{\underline{\tilde{K}}}_1\,{}^{\beta}_{c}\underline{\tilde{U}}_{,zz} + {}^{\beta}_{c}\underline{\underline{\tilde{K}}}_2\,{}^{\beta}_{c}\underline{\tilde{U}}_{,z} + {}^{\beta}_{c}\underline{\underline{\tilde{K}}}_3\,{}^{\beta}_{c}\underline{\tilde{U}} - {}^{\beta}_{c}\underline{\tilde{R}}\right)\cos(\beta\theta) = \underline{0}$$

as well as boundary conditions

$$\left({}^{0}\underline{\underline{\tilde{k}}}_1\,{}^{0}\underline{\tilde{U}}_{,z} + {}^{0}\underline{\underline{\tilde{k}}}_2\,{}^{0}\underline{\tilde{U}} - {}^{0}\underline{\tilde{r}}\right)\Big|_{z=0}^{z=2z_0} +$$

$$\sum_{\beta}\left({}^{\beta}_{s}\underline{\underline{\tilde{k}}}_1\,{}^{\beta}_{s}\underline{\tilde{U}}_{,z} + {}^{\beta}_{s}\underline{\underline{\tilde{k}}}_2\,{}^{\beta}_{s}\underline{\tilde{U}} - {}^{\beta}_{s}\underline{\tilde{r}}\right)\Big|_{z=0}^{z=2z_0}\sin(\beta\theta) + \qquad (6.29)$$

$$\sum_{\beta}\left({}^{\beta}_{c}\underline{\underline{\tilde{k}}}_1\,{}^{\beta}_{c}\underline{\tilde{U}}_{,z} + {}^{\beta}_{c}\underline{\underline{\tilde{k}}}_2\,{}^{\beta}_{c}\underline{\tilde{U}} - {}^{\beta}_{c}\underline{\tilde{r}}\right)\Big|_{z=0}^{z=2z_0}\cos(\beta\theta) = \underline{0}$$

for each β which, however, can be solved independently from each other by only considering the systems in the round brackets. Herein, each of the displacement function vectors $\underline{\tilde{U}}$ comprises all corresponding one-dimensional displacement functions $U^{(j)}(z)$, $V^{(j)}(z)$ and $W^{(j)}(z)$, while the $\tilde{K}$- and $\tilde{k}$-matrices are formulated in a closed-form manner. The exact formulations can be found in the appendix.

6.3.3 Semi-Analytical Solution

As already pointed out, each ordinary differential equation system

$$\underline{\tilde{\underline{K}}_1}\,\underline{\tilde{U}}_{,zz} + \underline{\tilde{\underline{K}}_2}\,\underline{\tilde{U}}_{,z} + \underline{\tilde{\underline{K}}_3}\,\underline{\tilde{U}} = \underline{\tilde{R}} \tag{6.30}$$

in (6.28) can be solved by means of the so-called state-space approach [19] wherein the state-space variable is defined as:

$$\underline{\tilde{X}}(z) = \underline{\tilde{U}}_{,z} \tag{6.31}$$

Consequently, the system of inhomogeneous, ordinary differential equations of second order can be reformulated into a system of differential equations of first order:

$$\begin{pmatrix} \underline{\tilde{U}} \\ \underline{\tilde{X}} \end{pmatrix}_{,z} = - \begin{bmatrix} \underline{0} & -\underline{I} \\ \underline{\tilde{K}_1^{-1}}\,\underline{\tilde{K}_3} & \underline{\tilde{K}_1^{-1}}\,\underline{\tilde{K}_3} \end{bmatrix} \begin{pmatrix} \underline{\tilde{U}} \\ \underline{\tilde{X}} \end{pmatrix} - \begin{pmatrix} \underline{0} \\ \underline{\tilde{K}_1^{-1}}\,\underline{\tilde{R}} \end{pmatrix}, \tag{6.32}$$

or rather summarized as $\underline{\hat{X}}_{,z} = \underline{\hat{\underline{K}}}\,\underline{\hat{X}} + \underline{\hat{R}}$. Employing the approach

$$\underline{\hat{X}} = \underline{\hat{\underline{A}}}\,\underline{\hat{Y}} \tag{6.33}$$

wherein $\underline{\hat{\underline{A}}}$ is the matrix of eigenvectors of $\underline{\hat{\underline{K}}}$ and $\underline{\hat{Y}}$ is a vector of unknown variables, yields the following uncoupled inhomogeneous ordinary differential equations:

$$\underline{\hat{Y}}_{,z} - \underline{\underline{\Lambda}}\,\underline{\hat{Y}} = \underline{\hat{\underline{A}}}^{-1}\,\underline{\hat{R}} \tag{6.34}$$

Herein, $\underline{\underline{\Lambda}} = \mathrm{diag}\left(\lambda_1, \ldots, \lambda_{\kappa(\Psi N_L + 1)}\right)$ is the diagonal matrix consisting of the eigenvalues of $\underline{\hat{\underline{K}}}$. The homogeneous solution of (6.34) is denoted as:

$$\underline{\hat{X}} = \underline{\hat{\underline{A}}}\,\underline{\underline{E}}\,B \tag{6.35}$$

wherein $\underline{\underline{E}}(z) = \mathrm{diag}\left(\exp(\lambda_1 z), \ldots, \exp(\lambda_{\kappa N_I} z)\right)$ and $\underline{B}$ is a vector consisting of the free constants that have to be determined through the boundary conditions (6.29). Since the right-side vector only contains scalar values, only the homogeneous solution has to be considered in the further course. This concludes the development of the semi-analytical approach.

6.4 Results and Discussion

The following section provides an insight into the accuracy of the presented semi-analytical method ('SA') by comparing the numerical results with full-scale, three-dimensional finite element computations ('FE') carried out using the commercial tool Abaqus FEA. The FE model uses hexahedral, twenty-node 'C3D20R' elements with quadratic shape functions and reduced integration (see also Kappel and Mittelstedt [15]). In addition, it should be noted, that from a physical point of view, the interlaminar stresses σ_{rr}, τ_{rz} and $\tau_{r\theta}$ have to fulfill the condition of continuity across the interfaces

of the considered cross-ply laminated shells. However, since the finite element method is not able to meet those requirements, in the following mean values in the interfaces of adjacent plies are presented [15].

The thickness of each laminate layer in all considered composite shells is defined as $d_L = 0.25$ mm. The computations are carried out by means of the following material properties for a Carbon/PEEK composite laminate [19]:

$$E_1 = 143\,\text{GPa}, \, E_2 = E_3 = 9.1\,\text{GPa},$$
$$G_{23} = 4.82\,\text{GPa}, \, G_{12} = G_{13} = 4.9\,\text{GPa},$$
$$\nu_{12} = \nu_{13} = \nu_{23} = 0.3$$

wherein the indices 1,2 and 3 define the on-axis material coordinates. Further on, only the interlaminar stresses are investigated in detail and all numerical results are presented using the following non-dimensional coordinates [19]:

$$\bar{r} = \frac{r - R}{h}, \quad \bar{z} = \frac{z - z_0}{2z_0}$$

6.4.1 Verification of Accuracy for Cross-Ply Laminated Shells Undergoing Uniform Edge Loads

Figures 6.3 and 6.4 illustrate the decaying behavior of the localized interlaminar stress gradients in the three interfaces of the symmetric $[0°/90°]_S$ and unsymmetric $[0°/90°]_2$ cross-ply laminated shells that are subjected to uniform edge loads $\bar{M}$ and $\bar{F}$. As expected, σ_{rr} and τ_{rz} attain a striking stress peak directly at the traction-free edges and then converge to the stress state in the inner laminate region. The third interlaminar stress component $\tau_{r\theta}$, on the other hand, is characterized by a rather constant value across the length of the considered cross-ply laminated shells. Furthermore, it is important to take into account, that in both displayed examples, the out-of-plane normal stresses act as tensile stresses perpendicular to the laminate layer where a very low transverse strength is encountered and thus indicate a potential endangerment for free-edge delaminations which eventually will commence in interface 1 due to the potential positive singular stress of σ_{rr} at $\bar{z} = -0.5$. Other than that, an excellent accordance concerning the numerical results of the semi-analytical approach and the finite element method can be observed.

6.4.2 Verification of accuracy for cross-ply laminated shells undergoing sinusoidal outer perssure

Figures 6.5 and 6.6 present results concerning the interlaminar stress distribution in axial direction in all three interfaces for two different angles for the same cross-ply
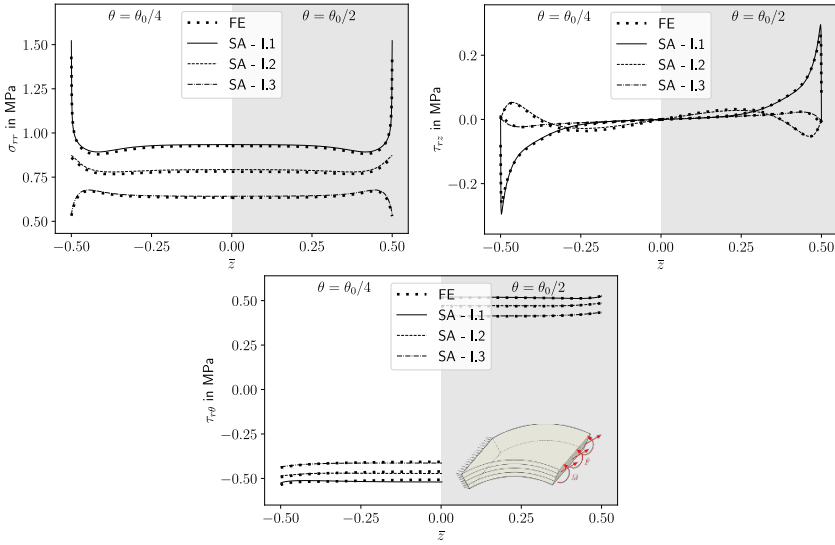
Fig. 6.3: Interlaminar stresses σ_{rr}, τ_{rz} and $\tau_{r\theta}$ in MPa in all interfaces at $\bar{r} = (-0.25, 0.0, 0.25)$ for the symmetric $[0°/90°]_S$ composite laminate ($R/h = 4$, $2z_0/h = 4$) subjected to uniform edge loadings $\bar{M} = 1$ N, $\bar{F}_r = 1$ N/mm and $\bar{F}_\theta = 1$ N/mm with $\theta_0 = 2\pi/3$.
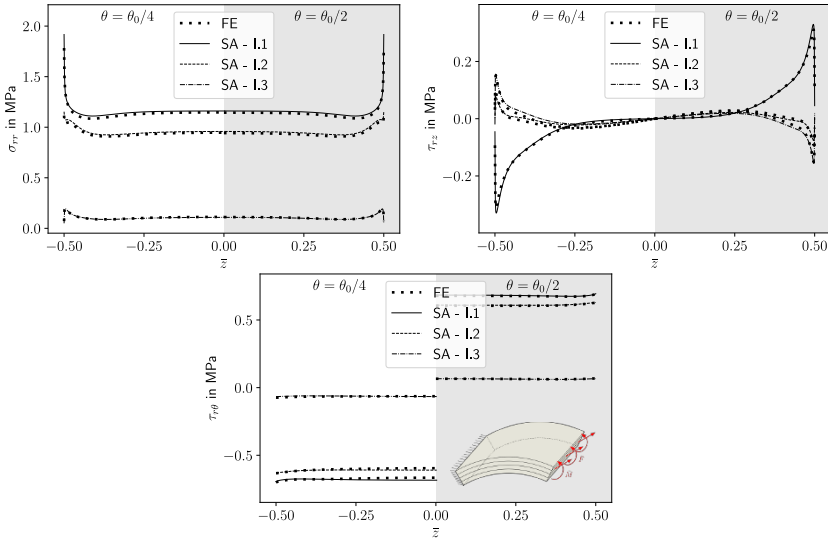
Fig. 6.4: Interlaminar stresses σ_{rr}, τ_{rz} and $\tau_{r\theta}$ in MPa in all interfaces at $\bar{r} = (-0.25, 0.0, 0.25)$ for the unsymmetric $[0°/90°]_2$ composite laminate ($R/h = 4$, $2z_0/h = 4$) subjected to uniform edge loadings $\bar{M} = 1$ N, $\bar{F}_r = 1$ N/mm and $\bar{F}_\theta = 1$ N/mm with $\theta_0 = 2\pi/3$.
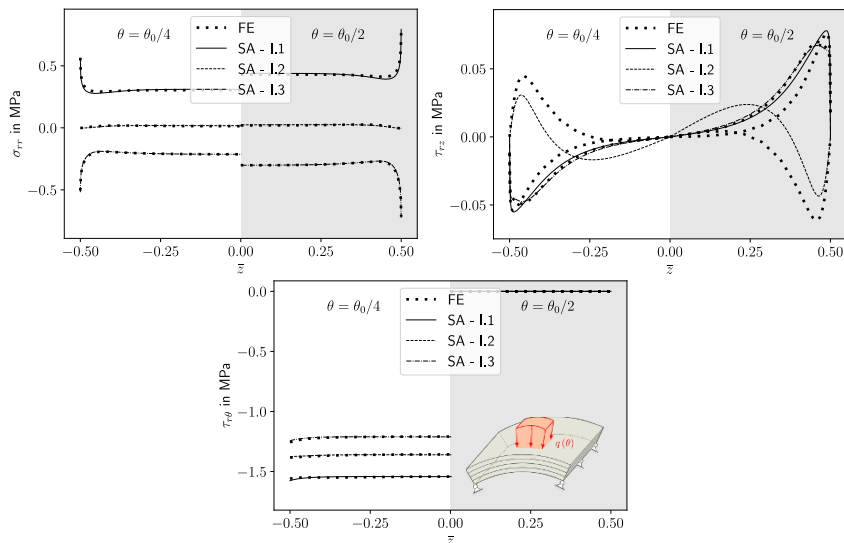
Fig. 6.5: Interlaminar stresses σ_{rr}, τ_{rz} and $\tau_{r\theta}$ in MPa in all interfaces at $\bar{r} = (-0.25, 0.0, 0.25)$ for the symmetric $[0°/90°]_S$ composite laminate ($R/h = 4$, $2z_0/h = 4$) subjected to a sinusoidal outer pressure $q(\theta) = \sin(\pi\theta/\theta_0)$ and $\theta_0 = \pi/3$.

laminated shells as already discussed in the previous section but now subjected to an outer surface load $q(\theta) = q\sin(\pi\theta/\theta_0)$ with $q = 1$ which acts in negative radial direction. With regard to the decaying behavior of the interlaminar stress gradients in the interfaces, similar accordance for the predictions as in Figs. 6.3 and 6.4 have been observed.

6.5 Concluding Remarks

In this contribution, a generalized semi-analytical model for the computation of the free-edge stress field in thick, finite length, circular cylindrical cross-ply laminated shells has been presented. The closed-form analytical method has been derived assuming a plane strain state and the resulting displacement components have been modified by three-dimensional, higher-order, displacement-based layerwise approaches in order to be able to investigate the free-edge stress field in the boundary-layer region of cross-ply laminated shells. The governing equations as well as the admissible boundary conditions are obtained by employing the general Euler-Lagrange equations and are solved by means of the state-space approach. The accuracy of the developed analysis methods has been verified through comparison with three-dimensional finite element computations, wherein hexahedral elements with quadratic shape functions and reduced integration were considered. The numerical results revealed excellent
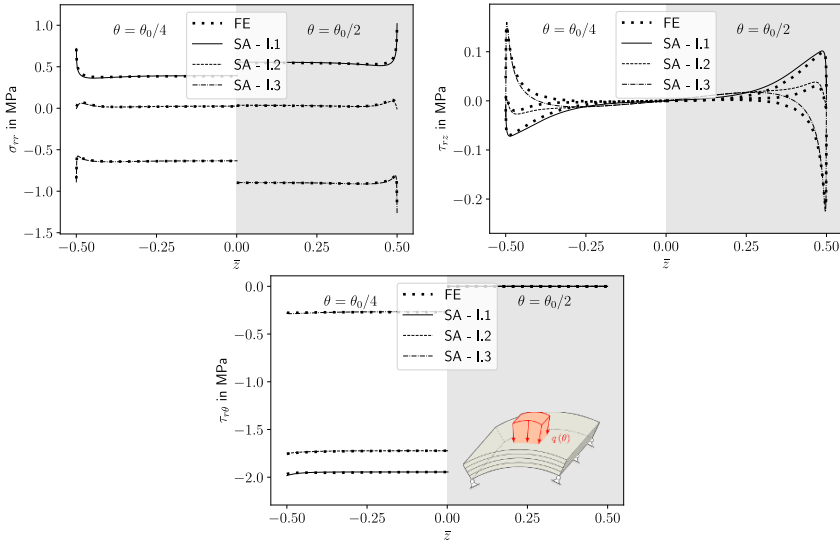
Fig. 6.6: Interlaminar stresses σ_{rr}, τ_{rz} and $\tau_{r\theta}$ in MPa in all interfaces at $\bar{r} = (-0.25, 0.0, 0.25)$ for the unsymmetric $[0°/90°]_2$ composite laminate ($R/h = 4$, $2z_0/h = 4$) subjected to a sinusoidal outer pressure $q(\theta) = \sin(\pi\theta/\theta_0)$ and $\theta_0 = \pi/3$.

agreement between both methods making the presented semi-analytical method especially useful for structural optimization due to its computational efficiency.

Appendix A

A.1 Stress Function Approaches

Fibre angle $\varphi = 0°$:

$$
{}^0 f(r) = {}^0C_1 r^2 + \sum_{k=3}^{4} {}^0C_k r^{1+\mu_{0,k}}, \quad {}^0\xi(r) = {}^0C_2 \ln(r) \tag{6.36}
$$

$$
{}_{s|c}^{1} f(r) = {}_{s|c}^{1}C_1 r + {}_{s|c}^{1}C_2 r \ln(r) + \sum_{k=3}^{4} {}_{s|c}^{1}C_k r^{1+\mu_{1,k}}, \quad {}_{s|c}^{1}\xi(r) = \sum_{k=5}^{6} {}_{s|c}^{1}C_k r^{\mu_{1,k}} \tag{6.37}
$$

$$\underset{s|c}{^\beta} f(r) = \sum_{k=1}^{4} \underset{s|c}{^\beta} C_k r^{1+\mu_{\beta,k}}, \qquad \underset{s|c}{^\beta} \xi(r) = \sum_{k=5}^{6} \underset{s|c}{^\beta} C_k r^{\mu_{\beta,k}} \tag{6.38}$$

wherein the material parameters are computed as:

$$\alpha_{\beta,1} = \tilde{S}_{22}, \quad \alpha_{\beta,2} = -\left(\tilde{S}_{11} + \tilde{S}_{22} + (2\tilde{S}_{12} + \tilde{S}_{66})\beta^2\right), \quad \alpha_{\beta,3} = \tilde{S}_{11}\left(\beta^2 - 1\right)^2$$

$$\mu_{0,3|4} = \pm\sqrt{\frac{\tilde{S}_{11}}{\tilde{S}_{22}}}, \quad \mu_{1,3|4} = \pm\sqrt{1 + \frac{\tilde{S}_{11} + 2\tilde{S}_{12} + \tilde{S}_{66}}{\tilde{S}_{22}}}, \quad \mu_{1,5|6} = \pm\sqrt{\frac{\tilde{S}_{55}}{\tilde{S}_{44}}} \tag{6.39}$$

$$\mu_{\beta,1|\ldots|4} = \pm\sqrt{-\left(\frac{\alpha_{\beta,2}}{2\alpha_{\beta,1}}\right) \pm \sqrt{\left(\frac{\alpha_{\beta,2}}{2\alpha_{\beta,1}}\right)^2 - \left(\frac{\alpha_{\beta,3}}{\alpha_{\beta,1}}\right)}}, \quad \mu_{\beta,5|6} = \pm\sqrt{\beta^2 \frac{\tilde{S}_{55}}{\tilde{S}_{44}}} \tag{6.40}$$

Fibre angle $\varphi = 90°$:

$$^0 f(r) = {^0}C_1 \ln(r) + {^0}C_3 r^2 + {^0}C_4 r^2 \ln(r), \quad {^0}\xi(r) = {^0}C_2 \ln(r) \tag{6.41}$$

$$\underset{s|c}{^1} f(r) = \underset{s|c}{^1}C_1 r + \underset{s|c}{^1}C_2 r \ln(r) + \sum_{k=3}^{4} \underset{s|c}{^1}C_k r^{1+\mu_{1,k}}, \qquad \underset{s|c}{^1}\xi(r) = \underset{s|c}{^1}C_5 r + \underset{s|c}{^1}C_6 \frac{1}{r}$$

$$\tag{6.42}$$

$$\underset{s|c}{^\beta} f(r) = \sum_{k=1}^{4} \underset{s|c}{^\beta} C_k r^{1+\mu_{\beta,k}}, \qquad \underset{s|c}{^\beta} \xi(r) = \sum_{k=5}^{6} \underset{s|c}{^\beta} C_k r^{\mu_{\beta,k}} \tag{6.43}$$

wherein the material parameters are computed as:

$$\alpha_{\beta,1} = \tilde{S}_{22}, \quad \alpha_{\beta,2} = -\left(2\tilde{S}_{22} + (2\tilde{S}_{12} + \tilde{S}_{66})\beta^2\right), \quad \alpha_{\beta,3} = \tilde{S}_{22}\left(\beta^2 - 1\right)^2$$

$$\mu_{1,3|4} = \pm\sqrt{2 + \frac{2\tilde{S}_{12} + \tilde{S}_{66}}{\tilde{S}_{22}}} \tag{6.44}$$

$$\mu_{\beta,1|\ldots|4} = \pm\sqrt{-\left(\frac{\alpha_{\beta,2}}{2\alpha_{\beta,1}}\right) \pm \sqrt{\left(\frac{\alpha_{\beta,2}}{2\alpha_{\beta,1}}\right)^2 - \left(\frac{\alpha_{\beta,3}}{\alpha_{\beta,1}}\right)}}, \quad \mu_{\beta,5|6} = \pm\beta \tag{6.45}$$

A.2 Global Interpolation Vector

Definition of the underlying sets with $N_L = N \times M$, $N_I = \Psi(N \times M) + 1$ and $I(k) = \Psi(k-1)$ being the last node of the $(k-1)^{\text{th}}$ numerical layer:

$$S_N = \{1, 2, ..., N\}, \quad S_M = \{1, 2, ..., M\}, \quad S_{N_L} = \{1, 2, ..., N \times M\},$$
$$S_{N_I} = \{1, 2, ..., \Psi(N \times M) + 1\}, \quad S_{N_{I,k}} = \{I(k)+1, I(k)+2, ..., I(k)+\Psi+1\},$$
$$S_{N_{I,r}} = \{I(k), I(k)+1, ..., I(k)+\Psi\}, \quad S_\Psi = \{1, 2, ..., \Psi+1\}$$

The global interpolation vector is described by $\Phi^{(j)}(r)$ which is defined as follows for an arbitrary interpolation order Ψ:

$$\Phi^{(1)}(r) = \psi_1^{(1)}(r), \, r_{(0)} \leq r \leq r_{(\Psi)}$$

$$\vdots$$

$$\Phi^{(\Psi k - \Psi + 1)}(r) = \psi_1^{(k)}(r), \, r_{(\Psi k - \Psi)} \leq r \leq r_{(\Psi k)} \, \left(k \in S_{N_L}\right)$$

$$\vdots$$

$$\Phi^{(\Psi k - 1)}(r) = \psi_{\Psi - 1}^{(k)}(r), \, r_{(\Psi k - \Psi)} \leq r \leq r_{(\Psi k)} \, \left(k \in S_{N_L}\right)$$

$$\Phi^{(\Psi k)}(r) = \psi_\Psi^{(k)}(r), \, r_{(\Psi k - \Psi)} \leq r \leq r_{(\Psi k)} \, \left(k \in S_{N_L}\right) \tag{6.46}$$

$$\Phi^{(\Psi k + 1)}(r) = \begin{cases} \psi_{\Psi+1}^{(k)}(r), & r_{(\Psi k - \Psi)} \leq r \leq r_{(\Psi k)} \\ \psi_1^{(k+1)}(r), & r_{(\Psi k)} \leq r \leq r_{(\Psi k + \Psi)} \end{cases} \, \left(k \in S_{N_L} \setminus N_L\right)$$

$$\vdots$$

$$\Phi^{(N_I)}(r) = \psi_{\Psi+1}^{(N_L)}(r), \, r_{(N_I - \Psi + 1)} \leq r \leq r_{(N_I - 1)},$$

with

$$\psi_j^{(k)} = \begin{cases} \prod_{p \in S_{N_{I,r}}, p \neq q} \left(\frac{r - r_{(p)}}{r_{(q)} - r_{(p)}}\right), & n \in S_\Psi \\ 0, & \text{other} \end{cases} \tag{6.47}$$

A.3 Abbreviations

$$\left\{ A_{op}^{mn\,(k)}, \bar{A}_{op}^{mn\,(k)} \right\} = \int_{r_{(k-1)}}^{r_{(k)}} C_{op}^{(k)} \left\{ \Phi^{(m)}\Phi^{(n)}, \Phi^{(m)}\Phi_{,r}^{(n)} \right\} dr \qquad (6.48)$$

$$\left\{ B_{op}^{mn\,(k)}, \bar{B}_{op}^{mn\,(k)} \right\} = \int_{r_{(k-1)}}^{r_{(k)}} C_{op}^{(k)} \left\{ \Phi^{(m)}\Phi^{(n)}, \Phi^{(m)}\Phi_{,r}^{(n)} \right\} \frac{1}{r} dr \qquad (6.49)$$

$$\left\{ \tilde{A}_{op}^{mn\,(k)}, D_{op}^{mn\,(k)} \right\} = \int_{r_{(k-1)}}^{r_{(k)}} C_{op}^{(k)} \left\{ \Phi_{,r}^{(m)}\Phi_{,r}^{(n)}, \Phi^{(m)}\Phi^{(n)} \frac{1}{r^2} \right\} dr \qquad (6.50)$$

$$\left\{ a_{op}^{mn\,(k)}, \bar{a}_{op}^{mn\,(k)} \right\} = \int_{r_{(k-1)}}^{r_{(k)}} C_{op}^{(k)} \left\{ \Phi^{(m)}\Phi^{(n)}, \Phi^{(m)}\Phi_{,r}^{(n)} \right\} r\, dr \qquad (6.51)$$

$$\left\{ N_{zz,\infty}^{(i)}, Q_{\theta z,\infty}^{(i)}, Q_{rz,\infty}^{(i)} \right\} = \int_{r_{(k-1)}}^{r_{(k)}} \left\{ \sigma_{zz,\infty}^{(k)}, \tau_{\theta z,\infty}^{(k)}, \tau_{r\theta,\infty}^{(k)} \right\} \Phi^{(i)} dr \qquad (6.52)$$

$$\left\{ \bar{N}_{\theta\theta,\infty}^{(i)}, \bar{Q}_{\theta z,\infty}^{(i)}, \bar{Q}_{r\theta,\infty}^{(i)} \right\} = \int_{r_{(k-1)}}^{r_{(k)}} \left\{ \frac{1}{r}\sigma_{\theta\theta,\infty}^{(k)}, \frac{1}{r}\tau_{\theta z,\infty}^{(k)}, \frac{1}{r}\tau_{r\theta,\infty}^{(k)} \right\} \Phi^{(i)} dr \qquad (6.53)$$

$$\left\{ \tilde{N}_{rr,\infty}^{(i)}, \tilde{Q}_{r\theta,\infty}^{(i)}, \tilde{Q}_{rz,\infty}^{(i)} \right\} = \int_{r_{(k-1)}}^{r_{(k)}} \left\{ \sigma_{rr,\infty}^{(k)}, \tau_{r\theta,\infty}^{(k)}, \tau_{rz,\infty}^{(k)} \right\} \Phi_{,r}^{(i)} dr \qquad (6.54)$$

$$\left\{ \bar{F}_r^{(i)}, \bar{F}_\theta^{(i)}, q^{(i)}, \bar{M}^{(i)} \right\} = \int_{r_{(k-1)}}^{r_{(k)}} \left\{ \bar{F}_r\Phi^{(i)}, \bar{F}_\theta\Phi^{(i)}, q\Phi^{(i)}, \bar{M}\Phi_{,r}^{(i)} \right\} dr \qquad (6.55)$$

A.4 Coefficient Matrices

Provided that not mentioned positions in the matrix are set to zero and with

$$(i,j) = I(k) + (i,j) = \Psi(k-1) + (i,j)$$

the coefficient matrices are built as (with $\beta \in \left\{ 1, \frac{n\pi}{\theta_0} \right\}$ $(n = 1,2,...))$:

$$\left\{ {}^0\tilde{K}_1, {}^0\tilde{K}_2, {}^0\tilde{K}_3 \right\} := \left\{ \begin{bmatrix} {}^0K_1 & 0 & 0 \\ 0 & {}^0K_2 & 0 \\ 0 & 0 & {}^0K_3 \end{bmatrix}, \begin{bmatrix} 0 & 0 & {}^0K_4 \\ 0 & 0 & 0 \\ {}^0K_5 & 0 & 0 \end{bmatrix}, \begin{bmatrix} {}^0K_6 & 0 & 0 \\ 0 & {}^0K_7 & 0 \\ 0 & 0 & {}^0K_8 \end{bmatrix} \right\}$$

$${}^0\tilde{K}_1: \quad {}^0K_1 = \left[-A_{55}^{ij\,(k)} \right], \quad {}^0K_2 = \left[-A_{44}^{ij\,(k)} \right], \quad {}^0K_3 = \left[-A_{33}^{ij\,(k)} \right],$$

$${}^0\tilde{K}_2: \quad {}^0K_4 = \left[\bar{A}_{13}^{ji\,(k)} - \bar{A}_{55}^{ij\,(k)} + B_{23}^{ij\,(k)} \right], {}^0K_5 = - {}^0K_4^T$$

$${}^0\tilde{K}_3: \quad {}^0K_6 = \left[\tilde{A}_{11}^{ij\,(k)} + \bar{B}_{12}^{ij\,(k)} + \bar{B}_{12}^{ji\,(k)} + D_{22}^{ij\,(k)} \right], {}^0K_7 = \left[\tilde{A}_{66}^{ij\,(k)} - \bar{B}_{66}^{ij\,(k)} - \right.$$
$$\bar{B}_{66}^{ji\,(k)} + D_{66}^{ij\,(k)} \right], {}^0K_8 = \left[\tilde{A}_{55}^{ij\,(k)} \right]$$

$$\left\{ {}^{\beta}_{s}\underline{\underline{\tilde{K}}}_1, {}^{\beta}_{s}\underline{\underline{\tilde{K}}}_2, {}^{\beta}_{s}\underline{\underline{\tilde{K}}}_3 \right\} := \left\{ \begin{bmatrix} {}^{\beta}_{s}\underline{\underline{K}}_1 & \underline{\underline{0}} & \underline{\underline{0}} \\ \underline{\underline{0}} & {}^{\beta}_{s}\underline{\underline{K}}_2 & \underline{\underline{0}} \\ \underline{\underline{0}} & \underline{\underline{0}} & {}^{\beta}_{s}\underline{\underline{K}}_3 \end{bmatrix}, \begin{bmatrix} \underline{\underline{0}} & \underline{\underline{0}} & {}^{\beta}_{s}\underline{\underline{K}}_4 \\ \underline{\underline{0}} & \underline{\underline{0}} & {}^{\beta}_{s}\underline{\underline{K}}_5 \\ {}^{\beta}_{s}\underline{\underline{K}}_6 & {}^{\beta}_{s}\underline{\underline{K}}_7 & \underline{\underline{0}} \end{bmatrix}, \begin{bmatrix} {}^{\beta}_{s}\underline{\underline{K}}_8 & {}^{\beta}_{s}\underline{\underline{K}}_9 & \underline{\underline{0}} \\ {}^{\beta}_{s}\underline{\underline{K}}_{10} & {}^{\beta}_{s}\underline{\underline{K}}_{11} & \underline{\underline{0}} \\ \underline{\underline{0}} & \underline{\underline{0}} & {}^{\beta}_{s}\underline{\underline{K}}_{12} \end{bmatrix} \right\}$$

$${}^{\beta}_{s}\underline{\underline{\tilde{K}}}_1 : \quad {}^{\beta}_{s}\underline{\underline{K}}_1 = {}^{0}\underline{\underline{K}}_1, \; {}^{\beta}_{s}\underline{\underline{K}}_2 = {}^{0}\underline{\underline{K}}_2 \; {}^{\beta}_{s}\underline{\underline{K}}_3 = {}^{0}\underline{\underline{K}}_3,$$

$${}^{\beta}_{s}\underline{\underline{\tilde{K}}}_2 : \quad {}^{\beta}_{s}\underline{\underline{K}}_5 = \left[-\left(B_{23}^{ij(k)} + B_{44}^{ij(k)} \right)\beta \right], \; {}^{\beta}_{s}\underline{\underline{K}}_4 = {}^{0}\underline{\underline{K}}_4, \; {}^{\beta}_{s}\underline{\underline{K}}_6 = -{}^{0}\underline{\underline{K}}_4^T, \; {}^{\beta}_{s}\underline{\underline{K}}_7 = -{}^{\beta}_{s}\underline{\underline{K}}_5^T$$

$${}^{\beta}_{s}\underline{\underline{\tilde{K}}}_3 : \quad {}^{\beta}_{s}\underline{\underline{K}}_8 = \left[\tilde{A}_{11}^{ij(k)} + \bar{B}_{12}^{ij(k)} + \bar{B}_{12}^{ji(k)} + D_{22}^{ij(k)} + D_{66}^{ij(k)}\beta^2 \right], \; {}^{\beta}_{s}\underline{\underline{K}}_9 = \left[\left(\bar{B}_{66}^{ij(k)} - \right. \right.$$

$$\left. \left. \bar{B}_{12}^{ji(k)} - D_{22}^{ij(k)} - D_{66}^{ij(k)} \right)\beta \right], \; {}^{\beta}_{s}\underline{\underline{K}}_{11} = \left[\tilde{A}_{66}^{ij(k)} - \bar{B}_{66}^{ij(k)} - \bar{B}_{66}^{ji(k)} + \right.$$

$$\left. D_{66}^{ij(k)} + D_{22}^{ij(k)}\beta^2 \right], \; {}^{\beta}_{s}\underline{\underline{K}}_{12} = \left[\tilde{A}_{55}^{ij(k)} + D_{44}^{ij(k)}\beta^2 \right], \; {}^{\beta}_{s}\underline{\underline{K}}_{10} = {}^{\beta}_{s}\underline{\underline{K}}_9^T$$

$$\left\{ {}^{\beta}_{c}\underline{\underline{\tilde{K}}}_1, {}^{\beta}_{c}\underline{\underline{\tilde{K}}}_2, {}^{\beta}_{c}\underline{\underline{\tilde{K}}}_3 \right\} := \left\{ \begin{bmatrix} {}^{\beta}_{c}\underline{\underline{K}}_1 & \underline{\underline{0}} & \underline{\underline{0}} \\ \underline{\underline{0}} & {}^{\beta}_{c}\underline{\underline{K}}_2 & \underline{\underline{0}} \\ \underline{\underline{0}} & \underline{\underline{0}} & {}^{\beta}_{c}\underline{\underline{K}}_3 \end{bmatrix}, \begin{bmatrix} \underline{\underline{0}} & \underline{\underline{0}} & {}^{\beta}_{c}\underline{\underline{K}}_4 \\ \underline{\underline{0}} & \underline{\underline{0}} & {}^{\beta}_{c}\underline{\underline{K}}_5 \\ {}^{\beta}_{c}\underline{\underline{K}}_6 & {}^{\beta}_{c}\underline{\underline{K}}_7 & \underline{\underline{0}} \end{bmatrix}, \begin{bmatrix} {}^{\beta}_{c}\underline{\underline{K}}_8 & {}^{\beta}_{c}\underline{\underline{K}}_9 & \underline{\underline{0}} \\ {}^{\beta}_{c}\underline{\underline{K}}_{10} & {}^{\beta}_{c}\underline{\underline{K}}_{11} & \underline{\underline{0}} \\ \underline{\underline{0}} & \underline{\underline{0}} & {}^{\beta}_{c}\underline{\underline{K}}_{12} \end{bmatrix} \right\}$$

$${}^{\beta}_{c}\underline{\underline{\tilde{K}}}_1 : \quad {}^{\beta}_{c}\underline{\underline{K}}_1 = {}^{0}\underline{\underline{K}}_1, \; {}^{\beta}_{c}\underline{\underline{K}}_2 = {}^{0}\underline{\underline{K}}_2 \; {}^{\beta}_{c}\underline{\underline{K}}_3 = {}^{0}\underline{\underline{K}}_3,$$

$${}^{\beta}_{c}\underline{\underline{\tilde{K}}}_2 : \quad {}^{\beta}_{c}\underline{\underline{K}}_4 = {}^{0}\underline{\underline{K}}_4, \; {}^{\beta}_{c}\underline{\underline{K}}_5 = -{}^{\beta}_{s}\underline{\underline{K}}_5^T, \; {}^{\beta}_{c}\underline{\underline{K}}_6 = -{}^{0}\underline{\underline{K}}_4^T, \; {}^{\beta}_{c}\underline{\underline{K}}_7 = {}^{\beta}_{s}\underline{\underline{K}}_5$$

$${}^{\beta}_{c}\underline{\underline{\tilde{K}}}_3 : \quad {}^{\beta}_{c}\underline{\underline{K}}_8 = {}^{\beta}_{s}\underline{\underline{K}}_8, \; {}^{\beta}_{c}\underline{\underline{K}}_9 = -{}^{\beta}_{s}\underline{\underline{K}}_9, \; {}^{\beta}_{c}\underline{\underline{K}}_{10} = -{}^{\beta}_{s}\underline{\underline{K}}_9^T, \; {}^{\beta}_{c}\underline{\underline{K}}_{11} = {}^{\beta}_{s}\underline{\underline{K}}_{11}, \; {}^{\beta}_{c}\underline{\underline{K}}_{12} = {}^{\beta}_{s}\underline{\underline{K}}_{12}$$

$$\left\{ {}^{0}\underline{\underline{R}}, {}^{\beta}_{s}\underline{\underline{R}}, {}^{\beta}_{c}\underline{\underline{R}} \right\} = \left\{ \begin{pmatrix} {}^{0}\underline{\tilde{R}}_1 \\ {}^{0}\underline{\tilde{R}}_2 \\ \underline{0} \end{pmatrix}, \begin{pmatrix} {}^{\beta}_{s}\underline{\tilde{R}}_1 \\ {}^{\beta}_{s}\underline{\tilde{R}}_2 \\ {}^{\beta}_{s}\underline{\tilde{R}}_3 \end{pmatrix}, \begin{pmatrix} {}^{\beta}_{c}\underline{\tilde{R}}_1 \\ {}^{\beta}_{c}\underline{\tilde{R}}_2 \\ {}^{\beta}_{c}\underline{\tilde{R}}_3 \end{pmatrix} \right\}$$

$${}^{0}\underline{\underline{R}} : \quad {}^{0}\underline{\tilde{R}}_1 = \left(\bar{F}_r^{(i)} - {}^{0}\tilde{N}_{rr,\infty}^{(i)} - {}^{0}\bar{N}_{\theta\theta,\infty}^{(i)} \right), \; {}^{0}\underline{\tilde{R}}_2 = \left(\bar{F}_\theta^{(i)} + \bar{M}^{(i)} \right)$$

$${}^{\beta}_{s}\underline{\underline{R}} : \quad {}^{\beta}_{s}\underline{\tilde{R}}_1 = \left(q^{(N_I)} - {}^{\beta}_{s}\tilde{N}_{rr,\infty}^{(i)} - {}^{\beta}_{s}\bar{N}_{\theta\theta,\infty}^{(i)} \right) \; {}^{\beta}_{s}\underline{\tilde{R}}_2 = \left({}^{\beta}_{s}\bar{Q}_{r\theta,\infty}^{(i)} - {}^{\beta}_{s}\tilde{Q}_{r\theta,\infty}^{(i)} \right),$$

$$\qquad\qquad {}^{\beta}_{s}\underline{\tilde{R}}_3 = \left({}^{\beta}_{s}\tilde{Q}_{rz,\infty}^{(i)} \right)$$

$${}^{\beta}_{c}\underline{\underline{R}} : \quad {}^{\beta}_{c}\underline{\tilde{R}}_1 = -\left({}^{\beta}_{c}\tilde{N}_{rr,\infty}^{(i)} + {}^{\beta}_{c}\bar{N}_{\theta\theta,\infty}^{(i)} \right) \; {}^{\beta}_{c}\underline{\tilde{R}}_2 = \left({}^{\beta}_{c}\bar{Q}_{r\theta,\infty}^{(i)} - {}^{\beta}_{c}\tilde{Q}_{r\theta,\infty}^{(i)} \right),$$

$$\qquad\qquad {}^{\beta}_{c}\underline{\tilde{R}}_3 = \left({}^{\beta}_{c}\tilde{Q}_{rz,\infty}^{(i)} \right)$$

$$\left\{ {}^{0}\underline{\underline{\tilde{k}}}_1, {}^{0}\underline{\underline{\tilde{k}}}_2, {}^{0}\underline{\tilde{r}} \right\} := \left\{ \begin{bmatrix} {}^{0}\underline{\underline{k}}_1 & \underline{\underline{0}} & \underline{\underline{0}} \\ \underline{\underline{0}} & {}^{0}\underline{\underline{k}}_2 & \underline{\underline{0}} \\ \underline{\underline{0}} & \underline{\underline{0}} & {}^{0}\underline{\underline{k}}_3 \end{bmatrix}, \begin{bmatrix} \underline{\underline{0}} & \underline{\underline{0}} & {}^{0}\underline{\underline{k}}_4 \\ \underline{\underline{0}} & \underline{\underline{0}} & \underline{\underline{0}} \\ {}^{0}\underline{\underline{k}}_5 & \underline{\underline{0}} & \underline{\underline{0}} \end{bmatrix}, \begin{pmatrix} \underline{0} \\ {}^{0}\underline{\tilde{r}}_2 \\ {}^{0}\underline{\tilde{r}}_3 \end{pmatrix} \right\}$$

$$
\begin{aligned}
&{}^{0}\underline{\underline{\tilde{k}_1}}: \quad {}^{0}\underline{\underline{k_1}} = \left[a_{55}^{ij\,(k)} \right], \; {}^{0}\underline{\underline{k_2}} = \left[a_{44}^{ij\,(k)} \right], \; {}^{0}\underline{\underline{k_3}} = \left[a_{33}^{ij\,(k)} \right], \\
&{}^{0}\underline{\underline{\tilde{k}_2}}: \quad {}^{0}\underline{\underline{k_4}} = \left[\bar{a}_{55}^{ij\,(k)} \right], \; {}^{0}\underline{\underline{k_5}} = \left[\bar{a}_{13}^{ij\,(k)} + b_{23}^{ij\,(k)} \right], \\
&{}^{0}\underline{\tilde{r}}: \quad {}^{0}\underline{\tilde{r}_2} = \left(-{}^{0}\tilde{Q}_{\theta z,\infty}^{(i)} \right), \; {}^{0}\underline{\tilde{r}_3} = \left(-{}^{0}\tilde{N}_{zz,\infty}^{(i)} \right)
\end{aligned}
$$

$$
\left\{ {}^{\beta}_{s}\underline{\underline{\tilde{k}_1}}, \, {}^{\beta}_{s}\underline{\underline{\tilde{k}_2}}, \, {}^{\beta}_{s}\underline{\tilde{r}} \right\} := \left\{
\begin{bmatrix} {}^{\beta}_{s}\underline{\underline{k_1}} & 0 & 0 \\ 0 & {}^{\beta}_{s}\underline{\underline{k_2}} & 0 \\ 0 & 0 & {}^{\beta}_{s}\underline{\underline{k_3}} \end{bmatrix}, \;
\begin{bmatrix} 0 & 0 & {}^{\beta}_{s}\underline{\underline{k_4}} \\ 0 & 0 & {}^{\beta}_{s}\underline{\underline{k_5}} \\ {}^{\beta}_{s}\underline{\underline{k_6}} & {}^{\beta}_{s}\underline{\underline{k_7}} & 0 \end{bmatrix}, \;
\begin{pmatrix} {}^{\beta}_{s}\underline{\tilde{r}_1} \\ {}^{\beta}_{s}\underline{\tilde{r}_2} \\ {}^{\beta}_{s}\underline{\tilde{r}_3} \end{pmatrix}
\right\}
$$

$$
\begin{aligned}
&{}^{\beta}_{s}\underline{\underline{\tilde{k}_1}}: \quad {}^{\beta}_{s}\underline{\underline{k_1}} = {}^{0}\underline{\underline{k_1}}, \; {}^{\beta}_{s}\underline{\underline{k_2}} = {}^{0}\underline{\underline{k_2}}, \; {}^{\beta}_{s}\underline{\underline{k_3}} = {}^{0}\underline{\underline{k_3}}, \\
&{}^{\beta}_{s}\underline{\underline{\tilde{k}_2}}: \quad {}^{\beta}_{s}\underline{\underline{k_5}} = \left[b_{44}^{ij\,(k)}\beta \right], \; {}^{\beta}_{s}\underline{\underline{k_6}} = \left[\bar{a}_{13}^{ij\,(k)} + b_{23}^{ij\,(k)} \right], \; {}^{\beta}_{s}\underline{\underline{k_7}} = -\left[b_{23}^{ij\,(k)}\beta \right], \; {}^{\beta}_{s}\underline{\underline{k_4}} = {}^{0}\underline{\underline{k_4}} \\
&{}^{\beta}_{s}\underline{\tilde{r}}: \quad {}^{\beta}_{s}\underline{\tilde{r}_1} = \left(-{}^{\beta}_{s}\tilde{Q}_{rz,\infty}^{(i)} \right), \; {}^{\beta}_{s}\underline{\tilde{r}_2} = \left(-{}^{\beta}_{s}\tilde{Q}_{\theta z,\infty}^{(i)} \right), \; {}^{\beta}_{s}\underline{\tilde{r}_3} = \left(-{}^{\beta}_{s}\tilde{N}_{zz,\infty}^{(i)} \right)
\end{aligned}
$$

$$
\left\{ {}^{\beta}_{c}\underline{\underline{\tilde{k}_1}}, \, {}^{\beta}_{c}\underline{\underline{\tilde{k}_2}}, \, {}^{\beta}_{c}\underline{\tilde{r}} \right\} := \left\{
\begin{bmatrix} {}^{\beta}_{c}\underline{\underline{k_1}} & 0 & 0 \\ 0 & {}^{\beta}_{c}\underline{\underline{k_2}} & 0 \\ 0 & 0 & {}^{\beta}_{c}\underline{\underline{k_3}} \end{bmatrix}, \;
\begin{bmatrix} 0 & 0 & {}^{\beta}_{c}\underline{\underline{k_4}} \\ 0 & 0 & {}^{\beta}_{c}\underline{\underline{k_5}} \\ {}^{\beta}_{c}\underline{\underline{k_6}} & {}^{\beta}_{c}\underline{\underline{k_7}} & 0 \end{bmatrix}, \;
\begin{pmatrix} {}^{\beta}_{c}\underline{\tilde{r}_1} \\ {}^{\beta}_{c}\underline{\tilde{r}_2} \\ {}^{\beta}_{c}\underline{\tilde{r}_3} \end{pmatrix}
\right\}
$$

$$
\begin{aligned}
&{}^{\beta}_{c}\underline{\underline{\tilde{k}_1}}: \quad {}^{\beta}_{c}\underline{\underline{k_1}} = {}^{0}\underline{\underline{k_1}}, \; {}^{\beta}_{c}\underline{\underline{k_2}} = {}^{0}\underline{\underline{k_2}}, \; {}^{\beta}_{c}\underline{\underline{k_3}} = {}^{0}\underline{\underline{k_3}}, \\
&{}^{\beta}_{c}\underline{\underline{\tilde{k}_2}}: \quad {}^{\beta}_{c}\underline{\underline{k_4}} = {}^{0}\underline{\underline{k_4}}, \; {}^{\beta}_{c}\underline{\underline{k_5}} = -{}^{\beta}_{s}\underline{\underline{k_5}}, \; {}^{\beta}_{c}\underline{\underline{k_6}} = {}^{\beta}_{s}\underline{\underline{k_6}}, \; {}^{\beta}_{c}\underline{\underline{k_7}} = -{}^{\beta}_{s}\underline{\underline{k_7}}, \\
&{}^{\beta}_{c}\underline{\tilde{r}}: \quad {}^{\beta}_{c}\underline{\tilde{r}_1} = \left(-{}^{\beta}_{c}Q_{rz,\infty}^{(i)} \right), \; {}^{\beta}_{c}\underline{\tilde{r}_2} = \left(-{}^{\beta}_{c}Q_{\theta z,\infty}^{(i)} \right), \; {}^{\beta}_{c}\underline{\tilde{r}_3} = \left(-{}^{\beta}_{c}N_{zz,\infty}^{(i)} \right)
\end{aligned}
$$

References

[1] Kant T, Swaminathan K (2000) Estimation of transverse/interlaminar stresses in laminated composites – a selective review and survey of current developments. Composite Structures **49**(1):65–75

[2] Mittelstedt C, Becker W (2007) Free-edge effects in composite laminates. Applied Mechanics Reviews **60**(5):217–245

[3] Mittelstedt C, Becker W, Kappel A, Kharghani N (2022) Free-edge effects in composite laminates—a review of recent developments 2005–2020. Applied Mechanics Reviews **74**(1):010,801

[4] Srinivas S (1974) Analysis of laminated, composite, circular cylindrical shells with general boundary conditions. Nasa tr r-412, Langley Research Center,

Hampton, Va. 23665

[5] Ren JG (1987) Exact solutions for laminated cylindrical shells in cylindrical bending. Composites Science and Technology **29**(3):169–187

[6] Lekhnitskii SG (1963) Theory of elasticity of an anisotropic elastic body. Holden-Day series in mathematical physics, Holden-Day, San Francisco, CA

[7] Lekhnitskii SG (1968) Anisotropic plates. Gordon and Breach, London, UK

[8] Ko WL, Jackson RH (1989) Multilayer theory for delamination analysis of a composite curved bar subjected to end forces and end moments. Technical memorandum no. 4139, NASA Research Center, Edwards, CA, USA

[9] Varadan TK, Bhaskar K (1991) Bending of laminated orthotropic cylindrical shells—an elasticity approach. Composite Structures **17**(2):141–156

[10] Miri AK, Nosier A (2011) Interlaminar stresses in antisymmetric angle-ply cylindrical shell panels. Composite Structures **93**(2):419–429

[11] Miri AK, Nosier A (2011) Out-of-plane stresses in composite shell panels: layerwise and elasticity solutions. Acta Mechanica **220**(1-4):15–32

[12] Nosier A, Miri AK (2010) Boundary-layer hygrothermal stresses in laminated, composite, circular, cylindrical shell panels. Archive of Applied Mechanics **80**(4):413–440

[13] Tahani M, Andakhshideh A, Maleki S (2016) Interlaminar stresses in thick cylindrical shell with arbitrary laminations and boundary conditions under transverse loads. Composites Part B: Engineering **98**:151–165

[14] Schnabel JE, Yousfi M, Mittelstedt C (2017) Free-edge stress fields in cylindrically curved symmetric and unsymmetric cross-ply laminates under bending load. Composite Structures **180**:862–875

[15] Kappel A, Mittelstedt C (2020) Free-edge stress fields in cylindrically curved cross-ply laminated shells. Composites Part B: Engineering **183**:107,693

[16] Kappel A, Mittelstedt C (2021) Interlaminar stress fields in circular cylindrical cross-ply laminated shells subjected to transverse loadings. International Journal of Solids and Structures **228**:111,096

[17] Ahmadi I (2019) Free edge stress prediction in thick laminated cylindrical shell panel subjected to bending moment. Applied Mathematical Modelling **65**:507–525

[18] Ahmadi I (2020) A three-dimensional formulation for levy-type transversely loaded cross-ply shell panels. International Journal of Mechanical Sciences **167**:105,224

[19] Kappel A, Dillen S, Mittelstedt C (2021) Hygrothermomechanical analysis of the free-edge stress fields in cylindrical cross-ply laminated shells. Mechanics of Advanced Materials and Structures **30**(4):1–18

Chapter 7
Experimental Quantification of Barrier Effects for Microstructural Short Fatigue Crack Propagation in Martensitic Steel

Kevin Koschella and Ulrich Krupp

Abstract In the scope of the underlying study, microstructurally short fatigue crack propagation was observed and analyzed in a fully martensitic microstructure of the 0.5C-1Cr-Mo alloy steel SAE4010. For this purpose, a three-stage examination procedure was developed to prepare macroscopic shallow notched specimens, define and analyze area of interest by EBSD and afterwards applying fully reversal load cycles with a frequency of 95Hz. To predefine the crack path, small rhombic notches were added by focused ion beam (FIB) milling in the area of interest. In the second stage, the crack growth was monitored in-situ by light optical microscopy. The final stage comprised the combination and correlation of the crack path, the crack growth data and the documented microstructure with its crystallographic properties. Based on essential literature results, which comprises statistical boundary plane orientations for a martensitic microstructure, it was possible to analyze the barrier effect of different martensitic boundary types as well as the effect of the twist angle and residual burgers vector on the crack propagation behavior. By an additional consideration of common evaluation parameters, a detailed analysis of the prediction behavior of slip system activity was done. The results suggest the application of a combined criterion (twist angle, residual burgers vector, resolved shear stress) to describe the general barrier effect against fatigue crack propagation in a martensitic microstructure. In detail, there was no clear difference in barrier effect between the observed boundary types.

Kevin Koschella
University of Applied Sciences Osnabrück, Institute of Materials Design and Structural Integrity, Albrechtstraße 30, 49076 Osnabrück, Germany,
e-mail: k.koschella@hs-osnabrueck.de

Ulrich Krupp
RWTH Aachen University, IEHK Steel Institute, Intzestraße 1, 52072 Aachen, Germany,
e-mail: krupp@iehk.rwth-aachen.de

7.1 Introduction

In general, optimization of a technical product can be differentiated into two fields: the structural optimization, e.g. changing design, topology or external loads, and the material optimization, respectively. Despite the crucial impact of the material's mechanical behavior, very often the specific material selections or adjustments of the material properties is underestimated and not kept in mind. The adequate selection of material properties, for example to withstand complex fatigue loads and critical environmental effects, requires a holistic understanding of the underlying structural and metallurgical boundary conditions, though. This mainly leads to the question how fatigue damage sets in, and what are the key features to prevent or at least delay any fatigue damage.

Today, it is well known that crack initiation and crack propagation in the scale of the local microstructure determines up to 90% of the lifetime, in the high cycle fatigue regime (HCF) as well as in the very high cycle fatigue regime (VHCF). Different studies have also shown that initiation and propagation of microstructurally short fatigue cracks occur below the stress intensity threshold for long crack propagation (cf. Suresh et al. [1]). Within this regime, the cyclically growing short cracks show a growth behavior with pronounced oscillations in the crack propagation rate da/dN. Kitagawa and Takahashi [2] attributed this to the interaction with local barriers, like microstructural boundaries or imperfections. This characteristic growth behavior shows a crack growth deceleration or arrest when approaching a grain or phase boundary and subsequently, an acceleration after passing the boundary with growth rates da/dN higher than those expected by the long crack propagation analysis. For a quantitative explanation of the observed deceleration and arrest mechanisms, Tanaka and Mura [3] and Navarro and de los Rios [4] introduced dislocation blocking models, which takes boundaries in a generalized manner into account. With respect to the slip mechanism by dislocation movement, which is assumed to be the major driving force for the short crack growth, several geometry-based barrier models were introduced (cf. Zhai et al. [5]). Here, the misorientation between the individual slip systems at the grain boundary is considered as well as the spatial orientation of the grain boundary plane. For detailed examinations of such barrier effects and detailed linking to the underlying microstructure it is essential to understand the microstructure of the respective materials on various length scales.

In the following sections, current results of in-situ monitored crack propagation data are analyzed by applying different commonly used parameters to quantify the barrier strength and slip system selection. This analysis used statistical data to estimate spatial parameters of boundary plane orientation for specific hierarchical boundary types. This approach was applied for a martensitic microstructure under fully reversal cyclic loading of macroscopic specimens. The objective of this work is to understand the short crack propagation mechanisms and their link to the martensitic microstructure in a quantitative manner.

7.2 Material

For this study, a martensitic steel with 0.5 wt.-% C (Table 7.1) was austenitized at 860°C for 30 minutes, quenched in oil and tempered at 550°C for one hour resulting in a hardness of 37HRC. During quenching of martensitic steels, the original austenite structure is decomposed by diffusion-less martensitic transformation into fine substructures (Fig. 7.1b), i.e. laths of tetragonally distorted martensite (bct, body centered tetragonal). Between the original parent austenitic microstructure and the resulting martensite structure a strict orientation relationship can be found. For the underlying martensitic structure, the corresponding orientation relationship was identified as Kurdjumov-Sachs orientation relationship (KS OR). In Fig. 7.1c, the measured $\langle 110 \rangle$ plane normal vectors are compared to the one resulting by the KS OR from the parent austenite grain.

Along with this fine microstructure different hierarchical levels for clustering these can be defined based on the orientation relationship. This starts with martensite packets as a first hierarchical level, where within a single martensite packet all laths

Table 7.1: Chemical composition (wt.%) of the martensitic steel SAE4010 studied.

Material	C	Si	Mn	Cr	Mo	Fe
0.5C-1.0Cr-Mo	0.48	0.25	0.71	1.00	0.18	bal.
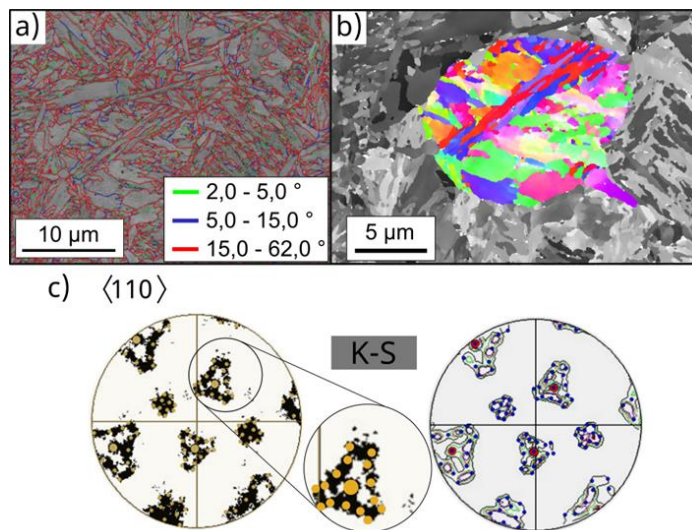
Fig. 7.1: Martensitic microstructure with mainly high-angle boundaries (marked by red lines) in a). The representative martensitic blocks within one prior austenitic grain are highlighted in b) by different colors. Overlay of ideal $\langle 110 \rangle$ planes resulting from KS OR (closed yellow circles) and the measured orientations are shown in c).

exhibit a common parallel crystallographic {110} plane. Each martensite packet is subdivided into blocks, which contain martensite laths with quasi-parallel ⟨111⟩ directions in addition to the parallel {110} planes. According to the Kurdjumov-Sachs OR, a single austenite grain may decay into four different packets, and for every packet into six different block variants (Fig. 7.2).

In some materials, the existence of two variants with a small misorientation range within one block was observed [6, 7]. However, the steel analyzed within the present study does not show such variant pairs within a single block structure (Fig. 7.1a). Based on the KS orientation relationship, up to 24 unique variants can be formed out of one single austenite grain. For this study, a mean block size of 0.4 μm was determined and a mean grain size of the prior austenite grains of 9 μm. The detailed analysis of the martensitic microstructure revealed a specific common block alignment within several packets. This observation agrees well with results of Beladi et al [8], where blocks and their habitus planes found to be near to a local (110) plane. Along with this alignment, the corresponding boundaries showed predominantly the identical orientation [8]. Figure 7.2 shows such a quasi-parallel alignment of blocks in the center and in the detail view, marked by black plane trace lines, where all blocks have in common within the white outlined martensite packet. Furthermore, in the lower part of the black outlined prior austenite grain area there are several blocks within a single martensite packet, which exhibit a more globular shape and deviating size. This can be explained by studies of Morsdorf et al. [9] and Zhang et al. [10], which associated this with the link between a self-accommodation process to minimize the transformation induced strain-stress state and the early-stage martensite transformation. The sum of the characteristics outlined above leads to a very complex microstructure providing a broad field of potential material properties associated with a complex fatigue behavior.
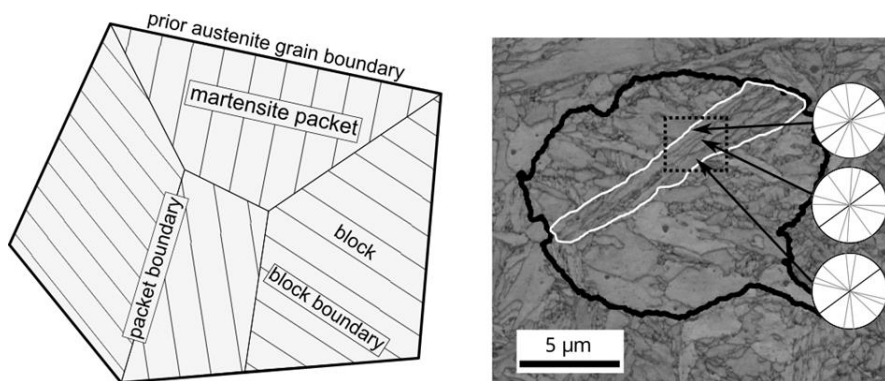
Fig. 7.2: Hierarchical levels of the martensitic microstructure based on the KS-orientation relationship in SAE4010. On the right-hand-side the parallel orientated ⟨110⟩-slip systems are shown within the white framed martensite packet.

7.3 Experiments and Methods

The measurements and observations of short crack growth in the order of the local microstructure under cyclic loading involve special requirements on the testing equipment as well as on the observation method itself. In general, for a very fine microstructure like in the present case for the underlying fully martensitic structure, the gold standard is applying in-situ testing in combination with SEM. Drawback of this testing method is the self-heating of the specimen in combination with a strongly reduced heat flux. This effect becomes increasingly dominant for high testing frequencies and can lead to overheating and to the destruction of the specimen or at least to significantly falsified results. Another aspect is the very limited specimen size which can lead to the size effect strongly reducing the result's quality. To overcome the above-mentioned issues, macroscopic cylindrical specimens with additional modifications were used. These modifications comprise the combination of a shallow notched area (notch factor of 1.2) in the specimen center with an additional rhombic-shaped notch, generated by focused ion beam milling (FIB) within the scanning electron microscope (SEM). As a result, the crack initiation site was predefined prior to any fatigue loading. Accordingly, the observation area was significantly reduced, which enabled the application of a higher magnification and resolution for the light optical microscopy. The only restriction on the observation resolution is set by the wavelength of the light.

The experimental procedure to evaluate the microstructural crack growth within the fully martensitic structure was carried out by three consecutive stages:

1. Specimen preparation,
2. Testing and observation,
3. Data correlation and evaluation.

In the scope of the first stage, the specimen notch surface area was polished mechanically followed by electropolishing [11]. Within the shallow notched region, the area of interest was selected and completely documented with respect to the crystallographic orientation distribution by automated electron back-scatter diffraction (EBSD). Afterwards, a rhombic-shaped micro notch with a length and depth varying from 12 μm up to 17 μm was cut out by means of FIB milling. This procedure was conducted within a ZEISS Auriga FEG scanning electron microscope (SEM). Objective of this stage was the documentation and final preparation of the unloaded and undamaged microstructure as well as the future crack path.

The second stage comprised the cyclic loading of the specimen using a resonance testing machine RUMUL Testronic 100 kN under stress-control. The fully reversed cyclic loading ($R = -1$) was applied under a testing frequency of 95 Hz and ambient temperature and environment, respectively. The prior selected and documented area of interest was monitored during cyclic testing with a high-resolution digital light optical microscope (HIROX MXG-10C – Fig. 7.3). The image capture rate was 0.19 Hz and 0.95 Hz for a lower stress amplitude and a higher stress amplitude, respectively. Along with the selected monitoring rate the microstructural crack was documented
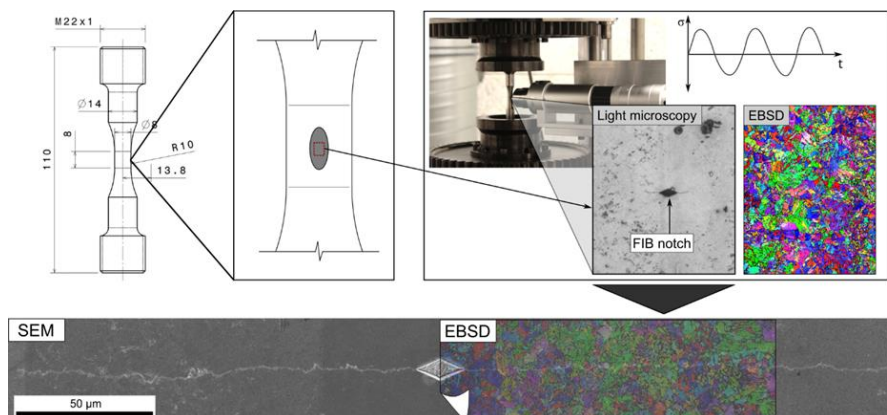
Fig. 7.3: Experimental sequence to measure the crack growth rate da/dN and correlate it with the crack path and the underlying microstructure. The sequence includes three experimental phases – specimen preparation (left top), testing and observation (right top) and finally, correlative actions of crack growth data with microstructural measurements (bottom).

at the peak of the upper tensile half-cycle to minimize the surface movement and increase the exposure time.

In the final stage of the experimental works, all collected data was correlated and combined to extract the characteristics of microstructurally short fatigue crack growth. In Fig. 7.3, an exemplary overlay result of post-mortem SEM crack path and the orientation data obtained from EBSD are shown. By using characteristic surface features as correlation fix points, the propagation of the crack tips was combined and correlated with SEM results and linked with the orientation data from ESBD maps. The mentioned data combination enabled the distinct study of crack growth rates associated with barrier interaction scenarios. In other words, with this final step it was possible to gain insight into the specific crack growth deceleration characteristics for every misorientation type within the martensitic structure. Though, this approach still neglected the three-dimensionality of the crack growth during the grain boundary transfer. In numerous studies [5, 12–17] it was observed that the barrier effect of grain boundaries against microstructurally short fatigue crack growth is strongly linked with spatial properties of these boundaries. In detail, it was reported that crack growth along primary slip systems is affected by the resulting twist angle between both corresponding slip systems at the grain boundary plane [5, 12–18]. This characteristic was also found for dislocation motion [19–22]. This similarity is not very surprising in the light of the dislocation movement in the plastic zone ahead the crack tip [23, 24]. In Fig. 7.4a, a detailed visualization of interacting slip systems and the resulting twist angle on the grain boundary plane is shown. This twist angle is determined by all three plane orientations and describes the angular discrepancy between the slip plane traces projected on the grain boundary plane.

To assess the missing information of spatial orientation of the grain boundary planes, results of Beladi et al. [8] were used. The authors found a strong systematic ori-
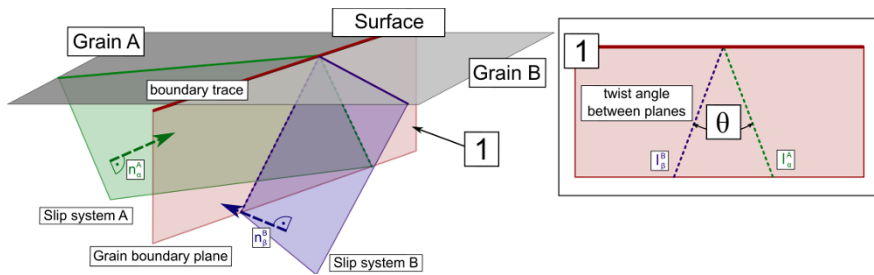
Fig. 7.4: Visualization of the evaluation parameters in a schematic slip system interaction, with corresponding main parameters of slip system plane normal $n_{\alpha,\beta}^{A,B}$ and the grain boundary plane.

entation characteristics of grain boundary planes for a fully martensitic microstructure following the Kurdjumov-Sachs orientation relationship. In terms of the underlying martensitic variants, it was possible to determine a statistical distribution of grain boundary orientation with one or more distribution peaks for each unique misorientation type. This data enabled a specific definition of the grain boundary plane for each variant pair.

For the orientation definition in this work, a grain boundary plane perpendicular to the surface was assumed in a first step for each martensitic variant pairing at a crack transition point. By rotating this boundary plane about the boundary plane surface trace, the plane orientation was approximated to the distribution peaks by the results of Beladi. This approximation step illustrated in Fig. 7.5 in an idealized manner, where the red dashed line in the pole figure describes the rotation movement to minimize the relative distance to the mean orientation. With this additional data of variant boundary plane orientations, the twist angle for each crack transition was determined and correlated with the crack growth data.
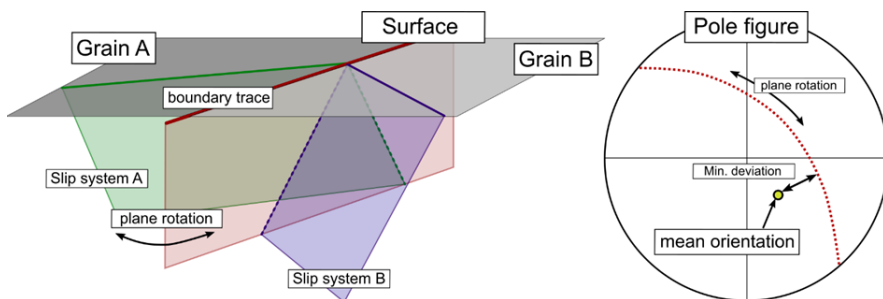
Fig. 7.5: Schematic visualization of the approximation for grain boundary plane orientations based on results of Beladi et al. [8]. The grain boundary plane was orientated with the minimum deviation of the plane normal with respect to the mean orientation from Beladi.

7.4 Results and Discussion

The examination and monitoring of five microstructural cracks under stress amplitudes ranging from $\Delta\sigma/2 = 500$ MPa up to $\Delta\sigma/2 = 630$ MPa results in ten separate crack tip examinations within the prior scanned and documented martensitic microstructure. By using the above introduced evaluation procedure, the crack growth was correlated with the underlying microstructure and typical growth characteristics were linked to changes of the crack path as well as to different martensitic boundary types. In Fig. 7.6, an exemplary correlation of crack growth data and the local microstructure from SEM and EBSD is shown. For any detailed evaluation, such transition events were considered, where a clear and pronounced crack growth sequence was apparent. In Fig. 7.6, four exemplary crack transition events are highlighted, which fulfill the evaluation condition. For transition points 1 and 2, a pronounced crack growth with an acceleration regime and a subsequent strong deceleration regime was apparent, which show local minima closely before passing the microstructural boundary. Afterwards, the crack tip started to increase its growth rate until the next grain boundary interaction occurred. Along with the identification of adequate crack transition events, the corresponding structures and their boundaries were evaluated. This included the identification of active crystallographic slip planes, which were carrying the crack path, the martensitic variant type as well as the spatial boundary plane orientation resulting of the procedure introduced in Sect. 7.3. In Fig. 7.7a, this correlation is shown by plotting crack growth deceleration rates against the twist angle on the boundary plane. Additional differentiations into block, packet and prior austenite grain boundaries enabled a detailed view on the barrier characteristics of different hierarchical boundary types. Due to missing statistical data, the twist angles for prior austenite grain boundaries were estimated by rotating the boundary planes and using the smallest resulting value. This approximation was used solely for visualization
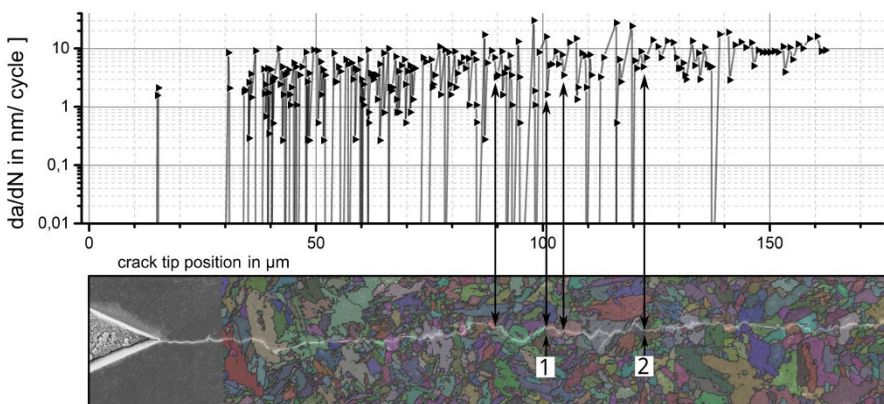
Fig. 7.6: Exemplary correlation between measured crack growth rates and the post-mortem crack path documentation by SEM and EBSD. Marked locations show the typical evaluation data to calculate the barrier effect at grain boundary transition.
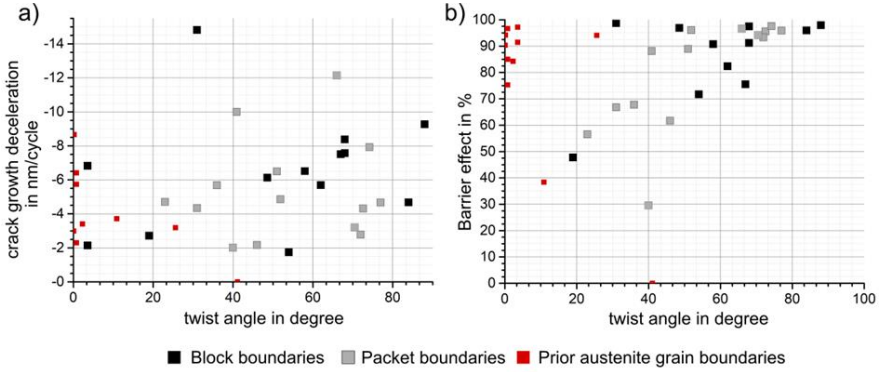
Fig. 7.7: Crack growth deceleration correlated with estimated grain boundary mismatch angle for active slip system in a). In b), the resulting barrier effect is shown with corresponding grain boundary mismatch angle for active slip systems. For both graphs the different hierarchical grain boundary types are shown with colored closed squares.

purpose. For all three boundary types in Fig. 7.7a, a strong scattering of deceleration rates for the twist angle range up to 80° was observed. Between block and packet boundaries no clear difference was observed in this graph.

However, due to the crack length and the linked crack tip stress field as well as the size of the plastic zone, even without any obstacles, the crack growth rate is highly dependent on the crack length as well as on the global loading. To minimize this effect for further evaluations, the measured decelerations of growth rate was normalized with respect to a local growth rate maximum. This local crack growth rate maximum was defined as the highest growth rate within the block structure corresponding to the crack transition site. This very simple definition of barrier effect is shown in Eq. (7.1)

$$B_{\text{effective,II}} = \frac{|\Delta \mathrm{d}a/\mathrm{d}N|}{\mathrm{d}a/\mathrm{d}N_{\text{max,I}}} = \frac{|\mathrm{d}a/\mathrm{d}N_{\text{transition,I}} - \mathrm{d}a/\mathrm{d}N_{\text{max,I}}|}{\mathrm{d}a/\mathrm{d}N_{\text{max,I}}} \tag{7.1}$$

The above introduced barrier effect $B_{\text{effective,II}}$ for slip-controlled fatigue crack propagation describes how strong the plastic zone is hindered due to the interaction with a grain boundary, which results in a successive deceleration of the crack growth. With this approach, decelerations of microstructurally short fatigue crack growth linked to grain boundary interactions will not be underestimated in situations of slow crack propagation.

Based on the definition of barrier effect $B_{\text{effective,II}}$, the results in Fig. 7.7a were re-evaluated and plotted in Fig. 7.7b. One of the key findings in this graph is, that aside from the small twist angles, prior austenite grain boundaries showed mainly high effective barrier effects. This result is in good agreement with findings of Zhang et al. [24, 25]. Additionally, the overall scatter of these barrier effects is substantially smaller than for the other observed boundary types. In contrast to this, Fig. 7.7b shows no clear difference in barrier effect for block and packet boundaries. Furthermore, a pronounced correlative trend of the barrier effect with increasing twist angle in Fig.

7.7b was observed. This behavior was observed also in numerous studies for short crack propagation [5, 13–15, 17, 18], as well as for plastic deformations [22, 26–28]. Another characteristic was observed regarding the scatter of the barrier effect with increasing twist angle.

In the scope of the underlying crack growth measurements, no complete crack stops were observed, though. Due to crack growth below the monitoring resolution several transition events occurred, which were interpreted as apparent crack stops, but resumed to grow into the adjacent block after a relatively small number of loading cycles. Based on these results, neither the scatter nor effects of the twist angle showed a distinct difference between the barrier effect of packet and block boundaries.

With respect to the scattering of barrier effect, the solely correlation to the twist angle seems not representative and highlighted the demand to expand the correlation parameters. This led to the extended consideration of additional parameters. In the scope of the present consideration, the fully geometrically based criterion of Shen et al. [19] was applied. Beside the twist angle, the authors considered the misorientation of slip directions of adjacent slip systems. Several studies successfully predicted the slip system activity at grain boundaries for the growth of plastic deformations with the additional incorporation of local shear stress on these slip systems [21, 22, 26, 29, 30]. In Eq. (7.2), the introduced parameters lead to the evaluation factor $M_{\alpha\beta}$, which describes the potential slip system activity ranging from 0 to 1 with increasing slip activity

$$M_{\alpha\beta} = (\boldsymbol{l}_\alpha^A \cdot \boldsymbol{l}_\beta^B)(\boldsymbol{d}_\alpha^A \cdot \boldsymbol{d}_\beta^B). \tag{7.2}$$

Shen et al. [19] incorporated within this evaluation factor the unit vectors of slip plane traces on the grain boundary plane $\boldsymbol{l}_{\alpha,\beta}^{A,B}$ as well as the slip direction $\boldsymbol{d}_{\alpha,\beta}^{A,B}$ for both interacting slip systems. This results in an evaluation matrix, considering every possible slip system encountering at the grain boundary. Plotting the barrier effects with the corresponding M factors led to the characteristics shown in Fig. 7.8a. With increasing M factor, the barrier effect is strongly decreasing and shows a
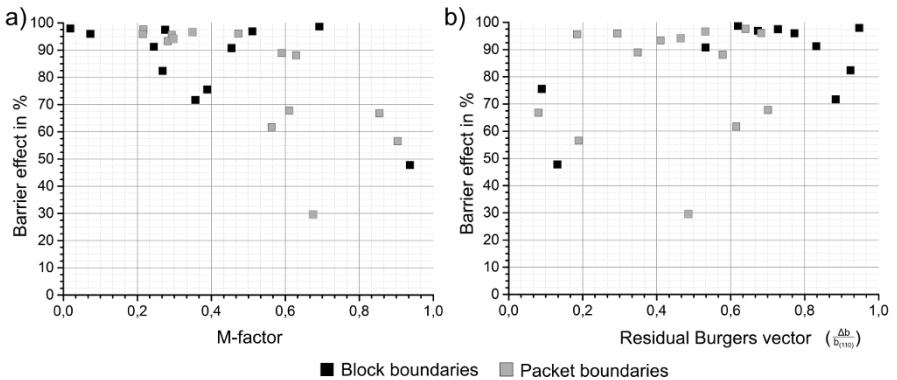
Fig. 7.8: Evaluated barrier effect correlated to the specific M-factor in a). Allocation of estimated residual burgers vector at the grain boundary transition to measured barrier effect values (b).

comparable scattering to the twist angle correlation. Again, it was not possible to derive any difference in barrier effect for packet or block boundaries. Along with the increased slip system activation potential described by an increasing M factor, the simultaneously increasing scatter in the barrier effect suggests the existence of further essential parameters.

This result was also observed in studies of Lee et al. [20]. They concluded that not only the twist angle is of major importance, but also the residual Burgers vector (RBV) in the grain boundary plane and the resolved shear stress on adjacent slip system. This concept (in the following called **L**ee-**R**obertson-**B**irnbaum-criterion) ranks all slip system pairs encountering at a boundary by their plastic slip transfer potential. To apply this concept, the residual Burgers vector in the structure boundary plane was estimated by Eq. (7.3) in a first step

$$\text{RBV} = \min|\boldsymbol{b}_\alpha^A - \boldsymbol{R}_{B,A} \cdot \boldsymbol{b}_\beta^B|. \tag{7.3}$$

Due to the existence of two possible slip directions for each of the six slip systems in the bcc crystallographic configuration, the minimum residual Burgers vector was used for each possible slip system pairings in this study. Equation (7.3) describes the necessary spatial modification of an edge dislocation passing from grain A into grain B in the coordinate system of grain A (by the transformation matrix $\boldsymbol{R}_{B,A}$). This modification must be beared by geometrical necessary grain boundary dislocations which is described by the residual Burgers vector. Contrary to the findings of Lee et al. [20] and others [26–28, 30, 31], the underlying barrier effects showed no clear sensitivity for varying RBVs, as it is visualized in Fig. 7.8b. For this graph, the resulting RBV was normalized by the Burgers vector length in the bcc (110)-slip system. For the whole range of RBV, the measured barrier effects are subjected to apparently constant scatter which varies from 50% up to nearly 100%. However, this result has to be discussed carefully, due to the assumption of minimum RBV by Eq. (7.3). To the current state of this study, the detailed examination of the true RBV, or the active Burgers vectors in both active slip systems, was not conducted.

The above introduced evaluations and examinations led to a concept of considering not only the slip system pairs encountering at the boundary, which was correlated to the crack path, but also the full range of available slip systems for each crack transition site, i.e. grain boundary. For this evaluation procedure the M factor and the LRB-criterion by Lee et al. were applied to rank every possible adjacent slip system by increasing factors. In Fig. 7.9a, the ranking based on the M factor is shown by color coding the results of Fig. 7.7b in an ascending order. Slip system pairs which are most favorable orientated by highest M factor are ranked on the first place (green). Considering the barrier effects in Fig. 7.9a, the observed slip system pairs with high twist angles show low rankings. This means that the M factor had only predicted the low barrier effects by ranking up the corresponding slip system pairs. For transition sites with high barrier effects and high twist angles, corresponding to the M factor ranking other slip system pairings would have been more favorable for an activation. This result shows that the evaluation by the M factor can capture quantitatively the
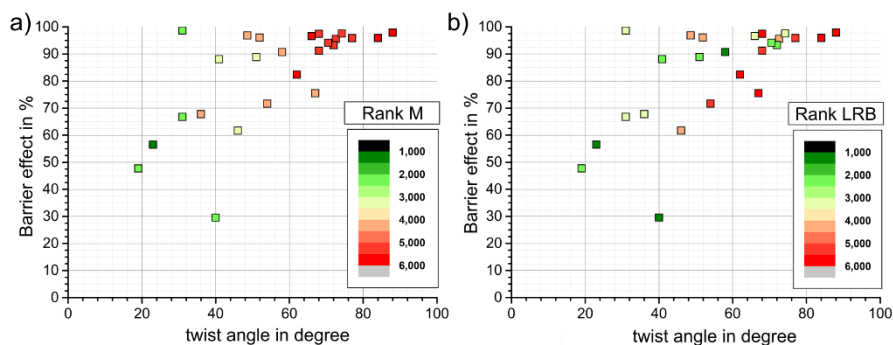
Fig. 7.9: Barrier effect plotted over grain boundary mismatch angle between interacting slip systems with an additional color coding of corresponding M factor (a) as well as for the LRB-criterion (b).

potential strength of the barrier, but not the discrete activation of a slip system for the growth of the plastic zone and the following crack.

Analogous to the evaluation method with the M factor, the LRB criterion was used to create a ranking of all available slip system pairs for each crack transition site. This ranking is shown in Fig. 7.9b with a color coding of the barrier effect data. This criterion considers - beside the RBV - also the twist angle and the resolved shear stress acting on the slip system. For the sake of approximation, the resolved shear stress was replaced by the crystallographic shear stress related to the corresponding Schmid factors of the slip systems. This is owed to the complex microscopic stress field at the crack tip and in the plastic zone, which was not monitored in the applied experimental procedure. Compared to the evaluation with M factors, this evaluation showed a higher number of predicted slip system activities. Interestingly, both evaluation methods showed a strong correlation to the barrier strength and consequently to the measured barrier effect. The inaccuracy of the activation prediction in the range of high twist angles can very likely attributed to the approximation by using the Schmid factor-based shear stresses. The general application of the LRB-criterion and its higher predictive accuracy was shown in experimental studies [21, 32] as well as in simulative studies [33–36].

Based on the above shown results, the important major role of the twist angle for the barrier effect on microstructural crack growth was observed. Regardless of the martensitic boundary type, this behavior is in good agreement with common literature and recent studies. Consequently, these results suggest to link the general barrier effect against microstructurally short fatigue crack growth and plastic deformation with geometrical characteristics rather than solely with the type of boundary. This explains the inconsistency in results of experimental works regarding the plastic deformations of martensitic blocks [36–41] and packets [42, 43]. The common observation of these studies is the predominant strong barrier effect of boundaries with high angle misorientation. This agrees well with the current results, since along with high

misorientation angles there is a high likelihood for high twist angles, regardless of the boundary plane orientation.

7.5 Summary and Conclusion

In the scope of this study, the barrier effect of different martensitic boundary types to microstructurally short fatigue cracks was analyzed. By monitoring a carefully selected region in a shallow notched specimen under fully reversed fatigue loading, several cracks emanating from artificial rhombic FIB-milled notches were in-situ observed by light optical microscopy and documented. After combining and correlating the in-situ measured crack propagation data with microstructural data from EBSD scans, crack transition sites were identified and evaluated. The evaluation was done in several steps by incorporating the specific slip systems pairs encountering at a boundary along with the respective boundary characteristics. Based on results of Beladi et al. [8], it was possible to estimate and define spatial characteristics of corresponding boundary planes for packet and block boundaries. Along with the fully defined boundary plane orientation, the resulting twist angle between adjacent slip system was derived and correlated with oscillations in the fatigue crack growth rate da/dN (deceleration and acceleration). Only by normalizing the crack growth deceleration rates to corresponding local peaks of the crack growth rate a detailed discussion was possible. Based on such derived barrier effects, there was no difference found between block and packet boundaries, regardless of the resulting twist angle. However, these boundaries showed increasing barrier effects with increasing twist angles.

The correlation to the M factor [19], considering the twist angle and the slip direction, led to comparable barrier characteristics for block and packet boundaries. For both types the M factor showed a high predictive accuracy for slip system pairs, where the observed barrier effects were low. However, for slip system pairings with high measured barrier effects, this concept identified different slip system combinations for those transition events. A slightly higher accuracy was reached applying the LRB-criterion [20]. By incorporating the residual burgers vector and the local shear stress, estimated by the Schmid factor, this approach showed a higher number of predicted slip system pairings, but still has blind spots for those pairings with high level barrier effects according to the measurements. Based on the applied approximations, it is expected to improve the prediction behavior by using the resolved shear stresses and consequently see a comparable predictive accuracy like in other studies.

The present study used in several steps approximations and estimations based on statistical data. With respect to the introduced results, the corresponding orientation of the grain boundary is subjected to a variation. Additionally, the experimental method to monitoring the crack during cyclic loading is subjected to a variation due to limits in the resolution of in-situ monitoring. In combination with the monitoring frequency, this led to blind spots in recognizing crack transition events and corresponding growth rate calculations.

Despite the above-mentioned sources for variation in measurements, the applied techniques and used equipment led to reasonable results, which agree well with results reported in more recent studies. However, to gain much more detailed insights, which is crucial with the underlying scale of microstructure, the experimental method should be extended to high-resolution monitoring within the SEM.

References

[1] Suresh S, Ritchie RO (1984) Propagation of short fatigue cracks. International Metals Reviews **29**(1):445–475

[2] Kitagawa H, Takahashi S (1976) Application of fracture mechanics to very small cracks or the cracks in the early stage. In: International Conference on Mechanical Behaviour of Materials, vol 2, Boston, pp 627–630

[3] Tanaka K, Mura T (1981) A Dislocation Model for Fatigue Crack Initiation. Journal of Applied Mechanics **48**(1):97–103

[4] Navarro A, de los Rios ER (1988) Short and long fatigue crack growth: A unified model. Philosophical Magazine A **57**(1):15–36

[5] Zhai T, Wilkinson AJ, Martin JW (2000) A crystallographic mechanism for fatigue crack propagation through grain boundaries. Acta Materialia **48**(20):4917–4927

[6] Kitahara H, Ueji R, Tsuji N, Minamino Y (2006) Crystallographic features of lath martensite in low-carbon steel. Acta Materialia **54**(5):1279–1288

[7] Morito S, Adachi Y, Ohba T (2009) Morphology and crystallography of sub-blocks in ultra-low carbon lath martensite steel. Materials Transactions **50**(8):1919–1923

[8] Beladi H, Rohrer GS, Rollett AD, Tari V, Hodgson PD (2014) The distribution of intervariant crystallographic planes in a lath martensite using five macroscopic parameters. Acta Materialia **63**:86–98

[9] Morsdorf L, Tasan CC, Ponge D, Raabe D (2015) 3D structural and atomic-scale analysis of lath martensite: Effect of the transformation sequence. Acta Materialia **95**:366–377

[10] Zhang S, Morito S, Komizo Y (2012) Variant selection of low carbon high alloy steel in an austenite grain during martensite transformation. ISIJ International **52**(3):510–515

[11] Koschella K, Krupp U (2019) Investigations of fatigue damage in tempered martensitic steel in the hcf regime. International Journal of Fatigue **124**:113–122

[12] Zhai T, Jiang XP, Li JX, Garratt MD, Bray GH (2005) The grain boundary geometry for optimum resistance to growth of short fatigue cracks in high strength al-alloys. International Journal of Fatigue **27**(10):1202–1209, Fatigue Damage of Structural Materials V

[13] Marx M, Schaef W, Vehoff H (2010) Interaction of short cracks with the local microstructure. Procedia Engineering **2**(1):163–171, fatigue 2010

[14] Schaef W, Marx M, Vehoff H, Heckl A, Randelzhofer P (2011) A 3-d view on the mechanisms of short fatigue cracks interacting with grain boundaries. Acta Materialia **59**(5):1849–1861

[15] Wen W, Zhai T (2011) Three-dimensional effects of microstructures on short fatigue crack growth in an Al–Li 8090 alloy. Philosophical Magazine **91**(27):3557–3577

[16] Künkler B, Düber O, Köster P, Krupp U, Fritzen CP, Christ HJ (2008) Modelling of short crack propagation – Transition from stage I to stage II. Engineering Fracture Mechanics **75**(3):715–725, international Conference of Crack Paths

[17] Pineau A (2015) Crossing grain boundaries in metals by slip bands, cleavage and fatigue cracks. Philosophical Transactions of the Royal Society A: Mathematical, Physical and Engineering Sciences **373**(2038):20140,131

[18] Abuzaid WZ, Sangid MD, Carroll JD, Sehitoglu H, Lambros J (2012) Slip transfer and plastic strain accumulation across grain boundaries in hastelloy x. Journal of the Mechanics and Physics of Solids **60**(6):1201–1220

[19] Shen Z, Wagoner RH, Clark WAT (1986) Dislocation pile-up and grain boundary interactions in 304 stainless steel. Scripta Metallurgica **20**(6):921–926

[20] Lee TC, Robertson IM, Birnbaum HK (1990) TEM in situ deformation study of the interaction of lattice dislocations with grain boundaries in metals. Philosophical Magazine A **62**(1):131–153

[21] Bieler TR, Eisenlohr P, Zhang C, Phukan HJ, Crimp MA (2014) Grain boundaries and interfaces in slip transfer. Current Opinion in Solid State and Materials Science **18**(4):212–226, Slip Localization and Transfer in Deformation and Fatigue of Polycrystals

[22] Genée J, Signor L, Villechaise P (2017) Slip transfer across grain/twin boundaries in polycrystalline ni-based superalloys. Materials Science and Engineering: A **701**:24–33

[23] Ohr SM (1985) An electron microscope study of crack tip deformation and its impact on the dislocation theory of fracture. Materials Science and Engineering **72**(1):1–35

[24] Zhang YH, Edwards L (1992) The effect of grain boundaries on the development of plastic deformation ahead of small fatigue cracks. Scripta Metallurgica et Materialia **26**(12):1901–1906

[25] Zhang C, Wang Q, Ren J, Li R, Wang M, Zhang F, Sun K (2012) Effect of martensitic morphology on mechanical properties of an as-quenched and tempered 25CrMo48V steel. Materials Science and Engineering: A **534**:339–346

[26] Guo Y, Britton TB, Wilkinson AJ (2014) Slip band–grain boundary interactions in commercial-purity titanium. Acta Materialia **76**:1–12

[27] Bamford TA, Hardiman B, Shen Z, Clark WAT, Wagoner RH (1986) Micromechanism of slip propagation through a high angle boundary in alpha brass. Scripta Metallurgica **20**(2):253–258

[28] Patriarca L, Abuzaid W, Sehitoglu H, Maier HJ (2013) Slip transmission in bcc fecr polycrystal. Materials Science and Engineering: A **588**:308–317

[29] Knorr AF, Marx M (2014) Calculating the resistance of a grain boundary against fatigue crack growth. In: 11th International Fatigue Congress, Trans Tech Publications Ltd, Advanced Materials Research, vol 891, pp 929–935

[30] Soer WA, De Hosson JTM (2005) Detection of grain-boundary resistance to slip transfer using nanoindentation. Materials Letters **59**(24):3192–3195

[31] Zheng Z, Balint DS, Dunne FPE (2017) Investigation of slip transfer across HCP grain boundaries with application to cold dwell facet fatigue. Acta Materialia **127**:43–53

[32] Javaid F, Pouriayevali H, Durst K (2021) Dislocation–grain boundary interactions: recent advances on the underlying mechanisms studied via nanoindentation testing. Journal of Materials Research **36**(12):2545–557

[33] Brandl C, Bitzek E, Derlet PM, Van Swygenhoven H (2007) Slip transfer through a general high angle grain boundary in nanocrystalline aluminum. Applied Physics Letters **91**(11):111,914

[34] Shanthraj P, Zikry M (2012) Optimal microstructure for martensitic steels. Journal of Materials Research **27**(12):1598–1611

[35] Shi J, Zikry MA (2009) Grain–boundary interactions and orientation effects on crack behavior in polycrystalline aggregates. International Journal of Solids and Structures **46**(21):3914–3925

[36] Maresca F, Kouznetsova VG, Geers MGD (2014) Subgrain lath martensite mechanics: A numerical–experimental analysis. Journal of the Mechanics and Physics of Solids **73**:69–83

[37] Du C, Hoefnagels JPM, Vaes R, Geers MGD (2016) Block and sub-block boundary strengthening in lath martensite. Scripta Materialia **116**:117–121

[38] Shibata A, Nagoshi T, Sone M, Morito S, Higo Y (2010) Evaluation of the block boundary and sub-block boundary strengths of ferrous lath martensite using a micro-bending test. Materials Science and Engineering: A **527**(29):7538–7544

[39] Kwak K, Mayama T, Mine Y, Takashima K (2016) Anisotropy of strength and plasticity in lath martensite steel. Materials Science and Engineering: A **674**:104–116

[40] Li S, Zhu G, Kang Y (2016) Effect of substructure on mechanical properties and fracture behavior of lath martensite in 0.1C–1.1Si–1.7Mn steel. Journal of Alloys and Compounds **675**:104–115

[41] Ohmura T, Minor AM, Stach EA, Morris JW (2004) Dislocation–grain boundary interactions in martensitic steel observed through in situ nanoindentation in a transmission electron microscope. Journal of Materials Research **19**(12):3626–3632

[42] Mine Y, Hirashita K, Takashima H, Matsuda M, Takashima K (2013) Micro-tension behaviour of lath martensite structures of carbon steel. Materials Science and Engineering: A **560**:535–544

[43] Sun C, Fu P, Liu H, Liu H, Du N, Cao Y (2020) The effect of lath martensite microstructures on the strength of medium-carbon low-alloy steel. Crystals **10**(3):232

Chapter 8

On the Difficulty to Implement the Coupled Criterion to Predict Failure in Tempered Glass

Dominique Leguillon, Isabell Ayvaz, and Philipp L. Rosendahl

Abstract Defining the tensile strength of a brittle material like glass is not easy and the presence of residual stresses further complicates the problem. Indeed, measuring the tensile strength by a standard bending test in glass specimens is more a measurement of the presence of surface defects than the determination of a material parameter. This explains that it has not a deterministic value but is defined through a probabilistic distribution which makes it difficult to use the Coupled Criterion (CC) which specifically requires the knowledge of the tensile strength together with the material toughness to be implemented so as to predict crack nucleation. In addition, the residual stresses move the stress peak inside the specimen while failure occurs at the surface due to a critical defect, which further hinders the implementation of the CC. We show that it is necessary to ensure that crack initiation does occur in the vicinity of a stress peak to obtain reliable fracture predictions thanks to the CC. The data of the tensile strength then provides a reliable critical failure load without it being necessary to finely model the defects which are at the origin of the rupture.

8.1 Introduction

Defining the apparent macroscopic or intrinsic material tensile strength of glass is challenging [1–3] and the presence of residual stresses (intentionally or unintentionally introduced during the manufacturing process) further complicates the problem

Dominique Leguillon
Institut Jean Le Rond d'Alembert, Sorbonne Université and CNRS UMR 7190, 4 place Jussieu, 75005 Paris, France,
e-mail: dominique.leguillon@upmc.fr

Isabell Schulz · Philipp L. Rosendahl
Institute of Structural Mechanics and Design, Technical University of Darmstadt, Franziska-Braun-Str. 3, 64287 Darmstadt, Germany,
e-mail: schulz@ismd.tu-darmstadt.de,rosendahl@ismd.tu-darmstadt.de

[4]. Indeed, measuring the tensile strength by a standard bending test (e.g., 4-point bending or ring-to-ring bending tests) in glass specimens is more a measurement of the presence of internal and surface defects than the determination of a constant material property, explaining that it leads to a large scattering [5]. While an intrinsic strength of glass has been suggested in a range of several GPa [5], the observable strength in bending tests is in a range of a few MPa (typically somewhere between 5 - 200 MPa [5, 6]. The strength of glass has been found to highly depend on environmental conditions and the size and favourable location of existing internal or surface flaws. Indeed, it is admitted that it has not a deterministic value but is defined through a probabilistic distribution, the so-called Weibull law [7]. Such a situation makes it difficult to use the Coupled Criterion (CC). The latter specifically requires the knowledge of the tensile strength of the material to implement the stress condition. This condition complements the energy condition derived from the energy balance to form a twofold criterion [8, 9]. However, in some cases, ceramic materials for instance, this difficulty can be partially overcome. It is well known that in bending tests, polishing the tested specimens leads to an increased load at failure. However the curves reach a plateau when the surface defects become smaller than a certain threshold, the so-called intrinsic strength (Fig. 8.1). In ceramic materials, this plateau is strongly related to the grain size, i.e., a microstructural length scale. It has been shown in [10] that this plateau is the value to be used by the CC to predict, for instance, crack nucleation at a sharp V-notch. A sharp V-notch is a major defect, stresses are singular and any statistical rule fails. Unfortunately, such a plateau does not exist in glass, due to its amorphous microstructure, and removing tiny extrinsic defects leads to higher and higher loads at failure which can exceed 10 GPa [5] [11], again emphasizing the interpretation of macroscopic strength as a measure for microstructural length scales - in this case the size of initial defects. In other words, not surprisingly, out of crack-like defects involving singularity exponents close to 1/2 (a crack), the CC will predict very high applied loads to trigger a failure. In addition, residual temper stresses, introduced into the glass by thermal or chemical tempering (see Fig. 8.2) move the stress peak inside the specimen while failure occurs at the surface due to a critical defect, which further hinders the implementation of the CC.
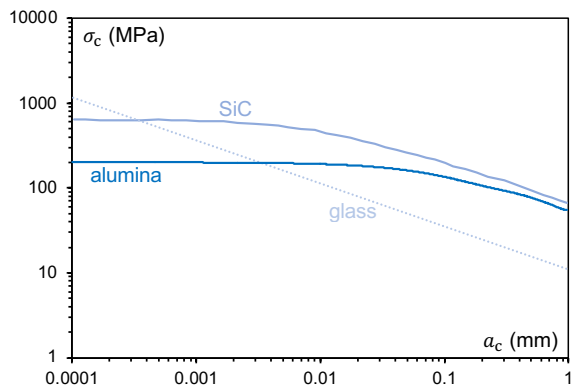
Fig. 8.1 Relationships between surface defect depth a_c and fracture stress σ_c for glass and ceramic materials, highlighting that the curves of alumina and SiC end in a plateau towards small surface flaws (data from [6]).
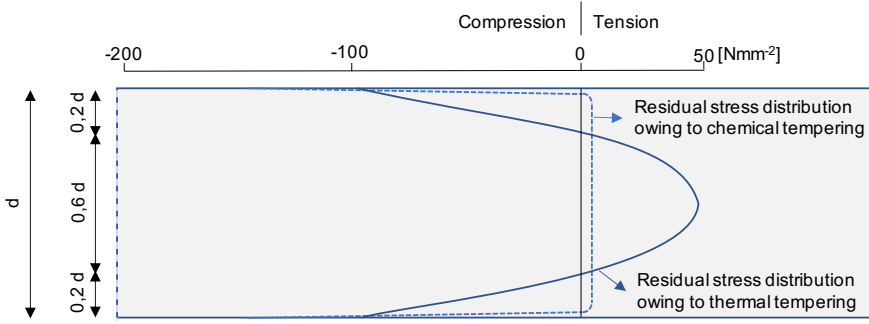
Fig. 8.2: Residual stress distribution in glass due to thermal and chemical tempering.

We show that it is necessary to ensure that crack initiation does occur in the vicinity of a stress peak to obtain reliable fracture predictions thanks to the CC. The data of the tensile strength then provides a reliable failure load without it being necessary to finely model the defects which are at the origin of the rupture.

8.2 Annealed Glass Specimen Under Bending

As discussed above, measuring the tensile strength by a bending test (Fig. 8.3) is, especially in glass specimens, more a measurement of the presence of surface defects than the determination of a constant material parameter [2, 12]. Thus, there is a relationship between σ_c and the defects size. For a crack-like defect, we can derive it from the formula found in [13] on stress intensity factors

$$K_I = \sigma \sqrt{\pi a} F(a/b) \tag{8.1}$$

K_I is the stress intensity at the tip of the surface crack, σ is the remote tensile stress, a the crack depth and b the specimen width. The function F depends on the ratio a/b and is approximately $F(a/b) \approx 1.122$ for small ratios.
According to Irwin's form of Griffith's criterion, the crack grows if $K_I = K_{Ic}$ where K_{Ic} is the material toughness. This occurs for the critical load σ_c and then the corresponding critical defect size a_c is

$$a_c = \frac{1}{1.259 \times \pi} \left(\frac{K_{Ic}}{\sigma_c} \right)^2 \tag{8.2}$$

On the other hand, the CC predicts crack initiation at stress concentration points from two parameters: the toughness and the tensile strength of the material [8] [9]. Unlike Griffith's criterion, it does not assume the existence of a pre-existing crack. It is a nucleation criterion while Griffith's criterion only concerns crack growth. The CC is

1. case: annealed glass
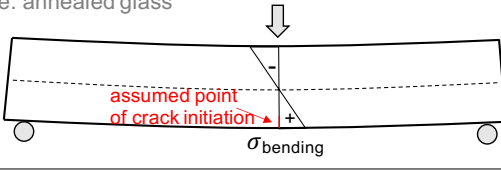
2. case: thermally tempered glass
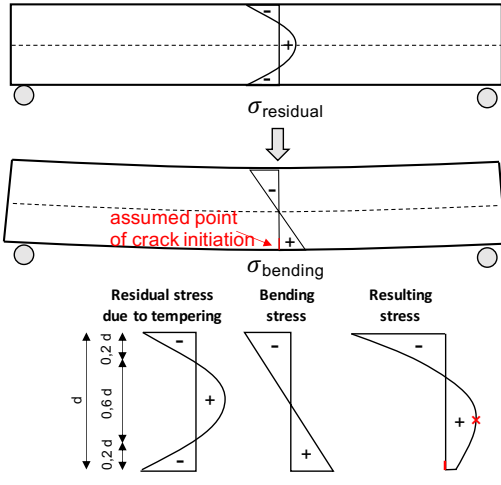
3. case: hypothetical tensile test
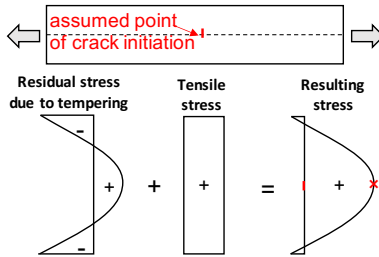
Fig. 8.3: Overview of considered test configuration - exemplary for the cases of annealed and tempered glass.

twofold: an energy condition, enough energy must be available to allow the creation of a crack of length a_{cc}, and a stress condition, the tensile stress prior to nucleation must be larger than the tensile strength σ_c all along the expected crack path with length a_{cc}. A consequence of these two conditions is that in general nucleation is an unstable process, there is a crack jump from 0 to a_{cc} without equilibrium in between. Fulfilling the two conditions allows calculating both a_{cc} and the critical load at failure. The initiation length a_{cc} differs from the critical flaw size a_c, however, these lengths both depend on Irwin's length $(K_{Ic}/\sigma_c)^2$ (see Table 8.1).

Table 8.1: The critical defect size a_c and the crack initiation length a_{cc} functions of the tensile strength σ_c, for K_{Ic}= 0.75 MPa m$^{1/2}$, according respectively to (8.2) and to the CC..

σ_c (MPa)	15	30	45	60	75	90
a_c (µm)	652	158	70	39	25	18
a_{cc} (µm)	764	277	135	79	53	38

The two approaches lead to very close predictions as shown in Fig. 8.4. The advantage of the CC is that it works from a model of smooth specimen whereas Griffith's criterion requires consideration of the small surface defect and a much more refined mesh accordingly. In general, the datum σ_c makes it possible to get rid of size and shape of micro-defects, again emphasizing its property as a proxy for the size of defects [10]. Note there are two ways to implement the CC, if a_{cc} is small enough compared to any dimension of the specimen, a quasi-analytical approach based on matched asymptotic expansions is possible [8], otherwise full FE calculations can be carried out. In the former case, the smallness is verified afterwards and validates or not the use of asymptotic expansions, while the second one does not require any smallness condition. In the present calculations the full FE approach was selected. The tensile stress was computed along the presupposed crack path in the uncracked domain, then a virtual crack with varying length was introduced to compute the strain energy as a function of a_{cc}.

8.3 Tempered Glass Specimen Under Bending

The most common method of strengthening glass by residual stresses is through a heat treatment. In a tempered glass, these residual stresses are classically modeled through the thickness by a second order polynomial, it is a compression –90 MPa at the surface and, to compensate, a tension inside, which reaches +45 MPa in the
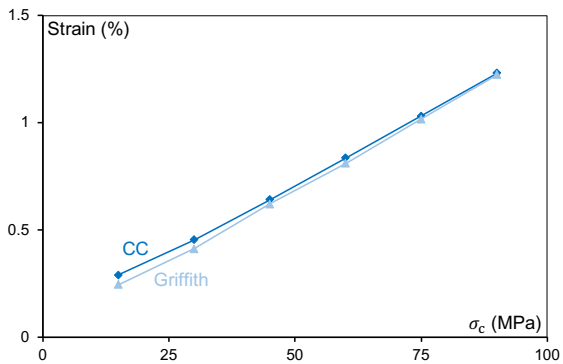
Fig. 8.4 Comparison between Griffith's criterion (in red) and the CC (in blue) in the prediction of the critical strain at failure as a function of the tensile strength.

middle of the specimen (Fig. 8.2) [4]. It should be noted that this profile corresponds to a pane thickness of 5 mm but that the intensity of the residual stresses decreases with the thickness [4].

In the previous section, the peak stress was at the free surface in tension and the standard situation of the application of the CC at a stress concentration point is met, i.e. the tensile stress is a decreasing function of the distance to the initiation point. Now, in the presence of thermal residual stresses, for small σ_c the applied stress at failure remains small and the peak stress is located far inside the specimen. Then, with an increasing σ_c, it moves toward the surface and thus approaches the supposed point of initiation.

However, it is observed during testing that the failure initiation continues to occur from surface defects while the peak stress is inside the specimen. In the forthcoming comparison, Griffith's criterion is still applied at the tip of the surface crack-like defect while the implementation of the CC assumes also an initiation from the (smooth) surface, abandoning the classical situation described above. The consequences can be seen in Fig. 8.5, the farther the peak stress is from the surface and thus from the supposed point of initiation, the more the CC prediction deviates from Griffith's criterion.

However, it is possible to somewhat temper this conclusion. Very small values of σ_c lead to larger and larger defect sizes (see Table 8.2) that can no longer be neglected when implementing the CC which predicts new crack initiation from a macroscopic point of view, i.e. without taking into account microscopic details of geometry.

Table 8.2: The critical defect size a_c and the crack initiation length a_{cc} functions of the tensile strength σ_c, for $K_{Ic}= 0.75$ MPa m$^{1/2}$, according respectively to (8.4) and to the CC..

σ_c (MPa)	15	30	45	60	75	90
a_c (µm)	796	199	88	50	32	22
a_{cc} (µm)	1470	411	192	115	79	60

Fig. 8.5 Comparison between Griffith's criterion (in red) and the CC (in blue) in the prediction of the critical strain at failure as a function of the tensile strength σ_c, in the presence of thermal residual stresses.
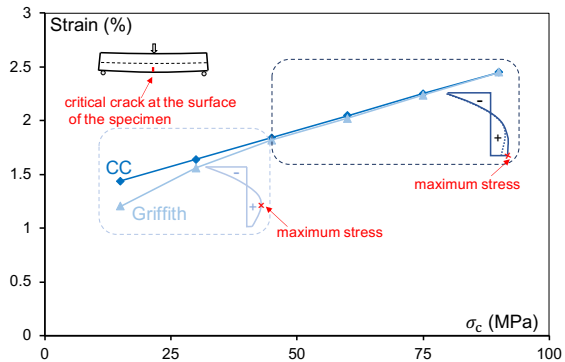
This discrepancy can worsen in case of a chemical tempering (Fig. 8.2). The chemical process leads to residual stresses located in a small band along the surface with a high gradient [14] and it is clearly visible in Fig. 8.6 that the CC predictions deviate significantly from Griffith's over a significant range of σ_c values.

It seems clearly that the location of the initiation point compared to that of the peak stress is determinant in the reliability of the CC. This will be clear in the next example.

8.4 The Hypothetical Case of a Critical Defect in the Bulk of a Thermally Tempered Glass Specimen Under Tension

We assume now, in presence of thermal residual stresses (Fig. 8.2) or not, that the crack initiates from the middle of the specimen under a tensile applied load (a priori an invented situation, the literature being sparse on tensile tests on glass specimens, except maybe on glass fibers alone or embedded in a composite). Thus the peak stress and the initiation point coincide. The corresponding stress intensity factor formula is now [13]

$$K_I = \sigma \sqrt{\pi \frac{a}{2}} F(a/b) \tag{8.3}$$

Note that usually this relationship is expressed in terms of the half length of the centered crack, noted $a/2$ here. The function $F(a/b)$ is close to 1 for small ratios and then

$$a_c = \frac{2}{\pi} \left(\frac{K_{Ic}}{\sigma_c} \right)^2 \tag{8.4}$$

Resulting in a similar tensile strength, the critical flaw size a_c derived from Griffith's criterion is significantly larger for inner defects than for surface ones (Tables 8.1 and 8.2) whereas practically only smaller and less critical flaws occur inside the material [15]. This could suggest a variable parameter σ_c through the thickness, significantly larger inside the material than at the surface. Although a variable parameter is not
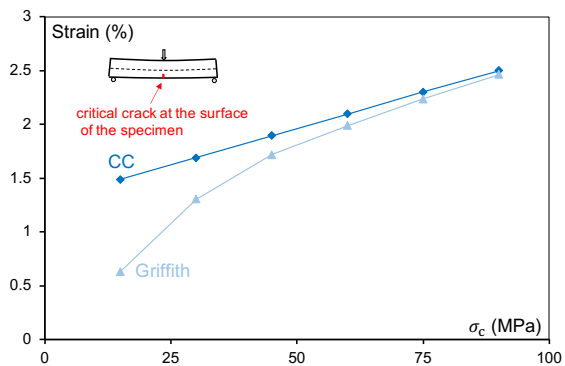
Fig. 8.6 Comparison between Griffith's criterion (in red) and the CC (in blue) in the prediction of the critical strain at failure as a function of the tensile strength σ_c, in the presence of chemical residual stresses.

excluded in the CC implementation as in oxide layers for instance [16], it has not been possible to implement this approach convincingly.

In this case there is a good agreement between Griffith's criterion and the CC in the presence or not of thermal residual stresses (Fig. 8.7). Clearly, in case of residual stresses, if $\sigma_c < 45$ MPa, failure could occur during the quenching process before any mechanical loading. Note that, in the absence of residual stresses, the CC is nothing else than the maximum tensile stress criterion.

This result confirms that of Sect. 8.2, the CC works properly as long as the initiation point is close to the peak stress, otherwise it exhibits a discrepancy. Once again, the datum σ_c allows a simple implementation of the CC which does not require modeling the defect at the origin of the failure, contrary to using Griffith's criterion.

8.5 Comparison with a Bending Test on Notched Zirconia Specimens

To enrich our examples of residual stresses, this section does not concern glass but zirconia. When such a sample is machined to create a notch, the honing causes a phase change that generates a very thin layer of residual stress on the surface. The compression in this layer, whose thickness does not exceed 7-8 μm, can reach 1800 MPa (Fig. 8.8). Moreover, these residual stresses depend also on the notch root radius r, which is one variable parameter of the experiments. They reach a maximum for r between 5 and 12 μm. For wider notches with radii above $\simeq 90$ μm created by cooled diamond grinding, they are significantly smaller. These specimens are tested under
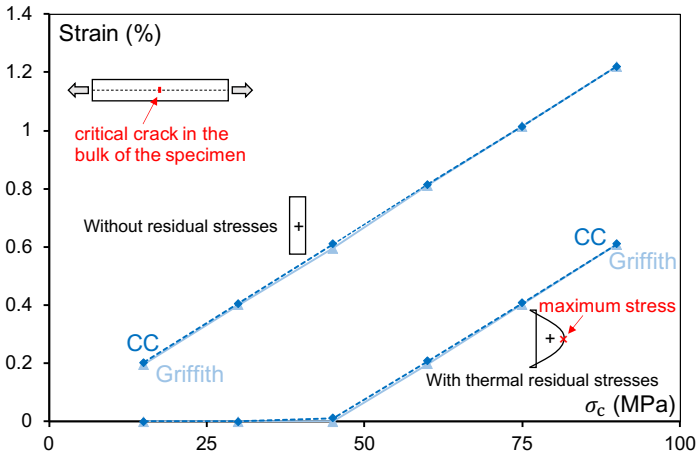
Fig. 8.7: Comparison between Griffith's criterion (in red) and the CC (in blue) in the prediction of the critical strain at failure as a function of the tensile strength σ_c, in case of a tensile test and the crack initiation in the middle of the specimen.
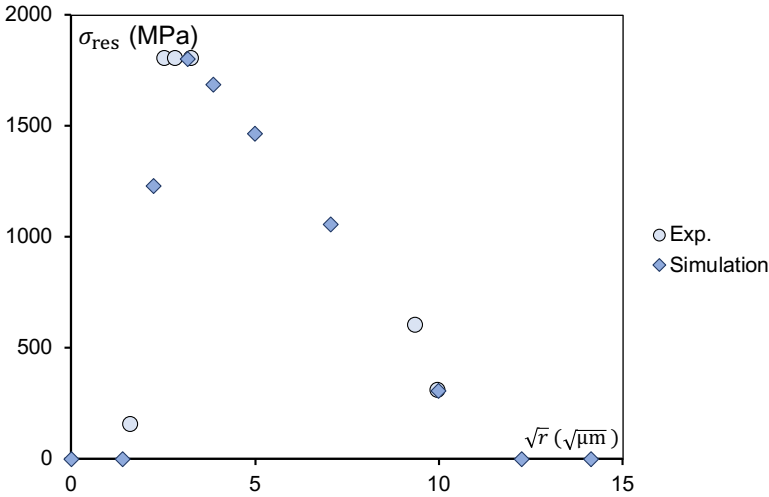
Fig. 8.8: Numerical simulation and experimental measurements of residual stresses due to the phase change caused by honing, function of the root radius r of the notch.

4-point bending loading (Fig. 8.9). In addition, a part of the samples undergoes a thermal post-treatment to release the residual stresses (Fig. 8.8) [17] [18].

The agreement between 4-point bending tests and the CC theoretical predictions is fully satisfactory (Fig. 8.10). There are two good reasons for this, the notch with a small root radius strongly concentrates the stresses (almost like a crack) and the residual stresses only slightly shift the stress peak inwards. Note that the parameter K_{Ic} in Fig. 8.8 is an equivalent K_{Ic}, the considered slit not being a real crack because of its rounding.
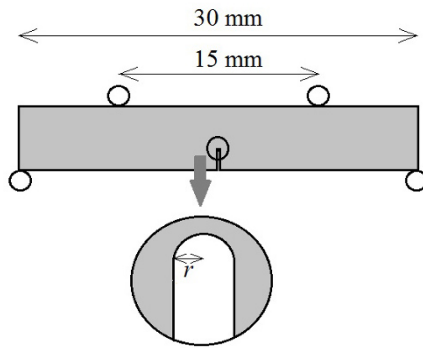
Fig. 8.9 4-point bending test on a notch specimen.
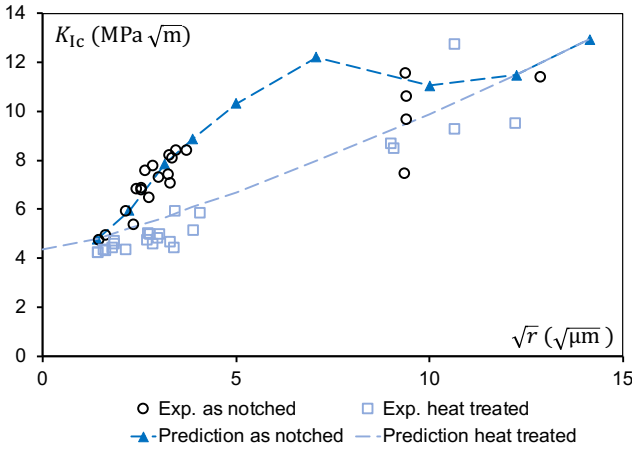
Fig. 8.10: Comparison between predictions using the CC (dashed lines) and experiments on notched specimens of zirconia.

8.6 Discussion and Conclusions

The CC makes it possible to predict the nucleation of new cracks from the data of two parameters: material toughness and tensile strength, without having to consider precisely any micro-structural particularity at the origin of the failure. This is, at large, because σ_c acts as a proxy for microstructure and incompasses information on microstructural length scales. This parameter can vary but it supposes that it characterizes the material not only a local property. Under these conditions, the hypothesis that the initiation of a crack occurs in the vicinity of a peak stress or more precisely of the maximum of the ratio σ/σ_c seems consistent, and this has been verified many times in the implementation of the CC when compared with experiments [9]. In contrast, in glass and tempered glass in particular, σ_c is ultimately just a measure of the surface finish because its armorphous microstructure does not exhibit length scales that are relevant to the fracture process. Moreover, since they are extremely brittle materials for which the theoretical σ_c is very high, they are only sensitive to crack-like defects. Under these conditions, ignoring micro-structural surface flaws when predicting failure, as the CC theoretically allows, turns out to be risky. It is then necessary to use the concept of equivalent crack length [6] and then the CC is no other than Griffith's criterion [8].

The CC is therefore effective provided that the ratio σ/σ_c is a decreasing function of the distance to the crack initiation point. On the other hand, the CC uses also the ratio G^{inc}/G_c where G_c is the fracture energy, related to K_{Ic} through Irwin's relationship, and G^{inc} is the incremental energy release rate, the incremental counterpart to the classical energy release rate defined as a derivative [8]. It is generally an increasing function of the virtual crack length but does not pose the same difficulties. Depending on the structural situation, it can eventually decrease (the so-called negative geometry

in [19]) or increase (positive geometry) with increasing crack size and this leads to different conclusions that are consistent with experiments.

References

[1] Kurkjian C, Gupta P, Brow R (2010) The strength of silicate glasses: What do we know, what do we need to know? International Journal of Applied Glass Science **1**:27–37

[2] Sugarman B (1967) Strength of glass (a review). Journal of material science **2**:275–283

[3] Veer F, Louter P, Bos F (2008) The strength of annealed, heat strengthened and fully tempered float glass. Fatigue & Fracture of Engineering materials & Structures **32**:18–25

[4] Nielsen J, Olesen J, Stang H (2009) The fracture process of tempered soda-lime-silica glass. Experimental Mechanics **49**:855–870

[5] Petzold A, Marush H, Schramm B (1990) Der Baustoff Glas: Grundlagen, Eigenschaften, Erzeugnisse, Glasbauelemente, Anwendungen. Hofmann, Schorndorf, 3rd edition

[6] Usami S, Kimoto H, Takahashi I, Shida S (1986) Strength of ceramic materials containing small flaws. Engineering Fracture Mechanics **23**:745–761

[7] Weibull W (1951) A statistical distribution function of wide applicability. Journal of Applied Mechanics **18**:293–297

[8] Leguillon D (2002) Strength or toughness? a criterion for crack onset at a notch. European Journal of Mechanics A/Solids **21**:61–72

[9] Weissgraeber P, Leguillon D, Becker W (2016) A review of finite fracture mechanics: Crack initiation at singular and non-singular stress-raisers. Archive of Applied Mechanics **86**:375—401

[10] Leguillon D, Martin E, Sevecek O, Bermejo R (2018) What is the tensile strength of a ceramic to be used in numerical models for predicting crack initiation? International Journal of Fracture **212**:89–103

[11] Rouxel T, Yoshida S (2017) The fracture toughness of inorganic glass. Journal of the American Ceramic Society **100**:4374–4396

[12] Alter C, Kolling S, Schneider J (2017) An enhanced non-local failure criterion for laminated glass under low velocity impact. International Journal of Impact Engineering **109**:342–353

[13] Tada H, Paris P, Irwin G (2000) The stress analysis of cracks handbook. ASME Press, 3rd edition, New York

[14] Haldimann M (2006) Fracture strength of structural glass elements – Analytical and numerical modelling, testing and design. Thèse – Ecole Polytechnique Fédérale de Lausanne

[15] Nielsen J (2017) Remaining stress-state and strain-energy in tempered glass fragments. Glass Structural Engineering **2**:45–56

[16] Leguillon D, Lafarie-Frenot M, Pannier Y, Matin E (2016) Prediction of the surface cracking pattern of an oxidized polymer induced by residual and bending stresses. International Journal of Solids and Structures **91**:89–101

[17] Leguillon D, Lube T, Bermejo R (2023) Failure of notched zirconia specimens under residual stress. In: The Seventh International Conference on Computational Modeling of Fracture and Failure of Materials and Structures CFRAC 2023 Prague, Czech Republic, 21–23 June 2023.

[18] Lube T, Luca M (2017) Measuring fracture toughness of y-tpz. In: 15th Conference & Exhibition of the European Ceramic Society, ECerS2017, Budapest, Hungary.

[19] Weissgraeber P, Hell S, Becker W (2016) Crack nucleation in negative geometries. Engineering Fracture Mechanics **168**:93–104

Chapter 9
Extended Reduced Bending Stiffness Method for Shear Deformable Laminated Plates

Philip Schreiber, Jakob C. Schilling, and Christian Mittelstedt

Abstract For the development of fast and simple computational methods for practical application in lightweight design, it is beneficial to simplify complex coupling behaviours of composite laminates. To this end, the RBS method is commonly used. Here, the method based on the framework of the classical laminated plate theory yields agreeable results for most configurations. However, the effect of shear deformation in laminates is not considered. Therefore, the novel formulation of the reduced bending stiffness (RBS) method for application in the framework of the third-order shear deformation theory (TSDT) is evaluated in the present work. Bending, buckling, and vibration are investigated for antisymmetric cross-ply laminates and antisymmetric angle-ply laminates. The presented results show the significant influence of the relative thickness which reduces the deviation of the RBS results relative to the Navier solution. The extended RBS method yields good agreement and presents the opportunity to simplify computational models in the framework of the TSDT.

9.1 Introduction

The design of lightweight structures greatly benefits from the properties of advanced materials. For example, the strength and stiffness properties of fibre-reinforced plastics are excellent and contribute greatly to the exploitation of the lightweight potential. However, the advantageous properties come at a price, one of them is the complex material behaviour. This is especially evident for unsymmetric laminated plates, where the out-of-plane behaviour is coupled with the in-plane behaviour, i.e. bending-

Philip Schreiber · Jakob C. Schilling · Christian Mittelstedt
Technical University Darmstadt, Institute for Lightweight Engineering and Structural Mechanics, Otto-Berndt-Straße 2, 64287 Darmstadt, Germany,
e-mail: philip.schreiber@lsm.tu-darmstadt.de,
jakob.schilling@lsm.tu-darmstadt.de,
christian.mittelstedt@lsm.tu-darmstadt.de

237

extensional coupling occurs. In analysis models where computational efficiency is of the utmost importance, this complex behaviour is often approximated by the reduced bending stiffness method (RBS). Especially in stringer-stiffened panels, the stringer foot is often approximated in this way in the context of stability analysis [1–6]. The RBS method reduces the complexity of the computational models significantly. Therefore, it is a suitable tool for practical application [7].

The present work focuses on the investigation of the RBS method in the context of the analysis of single unsymmetrical laminated plates, which is important for the advancement of the computational efficiency of approximate analysis models developed for application in preliminary design. The RBS method traces back to the work of Reissner and Stavsky [8], where the bending and stretching behaviour of unsymmetric laminated plates is investigated. The authors base their analysis on the semi-inverse constitutive equations. Consequently, they also evaluate results that are computed neglecting the compatibility of in-plane strains, which yield approximate but reasonable results. Chamis [9] investigates this approach in the context of a buckling analysis describing it as the method of reduced rigidities. The term reduced bending stiffness method is finally introduced by Ashton [10]. The main idea of the RBS method is to neglect the bending-extension coupling effects by replacing the bending stiffnesses with reduced bending stiffnesses.

Different aspects of the RBS method were investigated in the past. In a thorough study of the bending, vibration and buckling of antisymmetric laminates it is shown that especially for angle-ply laminates the quality of the approximate RBS method suffers although very good results are obtained for cross-ply laminates. Another benchmark especially aimed at typical stringer foot assemblies in stiffened panels where the bending-extension coupling results from the stacking of different cross-ply laminates with an excentric reference plane shows that the RBS method is a valid approximation in the context of a buckling analysis [11]. There, also a detailed review of the highly debated general aspects of the RBS method implemented in a linear buckling analysis and neglecting the prebuckling deformation is given. The RBS method is also investigated for the nonlinear bending of general-ply laminated plates showing its applicability and reliability when no shear coupling occurs [12]. By investigating the buckling and vibration of shallow curved panels made of unsymmetric cross- and angle-ply laminates it is found that the RBS method is curvature sensitive [13].

The mentioned works all employ classical laminated plate theory (CLPT) and neglect the effects of transverse shear deformation. Very few publications are known to the authors where the RBS method is evaluated for shear deformable laminates. Based on the first-order shear deformation theory (FSDT) the bending of unsymmetrical laminated plates is discussed including also elastically restrained plates [14]. The RBS method is applied analogously, as the constitutive law is only extended by shear stiffnesses that are uncoupled from the bending-stretching behaviour of the laminate. Recently, the RBS method was formulated based on the third-order shear deformation theory (TSDT) by the authors for application in buckling analyses [15]. However, this novel formulation has not yet been systematically discussed for bending and vibration analyses. Consequently, the present work aims to address the question of the validity

of the RBS method for laminates based on higher-order shear deformation theories (HSDT). Therefore, antisymmetric cross- and angle-ply shear deformable laminates are analysed regarding their bending, buckling, and vibration behaviour including the aspect of plate thickness. The results are compared to available Navier-type solutions for unsymmetric shear deformable laminates [16] and compared to results previously presented in the literature. The presented studies show that the new formulation of the RBS method achieves excellent agreement for the cross-ply configurations and good agreement in the case of angle-ply configurations. The results gain in accuracy for increasing the relative thickness of the plates. This will be shown after the brief presentation of the novel RBS formulation and the presentation of the reference Navier solution. First, bending, buckling, and vibration are investigated for antisymmetric cross-ply laminates, followed by an equivalent investigation for antisymmetric angle-ply laminates.

9.2 Basic Equations of Third-Order Shear Deformation Theory (TSDT)

In this section, the basic equations of the third-order shear deformation theory (TSDT) are given in a brief form. Extensive descriptions of TSDT can be found, for instance, in the publication [7, 16, 17].

The displacement field of TSDT (9.1) eliminates the normal hypothesis from CLPT as well as the requirement that the cross sections remain plane. The TSDT describes both the cross-section warping and transverse shear deformations. The assumption of a plane stress state is made, which leads to the fact that the laminate thickness h does not change in the deformed state, as illustrated in Fig. 9.1. The plate under consideration has the width b and a length of a and can be loaded with normal loads and transverse loads as shown in Fig. 9.2. The quantities u, v and w denote the displacements in the direction of the coordinates x, y and z, respectively. The cross-sectional rotations ψ_x and ψ_y are defined as rotations about the x and y axes.
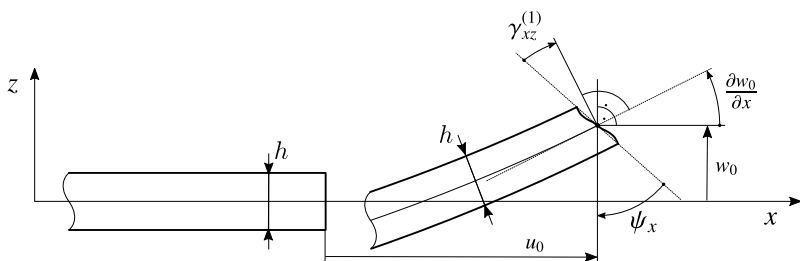
Fig. 9.1: Kinematics and cross-sectional deformation of the third-order shear deformation theory (TSDT), cubic cross-sectional deformation, cf. Eq. (9.1).
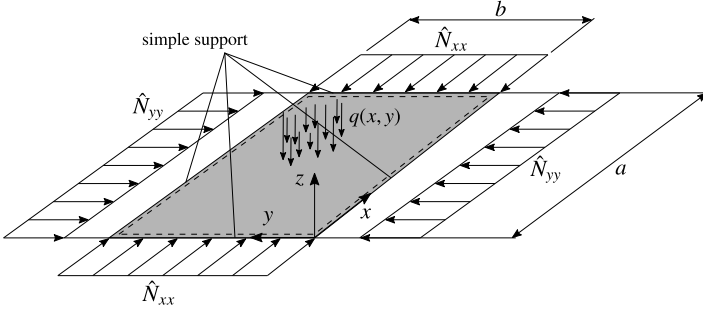
Fig. 9.2: Simply supported plate (Navier plate) with two normal line loads $\hat{N}_{xx}$ and $\hat{N}_{yy}$ as well as the transverse load $q(x,y)$.

$$u(x,y,z,t) = u_0(x,y,t) + z\psi_x(x,y,t) - \frac{4z^3}{3h^2}\left(\psi_x(x,y,t) + \frac{\partial w_0(x,y,t)}{\partial x}\right),$$

$$v(x,y,z,t) = v_0(x,y,t) + z\psi_y(x,y,t) - \frac{4z^3}{3h^2}\left(\psi_y(x,y,t) + \frac{\partial w_0(x,y,t)}{\partial y}\right),$$

$$w(x,y,t) = w_0(x,y,t). \tag{9.1}$$

The constitutive law from equation (9.2) contains on the left side the force and moment values per length, which are detailed in equation (9.3).

$$\underbrace{\begin{bmatrix} \underline{N} \\ \underline{M} \\ \underline{P} \\ \underline{Q} \\ \underline{R} \end{bmatrix}}_{\underline{N}} = \underbrace{\begin{bmatrix} \underline{\underline{A}} & \underline{\underline{B}} & \underline{\underline{E}} & \underline{\underline{0}} & \underline{\underline{0}} \\ \underline{\underline{B}} & \underline{\underline{D}} & \underline{\underline{F}} & \underline{\underline{0}} & \underline{\underline{0}} \\ \underline{\underline{E}} & \underline{\underline{F}} & \underline{\underline{H}} & \underline{\underline{0}} & \underline{\underline{0}} \\ \underline{\underline{0}} & \underline{\underline{0}} & \underline{\underline{0}} & \underline{\underline{A}}^{\mathrm{S}} & \underline{\underline{D}}^{\mathrm{S}} \\ \underline{\underline{0}} & \underline{\underline{0}} & \underline{\underline{0}} & \underline{\underline{D}}^{\mathrm{S}} & \underline{\underline{F}}^{\mathrm{S}} \end{bmatrix}}_{\underline{\underline{S}}} \underbrace{\begin{bmatrix} \underline{\varepsilon}^{(1)} \\ \underline{\varepsilon}^{(2)} \\ \underline{\varepsilon}^{(3)} \\ \underline{\gamma}^{(1)} \\ \underline{\gamma}^{(2)} \end{bmatrix}}_{\underline{\varepsilon}} \tag{9.2}$$

$$\underline{N} = \begin{bmatrix} N_{xx}^0 \\ N_{yy}^0 \\ N_{xy}^0 \end{bmatrix}, \quad \underline{M} = \begin{bmatrix} M_{xx}^0 \\ M_{yy}^0 \\ M_{xy}^0 \end{bmatrix}, \quad \underline{Q} = \begin{bmatrix} Q_y \\ Q_x \end{bmatrix}, \quad \underline{P} = \begin{bmatrix} P_{xx} \\ P_{yy} \\ P_{xy} \end{bmatrix}, \quad \underline{R} = \begin{bmatrix} R_y \\ R_x \end{bmatrix}. \tag{9.3}$$

The strains as well as shear strains are defined as follows:

$$\underline{\varepsilon}^{(1)} = \begin{bmatrix} \dfrac{\partial u_0}{\partial x} \\[2mm] \dfrac{\partial v_0}{\partial y} \\[2mm] \dfrac{\partial u_0}{\partial y} + \dfrac{\partial v_0}{\partial x} \end{bmatrix}, \quad \underline{\varepsilon}^{(2)} = \begin{bmatrix} \dfrac{\partial \psi_x}{\partial x} \\[2mm] \dfrac{\partial \psi_y}{\partial y} \\[2mm] \dfrac{\partial \psi_x}{\partial y} + \dfrac{\partial \psi_y}{\partial x} \end{bmatrix},$$

$$\underline{\varepsilon}^{(3)} = \begin{bmatrix} -\dfrac{4}{3h^2}\left(\dfrac{\partial \psi_x}{\partial x} + \dfrac{\partial^2 w_0}{\partial x^2}\right) \\[2mm] -\dfrac{4}{3h^2}\left(\dfrac{\partial \psi_y}{\partial y} + \dfrac{\partial^2 w_0}{\partial y^2}\right) \\[2mm] -\dfrac{4}{3h^2}\left(\dfrac{\partial \psi_x}{\partial y} + \dfrac{\partial \psi_y}{\partial x} + 2\dfrac{\partial^2 w_0}{\partial x \partial y}\right) \end{bmatrix},$$

$$\underline{\gamma}^{(1)} = \begin{bmatrix} \psi_y + \dfrac{\partial w_0}{\partial y} \\[2mm] \psi_x + \dfrac{\partial w_0}{\partial x} \end{bmatrix}, \quad \underline{\gamma}^{(2)} = \begin{bmatrix} -\dfrac{4}{h^2}\left(\psi_y + \dfrac{\partial w_0}{\partial y}\right) \\[2mm] -\dfrac{4}{h^2}\left(\psi_x + \dfrac{\partial w_0}{\partial x}\right) \end{bmatrix}. \tag{9.4}$$

The stiffness values of the constitutive law (9.2) result from the reduced stiffnesses which are defined by the engineering constants as follows:

$$Q_{11} = \dfrac{E_{11}}{1 - \nu_{12}\nu_{21}}, \ Q_{22} = \dfrac{E_{22}}{1 - \nu_{12}\nu_{21}}, \ Q_{12} = \dfrac{\nu_{12}E_{22}}{1 - \nu_{12}\nu_{21}}, \ Q_{16} = 0,$$

$$Q_{26} = 0, \qquad Q_{66} = G_{12}, \qquad C_{44} = G_{23}, \qquad C_{55} = G_{13} \tag{9.5}$$

These are subsequently transformed from the on-axis coordinate system into the laminate coordinate system:

$$\underline{\underline{\bar{Q}}} = \underline{\underline{T}}_Q \, \underline{\underline{Q}} \, \underline{\underline{T}}_Q^{\mathrm{T}}, \quad \underline{\underline{\bar{C}}} = \underline{\underline{T}}_C \begin{bmatrix} G_{23} & 0 \\ 0 & G_{13} \end{bmatrix} \underline{\underline{T}}_C^{\mathrm{T}} \quad \text{with} \quad \underline{\underline{T}}_Q = \begin{bmatrix} c^2 & s^2 & -2cs \\ s^2 & c^2 & 2cs \\ cs & -cs & c^2 - s^2 \end{bmatrix},$$

$$\underline{\underline{T}}_C = \begin{bmatrix} c & s \\ -s & c \end{bmatrix}, \quad s = \sin(\varphi), \quad c = \cos(\varphi). \tag{9.6}$$

Finally, the submatrices from equation (9.2) can be calculated as follows:

$$\left. \begin{aligned} A_{ij} &= \int_{-\frac{t}{2}}^{\frac{t}{2}} \bar{Q}_{ij}\mathrm{d}z, \quad B_{ij} = \int_{-\frac{t}{2}}^{\frac{t}{2}} \bar{Q}_{ij}z\,\mathrm{d}z, \quad D_{ij} = \int_{-\frac{t}{2}}^{\frac{t}{2}} \bar{Q}_{ij}z^2\mathrm{d}z, \\ E_{ij} &= \int_{-\frac{t}{2}}^{\frac{t}{2}} \bar{Q}_{ij}z^3\mathrm{d}z, \ F_{ij} = \int_{-\frac{t}{2}}^{\frac{t}{2}} \bar{Q}_{ij}z^4\mathrm{d}z, \ H_{ij} = \int_{-\frac{t}{2}}^{\frac{t}{2}} \bar{Q}_{ij}z^6\mathrm{d}z, \end{aligned} \right\} \ i,j = 1,2,6.$$

$$\left. A_{ij}^{\mathrm{S}} = \int_{-\frac{t}{2}}^{\frac{t}{2}} \bar{C}_{ij}\mathrm{d}z, \ D_{ij}^{\mathrm{S}} = \int_{-\frac{t}{2}}^{\frac{t}{2}} \bar{C}_{ij}z^2\mathrm{d}z, \ F_{ij}^{\mathrm{S}} = \int_{-\frac{t}{2}}^{\frac{t}{2}} \bar{C}_{ij}z^4\mathrm{d}z, \right\} \quad i,j = 4,5.$$

Only orthotropic laminates are considered in this publication. Consequently, the following entries in the stiffness matrices disappear:

$$A_{16} = A_{26} = D_{16} = D_{26} = F_{16} = F_{26} = H_{16} = H_{26}$$

$$= A_{45} = D_{45} = F_{45} = 0. \tag{9.7}$$

In the context of unsymmetrical laminates, this results in two laminate types. On the one hand, the unsymmetric cross-ply laminate has the following zero entries in addition to (9.7):

$$B_{16} = B_{26} = E_{16} = E_{26} = 0. \tag{9.8}$$

On the other hand, the antisymmetric angle-ply laminate, which, besides the zero entries of (9.7), shows the following:

$$B_{11} = B_{12} = B_{22} = B_{66} = E_{11} = E_{12} = E_{22} = E_{66} = 0. \tag{9.9}$$

The inertias can be calculated with:

$$I_i = \int_{-h/2}^{h/2} \rho z^i \, \mathrm{d}z, \text{ for } i = 0, 1, \ldots, 6. \tag{9.10}$$

For the class of laminates considered, the following entries are zero $I_1 = I_3 = I_5 = 0$.

9.3 Reduced Bending Stiffness Method

In the TSDT, besides the coupling terms B_{ij} from CLPT and FSDT, there are further coupling terms in the constitutive law (9.2) which have to be considered in the reduced stiffness method. In the first step, the semi-inverse of the constitutive law (9.2) with respect to $\underline{\varepsilon}_1$ and $\underline{N}$ is formed. This leads to the following relationship:

$$
\begin{bmatrix} \underline{\varepsilon_1} \\ \underline{M} \\ \underline{P} \\ \underline{Q} \\ \underline{R} \end{bmatrix} =
\begin{bmatrix}
\underline{\underline{A}}^* & -\underline{\underline{B}}^* & -\underline{\underline{E}}^* & \underline{\underline{0}} & \underline{\underline{0}} \\
\underline{\underline{B}}^{*T} & \underline{\underline{D}}^* & \underline{\underline{F}}^* & \underline{\underline{0}} & \underline{\underline{0}} \\
\underline{\underline{E}}^{*T} & \underline{\underline{F}}^{*T} & \underline{\underline{H}}^* & \underline{\underline{0}} & \underline{\underline{0}} \\
\underline{\underline{0}} & \underline{\underline{0}} & \underline{\underline{0}} & \underline{\underline{A}}^S & \underline{\underline{D}}^S \\
\underline{\underline{0}} & \underline{\underline{0}} & \underline{\underline{0}} & \underline{\underline{D}}^S & \underline{\underline{F}}^S
\end{bmatrix}
\begin{bmatrix} \underline{N} \\ \underline{\varepsilon_2} \\ \underline{\varepsilon_3} \\ \underline{\gamma_1} \\ \underline{\gamma_2} \end{bmatrix} \tag{9.11}
$$

with

$$
\begin{aligned}
\underline{\underline{A}}^* &= \underline{\underline{A}}^{-1}, & \underline{\underline{D}}^* &= \underline{\underline{D}} - \underline{\underline{B}}\,\underline{\underline{A}}^{-1}\underline{\underline{B}}, \\
\underline{\underline{B}}^* &= \underline{\underline{A}}^{-1}\underline{\underline{B}}, & \underline{\underline{F}}^* &= \underline{\underline{F}} - \underline{\underline{B}}\,\underline{\underline{A}}^{-1}\underline{\underline{E}}, \\
\underline{\underline{E}}^* &= \underline{\underline{A}}^{-1}\underline{\underline{E}}, & \underline{\underline{H}}^* &= \underline{\underline{H}} - \underline{\underline{E}}\,\underline{\underline{A}}^{-1}\underline{\underline{E}}.
\end{aligned} \tag{9.12}
$$

Considering the inner potential and substituting the relations from (9.2), it follows:

$$
\begin{aligned}
\Pi_i &= \frac{1}{2} \int_0^b \int_0^a \underline{\overline{\varepsilon}}^{\mathrm{T}} \underline{\overline{N}} \, \mathrm{d}x \, \mathrm{d}y, \\
&= \frac{1}{2} \int_0^b \int_0^a \left(\underline{\varepsilon_1}^T \underline{\underline{A}} \underline{\varepsilon_1} + 2\underline{\varepsilon_1}^T \underline{\underline{B}} \underline{\varepsilon_2} + 2\underline{\varepsilon_1}^T \underline{\underline{E}} \underline{\varepsilon_3} \right. \\
&\quad + \underline{\varepsilon_2}^T \underline{\underline{D}} \underline{\varepsilon_2} + 2\underline{\varepsilon_2}^T \underline{\underline{F}} \underline{\varepsilon_3} + \underline{\varepsilon_3}^T \underline{\underline{H}} \underline{\varepsilon_3}
\end{aligned}
$$

$$+\underline{\gamma_1}^T \underline{\underline{A}}^S \underline{\gamma_1} + 2 \underline{\gamma_1}^T \underline{\underline{D}}^S \underline{\gamma_2} + \underline{\gamma_2}^T \underline{\underline{F}}^S \underline{\gamma_2}\Big) \, \mathrm{d}x \, \mathrm{d}y. \tag{9.13}$$

Into this formulation (9.14), the new expression of $\underline{\varepsilon_1}$ from equation (9.11) is substituted which results in the following expression:

$$
\begin{aligned}
\Pi_i = \frac{1}{2} \int_0^b \int_0^a \Big(& \underline{N}^T \underline{\underline{A}}^* \underline{N} + \underline{\varepsilon_2}^T \underline{\underline{D}}^* \underline{\varepsilon_2} + 2 \underline{\varepsilon_2}^T \underline{\underline{F}}^* \underline{\varepsilon_3} \\
& + \underline{\varepsilon_3}^T \underline{\underline{H}}^* \underline{\varepsilon_3} + \underline{\gamma_1}^T \underline{\underline{A}}^S \underline{\gamma_1} + 2 \underline{\gamma_1}^T \underline{\underline{D}}^S \underline{\gamma_2} \\
& + \underline{\gamma_2}^T \underline{\underline{F}}^S \underline{\gamma_2}\Big) \, \mathrm{d}x \, \mathrm{d}y.
\end{aligned}
\tag{9.14}
$$

The newly obtained potential expression (9.14) shows a decoupling of $\underline{N}$ from the remaining strains ($\underline{\varepsilon_2}, \underline{\varepsilon_3}, \underline{\gamma_1}, \underline{\gamma_2}$). Thus, the potential (9.14) no longer exhibits bending-extension coupling. With this method, unsymmetric laminates can now be treated as effectively symmetric in the context of TSDT by using the reduced stiffnesses in the constitutive law (9.11). This is implemented by deleting the first three rows and columns in the constitutive law (9.11) and only considering the quantities $\underline{M}$, $\underline{P}$, $\underline{Q}$, and $\underline{R}$.

9.4 Navier Solution

Based on the orthotropic laminate behaviour considered, the general form of the ansatz functions provides a separation of the variables with respect to the x and y directions. Due to the different coupling effects in the stiffness matrix of the constitutive law, a distinction has to be made between cross- and angle-ply laminates as described in Equation (9.7), (9.8), (9.8), as well as (9.9). The boundary conditions of the Navier plate are to be chosen differently for unsymmetric cross-ply and antisymmetric angle-ply laminates with respect to their solvability, as described in [16, 18]. For the plate simply supported at all edges, the boundary conditions are described in the following. At the edge $x = 0, a$ applies:

$$
\left.
\begin{aligned}
&\text{cross-ply:} \\
&N_{xx}^0 = v_0 = 0, \\
&\text{angle-ply:} \\
&N_{xy}^0 = u_0 = 0,
\end{aligned}
\right\} w_0 = M_{xx}^0 = \psi_y = P_{xx} = 0. \tag{9.15}
$$

At the edges $y = 0, b$ the following applies:

$$
\left.
\begin{array}{l}
\text{cross-ply:} \\
N_{yy}^0 = u_0 = 0, \\
\text{angle-ply:} \\
N_{xy}^0 = v_0 = 0,
\end{array}
\right\}
\ w_0 = \psi_x = P_{yy} = M_{yy}^0 = 0.
\tag{9.16}
$$

The ansatz function for cross-ply laminates Φ_i^{CP} and angle-ply laminates Φ_i^{AP} are taken from [16] and can be found in Equation (9.17). These contain the abbreviation $\alpha = m\pi/a$ as well as $\beta = n\pi/b$ and fulfil the boundary conditions identically.

$$
\Phi_i^{\mathrm{CP}} =
\begin{bmatrix}
\sum\limits_{m,n=1}^{\infty} U_{mn}(t)\cos(\alpha x)\sin(\beta y) \\
\sum\limits_{m,n=1}^{\infty} V_{mn}(t)\sin(\alpha x)\cos(\beta y) \\
\sum\limits_{m,n=1}^{\infty} W_{mn}(t)\sin(\alpha x)\sin(\beta y) \\
\sum\limits_{m,n=1}^{\infty} X_{mn}(t)\cos(\alpha x)\sin(\beta y) \\
\sum\limits_{m,n=1}^{\infty} Y_{mn}(t)\sin(\alpha x)\cos(\beta y)
\end{bmatrix},
\quad
\Phi_i^{\mathrm{AP}} =
\begin{bmatrix}
\sum\limits_{m,n=1}^{\infty} U_{mn}(t)\sin(\alpha x)\cos(\beta y) \\
\sum\limits_{m,n=1}^{\infty} V_{mn}(t)\cos(\alpha x)\sin(\beta y) \\
\sum\limits_{m,n=1}^{\infty} W_{mn}(t)\sin(\alpha x)\sin(\beta y) \\
\sum\limits_{m,n=1}^{\infty} X_{mn}(t)\cos(\alpha x)\sin(\beta y) \\
\sum\limits_{m,n=1}^{\infty} Y_{mn}(t)\sin(\alpha x)\cos(\beta y)
\end{bmatrix}
\tag{9.17}
$$

The transverse load is also represented as a double series as:

$$
q(x,y,t) = \sum_{m,n=1}^{\infty} Q_{mn}(t)\sin(\alpha x)\sin(\beta y),
\tag{9.18}
$$

$$
Q(t) = \int_0^a \int_0^b q(x,y,t)\sin(\alpha x)\sin(\beta y)\,\mathrm{d}x\mathrm{d}y.
\tag{9.19}
$$

Substituting (9.17) into the differential equation, as described in [16], leads to the following system of linear equations:

$$
\underline{\underline{\hat{S}}}\,\underline{\Delta} + \underline{\underline{\hat{M}}}\,\underline{\ddot{\Delta}} = \underline{F} \quad \text{with}
\tag{9.20}
$$

$$
\underline{\Delta} =
\begin{bmatrix}
U_{mn}(t) = U_{mn}^0 \mathrm{e}^{i\omega t} \\
V_{mn}(t) = V_{mn}^0 \mathrm{e}^{i\omega t} \\
W_{mn}(t) = W_{mn}^0 \mathrm{e}^{i\omega t} \\
X_{mn}(t) = X_{mn}^0 \mathrm{e}^{i\omega t} \\
Y_{mn}(t) = Y_{mn}^0 \mathrm{e}^{i\omega t}
\end{bmatrix},
\quad
\underline{F} =
\begin{bmatrix}
0 \\
0 \\
Q_{mn}(t) \\
0 \\
0
\end{bmatrix}.
\tag{9.21}
$$

The entries of $\underline{\hat{S}}$ differ with regard to cross-ply laminate and angle-ply laminate. Those of the matrix $\underline{\underline{\hat{M}}}$ are the same for both. The entries of the matrices can be found in [16].

In the context of buckling analysis, the system of equations (9.20) leads to an eigenvalue problem. For this, $\omega = Q_{mn}(t) = 0$ must be used. The quantities $\hat{N}_{xx}, \hat{N}_{yy}$, which are contained in $\underline{\hat{S}}$, or their ratio is the eigenvalue of interest and reflects the buckling load. For frequency analysis, $\hat{N}_{xx} = \hat{N}_{yy} = 0$ is used and the eigenvalue is ω^2 where ω represents the natural frequency. In the bending analysis, however, $\hat{N}_{xx} = \hat{N}_{yy} = \omega = 0$ is employed, and the resulting system of linear equations can be solved directly.

9.5 Results and Discussion

For the evaluation of the validity of the new RBS formulation for antisymmetric cross- and angle-ply laminates, bending, buckling, and vibration are considered. The results are presented and discussed in the following sections, separately for antisymmetric cross-ply and antisymmetric angle-ply laminates. The results are obtained for the material defined in the following:

$$E_1 = 25E_2, \quad \nu_{12} = 0.25, \quad G_{12} = 0.5E_2, \quad G_{13} = 0.5E_2, \quad G_{23} = 0.2E_2.$$

The investigated parameters are the ratio between the modulus of elasticity parallel to the fibres and that perpendicular to the fibres $1 \leq E_1/E_2 \leq 50$, the aspect ratio of the plate $0.25 \leq a/b \leq 5$, and the relative length $2 \leq a/h \leq 100$.

9.5.1 Antisymmetric Cross-Ply Plates

The considered antisymmetric cross-ply laminates consist of N pairs of a $[0°/90°]_N$ layup. Here, the effect of bending-extension coupling is most prominent in the case of the two-layer laminate ($N = 1$) [19]. This remains consistent in the case of thick laminates.

9.5.1.1 Bending

The results for the bending analysis of the cross-ply laminates are obtained for the static and nondimensionalized centre deflection $\bar{w}$. The centre deflections are nondimensionlized as given in Equation (9.22).

$$\bar{w} = w\left(\frac{a}{2}, \frac{b}{2}\right) \frac{E_2 h^3}{a^4 q_0} 100 \tag{9.22}$$

For all following studies, the error is given in percent as defined in Eq. (9.23).

$$\% \text{ error} = \frac{\bar{w}_{\text{nav}} - \bar{w}_{\text{rbs}}}{\bar{w}_{\text{nav}}} 100 \tag{9.23}$$

The plate is loaded with transverse pressure q as introduced in Eqs. (9.18) and (9.19). The results presented in Table 9.1 are computed for uniform transverse pressure. The centre deflection is given for the exact results of the Navier solution and the RBS solution. Also, the error is computed. The results based on the FSDT are taken from Ref. [14]. Thus, the most commonly used laminated plate theories are shown in comparison. The results show that for an plate aspect ratio $a/b = 1$, while the relative length a/h and the ratio E_1/E_2 is varied. The deviation between the exact and the RBS solution is vanishing for the nondimensional centre deflection. This means that for this aspect ratio, the error of the RBS is independent of the other varied parameter ratios. However, between the different laminated plate theories, an expected deviation for the centre deflection is visible due to the effect of shear deformation.

    This is in contrast to the results presented in Table 9.2. Here, the plate aspect ratio is varied in addition to the variation of the relative thickness. Only the error between the Navier and RBS solution is presented. The table contains the results obtained in Ref. [20] and is extended to include the results for shear deformable

Table 9.1: Comparison of results for the nondimensional center deflection $\bar{w}$ for different thickness ratios a/h for different laminated plate theories and uniform loading. The results for the FSDT are available in literature [14].
($N = 2$, $E_2 = 1 \times 10^6$ psi, $\nu_{12} = 0.25$, $G_{12} = 0.6E_2$, $G_{13} = 0.6E_2$, $G_{23} = 0.5E_2$).

		$E_1/E_2 = 2$			$E_1/E_2 = 5$			$E_1/E_2 = 10$			$E_1/E_2 = 30$		
	a/h	Navier	RBS	Err	Navier	RBS	Err	Navier	RBS	Err	Navier	RBS	Err
TSDT													
	2	7.377	7.377	0.0	6.746	6.746	0.0	6.119	6.118	0.0	4.860	4.860	0.0
	5	4.058	4.058	0.0	3.512	3.512	0.0	3.007	3.007	0.0	2.041	2.041	0.0
	10	3.579	3.579	0.0	3.043	3.043	0.0	2.555	2.555	0.0	1.623	1.623	0.0
	30	3.437	3.436	0.0	2.904	2.904	0.0	2.420	2.420	0.0	1.498	1.498	0.0
	50	3.425	3.425	0.0	2.893	2.893	0.0	2.410	2.409	0.0	1.489	1.488	0.0
	100	3.420	3.420	0.0	2.889	2.888	0.0	2.405	2.405	0.0	1.484	1.484	0.0
FSDT													
	2	7.437	7.437	0.0	6.905	6.904	0.0	6.420	6.420	0.0	5.498	5.497	0.0
	5	4.062	4.062	0.0	3.530	3.529	0.0	3.046	3.045	0.0	2.124	2.124	0.0
	10	3.580	3.579	0.0	3.048	3.048	0.0	2.564	2.564	0.0	1.643	1.643	0.0
	30	3.437	3.437	0.0	2.905	2.905	0.0	2.421	2.421	0.0	1.501	1.501	0.0
	50	3.425	3.425	0.0	2.893	2.893	0.0	2.410	2.410	0.0	1.489	1.489	0.0
	100	3.420	3.420	0.0	2.889	2.889	0.0	2.405	2.405	0.0	1.484	1.484	0.0
CLPT													
	-	3.419	3.419	0.0	2.89	2.887	0.0	2.403	2.403	0.0	1.483	1.483	0.0

laminates. The loading is sinusoidal. The results show that for other aspect ratios, small deviations occur that are decreasing with increasing relative thickness, i.e. with decreasing relative length. The error reduces significantly for each plate aspect ratio. The number of layer pairs N and the ratio E_1/E_2 are chosen to present the highest errors following Ref. [20].

The present formulation of the RBS method in the framework of TSDT delivers accurate results for the centre deflection. However, it must be noted that the presented results do not allow making any assumptions regarding the accuracy of computed stress distributions using the RBS method. Since the bending-extension coupling is neglected, significant quantitative and qualitative deviations are expected. This is a topic that needs to be addressed in future publications.

9.5.1.2 Buckling and Vibration

The buckling results refer to a uniaxial constant compression $\hat{N}_{xx}$, which is evaluated for different values of m and n. The smallest buckling load was considered in the analyses. In the context of the vibration analyses, the first natural frequency ($m = n = 1$) is evaluated.

The comparison between the exact Navier solution and the Navier RBS solution for the cross-ply laminate is shown in Table 9.2. Regarding the buckling and vibration analysis, the comparative calculations for $a/h = 100$ show slightly smaller deviations than the literature value for the CLPT from [20]. The investigated a/b and a/h ratios do not show a clear tendency concerning the error behaviour. However, a good agreement between the two analyses can be observed.

Table 9.2: Errors of the comparison of the centre deflection, buckling load, and vibration obtained by the Navier and RBS-solution according to Equation (9.23) for an antisymmetric cross-ply under sinusoidal loading, constant axial compression, and natural frequency. The CLPT results are obtained from Ref. [20]. ($N = 2$; $E_1/E_2 = 2$).

		Deflection					Buckling					Vibration				
	a/h			a/b					a/b					a/b		
		0.25	0.5	1	2	5	0.25	0.5	1	2	5	0.25	0.5	1	2	5
TSDT																
	2	-0.09	-0.04	0.00	-0.02	0.00	0.17	0.23	0.17	0.05	0.01	-0.27	-0.39	-0.41	0.03	-7.50
	5	-0.17	-0.08	0.00	-0.05	-0.03	0.07	0.08	0.00	0.12	0.04	-0.47	-0.58	-0.81	-0.54	0.05
	10	-0.19	-0.08	0.00	-0.08	-0.10	0.03	0.02	0.00	0.09	0.12	-0.21	-0.26	-0.40	-0.58	-0.26
	100	-0.20	-0.09	0.00	-0.09	-0.22	0.02	0.01	0.00	0.00	0.00	0.01	0.00	-0.01	-0.01	-0.05
CLPT																
	-	-0.20	-0.09	0.00	-0.09	-0.22	0.20	0.09	0.00	0.09	0.22	0.10	0.04	0.00	0.04	0.11

9.5.2 Antisymmetric Angle-Ply Plates

After the investigation of the antisymmetric cross-ply laminates, antisymmetric angle-ply laminates are considered in this section. They consist of N-pairs of a $[\Theta/-\Theta]_N$-layup, where Θ denotes the fibre orientation of the individual layer. The validity of the introduced RBS formulation for the TSDT is again evaluated for bending, buckling, and vibration analysis.

9.5.2.1 Bending

For bending analysis in the present section only sinusoidal loading is considered. This allows to include the CLPT results of Ref. [20]. Hence, the following tabulated numerical results are following the mentioned literature results closely. In Table 9.3 the errors between the Navier and RBS solution in % (see Eq. (9.23)) are tabulated for the $E_1/E_2 = 15$ and $\Theta = \pm 15°$. The aspect ratio of the plate a/b is varied in order to find the most critical configurations, where high deviations occur.

By studying the presented values, it becomes apparent that the highest errors are computed for the utilization of the new RBS formulation for square plates and only one layer-pair. This confirms the results presented in Ref. [20]. However, the evaluation of an increasing relative thickness reveals that the highest deviations are visible for the ratio $a/b = 0.75$. The results are generally in good agreement and show again that the deviation vanishes with increasing relative thickness of the plate.

This can be also concluded from the tabulated errors in Table 9.4, where $a/b = 1$ and $\Theta = \pm 15°$. Here, the influence of the ratio E_1/E_2 is studied in combination of the ratio a/h again for different numbers of layer-pairs. In general, the highest deviations are

Table 9.3: Errors between the Navier and RBS solution in % for antisymmetric angle-ply laminates subjected to sinusiodal transverse loading. The ratio $E_1/E_2 = 15$ and the angle is set to $\Theta = \pm 15°$. The results are obtained on the basis of TSDT and CLPT, where the values for the CLPT are obtained from Ref. [20].

	$N = 1$					$N = 2$					$N = 3$				
	a/h (TSDT)				CLPT	a/h (TSDT)				CLPT	a/h (TSDT)				CLPT
a/b	2	5	10	100	-	2	5	10	100	-	2	5	10	100	-
0.25	-0.4	-1.8	-2.7	-3.2	-3.2	-0.2	-0.3	-0.4	-0.5	-0.5	-0.1	-0.1	-0.2	-0.2	-0.2
0.5	-0.9	-5.2	-8.2	-9.9	-9.9	-0.6	-1.0	-1.3	-1.6	-1.6	-0.3	-0.4	-0.6	-0.7	-0.7
0.75	-1.1	-7.2	-12.0	-14.9	-14.9	-0.9	-1.4	-1.9	-2.4	-2.4	-0.5	-0.6	-0.8	-1.0	-1.0
1	-0.8	-6.7	-12.0	-15.4	-15.5	-0.9	-1.3	-2.0	-2.5	-2.5	-0.5	-0.6	-0.8	-1.0	-1.0
1.5	-0.2	-3.2	-6.3	-8.5	-8.5	-0.5	-0.6	-1.1	-1.5	-1.5	-0.2	-0.3	-0.5	-0.6	-0.6
2	0.0	-0.8	-1.8	-2.6	-2.6	-0.1	-0.2	-0.3	-0.5	-0.5	-0.1	-0.1	-0.1	-0.2	-0.2
3	0.0	0.0	0.0	0.0	0.0	0.0	0.0	0.0	0.0	0.0	0.0	0.0	0.0	0.0	0.0
4	0.0	-0.1	-0.2	-0.4	0.0	-0.1	0.0	0.0	-0.1	0.0	0.0	0.0	0.0	0.0	0.0

Table 9.4: Errors between the Navier and RBS solution in % for antisymmetric angle-ply laminates subjected to sinusoidal transverse loading. The ratio $a/b = 1$ and the angle is set to $\Theta = \pm15°$. The results are obtained on the basis of TSDT and CLPT, where the values for the CLPT are obtained from Ref. [20].

	$N = 1$				CLPT	$N = 2$				CLPT	$N = 3$				CLPT
	a/h (TSDT)					a/h (TSDT)					a/h (TSDT)				
E_1/E_2	2	5	10	100	-	2	5	10	100	-	2	5	10	100	-
1	0.0	0.0	0.0	0.0	0.0	0.0	0.0	0.0	0.0	0.0	0.0	0.0	0.0	0.0	0.0
2.5	-0.2	-0.5	-0.5	-0.6	-0.6	-0.1	-0.1	-0.1	-0.1	-0.1	0.0	-0.1	-0.1	-0.1	-0.1
5	-0.8	-2.5	-3.3	-3.7	-3.7	-0.4	-0.6	-0.7	-0.8	-0.8	-0.2	-0.3	-0.3	-0.4	-0.4
7.5	-1.0	-4.3	-6.3	-7.3	-7.3	-0.6	-1.0	-1.3	-1.5	-1.5	-0.3	-0.4	-0.6	-0.6	-0.6
10	-1.0	-5.5	-8.7	-10.5	-10.6	-0.7	-1.2	-1.6	-1.9	-1.9	-0.4	-0.5	-0.7	-0.8	-0.8
15	-0.8	-6.7	-12.0	-15.4	-15.5	-0.9	-1.3	-2.0	-2.5	-2.5	-0.5	-0.6	-0.8	-1.0	-1.0
20	-0.6	-7.0	-13.7	-18.5	-18.6	-1.0	-1.3	-2.0	-2.7	-2.7	-0.5	-0.6	-0.9	-1.1	-1.1
30	-0.2	-6.4	-14.7	-21.5	-21.5	-1.1	-1.1	-1.9	-2.8	-2.8	-0.6	-0.5	-0.8	-1.1	-1.1
40	0.0	-5.4	-14.2	-22.2	-22.3	-1.1	-1.0	-1.7	-2.6	-2.7	-0.6	-0.4	-0.7	-1.1	-1.1
50	0.0	-4.5	-13.1	-22.0	-22.1	-1.2	-0.9	-1.4	-2.5	-2.5	-0.6	-0.4	-0.6	-1.0	-1.0

obtained for the case of only two layers ($N = 1$). For more layers very good agreement is obtained with an error that is maximal 2.8 %. In the most critical case, the error increases to up to 2.23×10^1 % for $E_1/E_2 = 40$. The critical areas shift depending on the relative thickness of the plate. This will be shown in the following paragraphs.

In the third table (Table 9.5) the focus lies on the variation of the fibre angle. The errors between the Navier and RBS solution in % are tabulated for different

Table 9.5: Errors between the Navier and RBS solution in % for antisymmetric angle-ply laminates subjected to sinusoidal transverse loading. The ratio $a/b = 1$ and the number of layer pairs is set to $N = 1$. The results are obtained on the basis of TSDT and CLPT, where the values for the CLPT are obtained from Ref. [20].

θ	$E_1/E_2 = 1$				CLPT	$E_1/E_2 = 15$				CLPT	$E_1/E_2 = 40$				CLPT
	a/h (TSDT)					a/h (TSDT)					a/h (TSDT)				
	2	5	10	100	-	2	5	10	100	-	2	5	10	100	-
5	0.0	0.0	0.0	0.0	0.0	-0.2	-2.1	-4.2	-5.7	-5.8	0.0	-2.9	-8.9	-16.9	-17.0
10	-0.1	-0.1	-0.1	-0.1	-0.1	-0.6	-5.5	-10.4	-13.8	-13.8	-0.1	-5.8	-16.3	-27.6	-27.8
15	-0.1	-0.2	-0.2	-0.2	-0.2	-0.8	-6.7	-12.0	-15.4	-15.5	0.0	-5.4	-14.2	-22.2	-22.3
20	-0.1	-0.2	-0.3	-0.3	-0.3	-0.7	-5.8	-9.8	-12.3	-12.3	0.0	-3.8	-9.5	-14.2	-14.3
25	-0.1	-0.3	-0.3	-0.3	-0.3	-0.5	-4.0	-6.5	-7.9	-7.9	0.0	-2.3	-5.6	-8.1	-8.2
30	-0.1	-0.2	-0.3	-0.3	-0.3	-0.3	-2.1	-3.4	-4.1	-4.1	0.0	-1.2	-2.8	-4.0	-4.0
35	-0.1	-0.2	-0.3	-0.3	-0.3	-0.1	-0.8	-1.3	-1.6	-1.6	0.0	-0.5	-1.0	-1.5	-1.5
40	-0.1	-0.2	-0.3	-0.3	-0.3	0.0	-0.2	-0.3	-0.4	-0.4	0.0	-0.1	-0.2	-0.3	-0.3
45	-0.1	-0.2	-0.2	-0.3	-0.3	0.0	-0.1	-0.1	-0.1	-0.1	0.0	0.0	0.0	0.0	0.0

relative thicknesses and for three different ratios E_1/E_2. The number of layer pairs is $N = 1$. In accordance with the results in Table 9.4, the highest deviations occur for the ratio $E_1/E_2 = 40$. As already mentioned in Ref. [20], the highest error is obtained for $\Theta = 10°$ with -2.76×10^1 %. This deviation quickly decreases for increasing relative thickness of increasing fibre angle. The literature results are in excellent agreement with the new RBS formulation.

A more qualitative description of the areas with excellent agreement and higher deviations of the RBS formulation compared to the Navier solution is depicted in Fig. 9.3 in the form of contour plots where the fibre angle Θ and ratio E_1/E_2 is varied for the four different investigated aspect ratios $a/h =$ 2, 5, 10 , 100. For very thick laminates $a/h = 2$ (Fig. 9.3a), the most critical area is for $E_1/E_2 \approx 10$ and $\Theta \approx 17.5°$, although it must be noted that the results are generally in very good agreement. If the ratio a/h is increased to 5 (Fig. 9.3b), the critical area shifts to the right with errors above -6 % in the range of E_1/E_2 from about 12.5 to 40 and fibre angles between $10°$

(a)

(b)

(c)

(d)
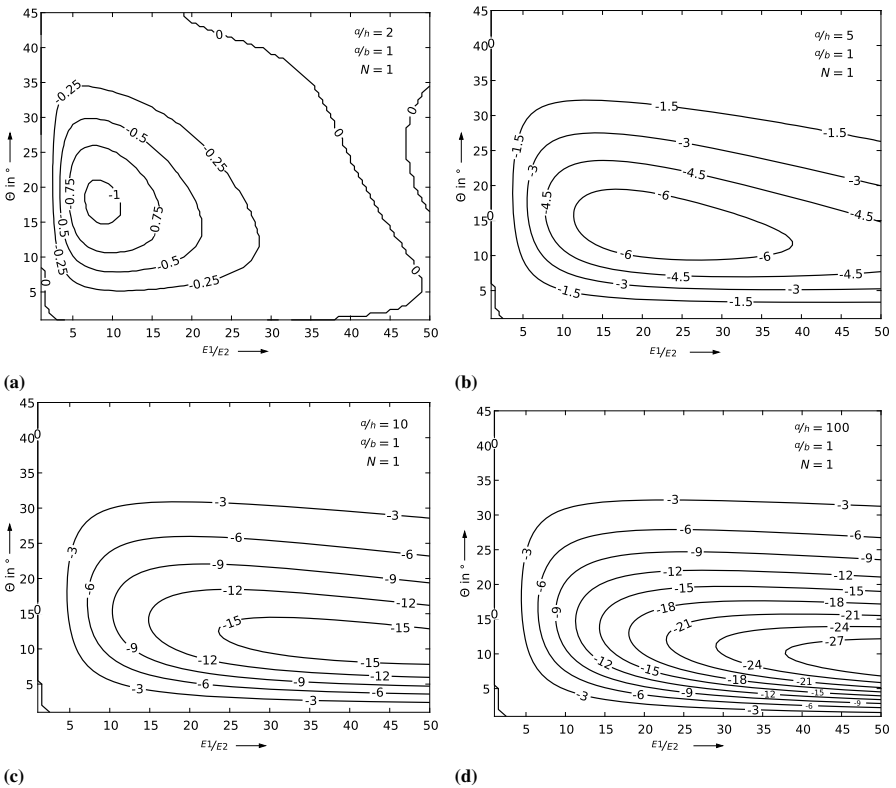
Fig. 9.3: Contour plots for the errors between the Navier and RBS solution in % for antisymmetric angle-ply laminates subjected to sinusoidal transverse loading, where the results are plotted for varying fibre angle Θ and ratio E_1/E_2 for the four different investigated aspect ratios $a/h =$ 2, 5, 10, 100.

to about 17.5°. This trend continues in Fig. 9.3c, for the ratio of $a/h = 10$ to the range of E_1/E_2 from about 25 to 50 and fibre angles between 10° and about 15°. Finally, the observations made in the description of Table 9.5 are reflected in the fourth figure (Fig. 9.3d). Here the a/h is set to 100. and the most critical parameter configuration are in area of E_1/E_2 approximately 40 to 50 and Θ approximately 7.5° to 12.5°.

9.5.2.2 Buckling

The RBS method shows a slightly different behaviour for the angle-ply laminates than before for the cross-ply laminates. On the one hand, the fibre angle θ is added as an additional parameter, on the other hand, the behaviour of the error between the exact method and RBS is somewhat more complex and shows the following behaviour regarding buckling. First we consider the ratio E_1/E_2 with constant θ and a/b, , as presented in Table 9.6.

For a layer repetition $N = 1$, the error increases with increasing θ from 0 up to 18%. It can be observed that for very thick laminates ($a/h = 2$) the error first increases with increasing E_1/E_2 ratio and then decreases again to 0 %. Only with increasing relative length is a constant increase observed. This behaviour changes for $N = 2$, here $a/h = 2$ and $a/h = 100$ show a similar error behaviour. For $N = 3$ an increasing error with increasing E_1/E_2 ratio can be observed as well, but the maximum deviations occur differently than before for $a/h = 2$ with 1.7 %.

For the investigation of the aspect ratio a/b, see Table 9.7, the E_1/E_2 ratio and θ are set constant. The comparison with literature values from [20] shows very good agreements for $a/h = 100$ for different a/b ratios as well as ply repetitions, as expected for thin plates. For $N = 1$ the largest deviations are observed between $a/b = 0.75$ and 1, which increase with increasing a/h ratio to 13 %. For the further layer repetitions ($N = 2, 3$) the errors decrease.

Table 9.6: Errors between the Navier and RBS solution in % for antisymmetric angle-ply laminates subjected to buckling load. The ratio $E_1/E_2 = 15$ and the angle is set to $\Theta = \pm 15°$.

	$N = 1$				$N = 2$				$N = 3$			
	a/h (TSDT)				a/h (TSDT)				a/h (TSDT)			
E_1/E_2	2	5	10	100	2	5	10	100	2	5	10	100
1	0.0	0.0	0.0	0.0	0.0	0.0	0.0	0.0	0.0	0.0	0.0	0.0
2.5	0.1	0.4	0.5	0.6	0.1	0.1	0.1	0.1	0.0	0.1	0.0	0.1
5	0.5	2.4	3.2	3.5	0.4	0.4	0.6	0.8	0.3	0.2	0.2	0.3
7.5	1.0	4.1	5.9	6.8	0.7	0.6	1.0	1.4	0.5	0.4	0.3	0.6
10	1.0	5.2	8.0	9.5	0.9	0.6	1.2	1.9	0.8	0.4	0.4	0.8
15	0.8	6.3	10.7	13.3	1.3	0.7	1.3	2.4	1.1	0.5	0.5	1.0
20	0.6	6.5	12.1	15.6	1.6	0.9	1.3	2.6	1.4	0.6	0.5	1.1
30	0.2	6.0	12.8	17.7	2.0	0.9	1.1	2.7	1.6	0.7	0.4	1.1
40	0.0	5.1	12.4	18.2	2.2	0.9	1.0	2.5	1.7	0.7	0.4	1.0
50	0.0	4.3	11.6	18.0	2.3	0.9	0.9	2.3	1.7	0.7	0.4	0.9

Table 9.7: Errors between the Navier and RBS solution in % for antisymmetric angle-ply laminates subjected to buckling load. The ratio $a/b = 1$ and the angle is set to $\Theta = \pm 15°$. The results are obtained on the basis of TSDT and CLPT, where the values for the CLPT are obtained from Ref. [20].

	$N = 1$					$N = 2$					$N = 3$				
	a/h (TSDT)				CLPT	a/h (TSDT)				CLPT	a/h (TSDT)				CLPT
a/b	2	5	10	100	-	2	5	10	100	-	2	5	10	100	-
0.25	0.4	1.8	2.6	3.1	3.1	0.3	0.2	0.3	0.5	0.5	0.2	0.1	0.1	0.2	0.2
0.5	0.9	5.0	7.6	9.0	9.0	0.9	0.7	0.9	1.5	1.6	0.7	0.3	0.3	0.6	0.7
0.75	1.0	6.7	10.7	13.0	13.0	1.3	0.9	1.3	2.3	2.3	1.1	0.5	0.5	1.0	1.0
1	0.8	6.3	10.7	13.3	13.4	1.3	0.7	1.3	2.4	2.4	1.1	0.5	0.5	1.0	1.0
1.5	0.0	2.0	5.9	7.8	7.9	0.8	1.1	0.9	1.4	1.4	0.7	0.9	0.5	0.6	0.6
2	0.0	1.7	6.3	2.5	2.5	2.4	1.1	0.9	0.5	0.5	1.5	0.9	0.6	0.2	0.2
3	0.4	0.1	3.3	7.8		1.5	1.6	1.1	1.4		1.1	1.3	0.7	0.5	
4	0.4	0.0	1.0	3.1		2.4	2.0	1.3	0.4		0.4	1.0	0.9	0.2	

The influence of the fibre angle θ on the error behaviour of the RBS is investigated in Table 9.8. In this table a/b and N are kept constant. The comparison for $a/h = 100$ with the literature values from [20] shows a very similar behaviour. For $E_1/E_2 = 1$ the maximum deviations for all investigated fibre angles as well as relative lengths are very low with 0.3 %. With increasing E_1/E_2 ratio the deviations become larger, these are maximum 13.3 % and 18.2 % respectively for $E_1/E_2 = 15$ and $E_1/E_2 = 40$. It can be observed that the error initially increases with increasing θ and has its maximum values between $\theta = 10°$ and $\theta = 15°$. Subsequently, the error decreases and shows very small values for $\theta = 45°$. As observed before, an increasing deviation with larger

Table 9.8: Errors between the Navier and RBS solution in % for antisymmetric angle-ply laminates subjected to buckling load. The ratio $a/b = 1$ and the number of layer pairs is set to $N = 1$. The results are obtained on the basis of TSDT and CLPT, where the values for the CLPT are obtained from Ref. [20].

	$E_1/E_2 = 1$					$E_1/E_2 = 15$					$E_1/E_2 = 40$				
	a/h (TSDT)				CLPT	a/h (TSDT)				CLPT	a/h (TSDT)				CLPT
θ	2	5	10	100	-	2	5	10	100	-	2	5	10	100	-
0	0.0	0.0	0.0	0.0	0.0	0.0	0.0	0.0	0.0	0.0	0.0	0.0	0.0	0.0	0.0
5	0.0	0.0	0.0	0.0	0.0	0.2	2.0	4.0	5.4	5.5	0.0	2.8	8.2	14.5	14.6
10	0.1	0.1	0.1	0.1	0.1	0.6	5.2	9.4	12.1	12.2	0.0	5.4	14.0	21.6	21.7
15	0.1	0.2	0.2	0.2	0.2	0.8	6.3	10.7	13.3	13.4	0.0	5.1	12.4	18.2	18.2
20	0.1	0.2	0.3	0.3	0.3	0.7	5.5	9.0	10.9	10.9	0.0	3.7	8.7	12.5	12.5
25	0.1	0.3	0.3	0.3	0.3	0.0	3.8	6.1	7.3	7.3	0.0	2.3	5.3	7.5	7.5
30	0.1	0.2	0.3	0.3	0.3	0.0	2.1	3.3	4.0	4.0	0.1	1.2	2.7	3.9	3.9
35	0.1	0.2	0.3	0.3	0.3	0.1	0.8	1.3	1.6	1.6	0.0	0.4	1.0	1.5	1.5
40	0.0	0.2	0.2	0.3	0.3	0.1	0.5	0.3	0.4	0.4	0.0	0.3	0.2	0.3	0.3
45	0.0	0.2	0.2	0.3	0.3	0.2	0.2	0.1	0.1	0.1	0.2	0.2	0.0	0.0	0.0

relative widths a/h can also be observed here, this is confirmed for different fibre angles.

An overview of the error behaviour can be found in Fig. 9.4. In the diagrams the error is plotted against E_1/E_2 ratio and θ. For $a/h = 2, 5, 10, 100$ one graph is shown respectively, where $a/b = N = 1$ is set. Regarding θ it can be seen that the maximum error is about $\theta \approx 15°$ for $a/h = 2$ and decreases to approximately $\theta \approx 10°$ for $a/h = 100$ with increasing E_1/E_2 ratio, compare Fig. 9.4a and 9.4d. As previously noted, there is a qualitative increase in the error with increasing relative length a/h and increasing E_1/E_2 ratio.

(a) .

(b) .

(c) .

(d) .
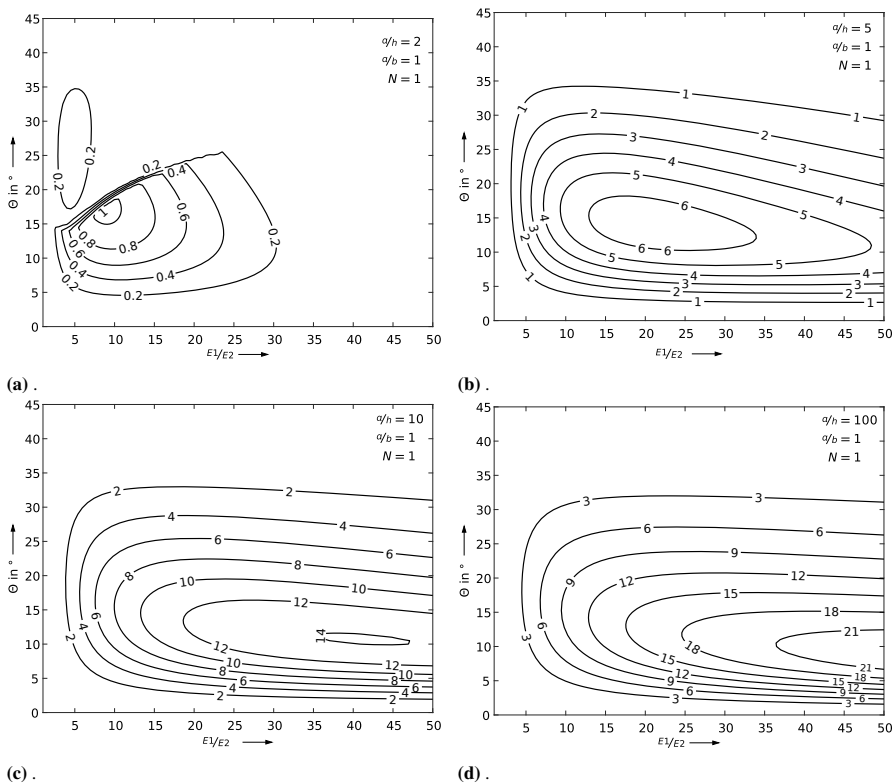
Fig. 9.4: Contour plots concerning buckling for the errors between the Navier and RBS solution in % for antisymmetric angle-ply laminates subjected to constant uniaxial compression, where the results are plotted for varying fibre angle Θ and ratio E_1/E_2 for the four different investigated aspect ratios $a/h = 2, 5, 10, 100$.

9.5.2.3 Vibration

The behaviour between the exact solution and the RBS shows a similar behaviour for the frequency analysis as the buckling analysis shown before. The differences and similarities are presented in the following. In Table 9.9 the error with respect to the E_1/E_2 ratio and a/h for different N is investigated. Quantitatively, a similar behaviour as for buckling is observed. For $N = 1$, the error increases with increasing a/h ratio. This effect reverses for $N = 3$. With increasing E_1/E_2 ratio, an increase in the error can be observed as well. The maximum amplitude of the error is significantly smaller with 9.5 % ($N = 1$). For $N = 3$ there are also evident negative errors of -1.1 %.

In Table 9.10 the aspect ratio a/b with regard to the relative length a/h is investigated for different N. The E_1/E_2 ratio and the fibre angle θ remain constant. The thin laminates ($a/h = 100$) allow a comparison to the CLPT and show good agreement with the values from [20] for all N considered. For $N = 1$ the largest deviations are observed, these lie in the range -1.7-6.9 %, with increasing N these become smaller. A clear influence of the aspect ratio is not evident.

The influence of θ and a/h for different E_1/E_2 ratios is investigated in Table 9.11. Very small influence is observed for $E_1/E_2 = 1$. With increasing E_1/E_2 ratio the error becomes larger and it can be seen that increasing a/h is correlated with increasing error. For θ a maximum error between 10° and 15° can be detected. For $a/h = 100$ good agreements with the CLPT values can be observed.

In the Fig. 9.5 the errors with respect to E_1/E_2 and θ are presented. Very small errors are observed for $a/h = 2$. The largest error is located at about $E_1/E_2 \approx 10$ and $\theta \approx 15°$. The minimum is located at about $\theta \approx 45°$. The extremal points of the error shift for $a/h = 5$ to higher E_1/E_2 values, as observed in Fig. 9.5a. This behaviour continues for $a/h = 10$ and 100. The maximum shifts to over $E_1/E_2 = 50$ with simultaneously decreasing θ.
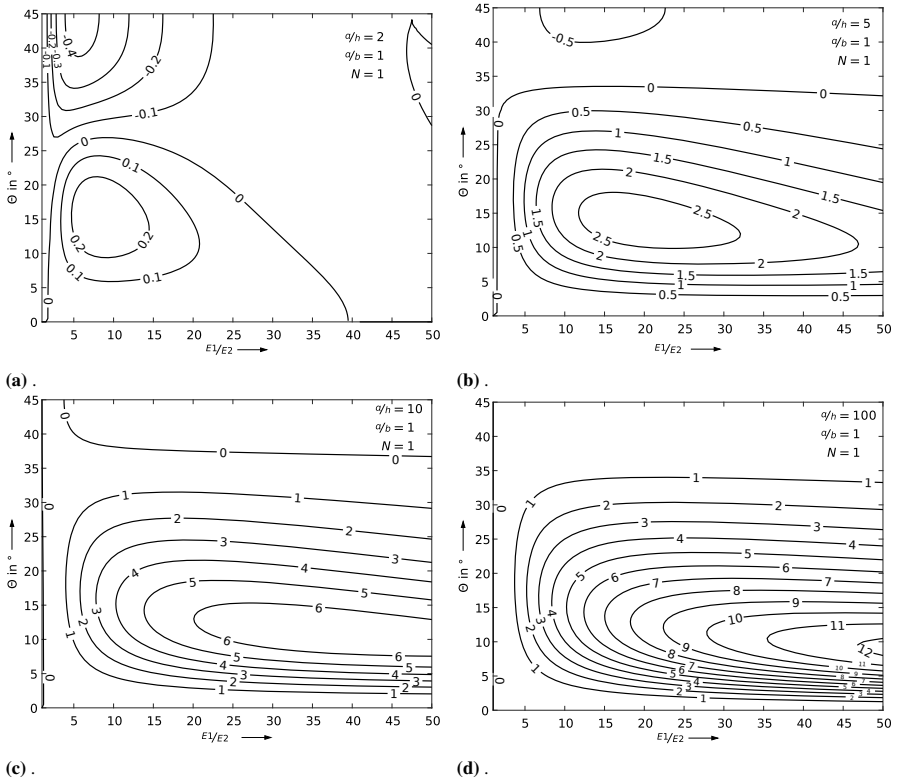
Table 9.9: Errors between the Navier and RBS solution in % for antisymmetric angle-ply laminates regarding natural frequency. The ratio $E_1/E_2 = 15$ and the angle is set to $\Theta = \pm15°$.

	$N = 1$				$N = 2$				$N = 3$			
	a/h (TSDT)				a/h (TSDT)				a/h (TSDT)			
E_1/E_2	2	5	10	100	2	5	10	100	2	5	10	100
1	0.0	0.0	0.0	0.0	0.0	0.0	0.0	0.0	0.0	0.0	0.0	0.0
2.5	0.0	0.1	0.2	0.3	0.0	0.0	0.0	0.1	0.0	0.0	0.0	0.0
5	0.2	1.0	1.5	1.8	0.1	0.1	0.2	0.4	0.0	0.0	0.1	0.2
7.5	0.3	1.8	2.8	3.5	0.1	0.2	0.4	0.7	0.0	0.1	0.1	0.3
10	0.3	2.3	3.9	4.9	0.2	0.2	0.5	0.9	0.1	0.1	0.1	0.4
15	0.2	2.7	5.2	6.9	0.2	0.3	0.5	1.2	0.0	0.1	0.2	0.5
20	0.1	2.8	5.8	8.1	0.2	0.3	0.5	1.3	-0.1	0.1	0.1	0.5
30	0.0	2.4	6.1	9.2	0.2	0.2	0.4	1.3	-0.4	0.1	0.1	0.5
40	0.0	2.0	5.8	9.5	0.1	0.2	0.3	1.3	-0.8	0.1	0.1	0.5
50	0.0	1.5	5.3	9.4	-0.1	0.2	0.3	1.2	-1.1	0.1	0.1	0.4

Table 9.10: Errors between the Navier and RBS solution in % for antisymmetric angle-ply laminates regarding natural frequency. The ratio $a/b = 1$ and the angle is set to $\Theta = \pm 15°$. The results are obtained on the basis of TSDT and CLPT, where the values for the CLPT are obtained from Ref. [20]..

| | N=1 | | | | | N=2 | | | | | N=3 | | | | |
| | a/h (TSDT) | | | | CLPT | a/h (TSDT) | | | | CLPT | a/h (TSDT) | | | | CLPT |
a/b	2	5	10	100	-	2	5	10	100	-	2	5	10	100	-
0.25	-1.7	-1.7	0.1	1.5	1.6	-1.6	-0.7	-0.4	0.2	0.3	-2.0	-0.5	-0.3	0.1	0.1
0.5	-0.5	0.8	3.0	4.6	4.6	-0.8	-0.2	0.1	0.8	0.8	-1.2	-0.2	-0.1	0.3	0.3
0.75	0.1	2.5	5.0	6.7	6.7	-0.1	0.1	0.4	1.1	1.2	-0.5	0.0	0.1	0.5	0.5
1	0.2	2.7	5.2	6.9	6.9	0.2	0.3	0.5	1.2	1.2	0.0	0.1	0.2	0.5	0.5
1.5	0.0	1.3	2.8	4.0	4.0	0.2	0.1	0.2	0.7	0.7	0.1	0.1	0.1	0.3	0.3
2	-0.1	0.1	0.7	1.3	1.3	-0.1	0.0	0.0	0.2	0.2	-0.2	0.0	0.0	0.1	0.1
3	0.0	-0.3	-0.3	0.0	0.0	-0.4	-0.1	-0.1	0.0	0.0	-0.5	-0.1	0.0	0.0	0.0
4	0.0	-0.1	-0.1	0.2	0.2	-0.4	-0.1	-0.1	0.0	0.1	-0.6	-0.1	0.0	0.0	0.0

Table 9.11: Errors between the Navier and RBS solution in % for antisymmetric angle-ply laminates regarding natural frequency. The ratio $a/b = 1$ and the number of layer pairs is set to $N = 1$. The results are obtained on the basis of TSDT and CLPT, where the values for the CLPT are obtained from Ref. [20].

| | $E_1/E_2 = 1$ | | | | | $E_1/E_2 = 15$ | | | | | $E_1/E_2 = 40$ | | | | |
| | a/h (TSDT) | | | | CLPT | a/h (TSDT) | | | | CLPT | a/h (TSDT) | | | | CLPT |
θ	2	5	10	100	-	2	5	10	100	-	2	5	10	100	-
0	0.0	0.0	0.0	0.0	0.0	0.0	0.0	0.0	0.0	0.0	0.0	0.0	0.0	0.0	0.0
5	0.0	0.0	0.0	0.0	0.0	0.1	0.9	1.9	2.8	2.8	0.0	1.2	3.9	7.5	7.6
10	0.0	0.0	0.0	0.1	0.1	0.2	2.3	4.6	6.3	6.3	0.0	2.2	6.6	11.5	11.5
15	0.0	0.0	0.1	0.1	0.1	0.2	2.7	5.2	6.9	6.9	0.0	2.0	5.8	9.5	9.6
20	0.0	0.0	0.1	0.1	0.1	0.1	2.2	4.3	5.6	5.6	0.0	1.3	3.9	6.4	6.5
25	-0.1	0.0	0.1	0.2	0.2	0.0	1.4	2.8	3.7	3.7	0.0	0.7	2.2	3.8	3.8
30	-0.1	0.0	0.1	0.2	0.2	-0.1	0.5	1.4	2.0	2.0	0.0	0.2	1.0	1.9	2.0
35	-0.1	0.0	0.1	0.1	0.1	-0.2	-0.2	0.3	0.8	0.8	0.0	-0.1	0.2	0.7	0.7
40	-0.2	-0.1	0.1	0.1	0.1	-0.2	-0.5	-0.2	0.2	0.2	0.0	-0.3	-0.2	0.1	0.1
45	-0.2	-0.1	0.1	0.1	0.1	-0.2	-0.6	-0.3	0.1	0.1	0.0	-0.3	-0.3	0.0	0.0

9.6 Conclusion

The novel formulation of the RBS method for the third-order shear deformation theory shows similar accuracy compared to the original formulation for the CLPT for plates that are not shear deformable.

In the bending analysis, the centre deflection is predicted with increasing accuracy for increasing relative thickness or decreasing relative length. This holds for antisymmetric cross-ply and angle-ply laminates. The configurations regarding the fibre angle Θ and the ratio E_1/E_2 are analysed with varying accuracy depending on the

Fig. 9.5: Contour plots concerning vibration for the errors between the Navier and RBS solution in % for antisymmetric angle-ply laminates regarding natural frequency, where the results are plotted for varying fibre angle Θ and ratio E_1/E_2 for the four different investigated aspect ratios a/h =2, 5, 10 , 100.

relative thickness. The most critical configurations are for $E_1/E_2 \approx 10$ and $\Theta \approx 17.5°$ for very thick laminates shifting towards $E_1/E_2 \approx 50$ and $\Theta \approx 10°$ for thin laminates. It must be noted that the agreement of centre deflections does not allow conclusions about the accuracy of the predicted stresses which must be investigated in future publications.

In the buckling analysis, a very good agreement is obtained between the exact solution and the RBS for the cross-ply laminate. The angle-ply laminate shows, as in the case of bending, an increasing error for increasing E_1/E_2 ratios and increasing relative lengths. The maximum deviations can be found for fibre angles from 10° to 15° and are up to 21 %. The vibration analysis shows a very similar behaviour as the buckling analysis, with deviations of up to 12 %. Apart from the critical points mentioned, there is good agreement between the RBS and the exact solution for angle-ply laminates.

References

[1] Herencia JE, Weaver PM, Friswell MI (2007) Optimisation of anisotropic plates that vary in thickness and properties. In: 16th International Conference on Composite Materials, Kyoto, pp 1–10

[2] Mittelstedt C, Beerhorst M (2009) Closed-form buckling analysis of compressively loaded composite plates braced by omega-stringers. Composite Structures **88**(3):424–435

[3] Coburn BH, Wu Z, Weaver P (2015) Buckling analysis and optimization of blade stiffened variable stiffness panels. In: 56th AIAA/ASCE/AHS/ASC Structures, Structural Dynamics, and Materials Conference, American Institute of Aeronautics and Astronautics, Kissimmee, Florida

[4] Vescovini R, Bisagni C (2015) Semi-analytical buckling analysis of omega stiffened panels under multi-axial loads. Composite Structures **120**:285–299

[5] Schilling JC, Mittelstedt C (2020) Local buckling analysis of omega-stringer-stiffened composite panels using a new closed-form analytical approximate solution. Thin-Walled Structures **147**:106,534

[6] Schilling JC, Atamann D, Voges J, Mittelstedt C (2022) Local buckling of omega-stringer-stiffened composite panels under compression–shear interaction. Thin-Walled Structures **180**:109,838

[7] Mittelstedt C, Becker W (2016) Strukturmechanik ebener Laminate, 1st edn. Studienbereich Mechanik, Technische Universität Darmstadt, Darmstadt

[8] Reissner E, Stavsky Y (1961) Bending and stretching of certain types of heterogeneous aeolotropic elastic plates. Journal of Applied Mechanics **28**(3):402–408

[9] Chamis CC (1969) Buckling of anisotropic composite plates. Journal of the Structural Division **95**(10):2119–2140

[10] Ashton JE (1969) Approximate solutions for unsymmetrically laminated plates. Journal of Composite Materials **3**(1):189–191

[11] Schilling JC, Mittelstedt C (2020) Validity of the reduced bending stiffness method for stacked laminates. In: Altenbach H, Chinchaladze N, Kienzler R, Müller WH (eds) Analysis of Shells, Plates, and Beams, Advanced Structured Materials, vol 134, Springer International Publishing, Cham, pp 389–408

[12] Zaghloul SA, Kennedy JB (1975) Nonlinear Analysis of Unsymmetrically Laminated Plates. Journal of the Engineering Mechanics Division **101**(3):169–186

[13] Sheinman I, Reichman Y (1992) A study of buckling and vibration of laminated shallow curved panels. International Journal of Solids and Structures **29**(11):1329–1338

[14] Jiaming Y, Suotai S (1993) Analysis of bending of unsymmetrical laminated plates using reduced bending stiffness method. Acta Materiae Compositae Sinica **10**(4):13–22

[15] Schreiber P, Mittelstedt C (2022) Buckling of shear-deformable unsymmetrically laminated plates. International Journal of Mechanical Sciences **218**:106,995

[16] Reddy JN (2004) Mechanics of laminated composite plates and shells: Theory and analysis, 2nd edn. Crc Press, Boca Raton, London, New York, Washington (D.C.)

[17] Reddy JN (1984) A simple higher-order theory for laminated composite plates. Journal of Applied Mechanics **51**(4):745–752

[18] Reddy JN, Phan ND (1985) Stability and vibration of isotropic, orthotropic and laminated plates according to a higher-order shear deformation theory. Journal of Sound and Vibration **98**(2):157–170

[19] Whitney JM, Leissa AW (1969) Analysis of heterogeneous anisotropic plates. Journal of Applied Mechanics **36**(2):261–266

[20] Ewing MS, Hinger RJ, Leissa AW (1988) On the validity of the reduced bending stiffness method for laminated composite plate analysis. Composite Structures **9**(4):301–317

Chapter 10
How Mechanically Inspired Design Rules Help in the Topology Optimization of Structures with Highly Nonlinear Behavior

Axel Schumacher

Abstract The efficient topology optimization of components based on purely mathematical algorithms is only possible for moderately non-linear structural behavior. This article is about the support of methods for topology optimization with design rules that are derived from expert knowledge. The use of these rules should help where mathematical methods cannot currently be used. The essential design rules of lightweight construction are presented and expanded to include design rules for crash-loaded structures. It is shown how these design rules can be algorithmized. These algorithmic design rules can be used as heuristics. They detect the situation in the mechanical structure and make topological changes based on this information. Different heuristics are used in competition with each other. Only a defined number of designs are allowed in the next iteration. The efficiency of the combination of mathematical optimization algorithms and algorithmic design tools is shown on various development tasks of crash structures. It is about optimizing the topology of laterally loaded profile structures made of metal and composite. In addition, topology optimizations of axially loaded structures are shown. The topology optimization of frame structures in three-dimensional space is also described.

10.1 Introduction

The algorithmic optimization of lightweight structures is about improving performance by finding optimal wall thicknesses and cross sections, by finding the optimal material, by finding the optimal shape and by finding the optimal topology, i. e. the position and arrangement of structural elements.

The optimal shape and the optimal topology are usually determined in a joint process. This works reliably because the special tasks can be transformed into a

Axel Schumacher
University of Wuppertal, Germany,
e-mail: schumacher@uni-wuppertal.de

formalized optimization task in which an objective function $f(\boldsymbol{x})$ dependent on the vector of the design variables is minimized [1, 2]:

$$\min f(\boldsymbol{x}) \qquad \text{(objective function)},$$

while considering the following constraints:

$$g_j(\boldsymbol{x}) \leq 0 \qquad j = 1, \dots, m_g \qquad \text{(inequality constraints)}$$
$$h_k(\boldsymbol{x}) = 0 \qquad k = 1, \dots, m_h \qquad \text{(equality constraints)}$$
$$x_i^l \leq x_i \leq x_i^u \qquad i = 1, \dots, n \qquad \text{(side constraints, upper and lower bounds)}$$

The restriction to "min $f(\boldsymbol{x})$" in the formulation does not pose a problem in practice, because the problem can easily be reformulated for maximization tasks with $\max f(\boldsymbol{x}) = -\min -f(\boldsymbol{x})$. The same applies to the inequality constraints and equality constraints, which should always be defined in the above form. All constraints formulations can be transformed to these forms. Optimization is based on the use of a structural analyses (usually finite element calculations). Their models are regarded as the correct representation of the structural behavior in the context of structural optimization.

The algorithmically determined optimization results often compete with solutions that have been created with the creativity and experience of the engineers. Sometimes the structures developed by the engineers are already quite good and are also more robust against changes in the assumed load cases, manufacturing accuracy and materials used.

A new quality of algorithmic structural optimization can be developed by integrating the experience of the engineers into the structural optimization process. This possibility is particularly interesting for problems where the structural analysis has difficulties in quickly providing the sensitivities of the objective and constraint functions according to the design variables. When optimizing the topology of structures with highly nonlinear behavior, working with sensitivities is very difficult, especially, e. g. crash structures. For this reason, this contribution shows what is possible with a combination of mathematical algorithms and a wealth of experience. So this is not about using an artificial intelligence that tries to find these rules with the help of neural networks.

In this contribution, the most important design rules for lightweight design are presented first. After these general rules, which also include a special consideration for composites, design rules are presented that are suitable for highly non-linear mechanical behavior. The main application here is the development of energy-absorbing structures in crash load cases. Especially for these rules it is shown how they can be integrated into the automatic structure optimization process. Then the Graph and Heuristic based Topology optimization (GHT) will be presented as an example. The GHT has been developed for more than 15 years [3–5]. At the end of the chapter, optimization results from different applications of crash optimization are shown and discussed.

10.2 Principal Design Rules for Lightweight Design

In this section, the principal design principles for lightweight structures are introduced and explained. It must be taken into account that lightweight structures not only have to meet requirements in terms of rigidity and strength. There are also, for example, dynamic requirements or acoustic requirements to be met.

The most important design principles for lightweight structures are:

- Avoidance of bending of the structural components: In Fig. 10.1 redesigning examples are shown.
- Multi-purpose design: A structural component should take on as many tasks as possible in the global lightweight structure. For example, the A-pillar of a passenger car is used and designed to support the door hinges, the windshield, and as a safety structure to maintain survival space when the car rolls over in a traffic accident.
- Short load transfer paths: If, for example, the length of a single loaded beam can be reduced, the maximum deflection is reduced to the third power.
- Consider stability issues such as (buckling of the structures)
- Use internal couplings of the structural components: Connecting structures that can support each other. Ribs, for example, are very effective in increasing the torsional stiffness of boxes.
- Use internal couplings of the structural components: Connecting structures that can support each other. Ribs, for example, are very effective in increasing the torsional stiffness of boxes.
- Depending on their design, beads can stiffen but also weaken sheet metal. Using beads is usually more efficient than open ribs.
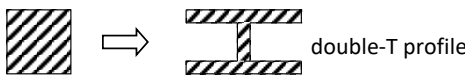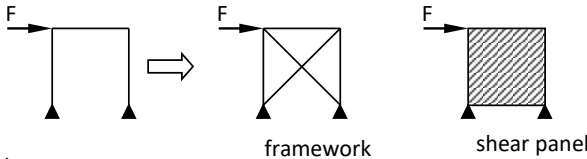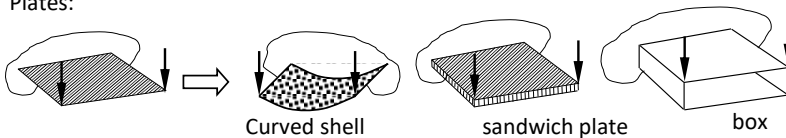
Fig. 10.1: Redesigning examples for avoiding bending of structural components.

- Avoid stress concentrations at force positions or cutouts (notches) and force redirection.

Depending on the material used, there are of course also specialized design rules. The following applies to composites, for example [6]:

- Design the laminate structure (stacking sequences) in such a way that all loads (load directions) are carried by fibers. The matrix only positions the fibers. Avoid high loads in the matrix.
- A laminate should have at least three different layer orientations.
- A cross-laminate design ("Cross-Ply" laminate) $\left[0_n^\circ \ 90_m^\circ\right]$ should be avoided.
- Normally, a $\left[0_n^\circ \ 90_m^\circ \ \pm45_k^\circ\right]$ laminate structure should be realized in which 4 different layer orientations are present.
- 3 layer orientations should only be used when there is clearly only one load orientation. Provide at least a proportion of 15–20% per layer orientation.
- 90° layers: Reduction of transverse contraction and coefficient of thermal expansion.
- Use 45°-layers for shear loads.

Regarding the stacking sequence:

- Normally use the sequence $[0° \ \pm45° \ 90°]$.
- Proportion of each layer: minimum $\approx 10\%$, maximum $\approx 60\%$.
- Maximum number of layers of the same orientation: 4.
- ±45° layer angles should be used on the outside of the laminate.
- Symmetrical layer structure.
- 0° layers to accommodate bending (tension and compression).
- ±45° layers to support shear loads (e. g., when a box is in torsion) and to increase buckling resistance (especially when located in the outer layers).
- 90° layers to stabilize necessary cutouts for joints.
- Symmetrical laminate structure in a component.

With regard to the tapering of the plies

- Main load direction: 1:20
- Other directions: 1:10

These rules are not integrated in current optimization algorithms for structures with linear or moderately non-linear behavior. This is also the case with the topology optimization algorithms. Here, in the standard procedure, the available design domain is divided into many small volumes and the optimization algorithm should decide which volume is filled with material and which is not [7]. The final component structure can be read from this. A typical application is shown in Fig. 10.2 [8].

These methods work very efficiently. Bending of the components is avoided and there are short load transfer paths. The main reason for the efficiency is that the finite element analysis provides the sensitivities of the objective functions and constraints according to the design variables. As a result, only one finite element calculation is required in each iteration [1, 2]. In the case of highly non-linear structural behavior, this analytical or semi-analytical calculation of the sensitivities is not so easy. There
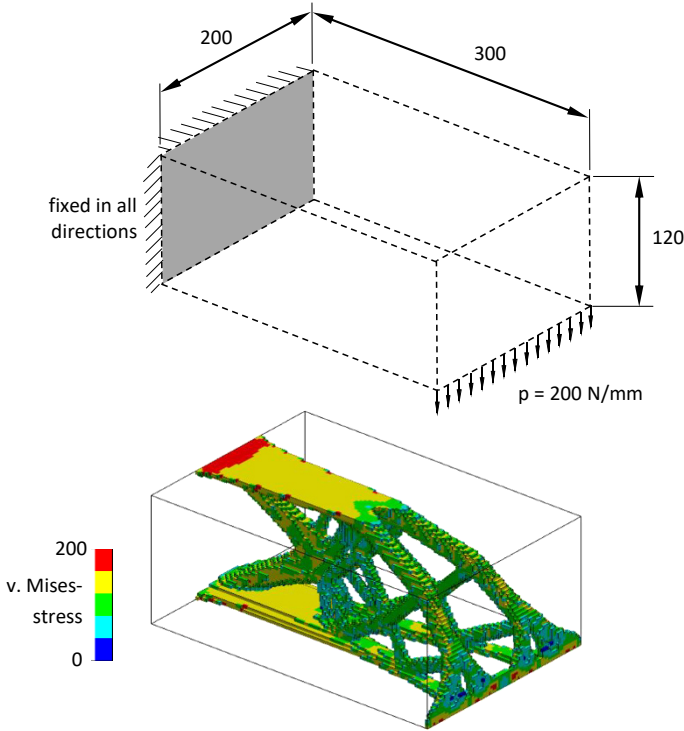
Fig. 10.2: Optimization of a cantilever (above: mechanical model and design domain, below: optimal structure) [8].

are initial approaches [9], but the effort is still so great that the topology optimization of crash structures must be done without analytical or semi-analytical sensitivities. For this reason, the use of mechanical inspired design rules is so interesting in this application.

10.3 Special Features in the Development of Crash Structures

The development of highly non-linearly loaded lightweight structures usually deals with crash structures of a passenger car, but also of trains, airplanes and ships. With all of these mobility systems, requirements for avoiding the severity of an accident in the event of a collision must be taken into account. However, this requirement is particularly important for passenger car. For this purpose, structures for energy absorbing are installed at many places in passenger cars. Regarding to these crash-

loaded structures with highly non-linear behavior, there are a lot of more complex objectives and constraints:

- Consideration of special acceleration values like the head injury criterion (HIC-value),
- Realize energy absorption possibilities,
- Fulfill special force levels in defined position of the automotive,
- Realize smooth force-displacement curve and smooth acceleration-time curve,
- Enable special force paths for special load cases,
- Make high stiffness of special parts possible, e. g. parts in a main force paths in the passenger area,
- Make low stiffness of special parts possible, e. g. at positions of the head contact of a pedestrian,
- Special safety criteria, e. g. intrusion of structural components in the battery system of an automotive.

In addition to these optimization functions, the behavior of the crash-loaded structures is strongly non-linear, normally calculated by the explicit finite element approach:

- Material plasticity and material failure models
- Geometric nonlinearities
- Contact phenomena
- Numerical and physical bifurcation points
- Non-smooth structural responses
- Mesh dependent results
- No analytical determination of the sensitivities (explicit time integration)
- Huge number of local optima in the design space

10.4 Design Rules for Crash Structures and Their Algorithms for use in the Automatic Structure Optimization Process

10.4.1 Principle Approach

Working with design rules always consists of three subtasks:

1. Detection of the situation in the component: Evaluation of the finite element calculation by extracting all essential output values.
2. Changing the structure: The basis is a flexible geometry model with which a new finite element model can be created with which the calculation can be carried out. Mathematical graphs [10] have established themselves as a very good tool here.
3. Evaluation of the structural improvement through the structural change using a finite element calculation.

A large number of competing heuristics are used. In the optimization, a user-defined number of designs can go into the next iteration. The selection of the design rules is based on the following questions:

1. How can the current situation in the component be identified in the batch?
2. How can the suggestions for improvement be automated in such a way that they carry out the structural change without a user interaction?

The programming effort for this can be very large.

10.4.2 Basic heuristics

In the following, 6 derived heuristics are presented (Fig. 10.3), which, unless otherwise stated, compete with each other:

1. Heuristic "Delete Needless Components": The simulation data used are the total internal energy densities of the individual walls. The wall with the lowest energy density is removed.
2. Heuristic "Support Buckling Components": It is about the homogenization of the buckling or deformation behavior of the structure. The heuristic is used for a) walls or profiles that offer little resistance to intrusion by other bodies or b) unstable walls or profiles. The simulation data used are the velocity vectors of the FE nodes, which can identify instabilities very well [11].
3. Heuristic "Balance Energy Density": By connecting loaded with unloaded components, the distribution of the internal energy density should be homogenized. The simulation data used are the total internal energy density of the individual walls or profiles.
4. Heuristic "Remove Small Chambers": The heuristic reduces the complexity of the structure.
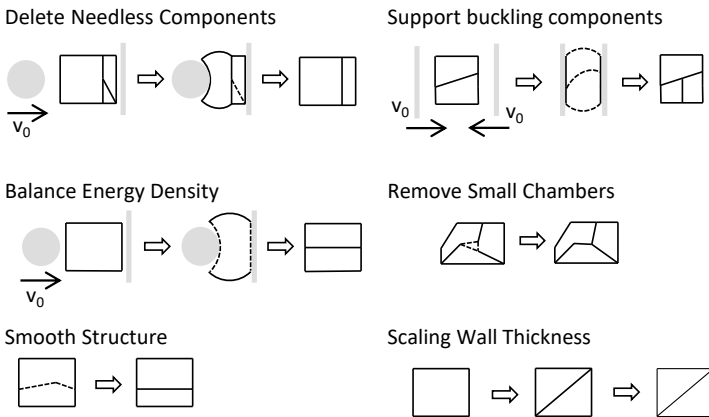
Fig. 10.3: Heuristics using the example of the design of profile structures in crash load cases [5].

5. Heuristic "Smooth Structure": Simplification of the structure by smoothing kinks inside the structure. This heuristic does not compete with other heuristics because no topology change is made. It is activated after each topology change of the structure.
6. Heuristic "Scaling Wall Thicknesses": Scaling the wall thicknesses of the structure to achieve a given mass. This heuristic also does not compete with other heuristics since no topology change is made. It is also activated after each topology change of the structure, so that the mass of the structure does not change due to the topology change (constant mass development).

The evaluation of the simulation data used can be very difficult and requires some investigations to ensure a safe process of automatic structure optimization. As an example, for the Heuristic "Support Buckling Components" the correlation between the very high velocity of the structural nodes and the buckling is shown in Fig. 10.4.

These 6 heuristics are used as basic heuristics in all applications. However, they have their origin in the topology optimization of laterally loaded profiles in a crash [4]. Additional heuristics have been developed for special applications, which are described below.

10.4.3 Special Heuristics for Laterally Loaded Profiles

Profiles are often loaded laterally in a crash. Common laterally loaded profiles are the automotive rocker or battery containment profiles in electric vehicles. Special heuristics for this class of crash structures are:

- Heuristic "Use Center of Gravity": The heuristic motivates the routing of a load path through the center of gravity of the profile. This is useful against global bending.
- Heuristic "Use Deformation Space": If there are large empty domains in the structure, they should be used.
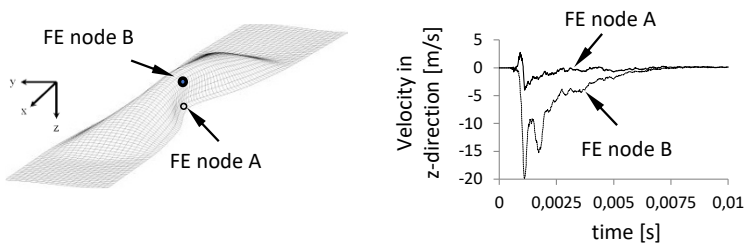
Fig. 10.4: Velocity of two nodes during the buckling of a wall [4].

10.4.4 Special Heuristics when Using Composite Material in Laterally Loaded Profiles

In themselves, composites are problematic in the production of high volumes in mass production. Nevertheless, composites are interesting as crash structures because of their very high specific energy absorption capacity [12]:

- Heuristic "Supporting Chamber Cracks": If cracks in the profile structure are detected in the axial direction, this area is reinforced by diagonal support [12].
- Heuristic "Thickening of High-energy Layers"
- Heuristic "remove unloaded layers"
- Heuristic "Adjust Ply Shares": This heuristic combines the two previously mentioned heuristics.
- Heuristic "Adjustment of the Fiber Orientation": Pre-defined orientations are set in the individual laminates depending on the detected stress.

10.4.5 Special Heuristics for Axially Loaded Profiles

The axial crash-loading of profiles enables a significantly higher specific absorption energy than laterally loaded profiles. For these axially loaded profiles, the following heuristics exist [13]:

- Heuristic "Create Lattice Structures": Lattice structures are common and efficient cross-section topologies. In the literature there is a large number of cross-section variants with good force-displacement curves
- Heuristic "Create Cross Structures": Crosses can also have a positive influence on the force-displacement curve.
- Heuristic "Connect Low Energy Walls": If two connected walls have a very low energy density, the connection is abbreviated by a diagonal.
- Heuristic "Split Long Walls": Long walls tend to buckle under axial loading. Splitting should allow fold buckling instead of global wall buckling.
- Heuristic "Create Different Wall Length": If cross-section geometries are irregular, there are different buckling wavelengths. With good tuning, this ensures more even force-displacement curves.
- Heuristic "Insert Small Chambers": Small chambers in the corners of axially loaded profiles increase energy absorption.
- Heuristic "Create Bitubular Structures": The heuristic builds new inner profiles into the existing profile. With good tuning, a more even force-displacement curve can be achieved.
- Heuristic "Incorporation of Triggers": Beads are good trigger elements that can be easily incorporated into the structure. They initiate fold buckling.

10.4.6 Special Heuristics for Frame Structures in the Three-Dimensional Space

The geometric realization of the designs generated by the heuristics is significantly more difficult in the case of three-dimensional frame structures [14]. The geometric situation of the Heuristic "Support Buckling Components" can be seen in Fig. 10.5. However, a few special heuristics are required:

- Heuristic "Split Long Profiles": Long profiles are at high risk of buckling under axial loads. Splitting is intended to reduce the risk of buckling.

10.5 The Procedure of the Graph and Heuristic Based Topology Optimization (GHT)

10.5.1 Basic Idea of the Method

The process of Graph and Heuristic based Topology Optimization (GHT) is based on the Bubble method [15], which changes the topology of the structure in the outer loop and optimizes the shape in the inner loop (Fig. 10.6). In the mechanically linear range, an analytical hole positioning criterion was developed for the bubble method, which evaluates the local stresses in the component. This hole positioning criterion has been replaced by heuristics in the GHT [3–5].
So the inner loop is executed with mathematical optimization algorithms while the outer loop uses the heuristics. The GHT process has a modular structure. For example, shape optimizations in individual iterations can be dispensed with and/or several heuristics can be pursued in parallel.

The basis for changing the geometry through the optimization software and for the automatic creation of input decks is a flexible description of the geometry using the mentioned mathematical graphs. The first scope of application for the GHT is the optimization of profile cross-sections, which can be described using a two-dimensional graph. However, the structure itself and all finite element simulations carried out are three-dimensional.
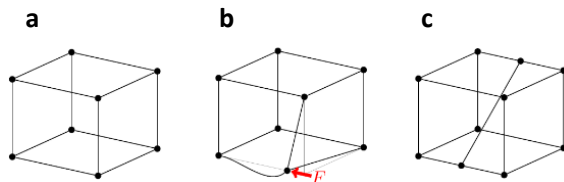
Fig. 10.5 Example of the scheme of the Heuristic "Support Buckling Components". **a)** Initial design. **b)** Fast deformation under loads. **c)** New structure with supported edge.
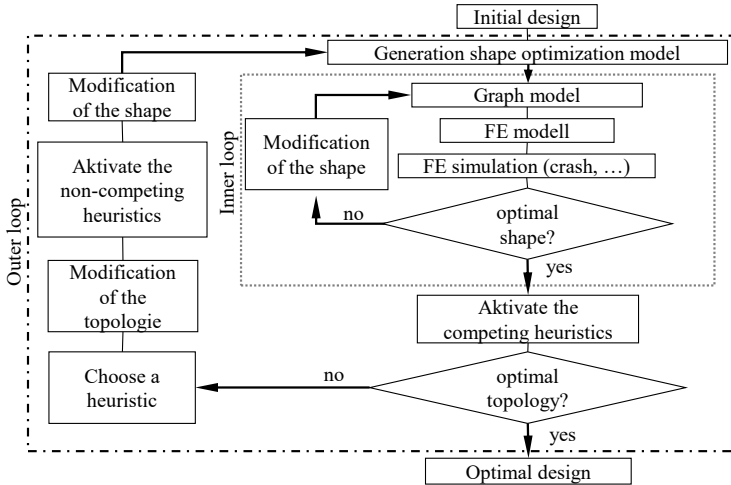
Fig. 10.6: Scheme of the GHT.

10.5.2 Essential Modules of the Fully Automatic Process

For the use in automatic structure optimization, the GHT modules are programmed in such a way that they run reliably in the batch process.

10.5.2.1 Use of Mathematical Graphs for a Flexibly Building of Complex Structures

The mathematical graph is used to describe the layout of a frame structure and the cross-sections of its profiles. It is used for the manipulation of the geometry and to check various geometrical constraints like minimum distances or connection angles. Fig. 10.7 shows the interaction of the 3D graph and the 2D graph.

Fig. 10.7 Mathematical graph of the 3D frame structure together with the graph of a profile [14].
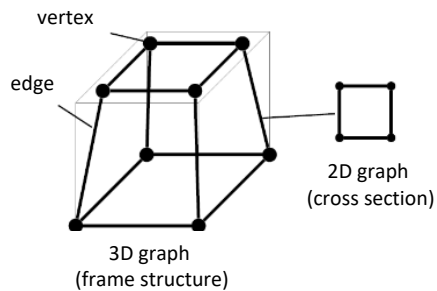
10.5.2.2 Automatic Generation of Geometry Details

The modelling of the relevant details is essential for the prediction quality of the crash simulation. In addition to the modeling of the profiles, the connection nodes are modeled as realistically as possible.

10.5.2.3 Automatic Generation of Finite Element Models for Crash Simulation

The geometry can be exported with an interface (e. g. to a STEP-file), so that state of the art finite element pre-processors can manage the meshing (Fig. 10.8). With the Include-Strategy of the finite element solvers (e. g. LS-DYNA®, Radioss® or PAM-CRASH®) the part to be optimized is integrated into the overall crash model.

10.5.2.4 Automatic Evaluation of the Results of the Crash Simulations

The heuristics need an automatic evaluation of the crash simulation. Self-developed programs are used together with commercially available post-processors.

10.5.2.5 Module of Heuristics

The heuristics described in Sect. 10.4 are integrated in the software. More than 20 heuristics are currently used.

10.5.2.6 Mathematical Algorithms for Shape Optimization and Dimensioning

Global optimization algorithms [1, 2] are used in the GHT process. This can be, for example, algorithms based on the evolution strategy. Simulated annealing or metamodel-based methods, such as those implemented in LS-OPT®, can also be used.
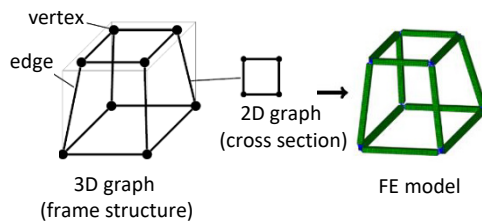
Fig. 10.8 From the graph to the finite element model [14].

10.5.2.7 Module for Control and Manage of Large Computing Clusters for Time-Consuming Crash Simulations

In each iteration, all heuristics provide design suggestions, of which a certain number (e. g. five) are pursued. This results in a large number of necessary crash simulations. If shape optimization and dimensioning are added, hundreds of simulations are necessary. Controlling a computing cluster is necessary.

10.6 Collection of Published Application Examples

10.6.1 Metal Profile Structure with a Lateral Load Case

The first application is the optimization of the cross-section of a vehicle rocker [4]. The manufacturing process is extrusion and the material is aluminum. Fig. 10.9 shows a sub-model of the vehicle rocker hitting a pile. The evaluation of the strains on the initial design in LS-DYNA®, i. e. the empty rocker profile, can be seen in Fig. 10.10.
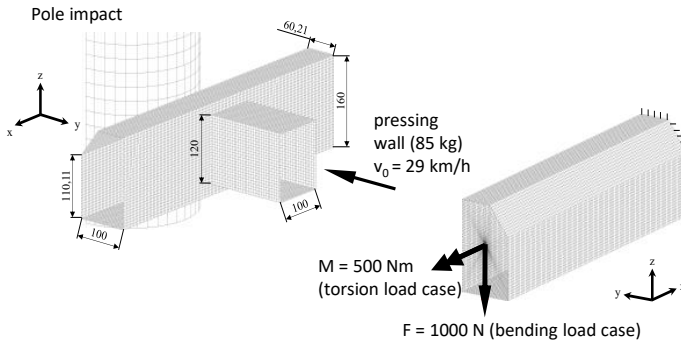
Fig. 10.9: Load cases of the rocker example [11].

Fig. 10.10 Evaluation of the strains in the initial design (blue: no strain, red: high strain) [11].
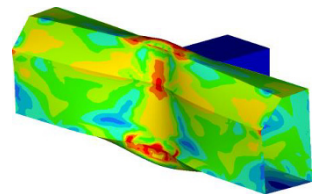
The optimization task is to find the optimal topology and shape of the cross section of the rocker profile by solving the following optimization task:

Minimize the maximal force at a moved rigid wall (velocity v_0), so that functional constraints

- Mass ≤ 2.801 kg
- Intrusion of the pole ≤ 70 mm
- Stiffness (bending and torsion) $\geq 50\%$ stiffness initial design

and the manufacturing constraints

- 1.6 mm $\leq$ wall thickness ≤ 3.5 mm
- Distance of walls ≥ 10 mm
- Connection angle of walls $\geq 15°$
- Maximum chamber size ration 1 : 20

are fulfilled.

Figure 10.11 shows the optimization history. In each iteration, the five best designs were followed up and shape optimization was only carried out in the 3rd iteration.

Fig. 10.12 shows the force-time curve of the starting design, the optimal design and the theoretical optimum (constant level during the crash time). The force-time curve of the optimal design is very close to the theoretical optimum, where the acceleration rises very quickly to a constant level and quickly drops back to zero.
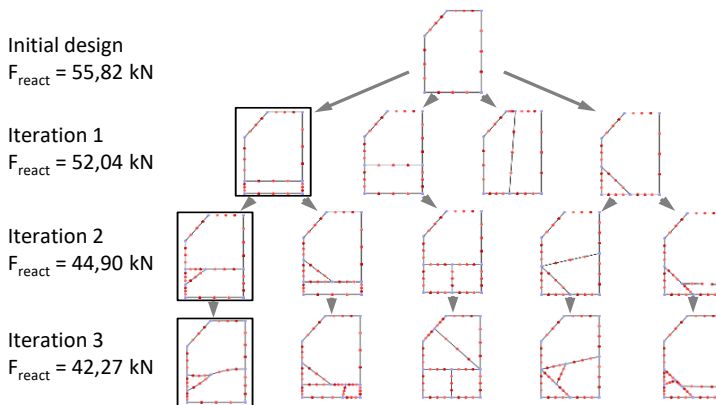
Fig. 10.11: Topology optimization of the rocker: Optimization history [11].
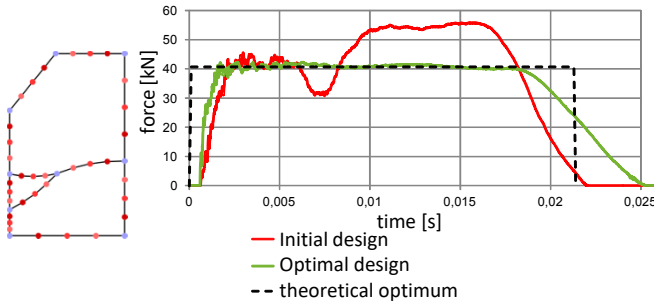
Fig. 10.12: Topology optimization of the rocker: Optimization result [11].

10.6.2 Composite Multi-Chamber Profile Structure with Lateral Load Cases

The optimization of a wrapped multi-chamber profile made of tapes with carbon fibers and a thermoplastic polyamide matrix is shown. The solver LS-DYNA® is used for the calculation. The structure rests on two rigid cylinders and is hit laterally by another cylinder and an initial velocity. The drop weight is inclined 2° around the x-axis to account for the fact that the drop body can tip a few degrees in a drop tower. In the model, the gravitational acceleration acts against the z-axis. The initial design consists of an inner and a surrounding outer chamber, each with a thickness of 3.12 mm and the fiber orientations of $\left[\pm87^\circ_2 \ \pm10^\circ_2 \ \pm45^\circ_2\right]$. In the FE model, the orientations with the same amount are combined into a layer group, which is modeled with a layer of shell elements and is connected to the adjacent layer groups with volume adhesive elements. The tape thickness is 0.13 mm and the tape width is 12 mm. The inner rounding radii are 6.5 mm. The orientations are slightly corrected prior to the simulations depending on the circumferential length to ensure wrapability. The load case with the initial design is shown in Fig. 10.13.

The mass is to be minimized and, as a constraint, the z-displacement of the drop weight must not be more than 60 mm in order to guarantee that the drop weight is
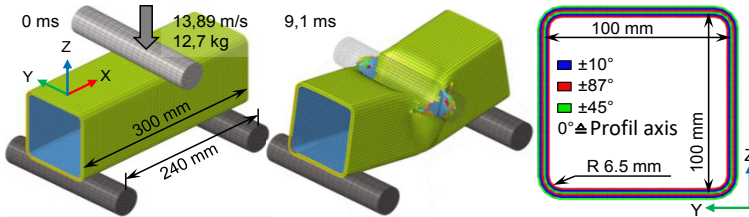
Fig. 10.13: Load case for the optimization of a wrapped multi-chamber profile [12].

stopped by the profile structure and its energy is almost completely absorbed. The manufacturing constraints are relatively restrictive in order to keep the manufacturing costs as low as possible. Due to a required symmetry to the local y-axis of the cross-section, a manufactured profile can be used up to twice in the structure. The optimization task reads as follows:

Minimize the mass, so that functional constraints

- z-Intrusion of the drop weight ≤ 60 mm

and the manufacturing constraints

- 1.04 mm $\leq$ wall thickness ≤ 5 mm
- Length of a walls ≥ 29 mm
- Distance of walls ≥ 10 mm
- Connection angle of walls $\geq 44.5°$
- Symmetry to local y-axis
- $10° \leq$ tape orientation $\leq 89.9°$
- Number of chambers ≤ 7
- Inner radius at corners ≥ 6.5 mm

are fulfilled.

In each optimization, the top five designs are passed to the next iteration, and all heuristic designs are evaluated in a dimensioning process in which all wall thicknesses are scaled by a uniform factor. The optimization history is shown in Fig. 10.14. The topology heuristics reduce the weight by 305 g in two iterations and achieve no further improvement in the third iteration, so that the layer construction heuristics are then activated. Here the mass can be reduced again by 29 g in the two following iterations. After the sixth iteration can no longer achieve any improvement, the optimization is terminated. A total of 337 simulations are run during the optimizations. The cross-sections of the designs generated by the topology heuristics are shown. The top five designs that are passed to the layer heuristics in the fourth iteration are marked with an asterisk.

The deformation behavior of the best design from iteration 5 is shown in Fig. 10.15. The penetration of the falling weight into the structure is severely restricted by the three upper chambers with relatively vertical walls. At the same time, there are two triangular profiles in the lower corners, which are laterally crushed by the large central profile during impact. With this mechanism, energy can be absorbed not only at the impact point of the falling weight, but also at both ends of the profile, so that a larger proportion of the structure is involved in the energy absorption and the wall thicknesses and consequently the mass can be reduced overall.

The two triangular profiles as well as the outer wraps have a thickness of 1.47 mm and all orientations contained therein [$\pm 87°$ $\pm 10°$ $\pm 45°$] have an equal proportion. The three remaining chambers in the upper half each have a thickness of 1.14 mm. Here, compared to the other chambers, the thickness of the $\pm 10°$ layers was reduced from 0.47 to 0.2 mm. Since the primary task of these chambers is to reduce intrusion into the profile, a smaller proportion of $\pm 10°$ layers is sufficient here. In a final step, the thicknesses of the individual layers must be corrected so that they correspond to a multiple of the discrete tape thickness in order to be produced.
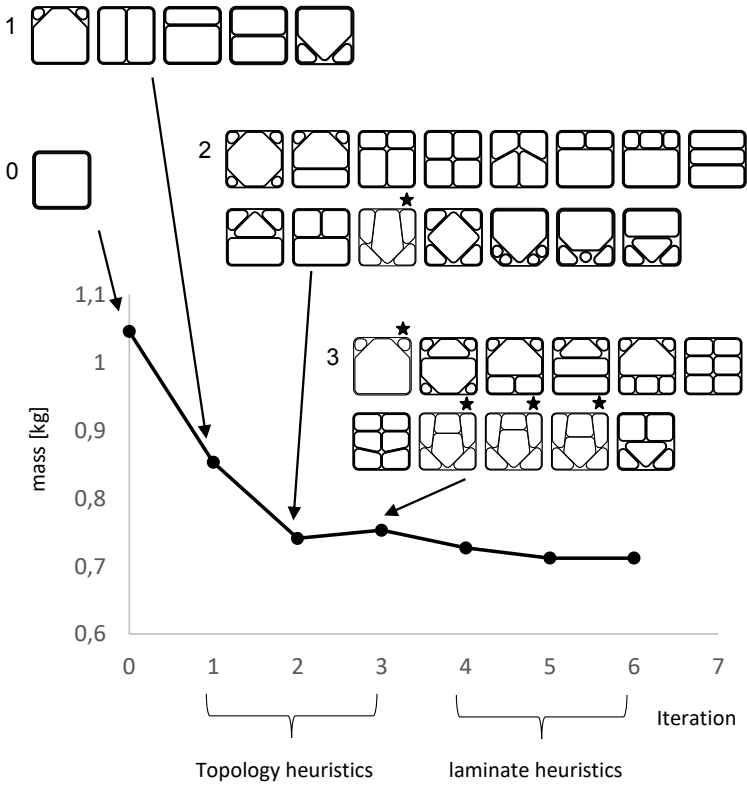
Fig. 10.14: Cross-sections of the designs generated by the topology heuristics, listed by iteration, highlighting the top five designs that are the starting point for the layer heuristics.
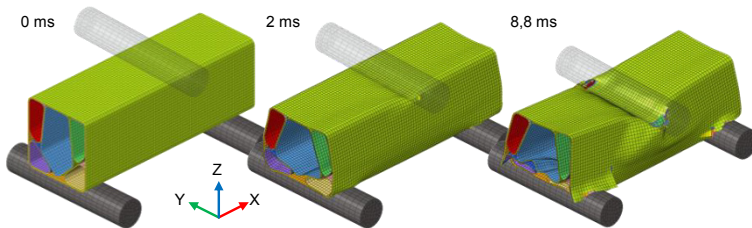
Fig. 10.15: Deformation behavior of the optimized profile at three different times.

10.6.3 Profile Structure with Axial Load Cases

In the drop tower load case shown in Fig. 10.16, a profile structure is to be optimized so that the impactor has a minimum intrusion into the profile structure. The impactor is modeled as a rigid body and has a mass of 500 kg and an initial velocity of $v_0 = 10$ ms. The angle of inclination of the impactor is 10° and is guided in the z-direction. The extrusion profile is firmly clamped on the side facing away from the impact, i. e. all translational and rotational degrees of freedom are blocked. A coefficient of friction of $\mu = 0.2$ is assumed at the contact between the impactor plate and the profile structure. The maximum contact force between impactor and profile structure is evaluated as the force. The optimization task reads as follows [13]:
Minimize the maximal z-intrusion of the impactor, so that functional constraints

• Mass ≤ 1.201 kg

and the manufacturing constraints

• 1.6 mm ≤ wall thickness ≤ 5 mm
• Distance of walls ≥ 10 mm
• Connection angle of walls ≥ 15°
• Symmetry to local x-axis and local y-axis

are fulfilled.

The optimization result is shown in Fig. 10.17, in which all available heuristics were able to deliver designs. For comparison, a structure is also shown that was created by simply applying the "Insert Small Chambers" heuristic. This structure exhibits global bending, which is due to the rapid reduction of the initially large force.

The final design of the GHT shows an even, almost rectangular force-displacement curve (after the buckling force level has been reached). The good performance of this design can be derived from the different chamber sizes and wall lengths, with the smallest chambers being found on the first crash-loaded side of the profile cross-section.
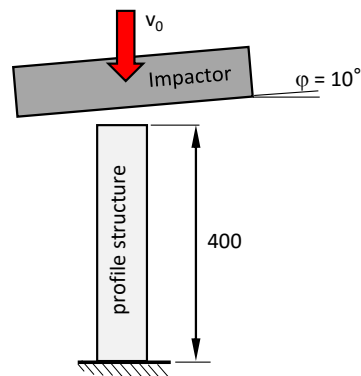
**Fig. 10.16** Axial load case of the drop tower [13].
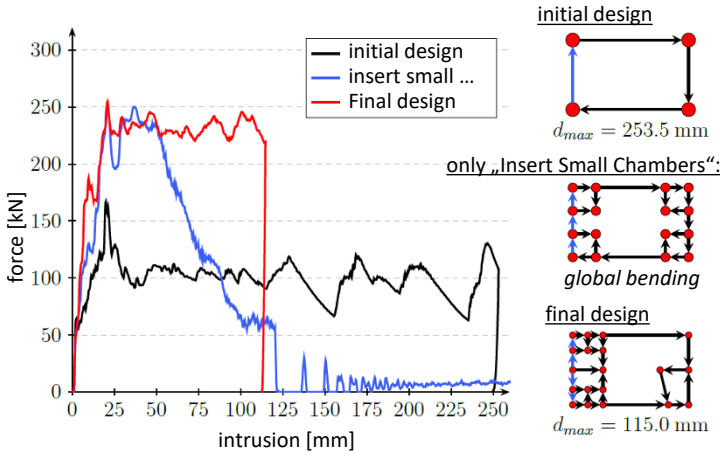
Fig. 10.17: Optimization results (the side hit first by the inclined impactor is shown in blue in the graph) [13].

10.6.4 Three-Dimensional Frame Structure

The optimization presented here is about the optimization of a three-dimensional frame structure (Fig. 10.18). Profiles can be arranged in the shown design space. These profiles should all have the same cross-section. In Fig. 10.19 the deformation of the initial design is shown. The optimization task reads as follows:

Minimize the maximum occurring contact force, so that functional constraints

- Intrusion of the pole $\leq$ 150 mm
- Mass $\leq$ 0.5 kg
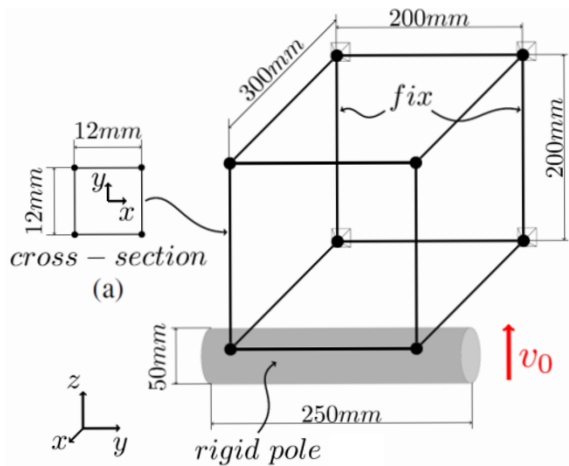
Fig. 10.18 Initial frame structure with quadratic cross-sections (12×12 mm) impacted by a rigid pole [14].

Fig. 10.19 Initial frame im-
pacted by rigid pole: Deformed
state at $t = 0.020$ s [14].
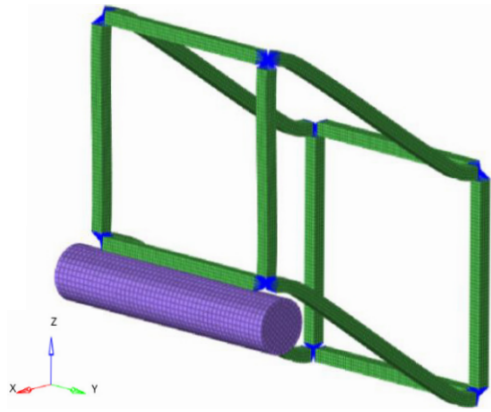
and the manufacturing constraints

- 0.8 mm ≤ wall thickness ≤ 3.5 mm
- Length of the profiles ≥ 35 mm
- Distance of walls ≥ 35 mm
- Connection angle of walls ≥ 15°
- Symmetry to y-axis

are fulfilled.

The optimization result can be seen in Fig. 10.20. In the two diagrams, contact force and displacement are plotted over the iterations. At the bottom of the picture the final structure is shown. The outer frame shape has been tapered in the shape optimization in the front upper area. The framework can be divided into two areas. The front area near the impact is more flexible, while additional profiles have developed in the rear area near the clamping. As a result, the rear of the frame provides the rigidity needed to stop the cylinder before 150 mm of displacement. Fig. 10.21 shows the diagram of the contact force over the displacement.

10.7 Conclusion

All presented optimization results strongly depend on the implemented heuristics. If these heuristics are further improved or supplemented by new heuristics, even better optimization results can most likely be achieved.
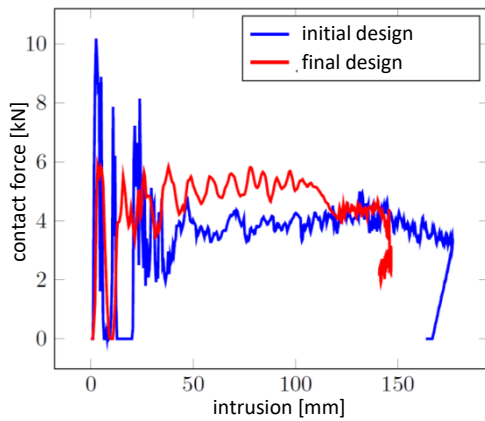
The idea of using heuristics to support mathematical optimization algorithms can also be transferred to other fields of application. However, the effort is only worthwhile if purely mathematical methods fail.
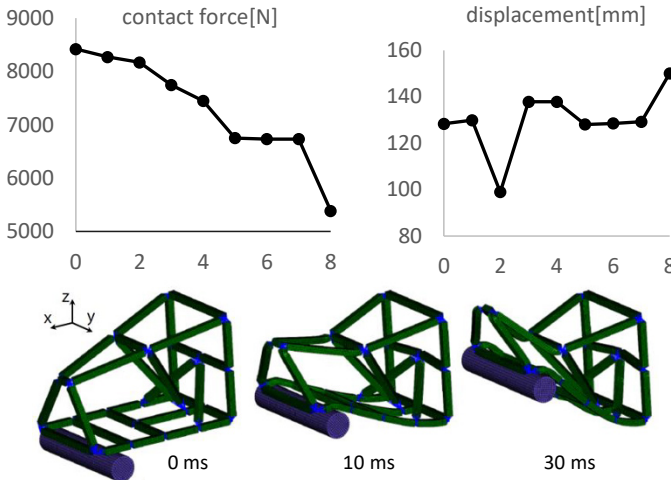
Fig. 10.20: Optimum of rigid pole model: Minimize the contact force. Initial state at $t_0 = 0.000$ s. Deformed state at $t = 0.010$ s. Deformed state at $t = 0.030$ s [14].

Fig. 10.21 Force-displacement behavior of the initial design and the final design [14].

References

[1] Harzheim L (2019) Strukturoptimierung: Grundlagen und Anwendungen, 3rd edn. Europa-Lehrmittel-Verlag, Haan-Gruiten

[2] Schumacher A (2020) Optimierung mechanischer Strukturen - Grundlagen und industrielle Anwendungen, 3rd edn. Springer Vieweg, Berlin, Heidelberg

[3] Olschinka C, Schumacher A (2008) Graph based topology optimization of crashworthiness structures. PAMM **8**(1):10,029–10,032

[4] Ortmann C, Schumacher A (2013) Graph and heuristic based topology optimization of crash loaded structures. Structural and Multidisciplinary Optimization **47**(6):839–854

[5] Ortmann C, Sperber J, Schneider D, Link S, Schumacher A (2021) Crashworthiness design of cross-sections with the graph and heuristic based topology optimization incorporating competing designs. Structural and Multidisciplinary Optimization **64**(3):1063–1077

[6] Seibel M (2012) Fiber composite technology. Lecture notes, Hamburg University of Applied Sciences, Hamburg

[7] Bendsøe MP, Kikuchi N (1988) Generating optimal topologies in structural design using a homogenization method. Computer Methods in Applied Mechanics and Engineering **71**(2):197–224

[8] Dienemann R, Schumacher A, Fiebig S (2017) Topology optimization for finding shell structures manufactured by deep drawing. Structural and Multidisciplinary Optimization **56**(2):473–485

[9] Weider K (2021) Topologische Ableitung zur Optimierung crashbelasteter Strukturen. Berichte aus dem Maschinenbau, Shaker Verlag, Düren

[10] Diestel R (2017) Graphentheorie, 5th edn. Springer Spektrum, Berlin and Heidelberg

[11] Ortmann C (2015) Entwicklung eines graphen- und heuristikbasierten Verfahrens zur Topologieoptimierung von Profilquerschnitten für Crashlastfälle. Berichte aus dem Maschinenbau, Shaker Verlag, Aachen

[12] Schneider D (2023) Graphen- und heuristikbasierte Topologieoptimierung von Profilstrukturen aus Faser-Kunststoff-Verbunden in Crashanwendungen. Berichte aus dem Maschinenbau, Shaker Verlag, Düren

[13] Sperber J (2022) Graphen- und Heuristikbasierte Topologieoptimierung axial belasteter Crashstrukturen. Berichte aus dem Maschinenbau, Shaker Verlag, Düren

[14] Beyer F, Schneider D, Schumacher A (2020) Finding three-dimensional layouts for crashworthiness load cases using the graph and heuristic based topology optimization. Structural and Multidisciplinary Optimization **63**(1):59–73

[15] Eschenauer HA, Kobelev VV, Schumacher A (1994) Bubble method for topology and shape optimization of structures. Structural and Multidisciplinary Optimization **8**(1):42–51

Chapter 11
Phase Field Modeling of Cracks in Ice

Rabea Sondershaus, Ralf Müller, Dietmar Gross, and Angelika Humbert

Abstract Calving of iceberg at ice shelves and floating glacier tongues is a poorly understood process, hence a physically motivated calving law is not yet existing. The demands on developing appropriate models for calving is large, as calving rates are needed for large scale ice sheet models that simulate the evolution of ice sheets. Here, we present a new approach for simulating fracture in ice. Our model is based on a finite strain theory for a viscoelastic Maxwell material, as the large simulation time leads to high strains. The fracturing process is simulated using a fracture phase field model that takes into account the elastic strain energy. We conduct simulations for a typical calving front geometry, with ice rises governing the formation of cracks. To represent the stress state adequately, we first conduct a spin-up to allow the viscous contribution to develop before the fracture phase field is computed. The analysis comprises the assessment of the crack path in comparison to observations, the influence of the spin-up, as well as elastic versus viscous strain contributions based on Hencky strain. Additionally, an estimate of released energy based on high resolution optical imagery of a Greenlandic calving front is presented.

11.1 Introduction

Ice at stresses and strain-rates typically occurring in ice sheets and ice shelves shows a dominant brittle behaviour [1]. The fracture toughness of polycrystalline ice was

Rabea Sondershaus · Ralf Müller · Dietmar Gross
Institute for Mechanics, Technical University of Darmstadt, Darmstadt, Germany,
e-mail: rabea.sondershaus@tu-darmstadt.de,
ralf.mueller@mechanik.tu-darmstadt.de, gross@mechanik.tu-darmstadt.de

Angelika Humbert
Alfred-Wegener-Institut Helmholtz Zentrum für Polar- und Meeresforschung, Bremerhaven, Germany and Department of Geoscience, University of Bremen, Bremen, Germany,
e-mail: angelika.humbert@awi.de

281

found in laboratory experiments to be $K_{Ic} = 95.35 \pm 16.69 \text{kPa m}^{1/2}$ [2]. Cracks in ice are evolving episodically. The length of such cracks is often on the order of kilometers. They either intersect the ice in vertical (thickness) direction entirely (so called rifts) when they propagate in horizontal direction, or they open up in vertical direction (crevasses) with crack face distance in the order to 1-10's meters. At calving fronts, crack propagation is eventually leading to the detachment of icebergs. This is a normal process of mass loss of floating ice masses. In contrast, ice shelf break-up events or the disintegration of floating tongues represent instability of ice masses. Understanding of fracture formation and evolution is thus of major importance for projecting the future of ice sheets. Yet physically based calving laws are not existing. In Fig. 11.1 the calving front situation at Greenland's largest floating ice tongue called Nioghalvfjerdsbræ is shown. The glacier tongue is grounded at several points which are called ice rises and are marked in blue. At these points cracks emerge in the ice shelf, as can be seen in the satellite imagery, Fig. 11.1b).

Glacial ice was found to be a viscolelastic fluid following a Maxwell rheology [3–5]. The elastic behavior is assumed to be compressible, as it is common for crystalline materials, while the viscous flow behavior originates from incompressible inelastic processes. The viscosity is strongly influenced by the temperature which varies in ice sheets primarily in vertical direction (cold at the top, warm at the base) and in flow direction (cold in the high elevated interior of the ice sheet, warmer at the lower ice sheet margins). In general, ice sheets and ice shelves are hot materials, as their homologous temperature is extremely high. Its characteristic time ranges from 30 days for $\eta = 10^{15} \text{Pa s}$ to 8.4 years for $\eta = 10^{17} \text{Pa s}$ assuming a Young's modulus
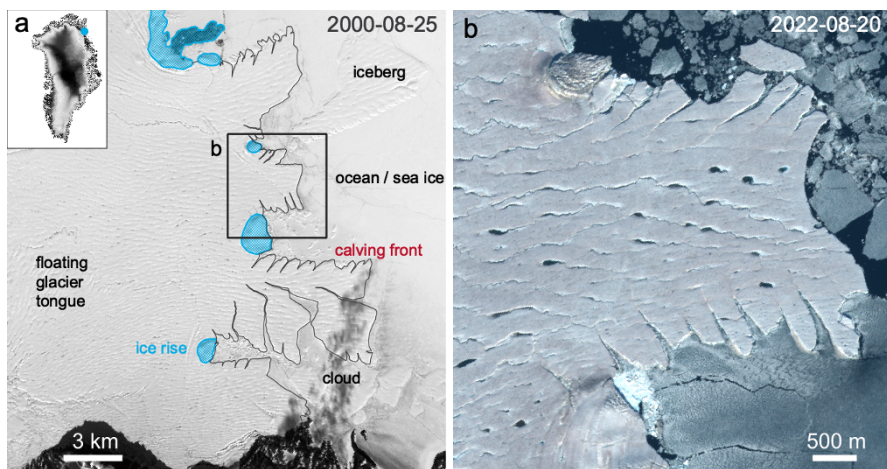
Fig. 11.1: Overview of a typical calving front situation. The left panel shows a Landsat-7 satellite image of the calving front (black line) of Nioghalvfjerdsbræ, Greenland's largest floating ice tongue. The blue areas are ice rises. The right panel (Sentinel-2 imagery) is a zoom into a part of the ice front (box in the left panel) where cracks around the ice rises and along the lateral margins of the ice are visible..

of 1 GPa and $\nu = 0.325$. This exemplifies that long computation times are needed to solve the problems adequately and as a consequence, a non-linear strain theory is required. For glacial ice a finite strain theory for a Maxwell rheology was first formulated by [6] and applied to a realistic ice shelf geometry in [7].

In the present investigation a fracture phase field model is proposed to describe the failure of ice due to crack formation and propagation. The general concept of phase field models is the representation of a sharp interface, such as for example crack surfaces or grain boundaries by means of a continuous scalar field $s(x, t)$. The order parameter s represents the 'phase' e.g. the state of the material, where for fracture the intact material is specified by $s = 1$ and the fractured material by $s = 0$. The transition between these states is smoothed out leading to a diffuse representation of the crack.

The benefit of the diffuse representation is the prevention of costly remeshing during crack growth. Furthermore, the fracture phase field method is capable to simulate crack propagation as well as crack initiation and crack branching. In the last decade, the phase field method has become well established for fracture simulations and was used for a variety of fracture processes such as brittle [8–10], dynamic [11–13], fatigue [14–16] and hydraulic fracture [17, 18]. Moreover, different material behaviours for instance anisotropy [19–21], plasticity [22–24] and viscoelasticity [25–27] were studied. In this contribution, we will focus on the latter by combining the phase field model with a viscoelastic material description to capture the long and short term deformation of ice adequately. Since large time scales are considered in this study, the theory of small strains is no longer sufficient and the framework of finite deformations is needed.

The first application of phase field modelling for fracture in ice was presented by [28], with a focus on hydrofracture. This study assumed a linear elastic material response of the glacier, disregarding any viscous deformation, and a 2D glacier geometry. [29] presented a stress-based phase field fracture formulation, which was used to simulate hydrofracture in 2D and 3D including a viscous rheology. Crack initiation at ice rises was studied in [30] based on a viscoelastic phase field formulation for Maxwell materials. All above mentioned studies were assuming linear strain.

This text is organised as follows: First, the visocelastic material model at finite strains is introduced before explaining the phase field for fracture. Subsequently, we present the numerical aspects of the implementation and the simulation concept. Sect. 11.3 is focusing on the simulation results. In a last part the energy release from observations is estimated.

11.2 Theory

11.2.1 Non-Linear Strain Theory for Viscoelastic Material

The viscoelastic behaviour of ice can be described by the rheological Maxwell model, where an elastic element is in series with a viscous element. The basics of such a viscoelastic material description are briefly outlaid in the following.

In a finite strain formulation of a viscoelastic material a distinction between a (stress-free) reference configuration κ_r and a current configuration κ_t at time t is made. Both configurations as well as their corresponding quantities are sketched in Fig. 11.2. A central quantity in the description of the kinematics is the deformation gradient $\mathbf{F}$, defined as

$$\mathbf{F}(\mathbf{X},t) = \frac{\partial \mathbf{x}}{\partial \mathbf{X}} = \mathbf{1} + \frac{\partial \mathbf{u}}{\partial \mathbf{X}}. \tag{11.1}$$

It is noted that $\mathbf{x}$ describes the position of a material point in the current configuration, whereas $\mathbf{X}$ describes the position of the same material point in the reference configuration. The vector $\mathbf{u} = \mathbf{x} - \mathbf{X}$ is referred to as displacement vector. As the deformation gradient also contains rigid body motion, it is not a useful measure for strain. To this end the Green-Lagrange strain tensor $\mathbf{E}$ is introduced

$$\mathbf{E} = \frac{1}{2}(\mathbf{C} - \mathbf{1}) \tag{11.2}$$

with the right Cauchy-Green tensor $\mathbf{C}$

$$\mathbf{C} = \mathbf{F}^{\mathrm{T}}\mathbf{F} \tag{11.3}$$

Fig. 11.2 Kinematics of the problem in the reference κ_r (light grey) and current configuration κ_t (dark grey). For viscoelastic materials the intermediate configuration κ_i (red dashed line) is the configuration in which the constitutive relation is derived.
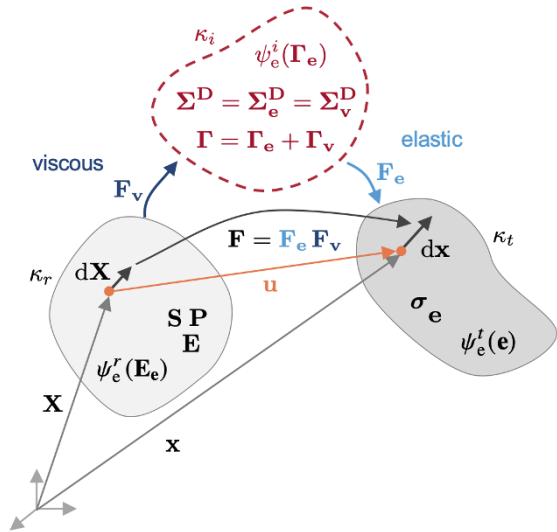
as a strain measure in the reference configuration κ_r. Its counterpart in the current configuration κ_t is the Euler-Almansi strain tensor $\mathbf{e}$

$$\mathbf{e} = \frac{1}{2}(\mathbf{1} - \mathbf{b}^{-1}) \tag{11.4}$$

that contains the left Cauchy-Green tensor $\mathbf{b}$

$$\mathbf{b} = \mathbf{F}\mathbf{F}^{\mathbf{T}}. \tag{11.5}$$

The kinematic equations are complemented by balance laws. To describe the motion of an ice sheet/ice shelf the balance of linear momentum is considered. As the focus is on horizontal plane of the extent of the ice sheet/ice shelf/glacier gravitational forces vanish. Furthermore, neglecting inertia terms the balance of linear momentum reduces to the equilibrium condition, given by

$$\mathrm{Div}\,\mathbf{P} = 0 \tag{11.6}$$

with the divergence in κ_r being denoted with $\mathrm{Div}(\cdot)$ and $\mathbf{P}$ the first Piola-Kirchhoff tensor, as a stress tensor referring to the reference configuration. The transformation between $\mathbf{P}$ and the Cauchy stress tensor $\boldsymbol{\sigma}$ in the current configuration κ_t is given by

$$\mathbf{P}\mathbf{N}\,\mathrm{d}A = \boldsymbol{\sigma}\mathbf{n}\,\mathrm{d}a \tag{11.7}$$

with $\mathbf{N}, \mathbf{n}$ the normal vectors and $\mathrm{d}A, \mathrm{d}a$ the infinitesimal area elements in the reference κ_r and current configuration κ_t, respectively. Infinitesimal area elements transform according to Nanson's formula

$$J\mathbf{F}^{-\mathbf{T}}\mathbf{N}\,\mathrm{d}A = \mathbf{n}\,\mathrm{d}a \tag{11.8}$$

with $J = \det(\mathbf{F})$.

To take the viscous part into account the intermediate configuration k_i (see Fig. 11.2) is introduced. The key concept for modelling finite viscoelasticity is the multiplicative decomposition of the deformation gradient into an elastic $\mathbf{F_e}$ and viscous $\mathbf{F_v}$ part

$$\mathbf{F} = \mathbf{F_e}\mathbf{F_v}, \tag{11.9}$$

which was introduced by [31] in the context of finite plasticity and first applied to ice deformation by [6]. As a consequence, the strain tensor $\boldsymbol{\Gamma}$ in the intermediate configuration is also decomposed into an elastic $\boldsymbol{\Gamma_e}$ and a viscous $\boldsymbol{\Gamma_v}$ part, but the decomposition is, comparable to the Maxwell model for small strains, additive

$$\boldsymbol{\Gamma} = \mathbf{F_v}^{-\mathbf{T}}\mathbf{E}\mathbf{F_v}^{-1} = \frac{1}{2}\mathbf{F_v}^{-\mathbf{T}}(\mathbf{F}^{\mathbf{T}}\mathbf{F} - \mathbf{1})\mathbf{F_v}^{-1} \tag{11.10}$$

$$= \frac{1}{2}(\mathbf{F_e}^{\mathbf{T}}\mathbf{F_e} - \mathbf{F_v}^{-\mathbf{T}}\mathbf{F_v}^{-1}) = \boldsymbol{\Gamma_e} + \boldsymbol{\Gamma_v}.$$

Accordingly the elastic strain is given by

$$\mathbf{\Gamma_e} = (1/2)(\mathbf{F_e}^{\mathrm{T}}\mathbf{F_e} - \mathbf{1}) \tag{11.11}$$

and the viscous strain in the intermediate configuration is obtained by

$$\mathbf{\Gamma_v} = (1/2)(\mathbf{1} - \mathbf{F_v}^{-\mathrm{T}}\mathbf{F_v}^{-1}). \tag{11.12}$$

It is important to note that the additive decomposition of the strain is only viable in the intermediate configuration [1].

The introduction of an intermediate configuration can be seen as a constitutive assumption. The stress tensor in intermediate configuration $\mathbf{\Sigma}$ depends on the elastic strain $\mathbf{\Gamma_e}$ as $\mathbf{\Sigma} = f(\mathbf{\Gamma_e})$, which for an isotropic material is given by

$$\mathbf{\Sigma} = \lambda\operatorname{tr}(\mathbf{\Gamma_e})\mathbf{1} + 2\mu\mathbf{\Gamma_e} \tag{11.13}$$

with the Lamé constants λ and μ. This form of material law is known as St. Venant-Kirchhoff material. Eq. (11.13) can be reformulated easily to

$$\mathbf{\Sigma} = \lambda\operatorname{tr}(\mathbf{\Gamma} - \mathbf{\Gamma_v})\mathbf{1} + 2\mu(\mathbf{\Gamma} - \mathbf{\Gamma_v}) \tag{11.14}$$

with the viscous strain in the intermediate configuration $\mathbf{\Gamma_v}$.

Similar to the additive composition of the strain in κ_i, the strain-rates are decomposed. Dealing with finite strains, objective time derivatives are needed. To this end, the lower Oldroyd rate is chosen.

$$\overset{\triangle}{\mathbf{\Gamma}}_e = \dot{\mathbf{\Gamma}}_e + \mathbf{l_v^T}\mathbf{\Gamma_e} + \mathbf{\Gamma_e}\mathbf{l_v} \tag{11.15}$$

is the elastic strain-rate, while

$$\overset{\triangle}{\mathbf{\Gamma}}_v = \dot{\mathbf{\Gamma}}_v + \mathbf{l_v^T}\mathbf{\Gamma_v} + \mathbf{\Gamma_v}\mathbf{l_v} \tag{11.16}$$

is the viscous strain-rate in κ_i. The viscous deformation gradient $\mathbf{l_v}$ is computed from

$$\mathbf{l_v} = \dot{\mathbf{F}}_v\mathbf{F_v^{-1}}. \tag{11.17}$$

The transformation (push forward operation) of the Green-Lagrange strain tensor into the intermediate configuration then reads

$$\overset{\triangle}{\mathbf{\Gamma}} = \mathbf{F_v}^{-\mathrm{T}}\dot{\mathbf{E}}\mathbf{F_v^{-1}} = \mathbf{F_v}^{-\mathrm{T}}\left(\overline{\mathbf{F_v^T}\mathbf{\Gamma}\mathbf{F_v}}\right)\mathbf{F_v^{-1}} = \dot{\mathbf{\Gamma}} + \mathbf{l_v^T}\mathbf{\Gamma} + \mathbf{\Gamma}\mathbf{l_v}. \tag{11.18}$$

To complete the viscoelastic constitutive model we need to define the stress in conjunction with an evolution law of the viscous strain, described by the viscous right Cauchy-Green tensor

$$\mathbf{C_v} = \mathbf{F_v^T}\mathbf{F_v}. \tag{11.19}$$

---

[1] Later on, we will introduce a strain measure that allows to compute the elastic and viscous strain components in the reference configuration.

We define a strain tensor in κ_r as the difference between total and viscous strains as

$$\mathbf{E_e} = \frac{1}{2}\left(\mathbf{C}-\mathbf{C_v}\right) \tag{11.20}$$

Setting the (deviatoric) elastic and viscous stresses equal

$$2\eta\overset{\triangle}{\mathbf{\Gamma}}_{\text{v}} = 2\mu\left(\mathbf{\Gamma}-\mathbf{\Gamma_v}-\frac{1}{3}\text{tr}(\mathbf{\Gamma}-\mathbf{\Gamma_v})\mathbf{1}\right) = 2\mu\mathbf{\Gamma_e^D}, \tag{11.21}$$

the evolution equation of the viscous part $\overset{\triangle}{\mathbf{\Gamma}}_{\text{v}}$ of the viscous strain tensor in the intermediate configuration is obtained as a function of the total strain difference $\mathbf{\Gamma}-\mathbf{\Gamma_v}$. Note that in the above equation the deviatoric part of $\mathbf{\Gamma}-\mathbf{\Gamma_v}=\mathbf{\Gamma_e}$ is used. This establishes an isochoric viscous deformation. The evolution law can also be expressed in terms of the right Cauchy-Green tensor $\mathbf{C_v}$, resulting in

$$\eta\dot{\mathbf{C}}_{\text{v}} = \mu\left(\mathbf{C}-\frac{1}{3}\text{tr}(\mathbf{CC_v^{-1}})\mathbf{C_v}\right). \tag{11.22}$$

Details are omitted here for the sake of compactness, but can be found in [6, 32]. Finally for the implementation the second Piola-Kirchhoff stress tensor is needed. It can be computed by a pull back of the stress $\mathbf{\Sigma}$ from the intermediate configuration κ_i on the reference configuration κ_r with the help of the viscous part of the deformation gradient $\mathbf{F_v}$

$$\begin{aligned}
\mathbf{S} &= \mathbf{F_v^{-1}}\mathbf{\Sigma}\mathbf{F_v^{-T}} \\
&= \frac{\lambda+(2/3)\mu}{2}\left[\text{tr}(\mathbf{CC_v^{-1}})-3\right]\mathbf{C_v^{-1}}+\mu\left[\mathbf{C_v^{-1}}\mathbf{CC_v^{-1}}-\frac{1}{3}\text{tr}(\mathbf{CC_v^{-1}})\mathbf{C_v^{-1}}\right].
\end{aligned} \tag{11.23}$$

As the viscous deformation is isochoric the $J_v = \det(\mathbf{F})$ does not appear in the above pull back operation.

The above derivations are formulated for the general 3D case. The adjustments for e.g. the computation of deviatoric tensor components in 2D have to be made, accordingly.

In the formulation of the fracture mechanical model the elastic energy density is needed. The elastic energy density of an isotropic St. Venant-Kirchhoff material in κ_i is given by

$$\psi_{\text{e}}^i(\mathbf{\Gamma_e}) = \frac{1}{2}\mathbf{\Gamma_e} : \mathbb{C}\mathbf{\Gamma_e} = \frac{\lambda}{2}\text{tr}(\mathbf{\Gamma_e})^2 + \mu\mathbf{\Gamma_e} : \mathbf{\Gamma_e} \tag{11.24}$$

with $\mathbb{C}$ the elasticity tensor defined by the Lamé constants λ, μ [33]. The elastic energy density of a St. Venant-Kirchhoff material in κ_r is given by

$$\psi_{\text{e}}^r(\mathbf{E_e}) = \frac{1}{2}\mathbf{E_e} : \mathbb{C}\mathbf{E_e} = \frac{\lambda}{2}\text{tr}(\mathbf{E_e})^2 + \mu\mathbf{E_e} : \mathbf{E_e} \tag{11.25}$$

as $J_v = 1$ due to $dV = dV^i$.

Finally, the elastic energy density of a St. Venant-Kirchhoff material in κ_t is given by

$$\psi_e^t(\mathbf{e}) = \frac{1}{2}\mathbf{e_e} : \mathbb{C}\mathbf{e_e} = \frac{\lambda}{2}\text{tr}(\mathbf{e_e})^2 + \mu\mathbf{e_e} : \mathbf{e_e}. \tag{11.26}$$

In order to evaluate the elastic and viscous components of strain, we introdue a logarithmic strain measure, the Hencky strain [34] that reads

$$\boldsymbol{\varepsilon}^{\mathbf{H}} = \frac{1}{2}\ln\left(\mathbf{F^T F}\right) = \frac{1}{2}\ln(\mathbf{C}) \tag{11.27}$$

and an additive decomposition of the Hencky strain as

$$\boldsymbol{\varepsilon_e^H} = \boldsymbol{\varepsilon^H} - \boldsymbol{\varepsilon_v^H} = \frac{1}{2}\ln(\mathbf{C}) - \frac{1}{2}\ln(\mathbf{C_v}) \tag{11.28}$$

With this the formulation of the finite strain theory for a viscoelastic Maxwell material is complete. Next, we introduce the fracture phase field model for viscoelastic materials under finite strains.
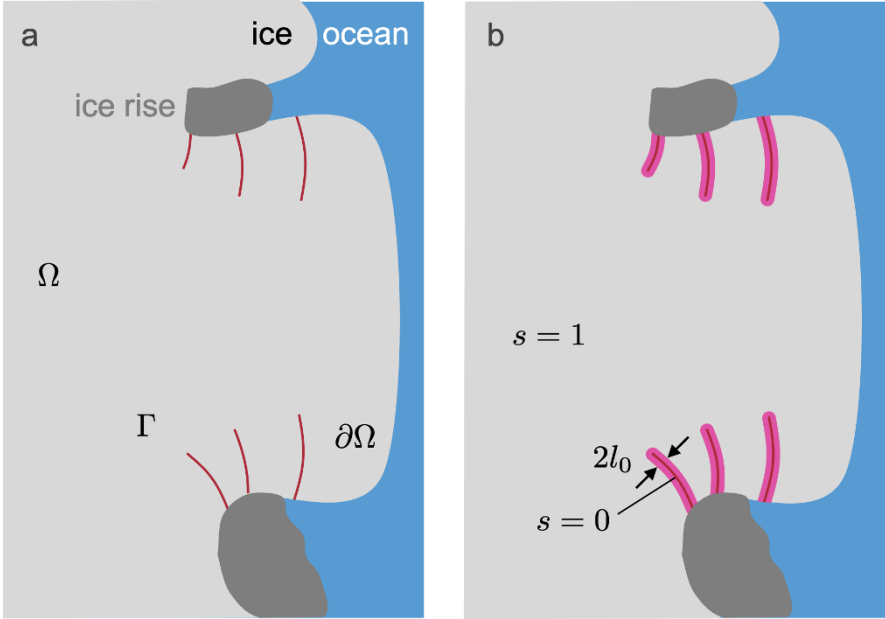
11.2.2 The Phase Field Model of Fracture

The general idea of the phase field method of fracture is based on Griffith's theory of fracture, in which failure occurs once a material specific critical value of the energy release rate $\mathcal{G}_c$ is reached. It is a material parameter that is related to the fracture toughness K_{Ic} by $\mathcal{G}_c = K_{Ic}^2(1 - \nu^2)/E$ in the plane strain case. The energy available for crack formation is given by the strain energy. Hence the energy potential Π of a body Ω with a sharp crack interface Γ_f reads

$$\Pi = \int_{\Omega\backslash\Gamma_f} \psi_e\, dV + \int_{\Gamma_f} \psi_f\, dA - \int_{\partial\Omega} \mathbf{t}_0 \cdot \mathbf{u}\, dA \tag{11.29}$$

with the first term describing the strain energy and the second term the energy required for fracture along the crack. The last term represents the traction boundary condition with a traction in the reference configuration $\mathbf{t}_0 = \mathbf{PN}$ and $\mathbf{u}$ the displacement. As mentioned above the sharp crack interface is smoothed out over a length scale l_0 as sketched in Fig. 11.3. The phase field method is hence approximating the energy for fracture as a volume integral over the critical energy release rate $\mathcal{G}_c$ multiplied by the crack surface (density) A_{l_0}

$$\int_{\Omega} \psi_f\, dV = \int_{\Omega} \mathcal{G}_c\, A_{l_0}\, dV \approx \int_{\Gamma_f} \mathcal{G}_c\, dA\ . \tag{11.30}$$

The crack surface density depends on the length scale l_0 which describes the transition width between intact and broken material as well as on the order parameter s. We use the Ambrosio and Tortorelli approximation [35] which is given by

Fig. 11.3: Sketch of the concept of phase field modelling of fracture. The left panel resembles sharp cracks, while the right panel highlights smeared out cracks represented by a continuous phase field. .

$$\int_\Omega \mathcal{G}_c A_{l_0} dV = \int_\Omega \mathcal{G}_c \left(\frac{(1-s)^2}{4l_0} + l_0 \nabla s \cdot \nabla s \right) dV \tag{11.31}$$

including a local part $(1-s)^2/4l_0$ and a non-local contribution $l_0 \nabla s \cdot \nabla s$ of the crack surface density. It satisfies the Γ-convergence criterion and converges for $l_0 \rightarrow 0$ to a sharp crack in case of a brittle material [36, 37].

With increasing damage due to crack formation and propagation, the material stiffness is reduced. This is introduced by a degradation function $g(s)$ given as a quadratic function $g(s) = s^2 + \eta_{RS}$ in which $\eta_{RS} \ll 1$ is a residual stiffness that ensures for an entirely broken material a numerically well conditioned system. For a vanishing residual stiffness η_{RS} the degradation function satisfies $g(s = 1) = 1$ as well as $g(s = 0) = 0$ and

$$\frac{\partial g}{\partial s} \leq 0, \quad \frac{\partial g}{\partial s}\bigg|_{s=0} = 0. \tag{11.32}$$

To ensure irreversibility of the crack, the phase field is set to 0 once it has reached a critical value.

The regularised energy potential including the work of the surface traction becomes

$$\Pi_r = \int_\Omega g(s)\psi_e \, dV + \int_\Omega \psi_f \, dV - \int_{\partial\Omega} \mathbf{t}_0 \cdot \mathbf{u} \, dA. \tag{11.33}$$

Next ψ_e is specified. Assuming a St. Venant-Kirchhoff material that was already introduced above, the elastic strain energy is split into a volumetric and a deviatoric part

$$\psi_e = \frac{\lambda}{2}\text{tr}(\mathbf{E_e})^2 + \mu\mathbf{E_e} : \mathbf{E_e} = \frac{1}{2}K\text{tr}(\mathbf{E_e})^2 + \mu\mathbf{E_e^D} : \mathbf{E_e^D} \tag{11.34}$$

with the bulk modulus $K = \lambda + \frac{2}{3}\mu$.

Crack evolution is assumed to occur under tension only, thus the volumetric strain energy density is split into a positive and a negative part. To this end the (signed) Macaulay brackets are defined as

$$\langle x \rangle_+ = \begin{cases} x & \text{for } x \geq 0 \\ 0 & \text{for } x < 0 \end{cases}$$
$$\langle x \rangle_- = \begin{cases} x & \text{for } x \leq 0 \\ 0 & \text{for } x > 0 \end{cases} \tag{11.35}$$

and are applied to the elastic volumetric strain $\text{tr}(\mathbf{E_e})$.

Incorporating all the above features the final version of the phase field potential is given by

$$\Pi_r = \int_\Omega g(s)\left(\frac{1}{2}K\langle\text{tr}(\mathbf{E_e})\rangle_+^2 + \mu\mathbf{E_e^D} : \mathbf{E_e^D}\right) dV + \int_\Omega \frac{1}{2}K\langle\text{tr}(\mathbf{E_e})\rangle_-^2 \, dV$$
$$+ \int_\Omega \mathcal{G}_c\left(\frac{(1-s)^2}{4l_0} + l_0\nabla s \cdot \nabla s\right) dV - \int_{\partial\Omega} \mathbf{t}_0 \cdot \mathbf{u} \, dA. \tag{11.36}$$

In the approach presented here, we only consider an elastic component to the strain energy, disregarding a direct influence of the viscous component. In this way we model elastic crack evolution in a viscoelastic material.

In order to solve the problem, Eq. (11.36) is minimized with respect to the displacement field $\mathbf{u}$ by setting the variation with respect to $\mathbf{u}$ to zero: $\delta_u\Pi = 0$. This renders the equilibrium conditions and the traction boundary conditions. To obtain an evolution equation for the phase field a time dependent Ginzburg-Landau equation is used to relate the change of the fracture field s to the variational derivative of the phase field potential with respect to s

$$\dot{s} = -M\delta_s\Pi_r \tag{11.37}$$

with M the mobility constant. The mobility constant M is introduced to ensure numerical stability and acts as a rate dependent regularization in situations with rapid crack evolution, such as crack initiation.

11.2.3 Numerics

The model was implemented in the finite element framework FEniCS [38], more specifically we implemented Eq. (11.36) and used the automatic derivative to obtain the variations with respect to the displacement $\mathbf{u}$ and the phase field variable s. Setting the variation with regard to $\mathbf{u}$ to zero renders the equilibrium condition. The variation with respect to s provides the driving force, c.f. Eq. (11.37), where we have chosen a mobility constant of $M = 10^5$. The rate of s in Eq. (11.37) is integrated in time using a backward Euler scheme. The residual stiffness η_{RS} in the degradation function has been chosen to be 0.001 and s is fixed to zero for all further time steps if $s \leq 0.05$. All model parameters used throughout the simulations can be found in Table 11.1. To solve the system of equations, a monolithic scheme is used and thus the displacement field $\mathbf{u}$ and the fracture field s are calculated simultaneously. The internal variable $\mathbf{C_v}$ is obtained from the evolution Eq. (11.38) where an forward Euler scheme is used to approximate the rate $\dot{\mathbf{C}}_\mathbf{v}$

$$\dot{\mathbf{C}}_\mathbf{v} = \frac{\mathbf{C_v}^{n+1} - \mathbf{C_v}^n}{\Delta t} \tag{11.38}$$

resulting in an equation for the $\mathbf{C_v}$ at time step $n+1$:

$$\mathbf{C_v}^{n+1} = \frac{\mu}{\eta}\Delta t \left(\mathbf{C}^n - \frac{1}{3}\text{tr}\left(\mathbf{C}^n (\mathbf{C_v}^n)^{-1} \right) \right) + \mathbf{C_v}^n . \tag{11.39}$$

The displacement field $\mathbf{u}$ and the fracture field s are interpolated linearly using triangular elements. The internal variable $\mathbf{C_v}$ is constant in each element. Due to the non-linear coupling of $\mathbf{u}$ and s a Newton-Raphson scheme is applied to obtain the values at a new time step t_{n+1} form the previous time step at t_n. The embedded linear system is solved using the solver MUMPS [39]. Especially in cases with rapid crack evolution, the Newton-Raphson scheme may not converge (relative and absolute tolerance). Thus, in cases where the Newton-Raphson scheme does not converge in 15 iterations the time step is halved. If the Newton-Raphson scheme converges

Table 11.1: Model parameters.

parameter	value	unit
η	$5 \cdot 10^{14}$	Pa s
E	1	GPa
ν	0.325	
$\mathcal{G}_c$ (for an ice thickness of 100 m)	901	J m^{-2}
l_0	198	m
M	10^5	
η_{RS}	0.001	

less than 5 iterations the time step is doubled. This heuristic time step adjustment improves the numerical stability and guarantees a certain efficiency.

11.2.4 Scenarios, Setup and Spin-ups

Different geometries are considered here, which are motivated by the typical calving front situations as shown in the right panel of Fig. 11.1. At first (Case 1) a square ice shelf area is used with inflow from left and a calving front on the right side as shown in Fig. 11.4. Upper and lower boundaries are assumed to be ice shelf internal boundaries. To mimic this situation vertical displacements are blocked while the horizontal motion is not constrained. The ice rises are modelled as holes, with a homogeneous Dirichlet boundary condition $\mathbf{u} = \mathbf{0}$. At the inflow boundary the displacement is also set to zero, whereas at the outflow a constant velocity of 0.2 m/day in horizontal direction is applied, leading to an overall tension of the domain. This setup resembles the situation at an ice shelf that is increasing in velocity towards the ice front.

In Case 2 a free floating ice tongue is anticipated. Thus from the inflow to the ice rise identical boundary conditions as in Case 1 are used. The ice rise are again modelled as fully attached ice by setting $\mathbf{u} = \mathbf{0}$ along both quarter-circles. As in the first example the lateral margins upstream of the ice rises are internal boundaries, where the vertical displacements are set to zero. The lateral boundary conditions of the ice tongue are traction free. The calving front is again loaded by a linearly in time increasing displacement load of 0.2 m/day. Both meshes were created in Gmsh [40] and have been refined towards the circles or quarter circles representing the ice rises.

In many engineering applications a load is applied to an initially unloaded body. The task is to simulate changes in stress, strain and associated crack formation during the application of a time dependent load. In the case under consideration here, a natural system is analysed that has undergone a long load and deformation
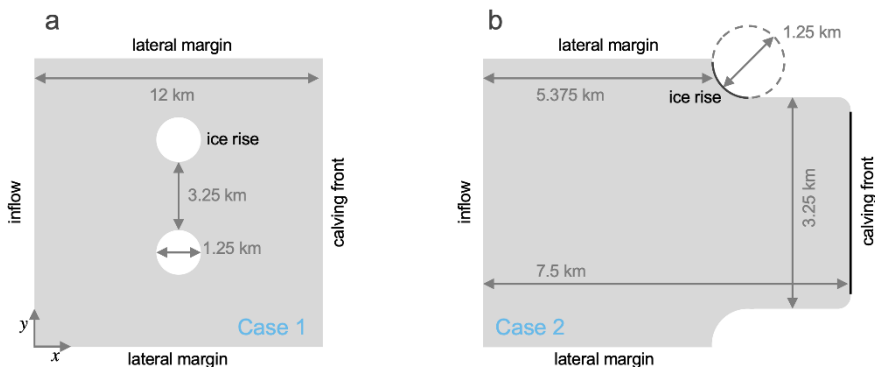

Fig. 11.4: Geometry setup of the numerical experiments, circles resemble ice rises.

history. Therefore, the viscous strain field is already well developed, while the elastic component is becoming more important in the vicinity of the calving front. This becomes more evident when considering the characteristic time again, as the viscous component only evolved over larger time scales of month to years. To capture this in this contribution, so called spin-up simulations were performed. In the spin-up the fracture phase field model is switched off, but the viscoelastic deformation is allowed to develop. As an order of magnitude for the time scale, the time span between the fracture formation of the lateral cracks visible in Fig. 11.1 is considered, which is about one year. As the fracture phase field is not solved for, only slow viscoelastic processes occur and the time steps in the spin-up runs can be larger, but due to the explicit time scheme a maximum time step of a day is allowed. After the completion of the spin-up runs, the displacement $\mathbf{u}$ and viscous strain field $\mathbf{C_v}$ are used as the initial state for subsequent fracture phase field simulations.
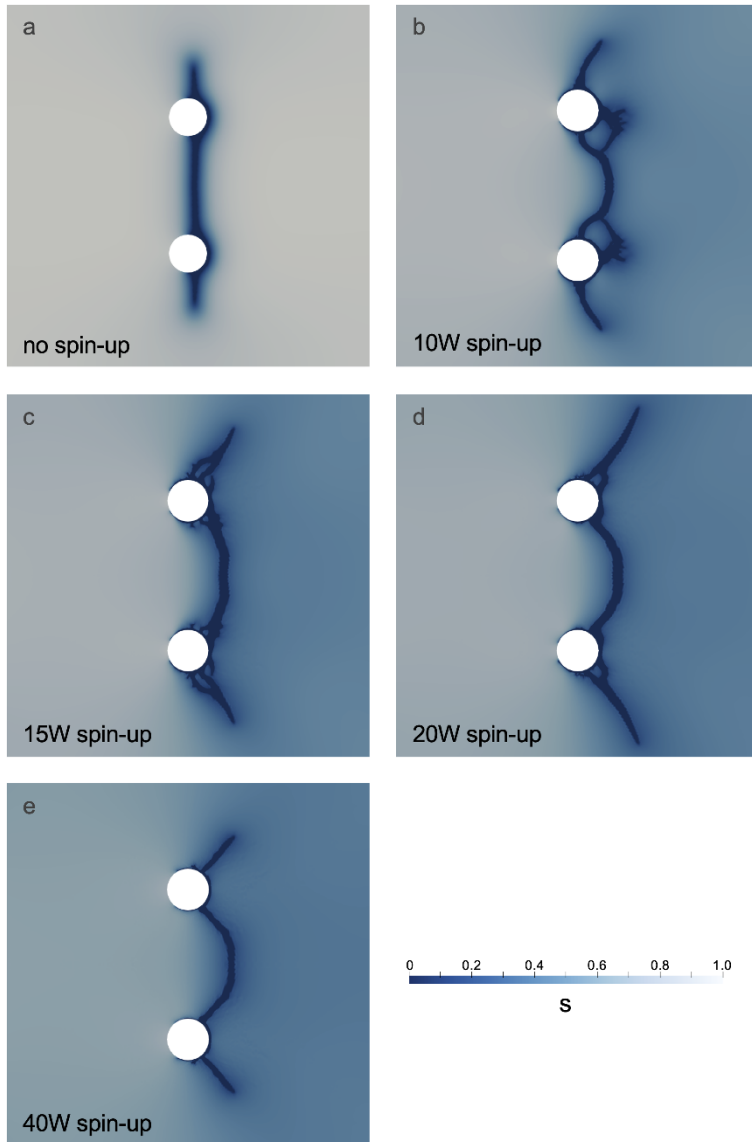
11.3 Results

11.3.1 Crack Evolution and Strain for Ice Rises Within the Ice Shelf

We present the fracture phase field of Case 1 in Fig. 11.5 for different initial conditions. We investigate the case of no spin-up and several spin-up simulations with different time periods varying between 10 up to 40 weeks. The crack paths differ in all experiments. In all cases the crack evolution starts at the downstream (lee) side of ice rises and then propagates along the circles until it deviates from the ice rise margin and cracks in the area between the ice rises are formed. Once the cracks are unified the fracture evolves towards the boundaries of the domain. For the experiment without spin-up the crack path is a nearly straight line between the ice rises and the lateral margins of the ice body. The crack paths for experiments with spin-up runs differ strongly from the experiment without spin-up. With shorter spin-up times, thus less viscous deformation, the crack path is more branched then with longer spin-up times. More than one crack forms at the ice rises. All cases with spin-up lead to a final crack path between the ice rises of a bow-like shape. Also between the ice rises and the lateral margins, the crack path is more inclined as compared to the experiment without spin-up. In the downstream part of the ice body, the phase field is also reduced for all pre-deformed cases, while the phase field without spin-up remains fully intact in almost all areas around except the main crack. While conducting the simulations, we observe that the transition between spin-up to the full problem including the fracture phase field is prone to numerical difficulties. The time step is becoming very small, as the spreading of the crack is very quick. This behaviour is referred to as model shock in the following.

In order to quantitatively capture the influence of elastic and viscous strain we resort to the additive decomposition of the Hencky strains as introduced in Eq. (11.28). For this purpose, Fig. 11.6 presents the ratio $\boldsymbol{\varepsilon_e^H}/(|\boldsymbol{\varepsilon_e^H}| + |\boldsymbol{\varepsilon_v^H}|)$ and $\boldsymbol{\varepsilon_v^H}/(|\boldsymbol{\varepsilon_e^H}| + |\boldsymbol{\varepsilon_v^H}|)$


for selected experiments: (a) no spin-up, (b) with 15 weeks spin-up and (c) with 40 weeks of pre-loading. The Hencky strains are shown at the same time as the phase field s in Fig. 11.5 It can be observed that elastic strains occur primarily as an instantaneous reaction to crack propagation and are thus very large in the area of the crack and at the crack tip. It is worth to note that this concentration of the elastic strains occurs more pronounced in the simulations with spin-up. This is an indication of the model shock. The system can only account for the stress redistribution by elastic responses. In the situation with no spin-up, elastic strain forms a compression arc to support the applied external load. In the simulations without spin up, the crack is almost invisible in the strain distributions, elastic or viscous, see Fig. 11.6a,b. In situations with spin-up the viscous strain contribution vanishes in the crack region, see Fig. 11.6 d,f. This is due to the longer viscous time scale, indication again the feature referred to as model shock.

To better understand the temporal evolution of the fracture process, Fig. 11.7 reports the fracture phase field and the elastic Hencky strain contribution for a spin-up of 10 weeks. The system is so highly stressed that not only one, but three cracks from at each ice rise (hole), see Fig. 11.7c. The two cracks towards the middle of the domain converge into one crack at each ice rise which afterwards grows further into the area between the ice rises. The two cracks this middle area unify and form a large crack that connects the two ice rises. Later the lateral cracks grow towards the boundaries resulting in a final splitting of the ice block. Again the different time scales of the crack propagation and the viscous flow are worth mentioning. Compared to the 'slow' flow process the crack propagates almost instantaneously. There is again a strong correlation between the elastic strain distribution and the crack path. To support this statement the arc-like tensile elastic strain distribution in Fig. 11.7d is mentioned. Later, see Fig. 11.7f, the crack path follows this arc-like distribution. In regions with compressive elastic strain, such as the upstream boundary of the ice rise, cracks are suppressed.

11.3.2 Crack Evolution and Strain for Floating Tongue

Here we present the results of a more realistic calving front geometry (see also Fig. 11.1). The evolution of the phase field is displayed in Fig. 11.8 for four instances in time without a spin-up run. The cracks emerge downstream of the ice rises and grow from the transition between ice rise and calving front in lateral direction. In the early stages of crack propagation the direction is more or less straight, while the crack path is slightly diverted as the cracks get closer to each other. The final stage is a slight bow form. The crack width grows wide at the calving front. In contrast to the case in which the ice rises are situated in the center of the ice body, the phase field downstream the crack is not impacted, as the ice does not have to detach form the ice rise.
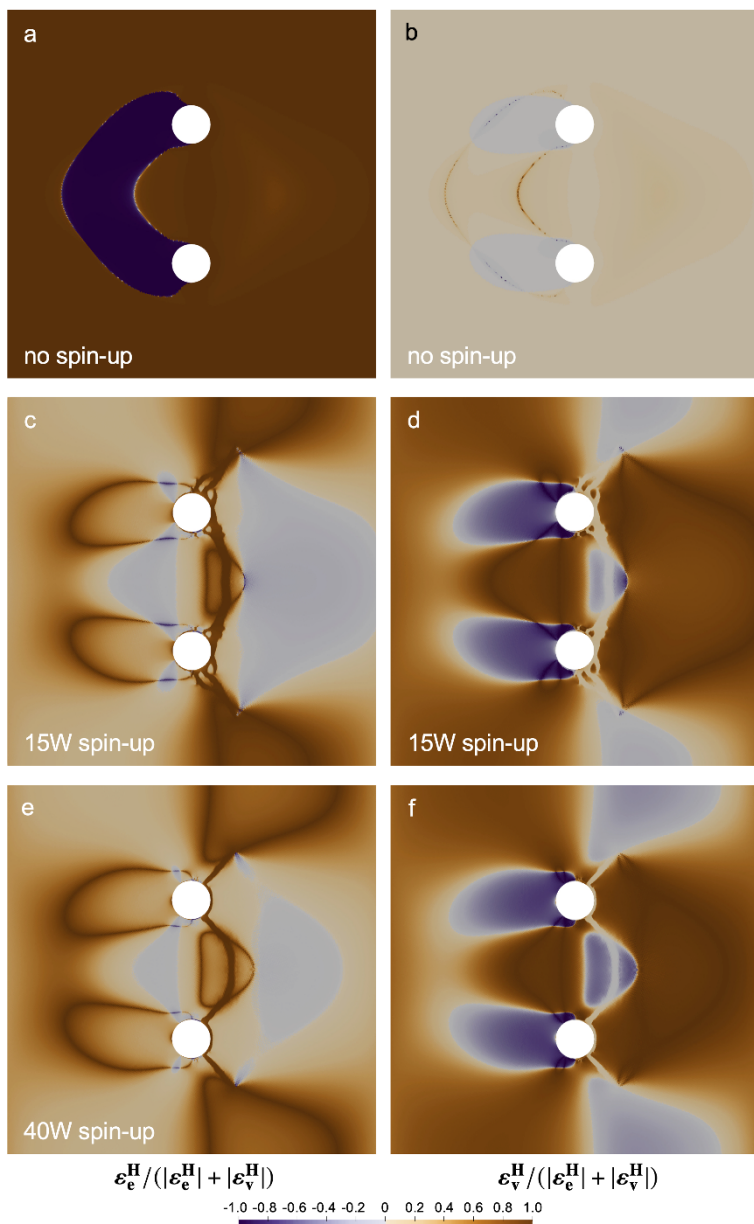
Fig. 11.6: Hencky strain in x-direction for different experiments. (a,c,e) display $\varepsilon_e^H/(|\varepsilon_e^H|+|\varepsilon_v^H|)$ for no spin-up, 15 and 40 weeks respectively. (b,d,f) display $\varepsilon_v^H/(|\varepsilon_e^H|+|\varepsilon_v^H|)$ for the same situations.
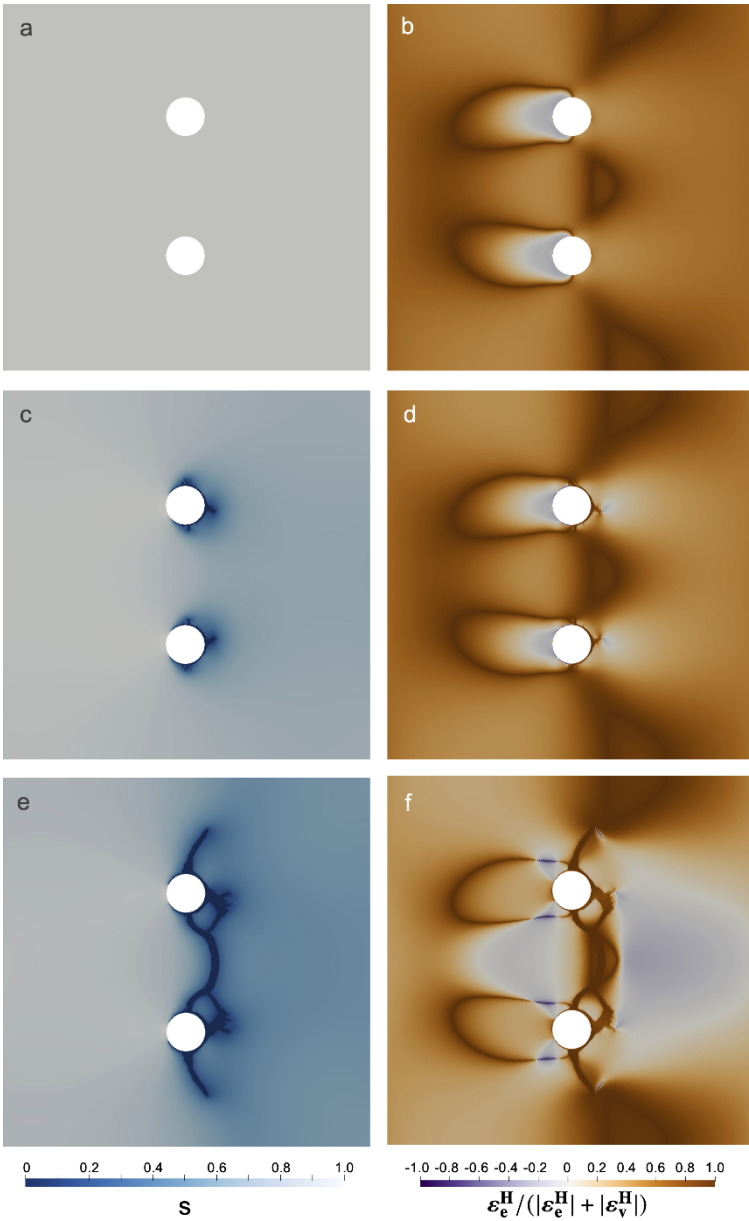
Fig. 11.7: Temporal evolution of the phase field s in the left panels and the corresponding elastic part of the Hencky strain $\varepsilon^{H}_{e\ xx}$ in the right panels for a pre-loading of 10 weeks. The Hencky strain is plotted relative $\varepsilon^{H}_{e}/(|\varepsilon^{H}_{e}| + |\varepsilon^{H}_{v}|)$. Upper row is for $\Delta t = 0$, middle row for $\Delta t = t - t_{SpinUp} = 1.9215 \cdot 10^{-9}$ s and bottom row for $\Delta t = 3.9343 \cdot 10^{-9}$ s.

Fig. 11.8 Temporal evolution of the phase field of the experiments with a floating tongue.

## 11.4 Released Energy Estimate Based on Observations

Satellite and airborne imagery, both optical and radar, can be used to identify cracks in ice. Although this provides only information of the position of the crack at the surface, either via the crack characteristics or additional airborne radar data, an estimate of the vertical dimension can be obtained. We use this to determine the area of the

crack faces and to compute the released energy. The satellite imagery we use here is Sentinel 2 (band 2,3,4) in 10 m (medium) resolution. In addition, we use high resolution (0.3 m) optical data (RGB) from the onboard MACS camera system on AWI's polar aircraft. More on the data and its processing is given in [41]. From this imagery we use data along one crack tip to constrain how much energy is released at a typical crack tip. In both cases, we use an energy release rate of $G_c = 8.071 \, \mathrm{J \, m^{-2}}$.

The medium resolution is used to measure the individual crack length of all rifts visible in the right panel of Fig. 11.1. The entire length of all cracks at the surface is 26 387 m. With an ice thickness of 90...100 m in this region, an area of $2.4...2.6 \, 10^6 \, \mathrm{m^2}$ and hence an energy of $\Delta E = 19.2\text{-}21.3 \, \mathrm{MJ}$ is released during the formation of the cracks.

The high resolution imagery in the right panel of Fig. 11.9 is used to measure the crack length of each individual crack face. To this end, the length of the crack at the ice shelf surface was determined and the ice thickness based on ice penetrating data was used to compute the newly formed area. The ice thickness is the same as above. The summing up the length of all individual cracks, we find with a total length of 767 m length and energy of 557.1...619.0 kJ.

Comparing to Sentinel-2 imagery in 10 m resolution at the same location and time of Fig. 11.9b, the crack ends 242 m further in the high resolution MACS imagery than in Sentinel-2 scenes. Next we use the estimated energy of such a rift tip field and add it for each rift in Fig. 11.1 (right panel). This leads to a total energy of all 15 cracks in this particular calving front situation of 19.2...21.3 MJ + 15·(557.1...619.0) kJ = 27.6...30.6 MJ, which is 44% more released energy than estimated without high resolution imagery.
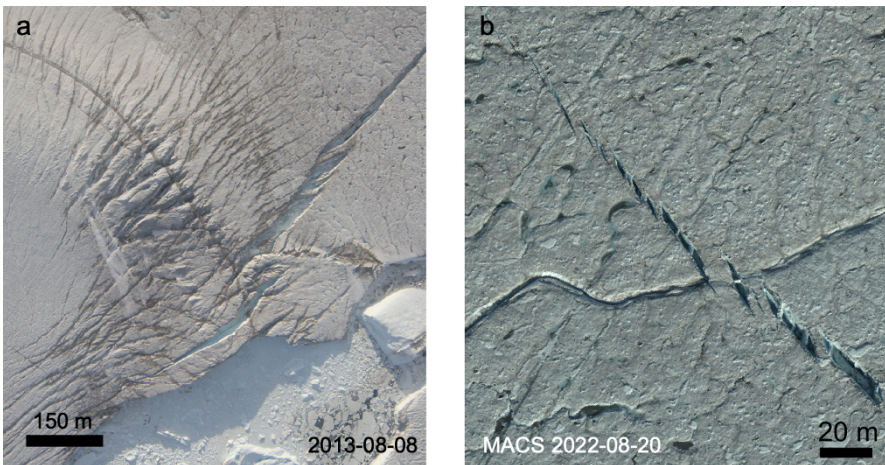
Fig. 11.9: The left panel displays an image of the onboard Canon camera from 2013-08-08 showing the calving front at the lower ice rise visible in the right panel of Fig. 11.1. In the right panel a high resolution optical image obtained with the MACS camera system in 30 cm ground resolution of a rift tip is shown. .

11.5 Discussion

In the simulations of Case 1 the crack path is leading to a separation at the downstream side of the ice rises, which is also found in nature. However, at typical calving front situations, the cracks form slightly further upstream than the simulations are showing. The simulated crack propagation in Case 2 is in very good agreement with observations (see Fig. 11.1 and Fig. 11.9).

The choice of the boundary condition is affecting the simulation results significantly. Currently, we are fixing the upper and lower boundary at their in vertical direction by choosing a zero displacement condition in vertical direction at those boundaries. This potentially leads to effects at the ice rise margins that are not intended. In future the computational model will be applied to more realistic, and thus irregular, geometries of ice rises. To do so, an extension of the boundary condition along the margin of the ice rise is necessary to prevent penetration, but to similarly allow the ice to disconnect from the grounded ice rises downstream. To this end a no penetration condition as is common in contact mechanics and ice sheet modelling has to be considered. The present investigation represents an extreme case, in which the ice is 'laterally frozen' (kinematically fixed) to the ice rise.

The natural system has a stress boundary condition at the calving front, with water pressure below sea level and traction-free at the ice-atmosphere boundary which was investigated in 2D vertical simulations by [6]. In future, a stress boundary condition along the calving front shall be considered too.

A comparison of the no spin-up simulations of Case 1 and the simulations of Case 2 shows a strong similarity between the crack paths. Both are nearly straight between the ice rises as we expected due to the same boundary conditions. Their are in good agreement with small strain results [30]. Further simulations especially for different spin-up times of Case 2 have to be carried out.

The spin-up runs were conducted to obtain an initial state that represents the stress and strain fields well prior to crack formation. Although this has been a useful method for the problem under consideration, it also caused issues in the transition between spin-up and solving the full problem including the fracture phase field. The pre-loading is so substantial, that the crack formation and propagation sets in nearly instantaneous after the spin-up. This needs further treatment in future, in order to better resemble the natural process. For the situation displayed in Fig. 11.1 the time between crack formation is about one year. In contrast, in our situation even after only five weeks of spin-up cracks form instantaneously. It is worth to note, that crack formation in ice shelves is happening extremely fast, with the time scale being narrowed by satellite observations to appear between two subsequent acquisitions, which may in summer be as close as within one day. That the crack propagation within the model is nearly instantaneous is consistent with observations, only the time period between two crack formation events is currently not matching observations.

In our approach a viscoelastic Maxwell material is applied, but we reduced complexity by assuming only an elastic fracture phase field model for crack formation, which can be extended in future to incorporate other crack driving mechanisms. Furthermore, a St. Venant-Kirchhoff material was used primarily for the sake of

simplicity. This material law is a widely used, but has issues for large compressive strains. Other material models such as neo-Hooke material formulations can be used as well, leading to a other constitutive relation for the second Piola-Kirchhoff stress tensor **S** and consequently to a different evolution equation for the internal variable $\mathbf{C_v}$ [42]. An investigation of the different material models and their influence on the spin-up and fracture phase field are very interesting.

In general, an incorporation of the phase field model of fracture approach into large scale ice sheet models is very favourable, as no adequate formulation of calving is currently incorporated in those models. There are two routes to consider here: (i) to use this approach in a micro-macro coupling, in which at local scale a fracture phase field model is applied. The micro scale fracture phase field model will than be used to derive calving rates, which are incorporated into the level-set method of calving front motion or (ii) to extend the phase field model into an ice sheet wide model with a high resolution mesh in calving front areas and to couple both models directly. In both cases, a velocity formulation of the phase field model for fracture is required, as ice sheet models are in velocity formulation. Both approaches are, however, quite challenging and remain subject of future research.

Comparing the estimate of released energy in medium and high resolution imagery makes evident, that it can only be estimated reliably when using high resolution imagery, as one may underestimate it massively. This highlights the need for high resolution airborne or satellite-borne data for fracture mechanical estimates.

Last but not least, the simulations depend on material parameters that are not well documented and constrained. The basis for $\mathcal{G}_c$ is only K_{Ic} [2], while cracks around the ice rises may also be mode II cracks in some occasion. In addition, the laboratory tests were not conducted for fully consolidated ice, but for very dense firn (experiments: 844.5 to 870.3 $\mathrm{kg\,m^{-3}}$, consolidated ice: 917 $\mathrm{kg\,m^{-3}}$). For polycrystalline ice $\mathcal{G}_c$ may thus be smaller than the value used here. Conducting laboratory tests to constrain the material parameters of polycrystalline ice further, would be highly beneficial.

11.6 Conclusions and Future Direction

We proposed a viscoelastic phase field method for fracture at finite strains and studied the influence of the loading history on the crack initiation and propagation. The influence of the viscous pre-loading is pronounced and shows the need of a carefully considered spin-ups as glaciers and ice shelves have a long deformation history, which is why large viscous strains occur. Comparison with simulations using small strain reveal that the crack path is similar if no pre-loading is considered, as the crack sets in quite rapidly.

All simulations show crack onset at the downstream side of ice rises. In reality, the downstream side of ice rises is often ice free, which is consistent with our simulations. The crack onset is in observations slightly further upstream, which is likely an effect of the choice of boundary conditions used here.

Ice shows a rate-dependent flow behavior, known by Glen's flow law, which should be incorporated in the future. Also a feedback between the phase field and the viscous deformation is to be evaluated and benchmarked against observations of crack formation.

Since this is the first work of a fracture phase field model for ice considering finite viscoelasticity a lot of open questions regarding the spin-ups and boundary conditions remain. More advanced treatment of the boundary condition is needed to resemble realistic ice shelf situations. Furthermore, a concept to combine large scale ice sheet simulations with fracture phase field simulation needs to be developed in future.

References

[1] Petrovic JJ (2003) Review mechanical properties of ice and snow. Journal of Materials Science **38**(1):1–6

[2] Christmann J, Müller R, Webber KG, Isaia D, Schader FH, Kipfstuhl S, Freitag J, Humbert A (2015) Measurement of the fracture toughness of polycrystalline bubbly ice from an antarctic ice core. Earth System Science Data **7**(1):87–92

[3] Reeh N, Christensen EL, Mayer C, Olesen OB (2003) Tidal bending of glaciers: a linear viscoelastic approach. Annals of Glaciology **37**:83–89

[4] Gudmundsson GH (2011) Ice-stream response to ocean tides and the form of the basal sliding law. The Cryosphere **5**(1):259–270

[5] Christmann J, Helm V, Khan S, Kleiner T, Müller R, Morlighem M, Neckel N, Rückamp M, Steinhage D, Zeising O, Humbert A (2021) Elastic deformation plays a non-negligible role in Greenland's outlet glacier flow. Communications Earth & Environment **2**(1)

[6] Christmann J, Müller R, Humbert A (2019) On nonlinear strain theory for a viscoelastic material model and its implications for calving of ice shelves. Journal of Glaciology **65**(250):212–224

[7] Humbert A, Christmann J, Corr HFJ, Helm V, Höyns LS, Hofstede C, Müller R, Neckel N, Nicholls KW, Schultz T, Steinhage D, Wolovick M, Zeising O (2022) On the evolution of an ice shelf melt channel at the base of Filchner Ice Shelf, from observations and viscoelastic modeling. The Cryosphere **16**(10):4107–4139

 [8] Francfort GA, Marigo JJ (1998) Revisiting brittle fracture as an energy minimization problem. Journal of the Mechanics and Physics of Solids **46**(8):1319–1342
 [9] Bourdin B, Francfort GA, Marigo JJ (2000) Numerical experiments in revisited brittle fracture. Journal of the Mechanics and Physics of Solids **48**(4):797–826
[10] Bourdin B (2007) Numerical implementation of the variational formulation for quasi-static brittle fracture. Interfaces and Free Boundaries **9**(3):411–430
[11] Borden MJ, Verhoosel CV, Scott MA, Hughes TJR, Landis CM (2012) A phase-field description of dynamic brittle fracture. Computer Methods in Applied Mechanics and Engineering **217-220**:77–95
[12] Schlueter A, Kuhn C, Müller R, Gross D (2016) An investigation of intersonic fracture using a phase field model. Archive of Applied Mechanics **86**:321–333
[13] Ren HL, Zhuang XY, Anitescu C, Rabczuk T (2019) An explicit phase field method for brittle dynamic fracture. Computers & Structures **217**:45–56
[14] Lo YS, Borden MJ, Ravi-Chandar K, Landis CM (2019) A phase-field model for fatigue crack growth. Journal of the Mechanics and Physics of Solids **132**:103,684
[15] Schreiber C, Kuhn C, Müller R, Zohdi T (2020) A phase field modeling approach of cyclic fatigue crack growth. International Journal of Fracture **225**:89–100
[16] Yan S, Schreiber C, Müller R (2022) An efficient implementation of a phase field model for fatigue crack growth. International Journal of Fracture **237**:1–14
[17] Heider Y (2021) A review on phase-field modeling of hydraulic fracturing. Engineering Fracture Mechanics **253**:107,881
[18] Aldakheel F, Noii N, Wick T, Wriggers P (2021) A global–local approach for hydraulic phase-field fracture in poroelastic media. Computers & Mathematics with Applications **91**:99–121, robust and Reliable Finite Element Methods in Poromechanics
[19] Teichtmeister S, Kienle D, Aldakheel F, Keip MA (2017) Phase field modeling of fracture in anisotropic brittle solids. International Journal of Non-Linear Mechanics **97**:1–21
[20] Bleyer J, Alessi R (2018) Phase-field modeling of anisotropic brittle fracture including several damage mechanisms. Computer Methods in Applied Mechanics and Engineering **336**:213–236
[21] Schreiber C (2021) Phase field modeling of fracture: Fatigue and anisotropic fracture resistance. Phd thesis, TU Kaiserslautern, Kaiserslautern
[22] Ambati M, Gerasimov T, De Lorenzis L (2015) Phase-field modeling of ductile fracture. Computational Mechanics **55**(5):1017–1040
[23] Miehe C, Aldakheel F, Raina A (2016) Phase field modeling of ductile fracture at finite strains: A variational gradient-extended plasticity-damage theory. International Journal of Plasticity **84**:1–32
[24] Noll T, Kuhn C, Olesch D, Müller R (2020) 3d phase field simulations of ductile fracture. GAMM-Mitteilungen **43**(2):e202000,008
[25] Shen R, Waisman H, Guo L (2019) Fracture of viscoelastic solids modeled with a modified phase field method. Computer Methods in Applied Mechanics and Engineering **346**:862–890

[26] Yin B, Kaliske M (2020) Fracture simulation of viscoelastic polymers by the phase-field method. Computational Mechanics **65**(2):293–309

[27] Dammaß F, Ambati M, Kästner M (2021) A unified phase-field model of fracture in viscoelastic materials. Continuum Mechanics and Thermodynamics **33**(4):1907–1929

[28] Sun X, Duddu R, Hirshikesh (2021) A poro-damage phase field model for hydrofracturing of glacier crevasses. Extreme Mechanics Letters **45**:101,277

[29] Clayton T, Duddu R, Siegert M, neda EMP (2022) A stress-based poro-damage phase field model for hydrofracturing of creeping glaciers and ice shelves. Engineering Fracture Mechanics **272**:108,693

[30] Sondershaus R, Humbert A, Müller R (2023) A phase field model for fractures in ice shelves. PAMM **22**(1):e202200,256

[31] Lee EH (1969) Elastic-Plastic Deformation at Finite Strains. Journal of Applied Mechanics **36**(1):1–6

[32] Haupt P (2000) Continuum Mechanics and Theory of Materials. Springer, Berlin, Heidelberg

[33] Becker W, Gross D (2002) Mechanik elastischer Körper und Strukturen. Springer, Berlin, Heidelberg

[34] Neff P, Ghiba ID, Lankeit J (2015) The exponentiated hencky-logarithmic strain energy. Part I: Constitutive issues and rank-one convexity. Journal of Elasticity **121**(2):143–234

[35] Ambrosio L, Tortorelli VM (1990) Approximation of functional depending on jumps by elliptic functional via t-convergence. Communications on Pure and Applied Mathematics **43**(8):999–1036

[36] Bourdin B (1998) Une méthode variationnelle en mécanique de la rupture. Phd thesis, Université Paris-Nord, Paris

[37] Chambolle A (2004) An approximation result for special functions with bounded deformation. Journal de Mathématiques Pures et Appliquées **83**(7):929–954

[38] Alnæs M, Blechta J, Hake J, Johansson A, Kehlet B, Logg A, Richardson C, Ring J, Rognes M, Wells G (2015) The fenics project version 1.5. Archive of Numerical Software **3**(100):9–23

[39] Amestoy PR, Duff IS, L'Excellent JY, Koster J (2001) A fully asynchronous multifrontal solver using distributed dynamic scheduling. SIAM Journal on Matrix Analysis and Applications **23**(1):15–41

[40] Geuzaine C, Remacle JF (2009) Gmsh: A 3-d finite element mesh generator with built-in pre- and post-processing facilities. International Journal for Numerical Methods in Engineering **79**(11):1309–1331

[41] Humbert A, Helm V, Neckel N, Zeising O, Rückamp M, Khan SA, Loebel E, Gross D, Sondershaus R, Müller R (2022) Precursor of disintegration of Greenland's largest floating ice tongue. The Cryosphere Discussions **in review**:1–29

[42] Christmann J (2017) Viscoelastic modeling of calving processes at antarctic ice shelves. Phd thesis, TU Kaiserslautern, Kaiserslautern